FINAL PROJECT REPORT # 00052346

GRANT: DTRT13-G-UTC45
Project Period: 5/1/2015 – 12/31/19

Influence of Casting Conditions on Durability and Structural Performance of HPC-AR: Changes In Workability And Air-Void System Of Concrete Due To Pumping

Participating Consortium Member:
Missouri University of Science and Technology

Authors:
Dimitri Feys, Assistant Professor, Missouri S&T
Kyle Riding, Associate Professor, University of Florida
Daniel Galvez Moreno, Alexis Salinas, Alexandra Wehar
Graduate Assistants, Missouri S&T

RE-CAST:
REsearch on Concrete Applications for Sustainable Transportation
Tier 1 University Transportation Center

DISCLAIMER

The contents of this report reflect the views of the authors, who are responsible for the facts and the accuracy of the information presented herein. This document is disseminated under the sponsorship of the U.S. Department of Transportation's University Transportation Centers Program, in the interest of information exchange. The U.S. Government assumes no liability for the contents or use thereof.

TECHNICAL REPORT DOCUMENTATION PAGE

1. Report No. RECAST UTC # 00052346	**2. Government Accession No.**	**3. Recipient's Catalog No.**
4. Title and Subtitle Influence of Casting Conditions on Durability and Structural Performance of HPC-AR: Changes in Workability and Air-Void System of Concrete due to Pumping		**5. Report Date** January 2020 **6. Performing Organization Code:**
7. Author(s) Dimitri Feys, Kyle Riding, Daniel Galvez Moreno, Alexis Salinas, Alexandra Wehar		**8. Performing Organization Report No.** Project # 00052346
9. Performing Organization Name and Address RE-CAST – Missouri University of Science and Technology 500 W. 16th St., 223 ERL Rolla, MO 65409-0710		**10. Work Unit No.** **11. Contract or Grant No.** USDOT: DTRT13-G-UTC45
12. Sponsoring Agency Name and Address Office of the Assistant Secretary for Research and Technology U.S. Department of Transportation 1200 New Jersey Avenue, SE Washington, DC 20590		**13. Type of Report and Period Covered:** Final Report Period: 5/1/2015 – 12/31/19 **14. Sponsoring Agency Code:**
15. Supplementary Notes The investigation was conducted in cooperation with the U. S. Department of Transportation.		

16. Abstract

This report summarizes the research performed on the influence of pumping operations on the changes in workability, rheology, air content, air-void system, freeze-thaw and scaling resistance of self-consolidating concrete (SCC). This project is a collaboration between the RE-CAST Tier-1 UTC the ACI Foundation, the Kansas State University (through funding from the Kansas DOT), EllisDon and CBM St-Marys. A portion of the results are summarized in the K-DOT report based on a research project on the effect of pumping on properties of low-slump concrete mixtures for bridge decks [1], as well as a paper in Materials and Structures [2]. This report discusses the continuation of the research work, as some dramatic results were observed especially for SCC.

When pumping concrete, a portion of the material is subjected to very high shear rates, and the lower the yield stress, the larger the concrete volume in the pipe which is exposed to shear. Shearing can cause substantial changes in rheology and workability, while a combination of pressure and shearing can induce major changes in the air-void system. Figure 1 shows the change in spacing factor, which is the difference between the spacing factor of the pumped and non-pumped concrete, due to the pumping process [2]. These results were obtained in an experimental campaign with EllisDon and CBM-St-Marys in Toronto, ON, Canada in May 2015. No major changes were imposed on the different SCC mix designs, apart from the workability level. Figure 1 shows that the spacing factor increases more with a faster flow rate, due to the increase in applied pressure and in shearing. The use of a reducer (triangles), also increases the change in spacing factor, due to the same reasons. It should also be mentioned that one of the tests when using a reducer caused segregation of the SCC. However, the most striking results are the magnitude of those changes: the spacing factor increased with values between 250 and 550 μm, significantly above the acceptable limits. Normal concrete shows changes up to 100-150 μm [1], making SCC more sensitive. This is why further investigation on SCC is necessary.

17. Key Words vibration-free, self-consolidating concrete	**18. Distribution Statement** No restrictions. This document is available to the public.	
19. Security Classification (of this report) Unclassified	**20. Security Classification (of this page)** Unclassified	**21. No of Pages** 304

Form DOT F 1700.7 (8-72) Reproduction of form and completed page is authorized.

RE-CAST PROJECT 1C-2:
INFLUENCE OF CASTING CONDITIONS ON DURABILITY AND STRUCTURAL PERFORMANCE OF HPC-AR: CHANGES IN WORKABILITY AND AIR-VOID SYSTEM OF CONCRETE DUE TO PUMPING

FINAL REPORT

(JANUARY, 2020)

By

Dimitri Feys, Associate Professor, Missouri S&T

Kyle Riding, Associate Professor, University of Florida

Daniel Galvez Moreno, Alexis Salinas, Alexandra Wehar, Graduate Assistants, Missouri S&T

Table of Contents

List of Figures

List of Tables

1 Introduction

This report summarizes the research performed on the influence of pumping operations on the changes in workability, rheology, air content, air-void system, freeze-thaw and scaling resistance of self-consolidating concrete (SCC). This project is a collaboration between the RE-CAST Tier-1 UTC the ACI Foundation, the Kansas State University (through funding from the Kansas DOT), EllisDon and CBM St-Marys. A portion of the results are summarized in the K-DOT report based on a research project on the effect of pumping on properties of low-slump concrete mixtures for bridge decks [1], as well as a paper in Materials and Structures [2]. This report discusses the continuation of the research work, as some dramatic results were observed especially for SCC.

When pumping concrete, a portion of the material is subjected to very high shear rates, and the lower the yield stress, the larger the concrete volume in the pipe which is exposed to shear. Shearing can cause substantial changes in rheology and workability, while a combination of pressure and shearing can induce major changes in the air-void system. Figure 1 shows the change in spacing factor, which is the difference between the spacing factor of the pumped and non-pumped concrete, due to the pumping process [2]. These results were obtained in an experimental campaign with EllisDon and CBM-St-Marys in Toronto, ON, Canada in May 2015. No major changes were imposed on the different SCC mix designs, apart from the workability level. Figure 1 shows that the spacing factor increases more with a faster flow rate, due to the increase in applied pressure and in shearing. The use of a reducer (triangles), also increases the change in spacing factor, due to the same reasons. It should also be mentioned that one of the tests when using a reducer caused segregation of the SCC. However, the most striking results are the magnitude of those changes: the spacing factor increased with values between 250 and 550 µm, significantly above the acceptable limits. Normal concrete shows changes up to 100-150 µm [1], making SCC more sensitive. This is why further investigation on SCC is necessary.

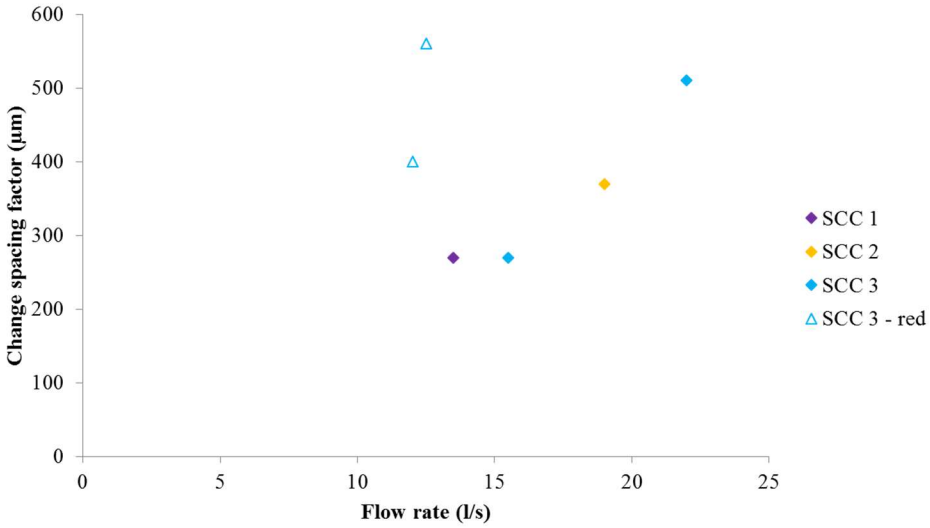

Figure 1. Change in spacing factor induced by pumping in SCC. Figure after [2].

The changes in spacing factor in Figure 1 are not the only changes observed in SCC. Feys has reported several changes in rheology due to pumping as well, especially for high-performance SCC mixtures [3, 4]. In order to provide a better understanding of the effect of pumping on fresh and hardened concrete properties, a proper understanding of the composition and thickness of the lubrication layer which is formed during pumping is essential. Furthermore, the physics of air dissolution under pressure and shear could provide an answer to the question why SCC seems more sensitive to pumping operations, compared to conventional concrete. As such,

those two topics are included in this research report, in parallel to the large scale pumping tests performed at Rolla Ready Mix in Missouri.

This report contains the following information:

- Chapter 2 is a review of the available literature on lubrication formation and composition, changes in rheology due to pumping, and changes in air-void system, freeze-thaw and scaling resistance induced by pumping operations.
- Chapter 3 contains an overview of a rheometer comparison campaign which has been conducted at Missouri S&T.
- Chapter 4 discusses an attempt to reverse-engineer the composition and thickness of the lubrication layer, through the science of rheology.
- Chapter 5 introduces the pumping experiments and the changes in fresh and hardened concrete properties induced by different pumping operations.
- Chapter 6 delivers an overview of rheological experiments on cement paste under pressure, in an attempt to understand the physics of air dissolution under combined pressure and shear.
- Chapter 7 summarizes the main findings of this research work.

2 Literature Review

2.1 Self-Consolidating Concrete

Self-Consolidating Concrete (SCC). Self-Consolidating Concrete (SCC) or self-compacting concrete is fresh concrete that does not require external vibration to consolidate within formwork or to flow around reinforcement but does so under its own weight [5]. This highly flowable concrete got its start in Japan in the 1980s. Conventional concrete requires consolidation to raise entrapped air out of the concrete. Consolidation creates a denser and less permeable concrete that will have better strength and durability. This manual consolidation must be performed properly by laborers, so decreases in the number of skilled workers in the 1980s in Japan lead to an increase in durability issues in concrete structures [6].

In 1986, Dr. Okamura, a professor at the University of Tokyo, proposed self-compacting concrete as the solution to poor consolidation leading to durability issues. In 1988 he developed the first prototype for this highly fluid concrete. The flowable concrete design was achieved by limiting the aggregate content, lowering the water-to-powder ratio, and using a chemical admixture called superplasticizer [6]. To achieve the desired properties, mix designs now can include micro-fillers, supplementary cementitious materials such as fly ash and silica fume, viscosity-modifying admixtures and different types of superplasticizers [7].

Figure 2 shows a typical example of mixture proportions of a conventional vibrated concrete (CVC) compared to a self-consolidating concrete (SCC) [8]. This includes an increased amount of fine material and a decrease of coarse aggregate content while holding the amount of water constant.

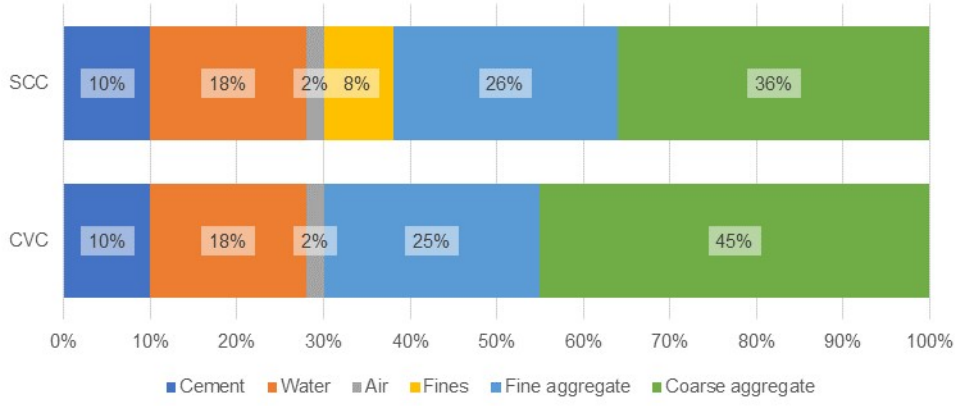

Figure 2. Typical Mix Design Proportions. Adapted from [8].

There are both benefits and limitations of using self-consolidating concrete. The concrete is less labor and equipment intensive, easier and quicker to place, easier to finish, and can be used in more complex designs. However, there is more pressure on the formwork due to the fluidity of the concrete and there is an increased importance of quality control and proper mix design. Additionally, in some instances, self-consolidating concrete will not be able to be used, for example if the concrete is required to hold a slope [9].

The three key characteristics self-consolidating concrete must have been filling ability, passing ability, and stability. Filling ability is the concrete's ability to flow and fill the formwork due to gravity without mechanical consolidation. Passing ability is the concrete's ability to flow through small openings without segregating or blocking. Stability means the concrete must remain stable and homogenous [10]. In the pursuit of achieving the desired passing and filling ability the concrete can become susceptible to stability issues. This includes segregation and excessive bleeding.

Since self-consolidating concretes fill formwork using only gravity, quantitative methods are needed to measure the fresh state properties. This need for more accurate quality control and mix designs mean the rheological properties are important, not only for pumpability but also for placement.

2.2 Rheology

Rheology is generally defined as "the science of deformation and flow of matter" [11]. In other words, it is that branch of physics that studies the interaction between force, deformation and time. Rheology is commonly used in the industry of paint, polymers, food (mayonnaise, ketchup, etc.), and others. It is also applicable for cement-based materials such as paste, mortar and concrete. With the implementation of more complex concrete types (anti-washout concrete, shotcrete, pumpable concrete, high-performance concrete with adapted rheology including SCC, etc.), rheology became a powerful tool to characterize its fresh behavior [12]. In this section, basic concepts of rheology are described including rheological models, rheometers (description, procedure and transformation equations), comparison between rheometers, and rheology of suspensions including the effect of volume fraction and viscosity amplification models.

2.2.1 Basic Relationships for Elastic Materials.

Mechanical properties of concrete in hardened state are well known in the engineering and construction field. In the 17th century, Robert Hooke defined the relationship between stress and strain for solids. Hooke's law, as shown in equations 1 and 2, is applicable for any material in the elastic range. Equation 1 identifies the shear modulus, as the proportionality factor between the angle of deformation and the shear stress. Equation 2 displays the well-known Young's modulus, reflecting axial stress and strain. It should be noted that the shear modulus and Young's modulus can be functions of the angle of deformation or the strain. In this case, the materials are non-linear elastic (such as rubber, hardened concrete).

$$\tau = G \cdot \gamma \qquad \textit{(Eq. 1)}$$

$$\sigma = E \cdot \varepsilon \qquad \textit{(Eq. 2)}$$

Where:

τ = Shear stress (Pa)
G = Shear modulus (Pa)
γ = Shear strain (-)
σ = Axial stress (Pa)
E = Young's modulus (Pa)
ε = Strain (-)

2.2.2 Basic Relationships for Fluid Materials.

The following definitions were obtained from the Guide to rheological nomenclature from the National Institute of Standards and Technology "NIST" [13]. Coefficient of viscosity or apparent viscosity: often abbreviated form as "viscosity" represents the ratio between the shear stress and shear rate. It can be easily visualized by the slope of the line connecting a point on the flow curve with the origin.

- Differential viscosity: the derivative of the shear stress with respect to shear rate.
- Plastic viscosity: when the material shows a Bingham behavior, the excess of the shear stress over the yield stress divided by the shear rate.
- Relative viscosity: Ratio of the viscosity in a suspension to the viscosity of the viscosity of the suspending medium.

2.2.2.1 Newtonian fluids

In 1687, Isaac Newton defined the viscosity as "the resistance which arises from the lack of lubricity or slipperiness of the parts of a fluid is, other things being equal, proportional to the velocity with which the parts of the fluid are separated from one another" [14]. In rheological terms, the applied shear stress is proportional to the viscosity multiplied by the velocity gradient (shear rate) as shown in Equation 3.

$$\tau = \eta \frac{dv}{dx} = \eta \dot{\gamma} \qquad \textit{(Eq. 3)}$$

τ = Shear stress (Pa)

$\dot{\gamma}$ = Shear rate (s^{-1})

$\frac{dv}{dx}$ = Velocity gradient (s^{-1})

η = Viscosity (Pa.s)

A fluid is Newtonian if it starts to flow as soon as stress is applied and if the relationship between stress and rate of deformation (i.e. the viscosity) is constant as shown in Figure 3, model 1. Examples of this kind of fluid include clear honey, oil, water, etc.

2.2.2.2 Non-Newtonian fluids

There are certain conditions that must be satisfied in order to classify a material as non-Newtonian.

- Condition 1: the applied shear stress must overcome an initial resistance to start the flow. In other words, the material has to "yield" to start the flow. If the viscosity is constant after exceeding the yield stress, the fluid is a so-called Bingham material, as can be seen in Figure 3, model 5.
- Condition 2: if the relationship between stress and rate of deformation is not linear even if no yield stress is present (Figure 3, models 2 and 3). Model 2 has an increase in viscosity at higher shear rate that can be described by the power law model shown in Figure 3, model 2
- Condition 3: if the material shows time-dependent behavior.

Any combinations of different conditions above are also non-Newtonian materials.

2.2.2.3 Rheological models for Cement-based Materials

The rheological properties of cementitious materials are critical to concrete science. However different models can result in different values for a certain physical entity, even for the same measurement [15]. It is typically accepted that cement-based materials are Bingham materials [16, 17]. But several authors have indicated non-linear rheological behavior. In some cases, the material behaves has a shear-thickening fluid [18, 19]. This can be attributed to low water/cement radio and to high shear rates applied. Yahia and Khayat observed shear-thinning behavior on high-performance concrete mixtures made with relatively low w/cm ratio, use of supplementary cementitious materials (SCMs) and rheology-modifying admixtures (RMAs) [20]. They also conclude that the Herschel-Bulkley model always results in the lowest value for yield stress compared to other models for shear-thinning materials, while for shear-thickening materials the highest yield stress value was systematically observed with Herschel-Bulkley. Since yield stress is obtained by extrapolating the curve to zero shear rate (impossible to measure), a fit with an available model is required. One possible problem using the Herschel-Bulkley model, shown in Equation 4, is the determination of the yield stress.

$$\tau = \tau_0 + k\dot{\gamma}^n \qquad \textit{(Eq. 4)}$$

Where:

τ = Shear stress (Pa)

$\dot{\gamma}$ = Shear rate (s^{-1})

τ_0 = Yield stress (Pa)

k = Consistency factor (-)

n = Consistency power index (-)

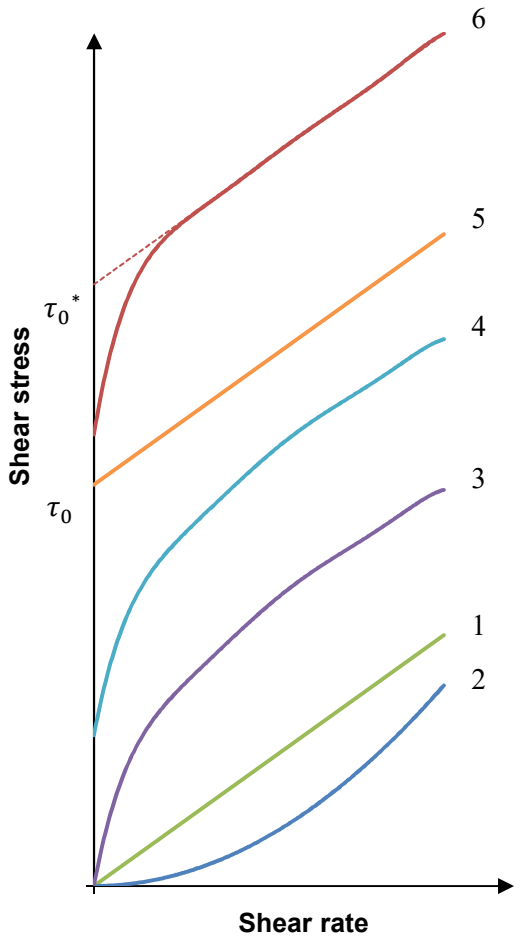

1. Newtonian: No shear stress required to initiate the flow, differential viscosity and apparent viscosity are independent of shear rate.

2. Shear-thickening power law: No shear stress required to initiate the flow, differential viscosity and coefficient of viscosity increase continuously with increasing shear rate.

3. Shear-thinning power law: No shear stress required to initiate the flow, differential viscosity and coefficient of viscosity decrease continuously with increasing shear rate.

4. Shear-thinning with yield response: shear stress required to initiate the flow, differential viscosity and coefficient of viscosity decrease continuously with increasing shear rate.

5. Ideal Bingham plastic: shear rate required to initiate the flow, differential viscosity is constant and is called plastic viscosity, while the coefficient of viscosity decreases continuously.

6. Non ideal Bingham plastic: Above the apparent yield stress, the coefficient of viscosity decreases continuously while the differential viscosity approaches a content value with increasing shear rate. Extrapolation of the curve from linear plastic region to the stress axis gives the apparent Bingham yield stress

Figure 3. Identification of flow curves based on their characteristic shape. From ACI committee 238 [21].

Mathematically, the value of the viscosity at zero shear rate is a concern for the Herschel-Bulkley model. The viscosity (slope of the rheogram) is a resistance to flow and for cement-based materials, most of the time, an initial stress is required to initiate the flow. If n < 1 in the Herschel-Bulkley model, the viscosity at zero shear rate is infinite. While if n > 1, the viscosity at zero shear rate is 0. The solution for this problem is to add a linear term (μ in Pa.s) to the model. Therefore, the modified Bingham model (Equation 5). Can provide a better description of rheological parameters [20].

$$\tau = \tau_0 + \mu\dot{\gamma} + c\dot{\gamma}^2 \qquad \textit{(Eq. 5)}$$

Figure 3 shows the most common models, following the classification from ACI committee 238 [21] while Table 1 shows their nomenclature. To obtain the rheological properties of a fluid, the use of a rheogram is required and the best fit to a rheological model is critical.

Table 1. Rheological models applied to cement-based materials [21].

RHEOLOGICAL MODELS FOR MATERIALS WITHOUT YIELD STRESS	
NEWTON'S LAW	$\tau = \eta\frac{dv}{dx} = \eta\dot{\gamma}$
POWER LAW	$\tau = K\dot{\gamma}^n$
RHEOLOGICAL MODELS FOR MATERIALS WITH YIELD STRESS	
BINGHAM	$\tau = \tau_0 + \mu\dot{\gamma}$
MODIFIED BINGHAM	$\tau = \tau_0 + \mu\dot{\gamma} + c\dot{\gamma}^2$
HERSCHEL-BULKLEY	$\tau = \tau_0 + K\dot{\gamma}^n$
CASSON	$\tau = \tau_0 + \eta_\infty\dot{\gamma} + 2(\sqrt{\tau_o\eta_\infty})\sqrt{\dot{\gamma}}$
DE KEE	$\tau = \tau_0 + \mu\dot{\gamma}e^{-2\propto\dot{\gamma}}$
YAHIA-KHAYAT	$\tau = \tau_0 + 2\,(\sqrt{\tau_o\eta_\infty})\,\sqrt{\dot{\gamma}e^{-2\propto\dot{\gamma}}}$

Where:

τ = Shear stress (Pa)

$\dot{\gamma}$ = Shear rate (s^{-1})

τ_0 = Yield stress (Pa)

K = Consistency factor (-)

n = Consistency power index (-)

μ = Coefficient of viscosity (Pa.s)

c = Second order parameter (Pa s^2)

$\propto$ = Time-dependent parameter (s)

η_∞ = Apparent viscosity at high shear rate (Pa)

2.2.3 Rheometers for Cement-Based Materials

2.2.3.1 ICAR rheometer

The ICAR rheometer is, according to the manufacturer, a rugged portable instrument for measuring rheological properties of fresh concrete. This instrument was developed at the International Center for Aggregate Research (ICAR) (Figure 4). This rheometer works under the principle of concentric cylinders for particles suspensions where the vaine representes an inner cylinder that rotates while the container stays stationary.

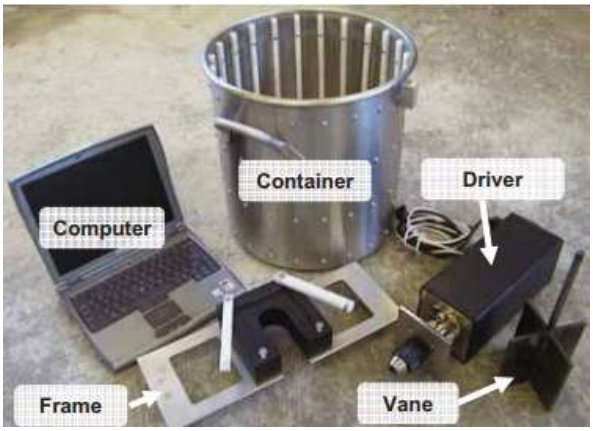

Figure 4. ICAR rheometer hardware.

Shear is applied to concrete by the rotation of the inner cylinder, while the torque necessary to keep certain velocity is recorded. The measurements are performed by decreasing rotational velocities in a set of steps. Following the standard procedure of the software, a pre-shear time of 20 seconds occurs before the measurement starts to avoid errors due to thixotropy. A procedure consisting of seven steps is conducted while torque is recorded during 5 seconds per step. By default, the software omits one second of torque data at the beginning of each before computing the rheological properties. Nevertheless, an independent custom-made analysis was performed using the raw data file captured by the ICAR rheometer software where 1.4 seconds were omitted at start and 0.3 at the end of each step to guarantee proper equilibrium at each velocity step. Figure 5 shows the typical torque vs. time profile as obtained from the raw data file. The average of torque measurements is obtained per step and from there the relationship between torque at each step and velocity (equation 6) is determined. G is obtained by extrapolating the linear equation and obtaining the intersection with the torque axis. H is obtained by determining the slope of the relationship between torque and velocity (Figure 6). The Reiner–Riwlin equation (see equations 8 and 9 further) is used to transform the relationship between torque and velocity into a relationship between shear stress and shear rate.

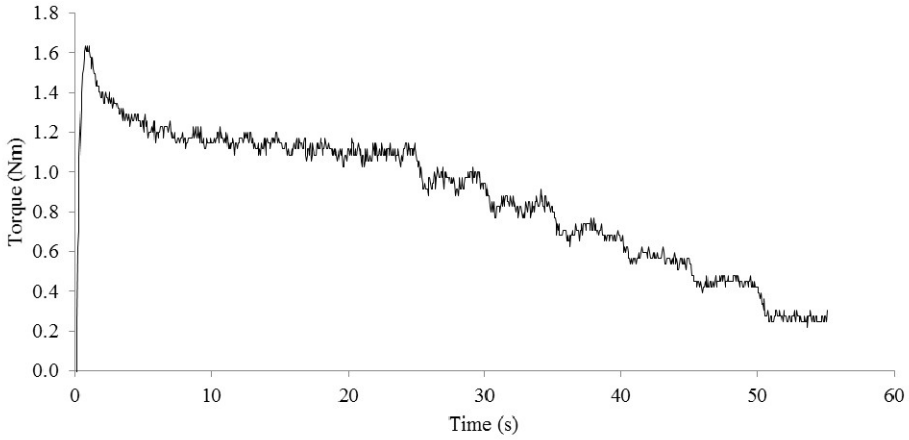

Figure 5. Typical profile of torque versus time for the ICAR rheometer.

$$T = G + HN \qquad \textit{(Eq. 6)}$$

Where:

T = Torque (Nm)

G = Intercept with the torque axis (Nm)

H = Slope of the relationship between torque and velocity (Nm.s)

N = Velocity (rps)

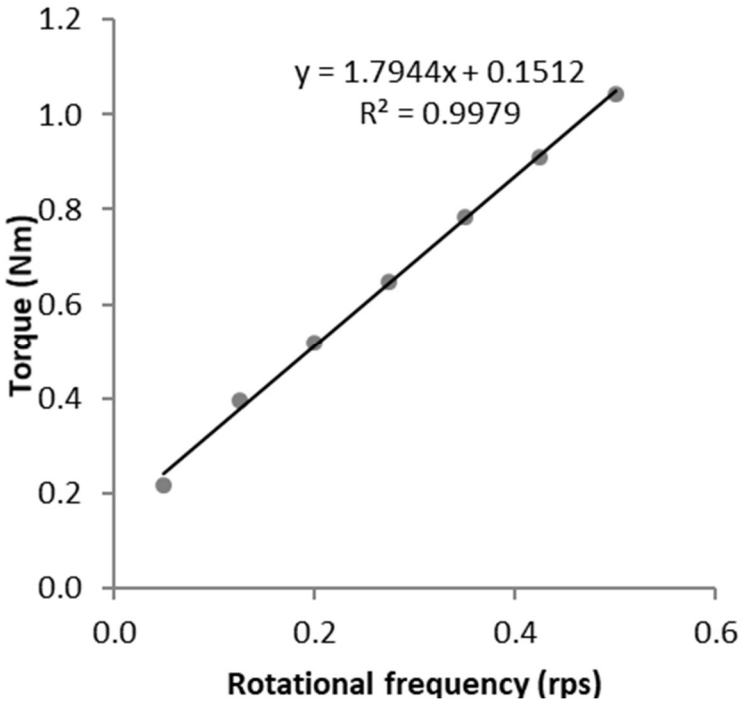

Figure 6. Torque vs velocity diagram.

2.2.3.2 ConTec Viscometer 5

The ConTec viscometer 5 is a non-portable instrument (Figure 7) for measuring the rheological properties of fresh mortar and concrete. The ConTec viscometer 5 has an inner cylinder divided in two parts. The upper part is used to measure torque and the lower part is used to eliminate the complex 3-D bottom flow. The system has two configurations. Further in this thesis referred as ConTec 5S which is used for mortar and ConTec 5W which is used for concrete:

- ConTec 5S configuration: R_i = 65 mm and R_o = 82 mm
- ConTec 5W configuration 2: R_i = 100 mm and R_o = 145 mm

This rheometer works under the principle of concentric cylinders for coarse particles suspensions where the ribbed vane representes a cylinder, which remains stationary, while the outer radius, composed by the bucket rotates. Both cylinders are equiped with vertical ribs that prevent the so-called “wall slip”.

Shear is applied to concrete by the rotation of the outer cylinder. The measurements are performed by decreasing rotational velocities in a set of steps. As an example, Figure 8 shows a 10-step procedure where 50 points of torque are recorded in a duration of 5 seconds per step with 1 second interval in between steps. A linear fit between torque and velocity was adapted.

Data analysis follow a similar approach like the used for the ICAR rheometer with the same transformation equations.

Figure 7. ConTec Viscometer 5.

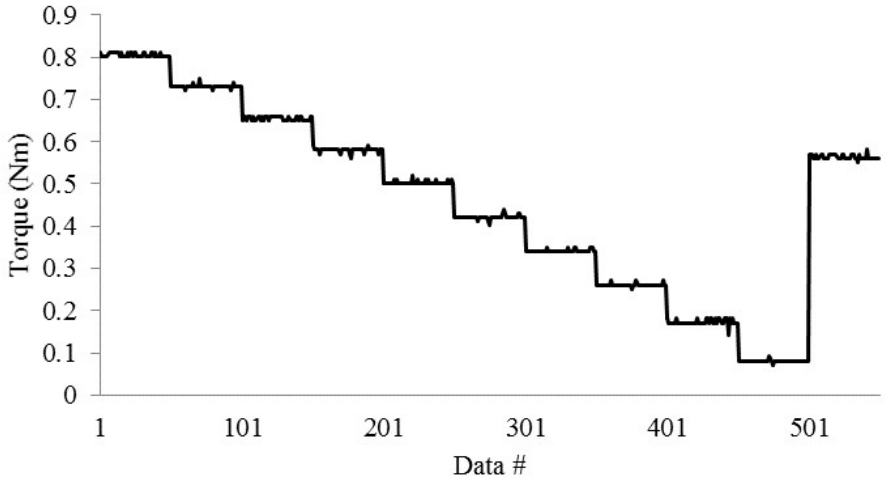

Figure 8. Typical measurement profile for the ConTec Viscometer 5.

2.2.3.3 ConTec viscometer 6

The ConTec viscometer 6 (Figure 9) is a smaller version of the ConTec viscometer 5 and suitable to measure the rheological properties of cement paste and mortar with a maximum particle diameter of 2 mm. It has only one configuration with R_o = 61.5 mm and R_i = 50 mm.

Figure 9. ConTec Viscometer 6.

2.2.3.4 Anton Paar MCR 302 rheometer.

The Anton Paar MCR 302 Rheometer (Figure 10) is a non-portable temperature-controlled instrument for measuring rheological properties for all kind of materials. This rheometer works based on the principle of concentric cylinders, although other geometries are available as well.

Shear is applied to cement paste by the rotation of the inner cylinder. The measurements can be performed by a linear decrease of rotational velocities or in a step wise procedure. The testing procedure in the Anton Paar rheometer is fully adjustable, in terms of shear rate range and profile. It is used in this thesis as a reference rheometer for the comparative tests, as the same pre-shear time and shear rate range of other rheometers can be imposed. The typical output is shown in Figure 11.

The Anton Paar software delivers directly fundamental units. After verification of their correctness, there is no need to transform torque measurements to fundamental units. The shear stress is obtained at every shear rate for each data point. In case of Bingham model, the yield stress is obtained by the extrapolation of the flow curve and intersection with the shear stress axis. Plastic viscosity is obtained by determining the slope of the flow curve.

Figure 10. Anton Paar MCR 302 rheometer

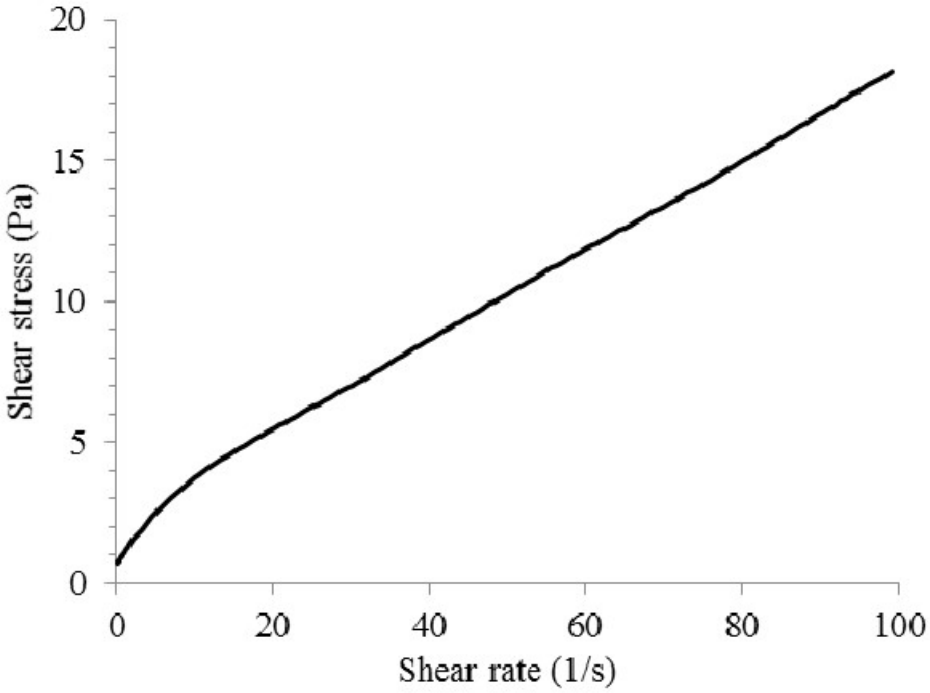

Figure 11. Typical flow curve from Anton Paar MCR 302.

2.2.4 Comparison of rheometers

Do all rheometers measure the same properties? They measure the same properties but deliver different values. The principle is the same for all rheometers: the required torque to maintain a certain speed is determined. However, due to design and sensitivity factors, the torque values differ from one rheometer to another. Two rheometer comparison campaigns have been done in the beginning of the 2000s. In 2000 in Nantes, France, 5 rheometers were compared, and 12 concrete mixes were tested with slump values ranging

from 90 mm to 235 mm, utilizing two types of coarse aggregate [22]. However, since SCC was becoming more and more popular, in 2003 in Cleveland, USA they decided to do another comparison in which 4 rheometers were tested. 17 concrete mixtures and five mortars were tested with a range of slump values from 121 mm to 248 mm, keeping the coarse aggregate type constant [23]. The rheometers compared were the ConTec BML Viscometer 3, the BTRHEOM rheometer, the IBB rheometer, the two-point workability rheometer, and the CEMAGREF-IMG rheometer. Results from empirical measurements (slump, slump flow) show correlations with the rheological measurements as shown in Figure 12. As the slump/slump flow increases, the yield stress decreases.

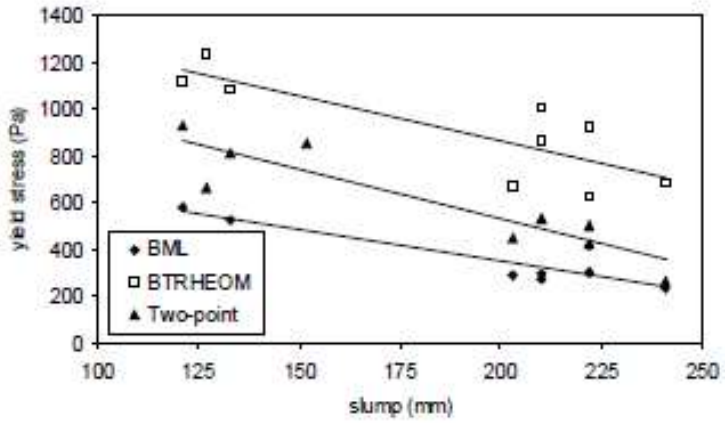

Figure 12. Comparison between yield stress and slump for different rheometers. Figure from [22].

Other empirical tests such as V-funnel flow time and T50 were compared with rheological parameters. However, a poor correlation between yield stress and V- funnel and T50 were shown, and a high correlation between V-funnel and T50 and plastic viscosity was observed as shown in Figure 13 and Figure 14. Regardless of the rheometer used, all rheometers show a similar trend for yield stress (Pa, Nm) and plastic viscosity (Pa s, Nm s), as shown in Figure 15 and Figure 16.

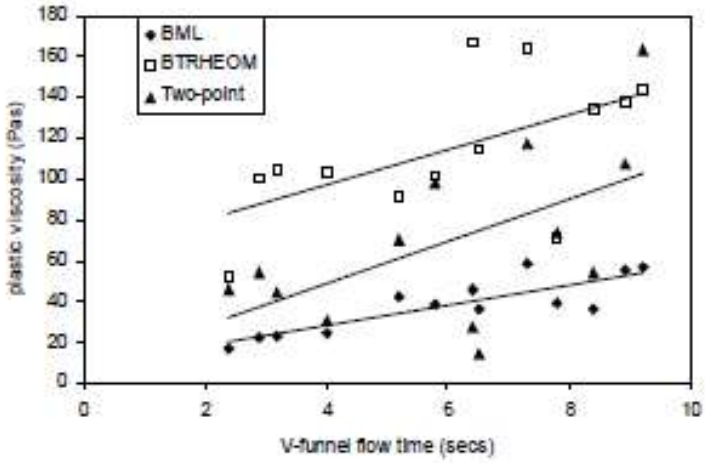

Figure 13. Correlation between plastic viscosity and V-funnel flow time for different rheometers. Figure from [22].

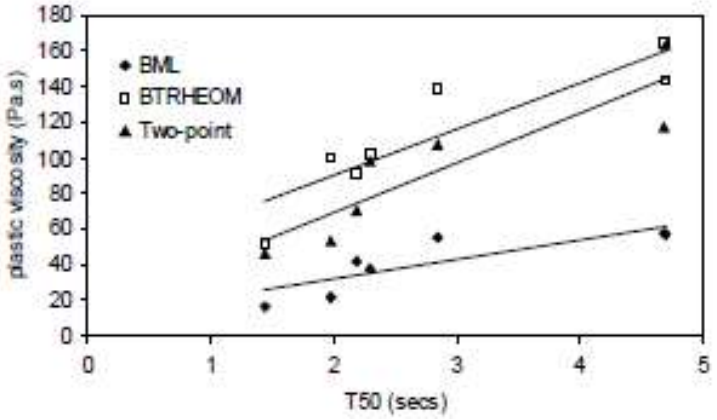

Figure 14. Correlation between plastic viscosity and T50 (from the slump flow test, for different rheometers. Figure from [22].

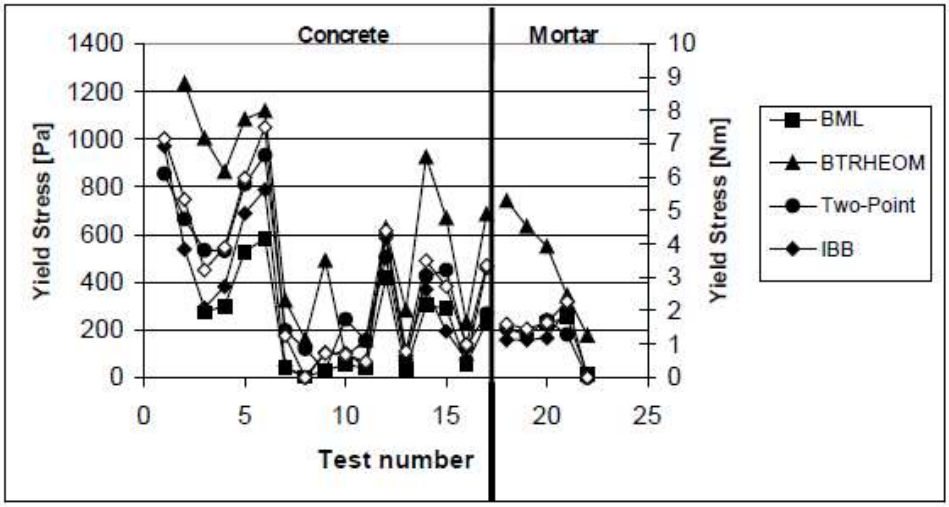

Figure 15. Yield stress for each test performed for all rheometers. Figure from [22].

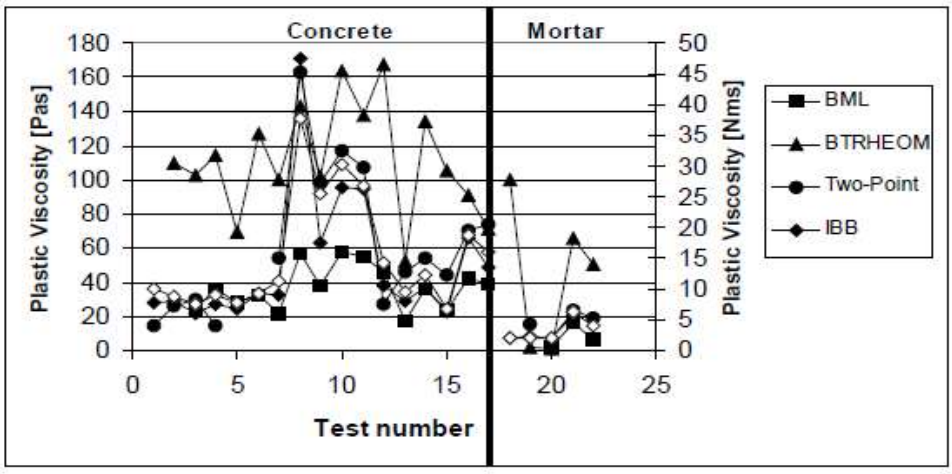

Figure 16. Plastic Viscosity for each test performed for all rheometers. Figure from [22].

2.2.5 Challenges in assessing rheological properties

2.2.5.1 Errors due to too large particles

Errors due to too large particles: Cement-based materials, such as concrete and even mortar are materials that have large solid particles (i.e., aggregates), and they must have enough space to flow. To avoid blockage in the rheometer, a gap of 10 times the size of the Maximum Aggregate Size (MAS) its recommended [15], although many commercial concrete rheometers suggest a factor 3 or 4. Too large particles for the gap of the rheometer will result in large fluctuations in torque values, potential blocking of the rheometer. Wrong selection of rheological model: As discussed before, different models result in different values and an inadequate selection of a model can lead to a different interpretation of properties, mostly for the yield stress. In order to conduct a valid experimental program, the same model must be used for all tests.

2.2.5.2 Errors due to time-dependent-behavior

Viscosity changes in cement-based materials can be non-time-dependent (i.e. shear thinning, shear thickening behavior), or time dependent. In case the time-dependent changes in viscosity are reversible, the effect is defined as thixotropy. Non-reversible changes in viscosity with time are also possible. "Thixotropy is a reversible, isothermal, time-dependent decrease in viscosity when a fluid is subjected to increased shear stress or shear rate, and a gradual recovery of that said viscosity when shear rate is removed" [24]. The mechanisms involved in the thixotropic behavior of cement-based materials are flocculation and hydration [25].When a concrete mixture is at rest, cement particles flocculate with time. This flocculated structure increases the viscosity and is the result of Van der Waals attraction and Brownian motion, and, at longer term, hydration bridges [24]. The opposite phenomenon happens when a flocculated concrete mixture is subjected to shear forces. The flocs can break down and viscosity can decrease [17].

Errors due to thixotropic behavior and structural breakdown can play a role in the assessment of rheological properties. Wallevik et al. recommended the following steps to minimize error due to thixotropy [24]:

- Pre-shearing the sample at the highest shear presented on the test.
- Measuring right after the pre-shear period
- Plot torque vs steps and verify that equilibrium is reached.
- Use of retarders

The time duration of the pre-shear is critical as an excessive pre-shear can enhance undesired effects such has workability loss or particle migration [26].

2.2.5.3 Errors due to plug flow

Based on the Cauchy stress principle [27] the stress for a cylinder can be calculated at a distance "r" as shown in Equation 7:

$$\tau = \frac{T}{2\pi r^2 h} \qquad \textit{(Eq. 7)}$$

One common procedure to transform torque-velocity measurements to fundamental units is equations 8 and 9, which is a rearrangement of the terms conforming the original Reiner-Riwlin equation. For coaxial cylinder rheometers, as the radius increases, the applied stress decreases and at some point, it is possible that the shear stress becomes lower than the yield stress of the material. If that happens the, material will not be sheared entirely, and the Reiner-Riwlin equations need to be re-evaluated since it considers that the material in the rheometer gap was entirely sheared during the duration of the test.

$$\tau_0 = \frac{\left(\frac{1}{Ri^2} - \frac{1}{R_0^2}\right)}{4\pi h l \left(\frac{R_0}{R_i}\right)} G \qquad \textit{(Eq. 8)}$$

$$\mu = \frac{\left(\frac{1}{Ri^2} - \frac{1}{R_0^2}\right)}{8\pi^2 h} H \qquad \textit{(Eq. 9)}$$

Where:

$\tau_0 =$ Yield stress (Pa)

$\mu =$ Plastic viscosity (Pa s)

$R_i =$ Inner cylinder radius (m)

$R_o =$ Outer cylinder radius (m)

$h =$ Height of the inner cylinder

$G =$ Intercept of the Torque vs Velocity diagram with the Y-axis (Nm)

$H =$ Slope of the Torque vs Velocity diagram (Nm s)

If R_p is defined as "the distance at which applied shear stress equals the yield stress", R_s is term utilized to determine the outer boundary of the flow domain [28]. If: $R_p < R_o$, not all material is being sheared (i.e., high yield stress material); then $R_s = R_p$. If $R_p > R_o$, all material is being sheared; $R_s = R_o$, as shown in Figure 17. In the case only a part of the gap is being sheared (Figure 17 (left)), the Reiner-Riwlin equations, with R_o being replaced by R_s are still valid, but R_s depends on an unknown yield stress value and the applied torque. To obtain the rheological properties, plug radius, yield stress and viscosity are adjusted in an iterative procedure until the input and output values converge satisfactorily.

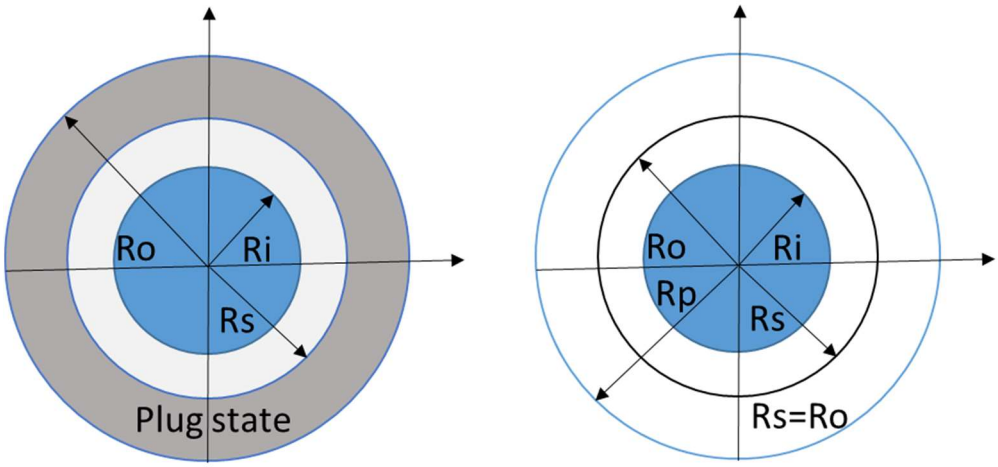

Figure 17. Potential conditions for flow of a yield stress material in a coaxial cylinders rheometer. Left: the system shows a reduction in flow domain and the Reiner-Riwlin equations need to be adjusted. Right: the entire flow domain is sheared. Figure after [15].

2.2.6 Influence of particles on suspension rheology

A suspension is a mixture of solid particles in a liquid medium. Concrete and mortar are considered suspensions since they are a mixture of solid particles in a liquid medium (i.e. aggregates in paste) which at the same time complicates the measurements of rheology due to the large range of particle sizes [29]. This section discusses some of the critical concepts necessary to understand the influence of particles and particle concentration on the rheological properties of cement-based materials.

Volume fraction describes at what degree a unit volume is filled with particles, which is defined as the ratio of the solid volume of particles to the entire volume of the suspension [30] as expressed by Equation 10. Usually, maximum packing density of aggregates has a value of 0.50-0.70 [31, 32]. Paste is required not only to fill the voids but to lubricate particles, decreasing interparticle friction.

$$\varphi = \frac{V_p}{V_b} \quad \textit{(Eq. 10)}$$

where:

$\varphi =$ Particle volume fraction (-)

$V_p =$ Solid volume of particles

$V_b =$ Volume occupied by the suspension

Einstein [33] [34] defined the relationship between the viscosity of a suspension and that of the suspending medium and the volume fraction, as follows: "the coefficient of internal friction increases by a fraction that is equal to the total volume of the spheres suspended in the unit volume" This can be translated to a simple Equation 11.

$$\eta_s = \eta_m(1 + 2.5\varphi) \quad \textit{(Eq. 11)}$$

where

$\eta_s =$ Viscosity of the suspension (Pas)

$\eta_m =$ Viscosity of the suspending medium (Pas)

$\varphi =$ Volume fraction (-)

But Einstein's formula was limited to dilute systems ($\varphi < .10$). Batchelor and Green [35] added a third term to the formula (equation 12) considering the interactions between distortions in the fluid field caused by neighboring particles [35].

$$\eta_s = \eta_m(1 + 2.5\varphi + 7.6\varphi^2) \quad \textit{(Eq. 12)}$$

As the volume fraction of particles increases more, the interaction between them becomes challenging. Two new terms were introduced: maximum volume fraction represents the maximum packing density which ranges from 0.64 (random close packing) to 0.74 (hexagonal close packing) for uniform spheres [36]. Yammine et al have shown there is a critical value of volume fraction where particle concentrations reach a transition from a suspension to granular material (0.55-0.62) [37]. Intrinsic viscosity; which has a value of 2.5 if spheres are used in the suspension [38]. However, a different value is expected for cement-based materials. The most popular equation to describe the viscosity amplification with the increase of particles in suspensions for high concentration of particles is the Krieger-Dougherty equation (Equation 13)

$$\eta_r = \left(1 - \frac{\varphi}{\varphi_{max}}\right)^{-[\eta]\cdot\varphi_{max}} \quad \textit{(Eq. 13)}$$

Where:

$\eta_r =$ Relative viscosity (-)

$\varphi =$ Volume fraction (-)

$\varphi_{max} =$ Maximum packing density (-)

$[\eta] =$ Intrinsic viscosity (Pa. s)

2.3 Pumping characterization

2.3.1 Flow or friction?

Rheology is used to quantify the fresh properties of concrete using fundamental quantitative units. For the pumping process, rheological properties are a powerful tool to predict how much pressure would be needed to make the concrete flow at a certain flow rate. But not only the rheological properties of bulk concrete are relevant, the rheological properties of the lubrication layer are as well, or even more, and for that, the interface properties are the key.

The following sections discuss different aspects of pumping concrete, including major flow behavior inside a pipe, type of flow presented, importance of stability, formation of the lubrication layer, the main factors affecting the lubrication layer and prediction of the pumping pressure. Major flow behavior in pipes depends on the type of flow:

Plug Flow: Concrete flows as a solid material separated from the pipeline by a layer with lower rheological properties (the lubrication layer). The portion that is in plug is called “bulk concrete”.

Degree of Saturation: The resistance to flow of concrete in a pipe depends on the shearing of the lubrication layer and the friction of the solid particles with the wall. This friction depends on how saturated the concrete mixture is. Two types of flow could occur:

- Hydraulic flow: When concrete is in a saturated state, there is enough paste to lubricate the aggregates and the magnitude of friction is negligible. As a result, the pressure evolution in the pipeline is linear as shown in Figure 18.
- Frictional flow: When a concrete mixture is unsaturated, there is not enough paste to lubricate aggregates and frictional resistance increases dramatically. As a result of frictional flow, the pressure loss in the pipeline is not linear as shown in Figure 39.

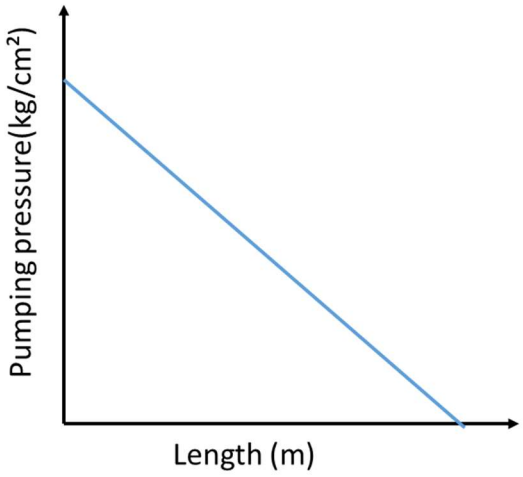

Figure 18. Saturated flow pressure loss from Browne and Bamforth [39].

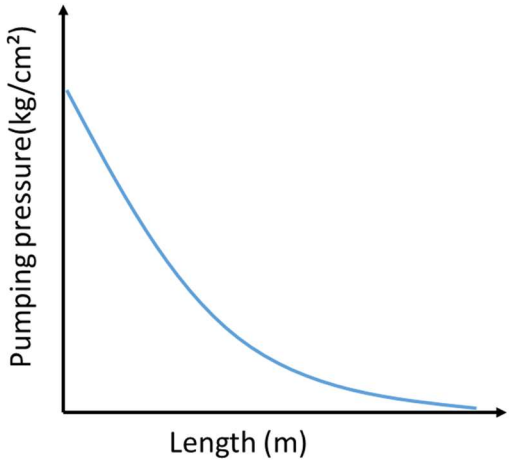

Figure 19. Frictional flow pressure loss from Browne and Bamforth [39].

Stability under Pressure: A concrete mixture that is pumped must remain homogenous in the direction of the flow. If heterogeneity of the concrete is induced inside the pipeline a blockage can occur which can potentially damage the equipment. Blockages may be caused by the separation of water from a concrete mixture caused by a high permeability as shown Figure 20.

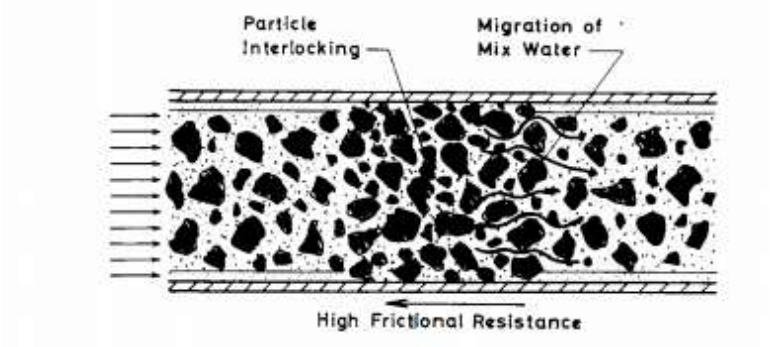

Figure 20. Cause of blockage inside a pipe from Browne and Bamforth [39].

In order to have low resistance to flow, the concrete must be saturated to reduce the risk of blockages. However, this is not the only parameter playing a role whether a blockage will occur. Saturated concrete with high permeability can become unsaturated due to water separating from the mixture in the direction of the flow in a short amount of time. Browne & Bamforth [39] developed a pumpability diagram that serves as a practical guide to evaluate whether concrete can be pumped without risking blockages (Figure 21), based on two empirical tests: the slump test and the pressurized bleeding test.

As mentioned before, concrete can be saturated or unsaturated, depending on the w/c ratio. For concrete mixtures in saturated state, the flow resistance can be represented with equation 14.

$$R = A + KV^n \qquad \textit{(Eq. 14)}$$

Where:

R = Pumping resistance (kg/cm^2)

A = Adhesion resistance (kg/cm^2)

K = Constant related to concrete velocity. (-)

$V =$ Factor related to velocity (kg/cm^2)

n = Constant related to concrete velocity (-)

While for concrete mixtures in unsaturated state (0.40 < w/c in Figure 22) the flow resistance can be represented with equation 15.

$$R = A + \mu P_r \qquad \textit{(Eq. 15)}$$

Where:

$\mu =$ Coefficient of friction between the concrete and the pipe wall. (-)

$P_r =$ Radial pressure (kg/cm^2)

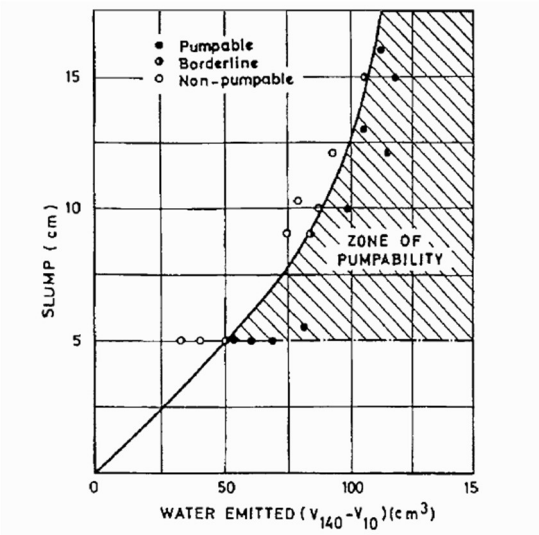

Figure 21. Pumpability diagram Browne and Bamforth [39].

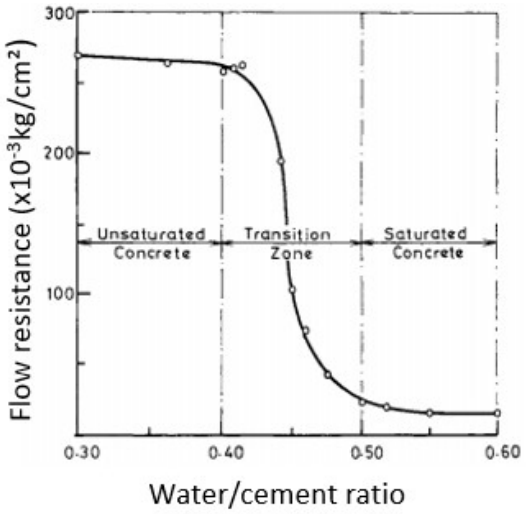

Figure 22. Effect of water to cement ratio on flow resistance from Browne and Bamforth [39].

2.3.2 Lubrication Layer

Kaplan and Chapdelaine were the first researchers to combine rheology and interface rheology to fully understand the flow behavior of concrete through a pipe [40, 41, 42]. The properties of the lubrication layer (LL) can be characterized with an interface rheometer (also called a tribometer) and the properties are typically expressed by equation 16.

$$\tau_{surface} = \tau_{oi} + \eta_i v \qquad \textit{(Eq. 16)}$$

Where:

$\tau_{surface}$ = Surface stress (Pa)

τ_{oi} = Yield stress of the LL (Pa)

η_i = Viscous constant of the LL (Pas/m)

v = Angular velocity of the LL (m/s)

By combining rheological and interfacial properties Kaplan [40] developed a bilinear model relating pumping pressure loss vs discharge flow as shown in Figure 23. As the name says, this model is divided in two parts:

Part A is purely attributed to the interface properties of the lubrication layer. The shear stress induced by the pressure loss is insufficient to overcome the yield stress of the concrete. As such, no shearing occurs in the bulk concrete. Generally, this part is formed at low velocities, and concrete moves as a plug. Equation 17 expresses the shear stress at the wall, and equation 18 predicts pressure in this zone of the graph.

Part B requires the interface properties of the lubrication layer and the flow properties of the concrete. There is a zone where the concrete is being sheared and that affects the flow rate. Generally, this part is formed at high velocities, the velocity is high enough that the applied shear stress closer to the central portion exceeds the yield stress initiating a viscous flow. A plug zone in the center of the pipe still forms but is reduced in diameter. Pressure prediction in this case is shown in equation 19.

$$\tau_w = \Delta_p \cdot \frac{R}{2} = \frac{\Delta p_{total}}{L} \cdot \frac{R}{2} \qquad \textit{(Eq. 17)}$$

$$\Delta p_{total} = \frac{2L}{R}\left(\frac{Q}{3600\pi\ {}^2k_r}\eta + \tau_{0i}\right) \qquad \textit{(Eq. 18)}$$

$$\Delta p_{total} = \frac{2L}{R}\left[\frac{\frac{v_p R_p^2}{R^2} - \frac{R}{4\mu}\tau_{0i} + \frac{R}{3\mu}\tau_0}{1 + \frac{R}{4\mu}\eta}\eta + \tau_{0i}\right] \qquad \textit{(Eq. 19)}$$

Where:

ΔP= Pressure loss (Pa/m)

ΔP_{total}= Total pressure loss (Pa)

L= Length of the pipe (m)

R= Pipe radius (m)

k_r= Filling coefficient

Q= Flow rate (m^3/s)

η= Interface viscous constant (Pa.s/m)

τ_{0i}= Interface yield stress (Pa)

v_p= Plug velocity (m/s)

R_p= Plug radius (m)

τ_0= Concrete yield stress (Pa)

μ= Concrete plastic viscosity (Pa.s)

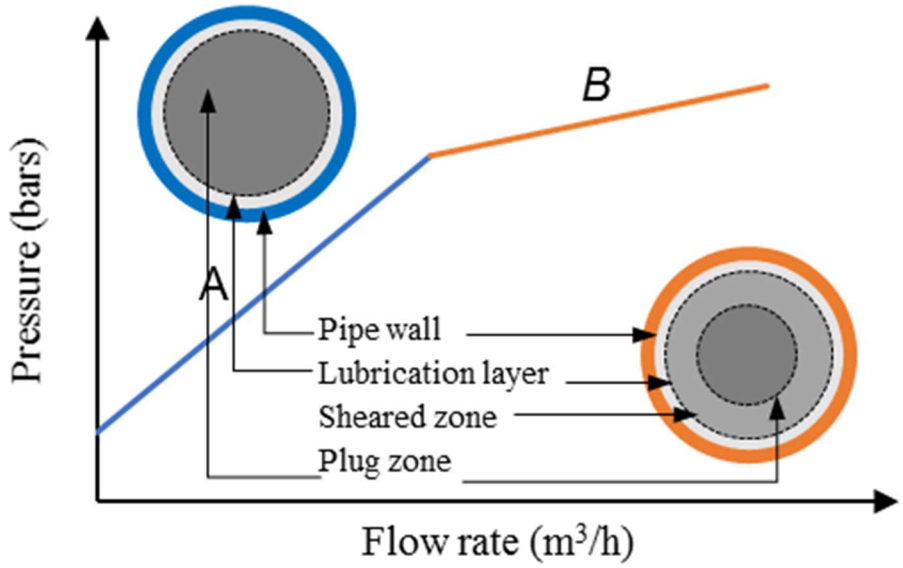

Figure 23. Kaplan's model Schematic representation of flow for the proposed bilinear model [40].

2.3.2.1 Formation of the lubrication layer.

Several mechanisms for the formation of the lubrication layer are reported in literature [40, 41, 42]. The following mechanisms are expected to contribute to the formation of the lubrication layer:

Wall effect: The concentration of particles tends to be lower close to the wall without external force applied on this system [40, 43]. This is applicable to the (coarse) aggregates in case of concrete, where the particle concentration is lower in the vicinity of the wall. The exclusion of particles close to the wall facilitates the formation of the lubrication layer. It is assumed that at a distance above half the diameter of the particles, this effect does not play a role anymore, as shown in Figure 24.

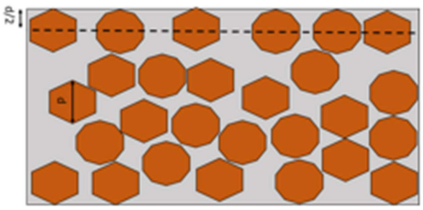

Figure 24. Schematic representation of wall effect (left) and particle migration (right) from [44].

Shear induced particle migration: The particle concentration tends to be lower close to the wall due to the application of an external force [43, 45] (i.e. pumping) because particles migrate from a zone of high shear rate (pipe wall) to a zone with low shear rate (center of the pipe). This leads to a heterogeneous mixture in the radial direction, as shown in Figure 25. This phenomenon is more noted in concrete than in mortar. It is

believed that increasing the coarse aggregates and the yield stress/viscosity ratio enhances the effect of particle migration [46]. This is the same phenomenon which also can lead to a wrong interpretation of rheological properties [15].

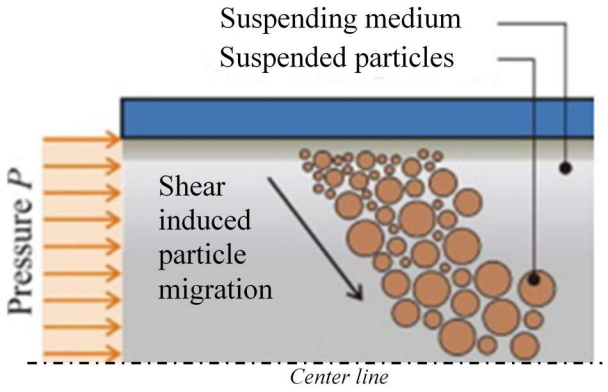

Figure 25. Particle concentration gradient due to shear-induced particle migration in pipe flow [47].

2.3.2.2 Measuring lubrication layer.

Secrieru et al. [47] performed a study that quantifies changes in rheology and the formation of the lubrication layer during pumping. In this study, the portable high-pressure filter press (PHPFP) (Figure 26) was used as an indication of stability of concrete and also to estimate the thickness of the lubrication layer. According to the model shown in Figure 27, under similar pumping pressures (maximum 100 bar) the rheologically effective water, which is the free water that helps concrete flow and is not required for chemical hydration or intrinsically volume, is expected to be pressed out.

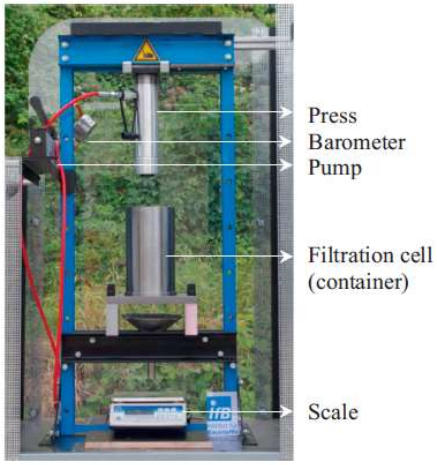

Figure 26. Portable high-pressure filter press. (PHPFP) [47].

According to Secrieru [47], the entire amount of rheologically effective water is interpreted to be available for the formation of the lubrication layer. With that assumption, the relative amount of paste required to build the lubrication layer of thickness "e" can be calculated using equation 20:

$$\pi[R^2 - (R - e)^2]L \qquad \textit{(Eq. 20)}$$

Where:

V_{paste} = Volume of paste (m^3)

R = Pipe radius (m)
L = Length of pipeline (m)
e = Thickness of the LL (m)

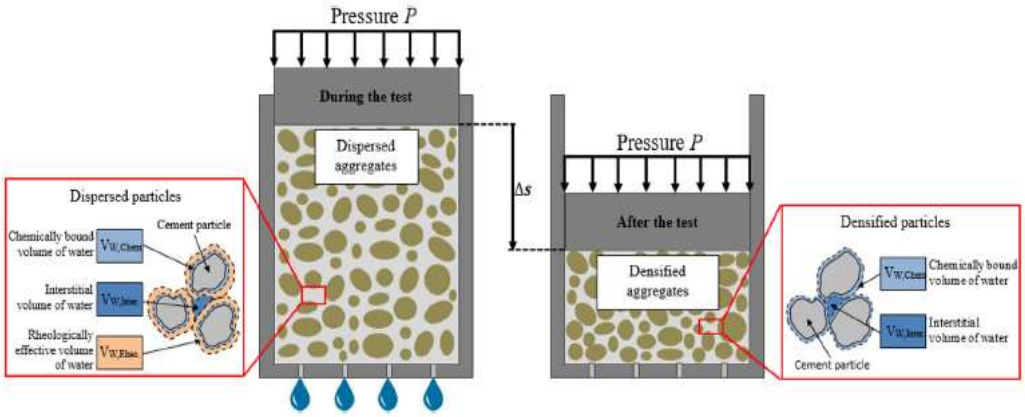

Figure 27. Schematic representation of filtrate extraction from concrete sample [46].

2.3.3 Prediction of Pumping Pressure.

Based on the technique developed by Secrieru [47], the total amount of filtrate pressed out is related to the formation of the lubrication layer. Based on Kaplan's equations, lubrication layer properties are related to the pumping pressure. Since the volume of material available for the formation of the lubrication layer is known from the PHPFP, the theoretical thickness of the lubrication layer can be calculated. This thickness is close to what Chapdelaine observed: 1 mm [42]. This calculation makes sense since mixtures with thicker lubrication layers require less pressure to be mobilized as shown Figure 28.

E (MM)	GRAVEL	M2A	M2B	M2C	M5A	M5B	M10A	M10B	SCC
BEFORE	1.31	1.65	1.48	1.91	2.15	1.74	1.13	1.18	0.85
AFTER	1.43	1.61	1.48	1.61	1.82	1.59	1.14	1.18	0.95

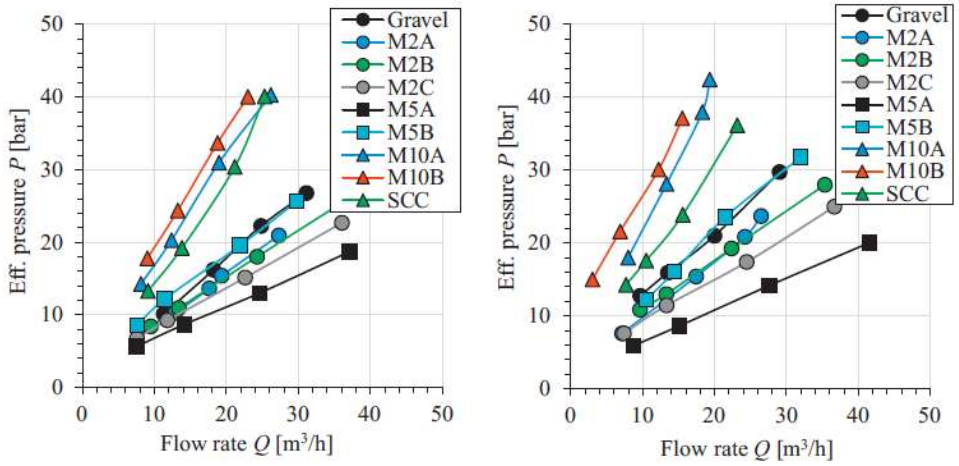

Figure 28. P-Q curves left at the beginning and b at the end of the pumping [47].

2.3.4 Factors Affecting Lubrication Layer Composition and Properties.

2.3.4.1 Effect of paste volume

It was shown by Chapdelaine that the paste content is a factor that plays a big role in concrete pumping. It is observed that the higher the paste volume, the easier it is to pump to concrete [48]. This makes sense since paste is required not only to fill the voids in between the aggregates, but to exceed this critical value to increase workability and reduce pumping resistance [39]. However, it was shown by Burns that paste is not directly a parameter that assesses the pumpability of a mixture. He observed a mixture with 13% of air and 37% of paste being able to be pumped but a mixture with 3% of air and 42.4% of paste was not pumpable. The question is: Does air content affect the pumping behavior? And how? The concept of "real paste" was then developed by Jolin and Burns [49]. Based on the hypothesis of Dryer [50], the bubbles dissolve under pressure in the water. As a result, the total volume is reduced. The real paste concept "is defined as the amount of paste (%) present in concrete while under pressure in the hose, which represents the amount of paste required to create the lubrication later against the pipe wall and fill the intergranular voids." When the pressure increases, the paste is reduced to the volume of binder and water. However, the calculation of the real paste is not only decreasing the volume of air from the paste, but the volume of the entire mixture is decreased by the same volume while keeping the same solid constituents.

2.3.4.2 Effect of aggregates

The composition of the lubrication layer is not completely constant since it is dependent on multiple factors (i.e. pump position, pipe material, diameter, length, and concrete composition). During concrete pumping the maximum stress is located at the walls and particles try to escape from the "high shear zone" to the lower shear zone [43]. This migration is dependent on the particle size [44]. As a result, coarse aggregates travel first to the center of the pipeline leaving paste and mortar behind suggesting that the lubrication layer is formed purely by paste. Other authors have claimed that the lubrication layer behaves as a mortar [51]. However, the composition of the lubrication layer is more complex since it is also dependent on the imposed shear rate. The layer could also be composed of micro-mortar [52].

2.3.4.3 Hose diameter and reducers

Chapdelaine [42] classifies 2 phenomena related with the reduction of the pipes: Increase of relative paste volume: Chapdelaine observed that the thickness of the lubrication layer is constant regardless of the pipe diameter. As a result, the smaller the diameter, the more paste required to form a lubrication layer as shown in Figure 29.

2.3.4.4 Increase in velocity

If the diameter is reduced, while the flow rate is constant, the velocity increases with the square of the diameter reduction.

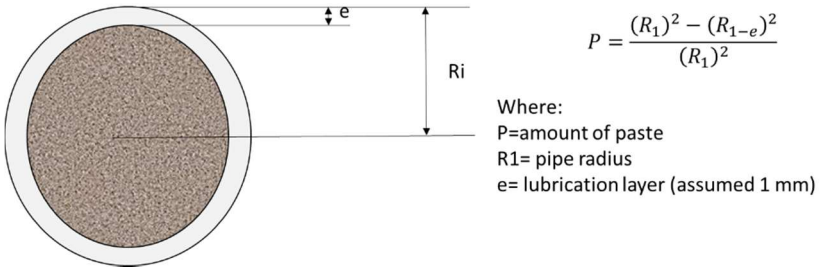

Figure 29. Representation of the required amount of paste to form the lubrication layer according to Chapdelaine [42].

2.4 Air entraining admixtures and the air void system

Air entraining admixtures (AEA) belong to the family of chemicals known as "surfactants". AEAs stabilize the air bubbles formed during the mixing process by reducing the surface tension of water, impeding coalescence and linking the bubbles to aggregate and cement particles [8]. It is hard to classify the AEA into a specific class of chemicals since are produced from chemically complex raw materials (Table 2) and can even be composed by a mixture of these plus additional ingredients [53]. A typical AEA consists of a non-polar hydrocarbon chain with an anionic polar group [54]. The polar group (carboxylic or sulfonic acid) gets oriented in direction of the water phase lowering the surface tension of water, promoting bubble formation and avoiding the coalescence of the dispersed bubbles due to electrostatic repulsion.

Table 2. Classification of common AEA according to their origin [53].

CLASSIFICATION	CHEMICAL DESCRIPTION	PERFORMANCE CHARACTERISTICS:
WOOD DERIVED ACID SALTS:	Alkali or alkanolamine salt of:	
• **VINSOL RESIN**	A mixture of tryclic acids, phenolics and terpenes	Minor air gain with initial mixing. Air loss with prolonged mixing. Midsized air bubbles formed. Compatible with most other admixtures.
• **WOOD ROSIN**	Tricyclic acids-major component. Tricyclic acids minor component.	Same as above.
• **TALL OIL**	Fatty acids-major component. Tricyclic acids-minor components.	Slower air generation. Air may increase with prolonged mixing. Smallest air bubbles of all agents. Compatible with most other admixtures.
VEGETABLE OIL ACIDS	Coconut fatty acids, alkanolamine salt.	Slower air generation than wood rosins. Moderate air loss with mixing. Coarser air bubbles relative to wood rosins. Compatible with most other admixtures.
SYNTHETIC DETERGENTS	Alkyl-aryl sulfonates and sulfates (e.g. sodium dodecylbenzenesulfonate)	Quick air generation. Minor air loss with mixing. Coarser bubbles. May be incompatible with some superplasticizers. Applicable to cellular concretes.
SYNTHETIC WORKABILITY AIDS	Alkyl-aryl ethoxylates	Primarily used in masonry mortars.
MISCELLANEOUS	Alkali/alkanolamine acid salts of lignosulfonate Oxygenated petroleum residues. Proteinaceous materials. Animal tallows.	Discontinued.

In presence of cement and aggregates, the surface charge of the stabilized bubble gets it attached to cement and aggregate surfaces forming aggregate-air-cement-air-aggregate type of bridges [55] as depicted in Figure 30. Such system would permit shear motion, since the air bubbles act like compressible bearings improving the cohesion and workability of the mixture [55].

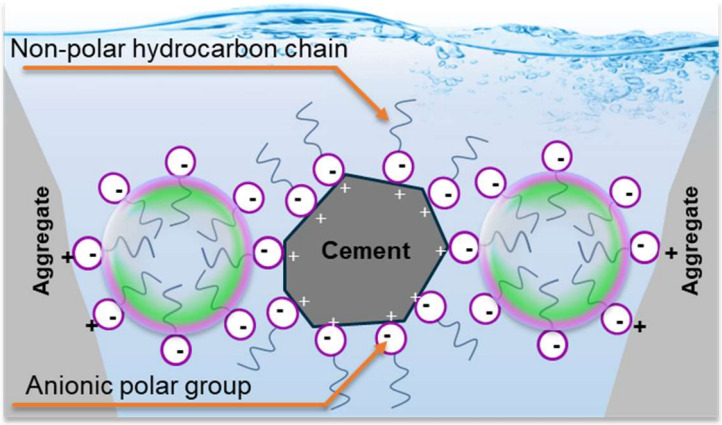

Figure 30. The air entraining admixtures create bonds between aggregates, bubbles and cement particles to stabilize the air void system [55].

The air void system of concrete can be described using three main parameters:

- Air content: Percentage of air per unit of volume.
- Specific surface: The surface area of the air voids divided by their volume.
- Spacing factor: The maximum distance of any point in the cement paste from the periphery of an air void.

These parameters are measured on polished hardened concrete sections examined under an optical microscope. The ASTM C457-16 describe three methods to determine the air void parameters:

- Linear-traverse
- Modified point-count
- Contrast enhanced method

The linear traverse method consists of the determination of the composition of concrete regarding to its volumetric proportions by adding up the distances traversed across by solids or air voids when these intersect a series of regularly spaced lines in one or more planes. The data is processed to determine the total traversed length, the length traversed by air voids and the length traversed by paste and the number of air voids intersected by the traverse line [56]. The modified point count method determines the volumetric composition of concrete based on the frequency with which paste, aggregates and air voids are observed using a grid of points equally separated. These points may be in one or more planes intersecting the specimen. The collected data is the linear distance between stops along the traverse, the number of stops and the number of stops in air voids intersected by the line of traverse over which the component data is gathered [56]. The contrast enhanced procedure consists of the determination of the volumetric composition of the concrete by summing distances measured in digital images of a prepared concrete surface using a series of regularly spaced lines in one or more digital images obtained with a flatbed scanner or an automated digital microscope [56]. The three methods require an exhaustive sample preparation. The hardened concrete specimen is cut in such size that it can be handled by the available equipment. The ASTM C457-16 specifies a minimal area of analysis based on the maximum aggregate size of the specimen. Then, the surface must be lapped using suitable abrasive media such silicon carbide or diamond pads decreasing the particle size in stepwise fashion as the sample becomes free of scratches or saw marks and it approaches total flatness. The sample is ready for microscopical analysis when is completely flat and can reflect light from a distance source. The contrast enhanced method requires coloring the surface using black ink and filling the air voids with a finely ground white powder. The image or images are captured by an automated microscope or a flatbed scanner with high-

enough resolution. Then, the acquired images are processed by an image analysis software to determine the air void parameters.

2.5 Frost Durability

There are two types of durability issues due to frost that will be discussed: freeze-thaw damage and salt scaling damage. The freeze-thaw test evaluates the risk of internal frost damage whereas the salt scaling test evaluates the risk of surface scaling. The air void system is a vital part of resistance to both damages. The results are often connected. Generally, when the concrete tests showed freeze-thaw damage they also showed scaling damage. However, the reverse was not always true. This is because the scaling test is a more severe procedure.

2.5.1 Freeze-Thaw Damage

Freeze-thaw damage is an internal damage. If stresses formed by freezing water are sufficiently large, micro-cracks within the concrete can form. These can expand and cause weakness in structural members. The damage from freeze-thaw cycles can decrease the compressive strength of the concrete. The overall damage can be relatively minor or detrimental to the structure depending on the air-void system and the amount of the freeze-thaw cycles endured.

Freeze-thaw resistance depends largely on the hardened air-void system found throughout the concrete. It is believed a system of entrained air-voids is needed to prevent freeze-thaw damage. The concrete must have an adequate system of air content, specific surface, and spacing factor. The air content is the volume of air per unit volume of hardened concrete expressed as a percent, the spacing factor is the average distance from a random point in the concrete to the nearest air void, and the specific surface is the voids' surface area per unit volume of voids.

There are many theories to explain how frost damages concrete. Pigeon and Pleau [57] cite the theories put forth by Powers [58], Powers and Helmuth [59], and Litvan [60] the only ones with "relatively complete theoretical explanations of the mechanisms causing damage to concrete during freezing," therefore these will be the ones discussed in the following paragraphs.

In 1945 Powers [61] proposed the critical saturation theory. This theory is based on the fact that as water freezes it expands by 9%. It states concrete's critical saturation point begins at 91.7%. When concrete is saturated past this point it is at risk for freeze-thaw damage. If the capillary pores are saturated stress will be generated when the water freezes.

Subsequently, in 1949 Powers [58] introduced the hydraulic pressure theory. The spacing factor was developed as part of this theory. The hydraulic pressure theory allowed for the water in the pores to behave according to Darcy's Law [58] and attributed frost damage to a buildup of hydraulic pressure. As the water freezes it expands and the excess liquid is forced ahead of the freezing front creating internal hydrostatic pressure. In non-air entrained concrete this pressure may disrupt the concrete causing internal cracks (when the spacing factor, the distance to the next void is too large or the freezing is too fast). In air entrained concrete, a system of small spherical air bubbles provide space for water to migrate to as the freezing advances. The hydrostatic pressure forces the water through small capillary pores to the closest air bubble. This relieves the pressure and prevents the concrete from being cracked. However, this only works if there is an adequate amount of air bubbles (air content) and they are spaced close enough (spacing factor). If not enough air is entrained or the pumping process negatively affects the air void system, air entrained concrete can also be susceptible to freeze thaw damage.

When the hydrostatic pressure theory was found to be inconsistent with experimental data, Powers and Helmuth [59] introduced the osmotic pressure theory. This theory used thermodynamics and osmosis to account for the dissolved alkalis in the pore water. These alkalis cause a gradual formation of ice with

decreasing temperature. In this theory, the water's freezing temperature depends on the pore size. Due to an energy imbalance caused by the differing freezing temperatures water flows from smaller pores to larger ones to reach equilibrium. The motion creates internal pressure and can cause cracking unless a sufficient air void system is present in the concrete. Powers and Helmuth [59] suggested limiting spacing factors to 250-300 μm to prevent damage within the concrete. For natural freeze-thaw cycles, Pigeon and Lachance [62] determined a slightly stricter limit of 200 μm.

Litvan's [60] later theory is based on the assumption water must travel through the paste and will only freeze on the exterior surface as due to changes in vapor pressure, water cannot freeze in the capillary pores. In this theory, if the freezing rate is too fast or the distance to the external surface is too large, internal pressure can cause damage.

Although the exact mechanisms which cause freeze-thaw damage are still unconfirmed, it is generally accepted that the freeze-thaw durability of concrete relies greatly on the quality of the concrete's air-void system [57]. Air-voids must be small in size, closely spaced, and uniformly distributed to ensure adequate resistance to freezing and thawing as well as satisfactory strength.

Overall, it has been observed that the spacing factor is the most critical factor to frost durability [63]. However, often in the United States, air content is associated with freeze-thaw and scaling resistance. In ACI 318 "Building Code Requirements for Structural Concrete," [64] the American Concrete Institute gives a target air value for concrete. This is a function of the nominal maximum aggregate size and the exposure of the concrete to freezing and thawing cycles. Concrete which is expected to be exposed to freeze-thaw cycles and frequently exposed to water is required to contain between 1-1.5 percent more air than those of the same maximum aggregate size that is not frequently exposed to water. This air content-to-frost durability association can be misleading because air content alone is not the best indicator for frost durability. Concretes at the same air content can result in a range of frost durability [65]. This is because the measurement only reports total air content. It gives no indication of size of air voids or space distance between voids, which are vital to frost durability [63].

A decrease in air content is not always connected to a decrease in quality of the air-void system [66, 67]. The exception is when the air content is low enough that the spacing factor is not able to be low enough to prevent freeze-thaw damage due to lack of air. Therefore, in concrete pumping, air loss itself is not necessarily detrimental to freeze-thaw durability. The relatively large bubbles do not aid as much in the freeze-thaw durability as the small air bubbles. It is generally accepted that a specific surface, which indicates the average air-void size, should be greater than 24 mm^2/mm^3 for frost durability [68]. So, if large air bubbles are lost in the pumping process, air content will decrease but the durability will not. These large bubbles are the ones removed when conventional concrete is vibrated. This act increases the quality of the concrete, particularly the strength [69]. When the fresh air content is measured, the size or distribution of air bubbles lost cannot be determined. Therefore, it is important to analyze the hardened air voids and calculate the specific surface and spacing factor to determine the durability.

Air content, spacing factor, and specific surface can all be altered due to pumping and are interconnected so a slight dissatisfactory value of one does not necessarily mean complete compromise of durability. Some of the studies examined reported that mechanisms in the pumping process resulted in unsatisfactory air-void parameters according to acceptance standards, however the overall system was not compromised enough to be detrimental to the freeze-thaw durability [67, 70, 71].

Two mix design factors that have the potential to affect the frost durability are fly ash and the water-to-cement ratio. Fly ash has the potential to decrease the frost durability by altering the effectiveness of the air entraining admixture. The use of fly ash can make identifying the correct air entertainer dosage difficult. On the other hand, a low enough water-to-cement ratio has the potential for rendering the air entraining admixture unnecessary to prevent frost damage.

Fly ash is a byproduct of coal combustion in coal-fired power plants. Fine, glassy, spherical particles with diameters less than 60 μm are liberated from mineral inclusions as the combustible coal is consumed. These particles are collected in particulate controls systems [72]. The fly ash collected requires no alterations before being used in concrete as long as it conforms to the properties and composition requirements listed in ASTM C618 "Standard Specification for Coal Fly Ash and Raw or Calcined Natural Pozzolan for Use in Concrete" [73]. Typically, fly ash is used to replace 15-30% of the cement content.

Unburned portions of coal in fly ash can adsorb organic material such as the surfactants used in air-entraining admixtures [74, 75, 76, 77] and inhibit the ability of the air-entraining admixture to stabilize air bubbles [72]. Typically, the higher the carbon content the larger the effect on the air entrainment [74, 77, 78, 79, 80, 81, 82]. Effects of using fly ash include a decrease in permeability of the concrete [83] and a decrease of air content with an increase in carbon content [53]. It has been observed that all concretes using fly ash require a higher dosage of air-entraining admixture and Class F requires larger dosages than Class C [78].

It is debated whether concretes with very low water-to-cement ratios, such as high performance concrete, need air entrainment for durability [84]. Durability is mainly dictated by the severity of the environment and the permeability of the concrete. Self-desiccation creates a somewhat disconnected network of capillaries and pores [84]. Additionally, the porosity of concrete decreases as the water-to-cement ratio decreases [84, 85, 86]. If water cannot penetrate the concrete, low temperatures may not result in frost damage.

Overall, frost durability relies strongly on the air-void system. Pumping can alter the air-void system in concrete [65, 66, 67, 68, 69, 70, 87, 88]. If this air-void system is significantly altered the resistance to freeze thaw cycles is decreased. If the air-void system is durable and robust to start with, the changes in the air void system will not affect the freeze-thaw durability of the concrete itself. Fundamentally durable concrete will not be affected by pumping [66].

2.5.2 Scaling Damage.

Salt scaling attacks the concrete surface a layer at a time and is an aesthetic damage rather than a structural damage. It usually only affects the top few millimeters of the concrete [57]. Though it has been observed to normally happen when deicer salts (commonly NaCl or $CaCl_2$) are being used, it was thought to predominantly be a physical damage and not chemical. is an example salt scaling damage (Figure 31).

Figure 31. Salt scaling damage.

Scaling is a complicated phenomenon and no single mechanism has been confirmed as the cause of damage. Over the years, there have been several mechanisms proposed to explain scaling, however according to Valenza II [89], none have accounted for all of the salt scaling characteristics. One common shortcoming of all of the physical explanations is that none of the theories can account for pessimum concentration. These theories include damage caused by internal crystallization from hydraulic pressure or crystallization pressure, thermal shock, a reduction in vapor pressure, and osmotic pressure.

Two theories which were first proposed to explain the cause of frost damage dealt with internal crystallization. The hydraulic pressure theory was one of the first theories suggested by Powers [58] to cause frost damage, this includes scaling damage. This theory has been previously discussed in the freeze-thaw damage section. Once laboratory research disproved the hydraulic pressure theory [59], Helmuth [90] theorized that crystallization pressure caused scaling damage. This theory is based on the fact that when porous bodies contain liquids that have larger specific volumes than the corresponding solid they are damaged when frozen [91]. However, neither theory can account for the lack of damage when there is not a pond of solution [89].

Another theory states: thermal shock or temperature shock can induce cracking when de-icer salts are applied to a thin layer of ice on top of the concrete. This is due to the temperature gradient induced by the salt [92, 93]. There are multiple shortcomings to this theory. According to the calculations performed by Valenza II [89] the required temperature drop is 8° C. Though this temperature drop has been reached in the lab, field tests have resulted in significantly lower changes in temperature. Between multiple researchers and studies, none reached a temperature drop of more than 4.3° C in the field [92]. Additionally, this theory cannot account for the studies which show freezing a saline solution rather than applying salt to ice on a concrete surface is more damaging [89].

Some researchers believed internal crystallization facilitated by vapor pressure is the cause of scaling damage. The salts lower the vapor pressure and decrease the temperature at which ice is formed. The decreased vapor pressure increases the degree of saturation in the concrete compared to a salt free concrete at the same relative humidity. Therefore, the damage is caused by internal crystallization [94, 95]. This is based on Raoult's Law which indicates pure water has a higher vapor pressure than a diluted salt solution [89]. However, the theory cannot explain why a concentration of approximately 3% salt results in a large increase of scaling but not in degree of saturation [89, 96].

The next theory that will be discussed involves the osmotic pressure. If the pore fluid salt concentration increases, the degree of saturation increases on the surface and reduces ice formation in pores [97, 98]. In this way the salts amplify the osmotic pressure due to freezing and there is an increase in vapor pressure difference between the water in the capillary pores and the ice on the external face [89]. However, the osmotic pressure will never reach a destructive level. Additionally, this theory does not account for the absence of damage when there is not a puddle of solution on the concrete surface [89].

Though there are many theories to explain salt scaling, none can fully explain the phenomenon which is observed. What is known is scaling attacks the surface layer which tends to be made of paste, making it more porous than the rest of the concrete and air entrainment is the most direct factor which affects the scaling resistance of concrete [63].

It has been observed that the same precautions can be taken to prevent scaling damage as freeze-thaw damage. Overall, either a robust air-void system is needed or a low enough water-to-cement ratio (w/c) [99]. Results have shown air entrainment to prevent scaling damage is not necessary in Ultra High Performance Concrete [100]. Additionally, fly ash [78, 101] and the water to cement ratio [96, 102, 103, 104, 105] affect scaling as discussed previously. The same critical spacing factor of 250-300 μm has been cited as the maximum spacing factor to prevent scaling damage as freeze-thaw damage [106, 107]. Some research has shown that when the critical spacing factor is exceeded, mass loss is proportional to the spacing factor [106, 107]. To prevent frost damage, the air-void system and permeability of the concrete are key properties.

2.6 Pumping and changes in the air-void system

Many experiments have been conducted to attempt to determine the effects pumping concrete has on the air-void system and consequently the freeze thaw and scaling durability. These include laboratory testing and

full-scale pumping experiments. A majority of these tests have been related to conventional concrete [66, 67, 68, 69, 70, 71, 108, 109] while fewer have examined the effects on self-consolidating concrete [65, 110]. Normal concrete and self-consolidating concrete have shown different results while being tested [65] and behave differently, therefore they must be considered independently.

Nearly every aspect and ingredient of mixing and placing concrete can affect the air void system [71]. Therefore, a cross-section of mix designs must be analyzed when attempting to generalize the effects pumping concrete has on the air-void system and freeze-thaw and scaling durability. Additionally, there must be a large amount of data points from which to draw conclusions because isolated reports from the field may be misleading because of other variances.

There are precautions that have to be taken in order to isolate the cause of the air-void change. Hover, Phares, and Ozyildirim [66, 71] all observed the truck-to-truck variation is often times greater than the in-truck variation due to pumping or handling. Therefore, it is equally important to carefully mix and monitor each truckload of concrete in a project. When testing the effects of pumping, it was suggested using one truck of concrete to eliminate the truck-to-truck variation. Additionally, when testing the effects of pumping conventional concrete it can be hard to tell if the same "slug" of concrete is being tested before and after pumping. This makes it necessary to determine the normal variability for concrete from the same load. In the test performed by Hover, Phares and Yingling et al. [66, 69, 108] none reported the air content more accurately than the air meter reading plus or minus the variation found within the truck from multiple samples before pumping.

Laboratory testing has been conducted to isolate mechanisms which are suspected to affect the air-void system during the pumping of concrete [68, 108, 109]. These studies show possibilities of what will result when concrete is being pumped. However, pumped concrete specimens will not directly follow the trends observed because during pumping, concrete is subjected to multiple mechanisms at the same time, therefore the results are more complicated.

Yingling et al. [108] confirmed that impact can cause air to be removed from concrete. This air does have the possibility of being entrapped back in the concrete [68]. Concrete being discharged at high velocities into concrete at rest creates conditions that are comparable to those in the concrete mixer. This can cause a remixing of the concrete, allowing it to entrain/entrap additional air. The amount of air forced back into the concrete at this point can cancel out or even overcome the negative effects from the previous impact on the air content. Additionally, the concrete at rest can cushion the flowing contact, reducing the effect of the impact by absorbing some of the kinetic energy [65]. Due to the higher internal pressure of the small air bubbles, they will be less susceptible to the negative effects of the impact. Therefore, mainly larger air voids are lost due to impact because of their higher buoyancy and consequently lower stability. Since primarily the large air bubbles are lost, the spacing factor is not greatly increased due to it [67]. As a result, the impact can cause a loss of air content but is unlikely to reduce the frost durability of the concrete.

Elkey et al. and Boulet et al. [68, 109] investigated the effects of pressure on concrete. The results from both researchers indicate that applying pressure to concrete negatively affects the air void system. Elkey et al. [68] found as the pressure increased the chord length of the concrete also increased. This increase in chord length resulted in fewer and larger air voids. Figure 32 shows results obtained by Elkey et al. [68]. Boulet et al. [109] reported that the pressure yielded a decrease in total number of air-voids and in increase in the average size of air-voids. A notable relationship between the pressure and the specific surface was also observed. This test showed that the spacing factor of the concrete increased linearly with the pressure applied to the concrete, which can be seen in Figure 33. The conclusion from this laboratory study was that the duration of the pressure was not as much of a factor because the damage done to the air-void system only took a few moments to complete. It is worth to mention that Elkey et al [68] obtained similar increases in the spacing

factor as the pressure applied to the sample of concrete increased, but when fly ash class F was incorporated as part of the paste the changes in the spacing factor were minimized (Figure 34).

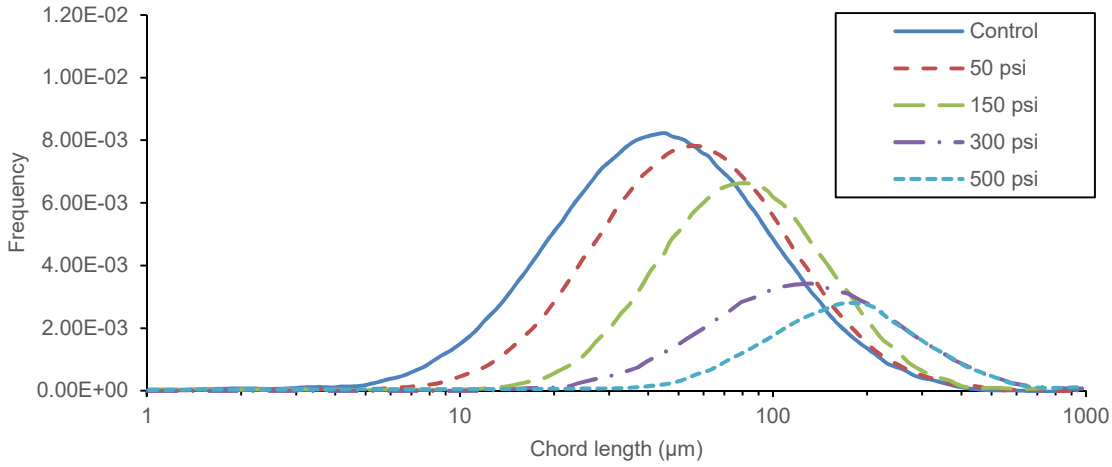

Figure 32. Effect of Pressurization on the Chord Length [68].

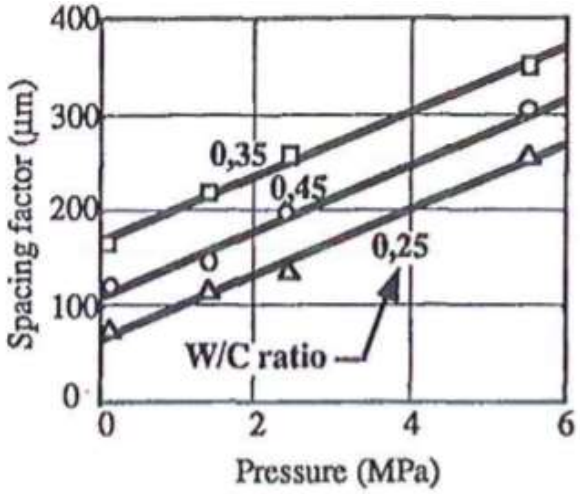

Figure 33. Spacing Factor and Pressure Applied for 10 Seconds Relationship [109].

Full-scale pumping experiments have rendered a variety of results. Kenneth Hover [69] said, "The only certainty in regard to the effect of pumping on the air content of fresh concrete is that pumping has been observed to increase air content, to decrease air content, or to have no measurable effect." Ozyildirim's [71] observations suggested the composition of the concrete and beginning air-void system plays a large role on the effects pumping has on the concrete.

For conventional concrete, Ozyildirim [71] found that generally, pumping reduces air content. Similar results were observed by both Lessard et al. and Pleau et al. [67, 70] when pumping horizontally. Both studies found a slight increase in spacing factor and a significant decrease in specific surface. However Lessard et al. [70] found horizontal pumping had no effect on slump or fresh air content while Pleau et al. [67] observed a small increase in air content. Both Lessard et al. and Pleau et al. [67, 70] observed that vertical pumping greatly increased the spacing factor of the concrete. However, Lessard et al. [70] measured small effects on the slump and air content and a significant reduction of the specific surface and confirmed that a reducer to the end of a vertical section can aid in conserving the air void system for normal concrete (Table 3) [70]. Pleau et al.

[67] measured significantly lower air content and a constant specific surface due to the vertical pumping (Table 4).

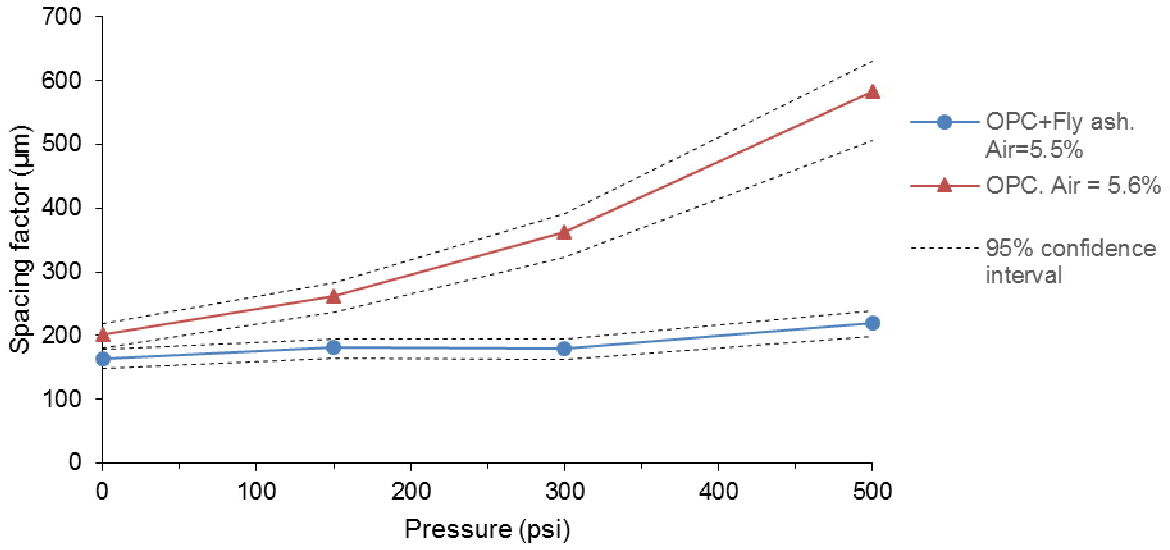

Figure 34. Effect of pressure on the spacing factor under the presence of fly ash type F. Adapted from [68].

Table 3. Effect of reducers placed at the boom discharge on freeze-thaw and de-icer scaling durability. Adapted from Lessard et al [70].

	BOOM SETUP						
	1st Horizontal pumping		2nd Vertical pumping		3rd Vertical pumping		
	Before	After	Before	After	Before	After	
						No reduced end	Reduced end
SLUMP, MM	105	110	95	85	90	115	115
AIR CONTENT (FRESH STATE), %	4.5	4.6	4.3	3.4	4.5	4.0	4.2
PUMPING PRESSURE (MAX), PSI		300		340		250	
AIR CONTENT (HARDENED STATE), %	5.1	5.7	3.9	3.1	5.9	4.8	4.1
SPACING FACTOR, µM	190	220	180	305	195	250	215
DE-ICER SCALING MASS LOSS AFTER 50 CYCLES, KG/M²	0.15	0.12	0.19	0.49	0.29	0.66	0.34
FREEZE-THAW DURABILITY FACTOR, %	99	99	102	97	99	98	101

Air loss has been observed to be associated with pumping for self-consolidating concrete. Based on the data collect by Vosahlik et al. [65], for self-consolidating concrete a relationship appeared to exist between flow rate and change in the spacing factor for concrete when pumped vertically. An increase in flow rate, increased

pumping pressure, and consequently increased the spacing factor. This could be due to the considerable loss of air.

It has been found for conventional concrete, that a reducer is beneficial in preserving the spacing factor by preventing partial emptying of the descending section of boom [70]. Test results indicate the opposite outcome on the air void system is true for self-consolidating concrete. A reducer can substantially coarsen the air void system. The pressure can rise by 50 to 75% when using a reducer. The reducer can also increase the risk of segregation due to the intense shearing. This can make it easier for the air bubbles to escape upon placement [65, 110].

Table 4. Summary of changes induced by horizontal and vertical pumping reported by Pleu et al. Adapted from [67].

		FRESH CONCRETE	HARDENED CONCRETE						
			Total air voids			Only air voids < 300 µm			
		Air content (%)	Air (%)	Specific surface (mm^{-1})	Spacing factor (µm)	Air (%)	Specific surface (mm^{-1})	Spacing factor (µm)	Flow length (mm)
HORIZONTAL PUMPING	Before	5.9	4.3	33.6	160	2.0	42.9	170	170
	After	6.1	4.7	23.1	225	2.1	37.5	190	195
VERTICAL PUMPING	Before	6.4	5.6	21.8	205	2.0	42.0	175	175
	After	4.8	3.6	21.6	265	1.1	40.0	235	305

However, in the study conducted by Vosahlik et al. [65], it was found that an increase in spacing factor can be directly related to an increase in pressure in the form of a higher flow rate. This was determined to be independent of the mix design. Additionally, in this experiment, it appeared the pressure-dissolution mechanism which negatively affects the air void system outweighed the shearing mechanism which positively affects the air void system.

In the same study, when a reducer was added to the vertical pumping configuration it was determined that the reducer, again, had a negative effect on the self-consolidating concrete. The spacing factor was significantly increased due to the use of a reducer. The author proposes two reasons for this result. First, some mixtures which showed this tendency were segregated and air is removed from segregated concrete much easier than non-segregated. The second reason was the large pressure induced on the concrete due to the reducer's small diameter. This increased the dissolution of the air due to the pressure-dissolution mechanism and increased the spacing factor out of specification in most cases. Results from this study can be found in Figure 1.

2.7 The effect of pressure on the rheology of air-entrained cement paste

2.7.1 Are air bubbles deformed?

Typically, air-entrained concrete shows lower viscosity than non-air-entrained concrete with the same w/c [12], but this is not necessarily true under pumping conditions. The role of entrained air on the rheological properties is one of the hardest to elucidate because when concrete flows under pressure, the air bubbles are prone to be dissolved in the water and reappear when pressure is removed, altering air bubble volume and size distribution [50, 66, 67, 68, 87, 88].

Bubbles in fluids act as soft particles susceptible to be deformed by the shearing forces acting on its surface [111]. This shape distortion is described in literature by the capillary number (equation 21) and it expresses the ratio between viscous forces and surface tension as follows:

$$Ca = \frac{\dot{\gamma}\eta a}{\Gamma} \qquad \textit{(Eq. 21)}$$

Where:

$Ca =$ Capillary number (-)

$\dot{\gamma} =$ Shear rate (s^{-1})

$\eta =$ Apparent viscosity of the suspending medium (Pa s)

$a =$ Bubble diameter (m)

$\Gamma =$ Surface tension at the water-air interface (N/m)

When $Ca \gg 1$, the shearing forces on the bubble surface are sufficiently high to overcome the surface tension, the bubble elongates and reduces the apparent viscosity of the fluid [112, 113]. At $Ca \ll 1$ the surface tension is strong enough to keep the bubbles spherical and amplify the overall rheological properties [111] (Figure 35).

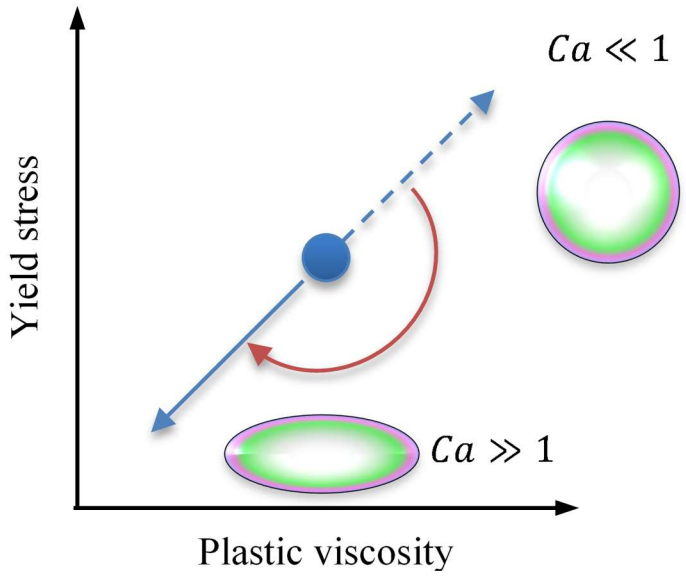

Figure 35. Effect of air bubbles as function of the capillary number on the rheological properties of suspensions.

The amplification of the rheological properties due to non-deformable solid particles is covered by the Krieger-Dougherty equation [38, 114], as it predicts the relative viscosity of a concentrated suspension in function of the solid volume fraction of suspended particles (equation 13). Figure 36 plots the Krieger-Dougherty equation and shows that if particles are taken out of the suspending medium, the relative viscosity of the suspension must decrease.

Therefore, the pressurization and subsequent dissolution of non-deformable air bubbles leads to a decrease in the apparent viscosity of suspensions [115]. It is important to mention that the Ca in concrete may be sufficiently large to deform a significant fraction of the air-void system if the surface tension is low and the shear rates experienced by the constituent paste are high. Furthermore, pressure is applied through pulses made by the pump pistons and decreases gradually as the concrete gets closer to exit the pipeline. Hence, during pumping operations, it would be possible for the air bubbles to dissolve and reappear between pulses as well as deform for a brief period of time while the concrete is being pressurized again by the next piston stroke and dissolution is taking place. However, the evaluation of the rheological properties under pressure is still more representative of the behavior during pumping at least during the fraction of time that one piston stroke last.

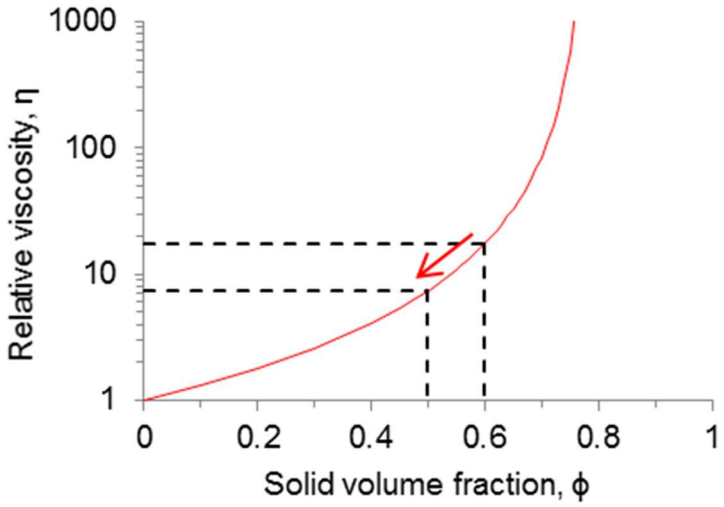

Figure 36. Effect of particles removal on the relative viscosity of suspensions.

2.7.2 The dissolution of air in water

The physical background for air dissolution and reappearance is covered by Henry's law (equation 22) which states that, in steady-state conditions and at constant temperature, the concentration of gas that can be dissolved in a liquid is proportional to the partial pressure of that gas in that liquid [68]:

$$p = kC \qquad \textit{(Eq. 22)}$$

Where:

$p =$ Partial pressure

$k =$ Henry's law constant (For common air at 20° C, k = 6.64)

$C =$ Concentration of the dissolved gas in solution at equilibrium

The parameter C in equation 22 describes the scenario where the gas molecules entering the liquid phase is equal to the amount of gas molecules being released from the liquid. It is clear from equation 22 that when pressure increases, the concentration of dissolved gas in solution must increase proportionally. Therefore, the minimum pressure to fully dissolve a concentration C_2 of a given gas parting from the initial conditions P_1 and C_1 can be calculated using equation 23.

$$P_2 = \frac{P_1 C_2}{C_1} \qquad \textit{(Eq. 23)}$$

Where:

$P_2 =$ Equilibrium pressure for concentration C_2

$P_1 =$ Initial pressure

$C_1 =$ Solubility of gas in water at pressure P_1 (% vol/vol)

$C_2 =$ Solubility of gas in water at pressure P_2 (% vol/vol)

At sea level, the solubility coefficient of air in water is 1.85 %v/v (% volume of gas/volume of water) at 20ºC [116]. To correct for the local altitude, 1.84 %v/v was used to compute the theoretical minimum pressure to fully dissolve the air bubbles into the liquid phase of the paste.

Furthermore, if a fluid is under shearing conditions dissolution is expected to happen faster. Favelukis et al [117] performed experiments where air and CO_2 bubbles were stabilized in polyisobutylene (PB24 and

PB32), a clear Newtonian low molecular weight polymer. The samples were subject to Couette flow within the range of 20-2 s^{-1} at ambient pressure (Figure 37). They found out that the diameter of the monitored bubbles decreased faster as the shear rate increased.

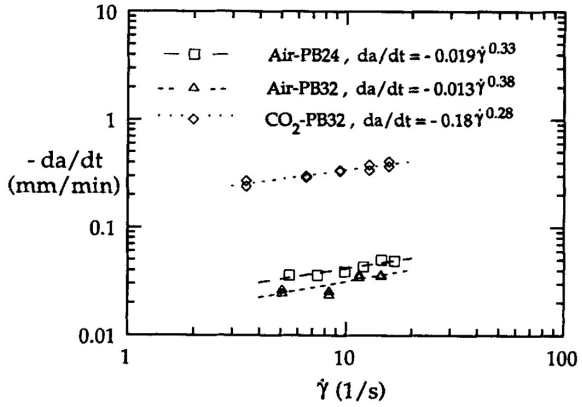

Figure 37. Dissolution rate of air and CO2, bubbles in PB24 and PB32 as a function of the shear rate at 30°C and ambient pressure [117].

Air exists in concrete as discrete air bubbles of different sizes that do not easily coalesce when air entrained polymers are added and are deemed to be stable. In order to be stable, the mass transfer from the bubble to the surrounding water must be minimum. As mentioned before, gases are susceptible to be dissolved in water and the capacity of water to carry dissolved gases depends on the nature of the gas, pressure and temperature [116]. Then, when concrete is under pressure, air will tend to be dissolved immediately due to the large bubble surface area that is in contact with water and diffuse further from the bubble film until the water becomes saturated. Another factor helping air dissolution is the fact that the smaller bubbles are the ones more susceptible to be dissolved or transfer their mass by diffusion to larger bubbles because small bubbles are already under higher internal pressure due to the surface tension of the surrounding liquid [116]. The air can be dissolved partially or totally depending on: the volume of air in the concrete, the water availability around the bubble and the pressure exerted [88], the portion of concrete sheared inside the pipe, degree of equilibrium between the air-water interface achieved during the pressurization time, filling coefficient of the pump pistons and the permeability of the air-entraining admixture bubble film [87].

3 Comparison of Rheometers available at Missouri S&T

This section contains a campaign undertaken to compare the results generated by the different rheometers available at Missouri S&T. This was essential for the work described in Section 4.

3.1 Objective

The purpose of this task is to derive transformation equations to translate rheological properties: i.e. yield stress and plastic viscosity, obtained from one rheometer to another. As will be discussed in Section 4, the rheological properties of paste, mortar and concrete were simultaneously used in one complex equation. Any differences in parameters from the rheometers causes issues in trying to understand how concrete constituent materials affect rheology and the lubrication layer.

3.2 Material

As different rheometers have different shear rate ranges, comparing cement pastes could not be performed, as the applied shear rate influences the rheological properties [118]. The chosen material was a replica of the NIST reference material for cement paste, composed of corn syrup, distilled water and limestone powder [119]. One large batch was created (the largest rheometer has a required volume of approximately 15 l) and evaluated in each rheometer. It should be noted that this is not the original NIST reference material, but a non-calibrated replica. Table 5 shows the composition of the reference material.

Table 5. Composition of the replica of the NIST reference material for cement paste.

MATERIAL	QUANTITY (KG)
CORN SYRUP	18.63
DISTILLED WATER	5.89
LIMESTONE POWDER	42.68

3.3 Rheometers

3.3.1 Anton Paar MCR 302

The Anton Paar MCR 302 served as reference rheometer, as it has the largest flexibility in setting the shear rate range and can be used at a wide range of different temperatures. It was used to mimic the shear rate range of each rheometer separately, in order to compare the results of each rheometer with the Anton Paar. The chosen geometry was a serrated concentric cylinder system, with an inner radius of 13.3 mm, and outer radius of 14.5 mm and a height of the vertical portion of the inner cylinder of 40.0 mm. The Anton Paar MCR 302 is capable of measuring on cement pastes with a maximum particle size of 0.2 mm in the chosen configuration.

3.3.2 ConTec Viscometer 6

The ConTec Viscometer 6 is a robust mortar rheometer based on coaxial cylinders. It has an inner radius of 50 mm and an outer radius of 61.5 mm. The inner cylinder is composed of two parts: the top part is connected to the load cell and registers torque. The bottom part is not connected to the load cell and serves to eliminate the complex 3-D flow at the bottom of the rheometer. Due to different filling heights of the reservoir, the height of the portion of the top part of the rheometer submerged in the material must be measured after every test, as the top ring was not used. The inner cylinder is equipped with ribs to minimize wall slip, the outer

cylinder is coated with a serrated rubber for the same purpose. The ConTec Viscometer 6 can be used to measure the rheological properties of mortars with a maximum particle size of 2 mm.

3.3.3 ConTec Viscometer 5

The ConTec Viscometer 5 is a larger version of the ConTec Viscometer 6, and its working principle, design and layout are identical, including the composition of the inner cylinder with two pieces. Two configurations were evaluated with the ConTec Viscometer 5, named 5S and 5W. The 5S configuration is suitable for mortars with 5 mm max particle size, while in the 5W setup, concrete mixtures with particles up to 15 mm can be measured. The inner cylinder measures 65 and 100 mm, respectively for the 5S and 5W. The outer cylinder is 82 or 145 mm, for both configurations, respectively.

3.3.4 ICAR Rheometer

The ICAR rheometer is developed as a portable rheometer, able to measure the rheological properties of concrete mixtures with particles up to 20 mm, in the standard configuration. The inner cylinder is a 4-blade vane, with an inner radius of 63.5 mm and a height of 127 mm. The outer radius, composed of the bucket, is 143 mm. Similarly to the ConTec Viscometer 5, the bucket is equipped with vertical ribs to reduce wall slip. The vane geometry limits wall slip at the inner cylinder.

3.4 Rheometer procedures and analysis

3.4.1 Procedures

The ConTec Viscometers and the ICAR rheometer only allow stepwise velocity profiles to be used, with a preshear period if desired. The range of velocities is fixed by the capacity of the motors. For the ConTec Viscometer 6, 5S, 5W, and the ICAR rheometer, a maximum rotational velocity of 0.71, 0.50, 0.40 and 0.5 rps, respectively was imposed. The minimum velocity used was 0.03 rps for the ConTec 6, 0.025 rps of the ConTec 5S and 5W and 0.05 rps for the ICAR. All procedures had 7 steps, with a pre-shear period at the maximum rotational velocity of 20 s. All tests were executed at three different temperatures: low (2°C), room (20°C), and high (35°C). The reference material and all portable, non-electronic rheometer components were brought to each temperature prior to testing. Temperature of the sample was measured before and after each test. At each temperature, three measurements were performed.

For the Anton Paar MCR 302, the imposed procedure was a linearly decreasing ramp preceded by a pre-shear procedure. The pre-shear had the same duration as for each rheometer, while the maximum and minimum shear rate imposed were calculated from the other rheometer tests. Tests were thus performed at each measured temperature (for each rheometer), and at each shear rate range for each other rheometer separately.

3.4.2 Analysis

For all rheometers, the analysis was performed by fitting a linear relationship to the torque-rotational velocity data ($T = G + H N$), and transforming G and H into yield stress and plastic viscosity by means of the Reiner-Riwlin transformation procedure. Special attention was paid to measurement artefacts, as mentioned in [120], and an iterative correction was executed for plug flow if necessary. As such, at each test temperature, a set of rheological properties is available for each rheometer. Transforming the maximum and minimum torque, following the principles from the Reiner-Riwlin equation delivers an average shear stress. With these shear stress values, and the known rheological properties, the maximum and minimum shear rate were calculated.

Figure 38 shows the raw data profile for the material from the Anton Paar rheometer. Some shear thinning is clearly visible, which complicates the transformation. As no plug flow correction is yet available for non-linear rheological profiles (a procedure developed by the research group is very sensitive to small errors), the Bingham model had to be applied to the data. This means that the rheological properties are dependent on the used shear rate range (Table 6), and that a direct transformation between ConTec 6, ConTec 5S or 5W,

or ICAR is not possible. However, a transformation to the Anton Paar MCR 302 is available for each rheometer.

Table 6. Shear rate ranges for each rheometer at room temperature.

RHEOMETER	MIN SHEAR RATE (1/S)	MAX SHEAR RATE (1/S)
CONTEC 6	0.4	21.1
CONTEC 5S	0.4	13.2
CONTEC 5W	0.3	6.8
ICAR	0.7	3.9

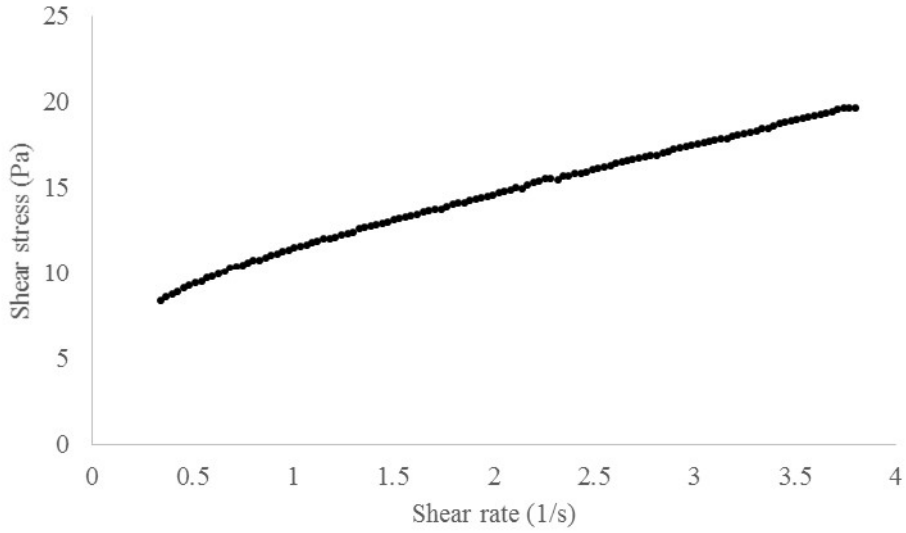

Figure 38. Shear rate profile in the Anton Paar MCR 302 for the reference material.

3.5 Comparison between rheometers

Figure 39 and Figure 40 show the comparison for yield stress and viscosity, respectively. The Y axes contain the values of ConTec 6, 5S, 5W and the ICAR, the X axes are the respective values in the Anton Paar MCR 302, at the same shear rate range. Good correlations can be observed between all rheometers, except for the yield stress in the ICAR rheometer. Each rheometer seems to have an individual correlation with the Anton Paar rheometer for the yield stress, and the range of yield stress values decreases with increasing gap size of the rheometer. For the viscosity, the ConTec 5S, 5W and ConTec 6 all have nearly the same correlation equation compared to the Anton Paar. The ICAR rheometer is a bit more difficult to evaluate. Regardless of the rheometer used, for viscosities inferior to 5 Pa s, all rheometers deliver nearly the same value.

The ICAR rheometer delivers a couple of issues. For the low temperatures, the measurement gives apparently negative yield stress values. Although the cause is unknown, it may be the consequence of large fluctuations in the signal, compared to the measured torque value, the extrapolation to zero shear rate, and the sensitivity of the sensors to temperature. The yield stress follows no logical correlation with the Anton Paar. As such, we will assume that the yield stress of the ICAR and the yield stress of the ConTec 5W are similar, for the devices in our possession. It should be noted that this statement is not universally valid. For viscosity, the results at room and high temperature coincide with the results from the Anton Paar rheometer. The result at

low temperature, when setting the yield stress artificially to zero, leads to a viscosity value between the ConTec rheometers and the Anton Paar.

Table 7 and Table 8 show the transformation equations between each rheometer and the Anton Paar for yield stress and plastic viscosity, respectively.

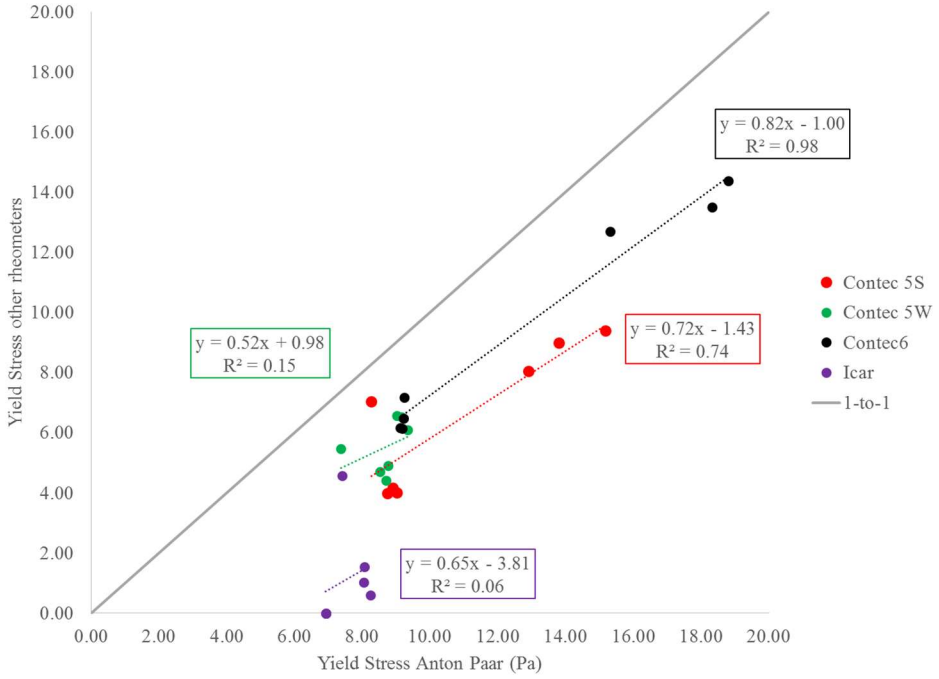

Figure 39. Yield stress comparison between ConTec 6, 5S, 5W and ICAR and the Anton Paar.

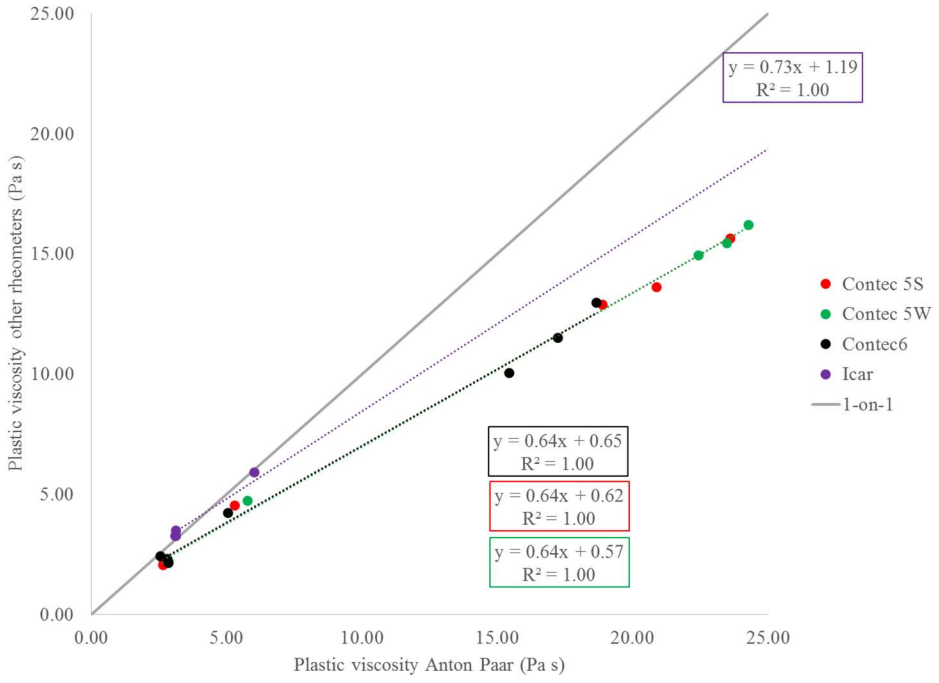

Figure 40. Plastic Viscosity comparison between ConTec 6, 5S, 5W and ICAR and the Anton Paar.

Table 7. Transformation equations for yield stress.

	TRANSFORMATION TO ANTON PAAR	TRANSFORMATION FROM ANTON PAAR
CONTEC 6	$\tau_{0,AP} = 1.18\tau_{0,C6} + 1.50$	$\tau_{0,C6} = 0.82\tau_{0,AP} - 1.00$
CONTEC 5S	$\tau_{0,AP} = 1.02\tau_{0,C5S} + 4.31$	$\tau_{0,C5S} = 0.72\tau_{0,AP} - 1.43$
CONTEC 5W	$\tau_{0,AP} = 0.28\tau_{0,C5W} + 7.15$	$\tau_{0,C5SW} = 0.52\tau_{0,AP} + 0.98$
ICAR	Not available	

Table 8. Transformation equations for viscosity, if the viscosity is above 5 Pas.

	TRANSFORMATION TO ANTON PAAR	TRANSFORMATION FROM ANTON PAAR
CONTEC 6	$\mu_{p,AP} = 1.56\mu_{p,C6} - 0.96$	$\mu_{p,C6} = 0.64\mu_{p,AP} + 0.65$
CONTEC 5S	$\mu_{p,AP} = 1.56\mu_{p,C5S} - 0.94$	$\mu_{p,C5S} = 0.64\mu_{p,AP} + 0.62$
CONTEC 5W	$\mu_{p,AP} = 1.56\mu_{p,C5W} - 0.88$	$\mu_{p,C5W} = 0.64\mu_{p,AP} + 0.57$
ICAR	$\mu_{p,AP} = 1.37\mu_{p,ICAR} - 1.64$	$\mu_{p,ICAR} = 0.73\mu_{p,AP} + 1.19$

3.6 Summary

A comparison was made between the ICAR rheometer, the ConTec Viscometer 6, the ConTec Viscometer 5 in small and large configuration and the Anton Paar MCR 302 rheometer. The material was a reproduction of the NIST reference material for cement paste and was evaluated at three different temperatures. Each rheometer, except the Anton Paar, is more or less limited in setting ranges of parameters, and as a consequence, a different shear rate range was applied in every rheometer. These shear rate ranges were reproduced in the Anton Paar to be able to complete the comparison, especially as the material shows shear thinning behavior, making the rheological properties dependent on the applied shear rate.

Transformation equations between each rheometer and the Anton Paar were developed for yield stress and viscosity, enabling for each rheometer to be compared with each other, with an intermediate step of comparison with the Anton Paar. Yield stress determination with the ICAR rheometer was more challenging and at low temperatures no feasible values of yield stress were found. Because of a lack of logical correlation for yield stress between the Anton Paar and the ICAR, it is assumed that the ConTec Viscometer 5W and the ICAR deliver similar yield stress values.

This portion of the research now allows to compare the results between different rheometers, which is necessary for the next task in determining the composition and thickness of the lubrication layer.

4 Lubrication Layer Thickness and Composition

4.1 Objective

Changes in fresh and hardened properties of concrete are caused by the exposure to pressure and shear rate during the pumping process. However, pressure and shear rate depend on the desired flow rate, the boom length and diameter, and on the rheological properties of the material. Furthermore, as discussed in the literature review, a lubrication layer is formed near the pipe wall, facilitating pumping operations: this means, it reduces pressure and shear rate in the concrete.

Several attempts have been made to characterize this lubrication layer and the velocity profile when concrete flows through a pipe, but regardless of the approach, the lubrication layer is regarded as a single homogeneous layer. However, according to the principles of shear-induced particle migration in suspensions with different particle sizes, each particle size should undergo migration away from the wall, with the larger particles migrating quicker. The current state-of-the-art is not capable of describing or simulating this phenomenon, but the general assumption of a single homogeneous layer is not valid. Instead, it should be composed of a concentration gradient of particles, which can be idealized as layers each with a different particle size, up to homogeneous bulk concrete. Even more, the thickness of these layers should see a statistical variation with space and time. The composition and thickness of each of these layers is unknown, and current techniques are not able to evaluate this effect. This section describes a first attempt to reverse-engineer the multi-layer composition of the lubrication layer.

4.2 Theoretical concept

This section describes a first attempt to reverse-engineer the multi-layer composition of the lubrication layer. When performing an interface rheometer test, the area around the inner cylinder is split in multiple layers, each with a fixed maximum particle size. In this work, six layers are assumed: paste (maximum particle size 75 µm), mortars with maximum sizes of 300 µm, 600 µm, 1.18 mm, 2.38 mm and 4.75 mm, followed by homogeneous concrete. Each layer is assumed to have constant rheological properties. When knowing the torque and rotational velocity in the interface rheometer, for each measured data point, and when knowing the rheological properties of each layer, one can calculate the best possible combination of layer thicknesses to fit the data from the interface rheometer, by using the following formula (equation 24):

$$\Delta N_x = \frac{T}{8\pi^2 h \mu_{p,x}} \left(\frac{1}{R_{i,x}^2} - \frac{1}{R_{o,x}^2} \right) - \frac{\tau_{0,x}}{2\pi\mu_{p,x}} ln \left(\frac{R_{o,x}}{R_{i,x}} \right) \qquad \textit{(Eq. 24)}$$

With ΔN the contribution to the rotational velocity of each layer, T the applied torque, R_i and R_o the (unknown) radii of each layer, and τ_0 and μ_p the yield stress and plastic viscosity of the respective layer. The index x indicates that this needs to be done over each layer. However, for each layer, one must calculate the plug radius $R_{p,x}$:

$$R_{p,x} = \sqrt{\frac{T}{2\pi h \tau_{0,x}}} \qquad \textit{(Eq. 25)}$$

If $R_{p,x}$ is larger than $R_{o,x}$, Eq. 24 can be applied. If $R_{p,x}$ is smaller than $R_{i,x}$, then the contribution of this layer to ΔN is zero, as the entire layer is in plug flow. If $R_{p,x}$ is in between $R_{i,x}$ and $R_{o,x}$, $R_{o,x}$ in Eq. 24 must be replaced by $R_{p,x}$, as the layer is partially in plug flow. The boundary conditions are that $R_{i,1} = R_i$, $R_{o,conc} = R_o$, and that $R_{i,x+1} = R_{o,x}$. This means that the paste layer is adjacent to the smooth cylinder and the concrete layer touches the outer cylinder. None of the layers can overlap and are adjacent.

By iteratively adjusting each $R_{i,x}$ and $R_{o,x}$, one can try to approach as close as possible the calculated N (the sum of all ΔN) to the measured N, at each torque value. The best solution for the entire measurement, including all torque values, is retained. This assumes that the lubrication layer does not change during the measurement, which may or may not be true. However, with the six unknown boundaries between each layer, one needs at least six different data points to come to a stable solution.

The proposed strategy has though one major practical concern: how are the rheological properties of the different mortar layers going to be measured accurately? One can wet sieve the concrete on each used sieve size, but this process would be too time-consuming, and changes in rheological properties can occur with time. Another strategy would be to produce the cement paste and mortars separately, and measure their properties in the respective rheometers. Table 9 shows an attempt at this, by producing cement paste, mortar and concrete mixtures with different maximum particle sizes. The difference between each mix design is that the fraction of material larger than the listed size was sieved off and not included in the materials. All mixtures were produced separately and all quantities of the remaining materials remained constant. The order of values in Table 9, for each rheometer separately, are not logical on first sight. When removing larger particles from a mixture, and by keeping the quantity of each remaining material constant, the paste volume relative to the total volume increased as the total volume decreased. One would expect a decrease in rheological properties under this scenario. The yield stress does not follow that principle systematically. One explanation is the difference in mixing energy inside the paste in the concrete or mortar, countering the change in aggregate size and quantity. A second concern is the mixer's mixing energy. The first three mixtures in Table 9 were mixed in a standard concrete drum mixer. The mixtures with an asterix* were produced in a large Hobart mixer, while the cement paste mixture (marked by the plus sign: $^{+}$) was produced in a small Hobart mixer. Comparing the two mixtures with 4.75 mm maximum particle size shows clearly the influence of mixer type. Thirdly, despite incorporating the rheometer correction factors from section 3.5, there are still considerable differences between the rheometers.

Table 9. Properties of different concrete, mortars and cement pastes with different maximum particle sizes, measured in different rheometers (YS = yield stress, PV = plastic viscosity, CT = ConTec, AP = Anton Paar).

	YS CT 5W	PV CT 5W	YS CT 6	PC CT 6	YS AP	PV AP
12.5 MM	360	34				
9.5 MM	450	28				
4.75 MM	550	9	448	5.3		
4.75 MM*			541	2.1		
1.16 MM*			426	0.6		
0.3 MM*			72	1.1	14	1.0
0.075 MM^{+}					16	1.1

From the above data, it is clear that this approach would give substantial issues, so a different strategy was followed. As the reference state in the cement paste is crucial, the cement paste was mixed intensively, while any sand or combination of sand and coarse aggregates was either mixed in by hand, or by slowly agitating the mixer. In this way, the mixing procedure does not influence the rheological characteristics of each component. However, this would induce a very time-consuming experiment if this needs to be done for each mortar. Instead, when producing the concrete, the cement paste was produced first and measured in the Anton Paar. All aggregates were incorporated and the mixer was slowly agitated in the drum mixer. Concrete

rheology was measured with the ConTec 5W, the interface rheometry with the ICAR. For the mortar mixtures, preliminary work was performed to obtain Krieger-Dougherty style curves for yield stress and viscosity, for each of the considered maximum particle sizes, as a function of volume fraction. Now, with known volume fraction for each particle size, the rheological properties of the mortar layer can be calculated based on the cement paste rheology.

4.3 Materials

4.3.1 Constituent materials

4.3.1.1 Cement and fly ash

A commercially available Type I/II Portland cement with a density of 3160 kg/m^3 and a locally available Class C fly ash, with a density of 2930 kg/m^3 were used for this part of the research.

4.3.1.2 Fine aggregate

Iron Mountain crushed Trap Rock was used as fine aggregate. This aggregate was chosen for its coarser grain size distribution to ensure adequate distinction between the different sieve sizes. Figure 41 show the grain size distribution of the trap rock compared to the ASTM C33 limits for sand. Table 10 shows the oven dry and SSD densities of the different portions of the trap rock with maximum particle sizes of 2.36, 1.18, 0.60 and 0.30 mm, determined according to ASTM C128, as well as the absorption values.

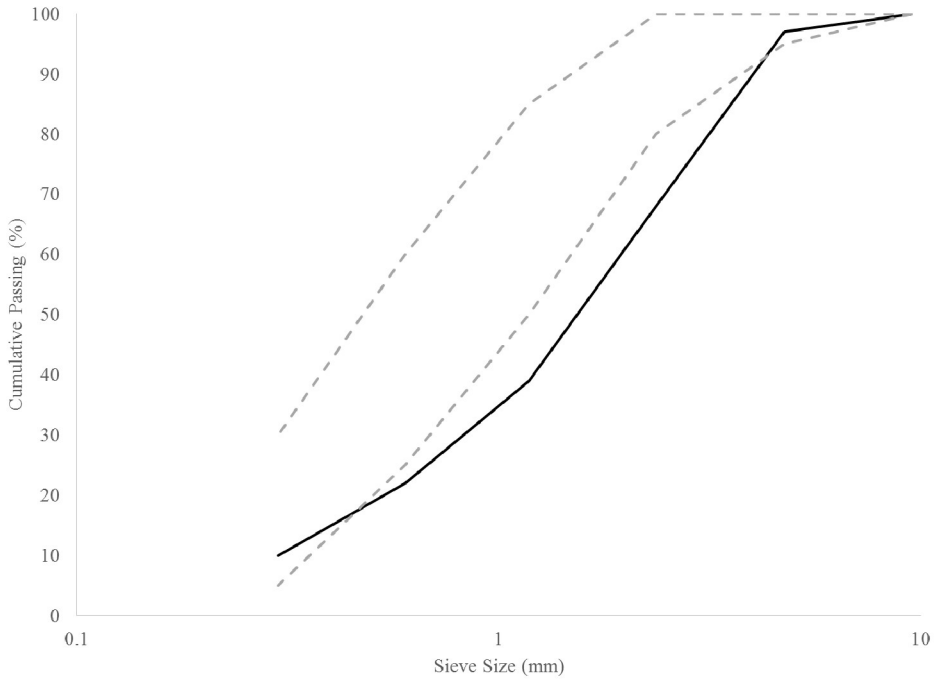

Figure 41. Grain size distribution of the Missouri trap rock (black line), compared to the ASTM C33 limits (gray dashed lines).

Table 10. SSD and oven dry densities and absorption of the different portion of the traprock.

SIEVE SIZE #	SSD DENSITY	OD DENSITY	ABSORPTION
8 (2.36 MM)	2580 kg/m^3	2550 kg/m^3	1.27%
16 (1.18 MM)	2560 kg/m^3	2520 kg/m^3	1.50%
30 (0.60 MM)	2560 kg/m^3	2520 kg/m^3	1.77%
50 (0.30 MM)	2550 kg/m^3	2490 kg/m^3	2.42%

4.3.1.3 Coarse aggregate

For the concrete mixtures, a 3/8" crushed limestone was used, with a density of 2700 kg/m^3 and an absorption of 0.66%.

4.3.1.4 Chemical admixtures

A PCE-based polycarboxylate (PCE) was used to enhance the fluidity of the pastes, mortar and concrete, as well as a hydration stabilizer (HS) to reduce the increase in rheological properties with time. These admixtures are identical to some of the admixtures used in the full-scale pumping tests. No air-entrainers or viscosity modifying agents were employed.

4.3.2 Mix designs and mixing procedures

4.3.2.1 Cement paste for Krieger-Dougherty curves

The cement paste mix design for the establishment of the Krieger-Dougherty curves is shown in Table 11. The w/cm for the mixtures was 0.40. The paste was mixed in a high shear mixer in 9 liter batches. First, the dry materials were homogenized, followed by approximately 90% of the mixing water. After mixing for 2 min at maximum speed, the PCE was added with some of the remaining mixing water. Mixing resumed for 2 min at maximum speed, after which the hydration stabilizer was added with the remaining mixing water. After 1 final minute of mixing, the cement paste was ready for evaluation.

Table 11. Mix design for 9 liter of cement paste to establish the Krieger-Dougherty curves.

MATERIAL	QUANTITY
CEMENT	9.97 kg
FLY ASH	2.49 kg
WATER	4.98 kg
PCE	32.4 g
HS	37.4 g

4.3.2.2 Mortars for Krieger-Dougherty curves

With the cement paste produced, mortars with different volume fractions were created. The amount of (sieved) sand necessary for each volume fraction was pre-weighed, including the amount of water to be added to compensate for the absorption (Figure 42). The aggregates were prepared on an air-dry basis. Prior to producing the mortar, the paste was remixed in the high shear mixer to impose the reference state. The correct mass of paste was sampled from the mixer and the predefined amount of sand and water were hand mixed with the paste to create the mortar sample. In this way, the reference state of the paste was not altered. Table 12 shows an example of the masses of sand and the masses of cement paste mixed to create mortars with different volume fractions of sand. The total volume of mortar was sufficient to fill the ConTec Viscometer

6, and it was kept approximately constant. Table 13 shows the selected volume fractions for each of the sieved portions of the sand. It should be noted that the initial intention was to measure at 20, 30, 40, 45 and 50% for each portion, but for the smaller particles, the larger volume fractions did not yield adequate results in the rheometer. As such, intermediate volume fractions were evaluated.

Table 12. Example of masses of sand and cement paste to create mortars with sand volume fractions of 20 to 50 %.

VOLUME FRACTION	SAND	CEMENT PASTE
20%	634 g	1873 g
30%	950 g	1639 g
40%	1267 g	1405 g
45%	1426 g	1288 g
50%	1584 g	1171 g

Figure 42. Prepared quantities of sand and water for different volume fractions.

Table 13. Selected volume fractions evaluated in the ConTec 6 rheometer, for each sand portion with different maximum particle sizes.

SIEVE SIZE	20%	30%	35%	40%	42.5%	45%	47.5%	50%
# 8	X	X		X		X		X
# 16	X	X		X		X	X	
# 30	X	X		X	X	X		
# 50	X	X	X	X				

4.3.2.3 Concrete for interface tests

Three different concrete mix designs were employed to evaluate the lubrication layer composition and thickness using the interface tests. The difference between the concrete mix designs was the paste composition. Mix designs 1 and 2 did not contain any fly ash. The w/c for mix design 1 was 0.35, while it was 0.40 for mix design 2. For mix design 3, mix design 2 was mimicked, but 20% by volume of the cement was replaced with fly ash. Admixture dosages were kept constant at 2 g/kg of cementitious materials for the

PCE and 4 g/kg of cementitious materials for the HS. All concrete mix designs contained 38% by volume of paste, 34.7% by volume of the traprock sand and 27.3% by volume of the crushed limestone.

The paste was produced in a similar fashion as for the mortars. The coarse aggregate and sand were premixed, with the water necessary to compensate for absorption, in a drum mixer with 150 l capacity. After the paste was added, the mixer was slowly agitated to homogenize the mixture. In this way, the effect of mixing on the reference state of the paste was minimized.

4.4 Testing procedures

4.4.1 Equipment

4.4.1.1 ConTec Viscometer 6

The ConTec Viscometer 6, described in section 3.3.2, was utilized for all measurements on the mortars. This includes the measurements on the cement pastes for the determination of the Krieger-Dougherty curves. As the maximum particle size is 2 mm for the ConTec 6, no mortars with larger particle sizes could be evaluated. The ConTec 6 was not utilized to evaluate any rheological properties when concrete was produced.

4.4.1.2 Anton Paar MCR 302

The Anton Paar MCR 302 with serrated concentric cylinders was used to determine the rheological properties of the cement paste for the concrete tests. This rheometer is described in section 3.3.1.

4.4.1.3 ConTec Viscometer 5W

The ConTec Viscometer 5, with the large configuration was used to determine the rheological properties of the concrete mixtures. More info on this rheometer can be found in section 3.3.3.

4.4.1.4 Interface rheometer

The hardware and software of the ICAR rheometer were used to create an interface rheometer. The interface rheometer utilizes a smooth cylinder instead of a vane, allowing the lubrication layer to form near the metal-concrete interface. This type of rheometer has proven useful in predicting pumping pressures, based on a single, homogeneous lubrication layer approach. The interface tool is a smooth aluminum cylinder with a radius of 125 mm and a vertical height of 200 mm. The bottom of the cylinder is conical in shape to provide easier insertion into the concrete if necessary.

4.4.2 Testing procedures

4.4.2.1 ConTec Viscometer 6

The testing procedure imposed on the ConTec Viscometer 6 was determined to minimize its influence on the reference state of the material. It had a minimal preshear period of 10 s, which includes the insertion of the inner cylinder, at 0.35 rps. Seven rotational velocity steps in descending order were imposed from 0.707 to 0.030 rps. Each step was maintained for only 2 s. This procedure deviates from the commonly accepted procedures with the sole goal to minimize the influence of the rheometer test on the rheology of the paste and the mortar.

As mentioned before, the ConTec Viscometer 6 was employed to evaluate the rheology of the cement paste and the mortars. After mixing the cement paste, a sample was taken and evaluated for yield stress and viscosity. This specific paste sample was returned to the mixer. For each of the mortars, the sample was discarded after evaluation. After measuring the rheological properties of the mortars, a new measurement on the (remaining) paste was performed. This measurement allowed for the evaluation of the time-dependency of the yield stress and viscosity. For each measurement, time of testing was recorded. Based on the linear evolution of yield stress and viscosity with time for the cement pastes, a linear interpolation was made for

every test. Figure 43 and Figure 44 show an example of the evolution for yield stress and viscosity of the cement paste with time.

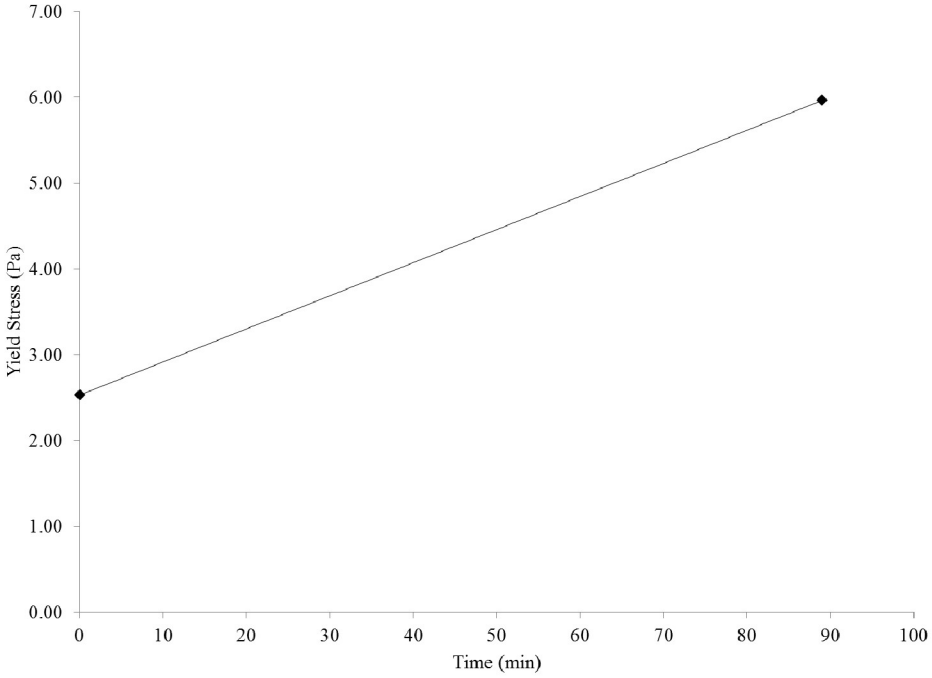

Figure 43. Example of yield stress evolution with elapsed time for the cement paste.

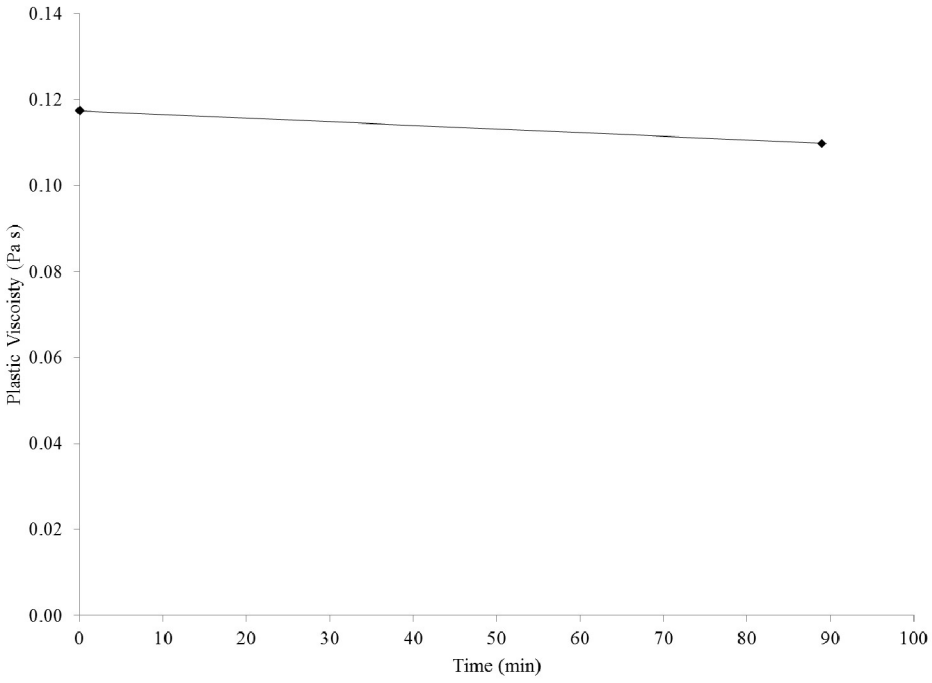

Figure 44. Example of plastic viscosity evolution with elapsed time for the cement paste.

4.4.2.2 Anton Paar MCR 302

A pre-shear of 100 s^{-1} was applied during 180 s to ensure equilibrium of the shear stress, followed by a decreasing ramp from 100 to 0.1 s^{-1} during 30 s.

4.4.2.3 ConTec Viscometer 5

The measurement of concrete rheology in the ConTec Viscometer 5 follows the same procedure as for the ConTec Viscometer 6. The procedure aimed to minimize disturbance.

4.4.2.4 Interface rheometer

The interface rheometer test consisted of imposing a rotational velocity of 0.5 rps for 20 s as preshear. This was necessary to create the lubrication layer. The pre-shear was followed by a stepwise decrease in rotational velocity from 0.5 to 0.05 rps, in seven steps of 5 s each.

4.4.3 Analysis

4.4.3.1 Rheometer data

The rheometer data were analyzed following the Reiner-Riwlin approach described in section 3.4.2. No attention was paid to equilibrium though, as the procedure attempted to measure the properties of the mortar or concrete as inserted in the rheometer. Plug flow corrections were performed if necessary. As such, a yield stress and plastic viscosity value are obtained for each paste, mortar and concrete measurement.

Figure 45. Vertical standing walls of mortar inside the rheometer after the test indicate the test might be invalid.

Special attention was paid to the condition of the sample after the measurement in the rheometer. With increasing volume fraction of sand, there is a risk that the material's behavior will change to frictional. Figure

45 shows an example of such case. After the removal of the inner cylinder, the mortar did not flow back, but kept a vertical position. This can only be achieved with a very high yield stress. In this case, the measurement was deemed invalid and no measurement could be recorded at this volume fraction.

4.4.3.2 Interface rheometer

For the interface rheometer, the averages of torque and velocity were determined at each step. This data serves as input for the solution of the lubrication layer estimate.

4.4.3.3 Estimation of lubrication layer thickness and composition

The ConTec 6 data were used to create Krieger-Dougherty style equations for yield stress and viscosity, allowing to calculate the properties of each mortar at each volume fraction from the paste rheology. For the mortar with 4.75 mm particles, for which no curves could be established, the equation of the 2.36 mm particles was used. The paste rheology and concrete rheology were measured. As such, Eq. 25 could be used to determine the location of the plug radius for each torque value of the interface rheometer and for each layer's properties. Eq. 24 was then used to calculate the total theoretical rotational velocity at each step, and the iterations delivered the best fitting values for each $R_{i,x}$ and $R_{o,x}$. As such, the best-fitting thickness of each layer was obtained, revealing the composition of the lubrication layer.

4.5 Krieger-Dougherty style curves for yield stress and plastic viscosity

For each of the volume fractions of sand mentioned in Table 13, a value for yield stress and viscosity was available. At the time of each test, an interpolated value for the yield stress and viscosity of the cement paste was also available from Figure 43 and Figure 44. As such, a relative viscosity and relative yield stress could be calculated, as the ratio of the suspension (mortar) to the medium (paste). Eq. 26 represents the viscosity amplification with increasing volume fraction, according to Krieger-Dougherty. This equation was fit to the obtained relative plastic viscosity data, for each sand portion separately. Fitted parameters are the maximum packing density φ_{max} and the intrinsic viscosity [η].

$$\frac{\eta_s}{\eta_m} = \eta_r = \left(1 - \frac{\varphi}{\varphi_{max}}\right)^{-[\eta]\varphi_{max}} \qquad \textit{(Eq. 26)}$$

$$\frac{\tau_{0,s}}{\tau_{0,m}} = \tau_{0,r} = \sqrt{(1-\varphi)\left(1 - \frac{\varphi}{\varphi_m}\right)^{-[\eta]\varphi_m}} \qquad \textit{(Eq. 27)}$$

Equation 27 shows a similar formula, but now for yield stress. Similarly, the relative yield stress values can be used to determine the parameters φ_m and [η]. However, φ_m should be lower than φ_{max}, as φ_m denotes the transition to frictional regime, but not full packing. The intrinsic viscosity for the yield stress might be different in value. For spheres, both equations have 2.5 as value for intrinsic viscosity, but it is not certain if this principle still stands for non-spherical particles. In fact, the results show it is better to fit separate intrinsic viscosities for yield stress and plastic viscosity.

Figure 46 and Figure 47 show the measured data and fitted curves for relative yield stress and relative plastic viscosity, respectively. Table 14 shows the obtained values for the maximum packing density and intrinsic viscosity for the plastic viscosity, and the φ_m and intrinsic viscosity values for the yield stress. A couple of trends can be observed: the maximum packing density, and the critical packing fraction for friction decrease with decreasing maximum particle size. This is logical due to the reduced polydispersity of sizes through the system. Intrinsic viscosities for yield stress and viscosity increase with decreasing maximum particle size. It could be that more irregularly shaped particles are found in this case, but no proof has been found for that statement. The maximum packing fraction for friction is approximately 85-90% of the maximum packing density, which is in line with the results from literature.

Based on the obtained parameters in Table 14, a prediction of the rheological properties of mortar with a certain volume fraction can be made based on the paste rheology.

Table 14. Obtained φ_m, φ_{max} and intrinsic viscosity values for the mortar mixtures with different particles size.

	ΦM	**[η] FOR YS**	**ΦMAX**	**[η] FOR PV**
#8	0.565	6.27	0.628	4.53
#16	0.511	6.01	0.579	4.52
#30	0.501	9.02	0.591	5.51
#50	0.455	12.38	0.494	7.05

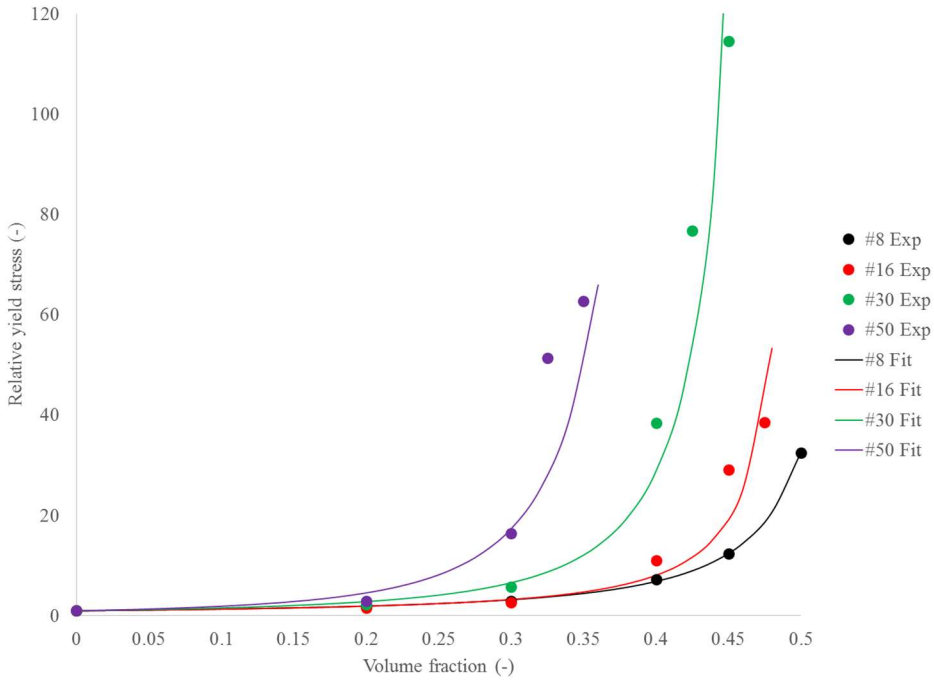

Figure 46. Experimental values for relative yield stress as a function of volume fraction for each sand fraction, combined with best-fitting curves, following Eq. 27.

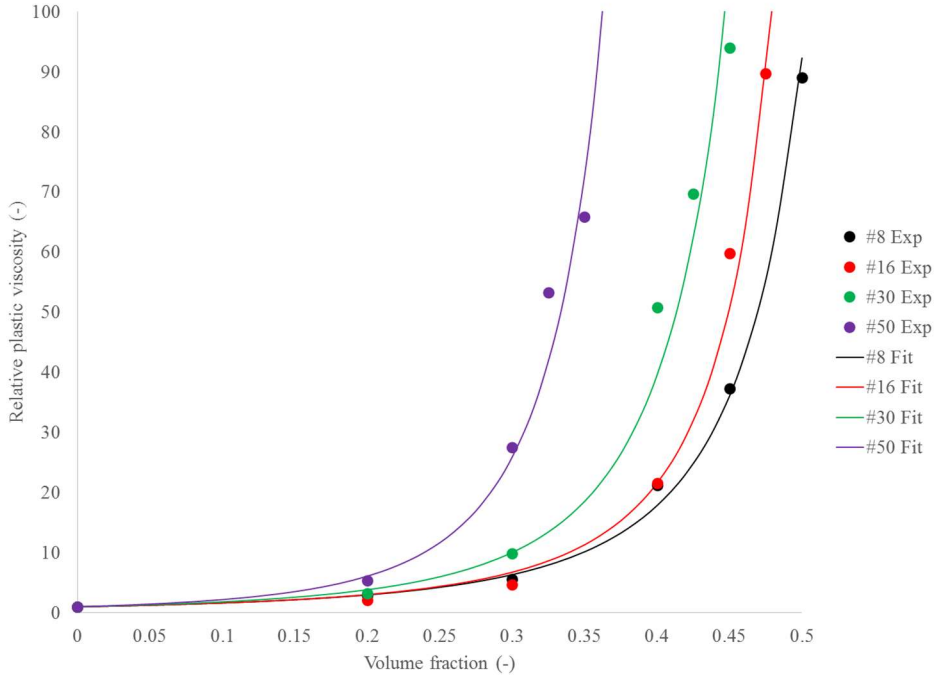

Figure 47. Experimental values for relative plastic viscosity as a function of volume fraction for each sand fraction, combined with best-fitting curves, following Eq. 26.

4.6 Estimation of lubrication layer thickness and composition

Table 15 shows the volume fractions of sand for each of the considered layers composing the lubrication layer. This was calculated as the total percent aggregate relative to the total volume of all materials with particle size smaller than the listed values. Table 16 shows the measured and calculated rheological properties of each layer. Paste and concrete rheology were measured. The mortar properties were calculated based on the values in Table 14. The properties for the layer with maximum particle size of 4.75 mm were calculated based on the values for 2.36 mm. Table 17 shows the torque and rotational velocity values in the interface rheometer for all mix designs evaluated.

Table 15. Volume fractions of sand for each of the considered mortar layers.

SIEVE SIZE	VOLUME FRACTION
#4	0.47
#8	0.38
#16	0.26
#30	0.17
#50	0.09

Table 16. Rheological properties of each layer. Yield stress in Pa, plastic viscosity in Pa s.

	PASTE	#50	#30	#16	#8	#4	CONCR
YS MIX 1	0.7	1.3	1.6	1.9	4.2	12.4	39.7
PV MIX 1	0.13	0.26	0.38	0.63	1.88	6.63	33.5
YS MIX 2	0.6	1.1	1.4	1.6	3.6	10.5	54.4
PV MIX 2	0.09	0.18	0.27	0.46	1.35	4.78	24.3
YS MIX 3	0.5	0.8	1.1	1.2	2.8	8.2	50.6
PV MIX 3	0.07	0.14	0.21	0.34	1.02	3.62	26.6

Table 17. Torque (Nm) and rotational velocity from the interface rheometer for each mix design.

ROT VELOCITY	TORQUE MIX 1	TORQUE MIX 2	TORQUE MIX 3
0.50	0.90	0.58	1.02
0.42	0.78	0.53	0.89
0.35	0.61	0.46	0.78
0.27	0.49	0.40	0.70
0.20	0.37	0.33	0.54
0.12	0.22	0.25	0.44
0.05	0.08	0.16	0.30

Figure 48 to Figure 50 show the experimentally obtained relationships between torque and rotational velocity in the interface rheometer (black), and the calculated values based on the best estimates for the different layer thicknesses (red). The green data are included to show the obtained relationship if no lubrication layer was present. The data in Figure 48 to Figure 50 for the lubrication layer results are based on a single cement paste layer. Other similar solutions are also found varying the thickness of each single layer and keeping all others at zero. The initial thought of combining multiple layers appears to over-estimate the calculated velocity, so the single layer approach has been chosen. Table 18 shows the different results for the thicknesses of each layer. Again, each result shows the thickness of that layer, without any other layers present. Plotting such results in Figure 48 to Figure 50 would deliver very similar results as the red data, except for the #4 layer, which shows a little more deviation.

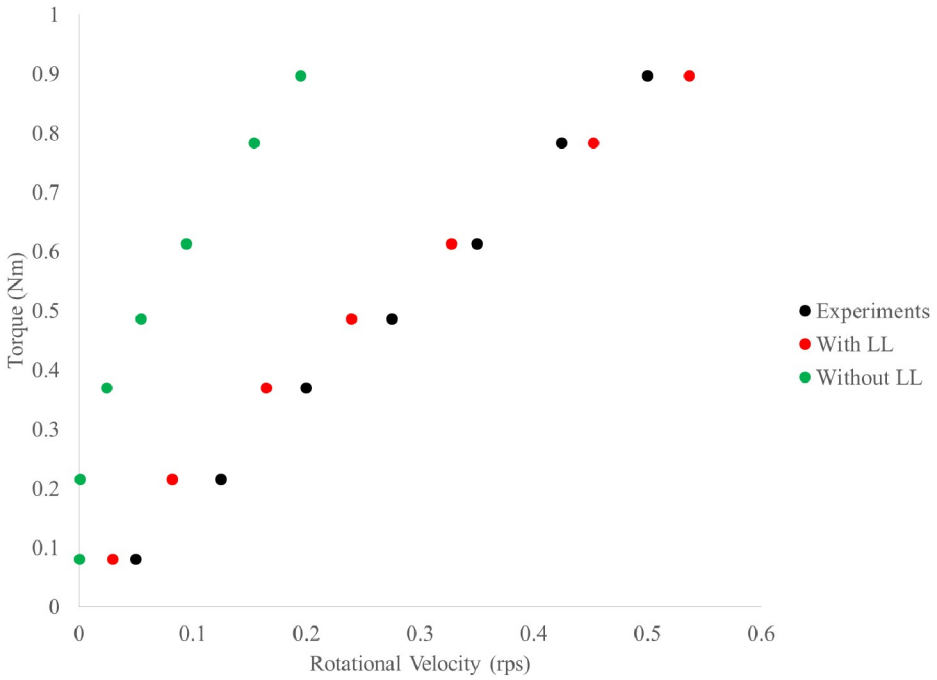

Figure 48. Experimental torque vs. rotational velocity (black) for mix design 1 in the interface rheometer. The red data show the result with the best-fitting lubrication layer while the green data show the theoretical results when no lubrication layer would be present.

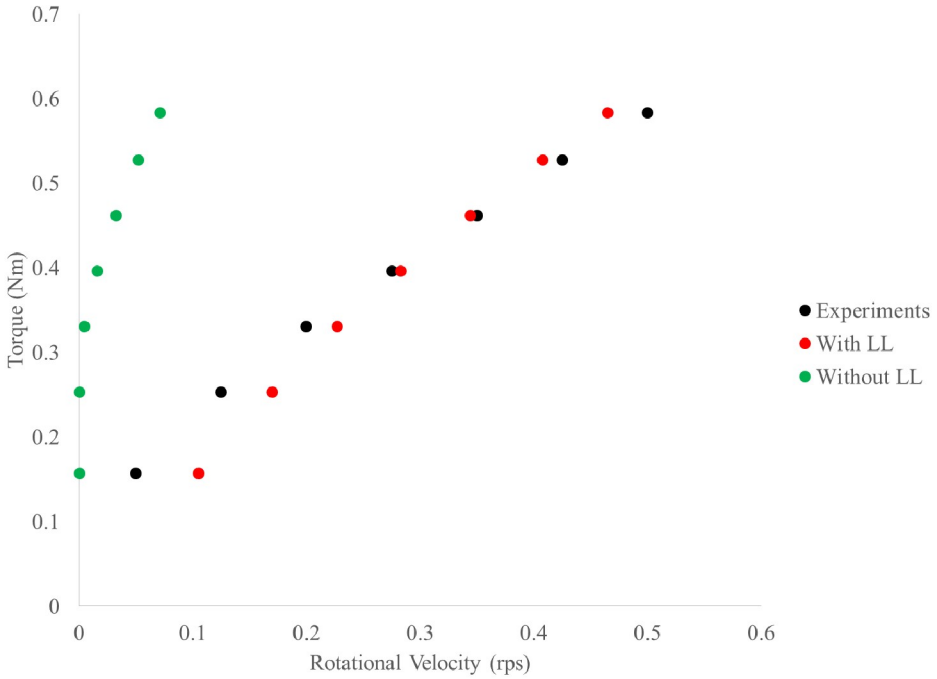

Figure 49. Experimental torque vs. rotational velocity (black) for mix design 2 in the interface rheometer. The red data show the result with the best-fitting lubrication layer while the green data show the theoretical results when no lubrication layer would be present.

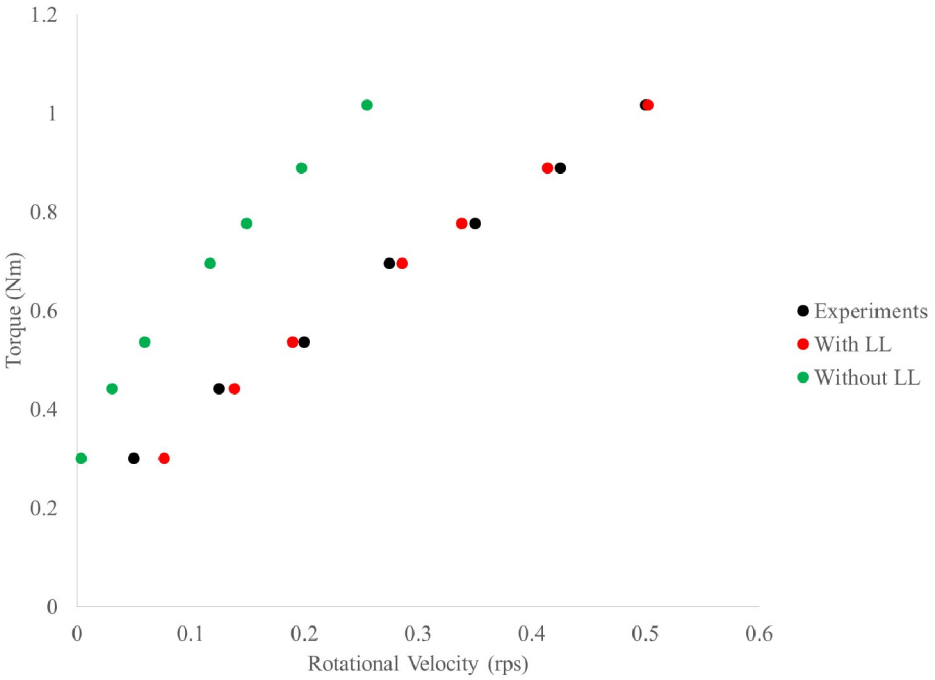

Figure 50. Experimental torque vs. rotational velocity (black) for mix design 3 in the interface rheometer. The red data show the result with the best-fitting lubrication layer while the green data show the theoretical results when no lubrication layer would be present.

Table 18. Thickness of lubrication layer for each mix design, dependent on the maximum particle size of each layer.

MAX AGGR. SIZE	MIX 1	MIX 2	MIX 3
#200	0.096 mm	0.123 mm	0.033 mm
#50	0.191 mm	0.244 mm	0.066 mm
#30	0.282 mm	0.362 mm	0.098 mm
#16	0.48 mm	0.61 mm	0.17 mm
#8	1.53 mm	1.96 mm	0.51 mm
#4	7.46 mm	9.59 mm	2.08 mm

Referring back to literature, some discussion is made about the composition of the lubrication layer [51, 52]. Is it fully composed of the constituent mortar, or is it a micromortar or a cement paste? Assuming the homogeneous approach (because the heterogeneous does not deliver adequate data), if the lubrication layer would be the mortar, its thickness would vary between 2 and 10 mm. Although this upper range has been reported, it does not seem realistic. Assuming the layer is a micromortar with 1 or 2 mm maximum particle size, the thickness of the lubrication layer is between 0.5 and 2 mm, which is more in accordance with reported assessments. For mix design 3, the thicknesses of the lubrication layer is much smaller. Extrapolating to cement paste, thicknesses of 96, 123 or 33 µm are found to be able to lubricate the material as well. Besides, the major concern which can be raised for most of these values is that the thickness of the layer is smaller than the maximum particle size. This is physically impossible. However, for the cement paste, this is not true, although doubt can be raised for mix design 3.

The main question remaining though is whether an error in assessment of the rheological properties, the obtained Krieger-Dougherty parameters, or the rheometer comparison is having an influence on the results. This could change the obtained values in the right range for the lubrication layer. It should also be questioned if a lubrication layer composed of cement paste is physically the correct solution. Yes, every particle undergoes shear-induced particle migration, but the larger particles move much quicker than the smaller particles. Unfortunately, the results here cannot answer the question for which size the particle migration has not yet occurred, as each layer thickness is a possible solution.

4.7 Summary

An approach was developed to estimate the composition and thickness of the lubrication layer as measured in the interface rheometer. This approach however required substantial care in considering that rheometers deliver different values, and that the shear rate in the paste, inside the mortar or concrete can change the rheological properties during mixing or during measuring. As such, a careful procedure was employed during mixing of mortar and concrete samples. Rheometer procedures were also modified to minimize the duration the sample is exposed to elevated shear rates.

The lubrication layer properties were reverse-engineered, by considering the interface rheometer as a combination of multiple concentric layers of paste, mortar and concrete, with different maximum particle sizes. Knowing the rheological properties of each layer allows to calculate, iteratively, the best-fitting thicknesses of each layer to approach the experimental torque-rotational velocity in the interface rheometer as good as possible. However, one cannot execute eight rheological experiments on materials with all different particle sizes within a timeframe in which the rheological parameters will not vary too much.

Instead, the research team elected to find Krieger-Dougherty style relationships between relative plastic viscosity and relative yield stress as a function of volume fraction for the different mortar portions. The results on the Krieger-Dougherty parameters indicate a decrease in maximum packing density and a decrease in the critical volume fraction, combined with an increase in intrinsic viscosity, with decreasing maximum particle size in the mortar. Also, the critical volume fraction for friction appears to be 85 – 90% of the maximum packing density, which is in agreement with literature. Different values for intrinsic viscosity for the yield stress and plastic viscosity fits were suggested.

Implementing the predicted rheological properties for mortar, with the rheological properties for paste and concrete into the developed model delivered some remarkable results. The best solutions are obtained when individual layers have a fixed thickness, not a combination of different layers. Regardless whether a cement paste, micromortar or mortar layer is imposed, similar solutions are obtained. However, apart from the cement paste solution, the layer thicknesses are smaller than the maximum particle sizes, which makes the solution physically impossible. Measurement errors, whether in each rheometer, the determination of the Krieger-Dougherty parameters, or the comparison of the rheometers, could alter the values of the obtained results, potentially making them physically feasible. Furthermore, seen particle migration velocity depends strongly on particle size, it is doubted whether all particles migrate to create a cement paste layer near the inner cylinder or the pipe wall, within the duration of the test.

5 Influence of Pumping on Fresh and Hardened Concrete Properties

5.1 Objectives

The literature review in section 2.6 pointed out that both the fresh and hardened properties of concrete can be altered due to pumping. This can mainly be attributed to the applied pressure, shearing, and impact at discharge. Figure 1 in the introduction showed some dramatic results in which the spacing factor of SCC increased substantially due to pumping, especially with increased flow rate, and when using a reducer. Practical guidelines on pumping concrete mainly try to restrict freefall in the downward section of an A-shaped boom configuration, but the results in the introduction appear to contradict this for SCC. The purpose of this research is to investigate which boom configurations and other concrete pumping parameters are affecting the fresh and hardened properties significantly, in order to potentially change the practical recommendations for more flowable concrete mixtures. This chapter discusses the results of a large scale pumping campaign conducted at Rolla Ready Mix. 18 concrete mixtures were evaluated. The influence of pumping on fresh properties, in terms of slump or slump flow, sieve stability, rheology, interface rheology, density and air content, as well as hardened properties: compressive strength, density, air content, spacing factor, freeze-thaw resistance and salt scaling, was determined. Each concrete mixture was subjected to four to six different pumping conditions, in which flow rate, boom configuration, the use of a reducer and submerging the hose in the concrete were evaluated. Results from pumped concrete were compared to non-pumped concrete samples.

5.2 Materials

5.2.1 Constituent materials

5.2.1.1 Cement and fly ash

All mixtures contained a commercially available Type I/II Portland cement with a density of 3160 kg/m^3. A Class C fly ash was incorporated in 16 of the 18 mixtures, with a density of 2930 kg/m^3. The cement and fly ash are identical to the materials sourced for the research in Section 4. No other supplementary cementitious materials were available at the ready-mix plant. The incorporation of half a ton of slag, metakaolin or limestone powder would be too laborious on-site, and even the use of 50-100 kg of silica fume in a full mixer would be an extensive task in unsafe conditions with the lack of a forklift. Additionally, mixing was provided by the truck itself, so the dispersion of silica fume could be doubted. As such, only Class C fly ash was evaluated as an SCM.

5.2.1.2 Aggregate

Missouri River sand was used as a fine aggregate. It has a density of 2630 kg/m^3 and an absorption equal to 0.24 %. The coarse aggregate was a locally available crushed limestone with a nominal maximum aggregate size of 12.5 mm (3/8”). The density of the coarse aggregate was 2700 kg/m^3 and the absorption was 0.66%. The concrete production plant does not have moisture meters for the aggregate. A “correction” for the water was performed by the operators based on experience. Any large deviations of water between mixtures can be discovered by the compressive strength results. Figure 51 shows the grain size distributions of the sand and coarse aggregates, as well as the ASTM C-33 limits for sand and for a size 7 coarse aggregate.

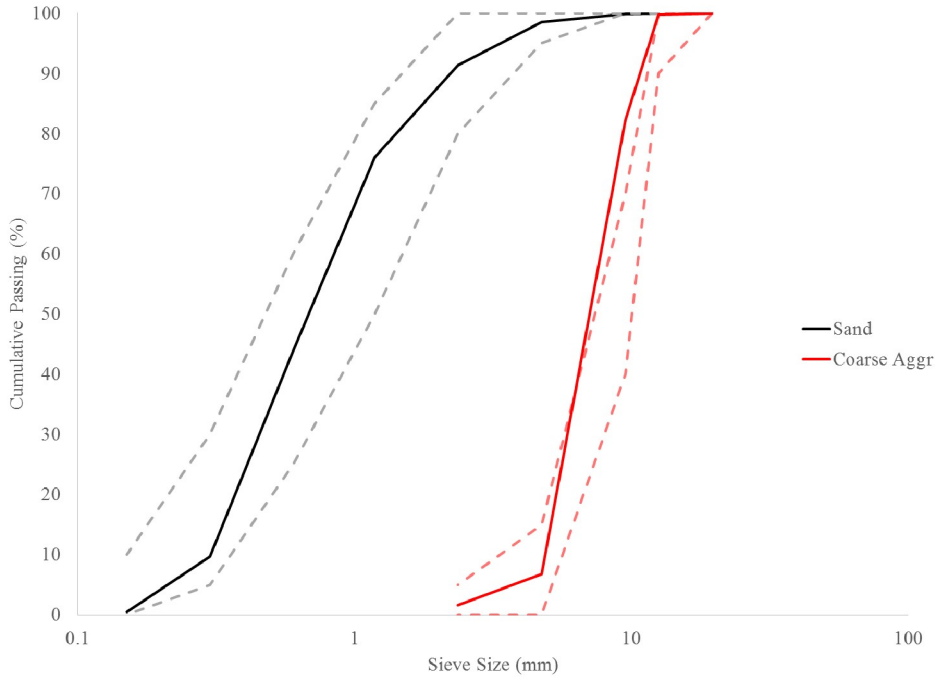

Figure 51. Grain size distribution of sand (black) and coarse aggregates (red), with their respective ASTM C33 limits (dashed lines).

5.2.1.3 Chemical admixtures

Several chemical admixtures were employed during this research. The admixtures of two different producers were used in this work. Air-entraining agents were employed to achieve different air contents, as this is one of the main subjects of this study. Different superplasticizers were also used: three based on PCE design and one PNS. Retarders (Ret) and/or hydration stabilizers (HS) were introduced into the concrete to maintain workability as long as possible. A typical test with a concrete truck took approximately four hours between contact between cement and water and the last evaluation. Hydration was slowed down extensively, leading to delayed setting of the samples. A workability retaining admixture (WR) was also used to help maintain the workability level. A viscosity-modifying agent (VMA) was needed for the mixtures with PNS, as the quantity of PNS required to create SCC caused concerns about segregation. Some mixtures contained a defoamer (Def), especially to keep the quantity of air generated by the PCE under control. This was an issue encountered with both admixture producers, except for the mixtures with PNS. The following paragraph lists the different properties of each admixture:

- AEA 1: Density: 1.01 kg/m^3, solid content 6.1%
- AEA 2: Density: 1.01 kg/m^3, solid content 6.8%
- PCE 1: Density: 1.05 kg/m^3, solid content 25.0%
- PCE 2: Density: 1.05 kg/m^3, solid content 29.5%
- PCE 3: Density: 1.06 kg/m^3, solid content 35.4%
- PNS: Density: 1.19 kg/m^3, solid content 41.0%
- Ret: Density: 1.06 kg/m^3, solid content 13.1%
- HS: Density: 1.12 kg/m^3, solid content 18.0%
- WR 1: Density: 1.04 kg/m^3, solid content 20.8%
- WR 2: Density: 1.04 kg/m^3, solid content 21.6%
- Def: Density: 1.35 kg/m^3, delivered as a powder

- VMA: Density: 1.20 kg/m^3, solid content 42.3%

It should be stated that products of the different producers were never mixed and that achieving the desired air content and the desired fluidity level of the concrete on-site was not a straightforward task.

5.2.2 Mix designs and mixing procedures

The concrete mixtures were created in batches of 5.25 to 5.75 m^3 each, the latter being the maximum capacity of the drum mixer. Mixtures 1 through 16 all contained 25% class C fly ash, while the fly ash was omitted for mix designs 17 and 18. The w/cm was kept constant at 0.45. Although a typical SCC mixture would contain a lower w/cm, the w/cm of 0.45 was maintained to ensure that the air-void system was needed for freeze-thaw and scaling protection. At lower w/cm, the porosity of the concrete may be too low to allow the concrete to saturate, and the addition of air would not be necessary. In the current design, a change in air-void system induced by pumping should have repercussions on the freeze-thaw and scaling performance. Table 19 shows the mix design, without the admixtures, for all mixtures. As mentioned in section 5.2.1.2, the aggregate moisture content was not measured and corrections based on experience were performed. Tests were not performed on rainy days, and were postponed in case of prolonged rainfall or torrential storms in the days leading up to the tests.

Table shows the admixture quantities for all mix designs. Mixtures 1 through 4, and 6 and 7 all contained PCE-1. Mix design 8 was equivalent to the other mixtures, but used a different PCE. The PCE dosage was adjusted to obtain different workability levels. Mixture 5 was a CVC and did not contain any PCE. Mixtures 1 through 8 were produced with the products from one admixture producer, while the chemicals from the other producer were used in mixtures 9 through 18. Of those, mixtures 9 through 14 were made with PCE and 15 through 18 were produced with the PNS. Defoamer was added to mixtures 11 through 14 to lower the air content. The AEA, defoamer and PCE or PNS dosages were altered to obtained mixtures with different air contents and different workability levels.

All mixtures were produced at the ready mix plant. Sand and coarse aggregates and half of the mixing water were added to the truck and homogenized, followed by the air-entraining agent. The cement and fly ash and the remaining mixing water were further added and mixing continued. The truck moved from the plant to the yard across the street, to which the remaining admixtures were added. These were added separately in the mixer, each time with a 2-4 min mixing period in between. Typically, the PCE/PNS was added first, followed by the retarder, the WR or the VMA. Additional dosages of PCE/PNS, defoamer or AEA (mixtures 17-18) were added to adjust workability level and/or air content. Late additions of AEA were not as efficient, and it seems that a majority of the later entrained air was not as effectively stabilized in the concrete. Table 21 contains the initial slump flow and initial air content of the concrete mixtures.

Table 19. Mix designs without admixtures.

	MIXTURES 1-16	**MIXTURES 17-18**
CEMENT	315 kg/m^3	421 kg/m^3
CLASS C FLY ASH	105 kg/m^3	
FINE AGGREGATE	927 kg/m^3	930 kg/m^3
COARSE AGGREGATE	759 kg/m^3	761 kg/m^3
WATER	189 kg/m^3	190 kg/m^3

Table 20. Admixture quantities for each mixture. All units are in kg/m³.

	AE1	AE2	PC1	PC2	PC3	PNS	RET	HS	WR1	WR2	DEF	VMA
MIX 1	0.129		0.87				0.78		1.05			
MIX 2	0.129		0.77				0.79		1.05			
MIX 3	0.129		0.61				0.72		1.05			
MIX 4	0.129		0.44				0.79		0.79			
MIX 5	0.065						0.62		0.79			
MIX 6	0.065		0.82				1.05		1.05			
MIX 7	0.065		0.96				1.05		0.79			
MIX 8	0.065				0.37		0.79		0.79			
MIX 9		0.026		0.44				0.35		1.78		
MIX 10		0.026		0.44				0.70		1.78		
MIX 11		0.028		0.36				0.43		1.92	0.75	
MIX 12		0.094		0.28				0.43		1.92	0.19	
MIX 13		0.094		0.19				0.65		1.21	0.21	
MIX 14		0.140		0.37				0.49		1.72	0.19	
MIX 15		0.274				5.55		0.82				3.93
MIX 16		0.698				3.70		0.82				2.62
MIX 17		0.417				4.69		1.09				2.62
MIX 18		0.553				2.05		1.09				1.09

Although the required admixture dosages were predetermined on laboratory mixtures, field conditions, which include different mixing energy, concrete volume, different deliveries of cement and fly ash, and temperature, caused significant changes in expected behavior. In most cases, the concrete workability and air-content was adjusted individually for each mixture on-site, a process which could extend the concrete preparation time up to an hour.

Table 21. Initial slump flow (in mm) and air content (%) of all mixtures. The report value for mixture 5 is the slump.

	INITIAL SF	INITIAL AC
MIX 1	590	7.2
MIX 2	555	8.2
MIX 3	480	6.6
MIX 4	490	7.5
MIX 5	130*	3.2
MIX 6	575	9.2
MIX 7	790	6.7
MIX 8	710	8.0

MIX 9	655	8.2
MIX 10	790	6.9
MIX 11	690	3.2
MIX 12	610	3.1
MIX 13	445	5.4
MIX 14	685	3.1
MIX 15	780	2.8
MIX 16	690	3.1
MIX 17	800	2.5
MIX 18	645	4.4

5.3 Testing equipment and procedures

This section includes the information on testing procedures and equipment used.

5.3.1 Slump, slump flow and T50

The slump test is governed by ASTM C143 while the slump flow testing procedure is described in ASTM C1611. Both tests include filling the Abram's cone with concrete and lifting the cone. The slump measures the difference in height between the displaced top surface and the initial height, while the slump flow takes the average of two perpendicular concrete spread values. The main difference between the procedures is how the cone is filled. ASTM C143 requires the cone to be filled in three layers, rodding each layer 25 times. ASTM C1611 prescribes no external consolidation and filling the cone in a single layer. However, for flowable mixtures, which are not conventional concrete nor SCC, no rodding would leave too much entrapped air, while the full procedure could cause significant segregation. As such, based on literature [121], an intermediate procedure for highly-workable concrete (HWC) was introduced: 2 layers (although the original suggestion calls for 1 layer), each being rodded 10 times. The decision on which procedure to apply: i.e.: no rodding or reduced rodding, was determined by the initial slump flow of the mixture. If this value was superior to 550 mm, the mixture was considered SCC, if it was inferior, it was considered HWC. Once a decision was taken for a mixture, the process was maintained for this concrete mixture, regardless of the changes in slump flow. Mixture 5 was the only CVC, so it was the only concrete for which the procedure in ASTM C143 was followed.

The T50 was determined by measuring the time between lifting the cone and reaching 500 mm diameter. As the w/cm of the mixtures was elevated, and thus the viscosity low, the T50 values, typically less than 1 s, are deemed to be significantly influenced by operator error.

5.3.2 Sieve stability

The sieve stability test is a relatively quick test to establish the segregation potential of an SCC mixture. If the initial slump flow value was above 500 mm, the sieve stability test was executed. The test consists of pouring 5.0 ± 0.2 kg of concrete on a #4 sieve, and recording the mass which passed through the sieve after 2 min of rest. The segregation index is calculated as the mass passed through, relative to the original mass. The test is described in detail in the European guidelines for SCC [122]. The team deviated from the original guidelines by not performing the 15 min wait time prior to placing the concrete on the sieve.

5.3.3 Rheology and interface rheometry

For the determination of the rheological properties, the ICAR rheometer, as described in section 3.3.4, was employed. The testing procedure consisted of a pre-shear period of 20 s at 0.5 rps, followed by a stepwise decrease in rotational velocity from 0.5 to 0.05 rps, in 7 steps of 5 s each. The interface rheometer, which consists of replacing the vane by a smooth cylinder in the ICAR device, is described in section 4.4.3.2. The employed procedure was identical to the procedure for the rheology. The sequence in determining the rheological and interface properties was as follows:

- Empty test with interface device, preceded by a torque reset.
- Filling the concrete inside the container, without consolidation and without moving the hardware.
- Execution of interface test.
- Empty the container, without cleaning.
- Empty test with the rheometer vane, again preceded by a torque reset.
- Filling of the container with concrete without consolidation. The ICAR hardware was not moved.
- Execution of the rheometer test.
- Empty the container and clean of the rheometer.

A first attempt to analyze the rheometer data was done by applying the Reiner-Riwlin equations (eqs. 8 and 9) and correcting for plug flow. However, issues have been observed in determining the yield stress. Inaccuracies were amplified with the plug flow correction procedure. It should be noted that due to the low viscosity of the mixtures, significant plug flow was observed. Also, the obtained yield stress values from the rheometer did not deliver an adequate correlation with the slump flow values. A possible cause for this issue is the offset of the rheometer from zero torque, a feature previously observed despite the care taken not to influence the rheometer position between the empty and full tests. Instead, the yield stress values were calculated based on the slump flow by using the equation provided by Roussel and Coussot for slump flow [123]. This value was used as yield stress value in the plug flow calculations, and the viscosity was obtained by adjusting a torque translation for all measured points.

For the interface rheometer, once the rheological properties are known, one can calculate the lubrication layer properties. However, because of the problems observed in determining the rheological properties, this process was deemed too sensitive. Instead, the raw data were used, as the slope between torque and rotational velocity indicates the flow resistance inside the interface rheometer. Feys et al. have shown an adequate correlation between this slope (I_{trib}) and the total pumping pressure [52]. I_{trib} could also be used as an alternate measure of a parameter related to viscosity. The intercept of the T-N relationship in the interface rheometer was ignored.

5.3.4 Fresh concrete density and air content

The fresh concrete density was determined following ASTM C138, while the air content according to the pressure method was measured by the guidance of ASTM C231, with a Type B pressure meter. The main deviations from the standard were the filling procedures of the bowl. For mixture 5, the only CVC, the standard was followed: the bowl was filled in three layers, each layer receiving 25 roddings and 12 mallet strikes. For the SCC, the reservoir was filled in one layer without rodding and with 12 mallet strikes. For HWC, two layers with 10 roddings were used, combined with 12 mallet strikes per layer. The determination of the consolidation procedure was done based on the initial slump flow and remained unchanged for the concrete mixture.

5.3.5 Hardened concrete density, air content and compressive strength

Three 100 x 200 mm cylinders were cast for compressive strength per test. Like the slump flow, fresh concrete density, and air content tests, the consolidation energy differed depending on the initial slump flow. SCC was not consolidated, HWC and CVC were consolidated using a vibration table. In the latter case, cylinders were

filled in two lifts. The molds were covered with the lids to prevent evaporation and were brought to the lab and demolded the next day. Specimens were cured under lime-saturated water until 28 days after mixing. Density of the concrete was determined by weighing the specimens above and under water. Based on the theoretical density, an estimate of the air content could be made. Compressive strength tests were executed at 28 days following ASTM C39, with a loading rate of 250 N/s. The specimen ends were flattened by grinding. The average of three results was used to report compressive strength.

5.3.6 Hardened concrete air content and spacing factor

Similarly to the specimens for compressive strength, an additional specimen was cast for the hardened air-void analysis. The specimen production was done in the same way as for the compressive strength specimens. After hardening, a disk was cut from the cylinder approximately 80 mm from the bottom. The surface was carefully polished following the guidelines and suggestions from ASTM C457. Sandpapers with grit sizes of 80, 180, 320, 600 and 1200 were used in consecutive order. Between grits, the quality of the polishing was checked. The quality was assessed with the use of an air compressor, flash light and straight edge. The sample was first dried with the air compressor then checked for flatness and uniformity with a flash light and straight edge (Figure 52). It was ensured that any imperfections were removed from the surface and the surface was able to reflect light by the end of polishing.

Figure 52. Verification of flatness of surface after each polishing step.

Once polished, the concrete slices were contrasted, making the paste and aggregates black and the air-voids white. To accomplish this, the concrete was covered with black permanent marker and barium sulfate was applied to the surface. To achieve proper packing of the air-voids, a rubber disk was rolled across the concrete while it was covered with the barium sulfate. The barium sulfate was left in the filled air voids and the excess was carefully removed from the top with a straight edge and brush. The specimen was then examined and any voids in the aggregates that were filled with barium sulfate were colored black by the permanent marker. Once it was confirmed that only the air voids in the paste remained white, the concrete was covered with a small layer of mineral oil and was then ready to be analyzed. Figure 53 shows the preparation of the air-void

specimen. The air-void systems were measured by two methods: the Rapid Air 457 Air-Void Analyzer and the KSU Void Analyzer [124].

The air-void systems were first analyzed by the Rapid Air 457 Air-Void Analyzer. Procedure A, the linear-traverse method described in ASTM C457 was followed to determine the air-void system characteristics. A fixed threshold of 145 was determined and used for the analysis. This threshold served as the dividing line between what was considered black and what was considered white when the scanned image was converted to a binary image. The parameters used for the analysis included a paste content of 38.0 % by volume, which came from the mix design and a traverse length of 1,905 mm with 3 traverses/frame. The sample had a diameter of 100 mm and the area traversed was 65 mm by 65 mm.

The Rapid Air 457 provides a spreadsheet with a title page along with raw and calculated data. A chord length distribution table and graph that includes all chord lengths is generated. Additionally, a chord length distribution table for chords from 30 to 4000 μm is reported. The air content (%), specific surface (mm^{-1}), spacing factor (mm), void frequency (mm^{-1}), average chord length (mm), and paste to air ratio is calculated for all chord lengths and for chords from 30 to 4000 μm.

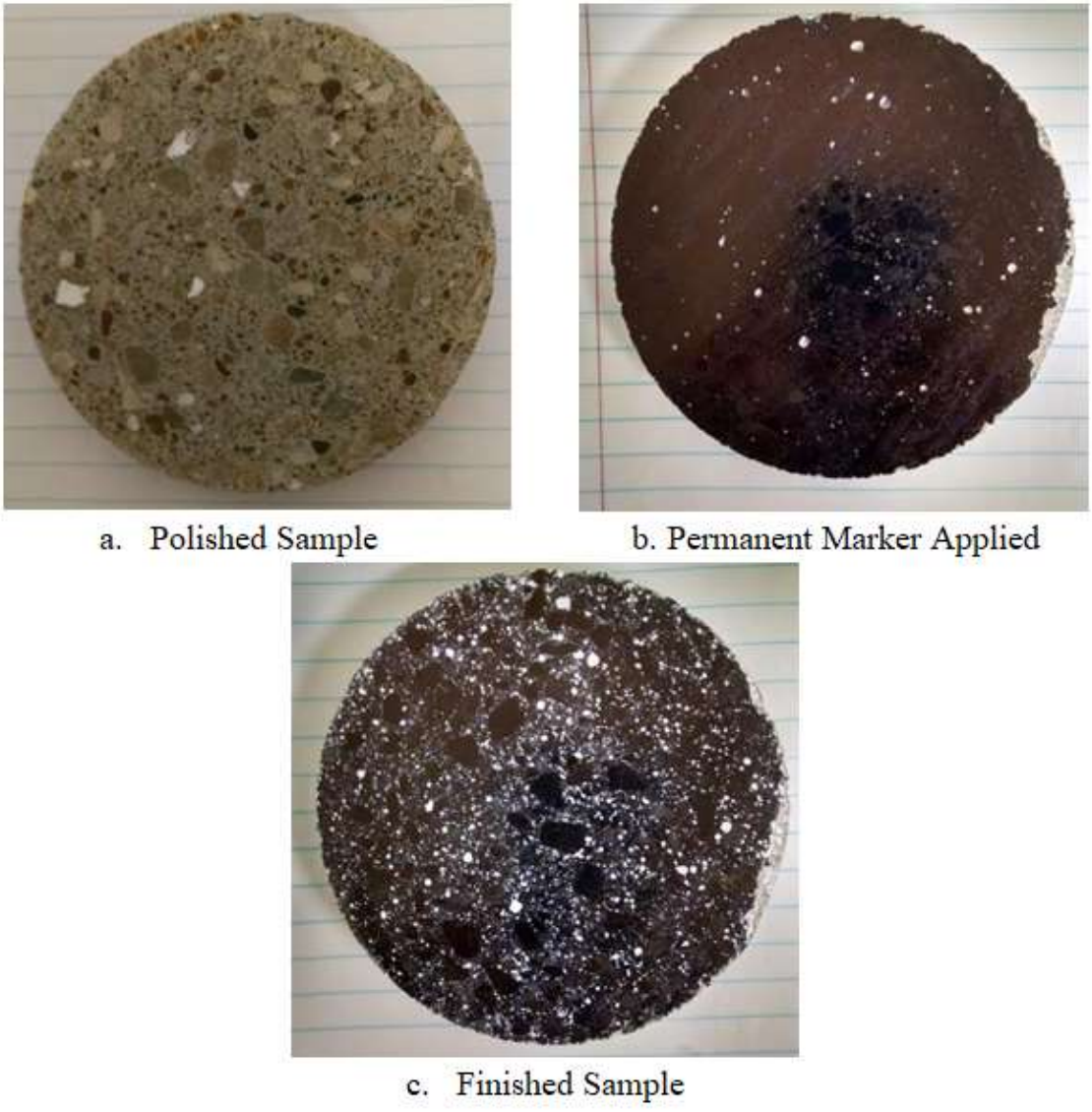

Figure 53. Preparation of samples for hardened air-void analysis.

The results from the Rapid Air 457 varied based on the starting point of the microscope on the concrete since only the line traversed is analyzed rather than the entire sample. For this reason, the analysis procedure was repeated 6 times. Each time the concrete was turned slightly so different lines were traversed across the sample. In total the sample was turned 90 degrees. After 3 trials the mineral oil was reapplied to the surface of the concrete to keep a consistent surface since the results varied if the specimen became dry. The average of the 6 measurements was calculated and considered in the data analysis. In this way, the variations in the data were averaged out so that more reliable results were obtained (Table 22).

Table 22. Example of analysis of 6 rotations of the sample in the Rapid Air analyzer.

PARAMETER	TEST 1	TEST 2	TEST 3	TEST 4	TEST 5	TEST 6	AVG	STDEV
AIR CONTENT (%)	2.23	1.39	1.58	1.87	1.70	1.70	1.75	0.29
SPACING FACOR (MM)	0.646	0.590	0.648	0.663	0.809	0.821	0.696	0.096

The air-void system was then analyzed by the KSU Void Analyzer. An Epson Perfection V550 Photo scanner was used to obtain 6400 dpi resolution scans of each sample. A 70 mm x 70 mm 16-bit grayscale scan was taken. This area is greater than that required by ASTM C457 for a 12.5 mm nominal maximum size aggregate. Photoshop was then used to adjust the contrast, brightness, and threshold of the picture to obtain a monochromatic picture which marked only the air-voids as white. This was done by overlaying the original scan with the altered photo and adjusting the settings until air voids visible in the original scan were the same size and shape as those in the adjusted photo and all noise created by reflecting light and porous aggregates was removed. Once the monochromatic picture was created, the KSU Void Analyzer was used to analyze the air void system.

The KSU Void Analyzer provides two spread sheets. The first includes analysis parameters, raw data pixel counts, and calculated air-void system parameters. This includes air content (%), spacing factor (mm), specific surface (mm^{-1}), entrapped air void content (%), and entrained air void content (%). The program provides data for the air voids smaller than 50 μm, air voids smaller than 10 μm, and irregular air voids each in terms of % by area, % by count and number. Finally, the maximum, average, and median air void size is listed. The second spreadsheet lists the raw data for the air void area for each air void by pixel count.

One major discussion point for the hardened air-void analysis is the lower threshold for air voids to be taken into consideration to calculate the spacing factor. Voids in the aggregates are manually removed, but it can be doubted if the smallest voids are actually visible with the naked eye. The scanner and KSU software eliminate automatically small air voids and irregularly shaped air voids. The Rapid Air takes all data into consideration. Figure 54 compares the values from the scanner with the Rapid Air, and the discrepancy is strongly noticeable. Figure 56 shows the same comparison, but the Rapid Air spacing factor is now calculated by omitting all air voids smaller than 30 μm, which is the deemed the lowest resolution which can be seen with the naked eye. The agreement between the values between the two apparatuses is stronger in this case. Figure 55 shows the influence on the spacing factor when removing the air voids smaller than 30 μm. Assessments of spacing factors, performed using a microscope by petrographers does typically not include any voids smaller than 30 μm either. Furthermore, the threshold between black and white in the scanner was adjusted for each sample, and it was kept fixed in the Rapid Air. The spacing factor values from the Rapid Air with air voids larger than 30 μm were used for analysis performed in this report.

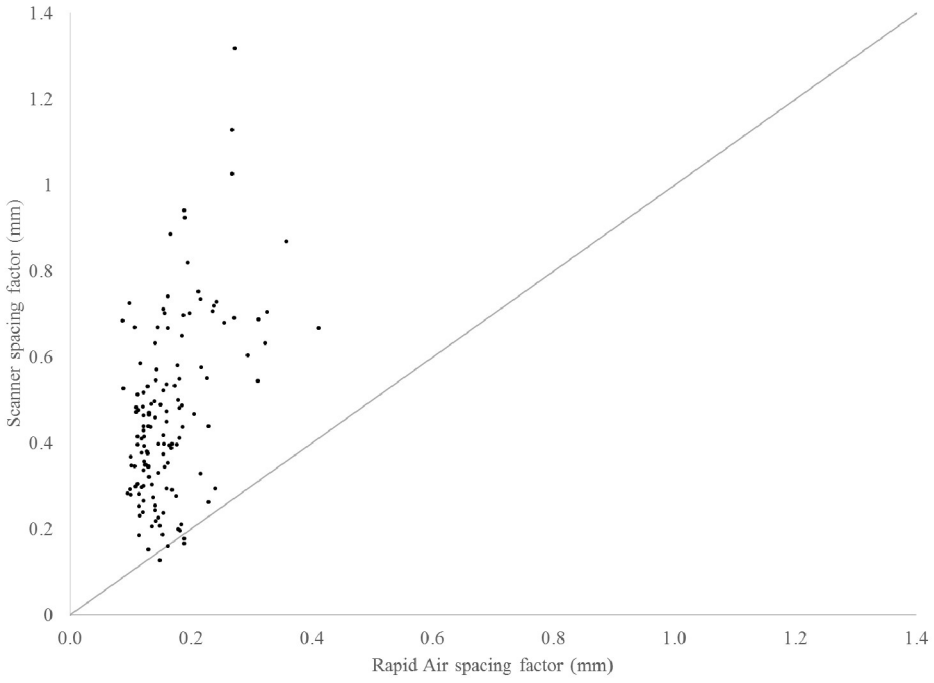

Figure 54. Comparing spacing factor from the Rapid Air with the spacing factor from the scanner and the KSU analyzer.

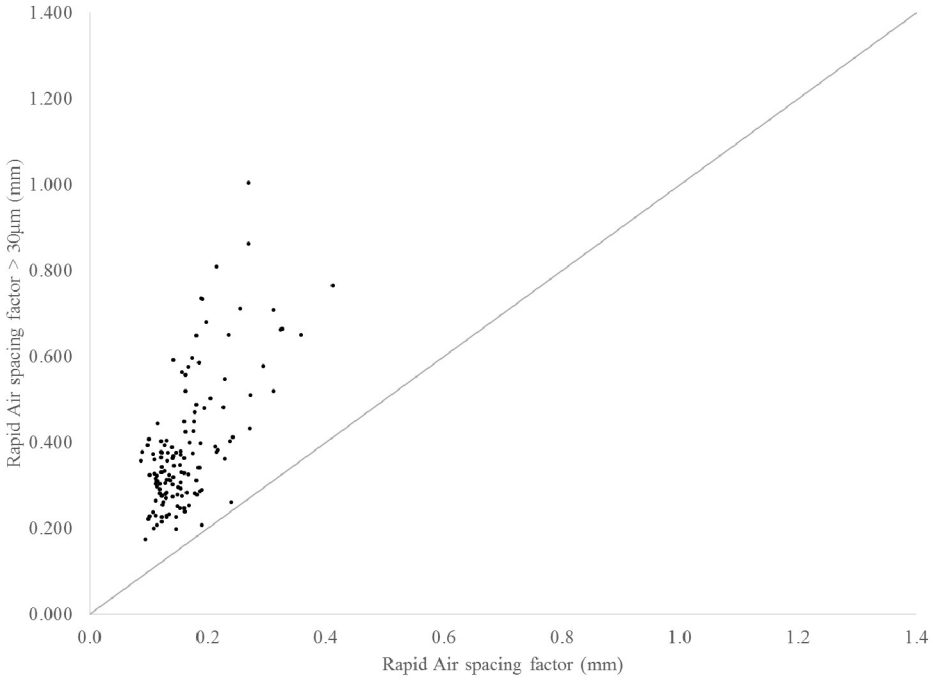

Figure 55. Comparing spacing factors from the Rapid Air without (horizontal) and with (vertical) the omission of air voids lower than 30 µm.

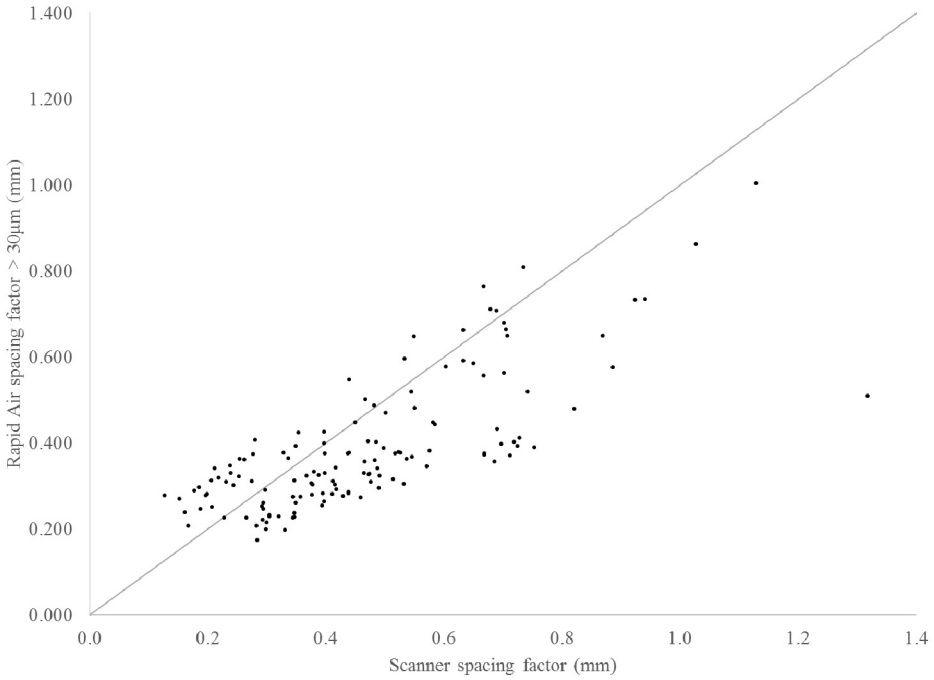

Figure 56. Comparing spacing factor from the Rapid Air by omitting any air void smaller than 30 µm to the spacing factor from the scanner and KSU analyzer.

5.3.7 Freeze-thaw resistance

During the pumping tests, one 80 x 100 x 400 mm beam was cast per test for freeze-thaw analysis. Although ASTM C666 requires at least two specimens to be evaluated, it was not feasible to test that many specimens in this project given equipment limitations. With the current procedure, a maximum of 18 beams were generated on a single day (two mixtures), which would be increased to 36 beams if the standard were exactly followed. The beams were cast on-site (Figure 57), vibrated on the vibration table in case of HWC or CVC, and finished with an aluminum trowel. Specimens were covered with a plastic sheet after production, and demolded in the lab the next day. The specimens were cured in lime-saturated water for 14 days.

The test method followed to determine the resistance of the concrete to rapid freezing and thawing was ASTM C666: Standard Test Method for Resistance of Concrete to Rapid Freezing and Thawing procedure A, rapid freezing and thawing in water. Concrete test specimen were submerged in water and cyclically frozen to -18°C and thawed to 4°C for 468 cycles. This was an extension from the 300 cycles required by ASTM C666. Every 36 cycles, the mass and ultrasonic pulse velocity of each bar was measured. Ultrasonic pulse velocity is a common way to measure deterioration of concrete due to frost. There is a reliable relationship between pulse velocity and dynamic elastic modulus that should produce a dynamic elastic modulus accurate within 10%.

The transducers were placed on either side of the concrete bar and the length of the specimen was measured to calculate the pulse velocity of the concrete. The transmitter sent an ultrasonic pulse (p waves were used) that traveled through the solid material to the receiver. If any crack or discontinuities occur in the concrete, the wave must move around the void since the wave cannot pass through air, causing a lower apparent pulse velocity. In this way, if the apparent pulse velocity slows compared to its original pulse velocity, it can be concluded the concrete is internally damaged [125, 126]. However, according to Bungey and Millard [125], the pulse velocity must change more than 2% to be larger than the variation induced by experimental error. To ensure all concrete bars were in identical conditions while being tested, the bars were placed in a water

bath which was held at 4°C previous to having the pulse velocity measured. In addition to the pulse velocity, the mass was also recorded each time.

From the acquired mass and pulse velocity measurement two parameters were calculated and evaluated. The first is the mass loss of the concrete. This was calculated as a percentage of the original weight. The change in pulse velocity was also calculated as a percentage of the original pulse velocity. As stated previously this change needs to be greater than 2% to be outside of the boundaries of error [125].

During delays required in testing specimens, the saturated specimen were wrapped in plastic and frozen at -18°C to limit the influence of continuing hydration. Once testing space became available and prior to beginning testing, the bars were brought back to 4°C and the pulse velocities and masses were measured before continuing freeze-thaw cycling, as is stated in ASTM C666.

Figure 57. Production of cylinders, freeze-thaw bars and scaling slabs in the field. After completion of all specimens, they were covered with a plastic sheet to minimize evaporation.

5.3.8 Scaling resistance

In similar fashion as the cylinders and the freeze-thaw bars, one 200 x 200 x 90 mm slab sample was produced per test in the field. Consolidation, if necessary, was performed with a vibration table and the sample was finished with a wooden strike-off board. Like for the freeze-thaw specimens, samples were covered with plastic once finished, and demolded in the lab the next day. The samples were cured for 14 days in lime-saturated water and stored in air for an additional 14 days.

This test was completed according to ASTM C672 to determine the scaling resistance of concrete surfaces exposed to deicing chemicals. Once the samples were cured for the designated time, waterproof silicone caulk was applied to the top surface to create a dike. The silicone was applied with a caulk gun while the specimen sat in the wooden molds in which they were cast. Petroleum jelly was used to prevent the caulk from sticking to the molds and the dike was finished at a 45° angle.

The concrete surface was covered with approximately 6 mm deep of a solution of 4% calcium chloride and water. It was subjected to 16 hours of 23°C followed by 8 hours of -18°C. The concrete surface was flushed and the scaled material was collected every 5 cycles up to 50 total cycles. The material was passed through a #100 sieve to prevent any undissolved calcium chloride from being collected (Figure 58). It was then dried in an oven and weighed; this is a deviation from ASTM C672 which calls for visual examination. The collection of the scaled material is based on the European standard procedure (CEN/TS 12390-9). It allows the damage to be quantified and a limit be applied to the damage [127].

ASTM 672 calls for the finished surface to be subjected to scaling, as this is closest to what the concrete will experience in practice. However, the scaling resistance will not only be influenced by the air-void system, but may also be affected by the bleeding of the concrete and finishing procedures required by ASTM C672 [128]. Seen the high w/cm, the high fluidity of the mixtures and the long retardation, bleeding cannot be excluded to be influencing the scaling behavior.

Figure 58. Setup to determine the mass of scaled material after each five cycles.

5.4 Pumping procedures

A standard truck-mounted double piston pump with a boom length of 40 m was used for the experiments. All pipes on the pump were 125 mm in diameter. The flow rate can be varied by the operator, and values between 1 to 47 l/s were employed in the experiments. The boom configuration was either in A-shape, distinctly making an upward and downward section (Figure 59), or in flat condition, i.e. fully extended horizontally (Figure 60). Other modifications in the testing procedure were the use of a reducer from 125 to 100 mm diameter at the end of the boom, and submerging the flexible hose under the concrete surface, instead of holding it within 1 m from the concrete surface. All concrete mixtures were subjected to 4, 5, or 6 pumping tests, pumping each time approximately 700 l in a formwork. 700 l was chosen as this is the approximate volume of concrete inside the boom. As such, the last portions of concrete in the formwork have undergone fully the pumping conditions as established for that test.

The flow rate was estimated by recording the time needed for a number of strokes of the pump. As the pump piston volume is known, the total volume can be estimated. It should though be considered that the pumping

cylinders do not entirely fill, but no calibration technique was available. As such, this estimation method is used.

All concrete was pumped inside a formwork which could hold approximately 800 l of concrete. Samples were removed by bucket from the formwork and transported in wheelbarrows to the places where fresh concrete testing or hardened concrete sample preparation was done. It was elected not to pump concrete directly into a wheelbarrow or in buckets, but rather in formworks to mimic as much as possible real-life scenarios. Furthermore, wheelbarrows or buckets could change the impact of the concrete and thus the air-void system.

Figure 59. Pumping boom in A-shape configuration.

Figure 60. Pumping boom in flat configuration.

Figure 61. Formworks to hold approximately 800 l of concrete.

For each concrete mixture, the concrete was pumped with four to six different pumping parameters. Before all pumping, after all pumping and at some point in the middle of the process, a sample was taken directly from the truck (without pumping). All fresh concrete tests were executed on those samples as well, and specimens were cast for hardened concrete evaluation. As will be discussed in the next section, these non-pumped samples, with their evolution with time, form the basis of the analysis in this research work.

Table 23 shows in which configuration each concrete was pumped. If a number is listed, it is the flow rate estimated by the stopwatch method. If multiple numbers are listed for the same configuration, it means that the concrete was pumped multiple times in that configuration. If no number is listed, the concrete was not pumped in this way.

Table 23. Testing parameters for each concrete mixture. A = A-frame, F = flat, R = reducer, S = submerged. The number indicates the estimated flow rate.

	A	A-R	A-S	A-R-S	F	F-R	F-R-S
MIX 1	11.1	14.6			10.3 17.2		
MIX 2	11.1	18.6		20.5	7.5 19.1 28.9		

MIX 3	20.2	20.0		20.8	5.2 20.3 33.2		
MIX 4	11.1	13.2		11.7	5.9 7.5 28.9		
MIX 5	22.3				5.7 16.8 32.0		
MIX 6	11.1	19.4		18.5	6.4 18.7 36.4		
MIX 7	21.3	22.6		19.1	1.1 21.1 38.0		
MIX 8	20.9	20.4		21.1	1.4 21.8 35.6		
MIX 9	20.4	20.3		21.2	2.1 22.7 37.8		
MIX 10	21.5	22.1		21.5	1.8 21.5 37.5		
MIX 11	6.1 26.0	25.8	6.0 25.0				
MIX 12	6.6 27.3	7.3 24.7	8.6 26.2				
MIX 13	5.5 32.1	5.3 32.5	5.5 31.9				
MIX 14	5.6 25.9	5.5 26.0	5.5 26.7				
MIX 15	5.6 29.1	5.5 28	5.6 29.1				
MIX 16	5.6 30.5	5.5 29.1	5.6 29.1				
MIX 17		5.6 40.8	5.6			5.7 40.5	
MIX 18		46.5	46.5			6.6 46.5	6.2 46.6

5.5 Main analysis strategy

The main purpose of this research work is to determine the influence of pumping on the change in fresh and hardened properties. As such, a comparison between the pumped and non-pumped samples must be established. Figure 62 shows an example of the procedure followed for the analysis. It shows the spacing factor for mix design 6. The black dots are the results for the non-pumped, truck samples. The red dots represent the pumped samples, with codes for F (flat) or A-frame, the use of a reducer (R), keeping the hose submerged (S), and the estimated flow rate in l/s. From the non-pumped samples, the best fitting linear relationship with time is established, and the difference in value of the red dot compared to the black line, at that specific time, is used to determine the difference. In the example of Figure 62, pumping the concrete in flat configuration at 6.4 l/s caused the spacing factor to increase by 0.14 mm. Pumping the concrete in A configuration with a reducer at 19.4 l/s reduced the spacing factor by 0.085 mm. As such, for each pumped sample, a Δproperty could be established, in this case a Δspacing factor. These Δ factors will be used for further analysis.

One of the problems encountered, especially for the spacing factor, is that there is one major outlier in the relationship. Because of the lack of repeat samples (despite the high number of samples taken), engineering judgement was used to delete a point if necessary.

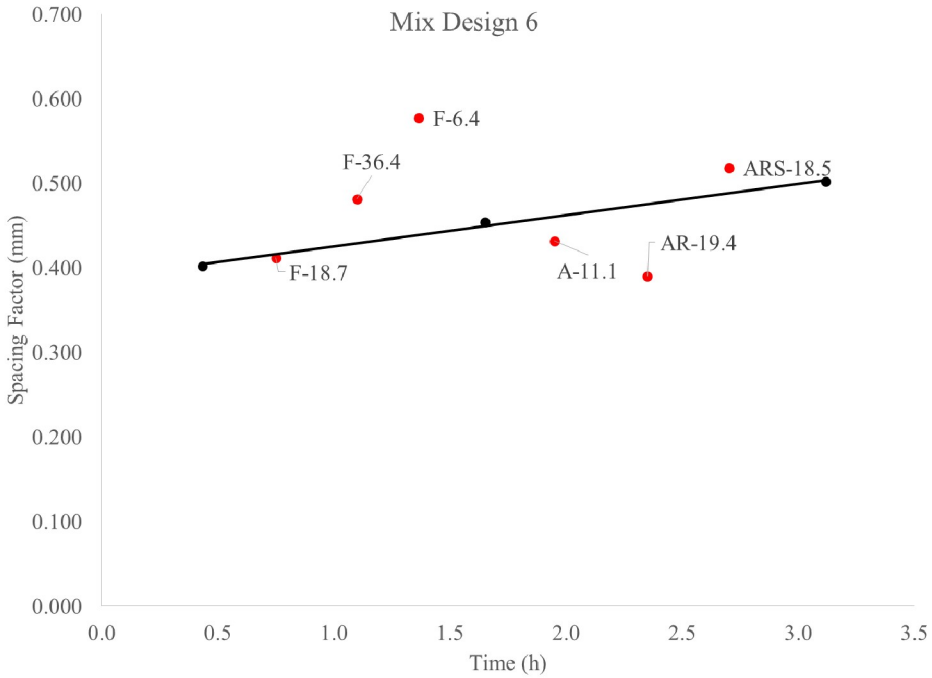

Figure 62. Example of analysis to determine the change in a certain concrete property. The red values are the pumped samples, with coding for the pumping conditions, while the black values are the non-pumped samples.

Some differences between the mix designs need to be taken into consideration during the analysis:

- Mixtures 1 through 8 have the admixtures from producer 1, mixtures 9 through 18 are from producer 2
- Mixtures 1 through 10 do not have defoamer, mixtures 11 through 14 do
- Mixtures 15 through 18 are made with PNS, mixtures 1 through 7 with PCE-1, mixture 8 with PCE-3 and mixtures 11 through 14 with PCE-2

- Mixtures 1, 7 through 12 and 14 through 18 are classified as SCC, mixtures 2 through 4, 6, and 13 are HWC and mixture 5 is a CVC

In the upcoming analyses, these differences are taken into consideration.

5.6 Changes in fresh properties

5.6.1 Slump flow

The change in slump flow was expected to be dependent on a number of factors. It was expected that higher shear rates would increase the observed differences in flow rate, but these findings were obtained on SCC and HWC with low w/cm, while these mixtures all have a more elevated w/cm. Appendix A1 contains all plots for slump or slump flow as a function of time. The analysis for slump flow follows the strategy explained in section 5.5. The following data shows how pumping affects the slump flow of the mixtures. Figure 63 shows all Δslump flow values, split according to workability level (HWC, initial slump flow < 550 mm, and SCC), as well as pumping boom configuration. The extreme values obtained were an increase in slump flow of almost 200 mm, and a decrease in slump flow of just over 130 mm. No clear trend can be observed from Figure 63 for which pumping parameter has which influence. A more individual approach must be used to see which parameter has a substantial influence on the change in slump flow.

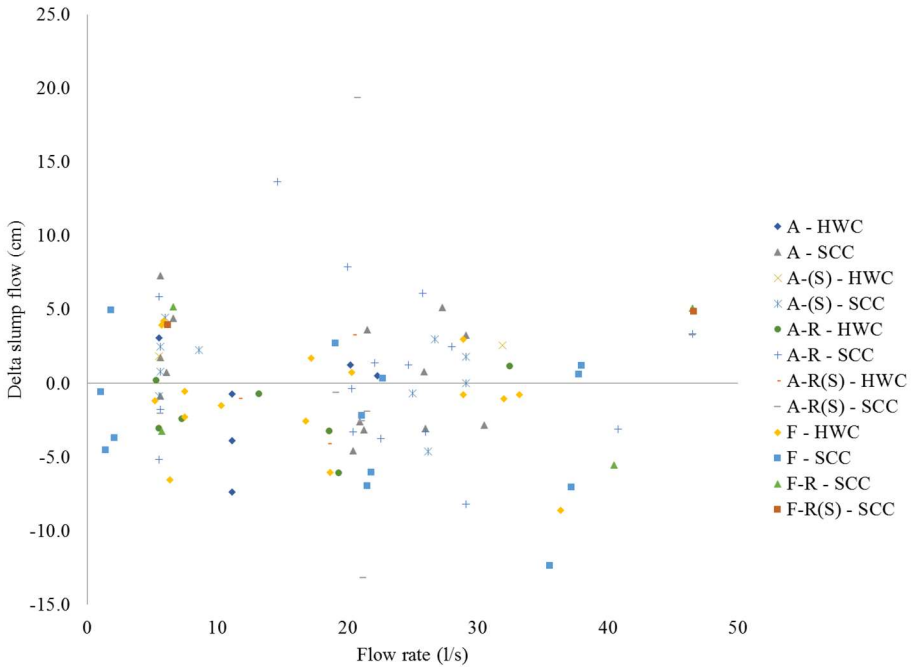

Figure 63. All ΔSlump flow values for the pumping mixtures, split according to pumping condition and according to workability level.

5.6.1.1 Influence of flow rate

Any results for each mix design where the difference was solely the flow rate were compared. This was done for mixtures 11 through 16 in A (Figure 64), A-S (Figure 65) and A-R (Figure 66) configuration, for mixtures 1 through 10 in F configuration (Figure 67 and Figure 68) and mixtures 17 and 18 in different F-R configurations (Figure 69). Figure 64 to Figure 66 show generally a constant Δslump flow or a decrease, which means that the increase is smaller or the decrease is larger. The exceptions are mix design 13 (the only HWC), mix design 12 (for A and A-R) and mix design 14 (for A-S). Strong decreases in Δslump flow are

seen for mix designs 8 and 10 in the F configuration, and for mixtures 4 or 5, at low flow rate as well. Otherwise, a rather constant or even an increase in Δslump flow is seen. Mixture 17 shows a decrease, mix design 18 remains unaffected.

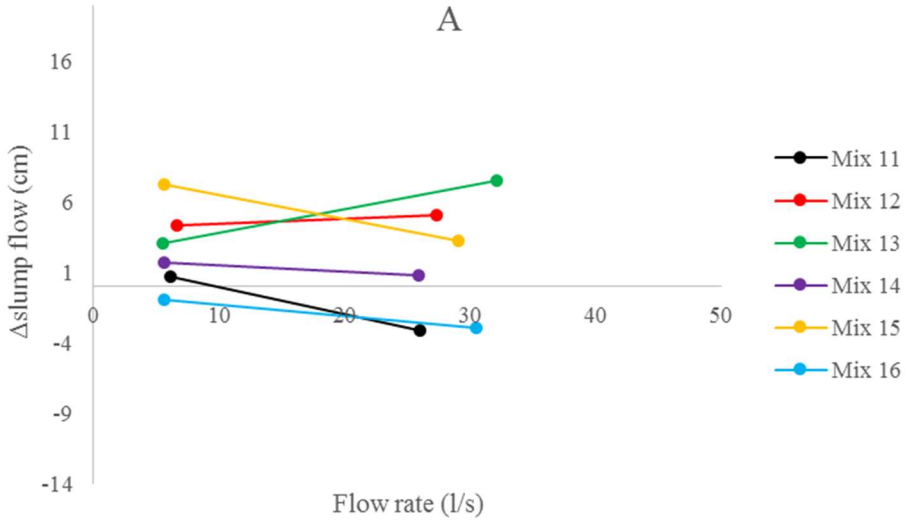

Figure 64. Influence of flow rate on change in slump flow for mixtures 11 to 16 in A configuration.

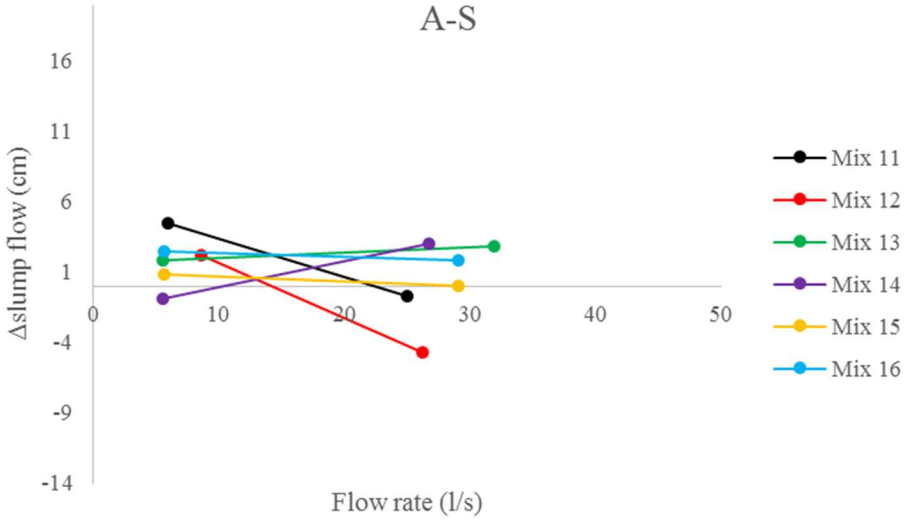

Figure 65. Influence of flow rate on change in slump flow for mixtures 11 to 16 in A-S configuration.

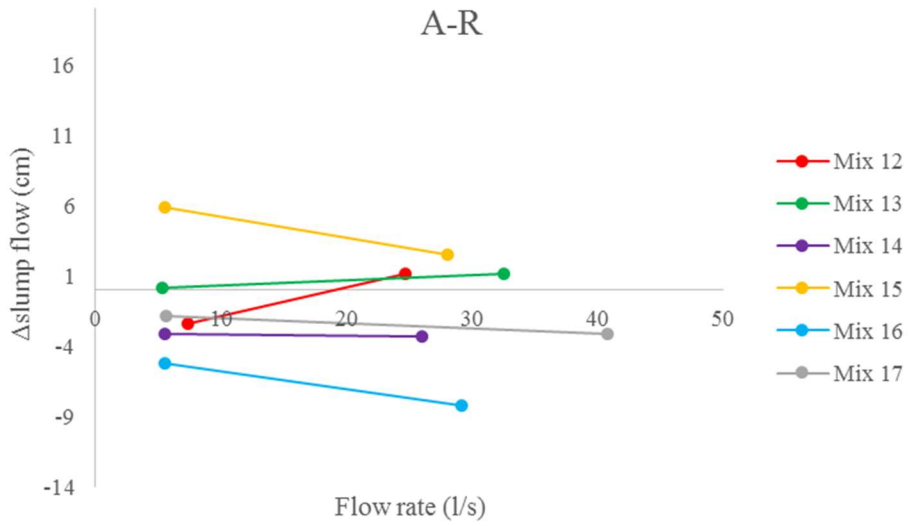

Figure 66. Influence of flow rate on change in slump flow for mixtures 12 to 16 in A-R configuration.

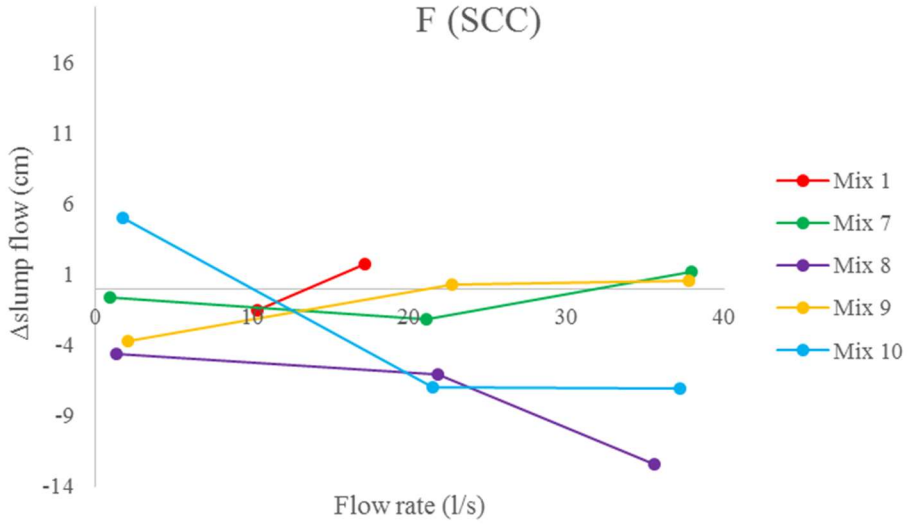

Figure 67. Influence of flow rate on change in slump flow for SCC mixtures 1, 7-10 in F configuration.

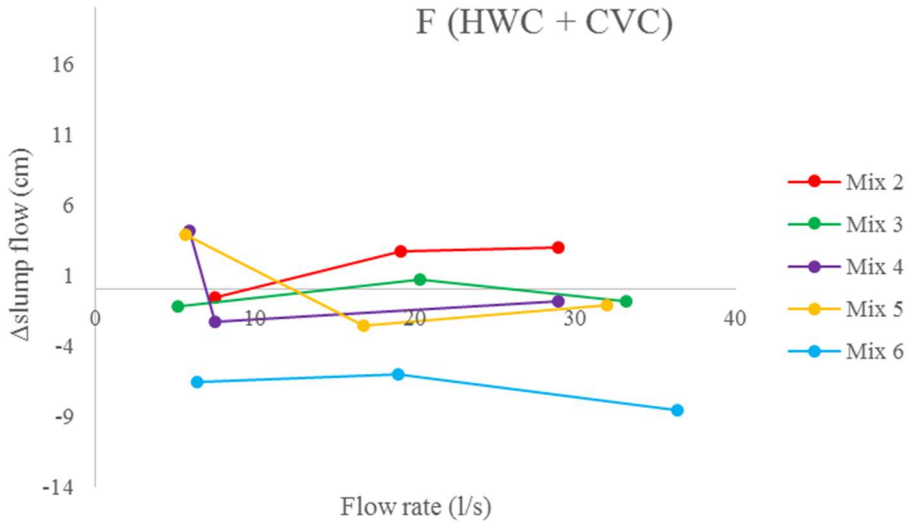

Figure 68. Influence of flow rate on change in slump flow for HWC and CVC mixtures 2 to 6 in F configuration.

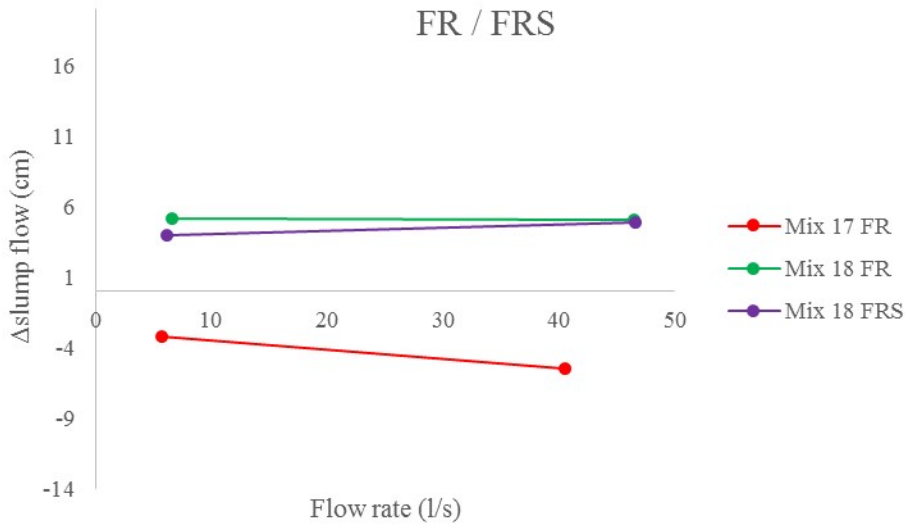

Figure 69. Influence of flow rate on change in slump flow for mixture 17 in F-R configuration and mixture 18 in F-R and F-RS configuration.

5.6.1.2 Influence of reducer

Similarly to the results in section 5.6.1.1, the influence of the reducer can be determined. This is performed for mixtures 2 through 10 in A configuration (Figure 70), and for mixtures 11 through 16 at different flow rates, also in A configuration (Figure 71). Δslump flow seems to be increasing for the HWC and CVC mixtures in Figure 70, and decreases for the SCC mixtures in Figure 70 and Figure 71, except for mix design 9. Mix design 13, also a HWC, shows a decrease in Δslump flow, contrary to the other HWC.

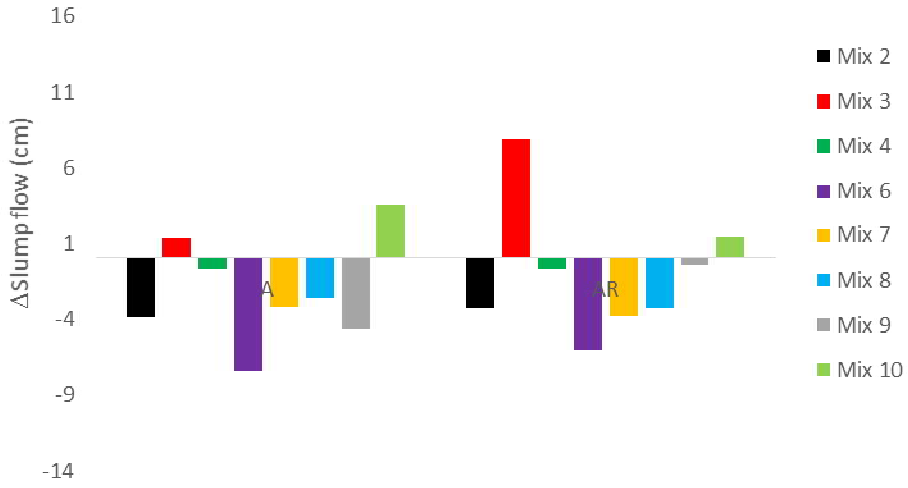

Figure 70. Change in slump flow when applying the reducer (A without on the left, A-R on the right) for mixtures 2-10.

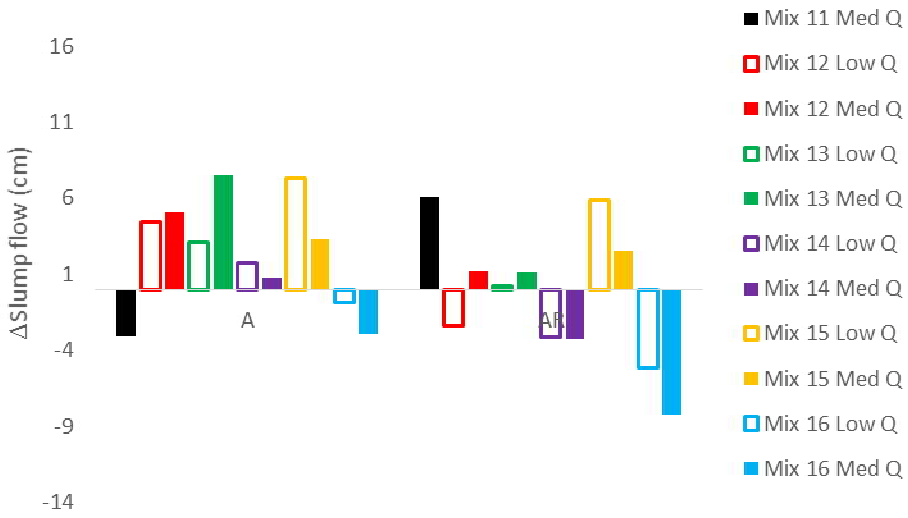

Figure 71. Change in slump flow when applying the reducer (A without on the left, A-R on the right) for mixtures 11-16, at two different flow rates.

5.6.1.3 Influence of submerging the hose

Figure 72 to Figure 74 show the influence of submerging the hose for mixtures 2 through 10, 11 through 16 and 17 through 18, respectively. Figure 72 shows the difference between A-R and A-R-S, Figure 73 compares A with A-S, and Figure 74 shows different comparisons for mixtures 17 and 18. Figure 72 shows an increase in Δslump flow when submerging the hose for mixtures 2 through 8, with some extreme changes. However, for mixtures 9 and 10, the opposite is seen. Figure 73 shows no clear trend, with differences between the mix designs, and even dependent on the flow rate. Figure 74 shows that submerging the hose only has a low influence.

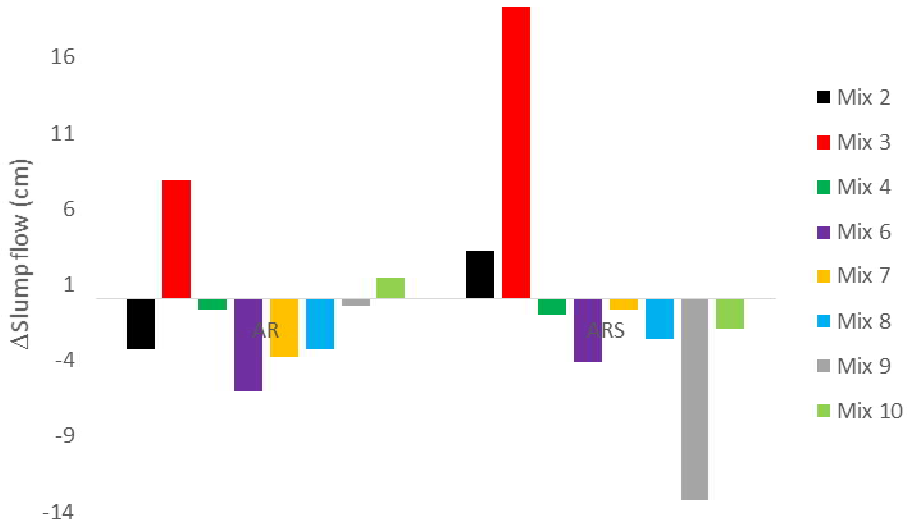

Figure 72. Change in slump flow when submerging the hose (left A-R, right A-R-S) for mixtures 2-10.

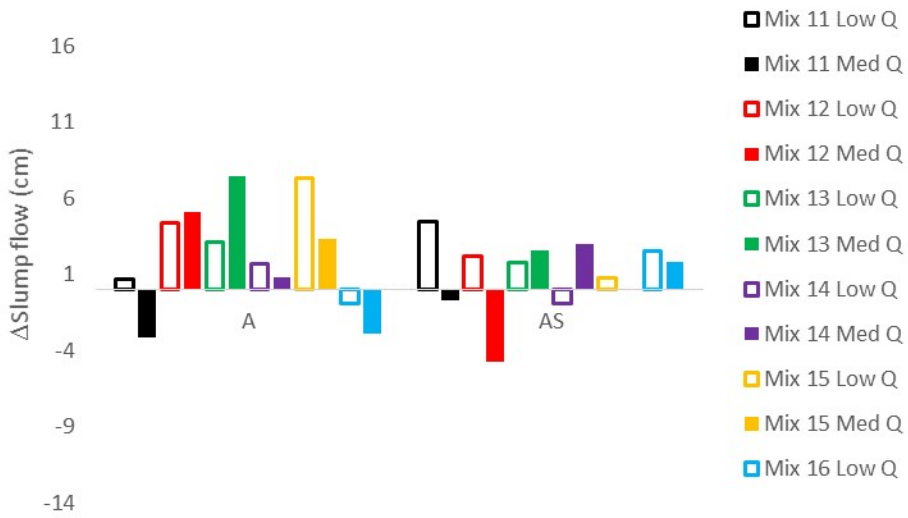

Figure 73. Change in slump flow when submerging the hose at different flow rates (left A, right A-S) for mixtures 11-16.

Figure 74. Change in slump flow when submerging the hose for mixtures 17 and 18.

5.6.1.4 Difference between flat and A configuration

Figure 75 to Figure 77 show how Δslump flow is influenced when changing from A to F configuration for SCC mixtures 1, 7 through 10, HWC and CVC mixtures 2 through 6, and mixtures 17 and 18, respectively. A mixed influence is observed throughout the different figures, not showing a clear influence.

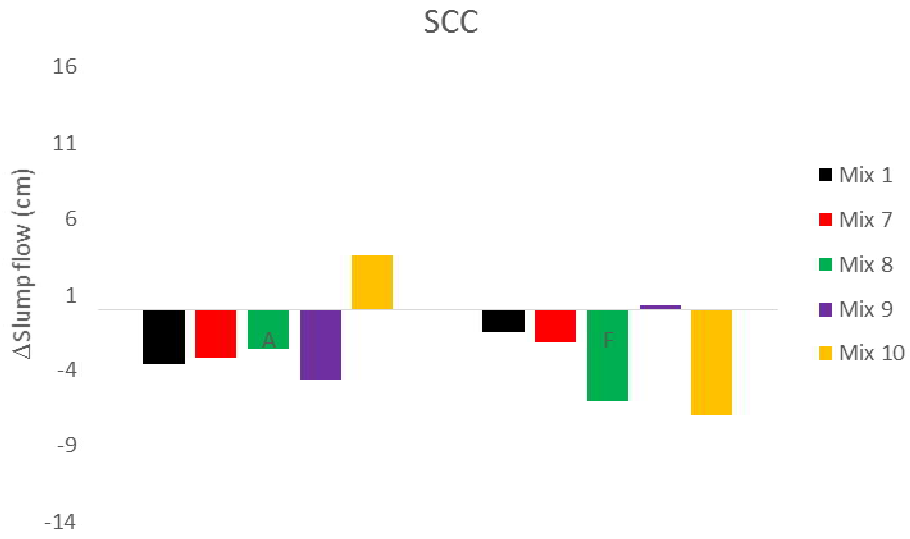

Figure 75. Change in slump flow when changing from A to F configuration for SCC mixtures 1, 7-10.

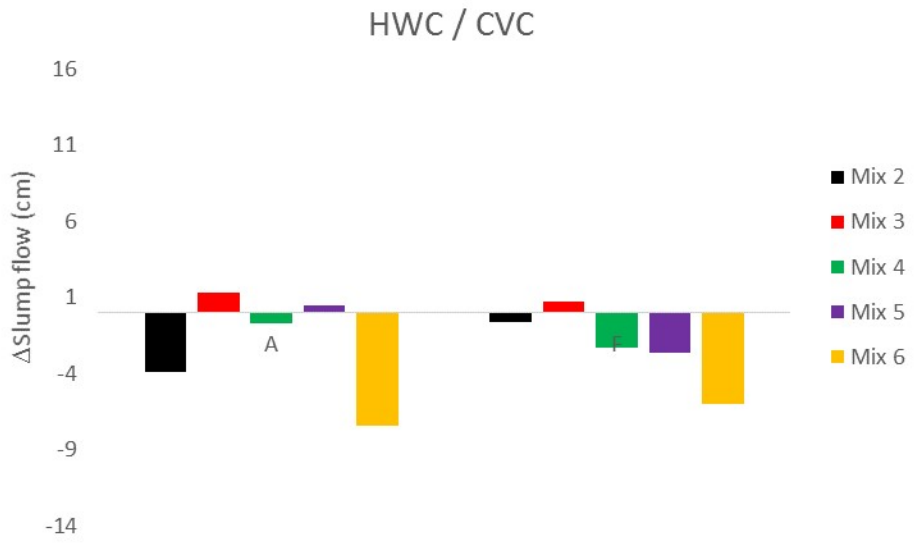

Figure 76. Change in slump flow when changing from A to F configuration for HWC and CVC mixtures 2-5.

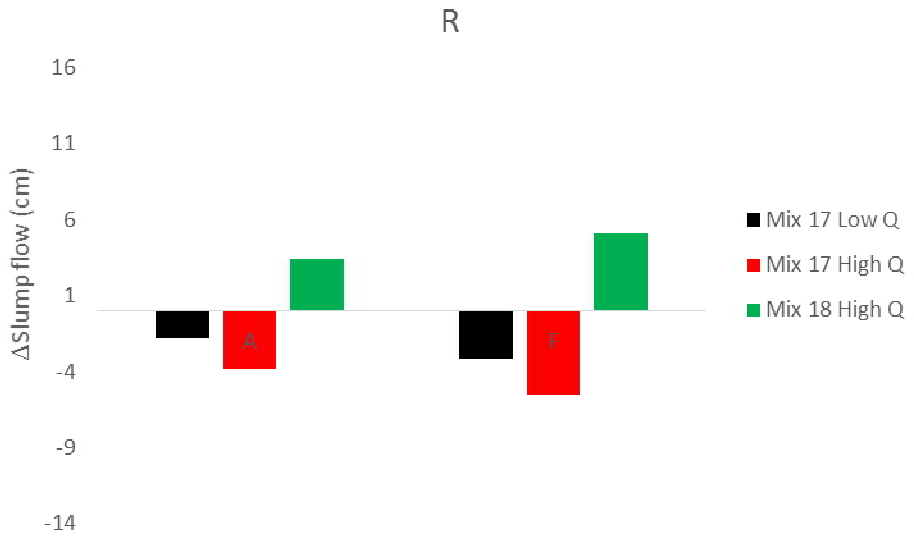

Figure 77. Change in slump flow when changing from A to F configuration for mixtures 17 and 18.

5.6.1.5 Influence of mix design

From the above results, no strong, uniform conclusions can be drawn, indicating that there is a mix design dependency. Although unfair to calculate the average Δslump flow for each mixture, as not all mixtures were exposed to the same pumping conditions, some mix design dependency can be identified by comparing the averages. Table 24 shows the average change in slump flow and the average of the absolute values in changes in slump flow. The latter parameter shows the sensitivity of the mix design to pumping in terms of slump flow. The former shows the average, and if the absolute value and the average value are similar in value (apart from the sign potentially), the slump flow changes systematically in the same direction. Mixtures 6, 3, 8, and 1 are the most sensitive mixtures evaluated. Mixtures 4, 7, 5, and 14 show the smallest variations. Mixtures 3, 18, and 15 show an almost systematic increase, while mixtures 6, 8 and 9 show an almost systematic decrease. The difficult part of this analysis is that mixtures 3 and 4 are HWC, showing opposite

behavior, same as 1 and 7 (SCC). A clear indication of which mix design, which admixture combinations, or which concrete workability class affects the changes in slump flow is not straightforward, despite the clear differences between the mix designs. There are no clear results showing that HWC and SCC behave differently, or whether the trends are influenced by the choice of admixture type or producer.

Table 24. Average and average of the absolute values of the Δslump flow for each mixture (in mm).

	AVERAGE Δ SLUMP FLOW	AVERAGE ABS Δ SLUMP FLOW
MIX 1	26	51
MIX 2	2	28
MIX 3	45	52
MIX 4	-2	16
MIX 5	2	20
MIX 6	-65	65
MIX 7	-15	19
MIX 8	-52	52
MIX 9	-35	38
MIX 10	-10	43
MIX 11	14	28
MIX 12	10	34
MIX 13	27	27
MIX 14	-3	21
MIX 15	33	33
MIX 16	-21	36
MIX 17	-18	35
MIX 18	43	43

5.6.1.6 Summary

There is a lot of variability in the results, and the changes in slump flow are strongly dependent on the mix design. In average, the magnitude of change in Δslump flow is the largest when submerging the hose or not, but, also in average, these is no clear tendency to increase or decrease. Applying a reducer causes a slightly smaller change in the magnitude of the Δslump flow, compared to submerging the hose, but in average, it shows a slight average increase. Increasing flow rate and changing from A to F configuration have a lower, average effect on the magnitude of change in Δslump flow, but both have, on average, a slightly positive effect: slump flow increases a bit more when using the reducer or when pumping in flat configuration. Of course, these changes are strongly dependent on the mix design, and this analysis gives the general trend, but it does not guarantee that each mix design will follow these trends.

5.6.2 Plastic viscosity

Section 5.3.3 describes the analysis procedure for the rheological properties. It mentions that due to issues with torque offset in the rheometer, the yield stress from the rheometer was not reliable. As such, Roussel

and Coussot's equation for yield stress from slump flow was employed to convert slump flow values to yield stress [123]. As such, there is a direct relationship between slump flow and yield stress, and all conclusions drawn for slump flow, above, are valid for the yield stress.

The reason why the yield stress values were obtained was to be able to perform the plug flow correction and determine plastic viscosity. The procedure can be found in 5.3.3. Appendix A.2 contains all plastic viscosity plots for the mixtures, except for mixture 5. Determining the plastic viscosity on a CVC is not a straightforward task. Even mixtures 13 and 12 show close to non-logical results. In general, for mixtures 1 to 14, the plastic viscosity values were very low, this due to the high w/cm of the mixtures. Mixtures 15 to 18 employed a PNS, which required a VMA, increasing the viscosity slightly compared to the PCE mixtures. However, the viscosity values were still low (< 15 Pa s in all cases), much lower than previous studies on pumping SCC. These latter mixtures show in general a decrease in plastic viscosity, which is in agreement with previous studies on pumping SCC. However, combining all results in Appendix A.2, it can be seen that the change in plastic viscosity is generally between -3 and +3 Pa s, with a few exceptions for the latter mixtures (and mix design 6, which we suspect may have had a lower water content). These values are in the accuracy range of any concrete rheometer, so a detailed analysis on which pumping parameters affect plastic viscosity, was not performed.

5.6.3 Interface rheology

The total flow resistance in the interface rheometer (I_{trib}), which was calculated as the slope of torque to rotational velocity, could be a good indicator of pumping pressure. It is influenced by the viscosity of the concrete, but a straightforward relationship is not available. However, this parameter is less sensitive to issues with the rheometer, as it is directly derived from the raw data and is independent of the torque offset. The time-plots for all mixtures are included in Appendix A.3. From these relationships, the ΔI_{trib} can be calculated following the main strategy elaborated in Section 5.5. Figure 78 shows all ΔI_{trib}, showing no clear relationship, similarly to the slump flow data, although a majority of the data points are negative, indicating a (slightly) more fluid concrete after pumping. The largest variations in I_{trib} are -0.5 Nms and 0.4 Nms. With I_{trib} values typically inferior to 1 for a majority of the mixtures, these variations might be substantial. Reliability of the test has not been established in this project, and the authors are not aware of repeatability studies on I_{trib}. On the other hand, it is a test method which is expected to be relatively accurate, as it is directly derived from raw data.

5.6.3.1 Influence of flow rate

Figure 79 to Figure 84 show how ΔI_{trib} is affected by the flow rate. Figure 79, Figure 80, and Figure 81 show the behavior for mixtures 11 through 16, in A, A-S, and A-R configuration, respectively. No clear trend can be observed, although the same mixtures typically behave consistently. For example, mixture 14 shows a decrease for all three configurations. Figure 82 shows a similar picture with no clear influence for SCC mixtures 1, and 7 through 10, while the same can be said for HWC and CVC mixtures 2 through 6 (Figure 83). It can be observed from both figures that ΔI_{trib} seems more dependent on the mix design than on the flow rate, at least for mixtures 1 through 10. Also, the influence of pumping on ΔI_{trib} seems more important for the HWC than for the SCC mixtures. For mixtures 17 and 18, a low influence can be seen (Figure 84).

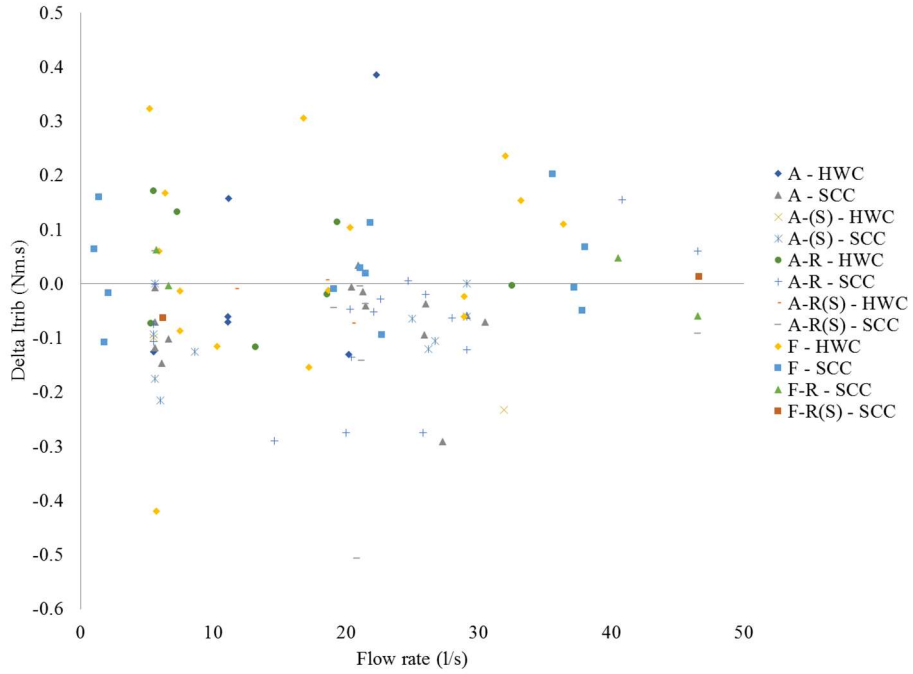

Figure 78. ΔI_{trib} for all mixtures and all pumping parameters.

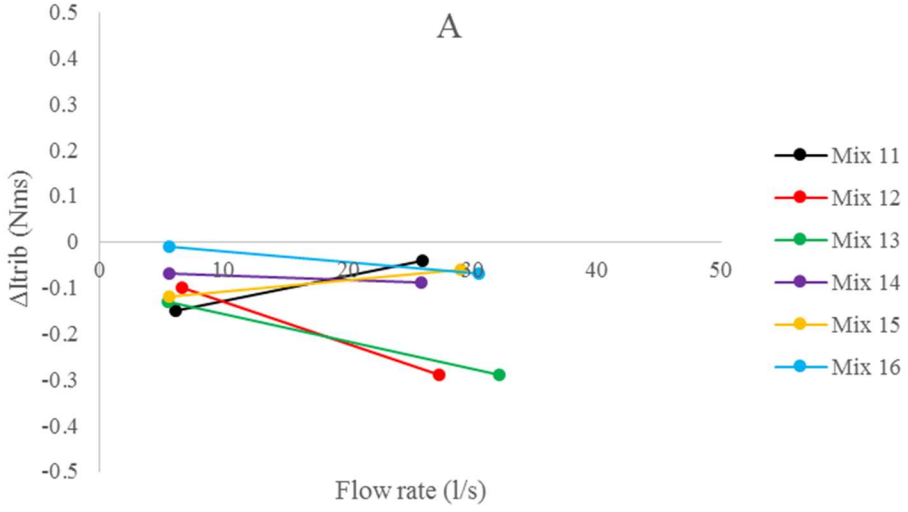

Figure 79. Change in total flow resistance in interface rheometer due to a change in flow rate for A-configuration.

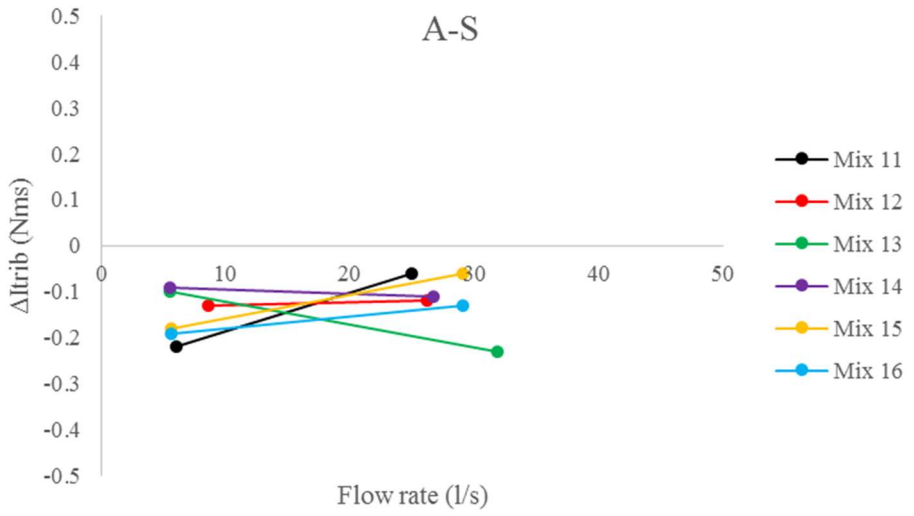

Figure 80. Change in total flow resistance in interface rheometer due to a change in flow rate for A-S configuration.

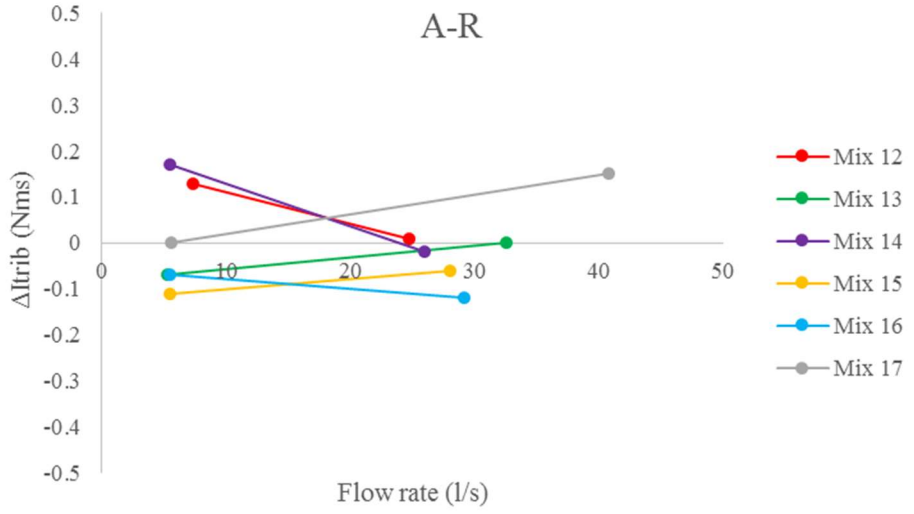

Figure 81. Change in total flow resistance in interface rheometer due to a change in flow rate for A-R configuration.

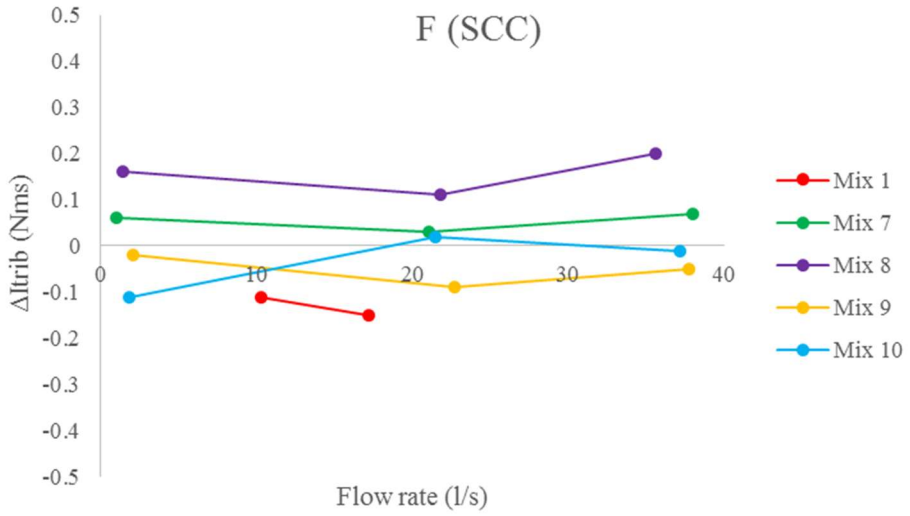

Figure 82. Change in total flow resistance in interface rheometer due to a change in flow rate for SCC in F configuration.

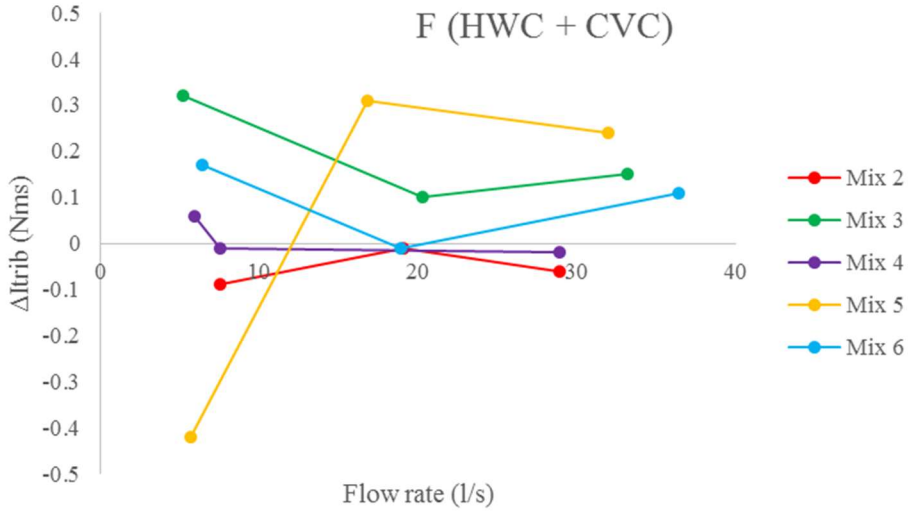

Figure 83. Change in total flow resistance in interface rheometer due to a change in flow rate for HWC and CVC in F configuration.

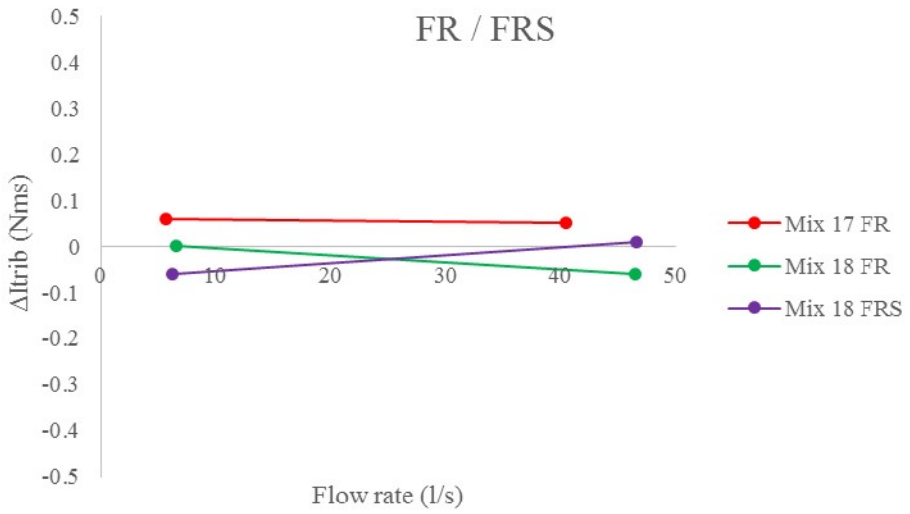

Figure 84. Change in total flow resistance in interface rheometer due to a change in flow rate for mixtures 17 and 18 in F configuration.

5.6.3.2 Influence of reducer

Figure 85 and Figure 86 show the influence of applying a reducer for mixtures 2 through 10 (except 5) and 11 through 16, respectively. Figure 85 shows that using the reducer decreases ΔI_{trib}, while the opposite is observed in Figure 86. Also, it seems that the ΔI_{trib} values for the A-configuration, apart from mixtures 4 and 16 (8 is negligible) are typically negative, while for A-R more positive ΔI_{trib} values are observed.

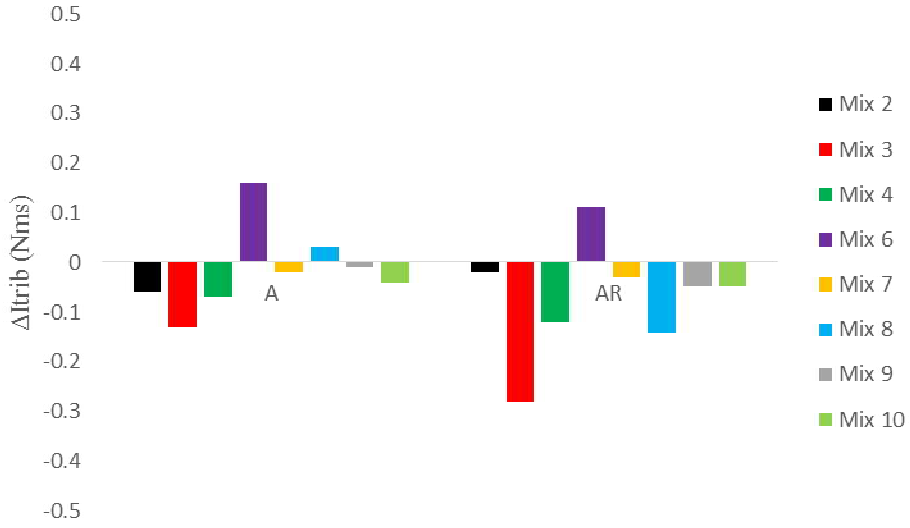

Figure 85. Change in total flow resistance in interface rheometer for A configuration (left) versus A-R configuration (right) for mixtures 2-10.

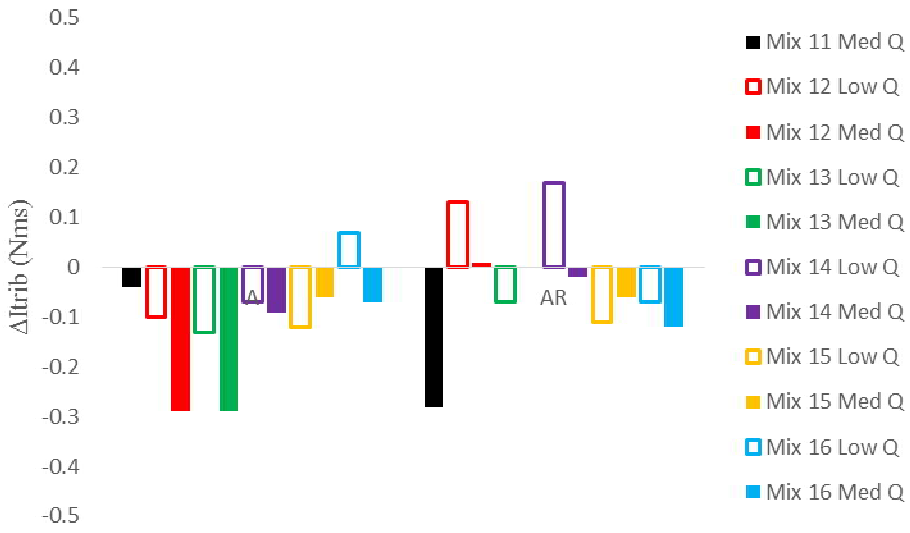

Figure 86. Change in total flow resistance in interface rheometer for A configuration (left) versus A-R configuration (right) for mixtures 11-16.

5.6.3.3 Influence of submerging the hose

Figure 87 to Figure 89 show the effect of submerging the hose on ΔI_{trib}. Although no definite increase or decrease can be detected, it is clear that submerging the hose causes almost all ΔI_{trib} values to be negative, fluidifying the concrete. The only exception seems mixture 17, which lost significant slump flow for each pumping operation (see Appendix A.1).

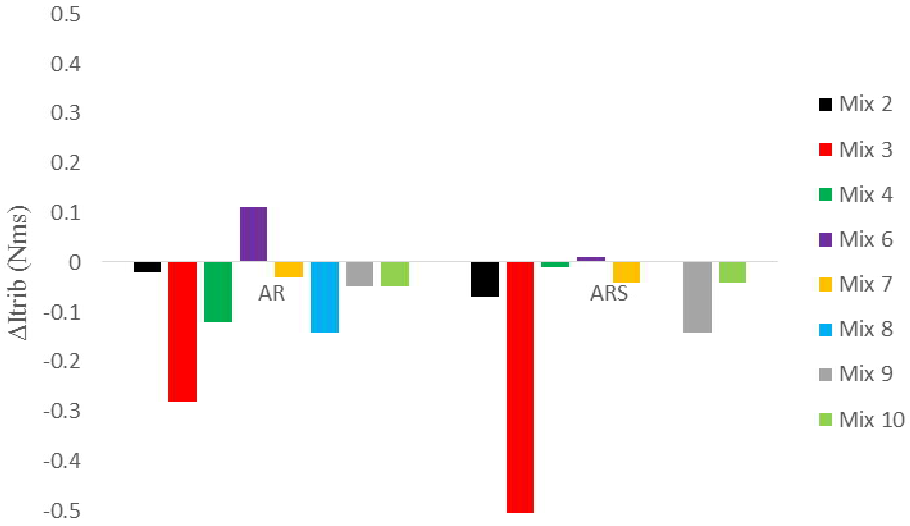

Figure 87. Change in total flow resistance in interface rheometer for A-R configuration (left) versus A-R-S configuration (right) for mixtures 2-10.

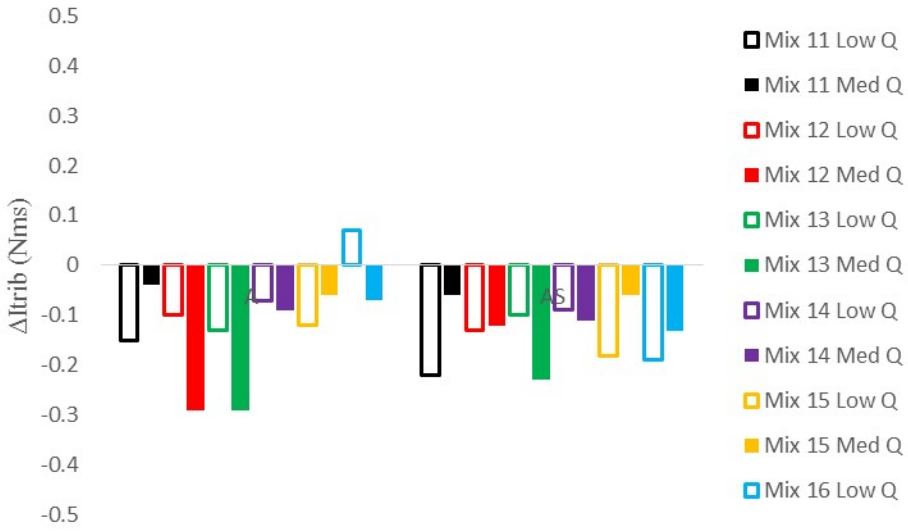

Figure 88. Change in total flow resistance in interface rheometer for A configuration (left) versus A-S configuration (right) for mixtures 11-16.

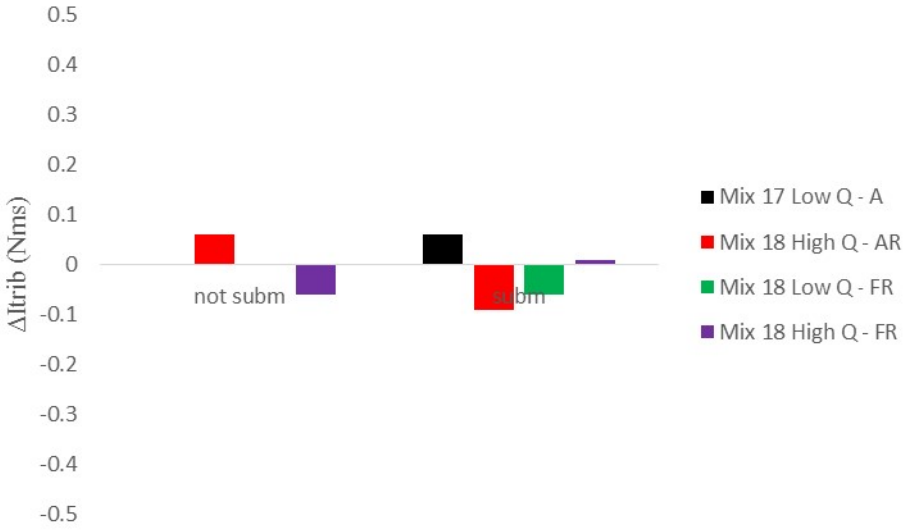

Figure 89. Change in total flow resistance in interface rheometer for non-submerged (left) versus submerged conditions (right) for mixtures 17-18.

5.6.3.4 Difference between A and flat configuration

Figure 90 to Figure 92 show the difference between the A and flat configuration. No clear influence of boom configuration can be observed.

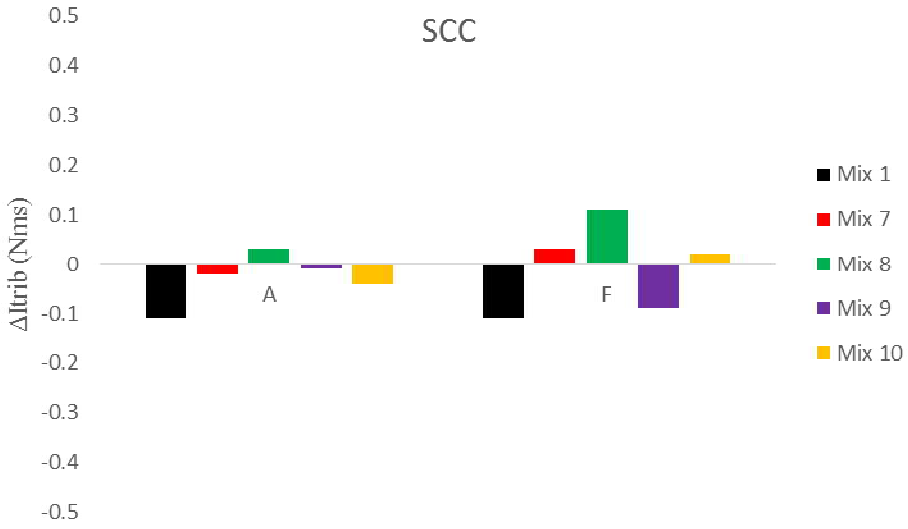

Figure 90. Change in total flow resistance in the interface rheometer between A (left) and F (right) configuration for SCC mixtures 1, 7-10.

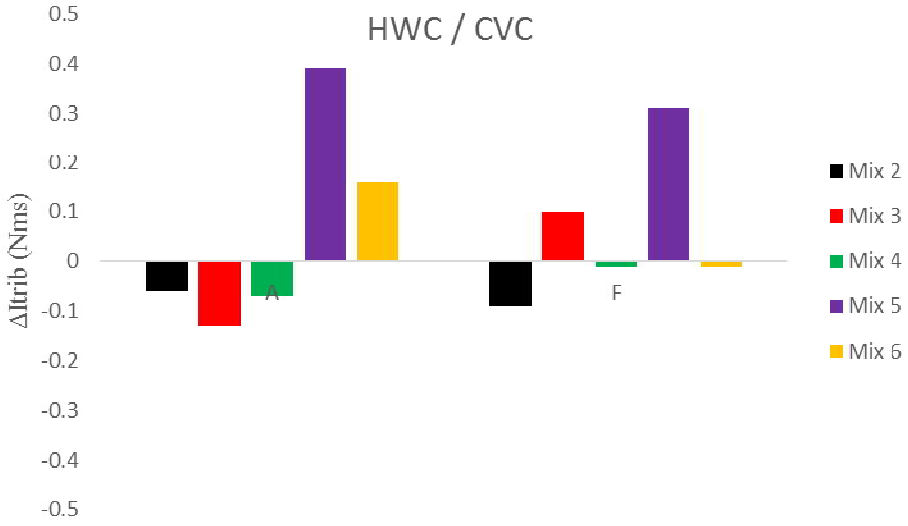

Figure 91. Change in total flow resistance in the interface rheometer between A (left) and F (right) configuration for HWC and CVC mixtures 2-6.

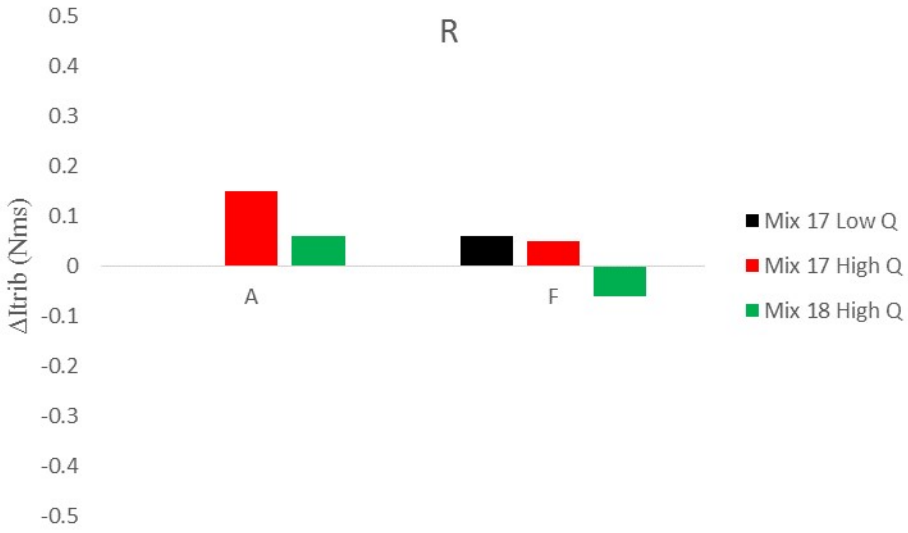

Figure 92. Change in total flow resistance in the interface rheometer between A (left) and F (right) configuration for mixtures 17 and 18.

5.6.3.5 Influence of mix design

Table 25 shows the average ΔI_{trib} for each mix design, and although mixtures have undergone different pumping conditions, this can sketch a general picture. Similarly as for the slump flow, the average of the absolute values of ΔI_{trib} show the sensitivity of the mixture to pumping. Most of the SCC mixtures show an average decrease in ΔI_{trib}, meaning that the concrete fluidifies due to pumping, with the exception of SCC 17. This latter mixture showed a systematic decrease in slump flow due to pumping, which could be translated in an increase in I_{trib}. The largest changes in ΔI_{trib} were found for mixtures 5, 3, and 1. Mixtures 3 and 1 also showed larger sensitivity for the slump flow (and mix 5 is a CVC). The smallest changes were found for mixture 7, 10, 2, 4, and 18. Similarly to slump flow, these is no clear indication why a certain mix design, admixture combination or workability class is more sensitive than another.

Table 25. Average and average of the absolute values for the change in ΔI_{trib} for each mix design.

	AVERAGE ΔI_{TRIB}	**AVERAGE ABS ΔI_{TRIB}**
MIX 1	-0.17	0.17
MIX 2	-0.05	0.05
MIX 3	-0.05	0.25
MIX 4	-0.03	0.05
MIX 5	0.13	0.34
MIX 6	0.09	0.09
MIX 7	0.01	0.04
MIX 8	0.06	0.11
MIX 9	-0.06	0.06
MIX 10	-0.04	0.04
MIX 11	-0.1	0.13

MIX 12	-0.08	0.13
MIX 13	-0.14	0.14
MIX 14	-0.04	0.09
MIX 15	-0.1	0.10
MIX 16	-0.08	0.11
MIX 17	0.05	0.06
MIX 18	-0.02	0.05

5.6.3.6 Summary

The main take-away from the effect of pumping on ΔI_{trib} is that the majority of the values are negative, especially for the A configuration and when submerging the hose. Changing flow rate and adding a reducer resulted in a slightly larger average change in magnitude of ΔI_{trib}, compared to submerging the hose or changing between A and F configuration.

5.6.4 Sieve stability

Appendix A.4 contains the time graphs of the sieve stability values for pumped and non-pumped samples. The sieve stability test was only executed on SCC mixtures, as HWC and CVC would show no results. Acceptance criteria in the European Guidelines for SCC vary from < 20%, over < 15% and < 10%, dependent on the application [122]. Mixtures 8, 12, 14, 16 and 18 do not show any form of segregation throughout the test, as all sieve stability values are below 10%. Mixtures 9 and 17 have a limited number of sieve stability values just over 10%, and it does not seem that pumping affects stability in these cases. Mixture 10 shows an initial, non-pumped value of around 18%, but all other subsequent values were below 10%.

Mix design 7 has sieve stability values between 10 and 15%, indicating some segregation sensitivity. However, pumping does not appear to increase segregation potential. Mix design 11 shows one value between 10 and 15%, corresponding to pumping at medium flow rate in A frame. Strangely, this same pumping condition induced a decrease in slump flow, and only a slight decrease in I_{trib}. So it is unsure whether this is a measurement error.

The non-pumped samples of mix design 15 show sieve stability values between 10 and 15%, while three tests cause the sieve stability results to rise between 15 and 20%, indicating some additional segregation. This occurs for A-S at medium flow rate, and at A and A-R at low flow rates, so no specific correlation between the different testing parameters. A-S at low flow rate and A and A-R at medium flow rates did not show such increase in sieve stability. The largest increases in slump flow due to pumping for mixture 15 were observed for A-S medium flow rate (+ 30 mm) and A-low flow rate (+ 17 mm). However, A-R at low flow rate showed a slump flow loss of 31 mm. The ΔI_{trib} values for SCC 15 were all negative, indicating a reduction in flow resistance in the tribometer, which may be caused by a decrease in viscosity. Together with mix design 11, mix design 15 did show the most negative ΔI_{trib} values, apart from mix design 1, for which no sieve stability measurements were performed.

If the concrete mixture is borderline unstable, pumping may render it more unstable, but this research has not shown cases in which a stable concrete has become unstable due to pumping. However, with further decreasing w/cm, and potentially more sensitivity of the rheological parameters to pumping operations, this statement may no longer be valid.

5.6.5 Density and air content

Appendix A.5 shows the density variation of the fresh concrete for non-pumped and pumped samples. Appendix A.6 shows the same information, but for the air content of the fresh concrete measured by means

of the pressure method. The analysis of the air content was performed in similar fashion as the analysis for slump flow and total flow resistance in the interface rheometer. Figure 93 shows the general results for the change in air content for all mixtures, taking the comment about the analysis of mix designs 7 and 8 below into consideration. The results again show a large variation, but a decrease in air content is more prominent than an increase. The lowest ΔAir is around -4.2 %, while the highest value is around +1.5%. The accuracy of the air content test for a single operator is ±0.88 % for a single operator, so any ΔAir values below 1% in absolute value could be considered within the variability of the test.

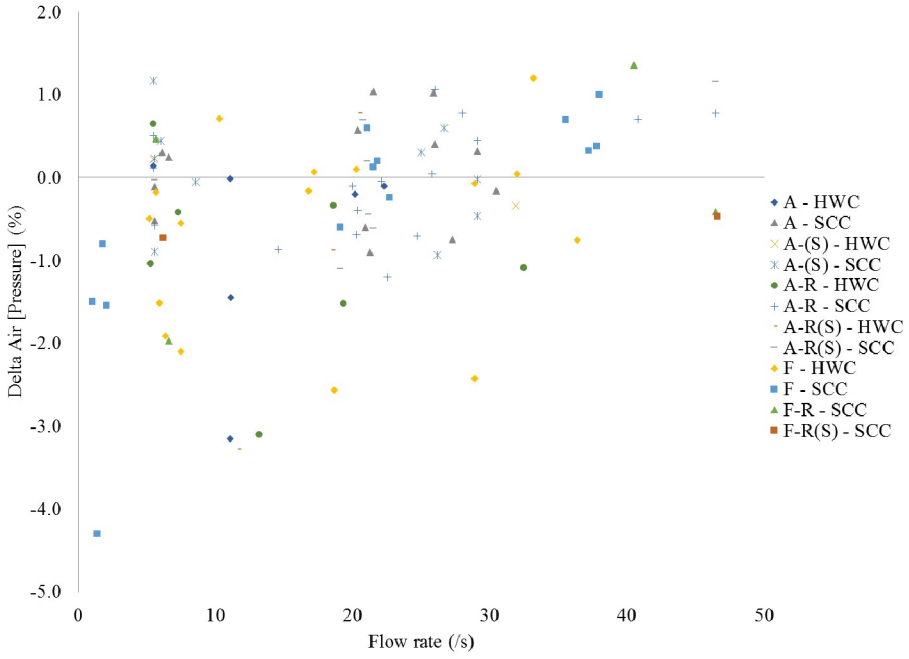

Figure 93. Change in fresh concrete air content for all mix designs and pumping configurations.

5.6.5.1 Mixtures 7 and 8

Mixtures 7 and 8 showed some visible signs of segregation at the moment the mixtures were produced. To avoid excessive segregation in the mixer truck, it was decided to continuously agitate the truck during the entire procedure, in contrast to all other mixtures. Figure 94 shows the evolution of the air content of the non-pumped samples over time (black dots). A clear increase with time, from 8% up to 14% of air, can be seen. However, it is believed that the increase in air content of the non-pumped samples is due to the continuous agitation of the truck. All pumped samples in Figure 94, except for the first, show an air content around 8%. Figure A6.7, which plots the same information for mix design 7, shows a similar trend. It is unclear if this is due to pumping, changes in workability, or sampling. However, agitating the mixture to increase the air content because it is "below spec" is not an acceptable procedure. The increase in air, which is captured by the pressure method for the non-pumped samples, will be completely removed due to the pumping procedure.

For the analysis of mix designs 7 and 8, instead of comparing the pumped results to the trendline for the non-pumped results, they were compared to the initial values instead.

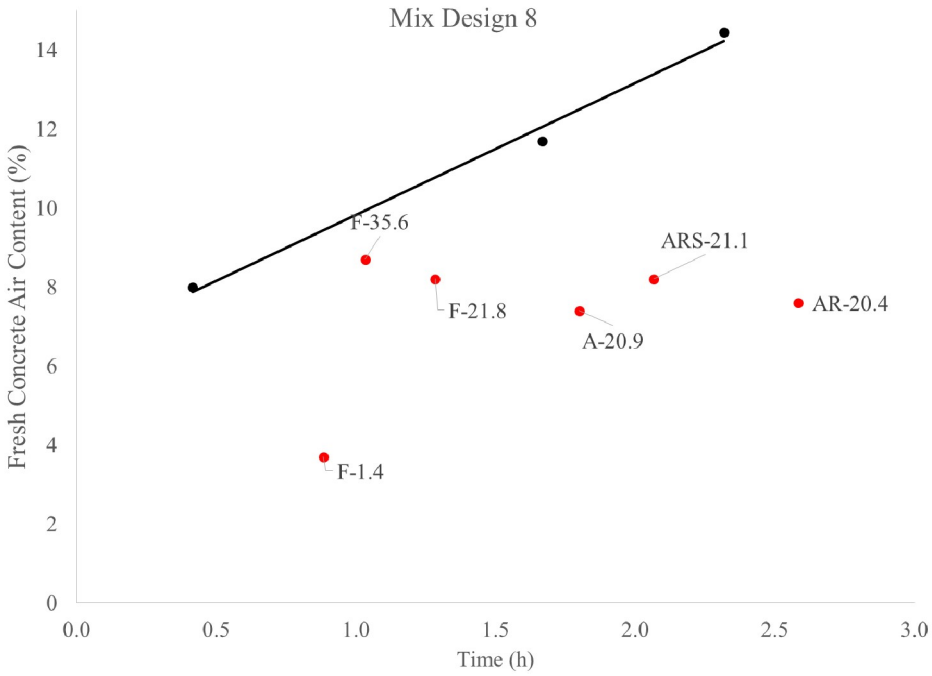

Figure 94. Fresh concrete air content for mix design 8.

5.6.5.2 Influence of flow rate

Figure 95 to Figure 97 show the change in fresh concrete air content for mixtures 11 through 16 in A, A-S and A-R configurations. The A-S results show a decrease in Δair with an increase in flow rate (Figure 96), mixture 16 being the exception. This means that with faster pumping, the concrete either gains less air or loses more air. For A-R configuration, a similar trend could be observed, but now mixtures 14 and 15 show the opposite behavior (Figure 97). The picture for the A configuration is more mixed (Figure 95). Figure 98 and Figure 99 show the effect of pumping flow rate on Δair in the flat configuration for SCC, and for HWC / CVC, respectively. Both figures show that with increasing flow rate, Δair increases, opposite to the findings from Figure 96, especially when increasing the flow rate to large values. This means that the largest losses of air occur at the lowest flow rates in F configuration, which is more or less opposite to any theory put forward on air losses. It might be that the impact of the concrete in the reservoir, which is proportional to the velocity squared, may have a non-negligible influence. Figure 100 shows a similar trend for the F configuration for mixtures 17 and 18.

It is possible that to study the influence of flow rate, a distinction needs to be made between flat and A configuration, as the influence of flow rate might be opposite. Mixture 17, the only one pumped at different flow rates in A and F configuration, shows a decrease in Δair for the A-configuration, and an increase for the F-configuration with increasing flow rate.

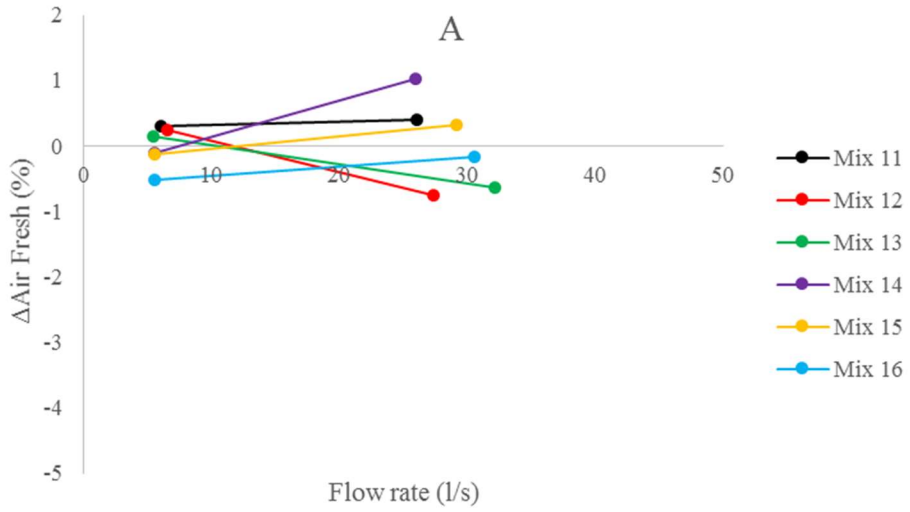

Figure 95. Change in fresh air content due to pumping as a function of flow rate for A configuration and mixtures 11-16.

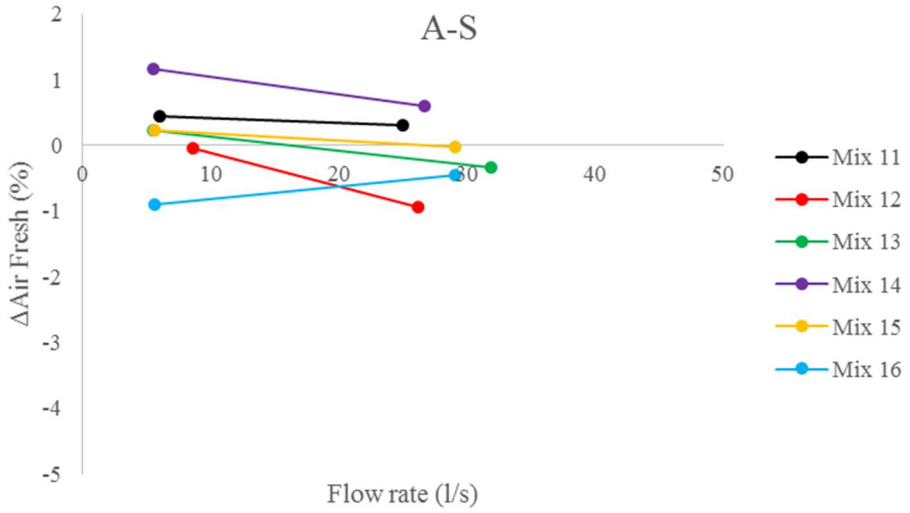

Figure 96. Change in fresh air content due to pumping as a function of flow rate for A-S configuration and mixtures 11-16.

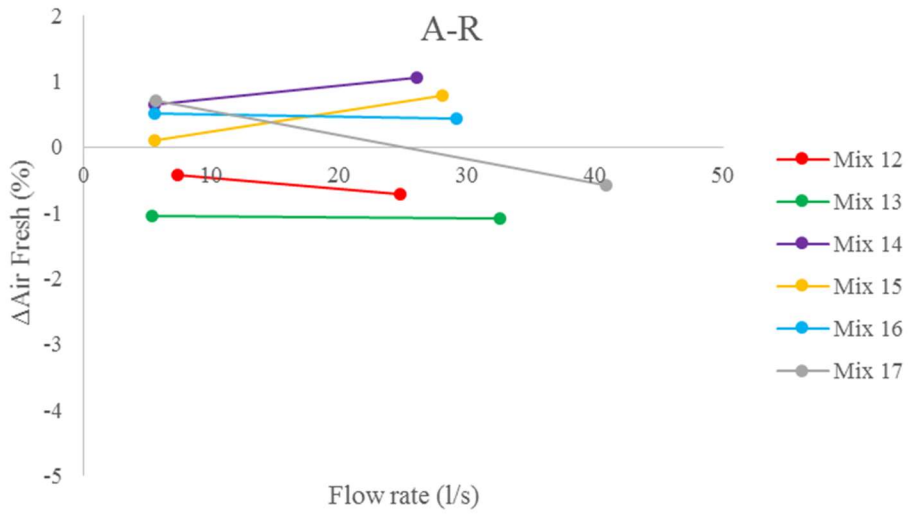

Figure 97. Change in fresh air content due to pumping as a function of flow rate for A-R configuration and mixtures 12-17.

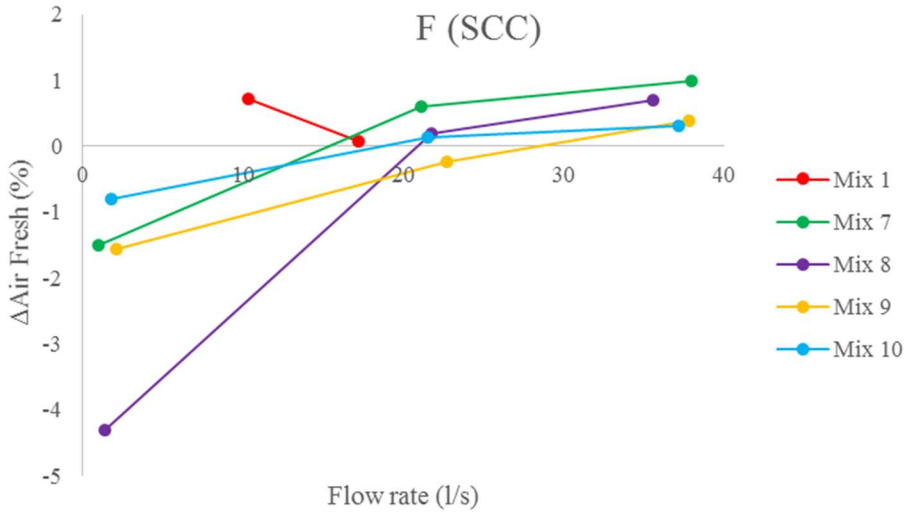

Figure 98. Change in fresh air content due to pumping as a function of flow rate for F configuration and SCC mixtures 1, 7-10.

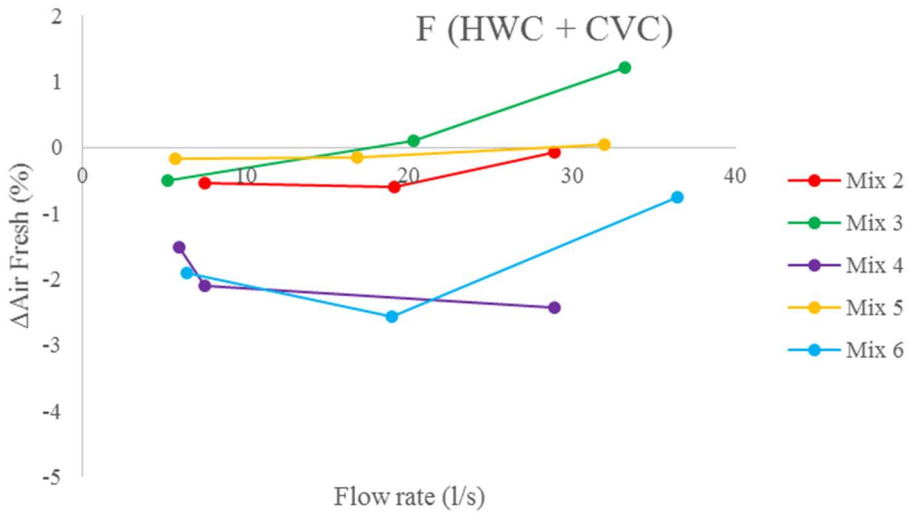

Figure 99. Change in fresh air content due to pumping as a function of flow rate for F configuration and HWC / CVC mixtures 2-6.

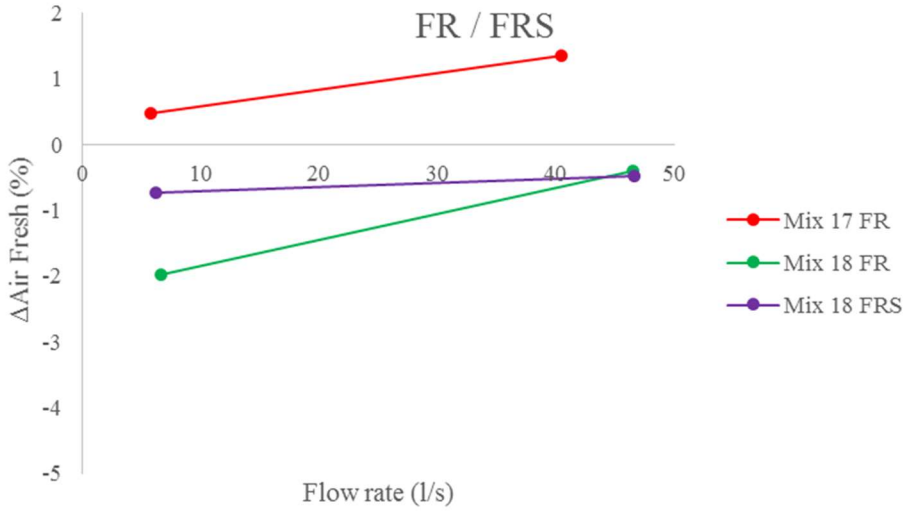

Figure 100. Change in fresh air content due to pumping as a function of flow rate for mixtures 17 and 18.

5.6.5.3 Influence of reducer

Figure 101 and Figure 102 show the change in air content when concrete is pumped with and without reducer. Figure 101 shows only minor influences of the reducer on the change in air content for mixtures 2 through 8, with somewhat larger changes for mixtures 9 and 10. Figure 102 shows a mixed picture, with no clear influence of the reducer.

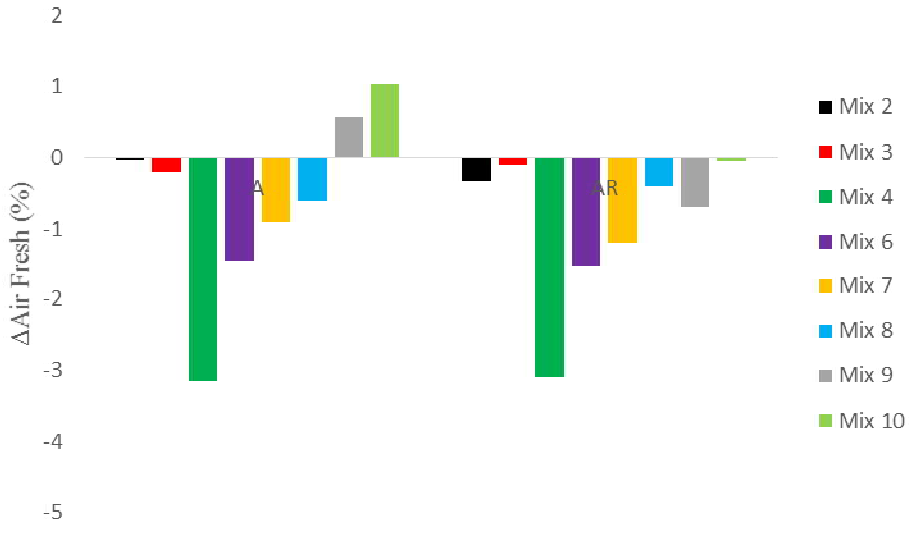

Figure 101. Change in fresh air content in A configuration (left) and A-R configuration (right) for mix designs 2-10.

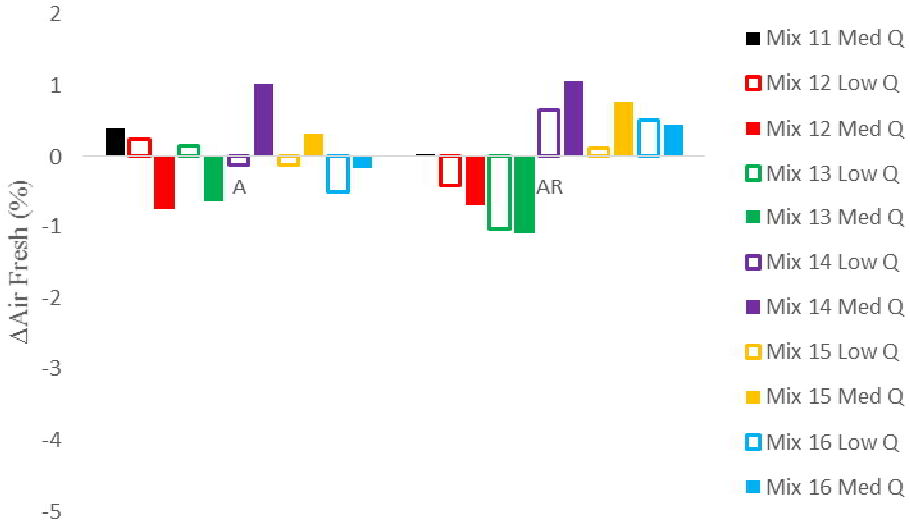

Figure 102. Change in fresh air content in A configuration (left) and A-R configuration (right) for mix designs 11-16.

5.6.5.4 Influence of submerging the hose

Figure 103 and Figure 104 show the change in air content with and without submerging the hose, for mixtures 2 through 10 and 11 through 16, respectively. Both figures show no major influence of submerging the hose on the change in air content, except for mixtures 1, 2 and 14. Figure 105 shows the effect for mixtures 17 and 18. A reduction in air loss due to pumping can be seen when submerging the hose.

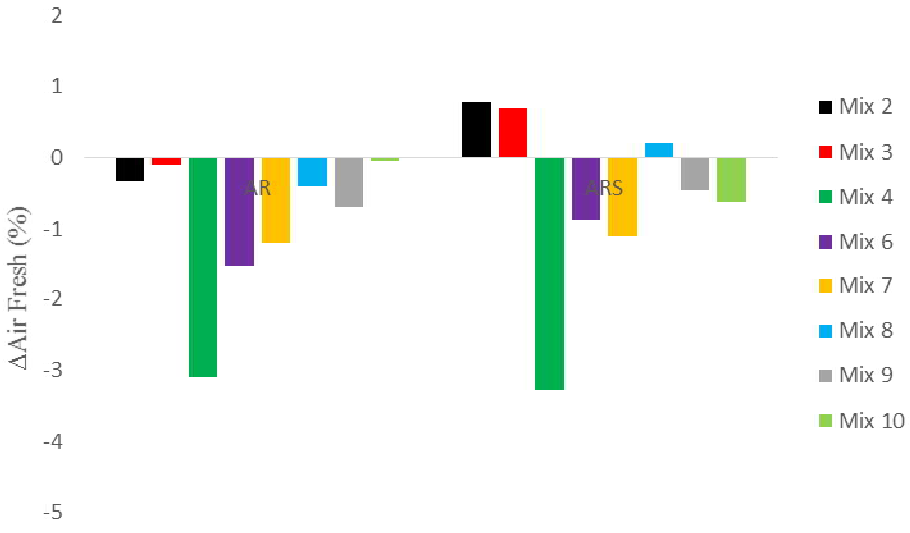

Figure 103. Change in fresh concrete air content for the A-R-configuration (left) and the A-R-S configuration (right) for mixtures 2-10.

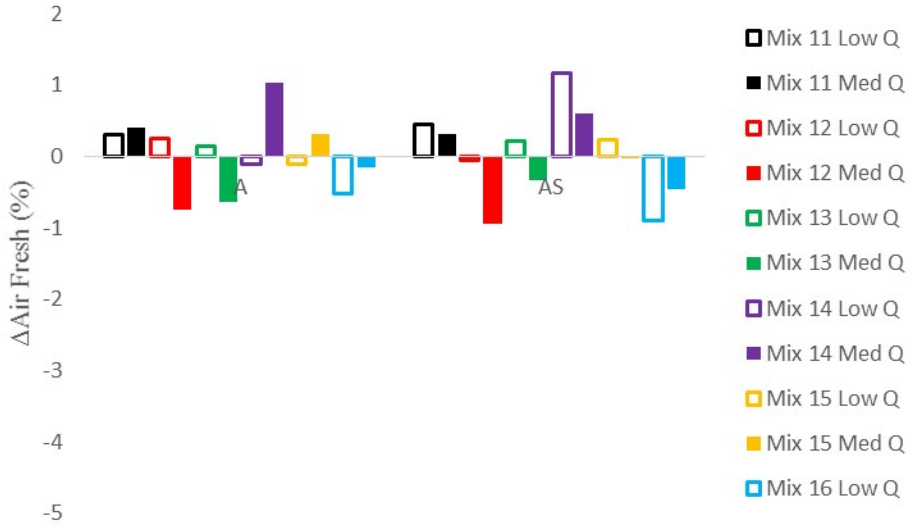

Figure 104. Change in fresh concrete air content for the A-configuration (left) and the A-S configuration (right) for mixtures 11-16.

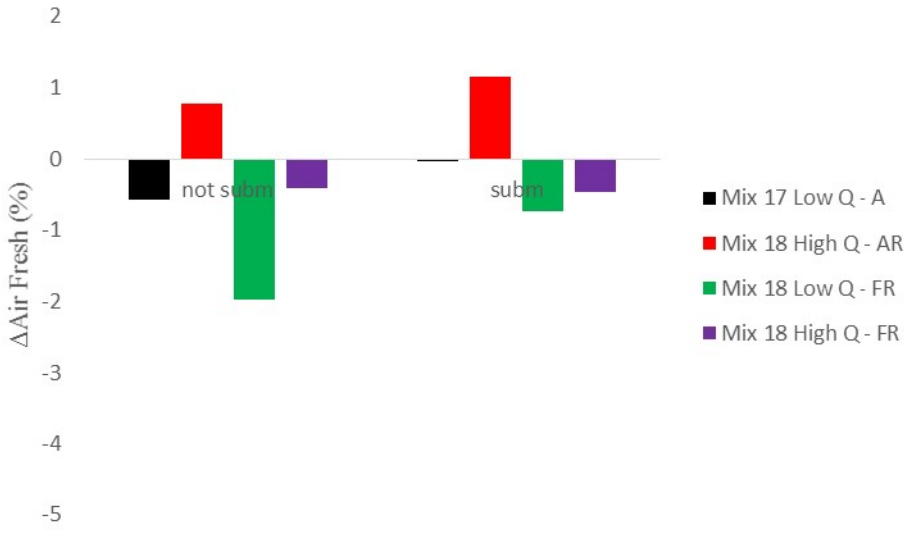

Figure 105. Change in fresh concrete air content when submerging the hose for mixtures 17 and 18.

5.6.5.5 Difference between flat and A configuration

Figure 106, Figure 107 and Figure 108 show the difference between A and F configuration for SCC mixtures 1, 7 through 10, HWC and CVC mixtures 2 through 6, and for mixtures 17 and 18, respectively. For mixtures 1, 4, 7, 8 and 17, the flat configuration results in a larger Δair. Mixtures 6, 9, 10 and 18 show the opposite. As such, no influence of the boom configuration is clear, and the behavior might be influenced by many more factors.

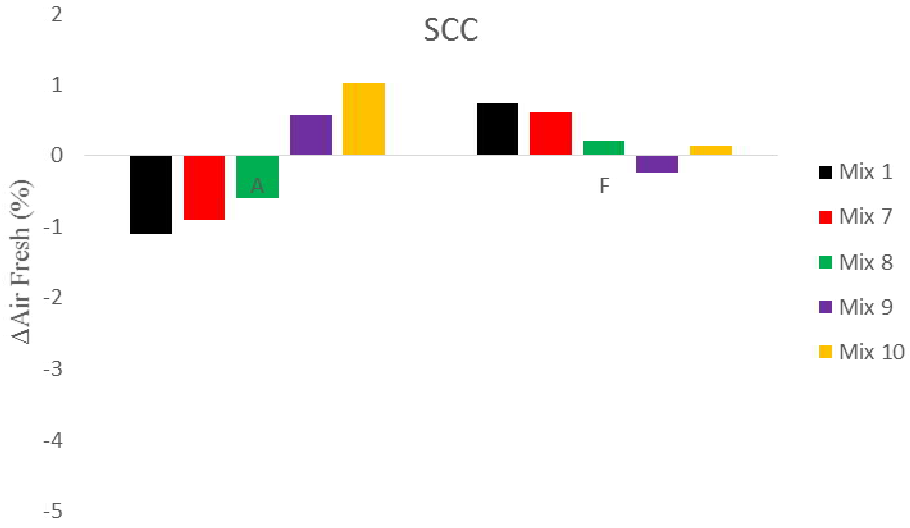

Figure 106. Change in fresh concrete air content between A (left) and flat (right) configurations for SCC mixtures 1, 7-10.

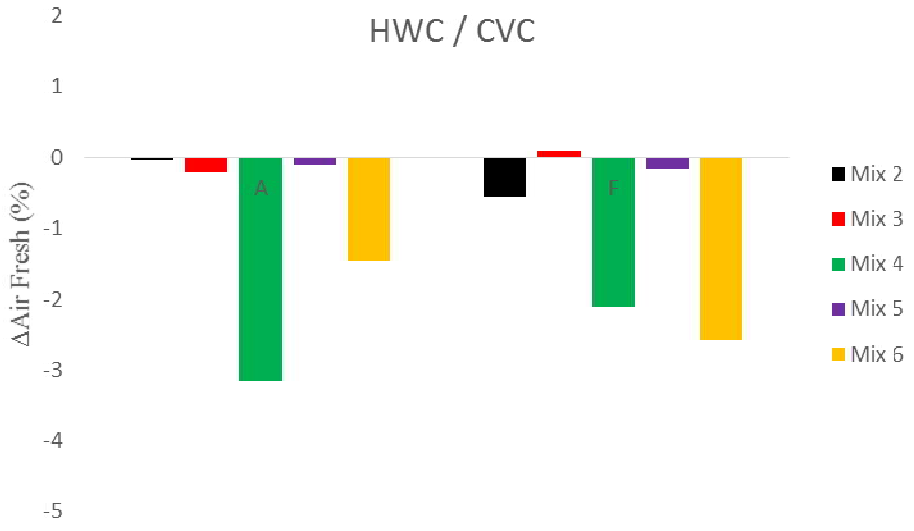

Figure 107. Change in fresh concrete air content between A (left) and flat (right) configurations for HWC / CVC mixtures 2-6.

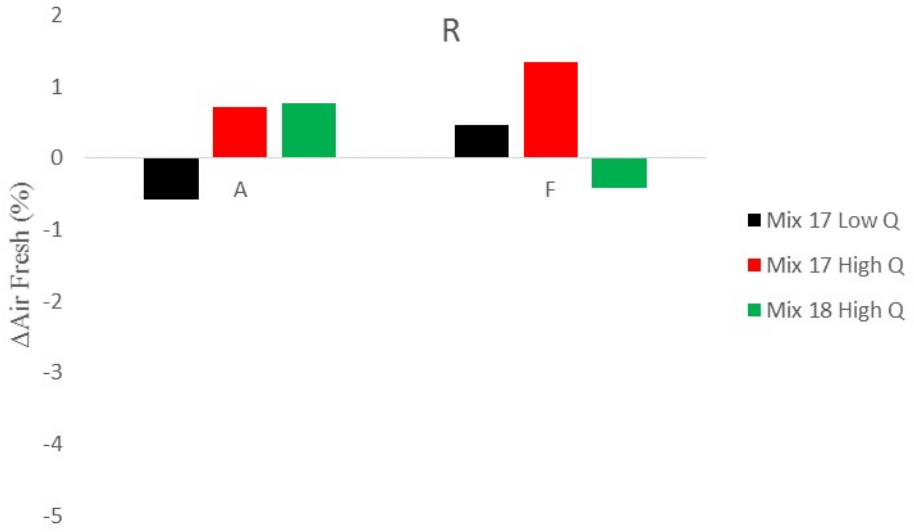

Figure 108. Change in fresh concrete air content between A (left) and flat (right) configurations for mixtures 17 and 18.

5.6.5.6 Influence of mix design

Table 26 shows that the mix design has a large influence on the average change in air content due to pumping. Again, this analysis strategy might not be entirely fair due to different pumping conditions for different mixtures, but this table gives at least an indication. It should be noted that mixtures 1 through 10 had a relatively high initial air content, and mixtures 11 through 18 had a lower initial air content (Table 26). The average of the absolute values show the sensitivity of the mixture to pumping. Mixtures with products from admixture producer 1 appear to be, in general, a little more sensitive than the mixtures with the products from producer 2. The low absolute values for mix designs 9 and 10 confirm this statement and cause this not to be attributed to the high air content. Mix designs 4 and 6 show the largest decrease in air content. Both are HWC mixtures. However, HWC mixtures 2 and 3 show the lowest sensitivity though.

Table 26. Average and average of absolute value for the change in air content for each mix design.

	AVERAGE ΔAIR	AVERAGE ABS ΔAIR
MIX 1	-0.30	0.69
MIX 2	-0.13	0.39
MIX 3	0.20	0.47
MIX 4	-2.6	2.60
MIX 5	-0.10	0.12
MIX 6	-1.51	1.51
MIX 7	-0.52	1.05
MIX 8	-0.70	1.07
MIX 9	-0.33	0.65
MIX 10	0.00	0.49
MIX 11	0.02	0.50
MIX 12	-0.43	0.52
MIX 13	-0.46	0.58
MIX 14	0.73	0.77
MIX 15	0.22	0.26
MIX 16	-0.18	0.50
MIX 17	-0.01	0.85
MIX 18	-0.27	0.92

5.6.5.7 Summary

Apart from the obvious mix design dependency, there is a difference between pumping in A or in F configuration in how the fresh concrete air content is affected. F configuration results in higher ΔAir. More important is how the flow rate affects the results. In the A-configuration, an increase in flow rate has a tendency to make the air loss worse, while for F-configuration, the increase in flow rate makes the air loss better (or the air gain higher). The difference between the two configurations is striking, and for the F-configuration, the result is strong. Pumping at low flow rate in F configuration appears to reduce the air content more strongly. Using a reducer or submerging the hose only have a minor influence of the change in fresh concrete air content. However, results on spacing factor, freeze-thaw resistance and scaling behavior are needed to indicate whether this change in air content is a good indicator.

5.6.6 Correlations between factors

Figure 109 to Figure 113 investigate if correlations between the changes in each of the properties exist. Slump flow may influence flow resistance in the interface rheometer, as a decrease in yield stress makes more concrete flow at the same shear stress. Figure 109 shows a weak, but existing correlation between those two parameters, showing that to some extent the measured changes actually correspond with reality in pumping.

Changes in air content could have an effect on yield stress and viscosity, and as such, on slump flow and interface rheology. The presence of a correlation would thus indicate that the changes in air content are a cause, although maybe not exclusively, of the changes in workability. However, in Figure 110 and Figure

111, there is no correlation visible between the change in air content and the change in slump flow or interface rheometer flow resistance, respectively. This means that the workability changes due to pumping are not influenced significantly by the changes in air content.

Changes in workability should cause changes in segregation resistance, as segregation is governed by yield stress and viscosity. However, Figure 112 and Figure 113 show very weak correlations. This is most likely attributed to the lack of segregation of the mixtures, as only a few data points had segregation concerns.

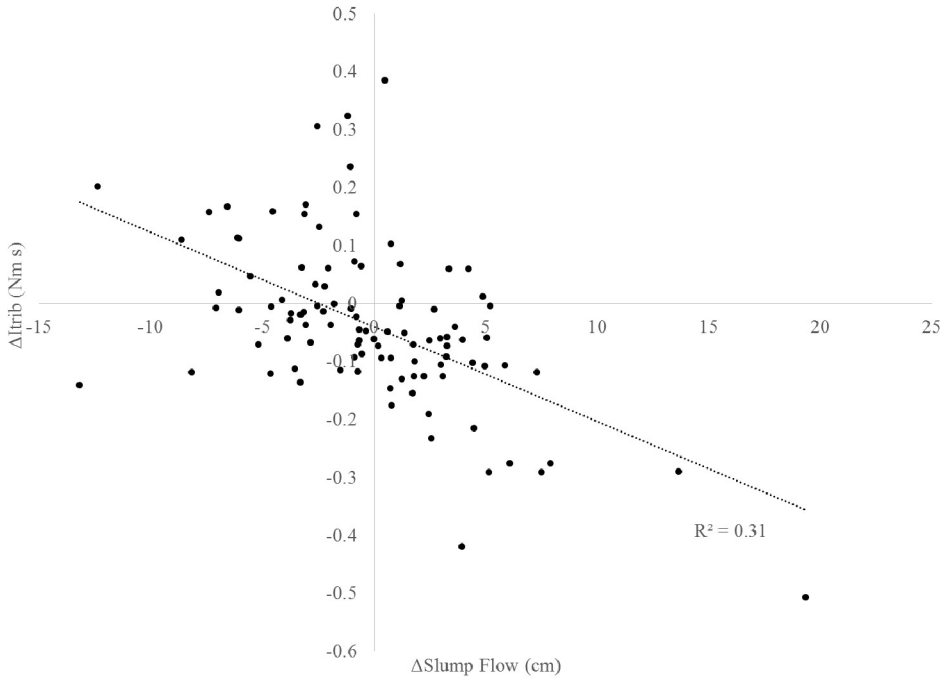

Figure 109. Correlation between the change in flow resistance in the interface rheometer and the change in slump flow.

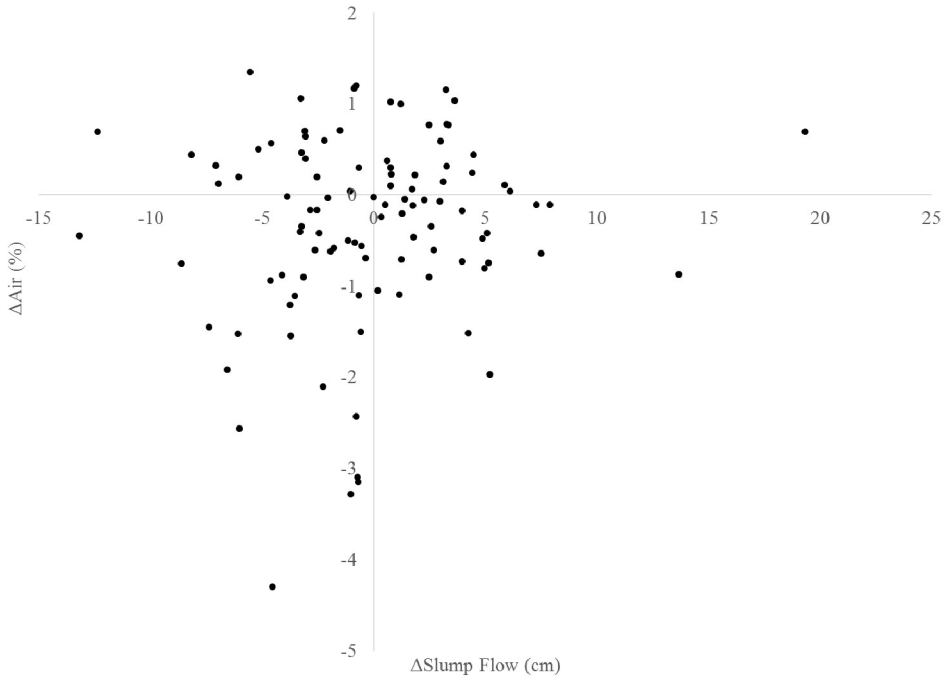

Figure 110. Correlation between the change in air content and the change in slump flow.

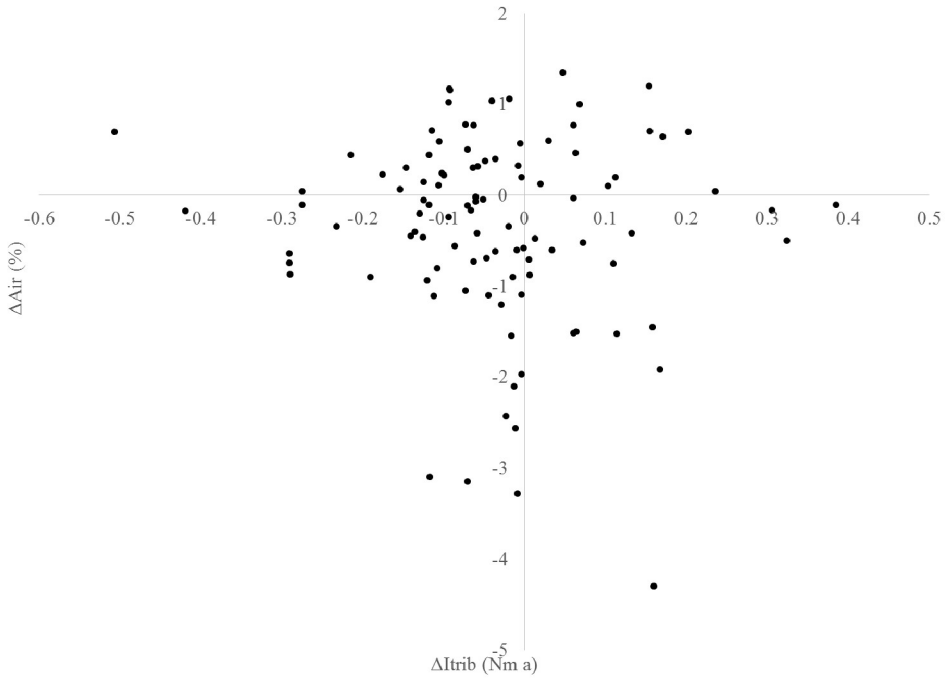

Figure 111. Correlation between the change in air content and the change in flow resistance in the interface rheometer.

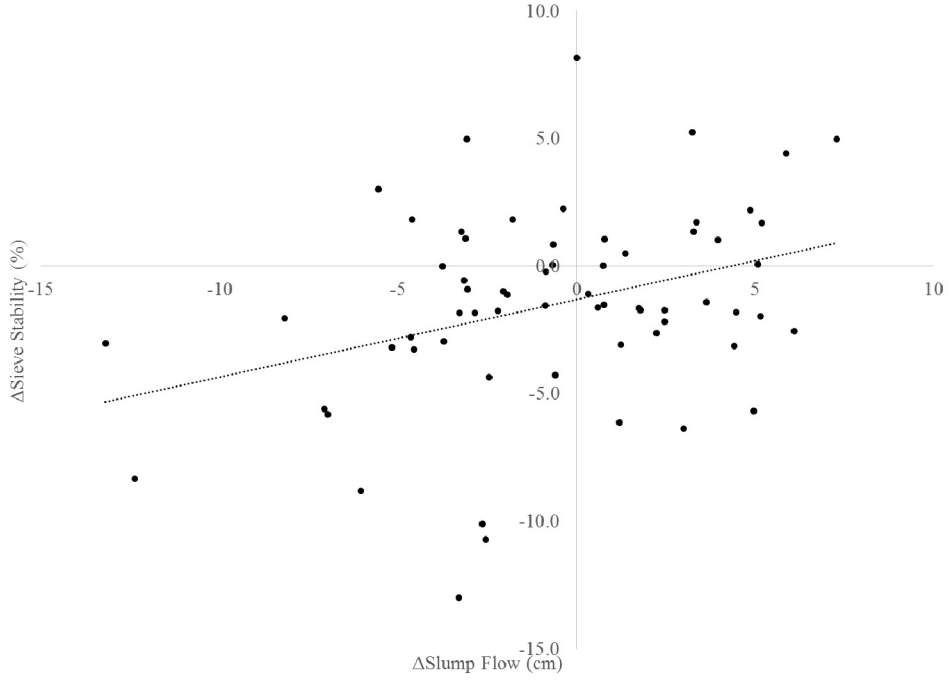

Figure 112. Correlation between the change in sieve stability and the change in slump flow.

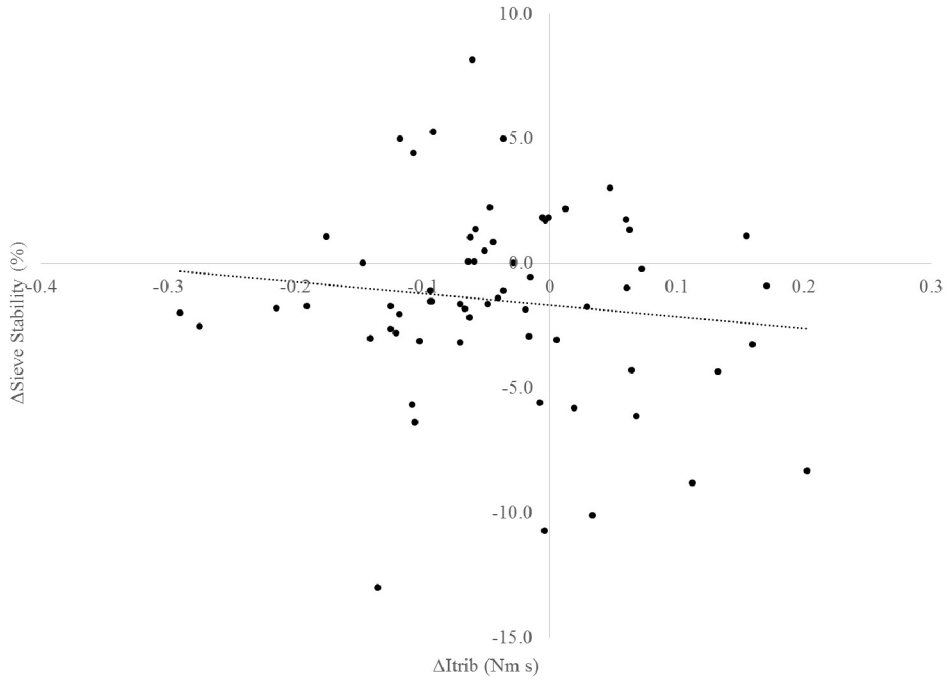

Figure 113. Correlation between the change in sieve stability and the change in flow resistance in the interface rheometer.

5.7 Changes in hardened concrete

5.7.1 Hardened concrete air content

The hardened concrete air content was determined using two methods. The first consisted of determining the density of the concrete cylinders for compressive strength, by weighing the saturated samples above and under water. By comparing with the theoretical density based on the mix design and properties of the constituent materials, the air content was calculated. This method is sensitive to errors in the mix design, especially given the industrial size of production and the non-exact consideration of the moisture content of the sand. However, it does give an indication of the air content. Appendix B.1 contains the time-evolution of the gravimetric hardened concrete air contents for non-pumped and pumped samples.

A second assessment of the air content was performed using the hardened air-void analysis. The details of the procedure are described in section 5.3.6. Spacing factor values obtained from different techniques were obtained and compared, and the spacing factor values of the Rapid Air Void Analyzer, with bubbles above 30 µm were retained. The air content values using the same procedure were also recorded, and are shown in Appendix B.2. Figure 114 compares the values obtained from both techniques, with the black dots representing non-pumped samples and the red dots are pumped concrete measurements. The correlations are close to the line of equality (gray line), but there is a lot of spread on the data. However, this gives an indication that the air content from the select spacing factor analyzing procedure could be reliable.

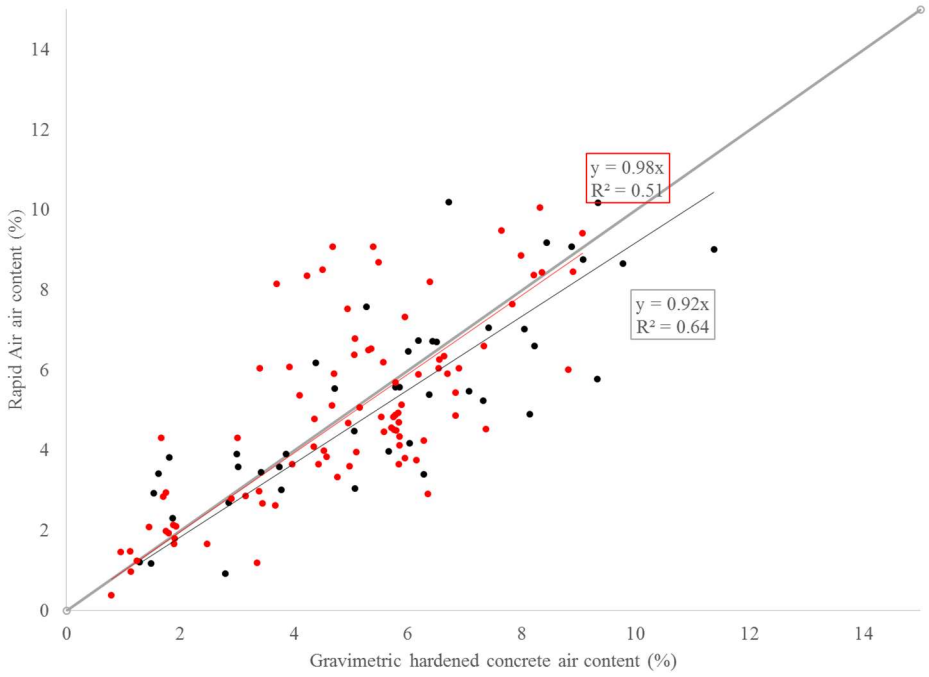

Figure 114. Comparison between the Rapid Air air content and the gravimetric air content. Black dots represent non-pumped samples, red data are pumped samples.

Figure 115 and Figure 116 show the comparison between the two methods to determine the hardened air content and the fresh concrete air content measured in the field. Decent correlations between hardened and fresh concrete air content can be observed. However, all correlations show a relationship below the line of equality, indicating that the fresh concrete air content is, in average, higher than the hardened concrete air content. As such, fresh concrete air content measurements performed shortly after pumping are reliable, as it

appears all air has returned to the concrete and is no longer dissolved. This is in agreement with the results from Vosahlik et al., who made similar observations for SCC and for CVC [2].

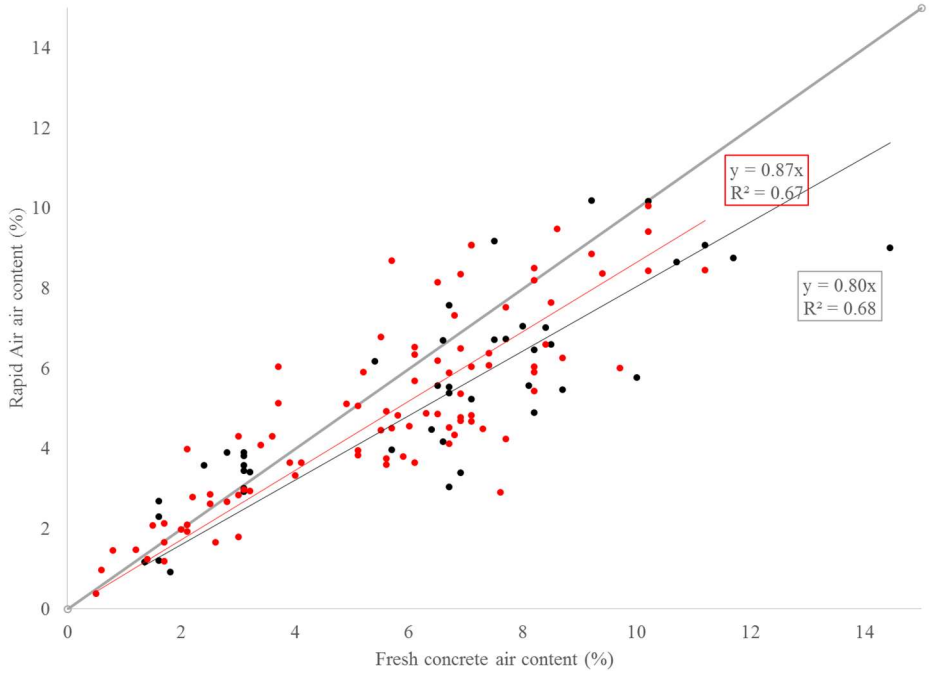

Figure 115. Comparison between Rapid Air air content and fresh concrete air content for pumped (red) and non-pumped samples (black).

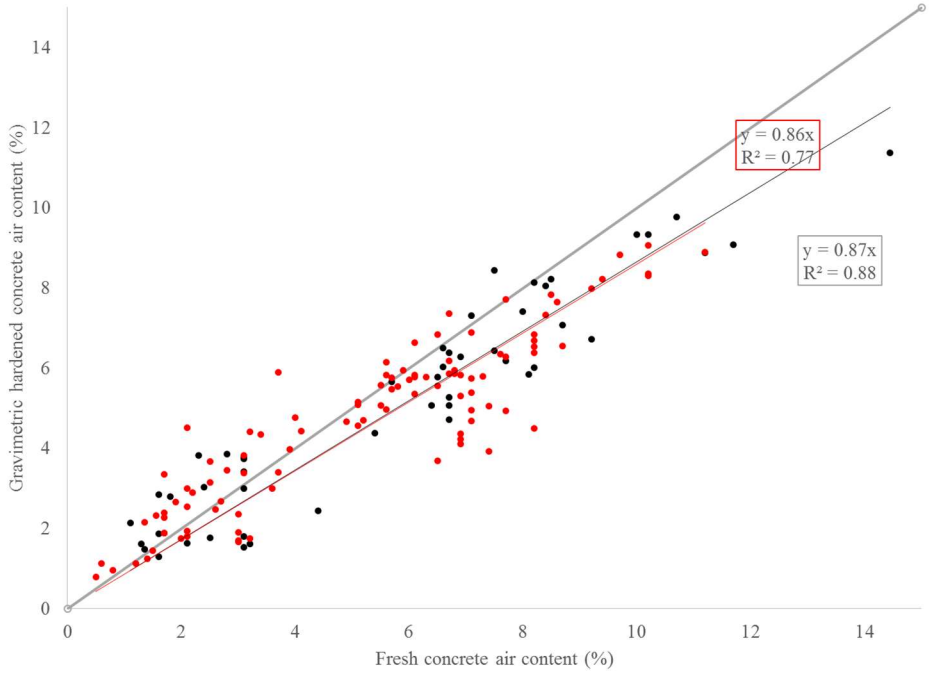

Figure 116. Comparison between gravimetric air content and fresh concrete air content for pumped (red) and non-pumped samples (black).

5.7.2 Compressive strength

Compressive strength is mainly influenced by the w/cm, air content, and the presence of SCMs. The air content is measured, the SCMs were only changed in mixtures 17 and 18, compared to the others. However, the water content was not entirely fixed due to changes in the moisture content in the sand. Consequently, compressive strength versus air content plots can be used to evaluate whether a significant change in w/cm has occurred. It is believed that at 28 days, the influence of the retarders has disappeared. Figure 117 to Figure 119 show the evolution of the compressive strength as a function of the gravimetric air content. For clarity, a trendline was added for each mix design. Mix designs 1 through 4 and 7 through 12 show similar values for compressive strength at equal air contents, indicating that the w/cm is approximately constant. Mix design 5 and 6 are above the other mixtures, showing two cases in which more water might have been withheld by the plant operator compared to the moisture content. For mix designs 13 through 16, especially the latter, the opposite might be true. Mixtures 17 and 18 logically show higher compressive strengths due to the absence of the fly ash, and both mixtures show similar strengths for similar air contents, thus the w/cm is estimated to be the same.

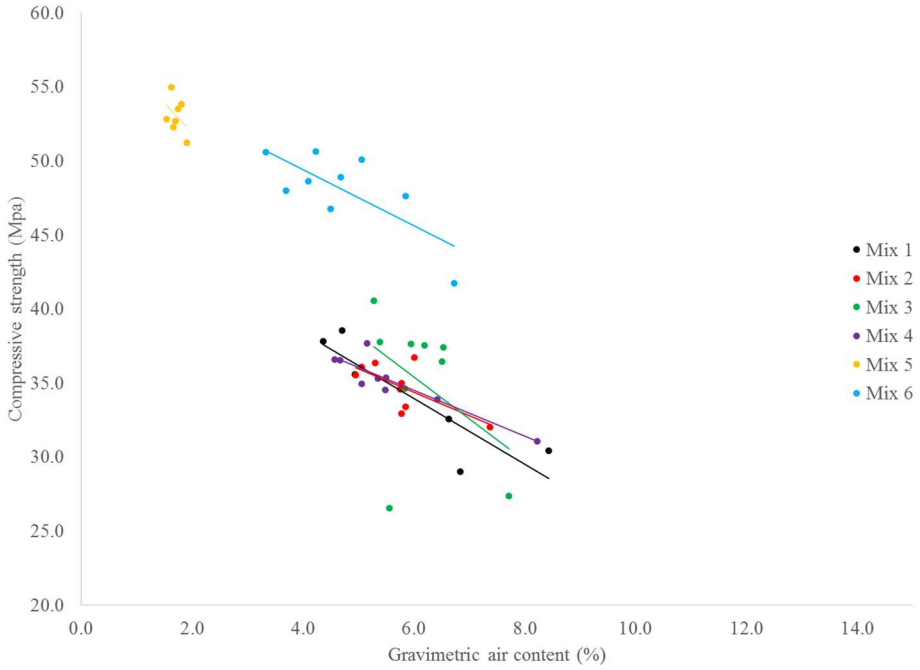

Figure 117. Comparison between compressive strength and air content for mixtures 1-6.

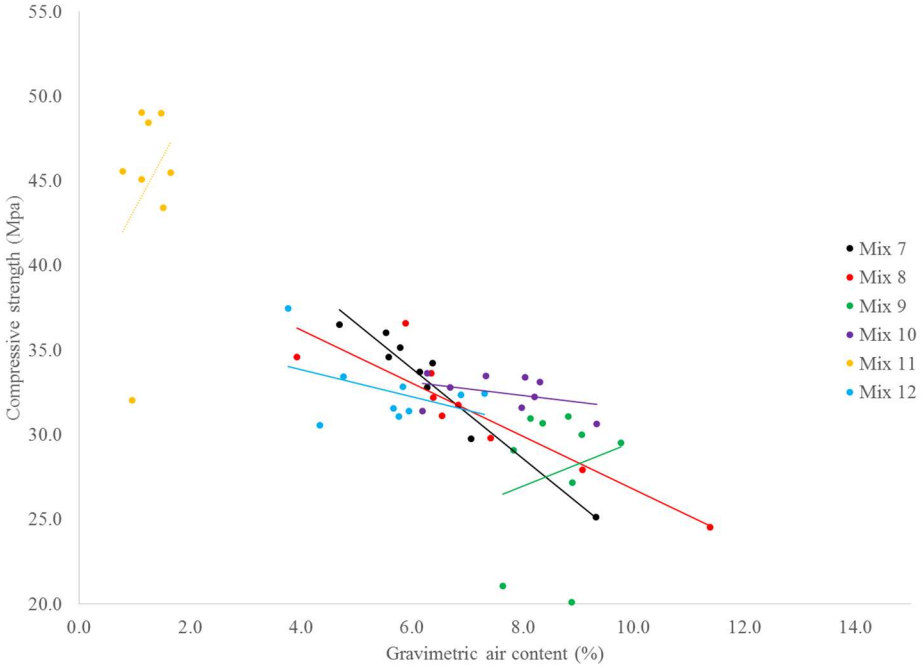

Figure 118. Comparison between compressive strength and air content for mixtures 7-12.

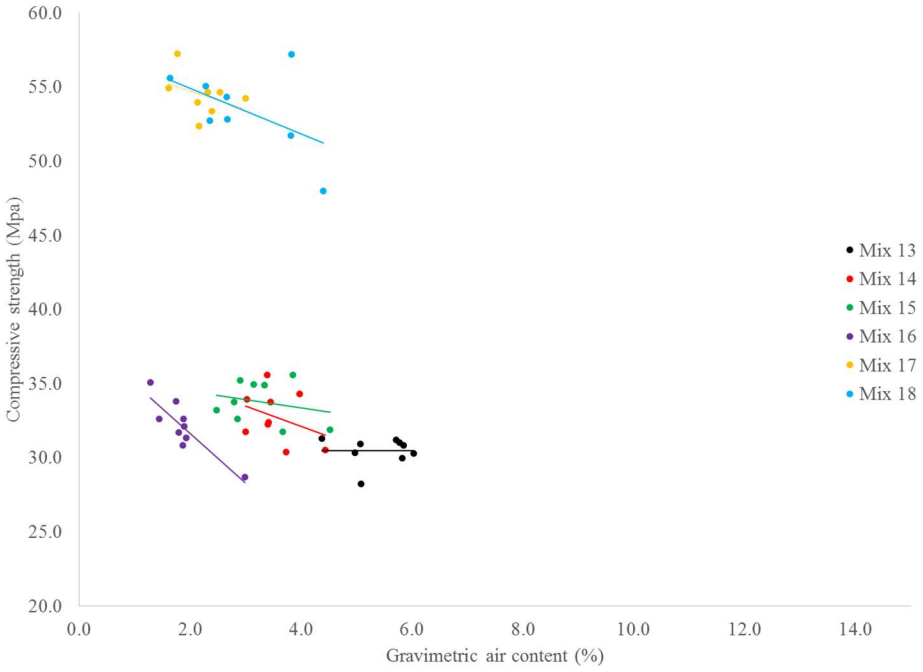

Figure 119. Comparison between compressive strength and air content for mixtures 13-18.

Appendix B.3 shows the compressive strength as a function of time for non-pumped (black) and pumped samples. In general, no major changes in compressive strength are observed, except for mix design 3 (ARS-med Q and F low Q (Figure 120)), mix design 9 (AR-med Q), mix design 11 (A-low Q), and mix design 12 (A-med Q). Mix design 18 shows a systematic decrease in compressive strength due to pumping (Figure 121). Mix design 7 and 8 show a strong decrease with time of the non-pumped samples, while the pumped

samples remain unaffected (Figure 122). This is in line with the observations of the air contents for those mixtures.

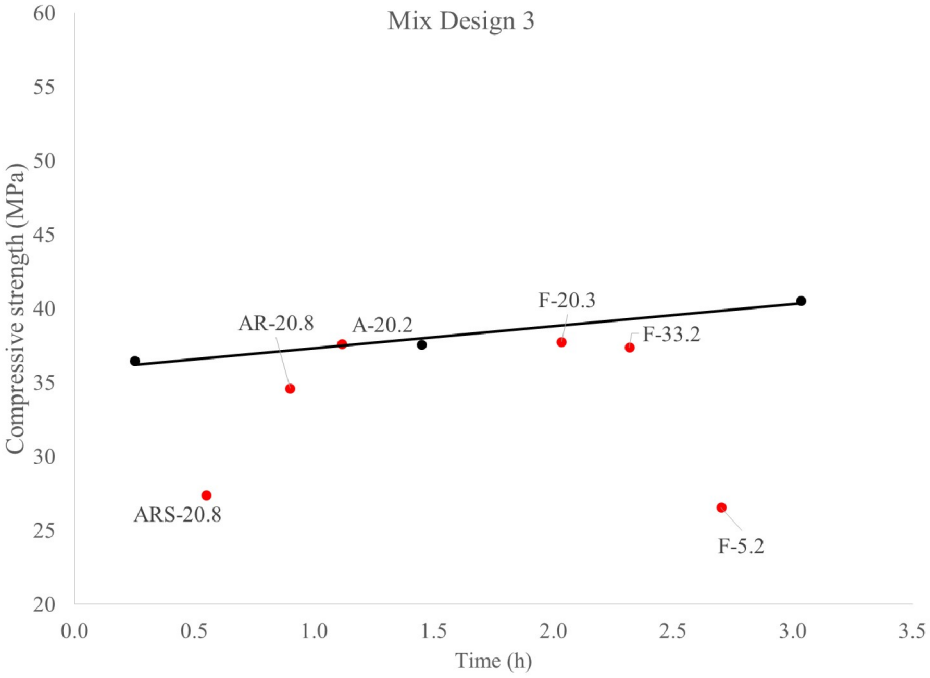

Figure 120. Example of changes in compressive strength due to pumping in some configurations.

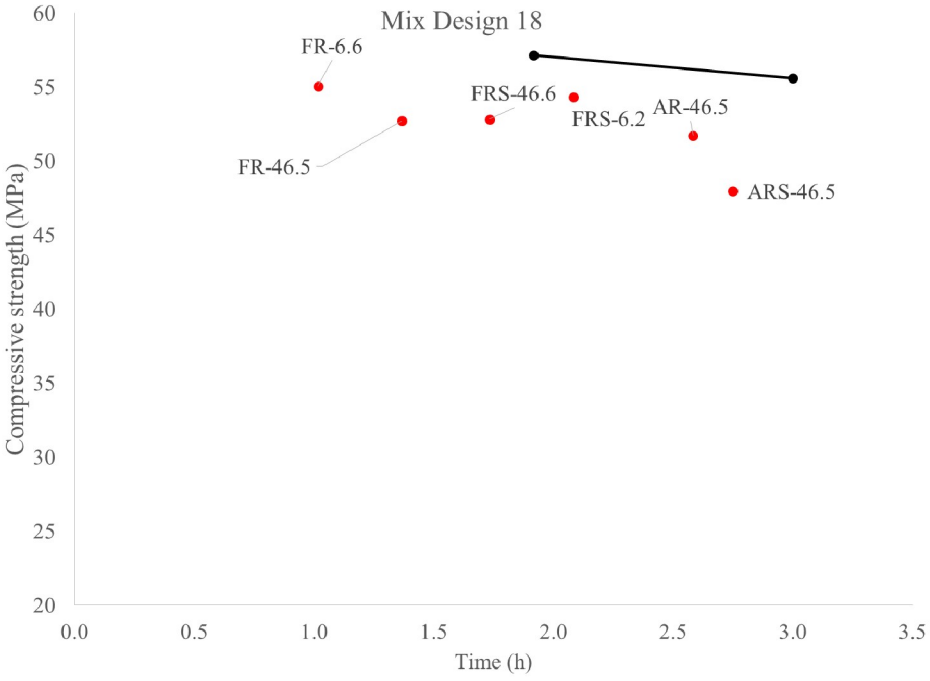

Figure 121. For mix design 18, strength decreased for every pumping operation.

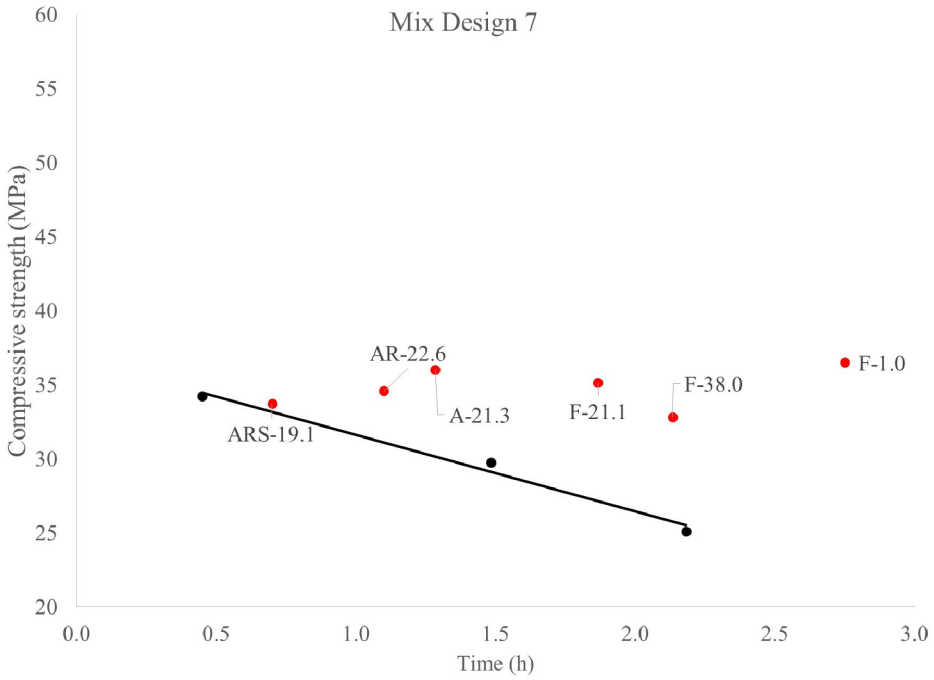

Figure 122. Changes in compressive strength for mix design 7 are corresponding to the changes in air content.

5.7.3 Spacing factor

Appendix B.4 contains the spacing factor results for all mixtures. The procedure selected was the spacing factor from the Rapid Air Void Analyzer, by omitting all "bubbles" below 30 µm. The detailed procedure is explained in section 5.3.6. Section 5.7.1 showed the correlations between the fresh and hardened air content, and between the hardened air content from the Rapid Air and the one determined gravimetrically from the cylinders for compressive strength. The adequate matches between the procedures show that the chosen strategy is valid. The following sections discuss the changes in spacing factor induced by the pumping parameters and the mix designs.

5.7.3.1 Influence of flow rate

Figure 123 to Figure 125 show the change in spacing factor for mixtures 11 through 16 (with low initial air contents), when pumped in A, A-S, and A-R configurations, respectively. For the A configuration, a general increase can be noted, except for mixture 14. Mixture 11 is sensitive to changes, as the air content is very low (Figure 123). However, Figure 124 shows an opposite picture for the A-S configuration, as only mixtures 13 and 14 show a similar change in spacing factor when increasing the flow rate, compared to the A configuration. The A-R configuration more or less follows the tendency of the A-S configuration (Figure 125). For the SCC mixtures with high initial air contents, the spacing factor change is barely influenced by the flow rate, in F-configuration (Figure 126). It can be noted that the sensitivity of mixtures 11 through 16 is much larger than for mixtures 1 and 7 through 10. The HWC/CVC mixtures show a sensitivity to the flow rate larger than for the SCC mixtures with high air contents, but lower than for the SCC mixtures with low air content (Figure 127). It also seems that pumping at low and at high flow rate is more disadvantageous than pumping at a medium flow rate. Figure 128 show a slightly decreasing trend in the change in spacing factor with increasing flow rate for mixtures 17 and 18.

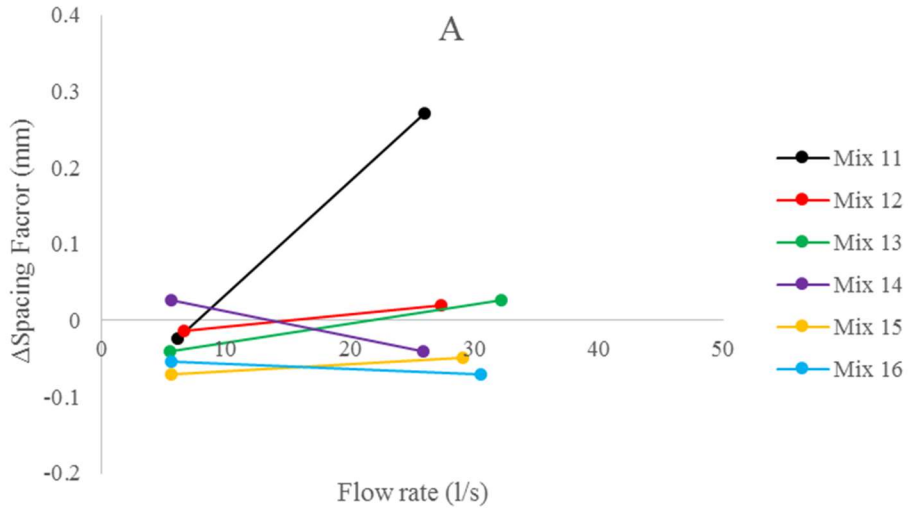

Figure 123. Change in spacing factor as a function of flow rate when pumping in A configuration for mixtures 11-16.

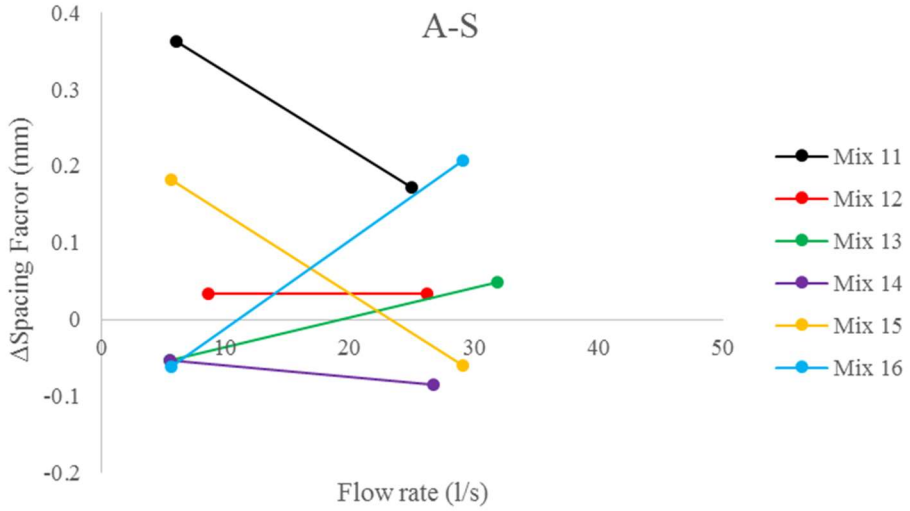

Figure 124. Change in spacing factor as a function of flow rate when pumping in A-S configuration for mixtures 11-16.

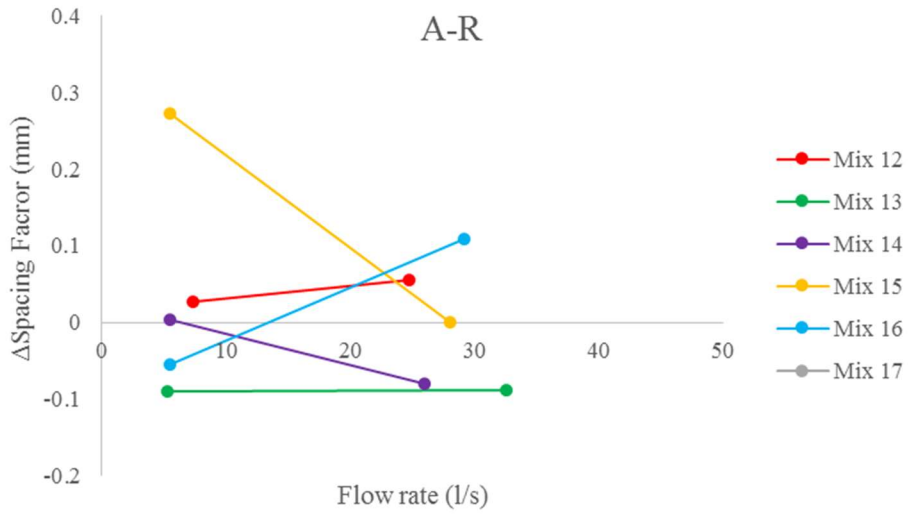

Figure 125. Change in spacing factor as a function of flow rate when pumping in A-R configuration for mixtures 11-16.

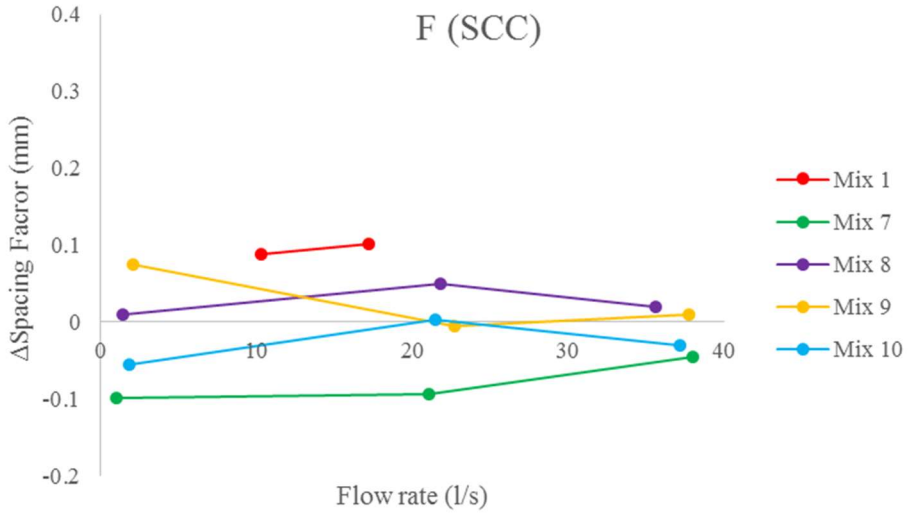

Figure 126. Change in spacing factor as a function of flow rate when pumping in F configuration for SCC mixtures 1, 7-10.

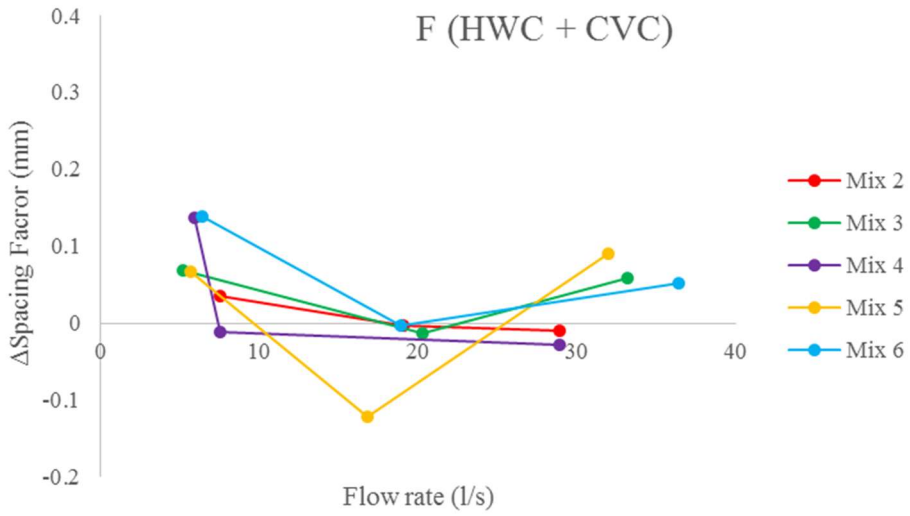

Figure 127. Change in spacing factor as a function of flow rate when pumping in F configuration for HWC / CVC mixtures 2-6.

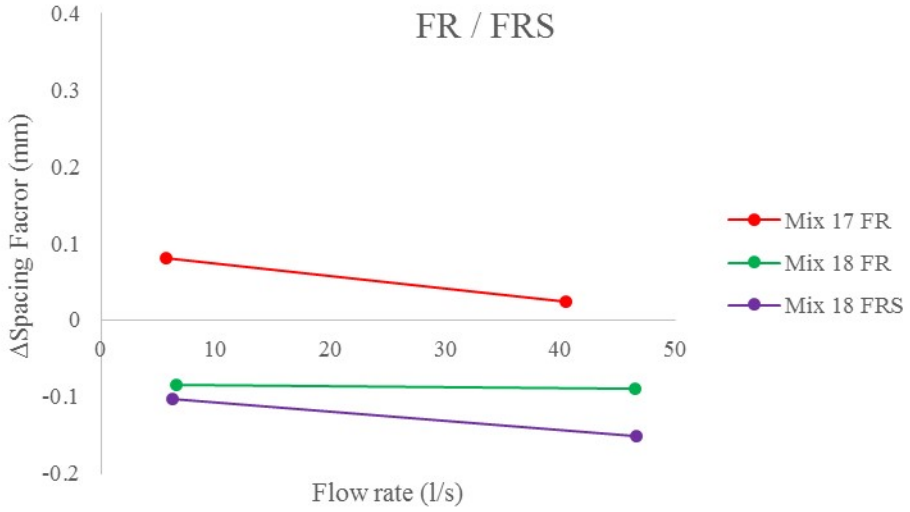

Figure 128. Change in spacing factor as a function of flow rate when pumping in F-R configuration for mixtures 17-18.

5.7.3.2 Influence of reducer

The use of a reducer to minimize the negative impact of pumping on the spacing factor is recommended for CVC. It is argued that using a reducer prevents the downward pipe from emptying under gravity, which induces pressures lower than atmospheric and bubble coalescence. Figure 129 confirms this behavior for all mixtures with high initial air contents: the spacing factor does not increase as much (or decreases more) due to pumping, except for mixtures 8 and 10. Figure 130 shows the same picture, except for mixtures 15 and 16, the two PNS mixtures evaluated in this graph. In those cases, the opposite behavior is observed: larger increases in spacing factor are noted for the A configuration with reducer compared to the values without reducer.

Figure 129. Change in spacing factor due to pumping with a reducer (right), compared to omitting the reducer (left) for mixtures 2-10.

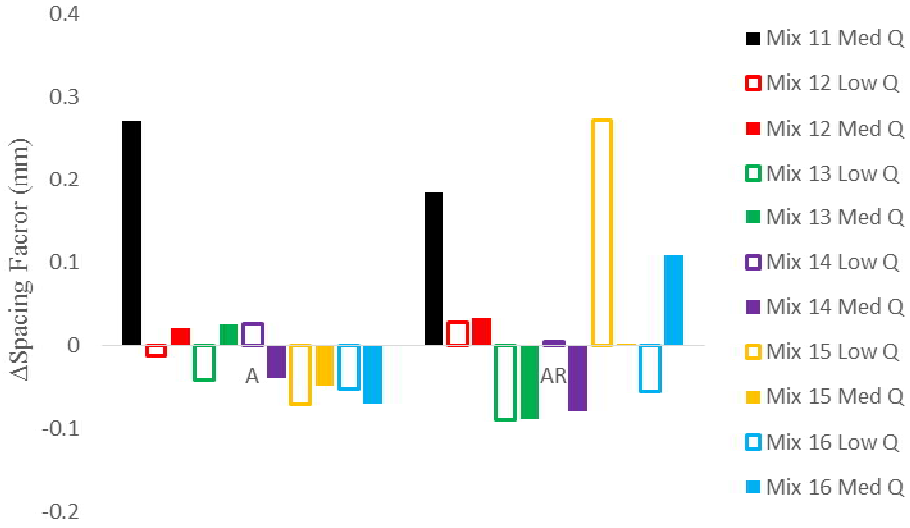

Figure 130. Change in spacing factor due to pumping with a reducer (right), compared to omitting the reducer (left) for mixtures 11-16.

5.7.3.3 Influence of submerging the hose

Figure 131 shows that submerging the hose does not largely influence the change in spacing factor, for mixtures 2 through 10. The largest increases are noted for mixtures 6 and 8. However, Figure 132 shows a much different picture. Submerging the hose can be positive (mixture 11, high Q, mixture 14), but in other cases, it seems to be detrimental (mixture 11, low Q, mixture 15 low Q, mixture 16 high Q). One could argue that mixtures 15 and 16 are PNS based, and that the behavior might be dependent on the mechanism of the dispersing agent, however Figure 133 shows the opposite for mixtures 17 and 18, also PNS-based mix designs.

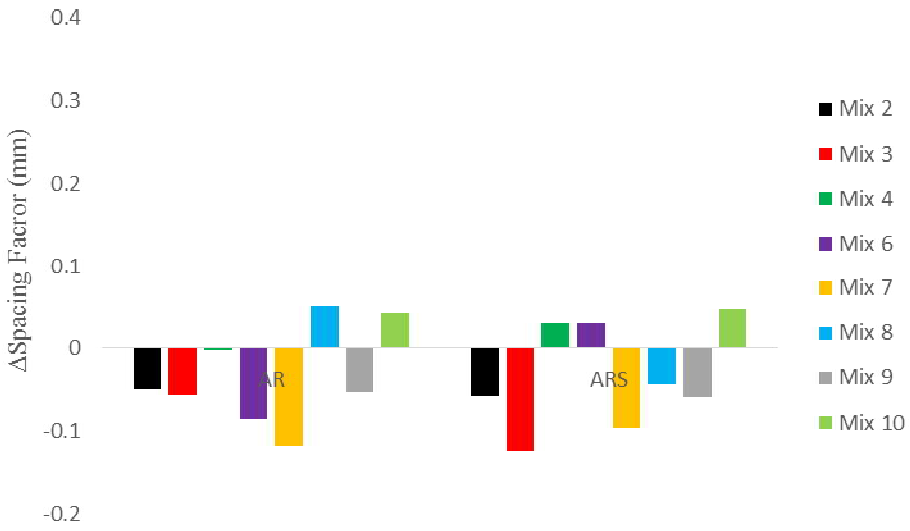

Figure 131. Influence of submerging the hose on the change in spacing factor due to pumping for mixtures 2-10.

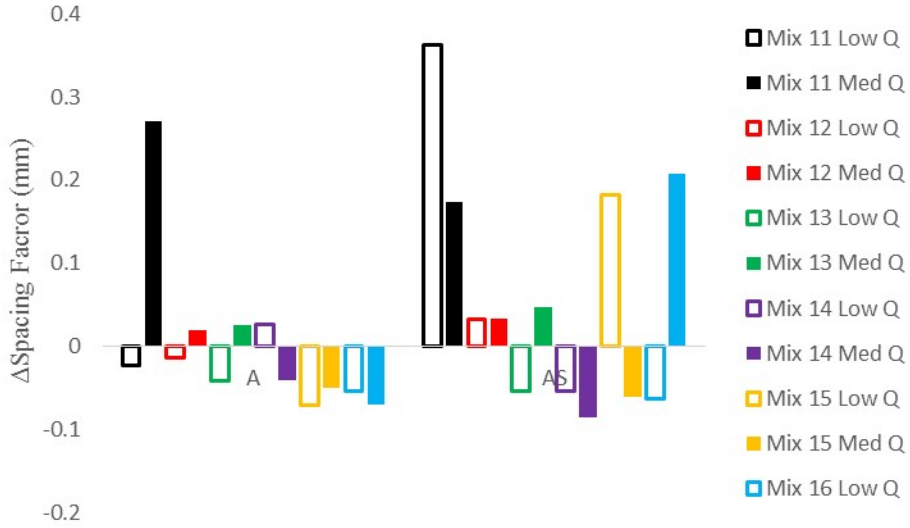

Figure 132. Influence of submerging the hose on the change in spacing factor for mixtures 11-16.

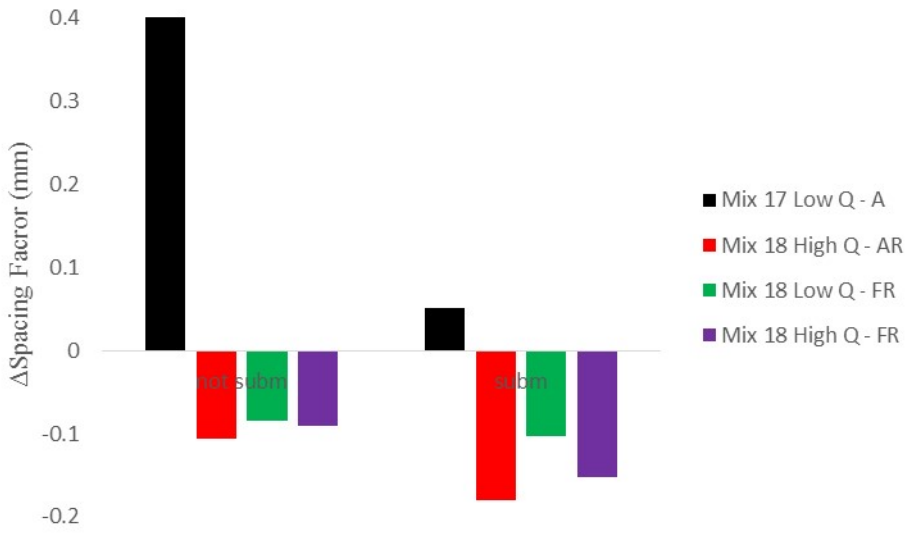

Figure 133. Influence of submerging the hose on the change in spacing factor for mixtures 17-18. Note that the value for mix 17, not submerged is off-chart (0.7 mm).

5.7.3.4 Difference between F and A configuration

Figure 134 to Figure 136 show the difference between pumping in A and F configuration for the spacing factor. For mixtures with sufficiently high air contents, no major difference can be observed. However, for mixtures with low initial air contents: CVC mixture 5, and SCC mixtures 17 and 18, the A configuration delivers worse results compared to the F configuration, which is in line with literature and findings on CVC.

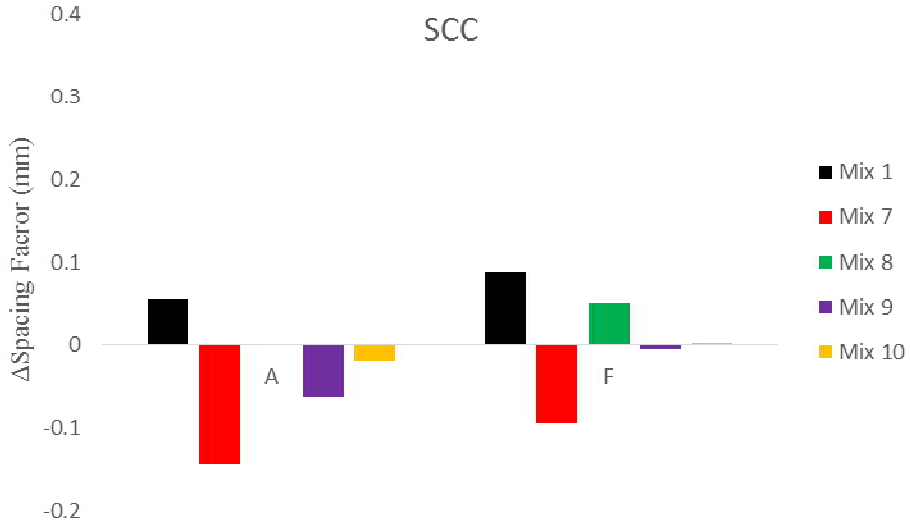

Figure 134. Change in spacing factor in A and F configuration for SCC mixtures 1, 7-10.

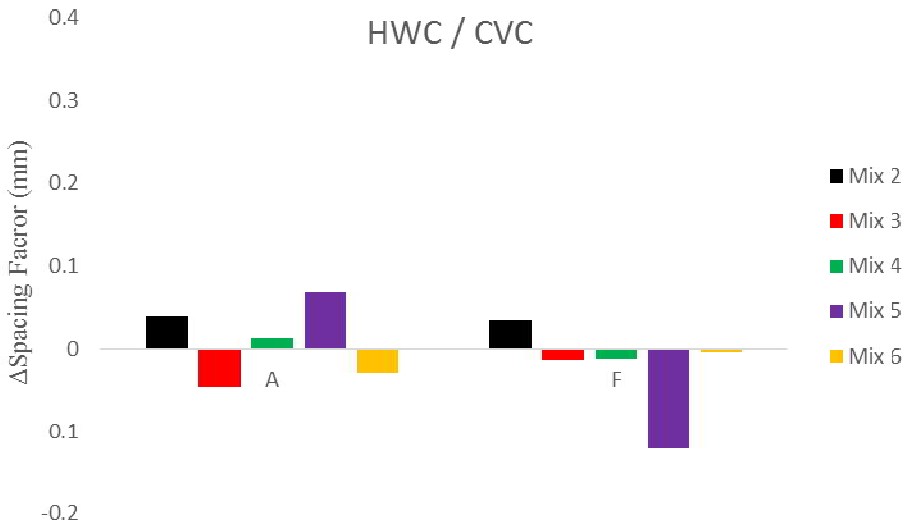

Figure 135. Change in spacing factor in A and F configuration for HWC/CVC mixtures 2-6.

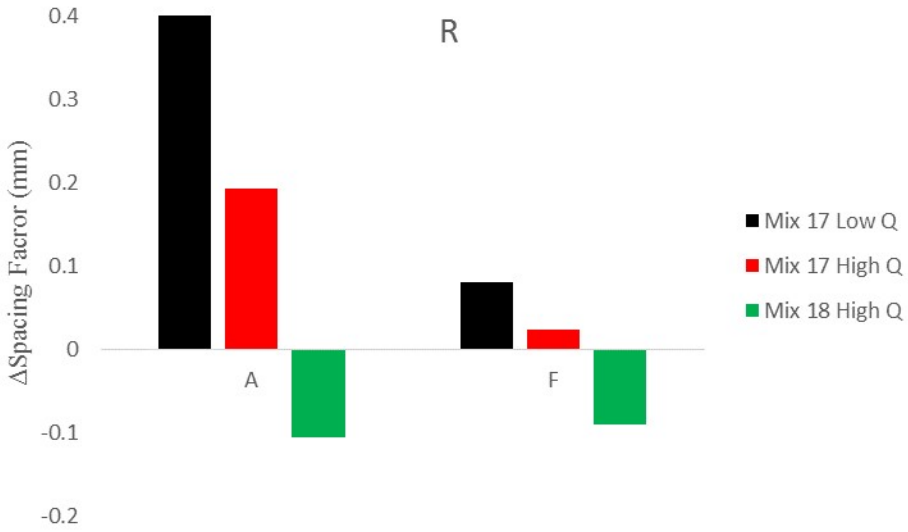

Figure 136. Change in spacing factor in A and F configuration for SCC mixtures 17-18. Note that the value for mix 17, A, low Q is off-chart (0.7 mm).

5.7.3.5 Influence of mix design

Similarly as for other parameters, the average change in spacing factor, and the average magnitude in change in spacing factor are listed in Table 27. The SCC mixtures with PCE-2 and high air content (mixtures 9 and 10) show the lowest sensitivity to changes in spacing factor. The HWC mixtures (mixtures 2-4, 6) are closely followed by the SCC mixtures with PCE-2 and low air contents (mixtures 11, 12 and 14), although mixture 11 shows somewhat larger dependency. The SCC mixtures with high air content and PCE-1/3 show even more sensitivity (mixtures 1, 7 and 8), and the highest sensitivity is found for the PNS mixtures (mixtures 15-18). The difference between the mixtures could not only be attributed to the workability range and dispersant type, but may also be dependent on the selected dosage of air-entraining agent.

Table 27. Average change in spacing factor and average of absolute values of change in spacing factor for the pumped mixtures.

	AVERAGE ΔSPACING F	AVERAGE ABS ΔSPACING F
MIX 1	0.084	0.084
MIX 2	-0.008	0.032
MIX 3	-0.018	0.061
MIX 4	0.023	0.037
MIX 5	0.026	0.087
MIX 6	0.017	0.056
MIX 7	-0.099	0.099
MIX 8	0.015	0.029
MIX 9	-0.015	0.043
MIX 10	-0.002	0.033
MIX 11	0.029	0.082
MIX 12	0.026	0.03
MIX 13	-0.033	0.058
MIX 14	-0.038	0.048
MIX 15	0.046	0.106
MIX 16	0.013	0.093
MIX 17	0.212	0.212
MIX 18	-0.107	0.107

5.7.3.6 Summary

The influence of pumping on the spacing factor is a complicated story. It seems that many parameters can either have a positive or negative effect on the change spacing factor. Concerning mix design, differences were noted in between mixture groups made with different admixture combinations. Some combinations perform better than others, although this effect could be dependent on the dosages of each admixture. The flow rate seemed to have a large effect on the spacing factor for mixtures with low air contents and the HWC mixtures. However, no uniform influence was found. Adding a reducer was generally beneficial, but it had a number of exceptions. If there is an effect of submerging the hose, it was rather negative. For the mixtures with high initial air contents, there was only a minor difference between A and F configuration. However, for the only two mixtures with low air content, a comparison delivered a significantly more negative effect for the A configuration.

5.7.4 Freeze-thaw resistance

Appendix C shows the raw data of the relative dynamic modulus, determined by means of ultrasonic pulse velocity for all specimens evaluated in the freeze-thaw chamber. Due to space restraint, the bars taken from the truck sample in the middle of all operations were not evaluated. As there are only 16 spaces available in the freeze-thaw chamber, the team could guarantee that all samples from the same mixture were evaluated in

the same chamber at the same time. For similar space restraints, after making the observations that mix designs 1 through 4 and 6 through 8 did not show damage, mixtures 9 and 10 were not evaluated as their air contents and spacing factors were in the same ranges as mixtures 1 through 8, except 5.

Appendix B.5 shows how many cycles the sample survived in the freeze-thaw chamber, with a maximum number of cycles set at 468. The purpose of the extension of this test was to see if any differences could be seen for more frost-resistant samples. Mix design 1, 2, 3, 4, 6, 7, 8 and 13 did not show any damage, when taking a criterion of 300 cycles. According to Table 26, these were all mixtures with an initial air content above 5.4%. All mixtures with lower air contents showed at least some kind of damage. These are discussed individually.

Mix design 5 was a CVC mixture, with the same mix design as mixture 6, but without the PCE. The significantly lower air content in mixture 5 showed some issues. The initial truck sample did not survive the 300 cycles, and neither did the pumped samples in A-frame at medium flow rate (the only A-frame configuration tested), and in F-frame at low flow rate. The samples pumped in F-frame at medium and high flow rate survived the freeze-thaw test, and even improved the resistance compared to the non-pumped samples, as showing in Figure 137.

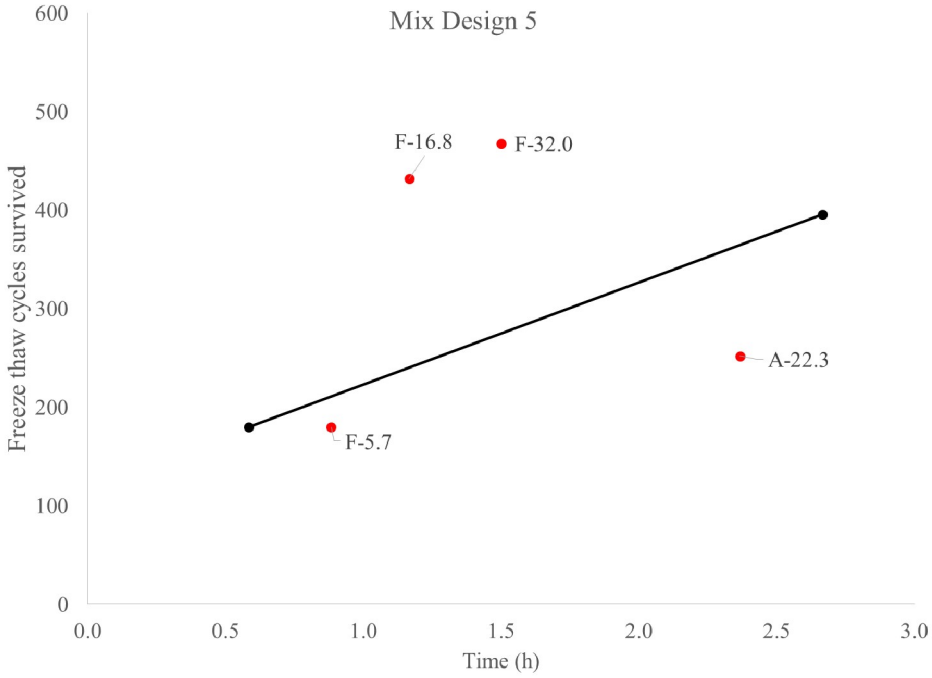

Figure 137. Freeze-thaw cycles survived for mixture 5. Black data are the truck samples, red dots represent the pumped samples.

Mix design 11 was an SCC mixture with a high dose of defoamer. All freeze-thaw bars were almost instantly damaged due to the lack of air (Figure 138).

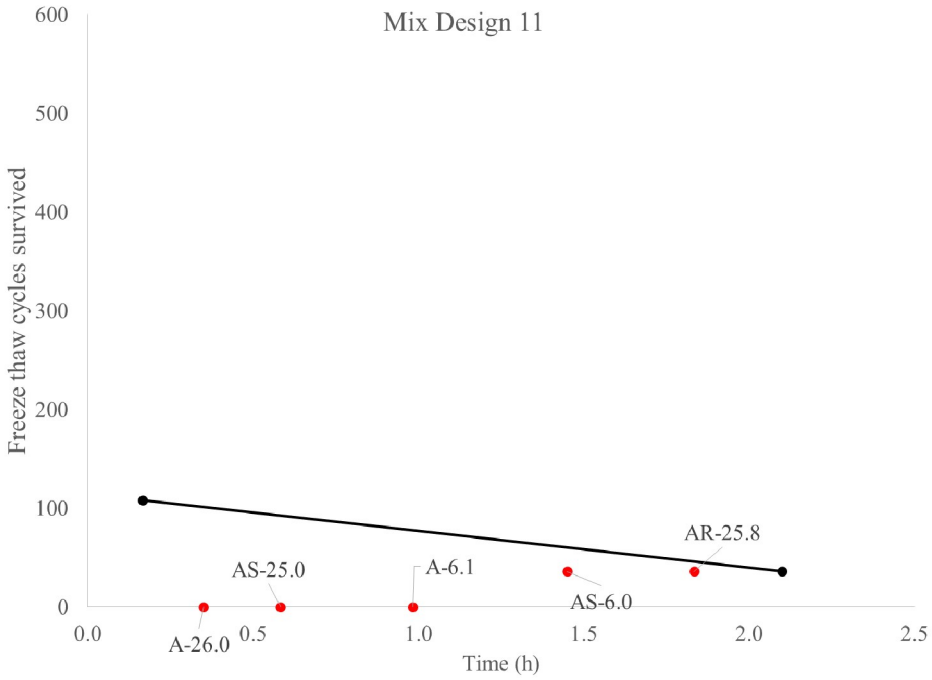

Figure 138. Freeze-thaw cycles survived for mixture 11. Black data are the truck samples, red dots represent the pumped samples.

Mix design 12 shows that all pumped samples performed similarly to the non-pumped samples, surviving the freeze-thaw test, except for the sample pumped in A-frame at medium flow rate (Figure 139).

Mix design 18 shows the last truck sample failing the freeze-thaw test, as well as both samples pumped at low flow rates (F-R and F-RS). All samples pumped at high flow rates (A-R, A-RS, F-R, F-RS) did survive the freeze-thaw test (Figure 140).

Mix design 17 shows rather strange behavior: the truck samples failed the freeze-thaw test severely, while all pumped samples showed an improvement. Even more, those pumped at high flow rate (barely) passed the 300 cycles in the freeze-thaw test.

Mixture 15 shows low resistance to freeze-thaw damage, but there seem to be no clear influence of pumping on how long the samples survived in the freeze-thaw chamber. Mixture 16 shows systematic failure after 72 cycles, most likely due to the higher w/cm caused by additional moisture in the aggregates.

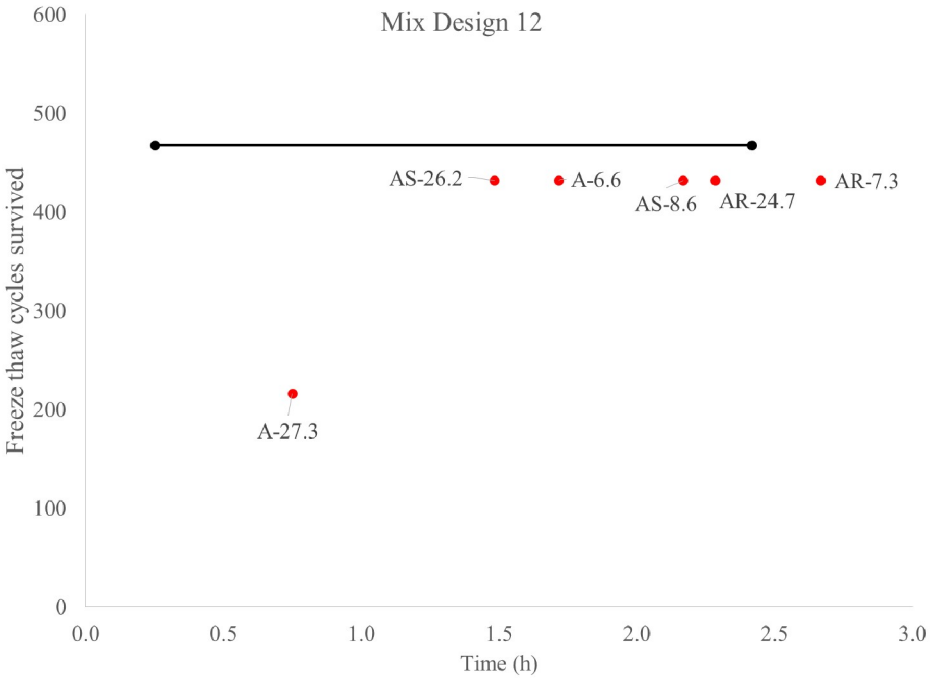

Figure 139. Freeze-thaw cycles survived for mixture 12. Black data are the truck samples, red dots represent the pumped samples.

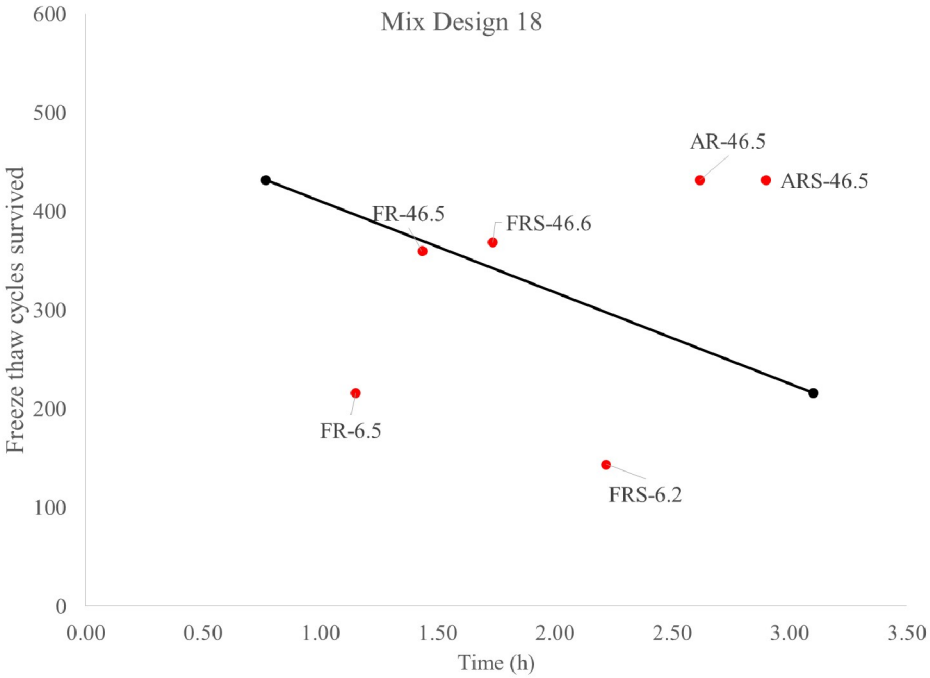

Figure 140. Freeze-thaw cycles survived for mixture 18. Black data are the truck samples, red dots represent the pumped samples.

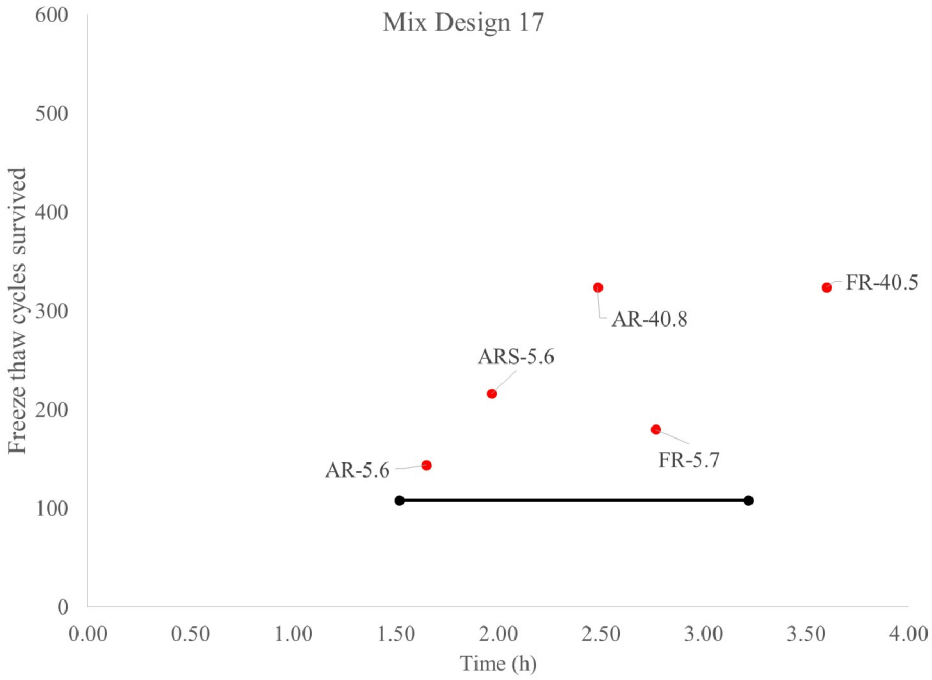

Figure 141. Freeze-thaw cycles survived for mixture 17. Black data are the truck samples, red dots represent the pumped samples.

5.7.5 Scaling resistance

5.7.5.1 General results

Appendix D shows the raw data for the scaling results on all top surfaces. Appendix B.6 shows the cumulative scaling after 50 cycles for all top surfaces, expressed in g/m^2 of surface. Depending on the regions, standards allow up to 500, 800, or 1500 g/m^2 of material to scale off. Mixtures 1, 2, 6, 7, 8, 9 and 10 do not show scaling issues for any of the samples. This includes all mix designs with an initial air content of 7%, except for mix design 4. Mix design 7 only had 6.7% and showed no scaling, but mix design 3 had 6.6% and showed some minor issues. The following paragraphs discuss the scaling resistance of the other mixtures.

Mixture 3 is a HWC with an initial air content of 6.6%. While the non-pumped samples perform under the most strict limit, pumping in A-RS, A-R and F at medium flow rate could increase concern, but not to a dramatic fashion. It should be noted that the A-RS and A-R configuration were only evaluated at medium flow rate for this mixture. Mixture 3 does not show any concerns for the freeze-thaw durability (Figure 142).

Mixture 4, also a HWC, which shows an initial air content of 7.5% shows no concerns for the non-pumped samples, but is the only mixture for which all pumping conditions worsened the scaling resistance. Pumping in A-RS configuration (at medium flow rate, the only one evaluated), and in flat configuration at low flow rate seems to significantly reduce the scaling resistance of mixture 4, causing a well-performing mixture before pumping to fail the most lenient specification in some pumping conditions (Figure 143).

Mixture 5, the CVC, which had a low air content to start with, showed scaling concerns before pumping. Pumping in A configuration (only evaluated at medium flow rate), or in F configuration at medium or high flow rate seems to improve the scaling resistance. However, pumping in F configuration at low flow rate made the scaling resistance worse (Figure 144).

Mixture 11 was the worst mixture in terms of scaling resistance. The use of the defoamer removed almost all air, especially after taking the first sample from the truck. All samples showed significant scaling, except the

first truck sample. Ignoring this sample, it seems that the A-S and A-R configuration result in worse scaling compared to the remaining truck samples. The A-S was evaluated at both low and medium flow rate, the A-R was only evaluated at medium flow rate (Figure 145).

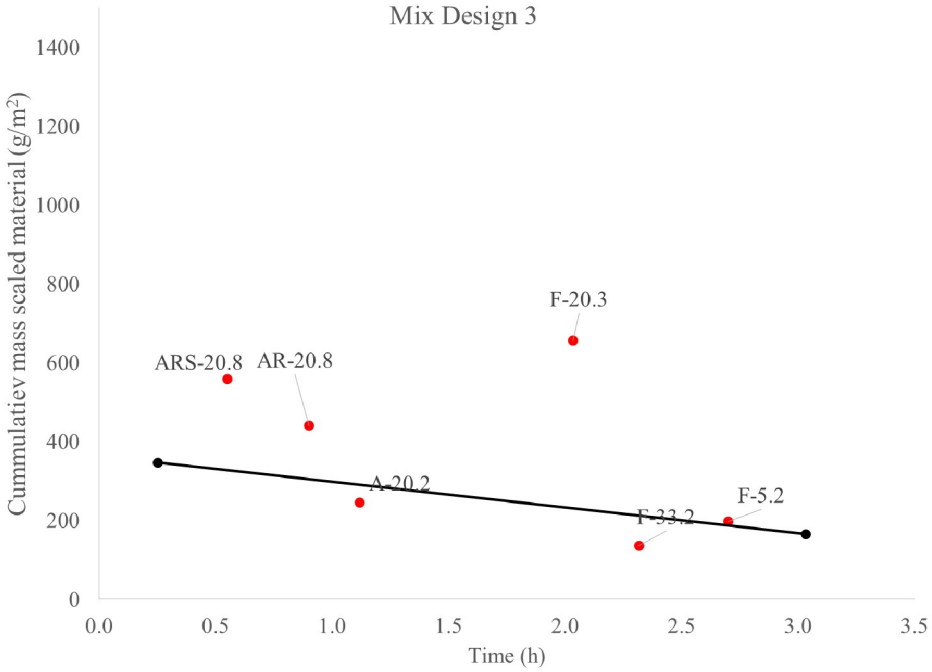

Figure 142. Scaling damage for non-pumped (black) and pumped (red) samples for mix design 3.

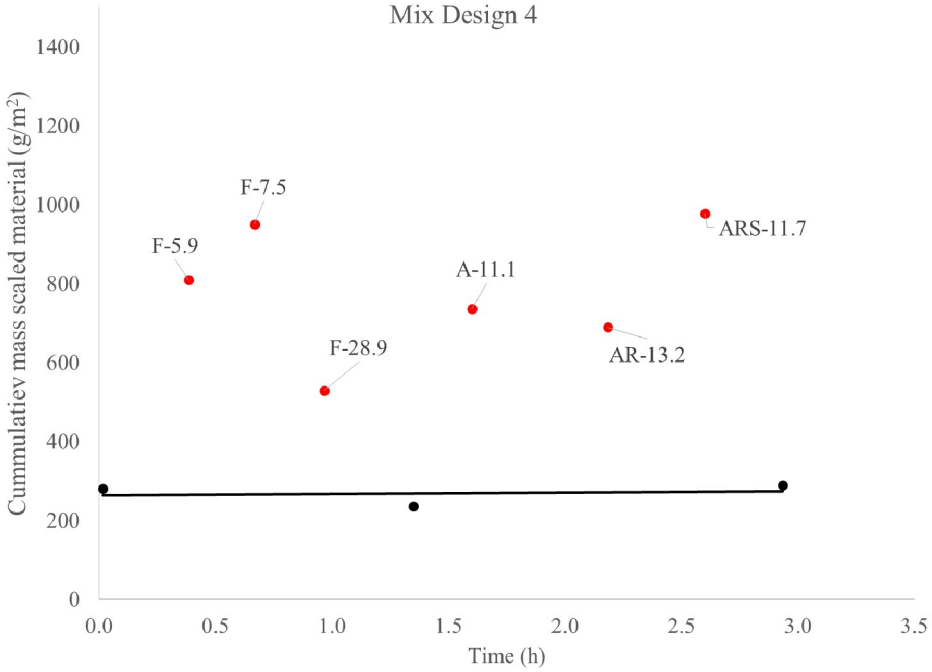

Figure 143. Scaling damage for non-pumped (black) and pumped (red) samples for mix design 4.

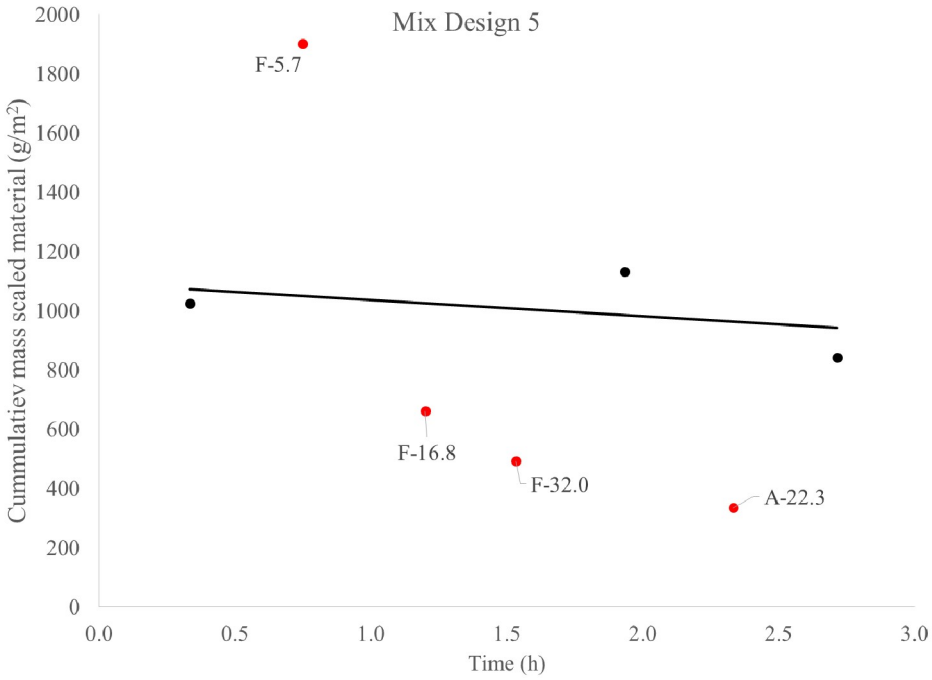

Figure 144. Scaling damage for non-pumped (black) and pumped (red) samples for mix design 5.

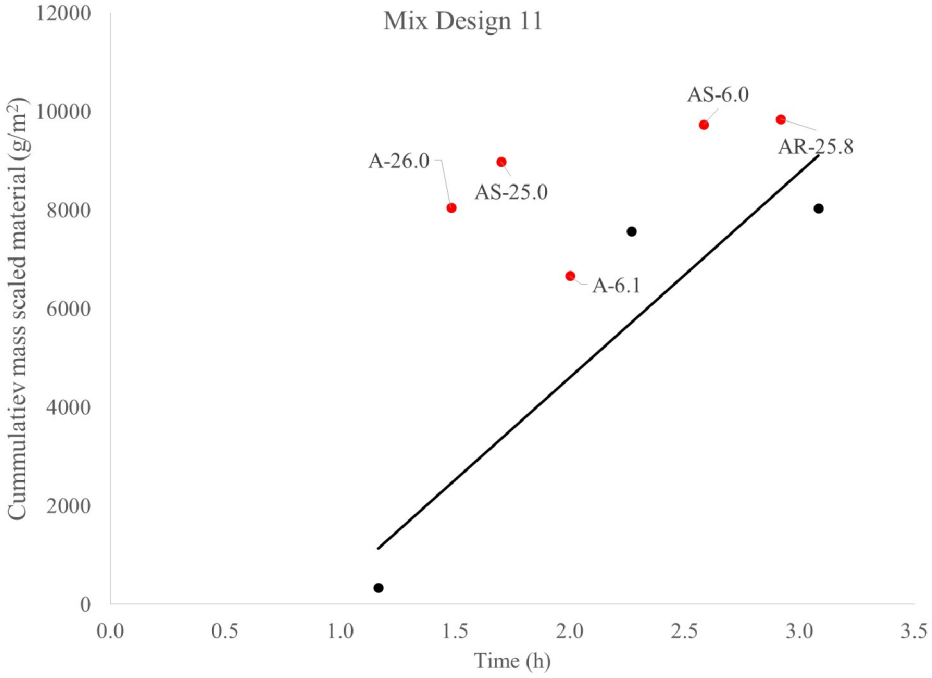

Figure 145. Scaling damage for non-pumped (black) and pumped (red) samples for mix design 11.

The non-pumped samples for mixture 12 show a strong decrease in amount of scaled material with time, and the pumped samples more or less follow that trend, except for the mixture pumped in A-configuration at medium flow rate, but not in A-S or A-R (Figure 146).

Mixture 13 shows poor scaling resistance, but pumping does not seem to affect this property, except for the mixture pumped at A-R-medium flow rate (Figure 147).

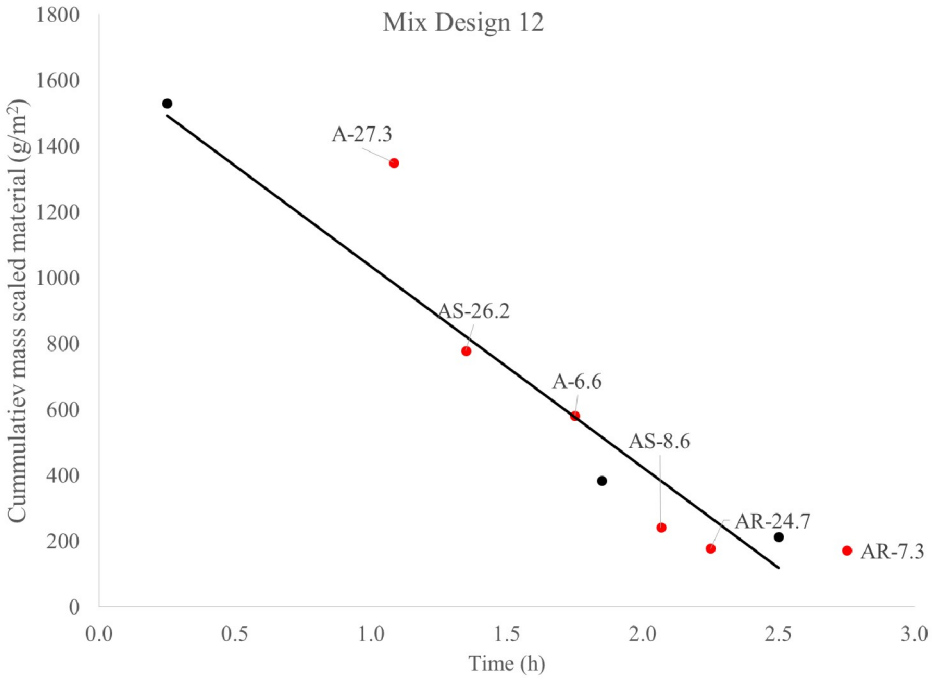

Figure 146. Scaling damage for non-pumped (black) and pumped (red) samples for mix design 12.

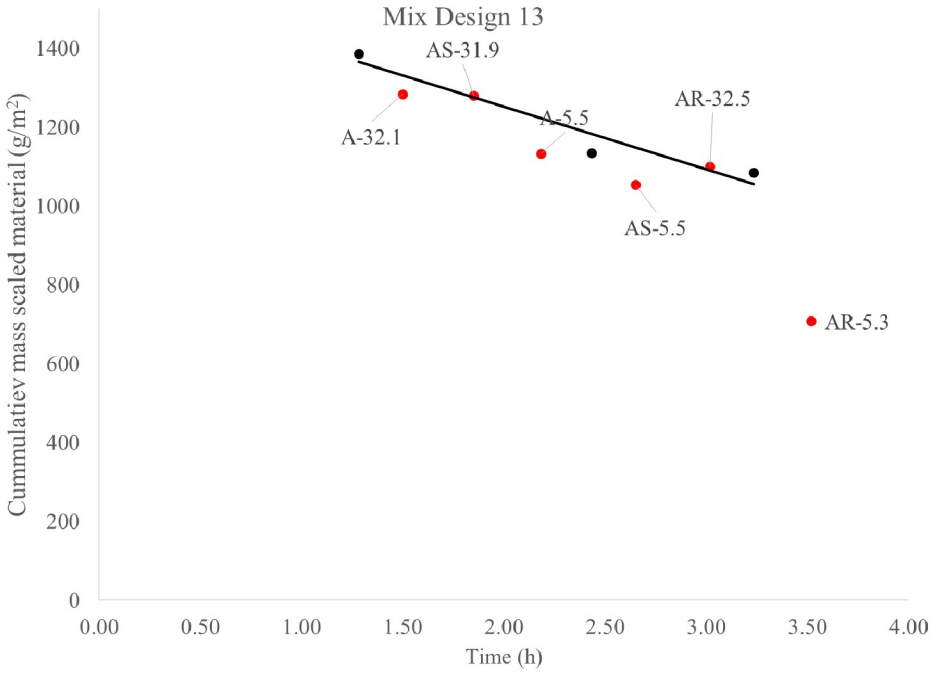

Figure 147. Scaling damage for non-pumped (black) and pumped (red) samples for mix design 13.

Mixture 14 shows complex behavior with the last scaling test of the non-pumped samples showing a substantially higher result. However, from the graph, it appears that pumping at medium flow rate seems to make scaling worse than at low flow rate, regardless of whether the hose was submerged, had a reducer, or not (Figure 148).

Mixture 16 shows better scaling resistance after pumping than before pumping, except for the AS low flow rate configuration (Figure 149).

Mixtures 15, 17 and 18 show surprisingly low values for the scaling tests, despite the more elevated spacing factors. It is suspected that there were some issues with the scaling chamber, not fully completing the thawing part of the cycles.

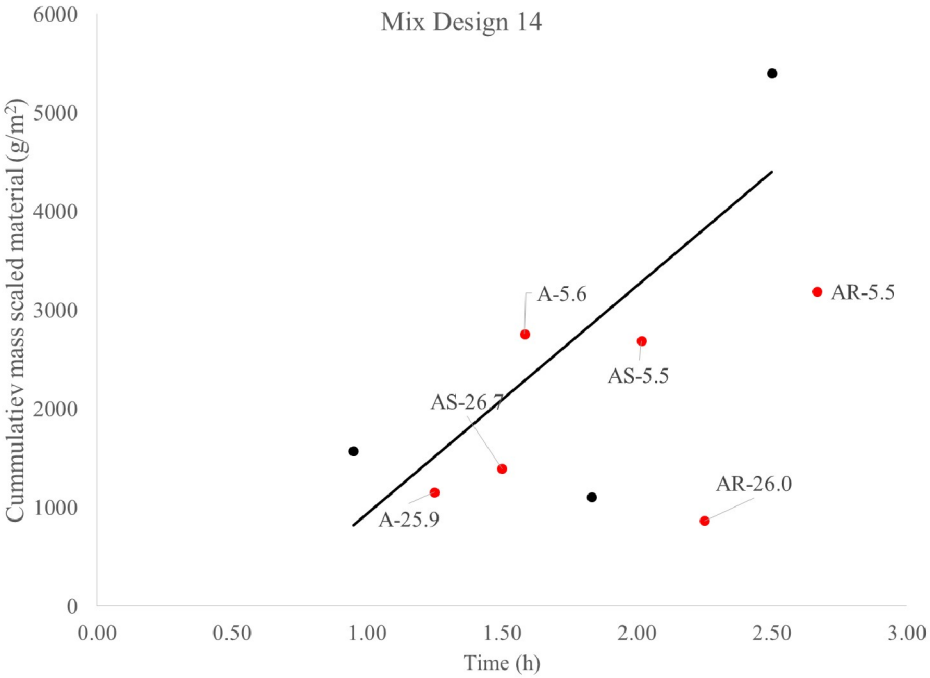

Figure 148. Scaling damage for non-pumped (black) and pumped (red) samples for mix design 14.

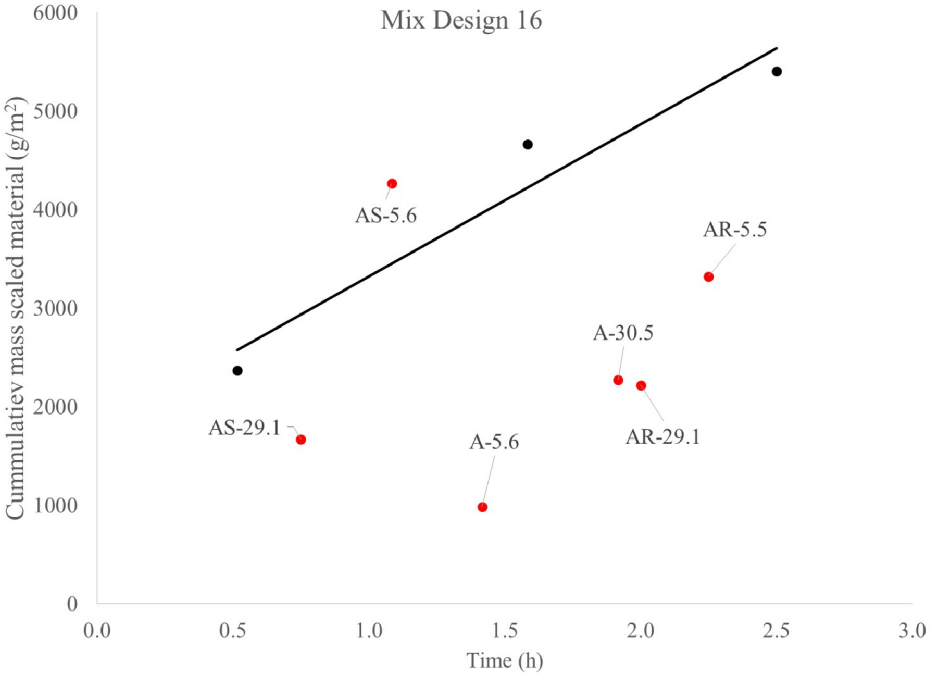

Figure 149. Scaling damage for non-pumped (black) and pumped (red) samples for mix design 16.

5.7.5.2 Influence of flow rate

Figure 150 to Figure 153 show the change in scaling due to pumping as a function of flow rate. Mixture 11 shows systematically more scaling with an increase in flow rate. For mixture 16, in A configuration, the change in scaling went up, but for A-R and A-S configuration, the change in scaling went down. For mixture 5, a decrease in scaling change was noted when increasing from low to medium flow rate.

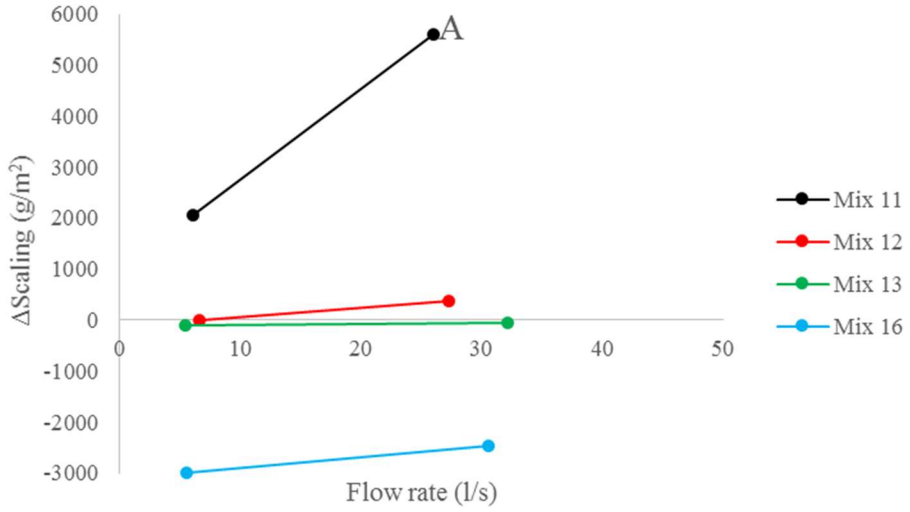

Figure 150. Influence of flow rate on the change in scaling values for A-configuration.

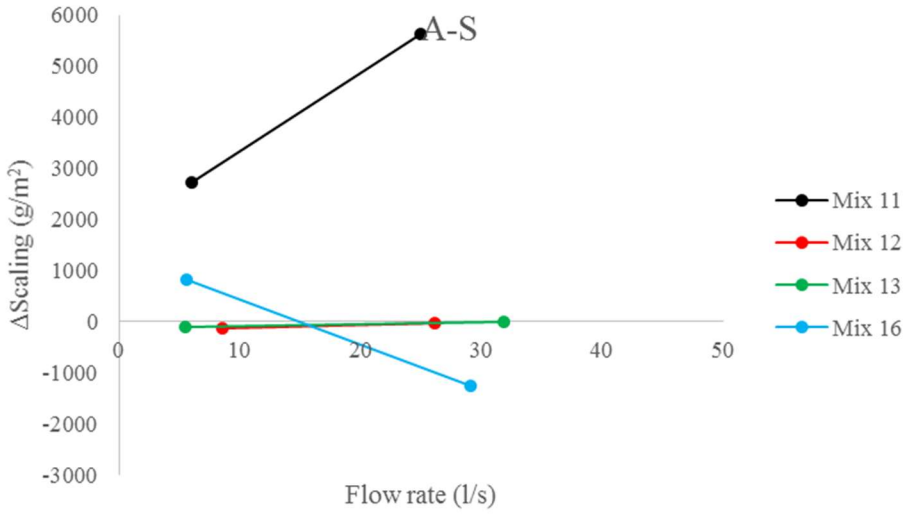

Figure 151. Influence of flow rate on the change in scaling values for A-S-configuration.

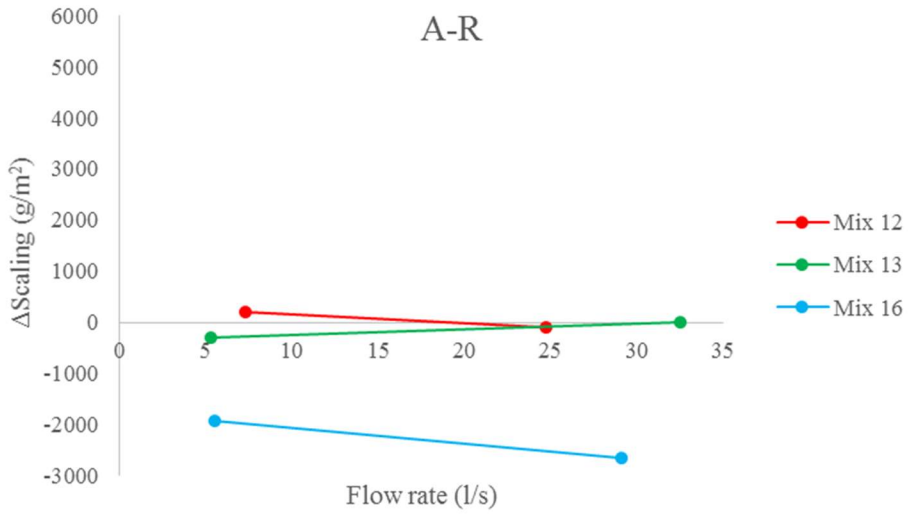

Figure 152. Influence of flow rate on the change in scaling values for A-R-configuration.

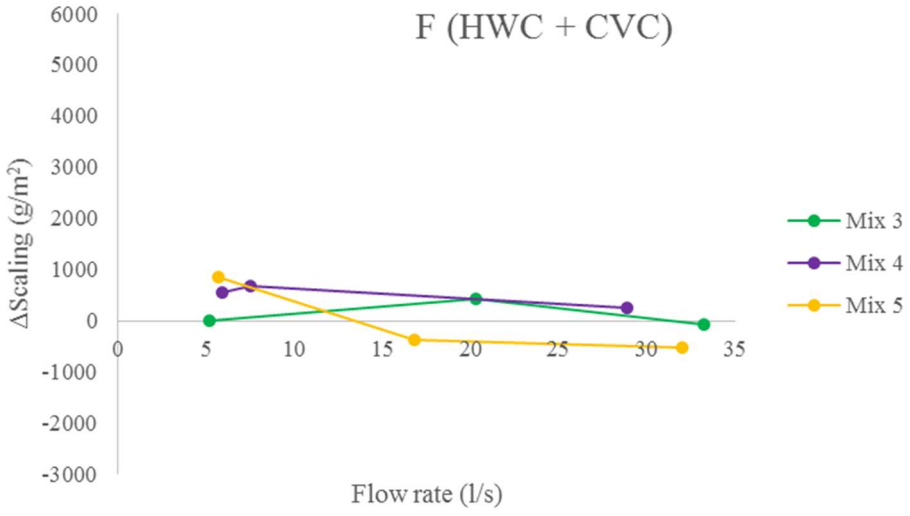

Figure 153. Influence of flow rate on the change in scaling values for F-configuration.

5.7.5.3 Influence of reducer

Figure 154 and Figure 155 show the influence of using a reducer on the change in scaling resistance. It appears that, if there is an influence on the scaling by using a reducer, in general, the negative effect is reduced, which is in line with the practical guidelines, except for mixture 16, at low flow rate.

Figure 154. Change in scaling resistance when using a reducer (right) versus not using a reducer (left).

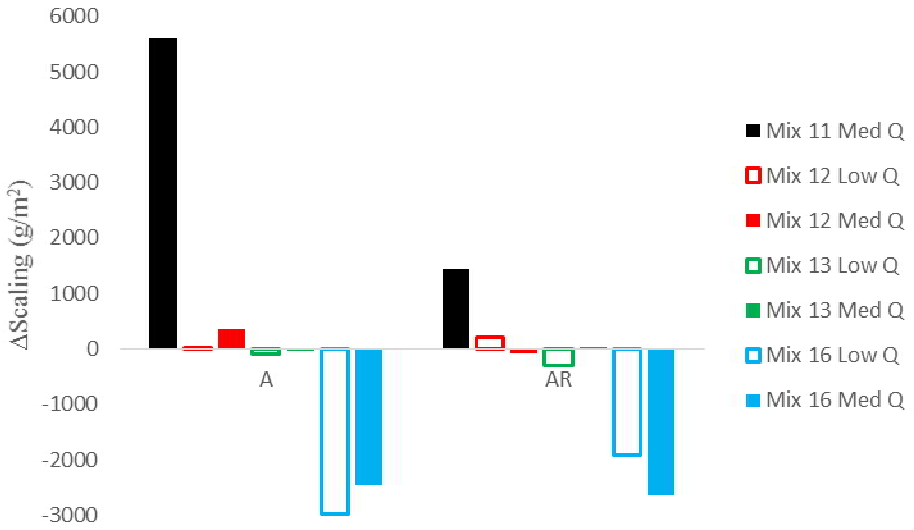

Figure 155. Change in scaling resistance when using a reducer (right) versus not using a reducer (left).

5.7.5.4 Influence of submerging the hose

Figure 156 and Figure 157 show the effect of submerging the hose. It appears that in general, when the hose is submerged, a larger increase in scaling value is observed. This is in line with the statements made above in section 5.7.5.1, as most of the mixtures which showed a larger scaling value were pumped in a submerged configuration. The exact reasoning is unknown.

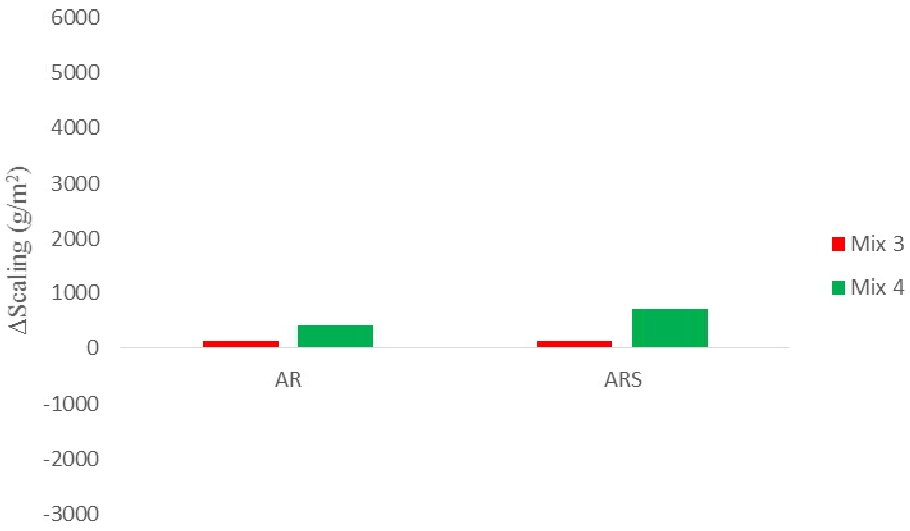

Figure 156. Change in scaling when submerging the hose (right) versus not submerging the hose (left).

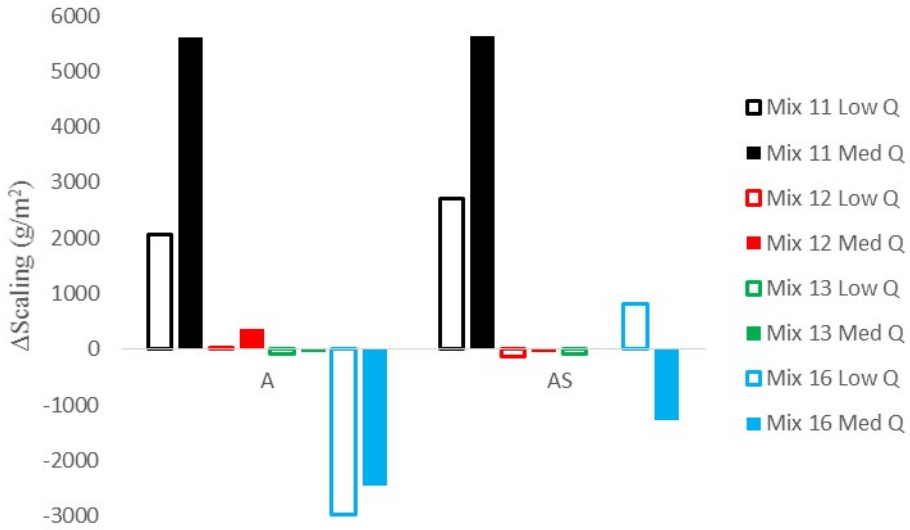

Figure 157. Change in scaling when submerging the hose (right) versus not submerging the hose (left).

5.7.5.5 A-configuration versus flat configuration

There are only two results in which the A and F configuration can be compared, being mixtures 3 and 4. No clear conclusions can be drawn from these results.

5.7.5.6 Summary

For mixtures with initial air contents of 7% and above, no issues with scaling were observed before or after pumping. For the other mixtures, the flow rate has a variable influence on the spacing factor, but stronger influences can be seen with lower initial air contents. Reducers generally result in a less negative effect compared to not using a reducer. Submerging the hose in the concrete typically has a more negative effect, if an effect is observed.

5.7.6 Correlations between factors

Figure 158 and Figure 159 show the relationship between spacing factor and air content, and between scaling and spacing factor, respectively, respecting any logical relationships. Figure 160 shows the change in spacing factor as a function of the change in air content, displaying almost no correlation, indicating that the observed change in spacing factor is not principally caused by a change in air content. Figure 161 and Figure 162 show the change in scaling as a function of the change in spacing factor. Figure 162 contains the same results as Figure 161, excluding the data with a small change in scaling (150 g/m^2). In that case, a weak correlation with $R^2 = 0.30$ is observed, indicating that when there is a change in scaling, it is influenced by the change in spacing factor. Figure 163 shows the correlation between the change in scaling and the change in air content, excluding the results with small changes in scaling. No correlation can be observed, showing that a change in air content due to pumping is not a good indicator for the change in scaling performance. No correlations between the changes in scaling or spacing factor with the changes in fresh properties were found based on this dataset.

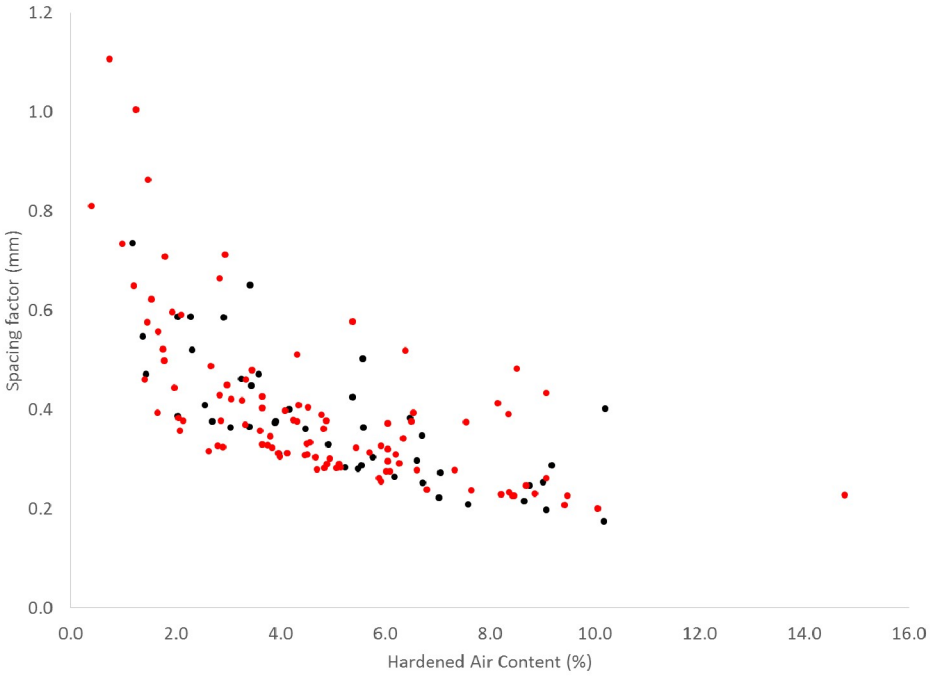

Figure 158. Relationship between spacing factor and hardened air content. Black points are non-pumped samples, red points are pumped.

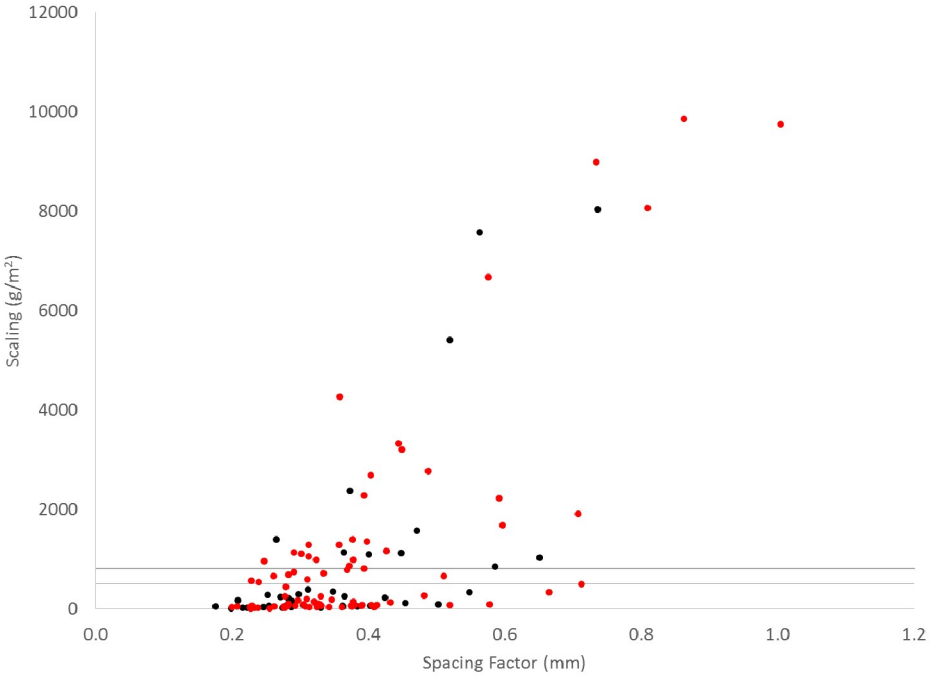

Figure 159. Relationship between scaling and spacing factor. Black dots are non-pumped, red dots are pumped. The gray lines indicate the 500 and 800 g/m² limits.

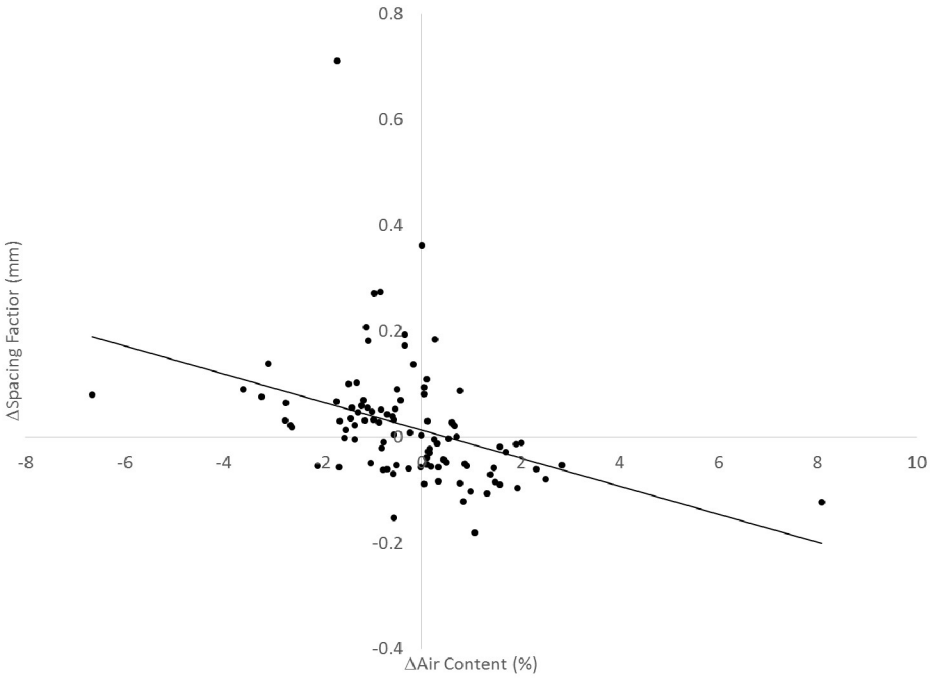

Figure 160. Correlation between the change in spacing factor and the change in air content.

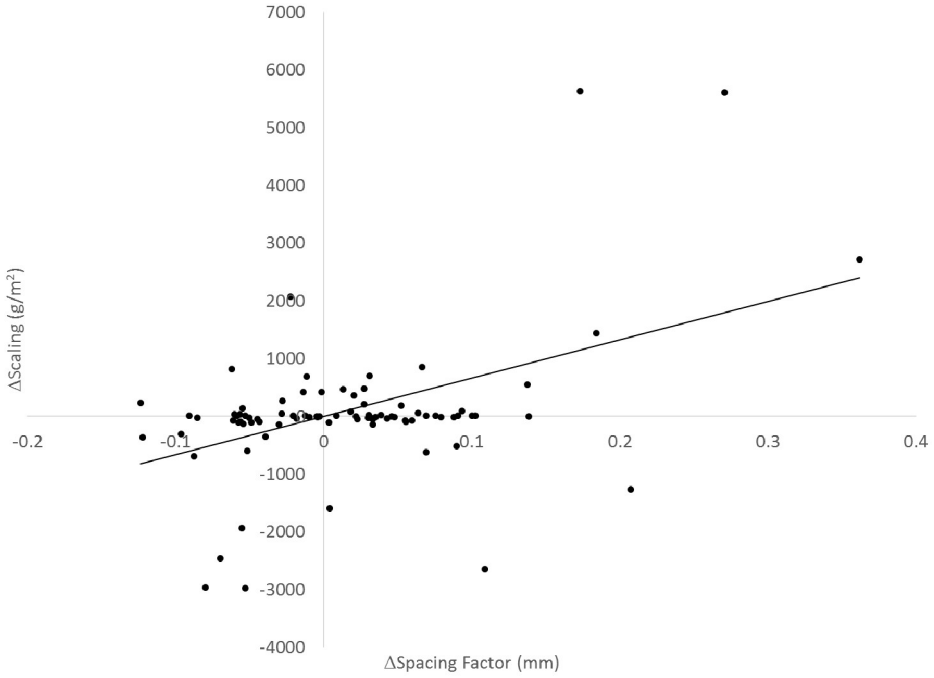

Figure 161. Correlation between the change in scaling measured and the change in spacing factor.

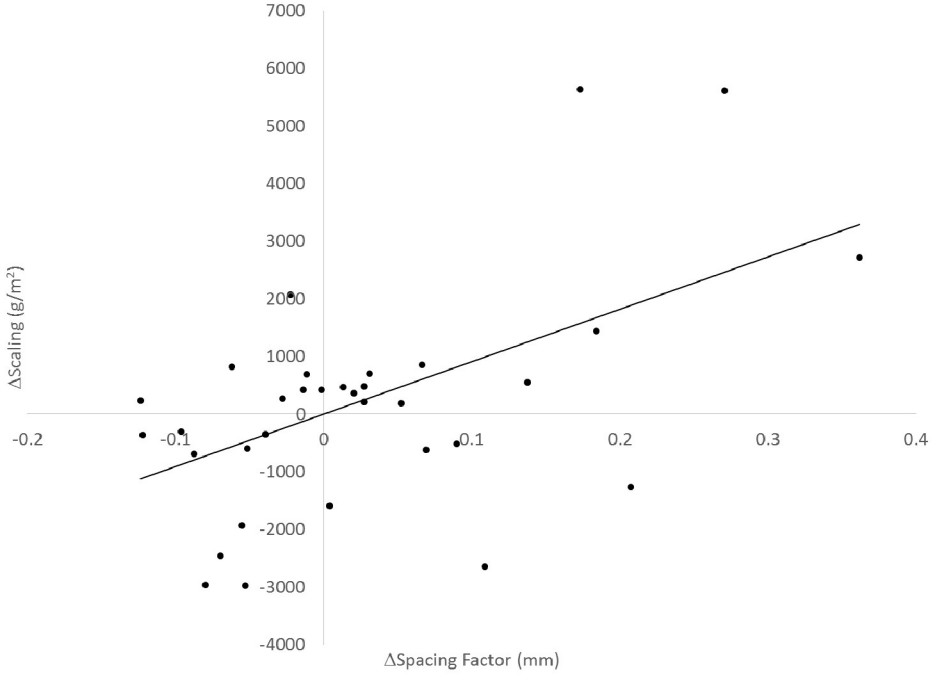

Figure 162. Correlation between chance in scaling and the change in spacing factor, excluding all results with a change in scaling < 150 g/m^2.

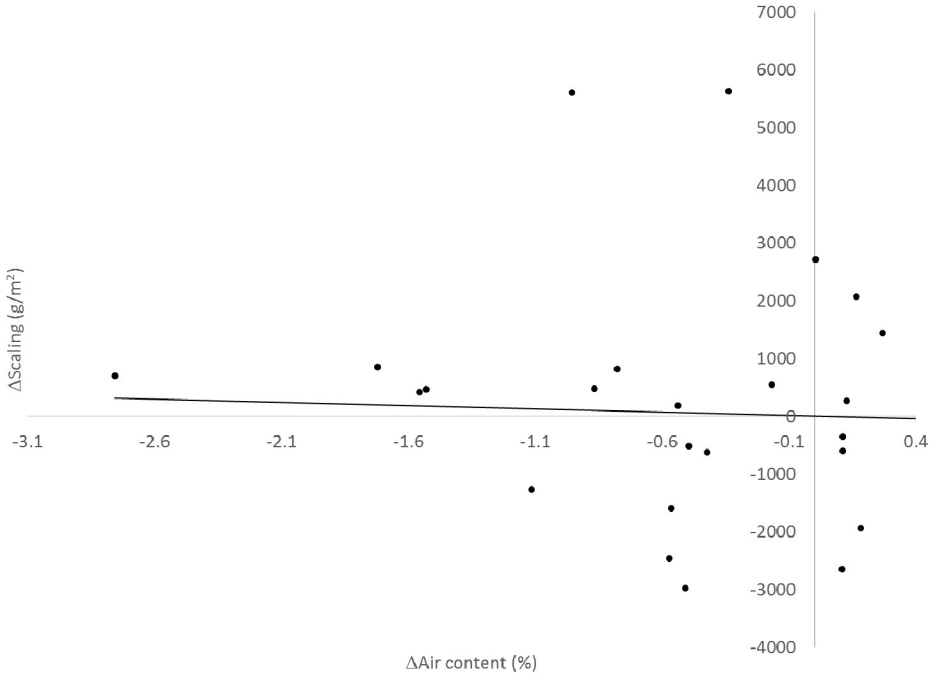

Figure 163. Change in scaling versus the change in air content, excluding all results which had a change in scaling < 150 g/m².

6 Air Dissolution in Cement Paste under Pressure and Shear

6.1 Objective

This section explores the capabilities of rheology to understand air dissolution and reappearance in cement paste under combined action of pressure and flow to emulate the conditions experienced by concrete when a pressure pulse is applied during pumping placement operations.

6.2 Materials and testing procedures

The cement pastes used in this study were composed by ordinary Portland cement (PC). The admixtures used were supplied by two different manufacturers, which divides them in two groups. The admixtures types were two polycarboxylate ether superplasticizer (SP), two retarders and two air-entraining admixtures (AEA). Tap water was used at water-to-cement ratios (w/c) of 0.45 and 0.35. In order to keep constant w/c regardless of the changing dose of the AEA, the solid residue of all the admixtures was determined by oven-drying as specified in ASTM C494-17 and the resulting mass loss was assumed to be water, which later was subtracted from the mixing water to preserve the design w/c. The admixtures relevant physical properties and the chemical composition (as extracted from their Material Safety Data Sheet) are shown in Table 28.

Table 28. Admixtures physical properties (density in g/l and solid residue in %) and chemical base.

ADMIXTURE	DENSITY	SOLID RESIDUE	BASE COMPOSITION
AEA1	1.01	6.1	Rosin, maleated
SP1	1.05	25.0	Polycarboxylate ether
RETARDER 1	1.06	13.1	Phosphonic acid
AEA2	1.01	15.7	Olefin Sulfonate
SP2	1.05	29.5	Polycarboxylate ether
RETARDER 2	1.12	18.0	Sodium hydroxide

The mixture proportions are shown in Table 29 and were designed to yield 1 liter of paste. The code names assigned to each mix design start with the w/c, followed by the level of AEA dose for each w/c system and the mixing procedure (see further). During the first phase of the experimental program, every mixture made had a replicate that was tested without pressurization and their code name starts with “NP” (Non-Pressurized). It can be seen in Table 29 that the volume of entrained air can theoretically be completely dissolved in the volume of mixing water at pressures that are well below the maximum applied during this phase of the experimental work (12 bar). However, this may not apply for some concrete mixtures where the ratio between the volume of air and volume of water is higher (%, Va/Vw) and the pressure exerted by the pump is relatively low.

Two different mixing procedures and high doses of AEA had to be used in order to achieve different volumes of entrained air. The main mixing procedure, using a small Hobart N50 mixer, consisted of first adding the water and the AEA to the mixing bowl, followed by the cement. Next, the mixer was started at speed 1 (139 rev/min) and the materials were mixed for one minute. Then, the mixer was stopped for 30 seconds, the mixing bowl was scraped, and the SP was added. Immediately after, the mixer was turned on at either speed 2 (285 rev/min) or speed 1 for one minute. The mixtures that were prepared using speed 1 on the second part

of the mixing procedure are identified with a letter "S" (slow), while the ones where speed 2 was used are "F" (Fast). By changing the mixing speed, it was possible to produce mixtures with different air contents and bubble size distributions. After one minute of mixing at speeds 1 or 2, the retarder was incorporated to the mixture without stopping the mixer and the paste was mixed for an additional minute.

Table 29. Mixture compositions (for 1 l) and measured air contents.

MATERIAL	W/C, BY MASS	WATER (G)	CEMENT (G)	AEA1 (G)	SP1 (G)	RETARDER 1 (G)	AIR (%/ML)	OVERALL WATER (ML)	PRESSURE FOR COMPLETE AIR DISSOLUTION (BAR)
045A1-S	0.45	561.5	1265	2.023	1.644	5.058	4.6/46.4	569.0	4.4
045A2-S	0.45	557.6	1264	6.068	1.644	5.057	5.9/58.8	568.9	5.6
045A3-S	0.45	553.7	1264	10.11	1.643	5.056	7.5/75.0	568.8	7.1
035A1-S	0.35	490.2	1453	11.62	3.196	5.812	4.1/41.2	508.5	4.4
035A1-F	0.35	490.2	1453	11.62	3.196	5.812	5.9/59.3	508.5	6.3
035A2-S	0.35	479	1452	23.23	3.195	5.808	3.8/38.2	508.2	4.1
035A2-F	0.35	479	1452	23.23	3.195	5.808	6.8/67.9	508.2	7.2
035M100-S	0.35	481.4	1449	23.18	2.029	5.796	4.5/45.5	507.1	4.8
035M100-F	0.35	481.4	1449	23.18	2.029	5.796	5.7/49.5	507.1	6.1
035M20-S	0.35	481.4	1449	23.18	2.029	5.796	5.4/53.7	507.1	5.7
035M20-F	0.35	481.4	1449	23.18	2.029	5.796	5.8/57.8	507.1	6.1

Self-consolidating consistency was desired to avoid slippage between the wall of the inner cylinder of the rheometer and the sample, plug-flow, and entrapment of unquantified air in the rheometer cup when the samples were inserted. Immediately after mixing, the air content was estimated using the procedure specified in ASTM C185-15a with the exception that the samples were not placed in layers inside the calibrated measure nor tamped. Two other samples were collected, one for rheological analysis and another for the estimation of the air-void size distribution using the AVA-3000 apparatus [129]. The AVA-3000 working principle is based on Stokes' law for bubble rise rate. In order to quantify the amount of bubbles of certain size that the sample has, it collects the air bubbles in an inverted pan which is hooked to a scale at the top of the water column (Figure 164). The test requires the use of glycerin-based release agent that is intermixed with the sample at the bottom of the water column which main function is to prevent the release of all the bubbles at the same time and to preserve their size. The device measures the change of weight of the inverted pan over time and estimates the amount of bubbles that could have induced such change based on the elapsed time.

The rheometer used was an Anton Paar MCR-302 equipped with a cylindrical pressure cell that encapsulated the inner cylinder (Figure 165). The rotation of the inner cylinder was driven by a magnetic coupler attached to the rheometer transducer. The pressure was supplied by a gas tank filled with common air and controlled manually by an ordinary pressure regulator. The volume of the sample inside the rheometer cup was 22 ml, which ensured that the inner cylinder wall was always covered even when pressure was applied. The Peltier control unit kept temperature constant at 20°C throughout the experiment.

Two testing procedures were used for this project and are denominated as "A" and "B". Procedure "A" is intended to assess the changes in the rheological properties caused by modifications in applied pressure, while procedure "B" evaluated the influence of a single pressure step on the rate of air dissolution and

reappearance. Procedure "A" (Figure 166) used a set of prolonged shearing stages at a fixed shear rate of 100 s^{-1} combined with 3 flow curves. Apparent viscosity during the prolonged shearing steps was calculated by dividing the shear stress by the shear rate. The pressure was supplied in stepwise fashion, starting from atmospheric conditions to approximately 12 bar. Although the pressure regulator was adjusted manually, care was taken regarding supplying the pressure as consistently as possible across all tests.

Figure 164. AVA-3000 bubble rise water column.

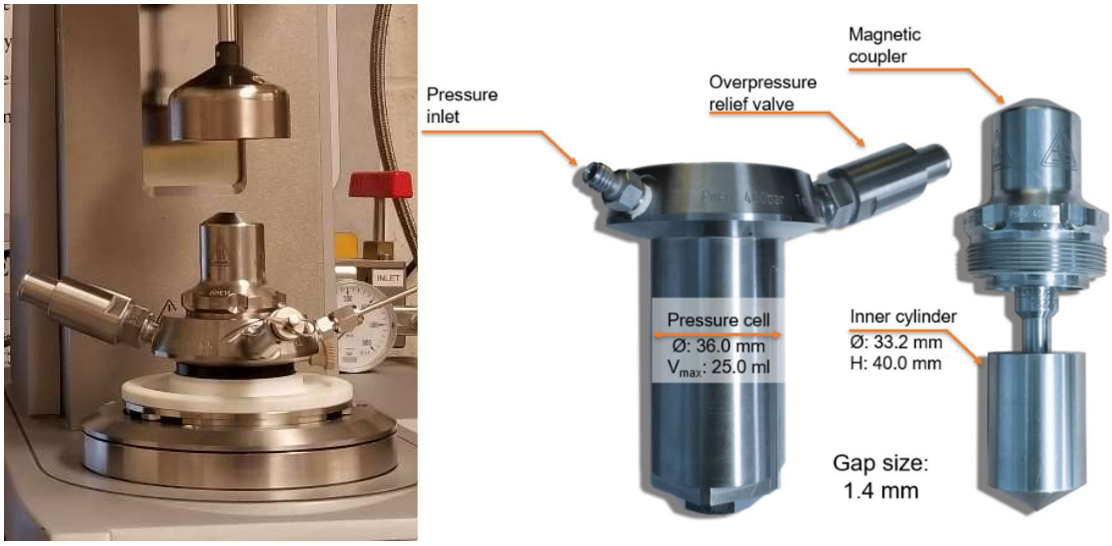

Figure 165. Pressure cell mounted in the rheometer MCR-302 (left) and geometry details (right).

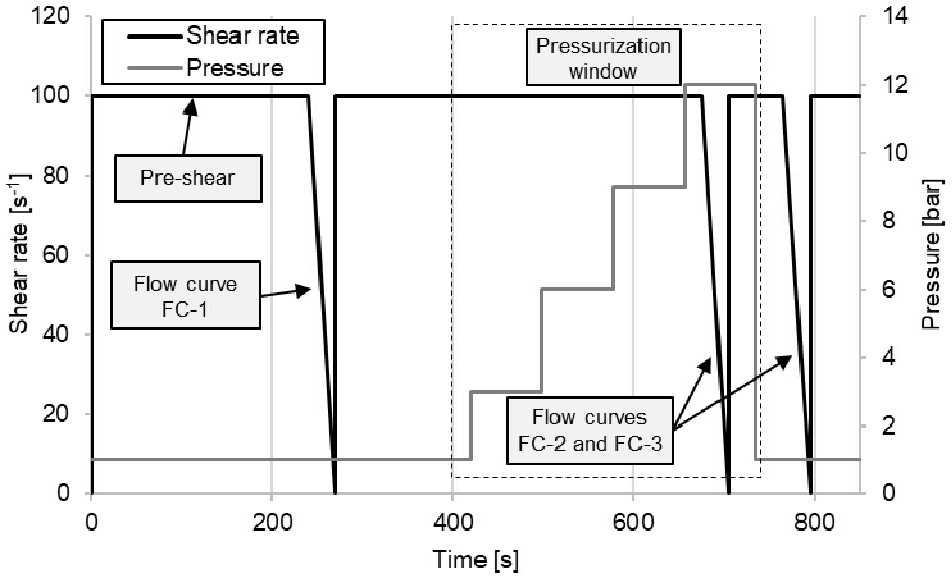

Figure 166. Testing procedure "A".

The flow curves were defined by linearly decreasing the shear rate from 100 to 10 s^{-1} in 25 s followed by a logarithmic decrease in shear rate from 10 to 0.01 s^{-1} during 5 s to obtain a better approximation of the yield stress. A 6th order polynomial was fitted to the whole data set conforming each flow curve and differentiated to the shear rate in order to define the differential viscosity at 50 s^{-1} [118]. The flow curves captured the rheological properties of the cement paste at the beginning of the test after structural breakdown (FC-1), under pressure (FC-2) and right after depressurization (FC-3).

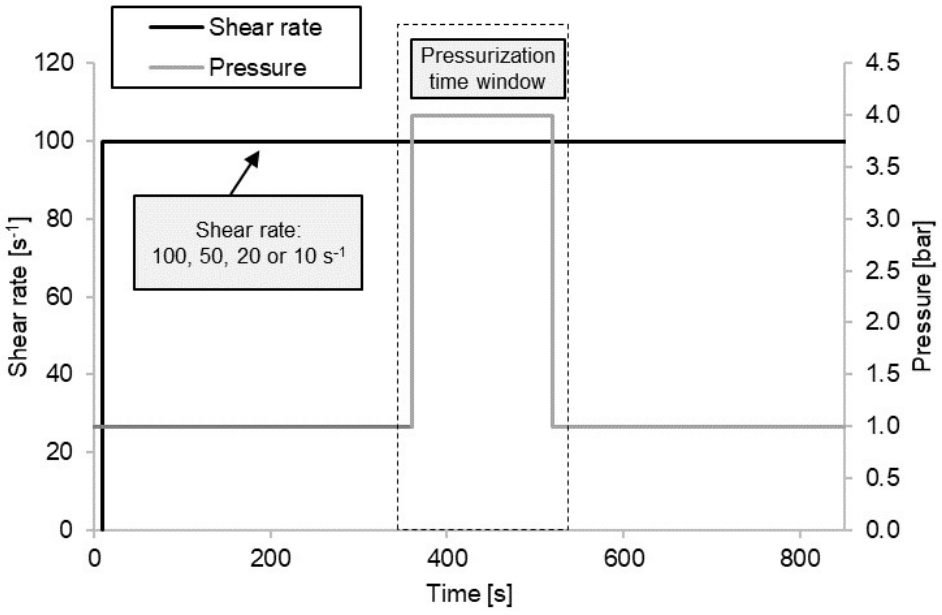

Figure 167. Testing procedure "B".

Procedure "B" (Figure 167) imposes uninterrupted shearing at either 100, 50, 20 or 10 s^{-1}. Since every shear rate requires different stabilization times to reach shear stress equilibrium [118], pressurization was not performed unless the shear stress was considered, visually, sufficiently stable. The pressure was supplied by opening the inlet valve of the pressure chamber in a single and fast maneuver exposing the sample from

atmospheric conditions to approximately 4 bar for 2 minutes. Although the pressure regulator was set up to the desired pressure previously to loading the sample in the pressure chamber, the way pressure built up over time changed randomly between samples from a single sudden increase to the desired pressure, or a combination of a sudden increase with a slight further increase in pressure over time. However, there was not an evident change in the rheometer output attributable to this artifact.

6.3 Results

6.3.1 Bubble size distribution and capillary number

Table 30 shows that most of the air bubbles of the pressurized samples were smaller than 500 µm. Considering a constant shear rate of 100 s^{-1}, an apparent viscosity of the suspending medium as η = 0.15 Pa s for w/c = 0.45 and η = 0.52 Pa s for w/c = 0.35, and assuming the surface tension of a combination of water-SP-AEA to be 0.040 N/m [130], the capillary number (Ca) would be less than 0.19 and 0.645, respectively, for bubbles sizes < 500 µm. Therefore, a large majority of the air bubbles behaved mostly as solid particles and had the tendency to amplify the rheological properties, similar to solid particles amplifying the rheology of suspensions [38]. One caution about the results is that the AVA-3000 software is not designed to measure the air-void distribution of cement paste as it is programed to stop the measurement automatically after 3 minutes of not recording significant changes in the recorded data. As consequence, the smaller bubble size fractions may be underestimated, however those bubbles are also less susceptible to being deformed.

Table 30. Bubble size distribution (expressed as % passing) for the w/c = 0.45 and 0.35 mixtures, obtained from the AVA 3000.

	SIZE (μm)							
	2000	**1000**	**500**	**300**	**200**	**150**	**125**	**100**
045A1-S	100	96.1	74.4	56.2	37.2	24.5	14.2	0
045A2-S	100	100	72	45.6	32.1	19.1	12.6	0
045A3-S	100	100	70.3	41.4	30.4	18.1	12.1	4.2
035A1-S	100	100	57.4	32.7	22.6	11.6	0	0
035A1-F	100	100	78.6	38.7	21.6	8.8	2.6	0
035A1-S	100	100	60.0	34.0	21.0	10.0	3.0	0
035A2-F	100	100	89.1	69.2	48.8	20.1	10.8	0
035M100-S	100	78.6	42.5	26.1	14.8	2.8	0	0
035M100-F	100	100	68.7	44.9	28.8	16.6	2.4	0
035M20-S	100	100	64.7	41.9	27.6	16	7.6	0
035M20-F	100	100	60.4	34.2	18.1	7.1	4.3	0

6.3.2 Testing procedure "A"

Mixtures 045A1-S, 045A2-S, 045A3-S, 035A1-S, 035A1-F, 035A2-S and 035A2-F and their corresponding non-pressurized replicates were tested using procedure "A". Table 31 shows a summary of the apparent viscosity recorded at specific points of procedure "A" for w/c = 0.45 and 0.35. These points correspond to the average apparent viscosity of the last 10 seconds before the system is pressurized, 10 seconds during pressurization where the rheological properties were at the lowest value and 10 seconds after the pressure was released. The column "Pressure" shows the pressure recorded after which the apparent viscosity did no longer change during the pressurization stage. As it was expected, the larger the volume of entrained air, the larger the pressure required to achieve full air dissolution in the liquid phase [66, 68] and the larger the reduction of the rheological properties [38]. However, the experimental pressure values for which the rheological properties stabilized are higher than the theoretical ones required to achieve full dissolution. The

w/c = 0.35 mixtures did not fully recover the apparent viscosity recorded right before the pressurization contrary to the mixtures with w/c = 0.45, suggesting changes in either air volume or distribution, which is discussed further. Regarding the results of the flow curves measured before, during and after pressurization, the changes in yield stress were too small to derive any conclusions. The results on differential viscosity followed the observations for the apparent viscosity.

Table 31. Summary of apparent viscosity changes due to pressurization.

	APPARENT VISCOSITY, η (PA S)			**PRESSURE (BAR)**	**AIR (%)**
	Pressurization				
	Before	**During**	**After**		
045A1-S	0.172	0.159	0.173	7.8	4.4
045A2-S	0.176	0.162	0.188	8.7	5.6
045A3-S	0.166	0.135	0.165	7.9	7.1
035A1-S	0.567	0.534	0.522	8.8	4.4
035A1-F	0.549	0.518	0.517	9.4	6.3
035A2-S	0.565	0.516	0.523	11.4	4.1
035A2-F	0.563	0.495	0.520	12.8	7.2

Figure 168 depicts the typical rheometer output for a pressurized and non-pressurized sample in terms of relative shear stress vs. time for the w/c = 0.45 mixtures. The relative shear stress is defined as *"the shear stress at any time t divided by the average shear stress recorded during 10 seconds previous to the pressurization step".* The effect of pressure can be clearly seen after t = 450 s. When the sample is suddenly pressurized to approximately 2.8 bar, a gradual reduction of the shear stress was experienced and was briefly stabilized for few seconds. When the next pressure step increment was supplied (4.8 bar), a gradual reduction of the shear stress was recorded once more. Further pressure additions did not provide significant changes in the rheometer output. The non-pressurized sample did not show any changes in rheological behavior during the same time period, indicating that the changes in rheology of the pressurized sample is solely caused by the pressure.

It is well known that the reduction of the (non-deformable) particle concentration of a suspension leads to a decrease in its rheological properties [38]. Since the only highly compressible phase present in the sample was air, the reduction in size and its eventual dissolution into the liquid phase due the pressure increase created a reduction in the bubble concentration and viscosity decreases. Figure 168 shows that when pressure was released at t = 736 s, the shear stress or viscosity was recovered to levels close to before pressurization, as can also be seen in Table 31. Once the cement paste was exposed again to atmospheric conditions, the air-dissolving capacity of the water was restored to its original level and the dissolved air was released almost instantly. The dynamic conditions of the sample during depressurization may accelerate this effect. The performed experiments cannot tell if the subsequent air nucleation created similar bubble size distributions or where the air reappeared. However, it is suggested by Dyer [50] that dissolved air will preferentially reappear in already formed bubbles since it is thermodynamically less energy consuming than forming a new bubble. As a consequence, a coarser air-void system is expected to occur after depressurization [68, 88]. At the end of the experiment, a thick layer of coarse foam was always observed on top of the inner cylinder, but only for the pressurized samples (Figure 169), suggesting that once pressure was released, air bubbles were formed somewhere in the rheometer cup, expanded due to the pressure decrease, and traveled to the surface due to buoyancy.

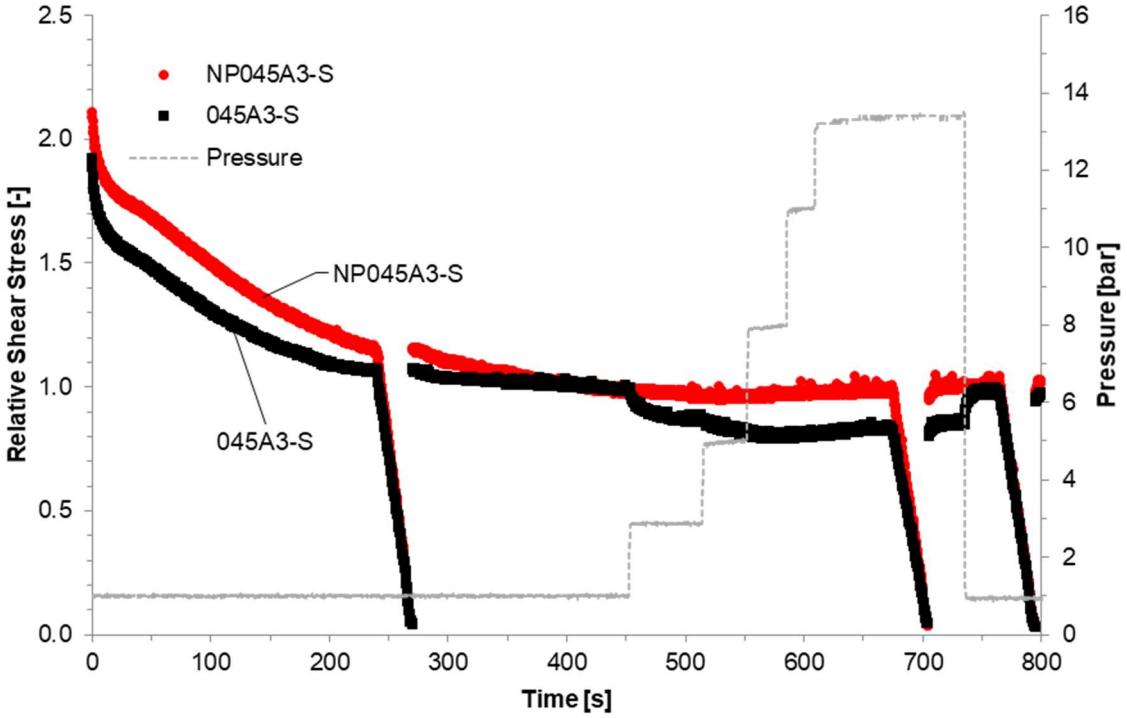

Figure 168. Rheological testing procedure "A" applied on mixture 045A3-S. The relative shear stress equals 1 just before the application of pressure.

Figure 169. The pressurization/depressurization of the samples yielded a substantial volume of foam on top of the inner cylinder of the pressure cell. Picture taken after removing the inner cylinder from the pressure cell.

Figure 170 illustrates the response to pressurization/depressurization of mixture 035A2-F. This mixture showed that at t = 450 s, the pressure was increased from atmospheric conditions to 3.9 bar leading to a sudden drop, followed by a gradual reduction of the rheological properties until equilibrium was reached. At t = 510 s the pressure was increased to 6.5 bar and a new (but smaller) drop in the shear stress was recorded. Figure 171 shows that the sudden drop of rheological properties was only observed in the mixtures 035A2-F

and less abruptly for 035A1-F. Such effect can be related to their finer bubble size distribution (Table 30). Part of the mixing process of 035A1-F and 035A2-F was performed at a higher mixing speed than the other samples. This change in the mixing energy produced a finer bubble size distribution. On the other hand, 035A1-S and 035A2-S were mixed using the same procedure as for all w/c = 0.45 mixtures. The reduced amount of water combined with relatively low mixing energy did not permit the incorporation of high volumes of air and resulted in the coarsest bubble size distribution of all the mixtures tested. Since for mixtures 035A1-F and 035A2-F, the concentration of small bubbles was larger than in the others, a small increase in pressure leads to the rapid dissolution of an important fraction of the air-void system. The internal air pressure due to surface tension is inversely proportional to the diameter of the bubble [68, 88, 116]. The solubility of air depends on the partial pressure surrounding the bubble, the small bubbles are the first ones to dissolve because their internal pressure is higher and any further increase in pressure will increase the degree of air under-saturation of water, promoting air diffusion from the bubbles [88]. In addition, small bubbles have larger specific surface, which accelerates the dissolution process [67]. Therefore, the rheological properties decrease consistently with the principle of particle concentration of suspensions as the air dissolves [38]. Figure 170 also shows that once the pressure was released, the rheological properties were not fully restored as was the case of the w/c = 0.45 mixtures, at least not within the remaining part of the test. This behavior was observed in all pressurized w/c = 0.35 samples. The lack of reestablishment of the rheological properties suggests a change in air volume and/or distribution.

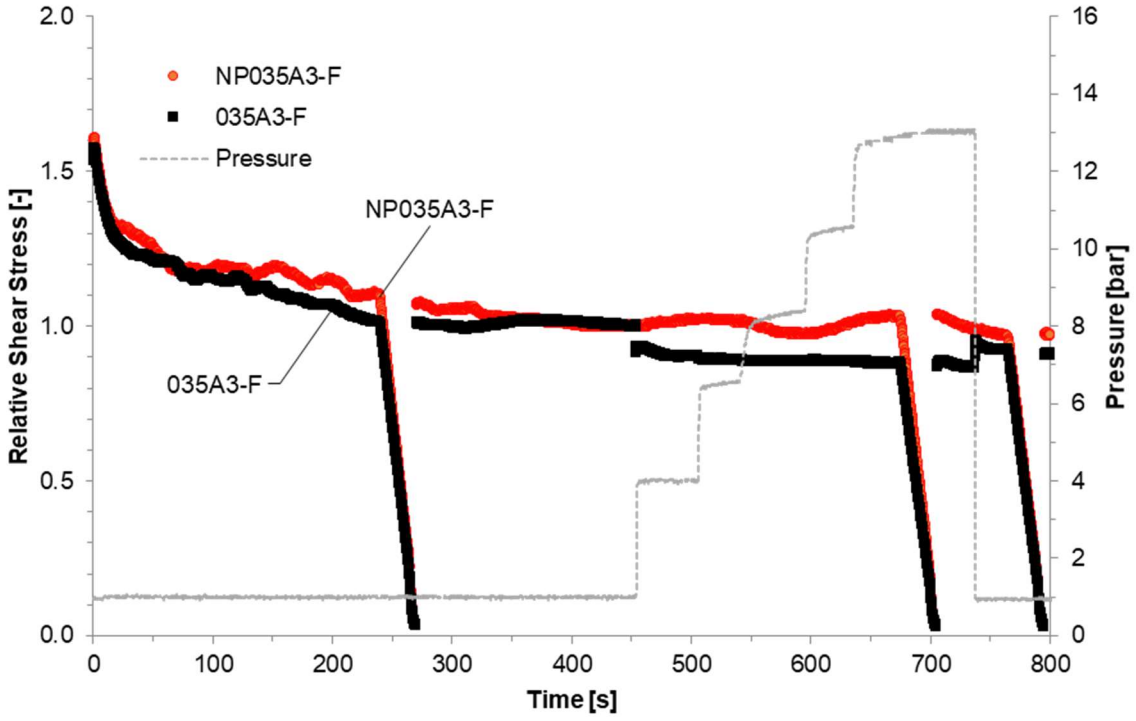

Figure 170. Rheological testing procedure "A" applied on mixture 035A2-F.

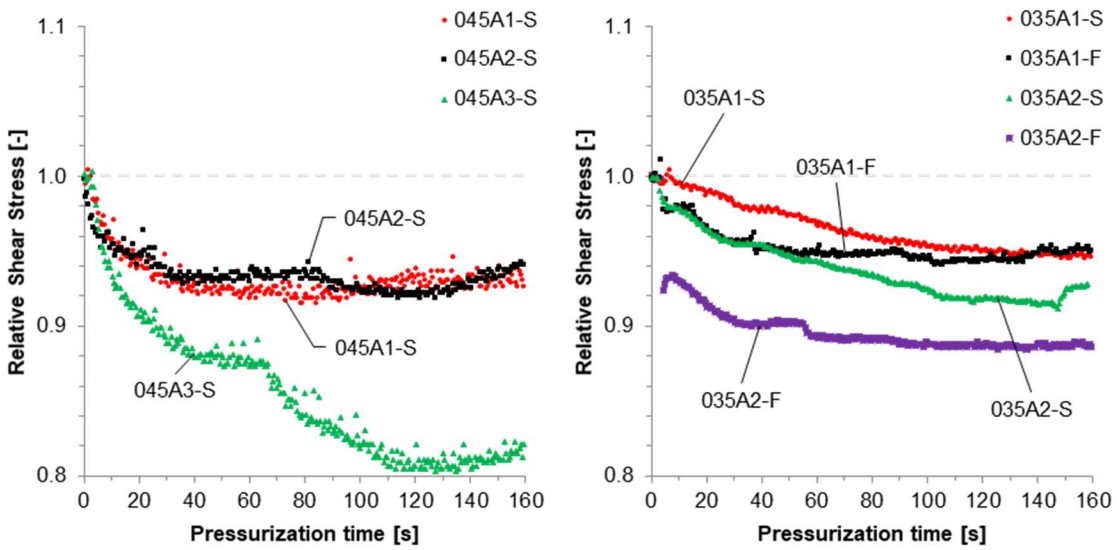

Figure 171. Comparison of the relative shear stress response to pressurization over time of w/c = 0.45 (left) and w/c = 0.35 (right) mixtures. Pressure steps are not shown.

6.3.3 Testing procedure "B"

For this testing series, replicates of mixture 035A2-F, all containing approximately 7% air by volume, were evaluated according to procedure B. The samples were exposed to a constant shear rate (100, 50, 20 or 10 s^{-1}), and were subjected to a sudden increase in pressure of approximately 4 bar, which was maintained for 2 min. A pre-shear period was applied on all samples in an attempt to reach equilibrium. Although visually, the shear stress appeared to be in equilibrium during the tests, analysis has shown this was not the case. As such, to eliminate the effect of structural breakdown, the shear stress-time curve before pressurization was fitted with a double exponentially decreasing function (eq. 28), adequately capturing the behavior (Figure 172)

$$\tau = A * e^{(-Bt)} + C * e^{(-D\ )} + E \qquad \textit{(Eq. 28)}$$

Where:

τ = shear stress (Pa)

t = time (s)

A, B, C, D and E = fitting constants

Then, the data of the pressurization stage at each shear rate were normalized point by point using the extrapolated fitted function.

Figure 173 to Figure 176 show the influence of the shear rate on the shear stress response caused by air dissolution at 100, 50, 20 and 10 s^{-1}. At 100 s^{-1} the changes in the rheological properties of the sample occur immediately and a small recovery hump was followed by a slight reduction and further stabilization of the rheological properties, as can be seen during the pressurization stage. When pressure is relieved, the rheological properties are partially restored after 6 seconds. At 50 s^{-1}, the same behavior can be seen but this time the instantaneous reduction on the shear stress was higher than the observed at 100 s^{-1} and, once the mixture got depressurized the shear stress partially recovered in approximately 2 seconds and stayed relatively constant for the rest of the test. At 20 and 10 s^{-1}, there is an abrupt drop in the rheological properties as well, with the main difference that the recovery hump that happens immediately after pressurizing the system is broader and takes approximately 40 seconds to get stable. Once that the pressure is released, it takes

only a few seconds to fully recover the initial relative shear stress but immediately after this it starts decreasing again.

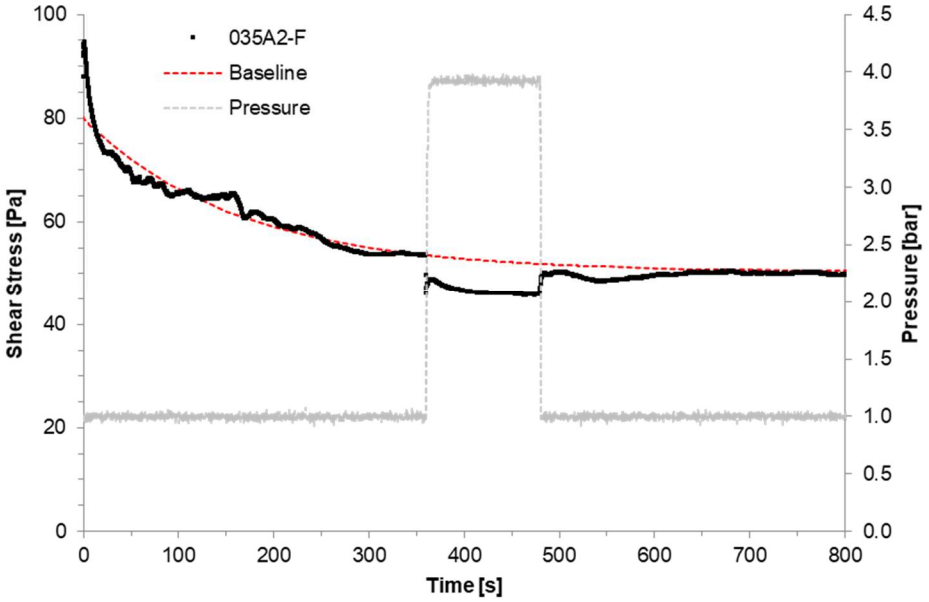

Figure 172. A double exponential approach based on data prior to pressurization was implemented to define a baseline for normalization.

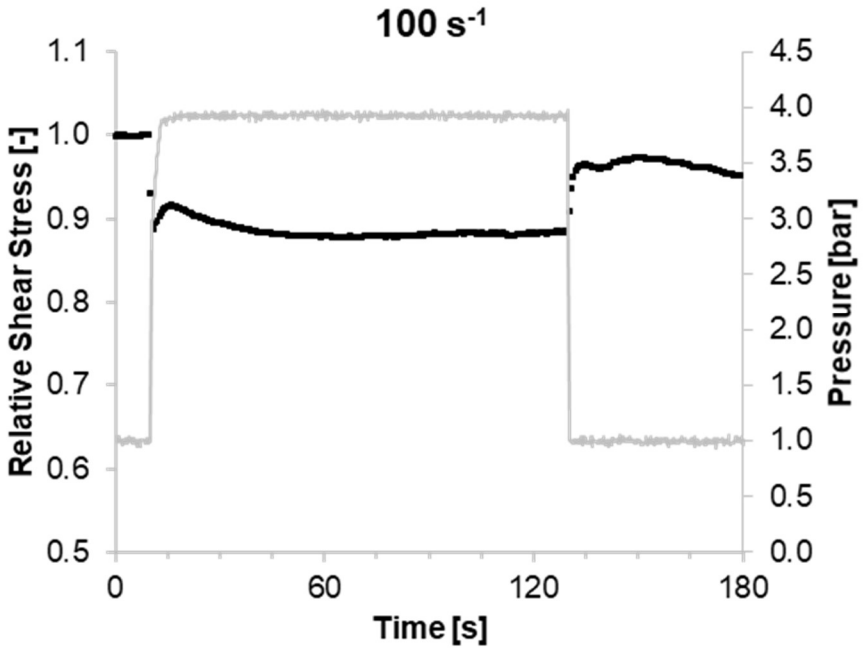

Figure 173. Rate of air dissolution and reappearance at a shear rate of 100 s^{-1} of sample 035A2-F.

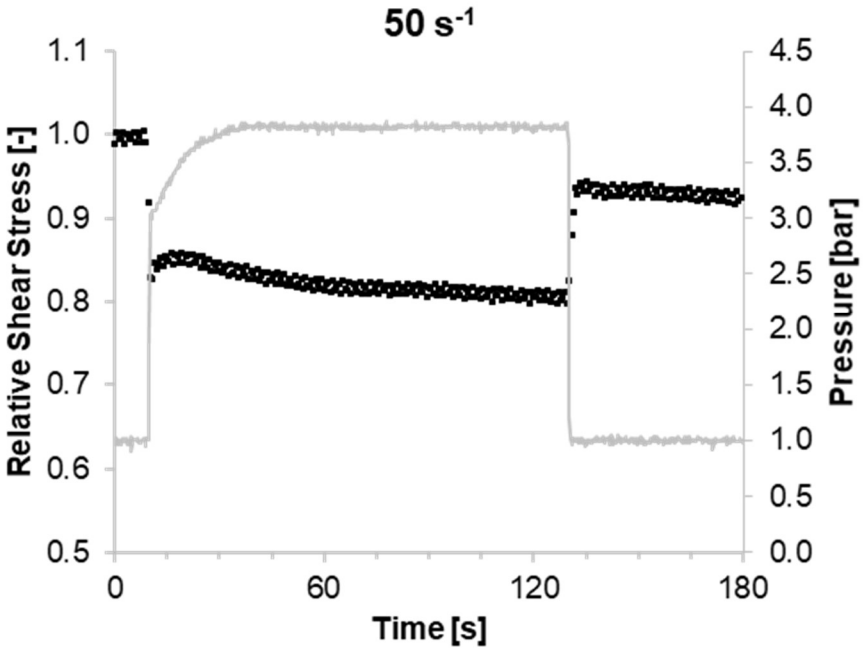

Figure 174. Rate of air dissolution and reappearance at a shear rate of 50 s^{-1} of sample 035A2-F.

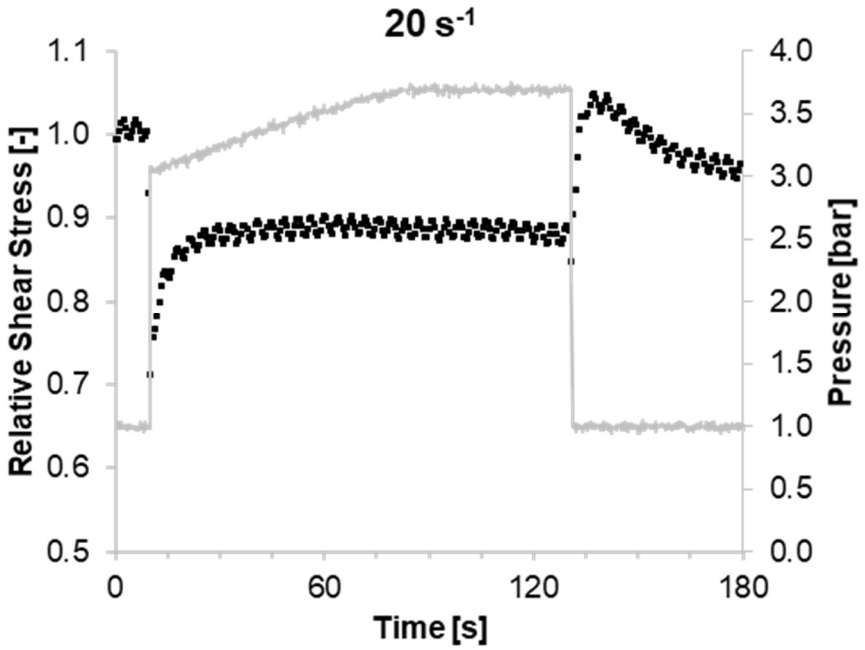

Figure 175. Rate of air dissolution and reappearance at a shear rate of 20 s^{-1} of sample 035A2-F.

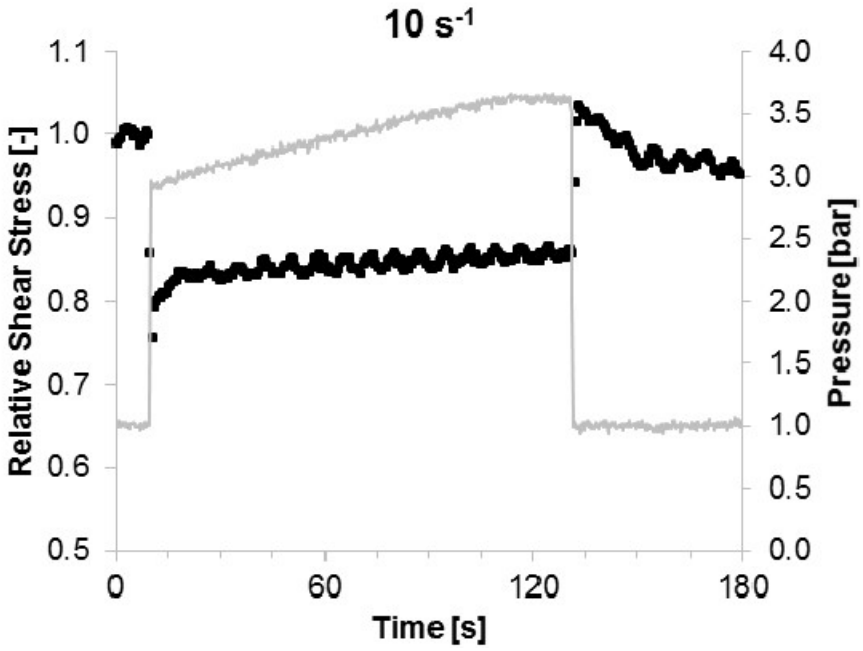

Figure 176. Rate of air dissolution and reappearance at a shear rate of 10 s^{-1} of sample 035A2-F.

From the results in Figure 173 to Figure 176, it can be concluded that air is dissolved almost instantaneously after application of the pressure, regardless of the applied shear rate. However, the evolution over time of rheological properties due to pressure application was different for mixtures 035A1-F and 035A2-F compared to the others (compare Figure 168 and Figure 170), it is believed that bubble size and shear rate will play an important role on air dissolution. This is also clear in Figure 171, as only 035A1-F and 035A2-F showed a sudden decrease in relative shear stress, while all others showed a gradual decrease with time. As mentioned before, smaller air bubbles dissolve more quickly, regardless of the applied shear rate. The larger air bubbles dissolve more slowly, and that process may be influenced by the applied shear rate. An explanation for the recovery of relative shear stress under pressure has not been found yet, but it may be related to the restructuration of the material after the sample volume gets suddenly reduced (vertical flow).

For the mixtures in Figure 173 to Figure 176, the recovery of relative shear stress is immediate after depressurization, and for the low shear rates (20 and 10 s^{-1}), the relative shear stress is fully recovered. At higher shear rates, the relative shear stress is not equal to 1 after depressurization, which may have several causes. This could indicate 1) an immediate air loss, 2) part of the air remains dissolved, or 3) the air-void system coarsens, creating larger air bubbles. The first hypothesis cannot be excluded. The second hypothesis seems unlikely, as at low shear, all air reappears. There are no physical reasons why all air would not reappear at higher shear rate, as on the contrary, increasing the shear rate should accelerate air reappearance. Hypothesis 3 is also possible. For the mixtures with w/c = 0.35, *Ca* starts to be close to 1, especially for the larger bubbles. This means that the deformation behavior of the air bubbles is uncertain. However, as air is assumed to reappear in existing bubbles at depressurization, the average bubble size increases, increasing the average *Ca*. As *Ca* is also proportional to the applied shear rate, increasing the bubble size could yield a lower amount of non-deformable air bubbles at high shear rates (50 and 100 s^{-1}), while this would not be observed at low shear rates (10 and 20 s^{-1}). Furthermore, all samples show a lower relative shear stress at and beyond 30 s after depressurization, indicating that air is escaping from the sample (Figure 169).

To verify the independence of the air dissolution and reappearance from the shear rate, another set of tests were performed using AEA2 listed in Table 28, which is based on a different chemical composition. These experiments were conducted at 100 s^{-1} and 20 s^{-1} on samples prepared with the two mixing protocols

described above. The samples were 035M100-S, 035M100-F, 035M20-S and 035M20-F, the code names are composed by the w/c, a letter to identify the admixture, shear rate applied and mixing protocol. In addition, the pressure cell was equipped with a custom-made profiled bob to minimize the risk of slippage between the sample and the inner cylinder wall. The pair of samples 035M100-S and 035M100-F have significantly different bubble size distributions. Figure 177 shows that the sample 035M100-S required approximately 10 seconds to stabilize itself after the pressure was applied, followed by a light gain of the relative shear stress. When the pressure was released, the maximum recovery of the rheological properties was achieved after 12 seconds and only reestablished up to 91%. On the other hand, the relative shear stress of the sample 035M100-F required only 2 seconds after pressurization to reach equilibrium and about 10 seconds to reach its maximum recovery after the pressure was released (Figure 178).

Table 30 shows that the sample 035M20-S had a finer bubble size distribution than 035M100-S. However, they show a completely different behavior when tested at different shear rates. At 20 s^{-1}, the relative shear stress of the mixture 035M20-S decreased gradually from 1.0 to 0.73 in approximately 150 seconds (Figure 179). After the pressure was released, the sample recovered its rheological properties up to a maximum of 94% in approximately 30 seconds. The sample 035M20-F showed a large data scattering (which is common when the profiled custom-made bob is used at low shear rates), but it is possible to identify a sudden drop on the relative shear stress right after pressure was applied on the system followed by a gradual reduction until it gets stabilized after approximately 90 seconds (Figure 180). Once that atmospheric conditions are reached after releasing the pressure, the relative shear stress is recovered at 94% after approximately 30 seconds. If Figure 177 and Figure 179 are compared, the contribution of the shear rate to the dissolution and reappearance of air in cement paste becomes evident. In this set of experiments, the dissolution of air bubbles in its surrounding water is enhanced greatly enhanced by the shear rate. The same is true for the samples 035M100-F and 035M20-F, although it is still a mystery why sometimes the relative shear stress increases during the pressurization step.

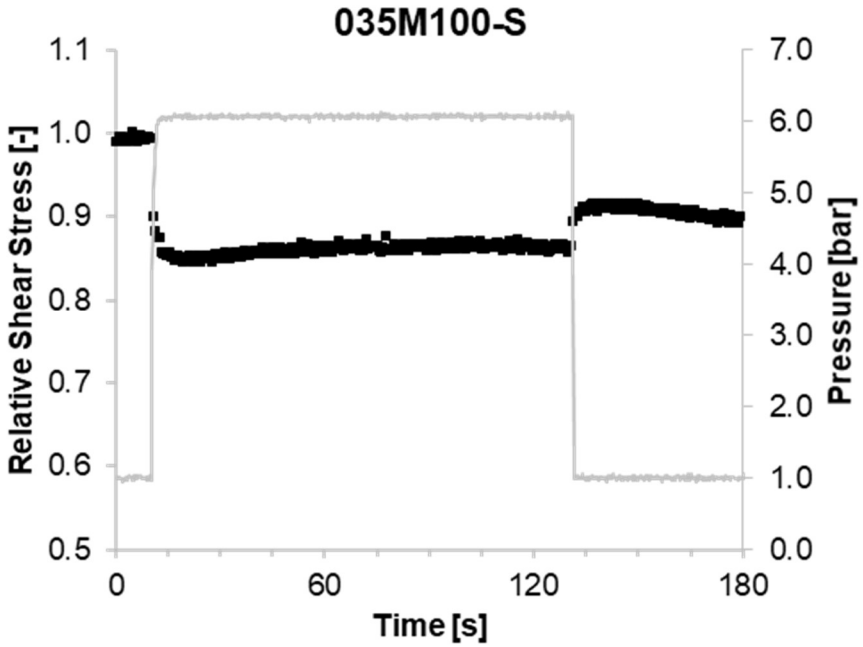

Figure 177. Rate of air dissolution and reappearance at a shear rate of 100 s^{-1} of sample 035M100-S.

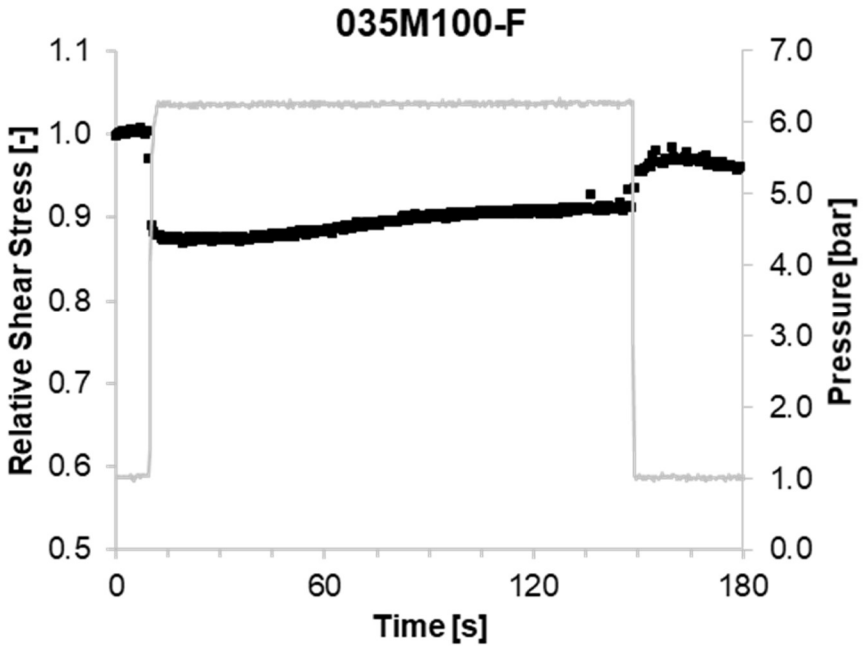

Figure 178. Rate of air dissolution and reappearance at a shear rate of 100 s^{-1} of sample 035M100-F.

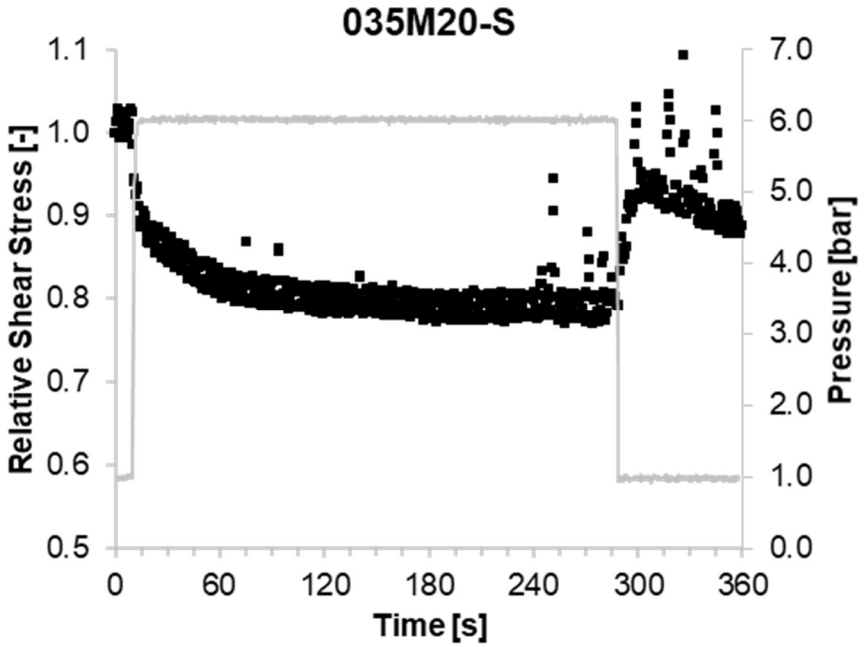

Figure 179. Rate of air dissolution and reappearance at a shear rate of 20 s^{-1} of sample 035M20-S.

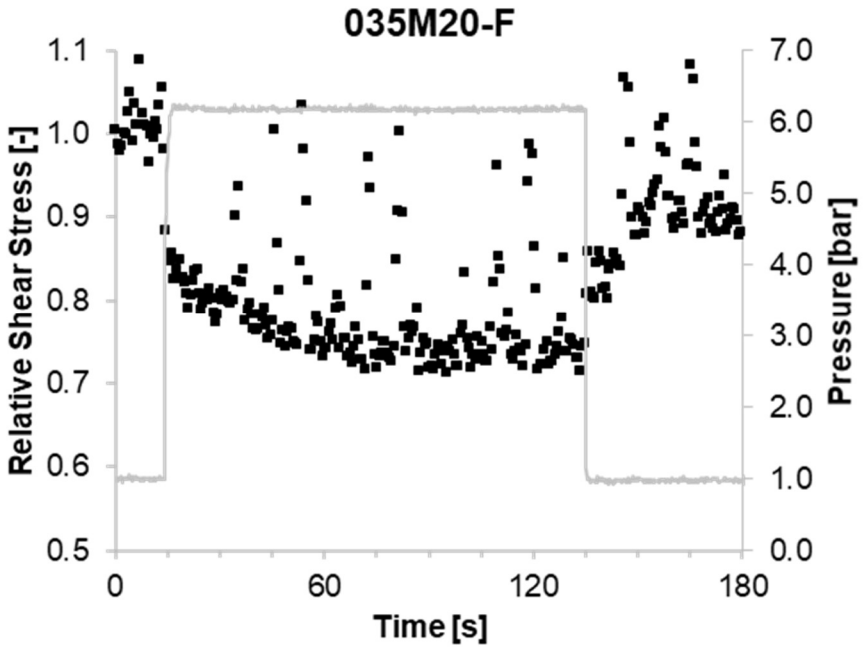

Figure 180. Rate of air dissolution and reappearance at a shear rate of 20 s^{-1} of sample 035M20-F.

6.4 Summary

A first important property to verify when studying the influence of air on the rheological properties of cement pastes is the Capillary number. This number determines whether the bubbles deform or stay spherical under shear, which has a significant consequence of the rheological behavior of the material. For this project, the Ca-number was typically lower than 1, resulting in an increase in rheological properties with increasing air content. When the air is removed, the rheological properties decrease.

The application of pressure leads to an increased capacity of water to carry dissolved air. As such, with each increase in pressure, more air is dissolved and a reduction in apparent viscosity or relative shear stress is observed, until all air is dissolved. The pressure values at which full dissolution is achieved are in the same range as the theoretical values for air dissolution. When the pressure is removed, the air returns almost instantly, and the rheological properties increase. However, the experience indicate that the air is no longer entirely stable and rises to the top surface of the cement paste. A thick foam layer is observed after each experiment, only when pressure was applied.

The experiments also showed a difference in the rate of air dissolution, characterized by the rate of decrease of the rheological properties with time. In case of coarser air void systems, air needs time to dissolve. For finer air void systems, the dissolution is almost instantaneous. This can be argued by the partial pressure inside the air bubbles, which is higher for smaller bubbles, as well as the increased surface area. Both effects lead to a quicker dissolution of small air bubbles.

Experiments on the sensitivity of the applied shear rate on the dissolution of air show a dependency on the used air-entraining agent. For one AEA, the dissolution rate was unaffected by the applied shear rate. For the evaluated shear rates, the dissolution happened nearly immediately. For a second AEA, the dissolution rate was dependent on the applied shear rate. Hence, it is suspected that dissolution rates are dependent on the used admixtures, the applied pressure and the applied shear rate. Oscillatory tests to investigate the effect of stationary samples were unsuccessful, as the pressure caused a vertical flow of the paste.

Releasing the pressure, regardless of the shear rate applied, resulted in an immediate full or partial recovery of the rheological properties. Higher recoveries of rheological properties when releasing pressure were observed at lower shear rates. Two hypothesis can explain the observations: either the air escapes immediately after releasing the pressure, or bubbles coalesce and result in larger Ca-numbers. If the Ca-number gets close to 1, the deformability of the bubble is uncertain. A third hypothesis, stating that some of the air may remain dissolved in the cement paste seems unlikely, as shear rate should accelerate reappearance of air. However, these measurements do not exclude this behavior for static conditions.

7 Conclusions

7.1 Conclusions of this research project

7.1.1 Investigation of lubrication layer thickness and composition

The lubrication layer formed when concrete flows near a smooth wall should show a concentration gradient of particles with space. This gradient is dependent on the particle size. However, all approaches in literature use a single layer, successfully, to predict pumping pressure and velocity profiles. This research project attempt to use a multilayer approach to discover the thickness and composition of the lubrication layer.

However, two major obstacles were found during this research. A first obstacle was the differences in rheological properties measured by each rheometer. This was addressed by using a reproduction of the NIST reference material in all rheometers, at three different temperatures. However, due to the non-linearity of this material at low shear rates, the shear rate ranges in each rheometer were also important. Comparison between the ConTec 5S, ConTec 5W, ConTec 6 and the ICAR rheometer delivered good correlations for plastic viscosity with the Anton Paar MCR 302. However for the yield stress, more inaccuracies were noted with increasing gap size, and for the ICAR, the results did not deliver an adequate interpretation.

The second obstacle observed was the dependency of the rheological properties of the mortar and concrete on the shear rate in the cement paste. Specific procedures were developed to minimize the influence of aggregate on the reference state of the paste during mixing and measurements.

Krieger-Dougherty style equations were used to determine the influence of volume fraction and maximum particle size of one specific sand on the amplification of yield stress and viscosity of the paste. The employed procedures attempted to minimize the impact of the shear rate inside the paste in the mortar on the rheological properties. From the results, it is seen that φ_m and φ_{max} decrease with decreasing maximum particle size due to a decrease in size variation. The intrinsic viscosities for both the yield stress and viscosity equations increased with decreasing maximum particle size, and the curve fits showed it was better to assign different values to intrinsic viscosity for the yield stress and viscosity equations. φ_m was approximately 85-90% of φ_{max}.

The derived amplification equations for yield stress and viscosity allowed to estimate the rheological properties of different mortars with different volume fractions and maximum particle sizes. Combined with the measured paste and concrete rheology, the results from an interface rheometer test could now be reproduced. The developed strategy considered six layers between the inner cylinder and the bulk concrete in the interface layer, each with increasing particle size. Theoretical calculations of the rotational velocity difference in each layer could be performed based on applied torque and the known (measured or predicted) rheological properties. By varying the inner and outer radii of each layer, the analytical solution showing the best fit with the experimental data was retained.

For three evaluated concrete mix designs, a solution with a good fit was found for each layer separately, mimicking the single-layer approach. Each solution gave a finite thickness for one layer, with all other layer thicknesses set at zero. The approximation of the experimental results was equally accurate when considering a cement paste layer as a mortar layer with 2.36 mm particles, as well as all layers in between. For the evaluated mixtures, mortar layers with 2.36 mm particles were between 0.5 and 2 mm thick, while cement paste layers between 30 and 130 µm thick delivered similar solutions. The former result is close to what is reported in literature. The latter result makes physically more sense as this is the only case where the maximum particle size is smaller than the layer thickness. However, it can be doubted whether a cement paste layer is the source of the lubrication layer, as it is suspected that the duration of the test is insufficient to cause shear-induced particle migration of the smaller sand particles. Furthermore, this study is sensitive to

many errors, including assessment of the rheological properties, determination of the Krieger-Dougherty-style curves and comparison of the rheometers.

7.1.2 Influence of pumping on fresh concrete properties

18 different concrete mix designs were evaluated by means of full-scale pumping tests. The mix design variations included changes in admixture producers, AEA dosages, and dispersant type and dosages. Pumping tests were performed by varying the flow rate, boom configuration in A or flat shape, the use of a reducer and submerging the hose slightly under the concrete surface. Truck samples were evaluated before, during and after the pumping procedures, and their time evolution serves as a baseline for the analysis of the differences. For each of the properties, the differences between pumped and non-pumped samples were investigated.

For most of the results, a substantial scatter was observed and a general strong increase or decrease in any of the parameters was not observed. Instead, pumping conditions with similar parameters had to be compared to determine which pumping parameter had a strong effect on the evaluated properties.

The changes in slump flow induced by pumping show a large scatter in the results. The values are strongly dependent on the mix design, but no clear distinction between initial workability level, admixture producer or admixture types can be established. Independent of the mix design, on average, the largest magnitude of changes in slump flow were observed when submerging the hose compared to keeping it above the surface. Applying a reducer caused the second largest average change in the magnitude of the change in slump flow. On average, the use of a reducer caused a slightly larger increase in the change in slump flow compared to similar pumping parameters without the reducer. Pumping made the concrete (on average) slightly more fluid. Other parameters, such as changing the flow rate and changing between A and F configuration have a less extensive effect.

For the developed mix designs, the changes in plastic viscosity were between -3 and +3 Pa s, which is too low compared to the accuracy of the rheometer to be able to draw conclusions. However, the change in slope of T versus N in the interface rheometer, named I_{trib}, shed a clearer and more significant picture. I_{trib} can be related to the pressure – flow rate relationship during pumping. The main conclusion when comparing I_{trib} after pumping to the truck samples is a general decrease in the value, indicating that the concrete, with the lubrication layer, has become more fluid. Pumping in A configuration and submerging the hose especially caused a lower I_{trib} due to pumping. The largest sensitivity was observed when changing the flow rate and using a reducer, which is logical as both parameters influence directly the applied shear rate in the concrete.

Sieve stability values were only evaluated for SCC mixtures and most mixtures did not show significant concerns. Only slightly unstable mixtures with sieve stability values between 10 and 15% led to some pumping combinations which could render the mixtures even more unstable.

Concerning the air content, there seems to be a larger sensitivity for the mixtures made with admixtures from producer 1 compared to producer 2. This might be caused by a larger sensitivity of the admixtures, but it might also be due to the selected dosages of admixtures. The pumping configuration (A or F) strongly influences how the air content changes are affected by the flow rate. In A configuration, an increase in flow rate increases the air loss. However, in F configuration, the largest air losses were observed for the lowest flow rates. A strong influence of flow rate in the F configuration was observed. The reason for this difference is currently unknown. Using a reducer or submerging the hose only appears to have a slightly different effect on the change in fresh concrete air content.

Two concrete mixtures were continuously agitated in the truck to avoid segregation. This caused a significant air content increase in the non-pumped samples, but pumping appeared to force this additional air out of the concrete. Hence, agitating concrete to compensate for a too low air content may increase the air in the truck,

but it is not recommended to do this when concrete is pumped, as the pumping procedure may remove all extra air.

Comparing the changes in slump flow, I_{trib} and air content has revealed a correlation between the Δslump flow and $\Delta I_{trib,}$ but no correlation between those two parameters and Δair. This means that the changes in air content do not significantly influence the changes in rheology.

7.1.3 Influence of pumping on hardened concrete properties

The hardened air content showed a good correlation with the fresh concrete air content, with the latter slightly higher than the former. This means that the hypothesis that air may remain dissolved for an extended time after pumping is not valid for the mixtures and conditions evaluated, which is in agreement with the results from the pressurized rheology on cement pastes.

The evolution of compressive strength versus air content was used to detect any potential changes in water content in the aggregates, and thus real w/cm, of the mixtures. Mix designs 5 and 6 appear to have a slightly lower w/cm, while the opposite is expected for mix design 16.

Following a similar procedure as for the fresh concrete properties, the influence of pumping on hardened concrete properties could be established. The spacing factor was determined by means of the Rapid Air 457, omitting all "bubbles" smaller than 30 μm. The changes in spacing factor due to pumping were strongly influenced by the mix design. SCC mixtures with PCE-2 and high air content showed the lowest sensitivity, followed by the HWC mixtures and the SCC mixtures with PCE-2 and low air contents. SCC mixtures with high air content and with PCE1/3 showed a larger influence and the highest sensitivity was found for the mixtures made with PNS. Similarly as explained for the fresh concrete air content, this difference in sensitivity of the admixtures can be attributed to the admixtures themselves, but also to the selected dosages. Detailed studies on air dissolution under pressure should give a clearer picture of the sensitivity of the admixtures. For the HWC mixtures and the SCC mixtures with low air contents, the flow rate seemed to have a large influence on the change in spacing factor, but no uniform trends were observed. Adding a reducer was generally beneficial, but it had a number of exceptions, especially for the mixtures with PNS. Submerging the hose generally did not show a positive effect: either the spacing factor remained constant, or it increased. The difference between A and F configuration was minor in case of mixtures with high air contents, but for the two mixtures with low air contents and with PNS, the A configuration delivered a significantly worse effect.

For freeze-thaw resistance, for the mixtures evaluated in this project with initial air contents above 5.5%, no freeze-thaw concerns were observed. For the other mixtures, there was an increased risk for freeze-thaw damage for pumped and non-pumped samples with a decrease in air content and an increase in w/cm.

Scaling was below the lowest threshold limit if the air content of the mixtures was above 7%. Some mixtures with lower air contents resisted scaling as well, while others showed failure, potentially caused by the pumping procedure. For the mixtures with significant scaling damage, some mixtures showed a significant influence of the flow rate on scaling resistance: mixture 11 with really low air content, mixture 16 with a higher w/cm and mixture 5, the CVC with low air content. Applying a reducer typically showed no effect on scaling, or caused an improvement on the scaling resistance, except for one scenario (mixture 16), when compared to pumping with similar parameter. Submerging the hose either caused no changes in scaling resistance or caused an increase in scaling, compared to not submerging the hose. This is in line with the results on the spacing factor changes, showing that submerging the hose, for the mixtures evaluated, did not provide a beneficial effect on the spacing factor and scaling resistance.

Comparing the changes in scaling to the changes in air content due to pumping delivered no correlation, while a weak correlation was observed between Δscaling and Δspacing factor. This indicates that the

monitoring the change in air content due to pumping is not a good methodology to capture potential durability issues induced by the pumping operation.

Regardless of which concrete property was investigated, these results showed that there is no single factor having a dominant influence. It is rather the additive effect of multiple factors, which were hard to distinguish, which cause the scatter in the data. This research focused on isolating some of these factors to show which factors affect certain properties.

7.1.4 The use of rheology to study the dissolution and reappearance of air under pressure

Rheology was successfully employed to study the dissolution and reappearance of air under pressure in cement pastes. However, to perform this study, the deformability of air bubbles must first be investigated. The Ca-number calculates the ratio of shearing forces to surface tension. For the studied cement paste systems, it was determined that for a majority of the measurements, the bubbles remained un-deformed and therefore caused an increase in rheological properties. The application of pressure, causing a decrease in the amount air in the paste, resulted in a decrease in apparent viscosity of the samples.

With each application of additional pressure, a new decrease, gradual or instantaneous, of apparent viscosity (or relative shear stress) was noted. This occurred up to a certain critical pressure below which no further changes were observed with increases in pressure. As such, at this critical pressure, all air is assumed to be dissolved. This critical pressure is dependent on the mix design, mainly the quantities of air and water, and correspond relatively well with the theoretical values for full air dissolution. In this work, full dissolution was observed roughly between 7 and 13 bar, but these pressure values are expected to be substantially higher for concrete due to the higher air to water ratio.

The change of relative shear stress with time under pressure showed two distinct evolutions. It was either a gradual change or an abrupt change. It is assumed that the way the relative shear stress changes is connected to how quickly the air dissolves. For the mixtures with a finer air void system measured by the AVA 3000, the change in relative shear stress was more instantaneous. For mixtures with a coarser air void system, it was more gradual. Finer air bubbles have more surface area and a higher partial pressure compared to coarser air bubbles, making them more susceptible to quick dissolution.

The effect of the applied shear rate on the dissolution rate of air appeared to be dependent on the chosen air-entraining agent. For one AEA, the change in relative shear stress was instantaneous regardless of which shear rate was applied. However, for another AEA, the change was more gradual at the lower shear rate compared to the higher shear rate. This shows that the dissolution rate of air in cement paste is dependent on the chosen admixtures, the applied pressure and the applied shear rate. Oscillatory measurements, to evaluate the dissolution of air at rest, did not deliver adequate results due to a vertical flow of the sample during pressurizing.

Removing the pressure caused almost instantaneous recovery of rheological properties, although some measurements did not show a full recovery. Observations on the samples after measuring revealed a thick foam on top of the sample, but only when it was pressurized. It is assumed that during depressurizing, the dissolved air is immediately regenerated, but most likely, not all air appears back in the original air bubbles. It can be questioned whether air bubble size increases (this is likely), and whether the AEA still has a stabilizing function (this may be reduced). It appears that large air quantities rise to the surface after the test due to buoyancy. However, it should be kept in mind that all measurements were performed in dynamic conditions and that applying a shear rate should accelerate reappearance of air.

The incomplete recovery of the rheological properties after depressurizing can be attributed to either an immediate air loss (vertical movement), or to bubble coalescence. Larger bubbles are more prone to deformation under shear, and it cannot be excluded that new air bubbles with Ca-numbers close to 1 are formed. In this case, their effect on rheology is uncertain. The hypothesis that air remains dissolved in the

water after depressurizing seems unlikely, as the incomplete recovery of rheology was more pronounced at high shear rates than at low shear rates. High shear rates should lead to equal or faster reappearance of air.

7.2 Future research

7.2.1 Shear-dependency of mortar and concrete

One of the main obstacles observed in this project is the shear-dependency of mortar and concrete. To be more precise, it is the dependency of the rheological properties of the cement paste to the shear rate of the paste inside the mortar or concrete. More research is needed to clarify this phenomenon and its magnitude to be able to fully understand the rheology and processing of cement-based materials.

7.2.2 Lubrication layer thickness and composition

The developed approach to determine the lubrication layer thickness and composition did not deliver the expected results. The obtained thickness ranges for mortars with 2 mm particle sizes were in the range of the literature, but a cement paste layer could have caused the same solution. A better understanding of the lubrication layer formation, thickness and composition will need to be achieved through a fundamental study on shear-induced particle migration. According to the research team, this is the only feasible strategy to fully discover the exact physical processes during pumping of concrete, and to a lesser extent the flow of concrete near a smooth wall (concrete truck chute or formwork). Only by fully understanding this process will the research community be able to predict pumping pressure, changes in rheology during pumping and changes in the air void system due to pumping.

7.2.3 Effect of pumping on fresh and hardened properties

As mentioned before, a large scatter was generally observed in the results, and only the more direct analyses procedures have revealed some of the stronger influence of pumping on the properties. It shows that the pumping procedure has a very variable influence and the combination of all parameters may lead to some complex results, dependent on which factor or combination of factors is dominant.

Concerning the workability, the research team will investigate how the climatic conditions influence the changes in fresh properties. Temperature may have an effect, as tests were performed over a period of a year and a half, including outside temperatures between 5 to 30°C. Similarly, any precipitation during the days before the experiments may be investigated to see if the degree of saturation of the aggregates may have had an influence.

For the air content and the spacing factor, the influence of some factors is totally opposite dependent on the mix design or pumping configuration. These effects need to be clarified, but most likely a more theoretical investigation would be needed, as described in the section below. The influence of other admixtures or admixture combinations, other SCMs, or a different mix design also needs to be investigated.

7.2.4 Pressurized rheology as a tool to understand air changes during pumping

Suggestions for future research on the pressurized rheology include a more detailed characterization of the air dissolution rate as a function of chosen mix design, admixtures and admixture combinations, applied pressure and shear rate. It is believed that pressurized rheology is the tool which will enable researchers to distinguish between the scatter in the pumping results. Air has only a limited time to get dissolved during the pumping process. As the air reappears after each pressure release, the pumping stroke time is a critical factor in how much air can be dissolved, especially if the process is gradual. Generating this knowledge, which will be material dependent, should explain why sometimes a lower flow rate gives a worse air void system compared to a higher flow rate. Despite the higher pressure in the latter case, the air has more time to dissolve at low flow rate (30-45 s), compared to the high flow rate (5-10 s). The applied pressure, influenced by flow rate, boom length, boom diameter or the application of a reducer, will determine how much air can be

dissolved. The time between pressure shocks, combined with the shear rate in the concrete will regulate if maximum air dissolution capacity can be achieved. As a consequence, the influence of pumping on the air-void system of concrete is a complex interaction between flow rate, pipe characteristics, admixture types and sources, the rheological properties of the concrete and the thickness and properties of the lubrication layer.

Acknowledgments

The research team would like to acknowledge all parties involved in this project: The RE-CAST UTC and the ACI CRC for the financial support of the project, as well as Kansas State University, EllisDon and Votorantim Cimentos (CBM-St-Marys) for their in-kind contributions. This work would also not have been possible without the help of many individuals, including all graduate students involved in this project: Daniel Galvez Moreno, Alexis Salinas and Alexandra Wehar, all undergraduate research students: Ana Messmer, Matthew Jokerst, Matthew Giacobbe, and Emily Hutcheson, as well as other graduate students from the research groups: Aida Margarita Ley Hernandez, Piyush Lunkad and Jan Vosahlik. The work of the technical staff from the Civil, Architectural and Environmental Engineering Department (John Bullock and Greg Leckrone), and from the Center of Engineering Infrastructure Studies (Jason Cox) at Missouri S&T cannot be under-estimated. This work would also not have been possible without the volunteering help of many other graduate and undergraduate students: Andrew Bryde, Shane Burkdoll, Rebecca Herndon, Emmanuel Botchway, TJ Daniels, Dakota Guthrie, Chris Moore, Nikkolas Edgmond, Bryce Tafolla, Kyle Krull, Casey Hecht, Nicholas Colbert, Simon Sargon, Matt Hopkins, Sarah Jemison, Scott Grier, and Diane Murph. We would like to thank the admixture producers for the technical assistance on the selection of the types and dosages of the admixtures and for their generosity in supplying the products. Last but not least, we would like to thank Rolla Ready Mix for preparing the concrete to our desires, for the use of the concrete truck on-site and for the use of their premises, and Dynamic Pumping for the pump rental and the adjustment of pumping parameters to our demands.

References

[1] K. Riding, J. Vosahlik, D. Feys, T. Malone and W. Lindquist, "Best practices for concrete pumping (No. K-TRAN: KSU-14-2)," Kansas Dept. of Transportation, 2016.

[2] J. Vosahlik, K. Riding, D. Feys, W. Lindquist, L. Keller, S. Van Zetten and B. Schulz, "Concrete pumping and its effect on the air void system," *Materials and Structures,* vol. 51, no. 4, p. 94, 2018.

[3] D. Feys, Interactions between rheological properties and pumping of self-compacting concrete, Ph-D thesis, Ghent University, 2009.

[4] D. Feys, G. De Schutter, K. Khayat and R. Verhoeven, "Changes in rheology of self-consolidating concrete induced by pumping," *Materials and Structures,* vol. 49, no. 11, pp. 4657-4677, 2016.

[5] ACI CT-13, "ACI Concrete Terminology," p. 32, 2013.

[6] H. Okamura and M. Ouchi, "Self-Compacting Concrete," vol. 1, no. 1, pp. 5-15, 2003.

[7] H. El-Chabib and M. Nehdi, "Effect of mixture design parameters on segregation of self-consolidating concrete," *ACI Materials Journal,* vol. 103, no. 5, pp. 374-383, 2006.

[8] M. L. KOSMATKA, Steven H.; WILSON, Design and Control of Concrete Mixtures – The Guide to Applications, Methods and Materials., 2011.

[9] J. A. Daczko, Self-Consolidating Concrete - Applying what we know, New York, NY: Spon Press, 2012, p. 305.

[10] ERMCO, "The European Guidelines for Self-Compacting Concrete," no. May, 2005.

[11] J. e. De Vicente, Rheology, Rijeka, Croatia: InTech, 2012.

[12] O. H. Wallevik and J. E. Wallevik, "Rheology as a tool in concrete science: The use of rheographs and workability boxes," *Cement and Concrete Research,* vol. 41, no. 12, pp. 1279-1288, 2011.

[13] V. A. Hackley and C. F. Ferraris, "The use of nomenclature in dispersion science and technology," *NIST Special Publication,* vol. 960, p. 76, 2001.

[14] I. Newton, Principia mathematica, London, England, 1687.

[15] O. H. Wallevik, D. Feys, J. E. Wallevik and K. H. Khayat, "Avoiding inaccurate interpretations of rheological measurements for cement-based materials," *Cement and Concrete Research,* vol. 78, pp. 100-109, 2015.

[16] G. H. Tattersall and P. F. G. Banfill, The rheology of fresh concrete, Pitman Advanced publishing program, 1983.

[17] O. H. Wallevik, "Rheology - a scientific approach to develop self-compacting concrete," in *International RILEM Symposium on Self-Compacting Concrete*, Reykjavik, Iceland, 2003.

[18] D. Feys, R. Verhoeven and G. De Schutter, "Fresh self compacting concrete, a shear thickening material," *Cement and Concrete Research,* vol. 38, no. 7, pp. 920-929, 2008.

[19] D. Feys, R. Verhoeven and G. De Schutter, "Why is fresh self-compacting concrete shear thickening?," *Cement and Concrete Research,* vol. 39, no. 6, pp. 510-523, 2009.

[20] A. Yahia and K. H. Khayat, "Analytical models for estimating yield stress of high-performance pseudoplastic grout," *Cement and Concrete Research,* vol. 31, no. 5, pp. 731-738, 2001.

[21] ACI Committee 238, Report on Measurements of Workability and Rheology of Fresh Concrete, 2008, p. 74.

[22] P. Banfill, D. Beaupré, F. Chapdelaine, F. de Larrard, P. Domone, L. Nachbaur, T. Sedran, O. Wallevik and J. Wallevik, "Comparison of concrete rheometers: international tests at LCPC (Nantes, France) in October 2000, NISTIR 6819," p. 157, 2000.

[23] L. E. Brower and C. F. Ferraris, "Comparison of concrete rheometers," *Concrete International,* vol. 25, no. 8, pp. 41-47, 2003.

[24] N. Roussel, G. Ovarlez, S. Garrault and C. Brumaud, "The origins of thixotropy of fresh cement pastes," *Cement and Concrete Research,* vol. 42, no. 1, pp. 148-157, 2012.

[25] F. Mahaut, S. Mokéddem, X. Chateau, N. Roussel and G. Ovarlez, "Effect of coarse particle volume fraction on the yield stress and thixotropy of cementitious materials," *Cement and Concrete Research,* vol. 38, no. 11, pp. 1276-1285, 2008.

[26] J. Wallevik, Rheology of Particle Suspensions - Fresh Concrete, Mortar and Cement Paste with Various Types of Lignosulfonates. Ph-D dissertation, Trondheim: The Norwegian University of Science and Technology, 2003.

[27] L. E. Malvern, "Introduction to the mechanics of continuous medium," p. 723, 1969.

[28] J. E. Wallevick, "Rheology of particle suspension: fresh concrete, mortar and cement paste with various types of lignosulfates," no. 3374, pp. 1-397, 2003.

[29] C. Ferraris, F. Larrard and N. Martys, "Fresh concrete rheology: recent developments," *Materials Science of Concrete,* vol. VI, pp. 215-241, 2001.

[30] D. P. Bentz, C. F. Ferraris, M. A. Galler, A. S. Hansen and J. M. Guynn, "Influence of particle size distributions on yield stress and viscosity of cement-fly ash pastes," *Cement and Concrete Research,* vol. 42, no. 2, pp. 404-409, 2012.

[31] M. R. Geiker, M. Brandl, L. N. Thrane and L. F. Nielsen, "On the effect of coarse aggregate fraction and shape on the rheological properties of self-compacting concrete," *Cement, Concrete and Aggregates,* vol. 24, no. 1, pp. 3-6, 2002.

[32] A. K. Kwan and W. W. Fung, "Packing density measurement and modelling of fine aggregate and mortar," *Cement and Concrete Composites,* vol. 31, no. 6, pp. 349-357, 2009.

[33] A. Einstein, "Eine neue bestimmung der moleküldimensionen," *Annalen der Physik,* vol. 324, no. 2, pp. 289-306, 1906.

[34] A. Einstein, "Berichtigung zu meiner Arbeit:„Eine neue Bestimmung der Moleküldimensionen”," *Annalen der Physik,* vol. 339, no. 3, pp. 591-592, 1911.

[35] G. K. BATCHELOR and J. T. GREEN, "the Determination of the Bulk Stress in a Suspension of Spherical Particles To Order C/Sup 2/.," *Journal of Fluid Mechanics,* vol. 56, no. (DECEMBER 12, 1972), pp. 401-427, 1972.

[36] S. Erdoğan, N. Martys, C. Ferraris and D. Fowler, "Influence of the shape and roughness of inclusions on the rheological properties of a cementitious suspension," *Cement and Concrete Composites,* vol. 30, no. 5, pp. 393-402, 1 5 2008.

[37] J. Yammine, M. Chaouche, M. Guerinet, M. Moranville and N. Roussel, "From ordinary rhelogy concrete to self compacting concrete: A transition between frictional and hydrodynamic interactions," *Cement and Concrete Research,* vol. 38, no. 7, pp. 890-896, 1 7 2008.

[38] I. M. Krieger, "Rheology of monodisperse latices," *Advances in Colloid and Interface Science,* vol. 3, no. 2, pp. 111-136, 1 1 1972.

[39] R. D. Browne and P. B. Bamforth, "Tests to establish concrete pumpability," *ACI Journal,* vol. 74, no. 5, pp. 193-203, 1977.

[40] D. Kaplan, F. de Larrard and T. Sedran, "Design of concrete pumping circuit," *ACI materials journal,* vol. 102, no. 2, p. 110, 2005.

[41] D. Kaplan, F. De Larrard and T. Sedran, "Avoidance of blockages in concrete pumping process," *ACI Materials Journal,* vol. 102, no. 3, pp. 183-191, 2005.

[42] F. Chapdelaine, "Étude fondamentale et pretique sur le pompage du béton," 2007.

[43] T. T. Ngo, E. H. Kadri, R. Bennacer and Cussigh, F., "Use of tribometer to estimate interface friction and concrete boundary layer composition during the fluid concrete pumping," *onstruction and Building Materials,* vol. 24, no. 7, pp. 1253-1261, 2010.

[44] S. Kwon, C. Park, J. Jeong, S. Jo and S. Lee, "Prediction of concrete pumping: Part II-analytical prediction and experimental verification," *ACI Materials Journal,* vol. 110, no. 6, pp. 657-667, 2013.

[45] R. J. Phillips, R. C. Armstrong, R. A. Brown, A. L. Graham and J. R. Abbott, "A constitutive equation for concentrated suspensions that accounts for shear-induced particle migration," *Physics of Fluids A,* vol. 4, no. 1, pp. 30-40, 1992.

[46] D. Feys and K. H. Khayat, "Particle migration during concrete rheometry: How bad is it?," *Materials and Structures,* vol. 50, no. 2, p. 122, 2016.

[47] E. Secrieru, D. Cotardo, V. Mechtcherine, L. Lohaus, C. Schröfl and C. Begemann, "Changes in concrete properties during pumping and formation of lubricating material under pressure," *Cement and Concrete Research,* vol. 108, pp. 129-139, 1 6 2018.

[48] D. Feys, G. De Schutter and R. Verhoeven, "Parameters influencing pressure during pumping of self-compacting concrete," *Materials and Structures,* vol. 46, no. 4, pp. 533-555, 2013.

[49] M. Jolin, D. Burns, B. Bissonnette, F. Gagnon and L.-S. Bolduc, "Understanding the pumpability of concrete," *Shotcrete for Underground Support XI Engineering Conferences International,* pp. 193-207, 2009.

[50] M. Dyer, "An investigation of concrete pumping and effects of pressure on the air void systeme of concrete," 1991.

[51] M. Choi, N. Roussel, Y. Kim and J. Kim, "Lubrication layer properties during concrete pumping," *Cement and Concrete Research,* vol. 45, pp. 69-78, 1 3 2013.

[52] D. Feys, K. H. Khayat and R. Khatib, "How do concrete rheology, tribology, flow rate and pipe radius influence pumping pressure?," *Cement and Concrete Composites,* vol. 66, pp. 38-46, 1 2 2016.

[53] D. A. Whiting and M. A. Nagi, Manual on control of air content in concrete, Portland Cement Assosiation, 1998, pp. 1-52.

[54] P. Mehta and P. J. M. Monteiro, Concrete: Microstructure, Properties, and Materials, McGraw-Hill Education, 2006.

[55] F. Lea, Chemistry of cement and concrete, 4th editio ed., P. C. Hewlett, Ed., Elsevier Science & Technology Books, 2004, p. 1057.

[56] ASTM C457 C457M-16, "Standard Test Method for Microscopical Determination of Parameters of the Air-Void System in Hardened Concrete," *Annual Book of ASTM Standards,* 2016.

[57] M. Pigeon and R. Pleau, Durability of Concrete in Cold Climates, CRC Press, 1995, p. 200.

[58] T. C. Powers and T. F. Willis, "The air requirement of frost-resistant concrete," in *Twenty-Ninth Annual Meeting of the Highway Research Board*, Washington, D.C., 1949.

[59] T. C. Powers and R. A. Helmuth, "Theory of volume changes in hardened Portland-cement paste during freezing," in *Thirty-Second Annual Meeting of the Highway Research Board*, Washington, D.C., 1953.

[60] G. G. Litvan, "Frost action in cement paste," *Matériaux et Construction,* vol. 6, no. 4, pp. 293-298, 1973.

[61] T. C. Powers, "A Working Hypothesis for Further Studies of Frost Resistance of Concrete," *ACI Journal Proceedings,* vol. 41, no. 1.

[62] M. Pigeon and M. Lachance, "Critical Air Void Spacing Factors for Concretes Submitted to Slow Freeze-Thaw Cycles," *ACI Journal Proceedings,* vol. 78, no. 4.

[63] M. Pigeon, J. Marchand and R. Pleau, "Frost resistant concrete," *Construction and Building Materials,* vol. 10, no. 5, pp. 339-348, 1 7 1996.

[64] ACI Committee 318, Building Code Requirements for Structural Concrete, Farmington Hills, MI.: American Concrete Institute, 2014.

[65] J. Vosahlik, K. A. Riding, D. Feys, W. Lindquist, L. Keller, S. Van Zetten and B. Schulz, "Concrete pumping and its effect on the air void system," *Materials and Structures,* vol. 51, no. 4, p. 94, 2018.

[66] K. C. Hover and R. J. Phares, "Impact of Concrete Placing Method on Air Content, Air-Void System Parameters, and Freeze-Thaw Durability," *Transportation Research Record,* vol. 1532, no. 1, pp. 1-8, 1996.

[67] R. Pleau, M. Pigeon, A. Lamontagne and M. Lessard, "Influence of Pumping on Characteristics of Air-Void System of High-Performance Concrete," *Transportation Research Record,* vol. 1478, no. 1, pp. 30-36, 1995.

[68] W. Elkey, D. J. Janssen and K. C. Hover, "Concrete Pumping Effects on Entrained Air-Voids," 1994.

[69] K. Hover, "Investigating effects of concrete handling on air content," *Aberdeen's Concrete Construction,* vol. 40, no. 9, 1995.

[70] M. Lessard, M. Baalbaki and R. C. Aïtcin, "Effect of pumping on air characteristics of conventional concrete," *Transportation Research Record,* no. 1532, pp. 9-14, 1996.

[71] C. Ozyildirim, "Air-Void Characteristics of Concretes in Different Applications," *Transportation Research Record,* vol. 1893, no. 1, pp. 70-74, 2004.

[72] K. J. Folliard, K. Hover, N. Harris and M. T. Ley, "Effects of Texas Fly Ash on Air-Entrainment in Concrete: Comprehensive Report," p. 578, 2009.

[73] ASTM C618-19, "Standard Specification for Coal Fly Ash and Raw or Calcined Natural Pozzolan for Use in Concrete," *Annual Book of ASTM Standards,* pp. 3-6, 2019.

[74] R. L. Hill, S. L. Sarkar, R. F. Rathbone and J. C. Hower, "An examination of fly ash carbon and its interactions with air entraining agent," *Cement and Concrete Research,* vol. 27, no. 2, pp. 193-204, 1 2 1997.

[75] L. Hachmann, A. Burnett, Y.-M. Gao, H. Robert H. and E. M. Suuberg, "Surfactant adsorptivity of solid products from pulverized-coal combustion under controlled conditions," *Symposium (International) on Combustion,* vol. 27, no. 2, pp. 2965-2971, 1 1 1998.

[76] C. Jolicoeur, T. C. To, É. Benoît, R. Hill, Z. Zhang and M. Pagé, "Fly ash-carbon effects on concrete air entrainment: Fundamental studies on their origin and chemical mitigation," *3rd World of Coal Ash, WOCA Conference - Proceedings,* 1 1 2009.

[77] Y.-M. Gao, H.-S. Shim, R. H. Hurt, E. M. Suuberg and N. Y. C. Yang, "Effects of Carbon on Air Entrainment in Fly Ash Concrete: The Role of Soot and Carbon Black," *Energy & Fuels,* vol. 11, no. 2, pp. 457-462, 1 3 1997.

[78] S. H. Gebler and P. Klieger, "Effect of Fly Ash on the Air-Void Stability of Concrete," *ACI Symposium Publication,* vol. 79, pp. 103-124, 1983.

[79] E. Freeman, Y.-M. Gao, R. Hurt and E. Suuberg, "Interactions of carbon-containing fly ash with commercial air-entraining admixtures for concrete," *Fuel,* vol. 76, no. 8, pp. 761-765, 1 6 1997.

[80] J. Yu, I. Külaots, N. Sabanegh, Y. Gao, R. H. Hurt, E. S. Suuberg and A. Mehta, "Adsorptive and Optical Properties of Fly Ash from Coal and Petroleum Coke Co-firing," *Energy & Fuels,* vol. 14, no. 3, pp. 591-596, 1 5 2000.

[81] R. C. Joshi and R. P. Lohtia, Fly ash in concrete: Production, properties and uses, Amsterdam, The Netherlands: Gordon and Breach, 1997, p. 269.

[82] E. Suuberg, I. Kuloats, K. Smith, N. Sabanegh, R. Hurt, W. Lilly and Y. Gao, "Fundamental Study of Low-Nox Combustion Fly Ash Utilization," Morgantown, West Virginia, 1997.

[83] R. L. Hill and K. Folliard, "The Impact of Fly Ash on Air-Entrained Concrete," *Concrete InFocus,* vol. 5, pp. 71-72, 1 1 2006.

[84] P. Aïtcin, "The durability characteristics of high performance concrete: a review," *Cement and Concrete Composites,* vol. 25, no. 4-5, pp. 409-420, 1 5 2003.

[85] M. H. Beygi, M. T. Kazemi, I. M. Nikbin and J. V. Amiri, "The effect of water to cement ratio on fracture parameters and brittleness of self-compacting concrete," *Materials & Design,* vol. 50, pp. 267-276, 1 9 2013.

[86] W. Piasta and B. Zarzycki, "The effect of cement paste volume and w/c ratio on shrinkage strain, water absorption and compressive strength of high performance concrete," *Construction and Building Materials,* vol. 140, pp. 395-402, 1 6 2017.

[87] S. Chitla,, D. Zollinger and R. K. Macha, "Effects on air entrainment on Portland cement concrete," Texas Transportation Institute, 1991.

[88] R. K. Macha, D. G. Zollinger and R. Szecsy, "Examination of Air Entrainment Stability Factors of Pumped Concrete," 1994.

[89] J. J. Valenza and G. W. Scherer, "A review of salt scaling: II. Mechanisms," *Cement and Concrete Research,* vol. 37, no. 7, pp. 1022-1034, 1 7 2007.

[90] R. A. Helmuth, "Discussion of the paper "Frost action in concrete"," in *4th International Congress on Chemistry of Cement*, Washington DC, 1962.

[91] J. J. Beaudoin and C. MacInnis, "The mechanism of frost damage in hardened cement paste," *Cement and Concrete Research,* vol. 4, no. 2, pp. 139-147, 1 3 1974.

[92] A. Rösli and A. B. Harnik, "Improving the durability of concrete to freezing and deicing salts," in *First Internatinal conference*, Ottawa, Canada, 1980.

[93] T. Ye, Z. Suo and A. Evans, "Thin film cracking and the roles of substrate and interface," *International Journal of Solids and Structures,* vol. 29, no. 21, pp. 2639-2648, 1 1 1992.

[94] G. G. Litvan, "Phase Transitions of Adsorbates: VI, Effect of Deicing Agents on the Freezing of Cement Paste," *Journal of the American Ceramic Society,* vol. 58, no. 1-2, pp. 26-30, 1975.

[95] C. MacInnis and J. D. Whiting, "The frost resistance of concrete subjected to a deicing agent," *Cement and Concrete Research,* vol. 9, no. 3, pp. 325-336, 1 5 1979.

[96] E. J. Sellevoid and T. A. Hammer, "Frost Resistance of High-Strength Concrete," *ACI Symposium Publication,* vol. 121, pp. 457-488, 1990.

[97] ,. J. Marchand, M. Pigeon, D. Bager and C. Talbot, "Influence of chloride solution concentration of salt scaling deterioration of concrete," *ACI Materials Journal,* vol. 96, no. 4, pp. 429-435, 1999.

[98] R. Beddoe and M. Setzer, "A low-temperature DSC investigation of hardened cement paste subjected to chloride action," *Cement and Concrete Research,* vol. 18, no. 2, pp. 249-256, 1 3 1988.

[99] J. J. Valenza and G. W. Scherer, "A review of salt scaling: I. Phenomenology," *Cement and Concrete Research,* vol. 37, no. 7, pp. 1007-1021, 1 7 2007.

[100] M. Thomas, B. Green, E. O'Neal, V. Perry, S. Hayman and A. Hossack, "Marine Performance of UHPC at Treat Island," in *HiPerMat, 3rd International Symposium on UHPC and Nanotechnology for High Performance Construction Materials*, Kassel, Germany, 2012.

[101] M. F. Pistilli, "Air-Void Parameters Developed by Air-Entraining Admixtures, as Influenced by Soluble Alkalies from Fly Ash and Portland Cement," *ACI Journal Proceedings,* vol. 80, no. 3, 1983.

[102] C. D. Johnston, "Effects of Microsilica and Class F Fly Ash on Resistance of Concrete to Rapid Freezing and Thawing and Scaling in the Presence of Deicing Agents," *ACI Symposium Publication,* vol. 100, 1987.

[103] K. Rose, B. Hope and A. Ip, "Statistical analysis of strength and durability of concrete made with different cements," *Cement and Concrete Research,* vol. 19, no. 3, pp. 476-486, 1 5 1989.

[104] D. Whiting, "Deicer Scaling Resistance of Lean Concretes Containing Fly Ash," *ACI Symposium Publication,* vol. 114, 1989.

[105] A. B. a. G. G. CaretteI, "Resistance of Condensed Silica Fume Concrete to the Combined Action of Freezing and Thawing Cycling and Deicing Salts," *ACI Symposium Publication,* vol. 114, 1989.

[106] B. Fournier, D. Vezina and M. A. Berube, "Condition Survey of Concrete Structures Built With Potentially Alkali-Reactive Limestone Aggregates from the Quebec City Area (Quebec, Canada)," *ACI Symposium Publication,* vol. 100, 1987.

[107] E. Siebel, "Air-Void Characteristics and Freezing and Thawing Resistance of Superplasticized Air-Entrained Concrete With High Workability," *ACI Symposium Publication,* vol. 119, pp. 297-320, 1989.

[108] J. Yingling, G. M. Mullings and R. D. Gaynor, "Loss of Air Content in Pumped Concrete," *Concrete International,* vol. 14, no. 10, pp. 57-61, 1992.

[109] D. Boulet, R. Pleau, P. Aitcin and M. Lessard, "Influence of Pumping on the Characteristics of the Air-Void System of Concrete," in *Annual Conference of the Canadian Society for Civil Engineering*, 1997.

[110] D. Feys, P. Zacarias, S. Van Zetten, L. Keller, B. Schulz and K. Riding, "Maintaining the Air-Void System during Pumping of Self-Consolidating Concrete: A Challenging Fluid Mechanics Problem!," in *8th Int. RILEM and the 6th North American Conference on Self-consolidating Concrete*, 2016.

[111] D. Feys, N. Roussel, R. Verhoeven and G. De Schutter, "Influence of air bubbles size and volume fraction on rheological properties of fresh self-compacting concrete," *3rd International RILEM Symposium on Rheology of Cement Suspensions Such As Fresh Concrete,* pp. 113-120, 1 1 2009.

[112] D. Feys, G. De Schutter, K. H. Khayat and R. Verhoeven, "Changes in rheology of self-consolidating concrete induced by pumping," *Materials and Structures/Materiaux et Constructions,* vol. 49, no. 11, pp. 4657-4677, 2016.

[113] A. Rust and M. Manga, "Effects of bubble deformation on the viscosity of dilute suspensions," *Journal of Non-Newtonian Fluid Mechanics,* vol. 104, no. 1, pp. 53-63, 20 4 2002.

[114] S. Mueller, E. W. Llewellin and H. M. Mader, "The rheology of suspensions of solid particles," *Proceedings of the Royal Society A: Mathematical, Physical and Engineering Sciences,* vol. 466, no. 2116, pp. 1201-1228, 8 4 2010.

[115] D. Gálvez-Moreno, D. Feys and K. Riding, "Characterization of air dissolution and reappearance under pressure in cement pastes by means of rheology," *Frontiers in Materials,* vol. 6, no. 73, 2019.

[116] L. K. Wang, N. K. Shammas, W. A. Selke and D. B. Aulenbach, "Gas Dissolution, Release, and Bubble Formation in Flotation Systems," in *Handbook of Environmental Engineering*, L. K. Wang, N. K. Shammas, W. A. Selke and D. B. Aulenbach, Eds., Totowa, NJ, Humana Press, 2010, pp. 49-83.

[117] M. Favelukis, Z. Tadmor and Y. Talmon, "Bubble dissolution viscous liquids in simple shear flow," *AIChE Journal,* vol. 41, no. 12, pp. 2637-2641, 1 12 1995.

[118] D. Feys and A. Asghari, "Influence of maximum applied shear rate on the measured rheological properties of flowable cement pastes," *Cement and Concrete Research,* vol. 117, pp. 69-81, 2019.

[119] C. Ferraris, Z. Li, M. Zhang and P. Stutzman, "Development of a reference material for the calibration of cement paste rheometers," *Advances in Civil Engineering Materials,* vol. 2, no. 1, pp. 140-162, 2013.

[120] O. Wallevik, D. Feys, J. Wallevik and K. Khayat, "Avoiding inaccurate interpretations of rheological measurements for cement-based materials," *Cement and Concrete Research,* vol. 78, pp. 100-109, 2015.

[121] A. Leclerc, Elaboration of procedures for testing and consolidation, and mix design of semi-self consolidating concrete for buildings, Sherbrooke: M.Sc. thesis (in French), Université de Sherbrooke., 2011.

[122] EFNARC, "The European Guidelines for Self-Compacting Concrete," 2005.

[123] N. Roussel and P. Coussot, "“Fifty-cent rheometer” for yield stress measurements: From slump to spreading flow," *Journal of Rheology,* vol. 49, pp. 705-718, 2005.

[124] J. Vosahlik, Air void clustering in concrete, PhD thesis, Kansas State University, 2014.

[125] J. Bungey and S. Millard, "Absorption and permeability tests," in *Testing of Concrete in Structures, 3rd edn*, London, Chapman and Hall, 1996.

[126] G. Skripkiūnas, D. Nagrockienė, G. Girskas, M. Vaičienė and E. Baranauskaitė, "The cement type effect on freeze–thaw and deicing salt resistance of concrete," *Procedia Engineering,* vol. 57, pp. 1054-1051, 2013.

[127] M. Glinicki and M. Zielinski, "Frost salt scaling resistance of concrete containing CFBC fly ash," *Materials and Structures,* vol. 42, no. 7, pp. 993-1002, 2009.

[128] K. Riding and B. Bortz, "Effects of Curing and Test Conditions on the Salt Scaling Durability of Fly Ash Concrete," *Advances in Civil Engineering Materials,* vol. 2, no. 1, pp. 551-565, 2013.

[129] C. G. Petersen, "Air void analyzer (AVA) for fresh concrete, latest advances," in *Ninth ACI International Conference on Superplasticizers and Other Chemical Admixtures in Concrete*, Sevilla, Spain, 2009.

[130] J. Szwabowski and B. Lazniewska-Piekarczyk, "Air-entrainment problem in self-compacting concrete," *Journal of Civil Engineering and Management,* vol. 15, no. 2, pp. 137-147, 2009.

Appendix A: Changes in fresh properties due to pumping

This appendix contains all time-plots of fresh properties for non-pumped (black) and pumped (red) samples;

- Section A.1: Slump flow or slump
- Section A.2: Plastic viscosity
- Section A.3: Total flow resistance in interface rheometer
- Section A.4: Sieve stability
- Section A.5: Fresh concrete density
- Section A.6: Fresh concrete air content.

A.1 Slump flow or slump

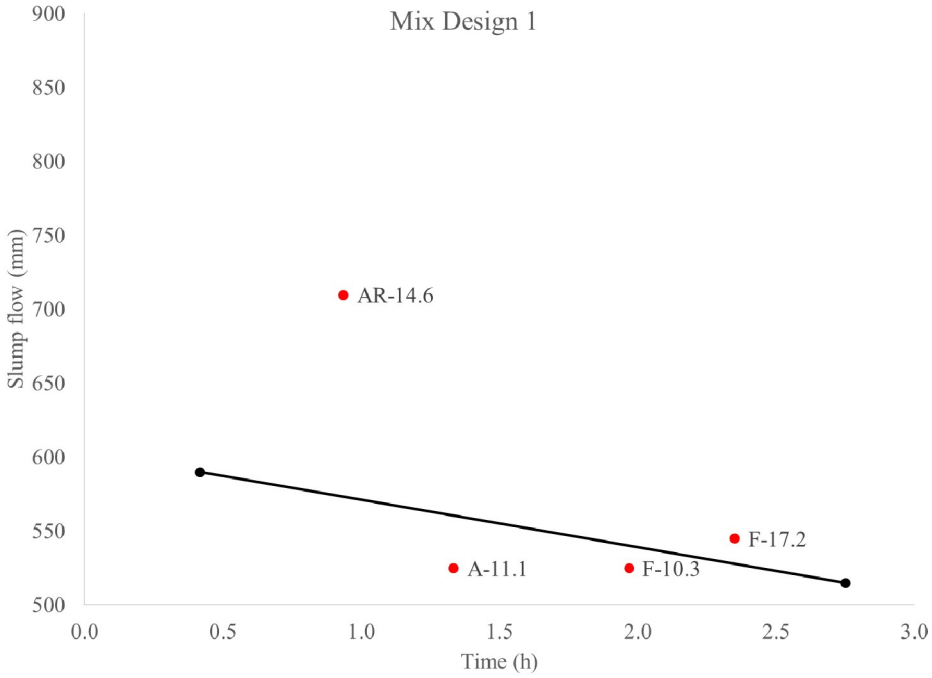

Figure A1.1. Slump flow for non-pumped (black) and pumped (red) samples for mix design 1.

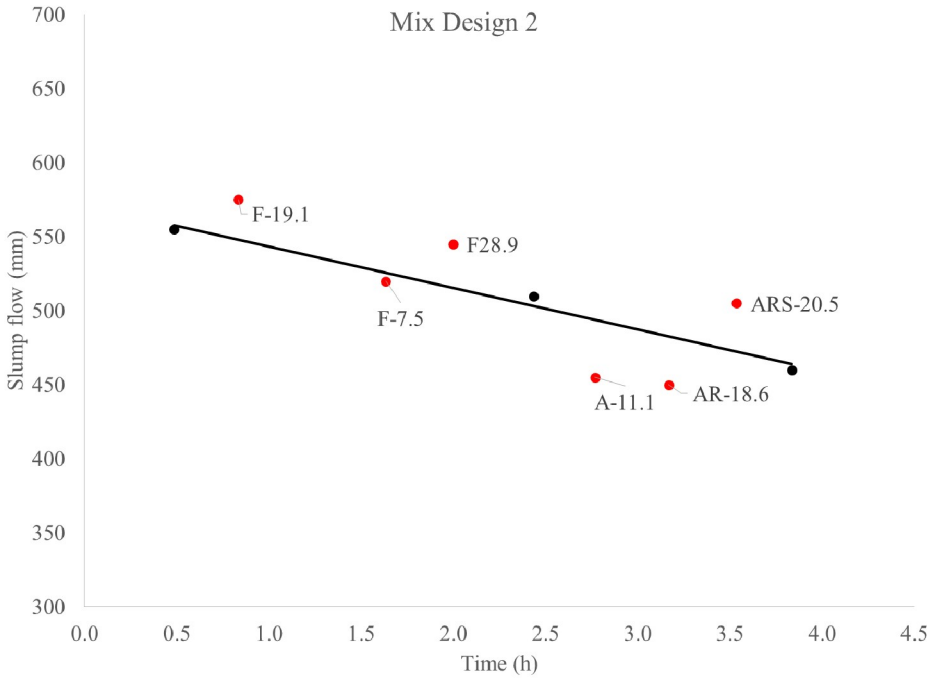

Figure A1.2. Slump flow for non-pumped (black) and pumped (red) samples for mix design 2.

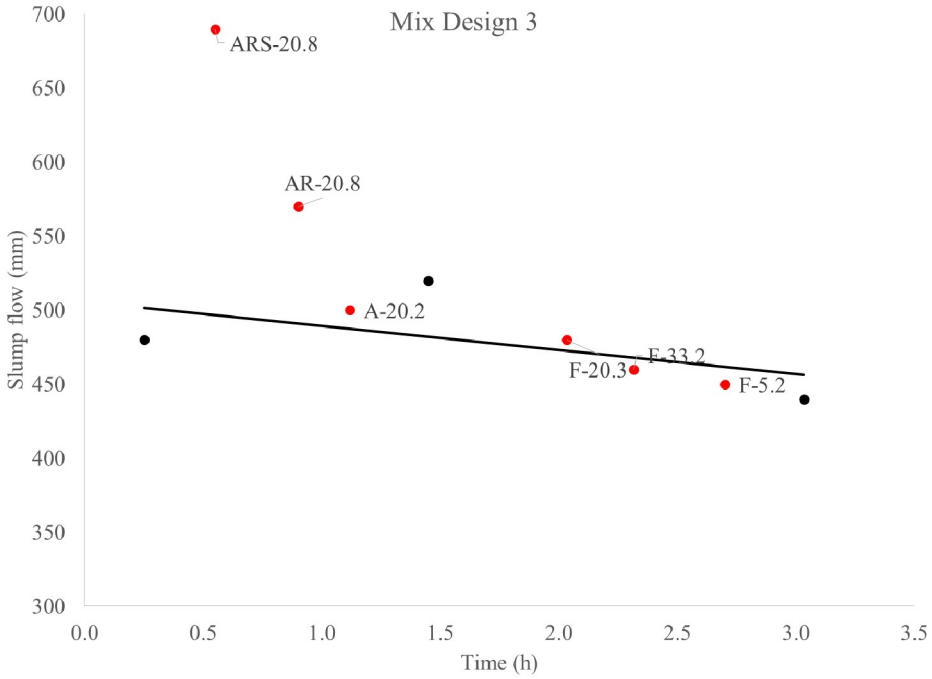

Figure A1.3. Slump flow for non-pumped (black) and pumped (red) samples for mix design 3.

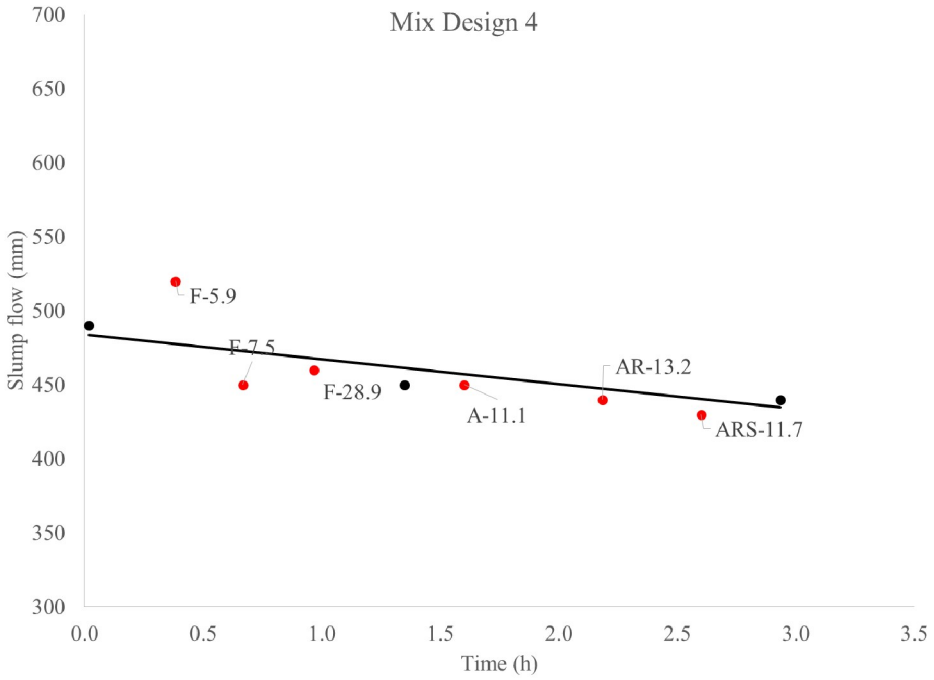

Figure A1.4. Slump flow for non-pumped (black) and pumped (red) samples for mix design 4.

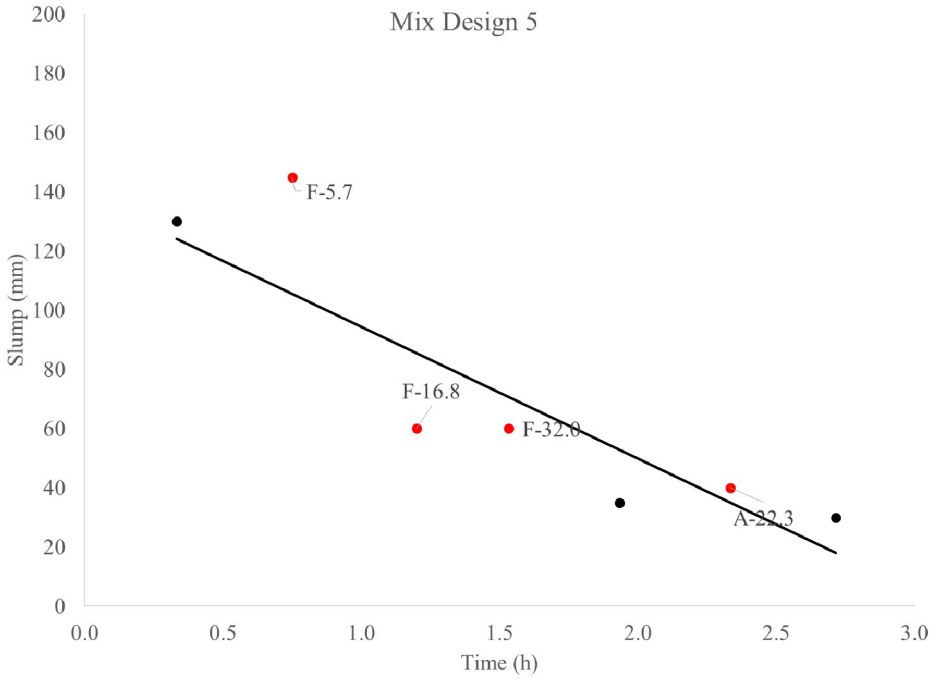

Figure A1.5. Slump for non-pumped (black) and pumped (red) samples for mix design 5.

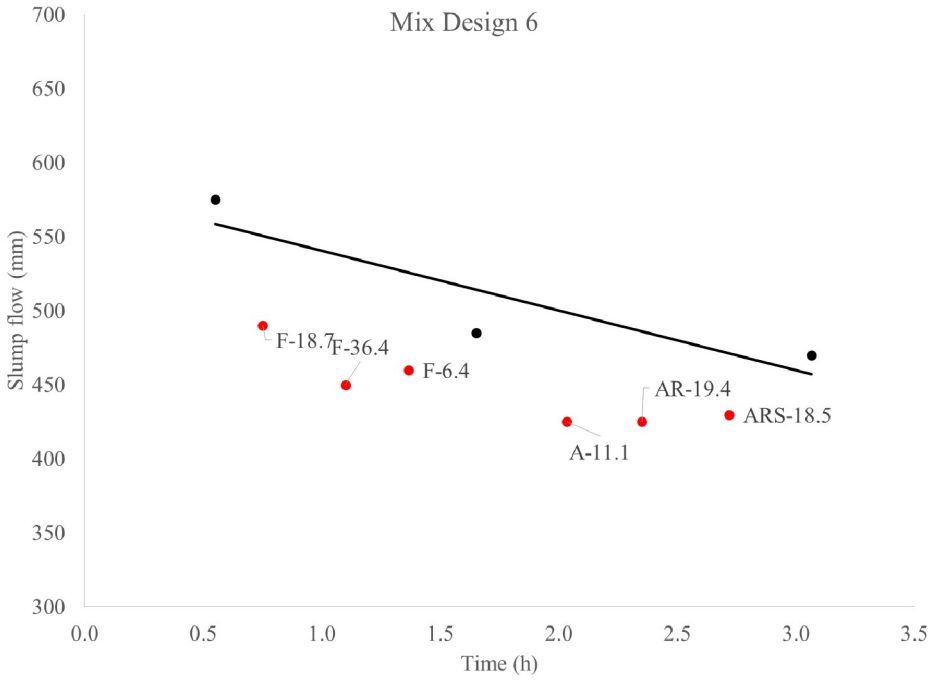

Figure A1.6. Slump flow for non-pumped (black) and pumped (red) samples for mix design 6.

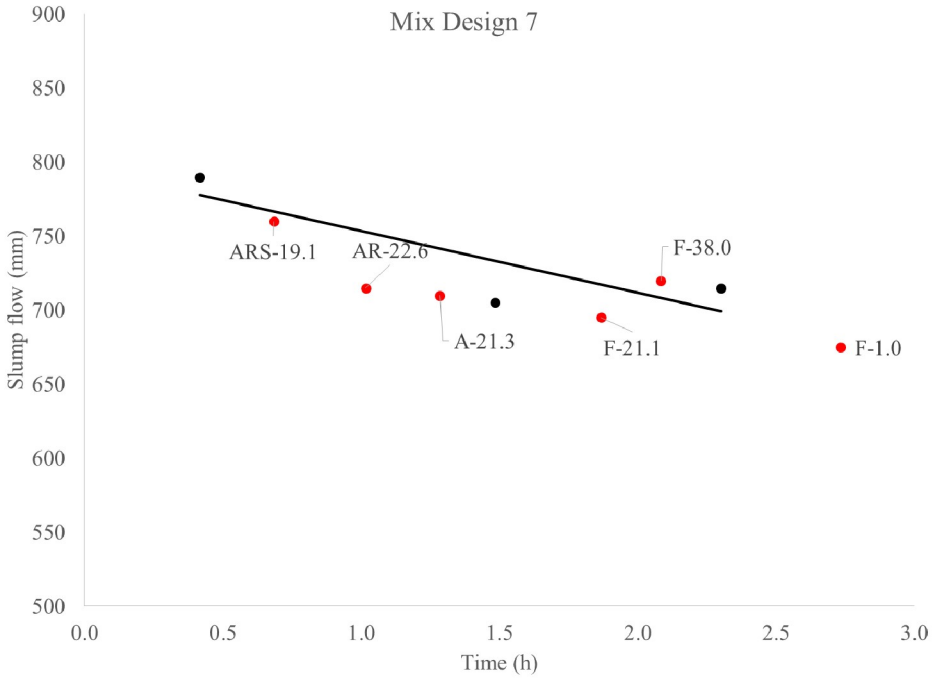

Figure A1.7. Slump flow for non-pumped (black) and pumped (red) samples for mix design 7.

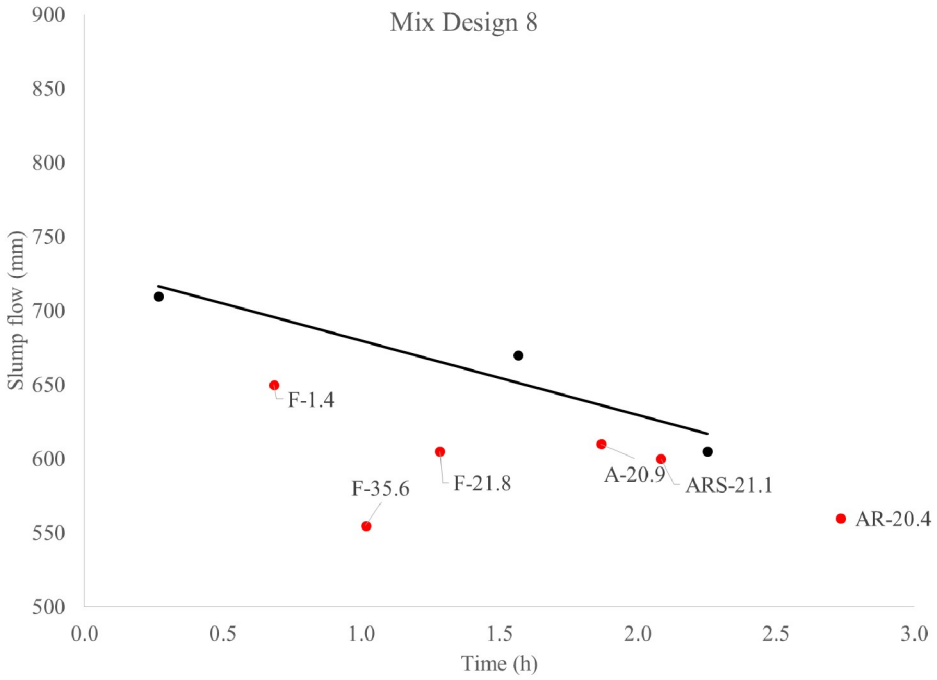

Figure A1.8. Slump flow for non-pumped (black) and pumped (red) samples for mix design 8.

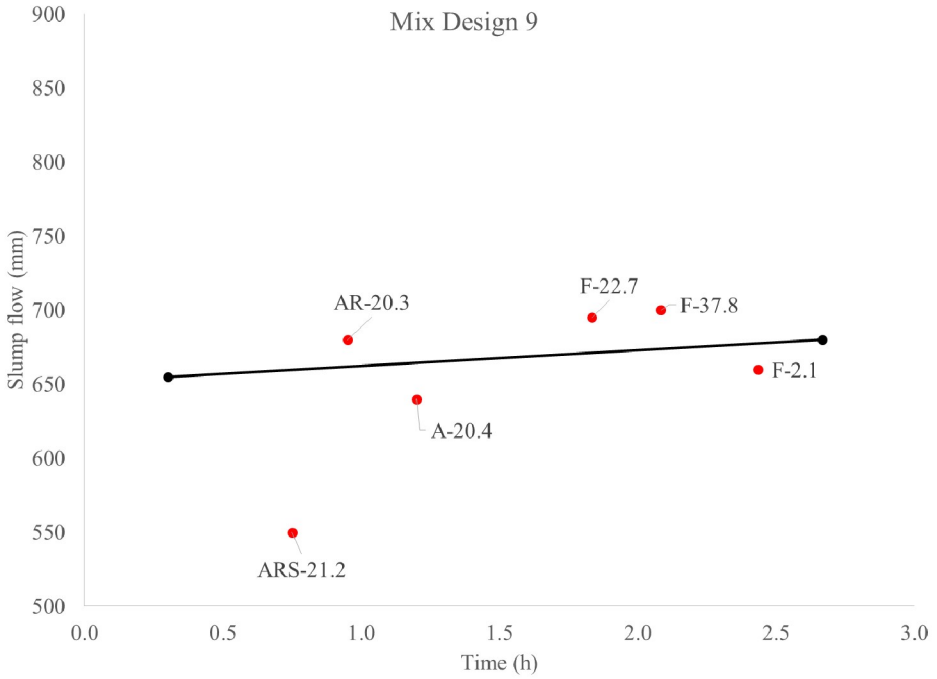

Figure A1.9. Slump flow for non-pumped (black) and pumped (red) samples for mix design 9.

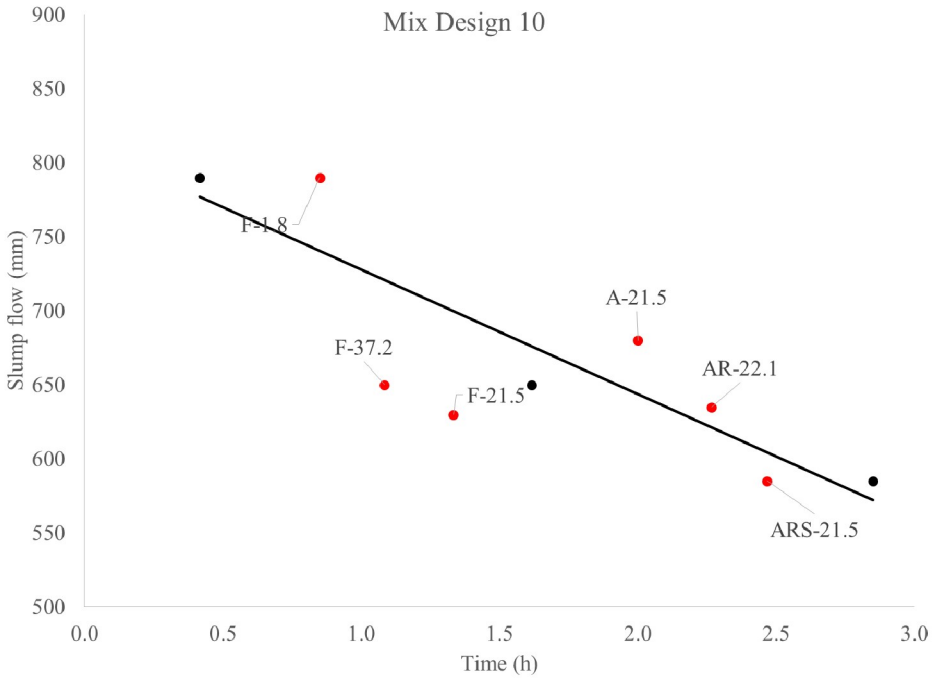

Figure A1.10. Slump flow for non-pumped (black) and pumped (red) samples for mix design 10.

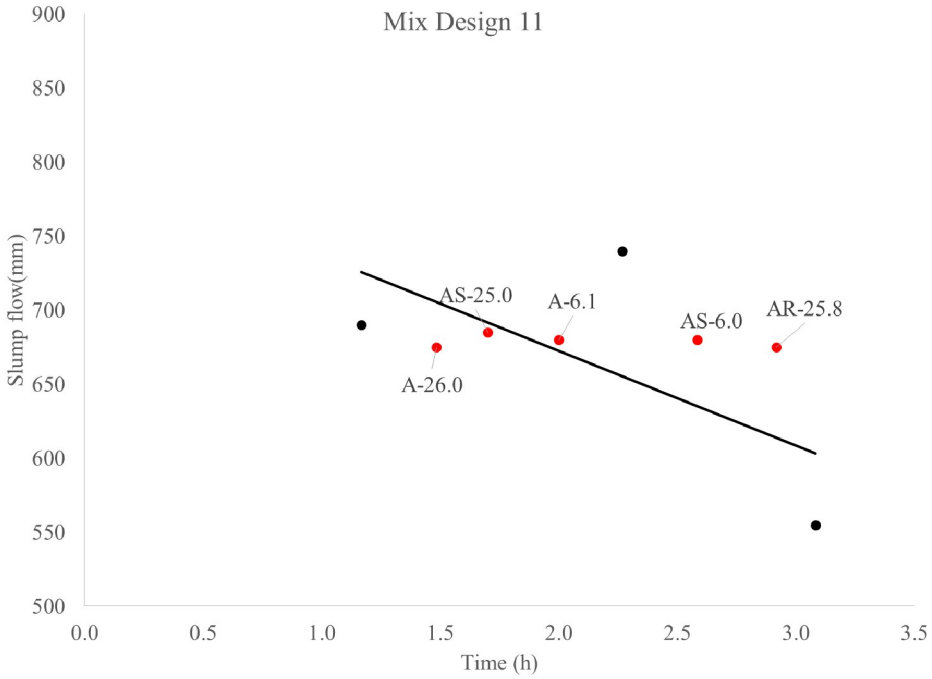

Figure A1.11. Slump flow for non-pumped (black) and pumped (red) samples for mix design 11.

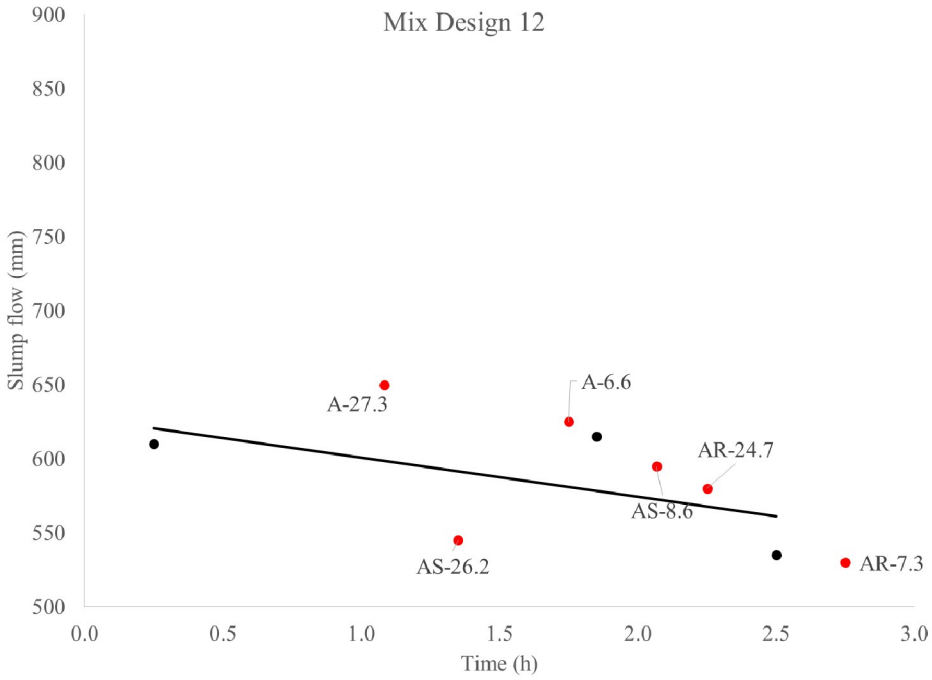

Figure A1.12. Slump flow for non-pumped (black) and pumped (red) samples for mix design 12.

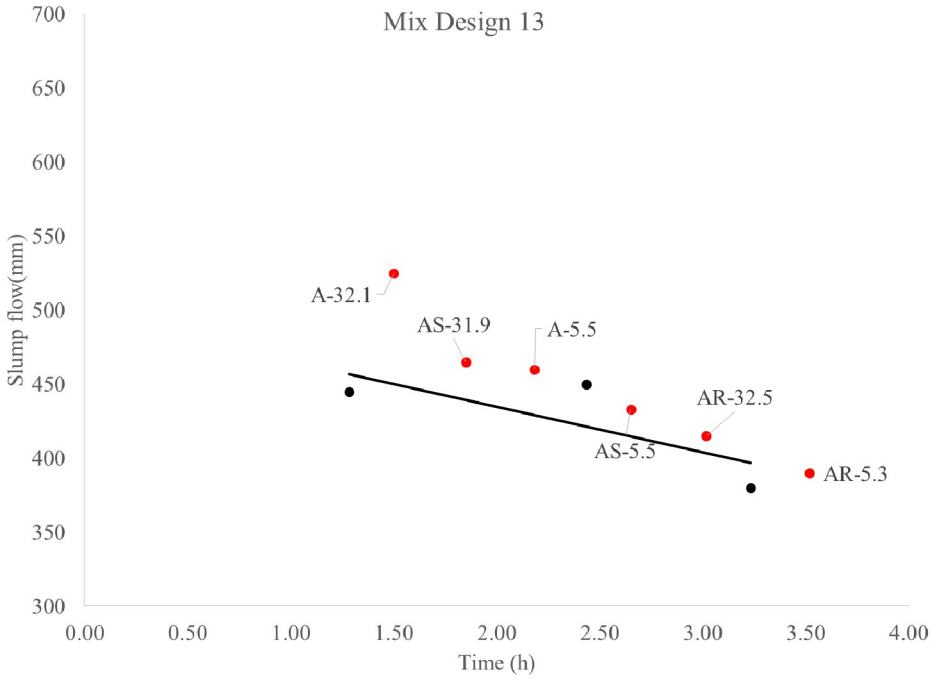

Figure A1.13. Slump flow for non-pumped (black) and pumped (red) samples for mix design 13.

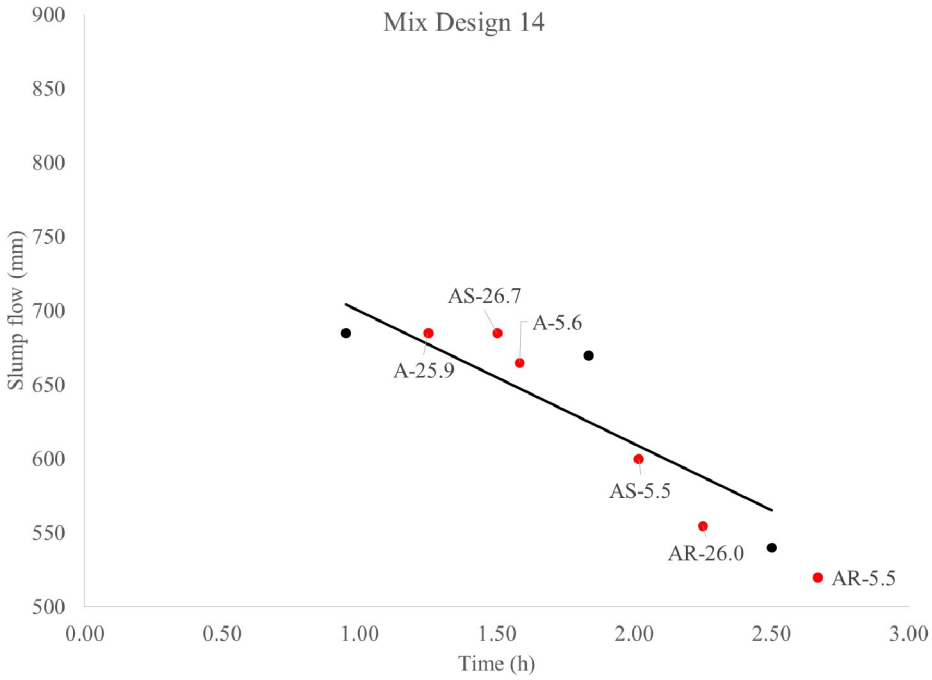

Figure A1.14. Slump flow for non-pumped (black) and pumped (red) samples for mix design 14.

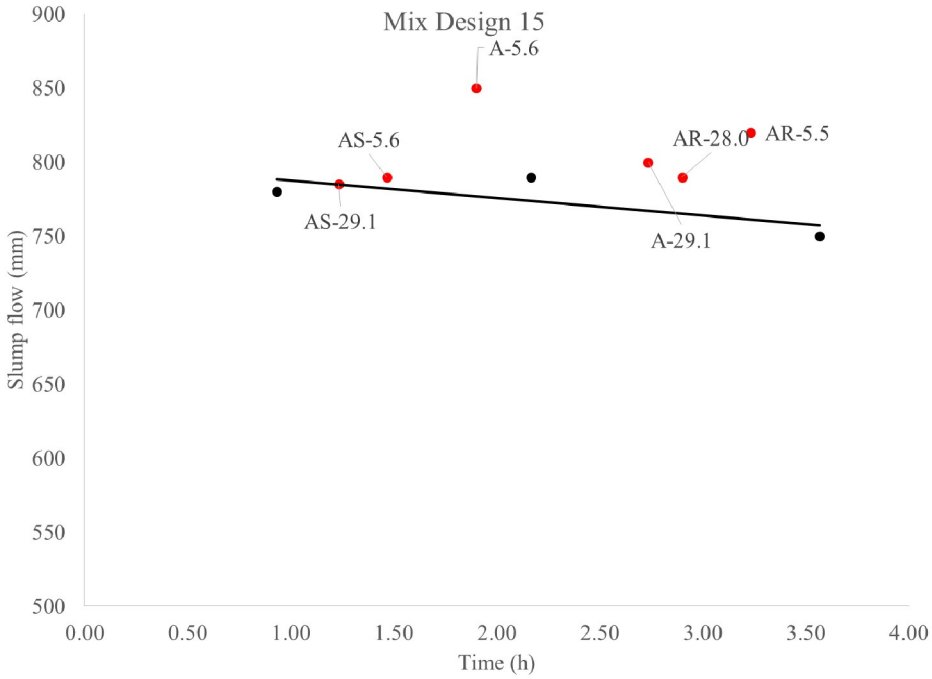

Figure A1.15. Slump flow for non-pumped (black) and pumped (red) samples for mix design 15.

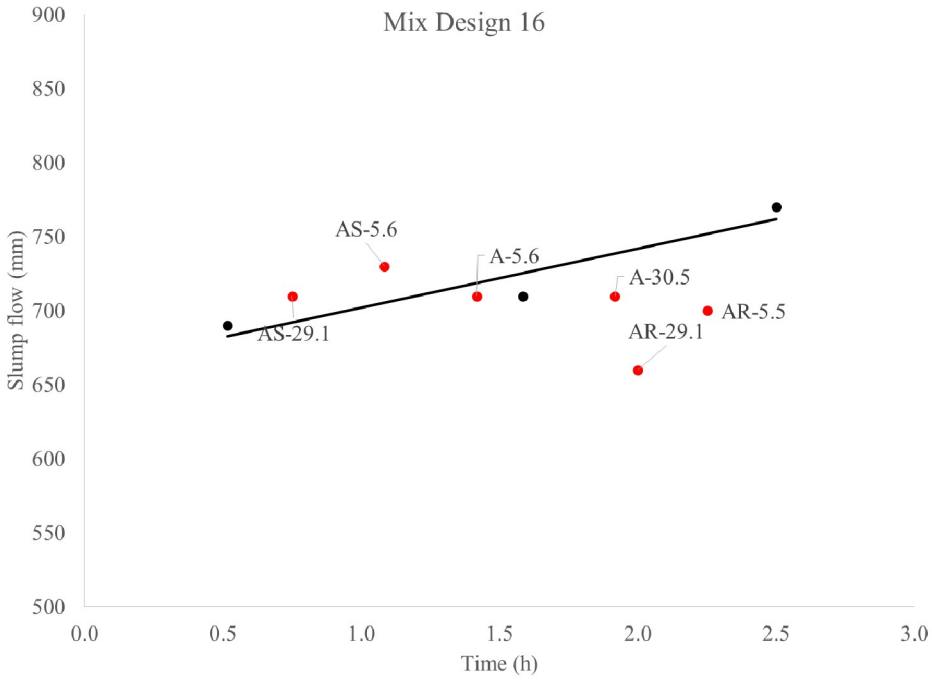

Figure A1.16. Slump flow for non-pumped (black) and pumped (red) samples for mix design 16.

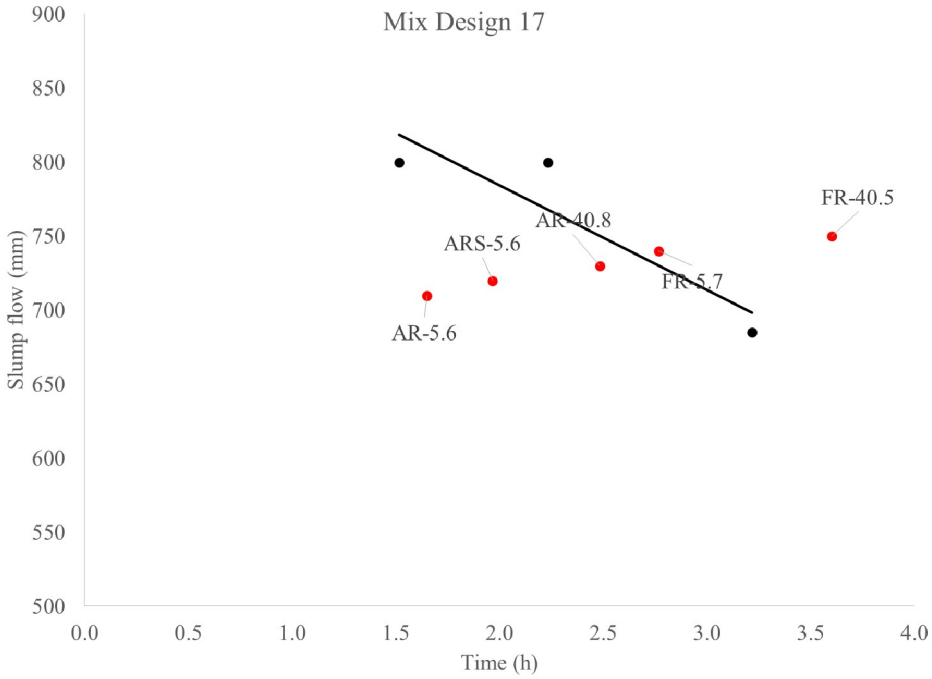

Figure A1.17. Slump flow for non-pumped (black) and pumped (red) samples for mix design 17.

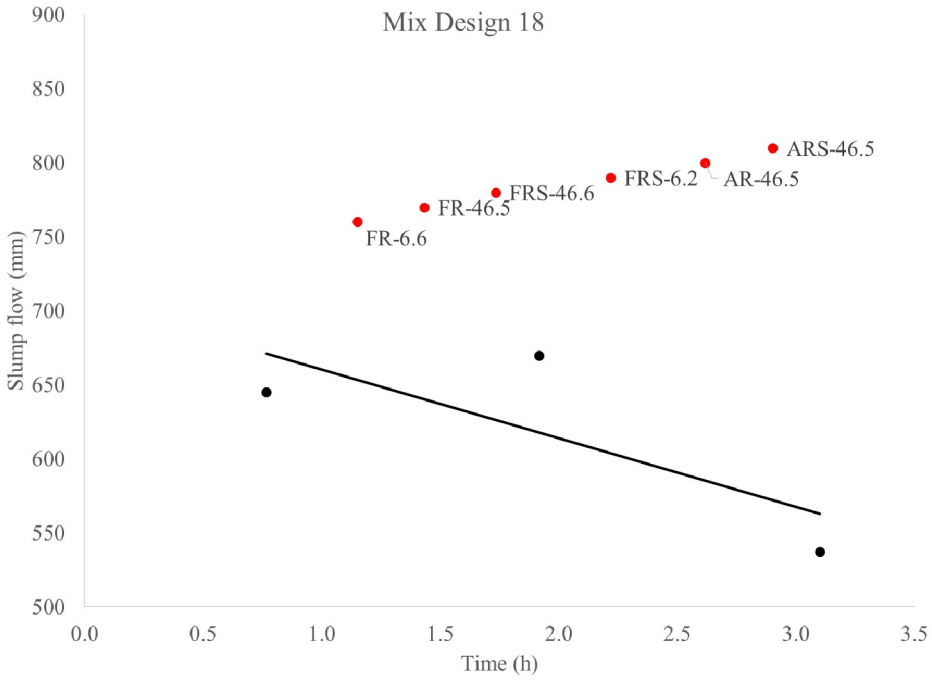

Figure A1.18. Slump flow for non-pumped (black) and pumped (red) samples for mix design 18.

A.2 Plastic Viscosity

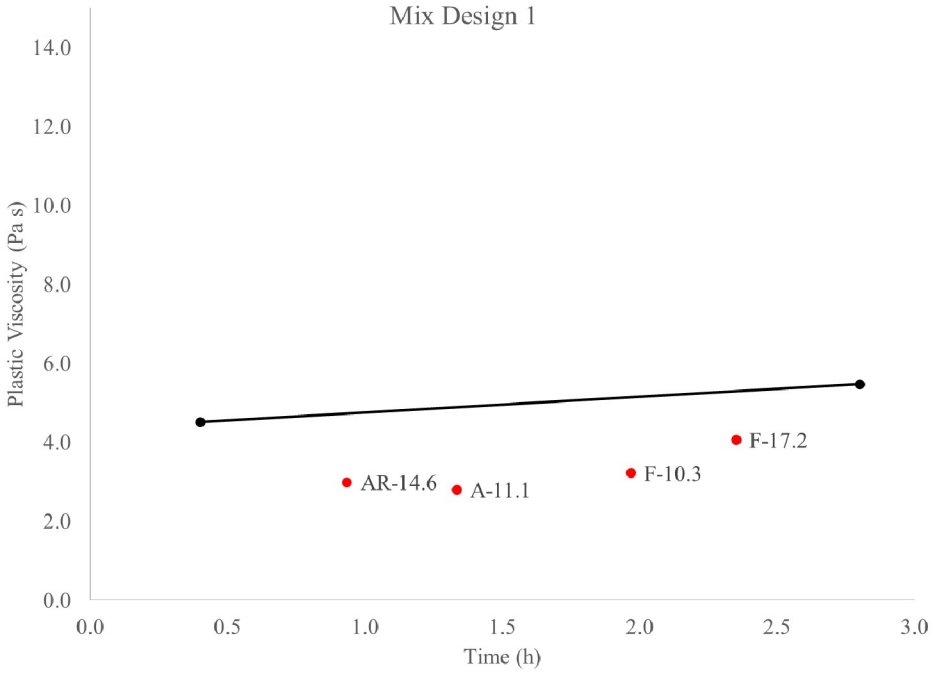

Figure A2.1. Plastic viscosity for non-pumped (black) and pumped (red) samples of mix design 1.

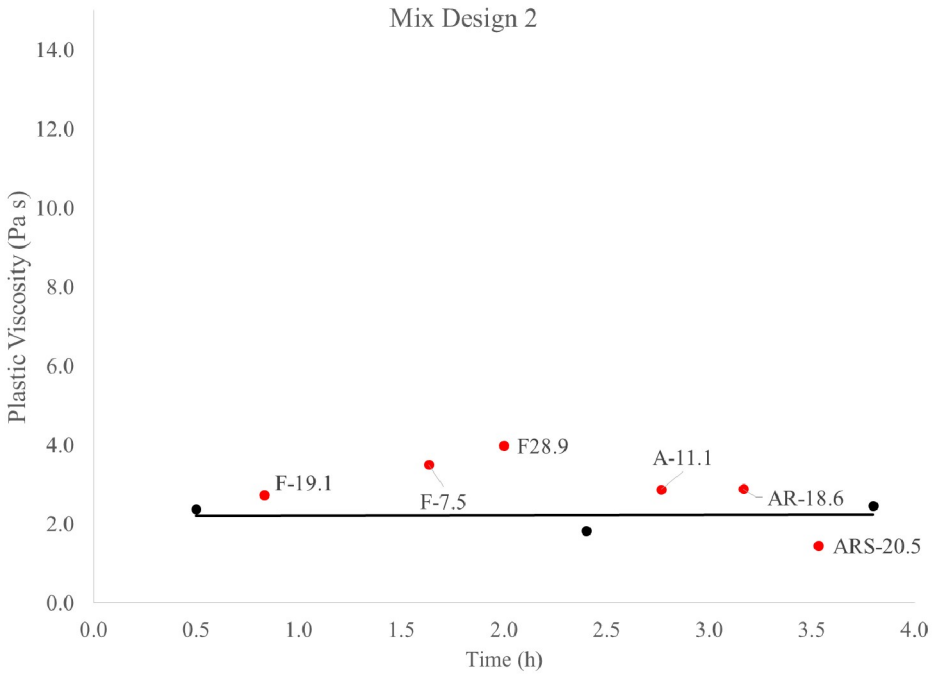

Figure A2.2. Plastic viscosity for non-pumped (black) and pumped (red) samples of mix design 2.

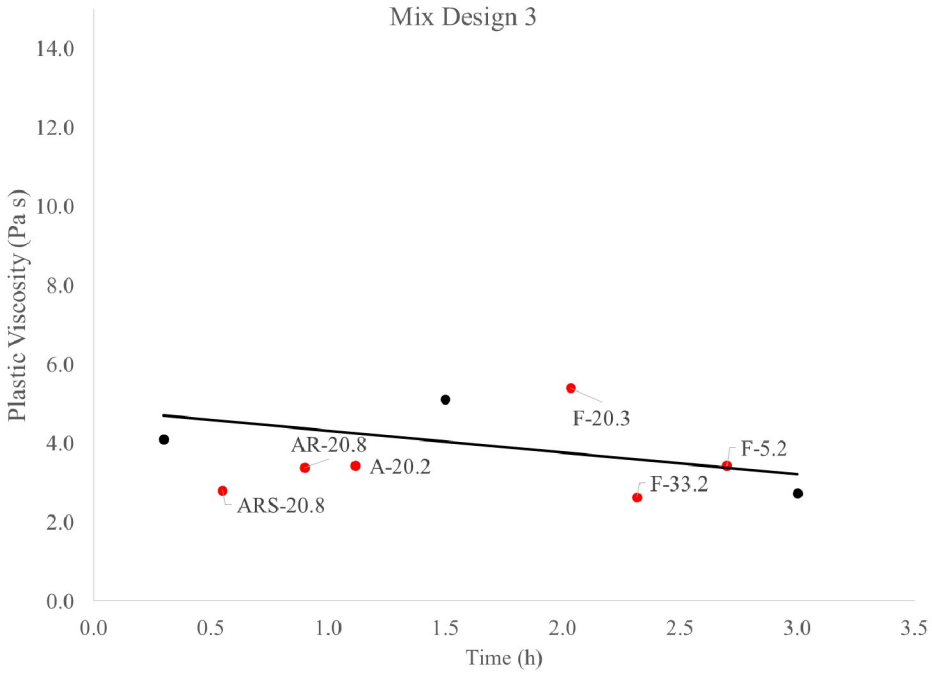

Figure A2.3. Plastic viscosity for non-pumped (black) and pumped (red) samples of mix design 3.

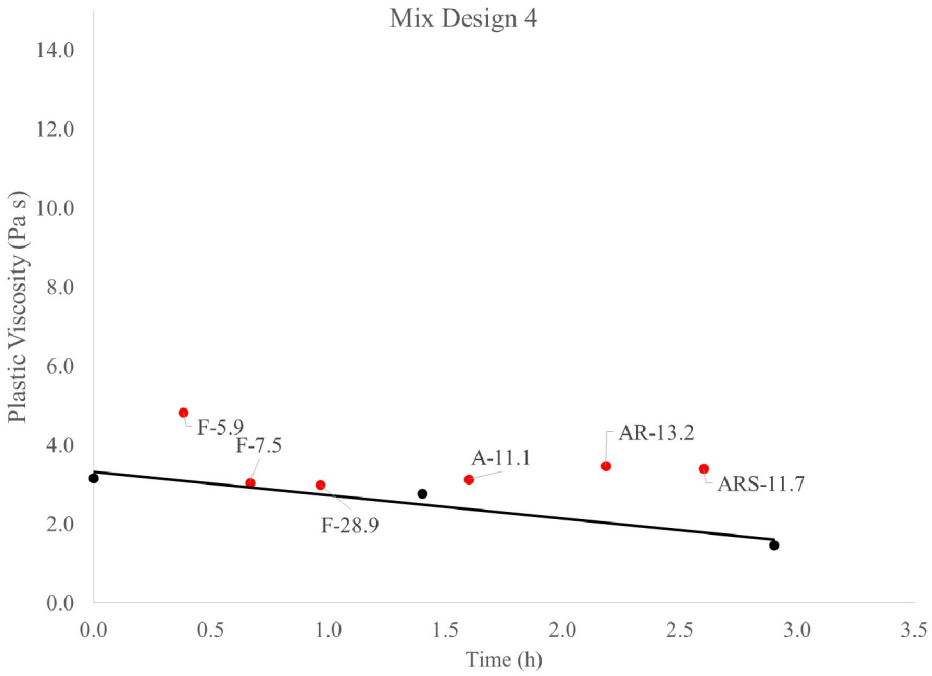

Figure A2.4. Plastic viscosity for non-pumped (black) and pumped (red) samples of mix design 4.

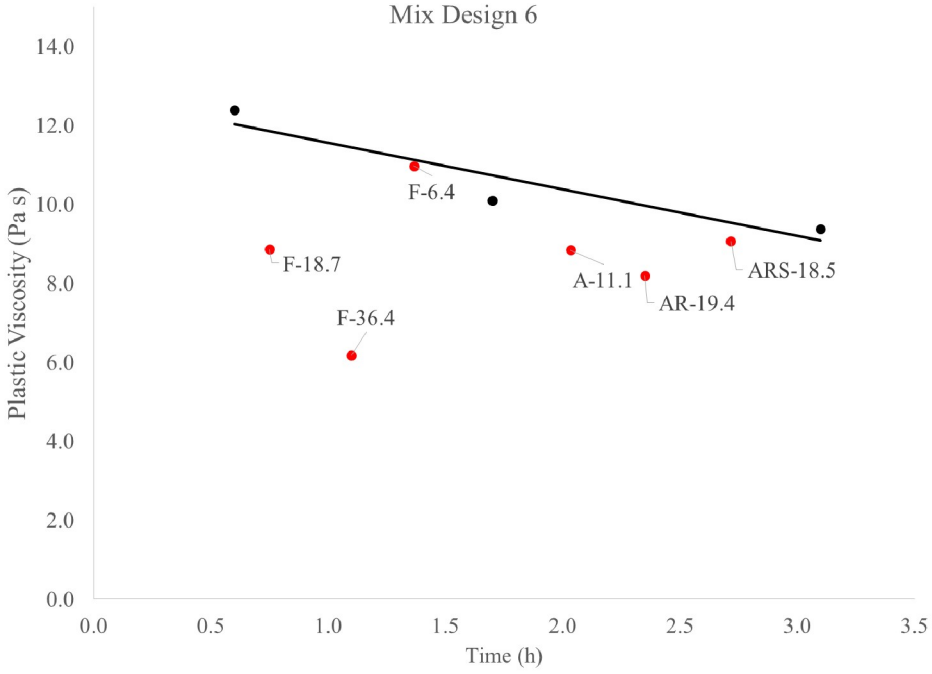

Figure A2.5. Plastic viscosity for non-pumped (black) and pumped (red) samples of mix design 6.

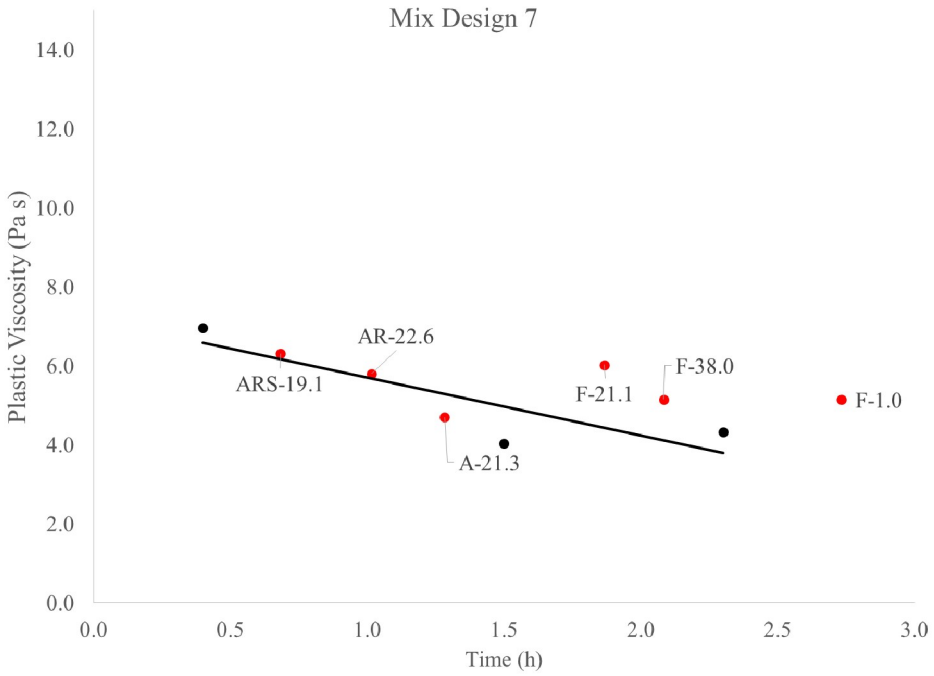

Figure A2.6. Plastic viscosity for non-pumped (black) and pumped (red) samples of mix design 7.

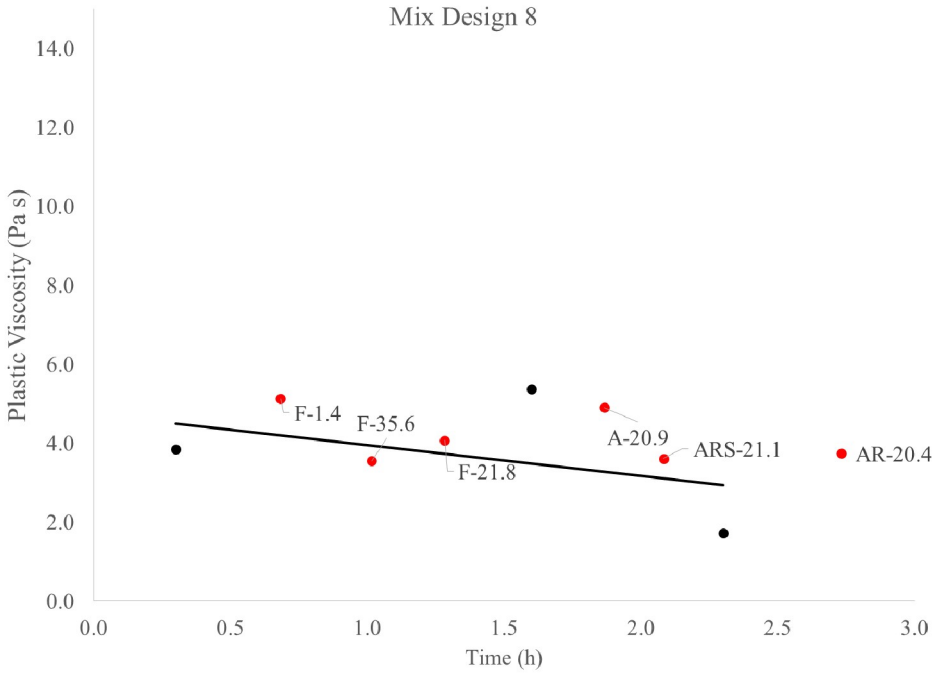

Figure A2.7. Plastic viscosity for non-pumped (black) and pumped (red) samples of mix design 8.

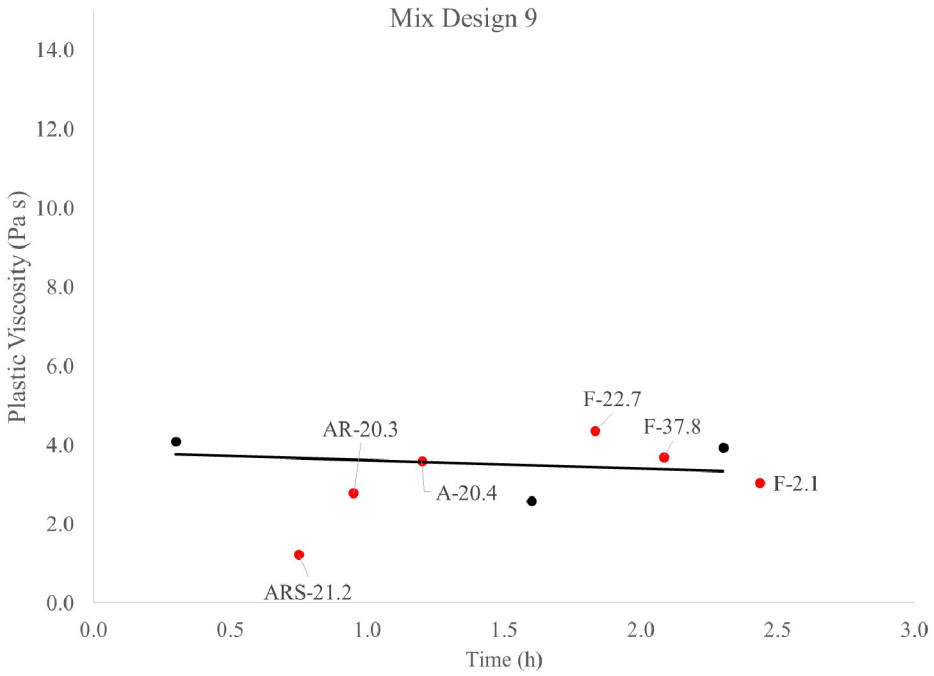

Figure A2.8. Plastic viscosity for non-pumped (black) and pumped (red) samples of mix design 9.

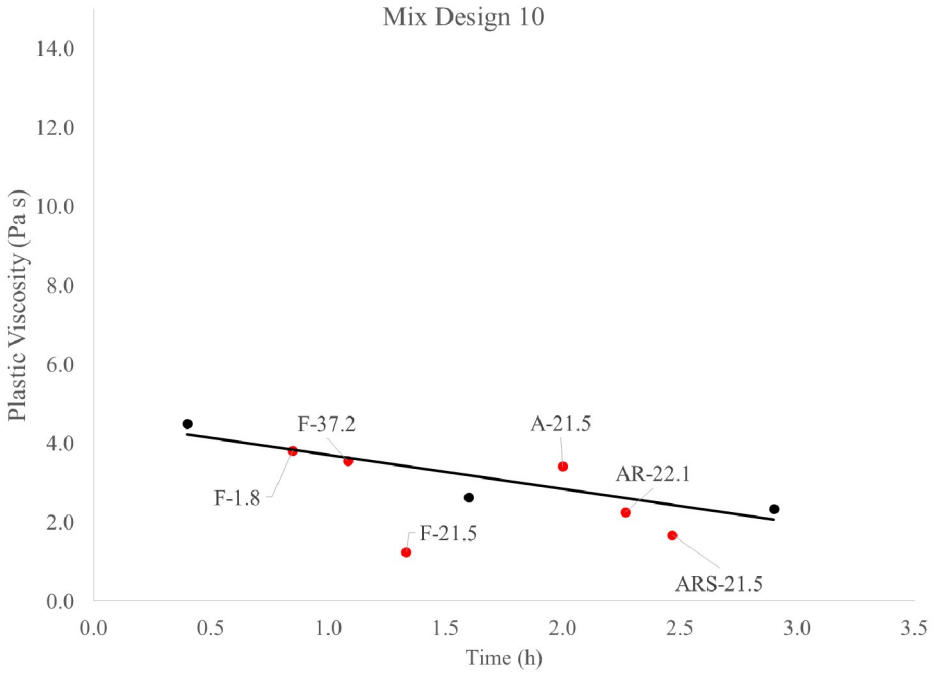

Figure A2.9. Plastic viscosity for non-pumped (black) and pumped (red) samples of mix design 10.

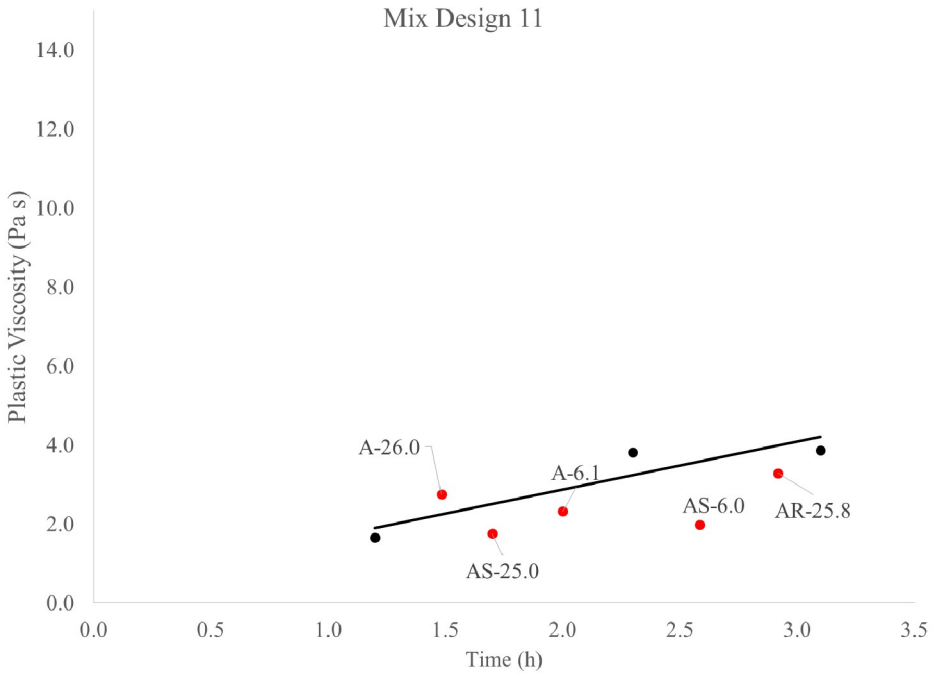

Figure A2.10. Plastic viscosity for non-pumped (black) and pumped (red) samples of mix design 11.

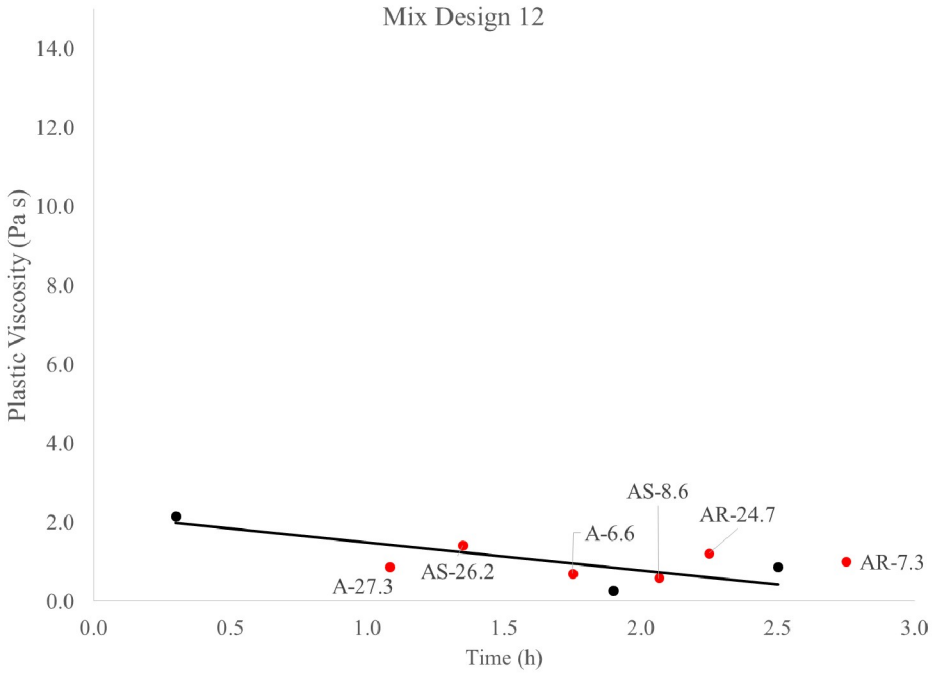

Figure A2.11. Plastic viscosity for non-pumped (black) and pumped (red) samples of mix design 12.

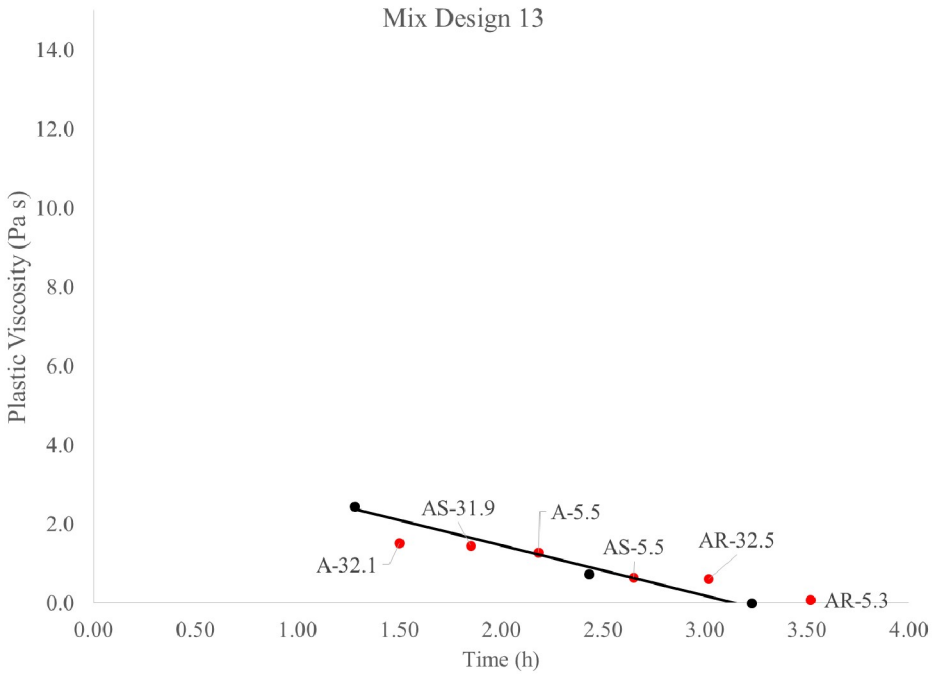

Figure A2.12. Plastic viscosity for non-pumped (black) and pumped (red) samples of mix design 13.

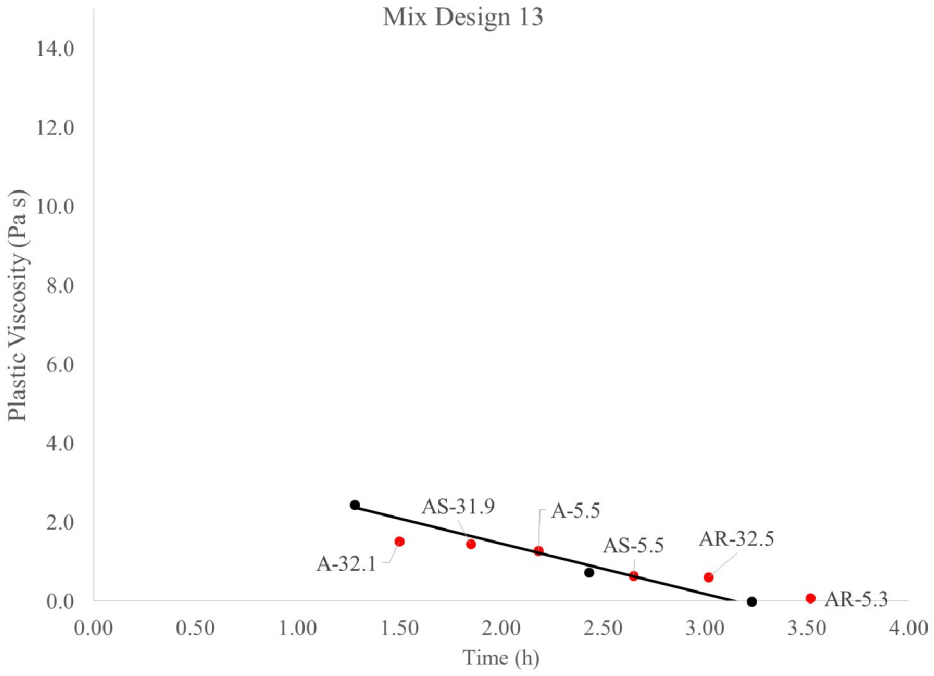

Figure A2.13. Plastic viscosity for non-pumped (black) and pumped (red) samples of mix design 14.

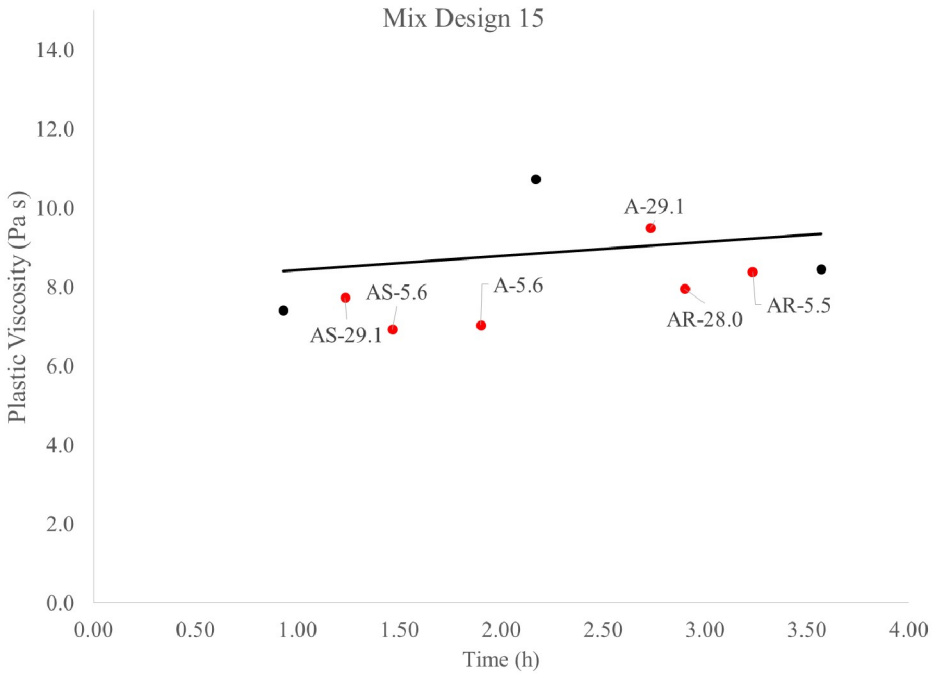

Figure A2.14. Plastic viscosity for non-pumped (black) and pumped (red) samples of mix design 15.

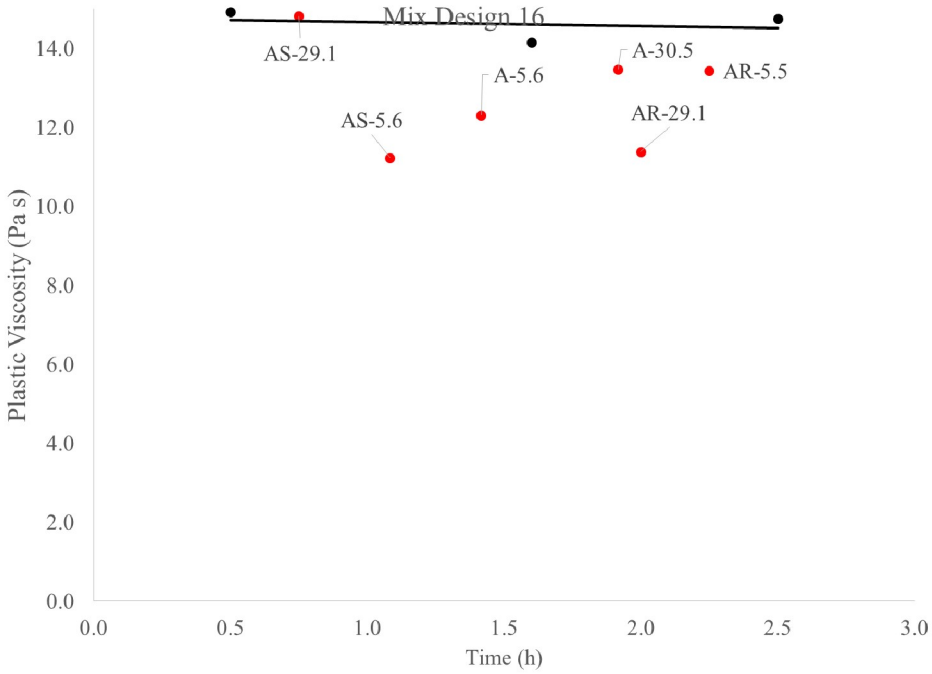

Figure A2.15. Plastic viscosity for non-pumped (black) and pumped (red) samples of mix design 16.

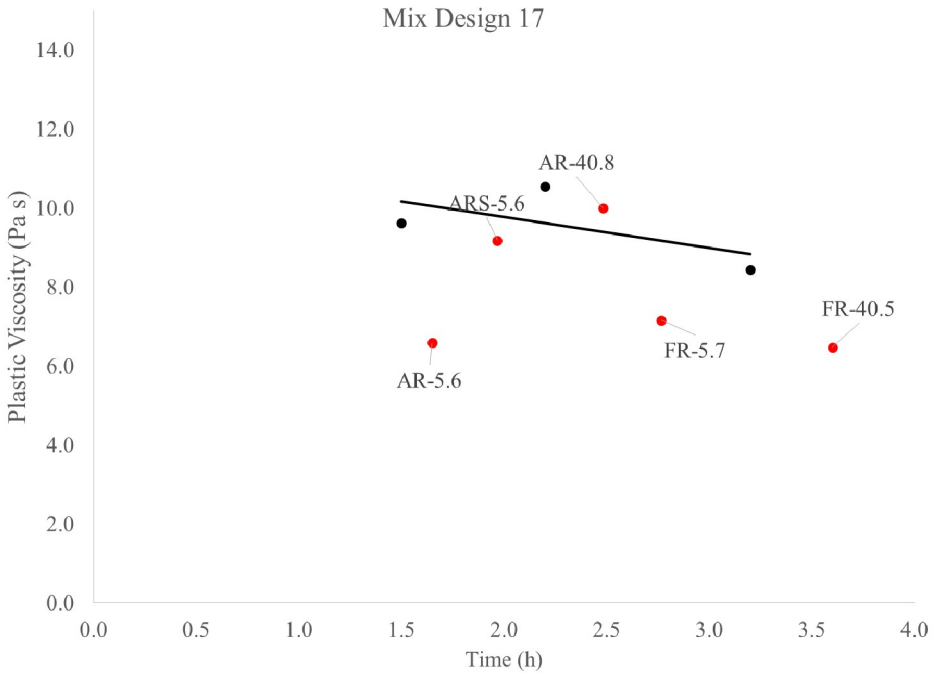

Figure A2.16. Plastic viscosity for non-pumped (black) and pumped (red) samples of mix design 17.

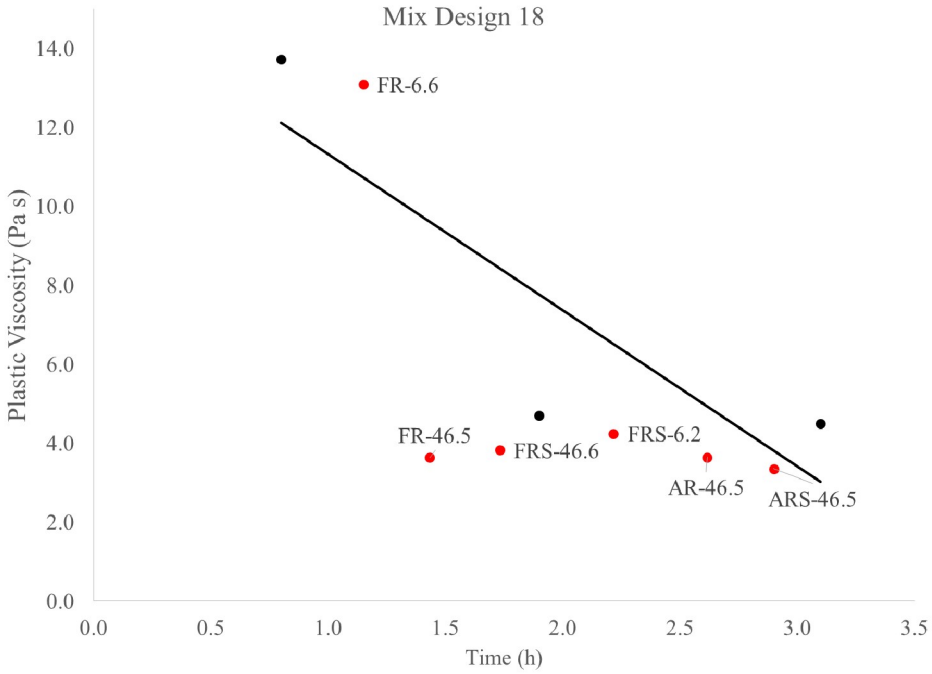

Figure A2.17. Plastic viscosity for non-pumped (black) and pumped (red) samples of mix design 18.

A.3 Flow resistance in interface rheometer

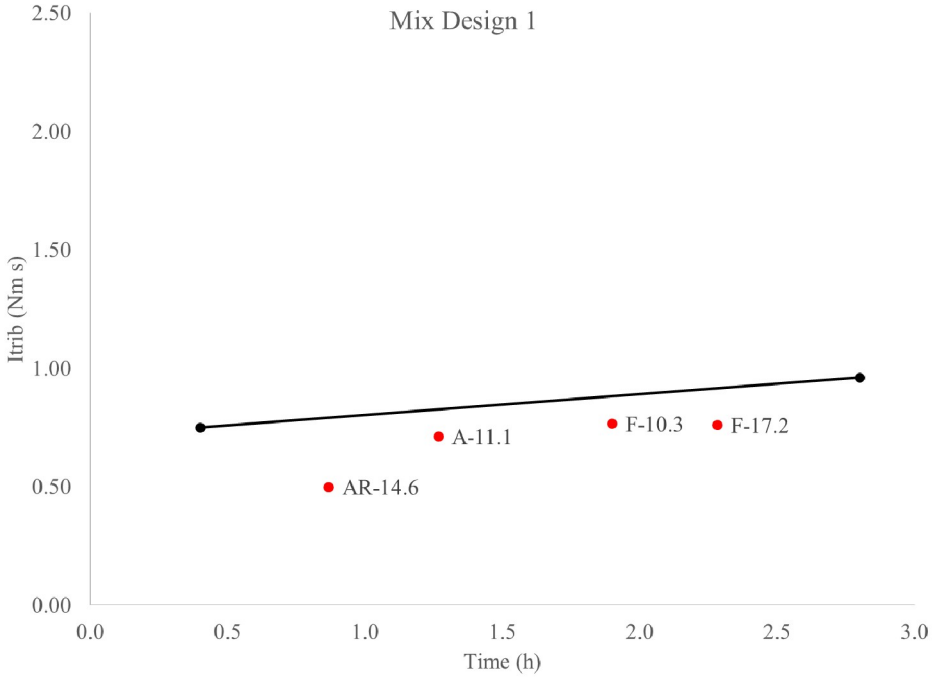

Figure A3.1. I_{trib} for non-pumped (black) and pumped (red) samples for mix design 1.

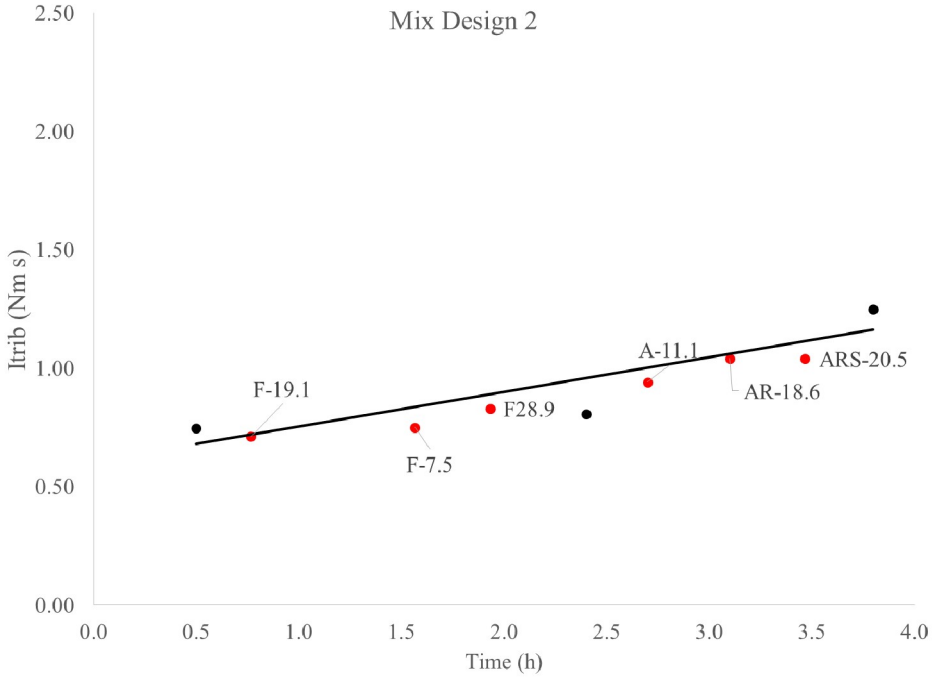

Figure A3.2. I_{trib} for non-pumped (black) and pumped (red) samples for mix design 2.

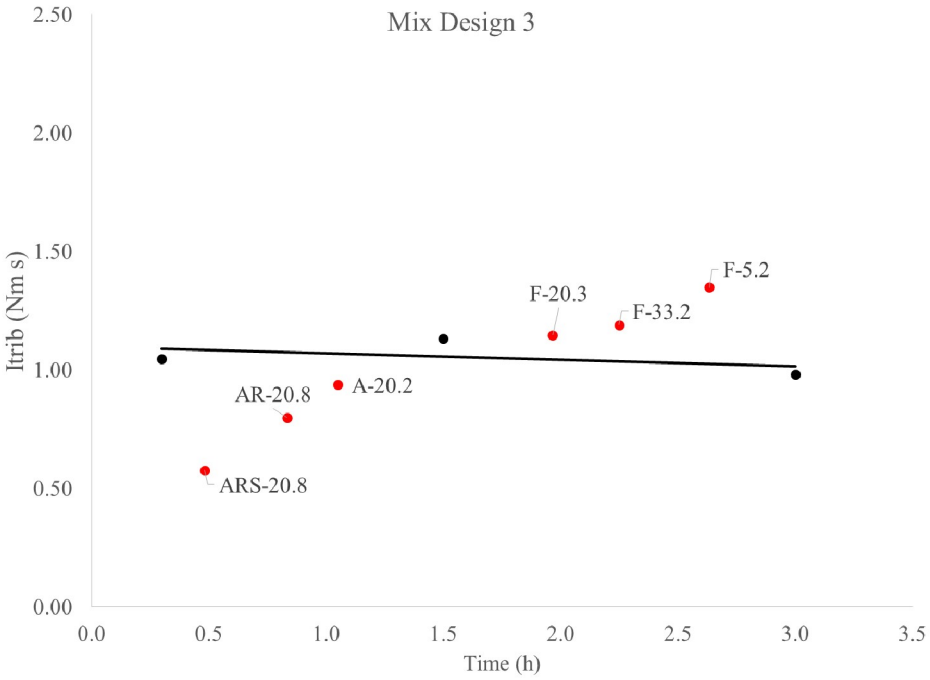

Figure A3.3. I_{trib} for non-pumped (black) and pumped (red) samples for mix design 3.

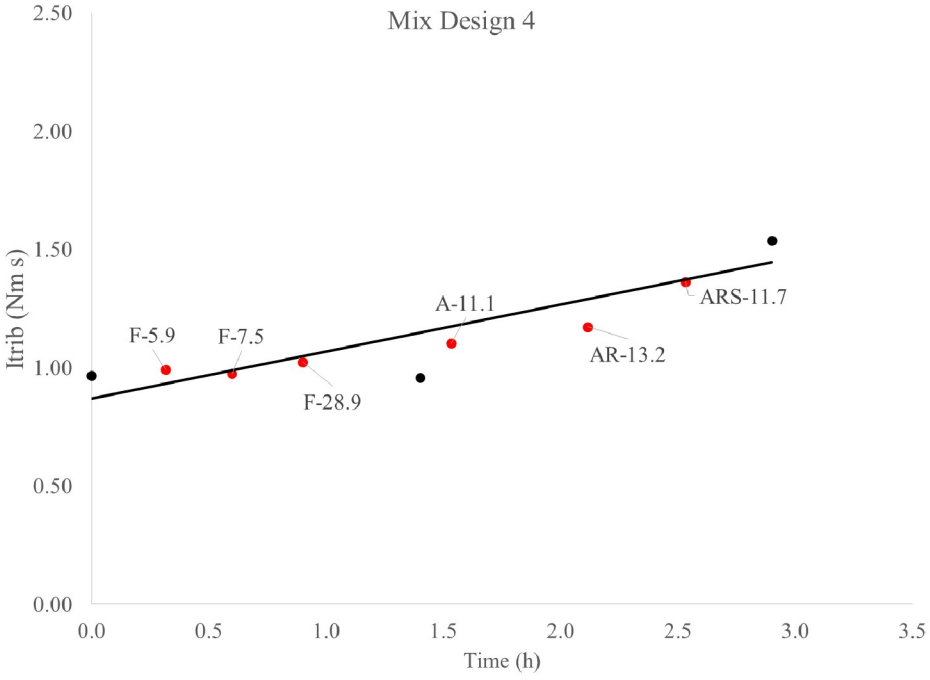

Figure A3.4. I_{trib} for non-pumped (black) and pumped (red) samples for mix design 4.

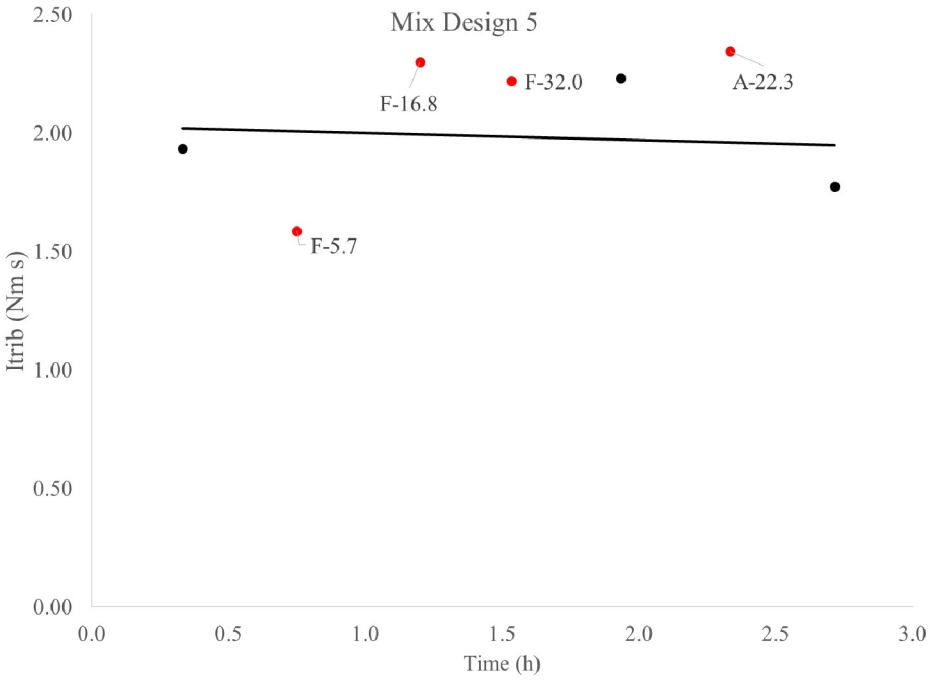

Figure A3.5. I_{trib} for non-pumped (black) and pumped (red) samples for mix design 5.

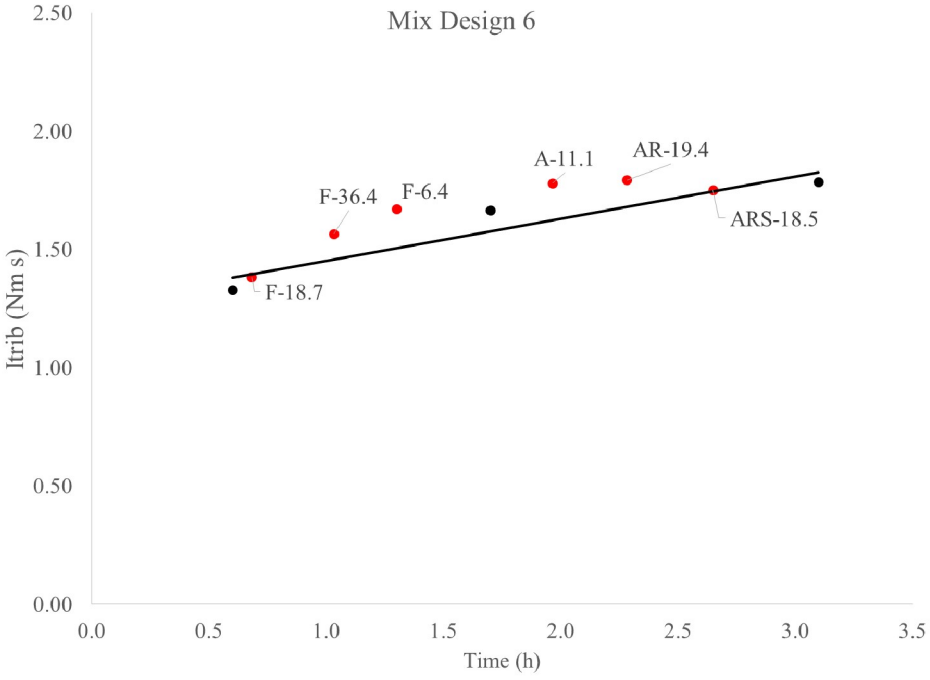

Figure A3.6. I_{trib} for non-pumped (black) and pumped (red) samples for mix design 6.

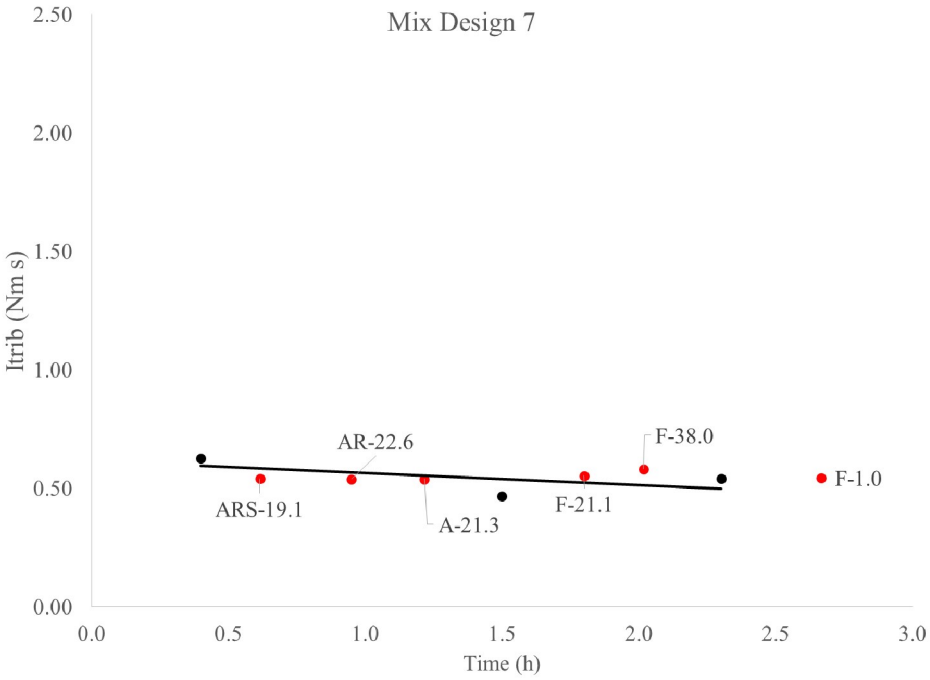

Figure A3.7. I_{trib} for non-pumped (black) and pumped (red) samples for mix design 7.

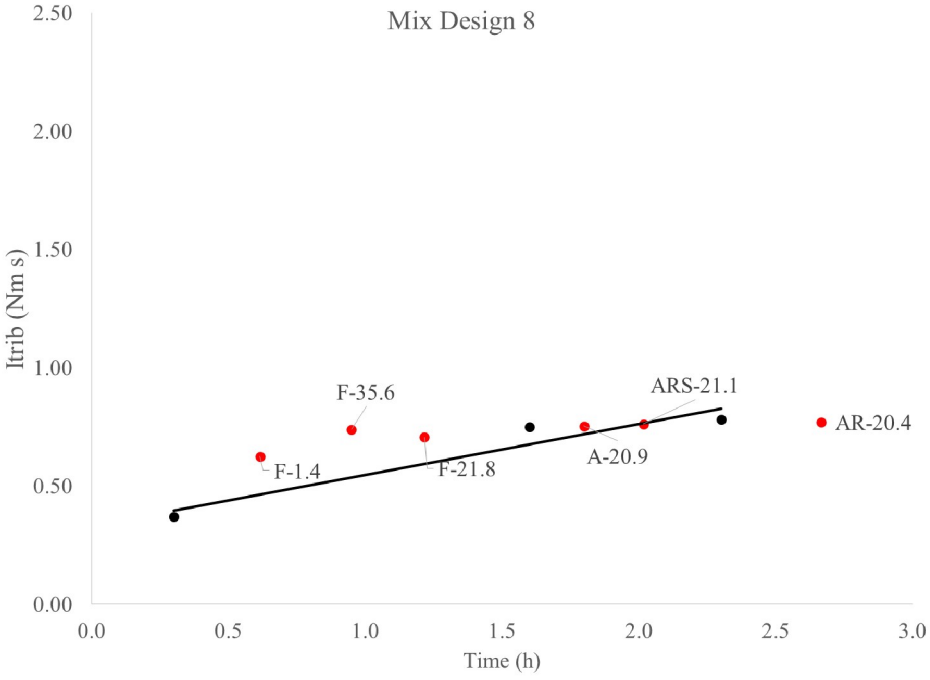

Figure A3.8. I_{trib} for non-pumped (black) and pumped (red) samples for mix design 8.

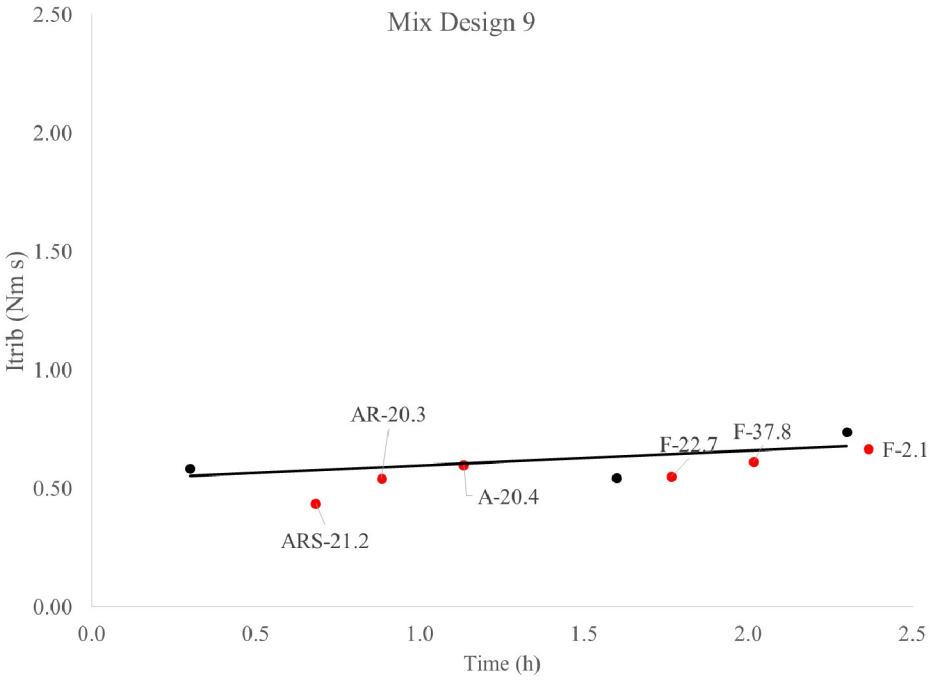

Figure A3.9. I_{trib} for non-pumped (black) and pumped (red) samples for mix design 9.

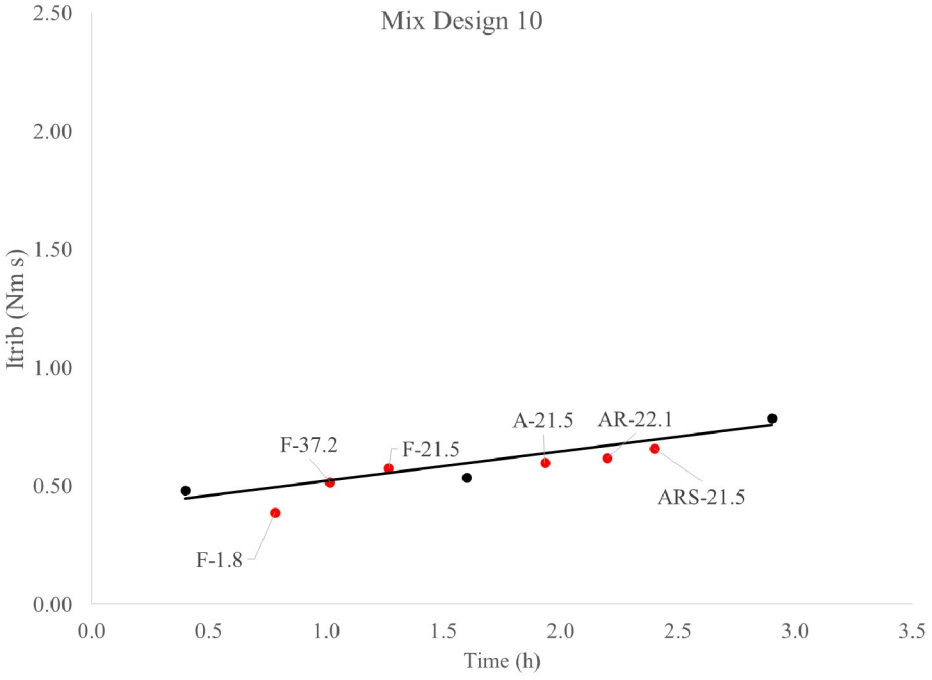

Figure A3.10. I_{trib} for non-pumped (black) and pumped (red) samples for mix design 10.

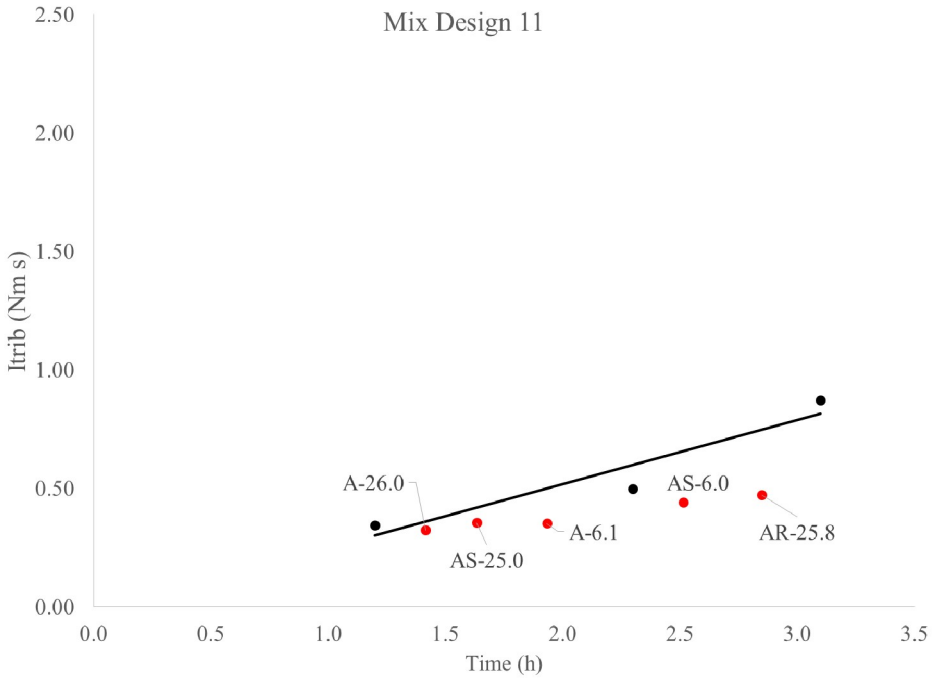

Figure A3.11. I_{trib} for non-pumped (black) and pumped (red) samples for mix design 11.

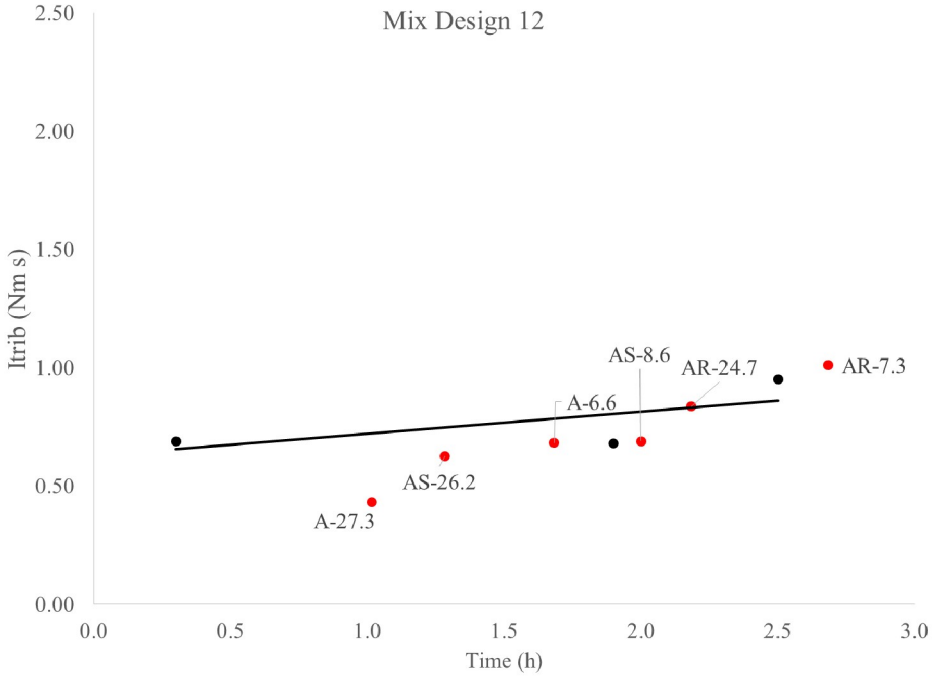

Figure A3.12. I_{trib} for non-pumped (black) and pumped (red) samples for mix design 12.

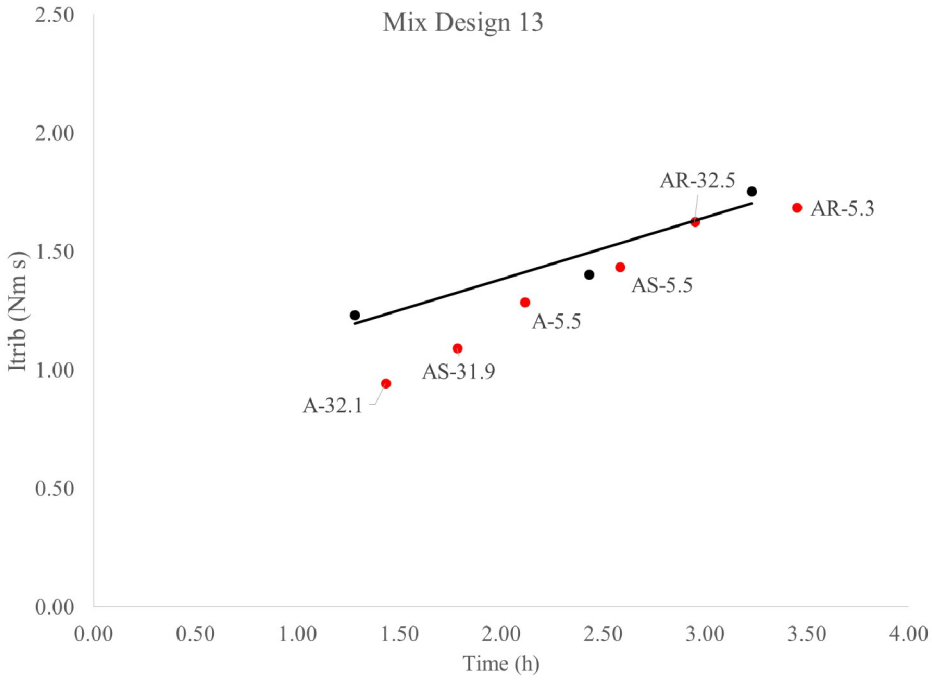

Figure A3.13. I_{trib} for non-pumped (black) and pumped (red) samples for mix design 13.

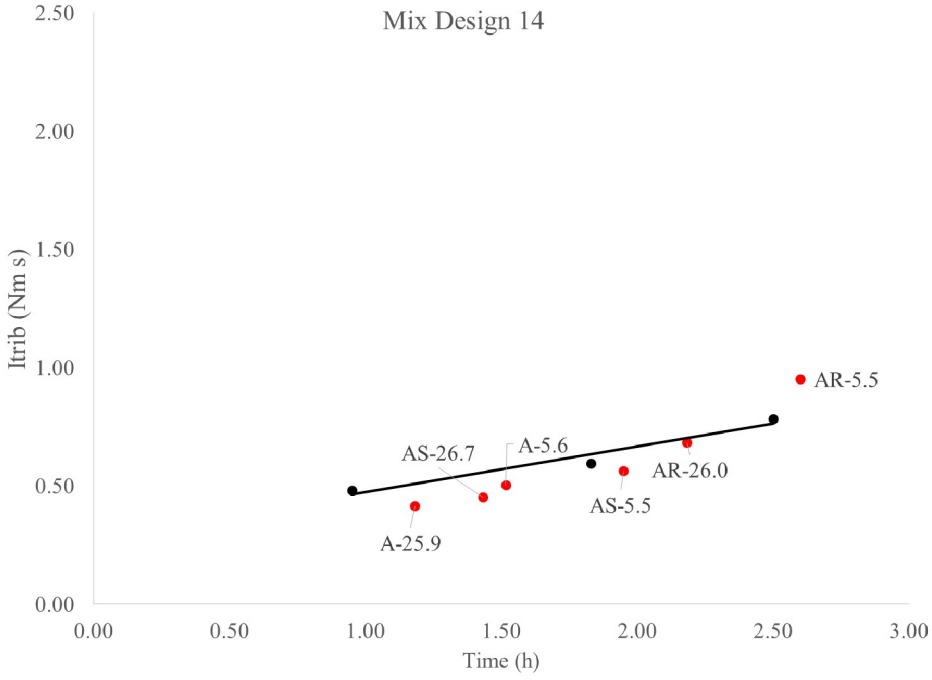

Figure A3.14. I_{trib} for non-pumped (black) and pumped (red) samples for mix design 14.

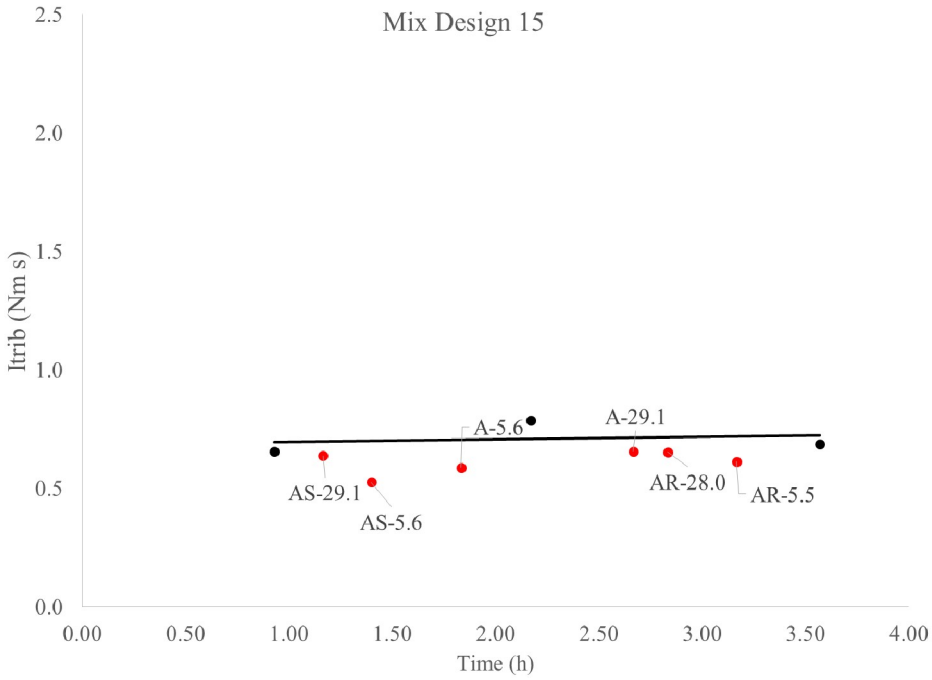

Figure A3.15. I_{trib} for non-pumped (black) and pumped (red) samples for mix design 15.

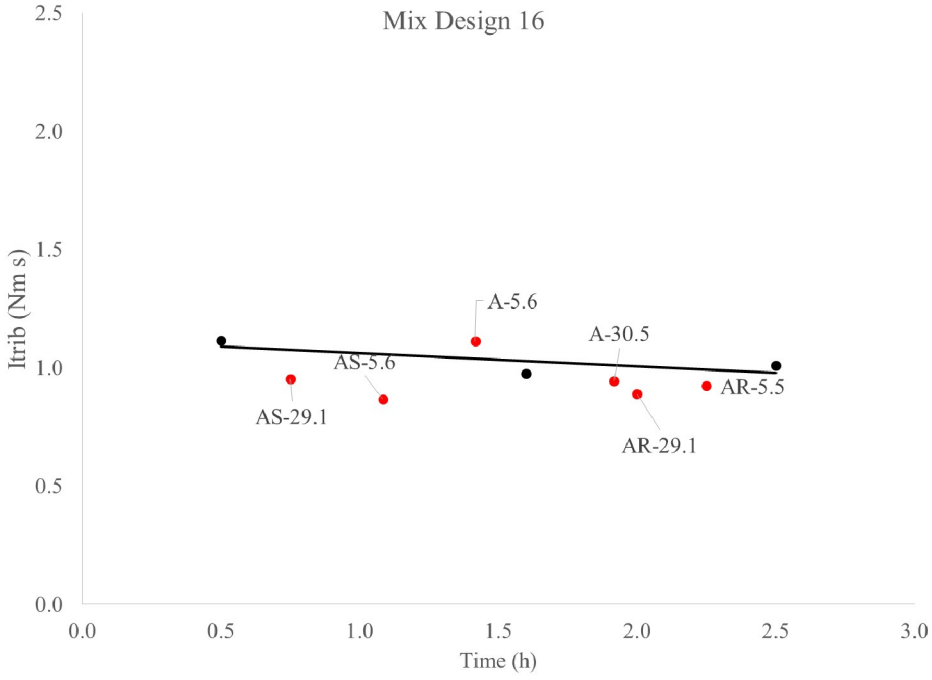

Figure A3.16. I_{trib} for non-pumped (black) and pumped (red) samples for mix design 16.

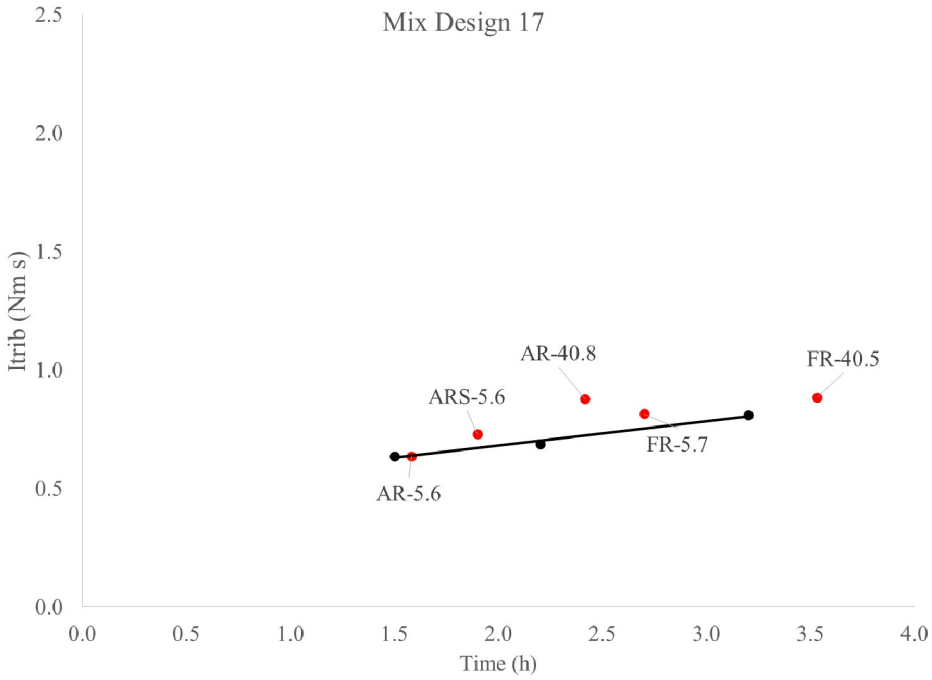

Figure A3.17. I_{trib} for non-pumped (black) and pumped (red) samples for mix design 17.

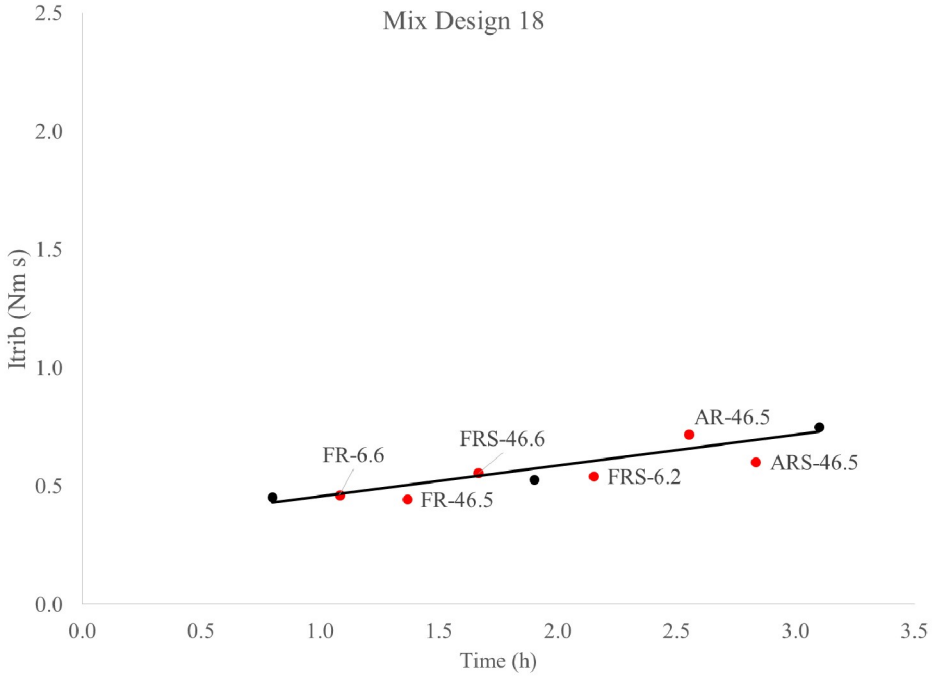

Figure A3.18. I_{trib} for non-pumped (black) and pumped (red) samples for mix design 18.

A.4 Sieve stability

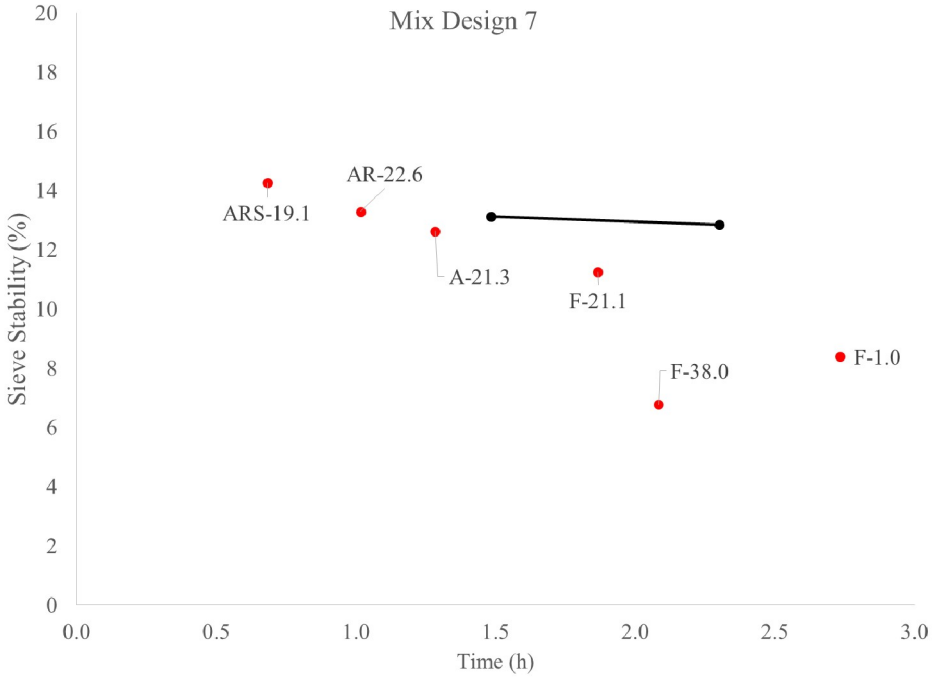

Figure A4.1. Sieve stability versus time for non-pumped (black) and pumped (red) samples for mix design 7.

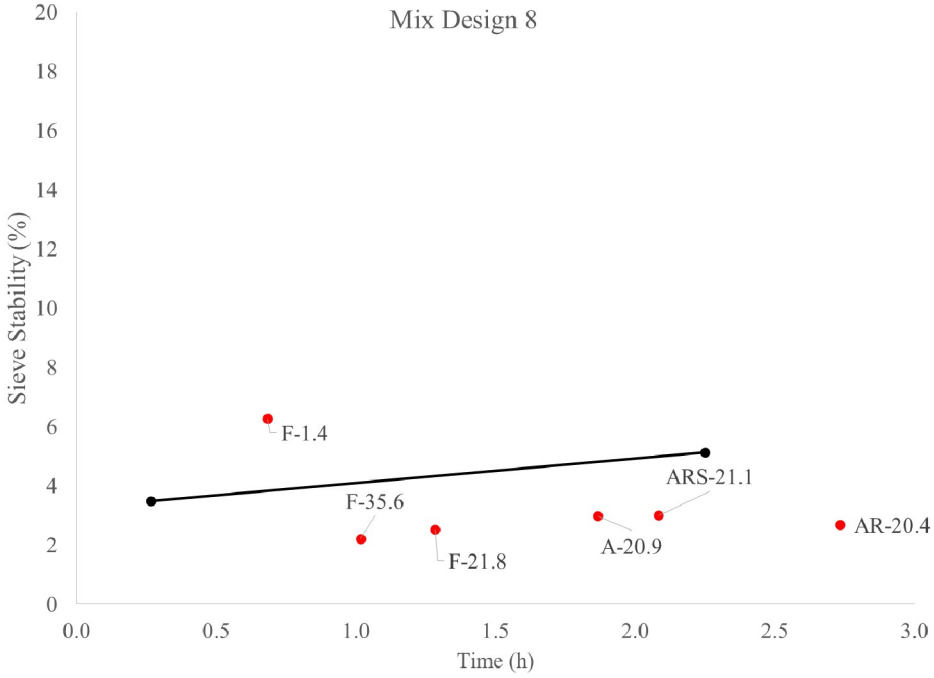

Figure A4.2. Sieve stability versus time for non-pumped (black) and pumped (red) samples for mix design 8.

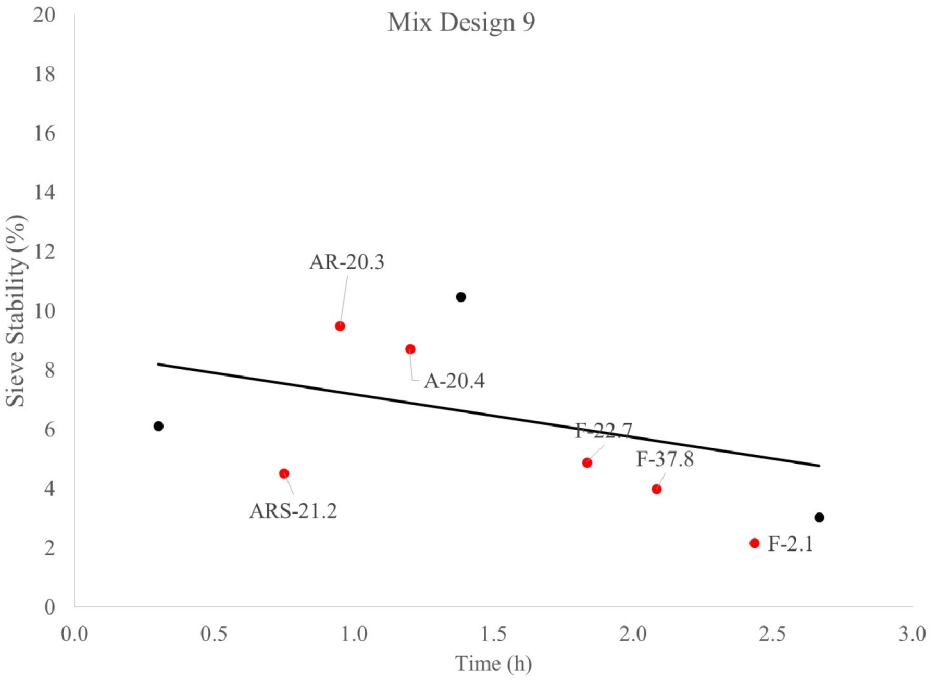

Figure A4.3. Sieve stability versus time for non-pumped (black) and pumped (red) samples for mix design 9.

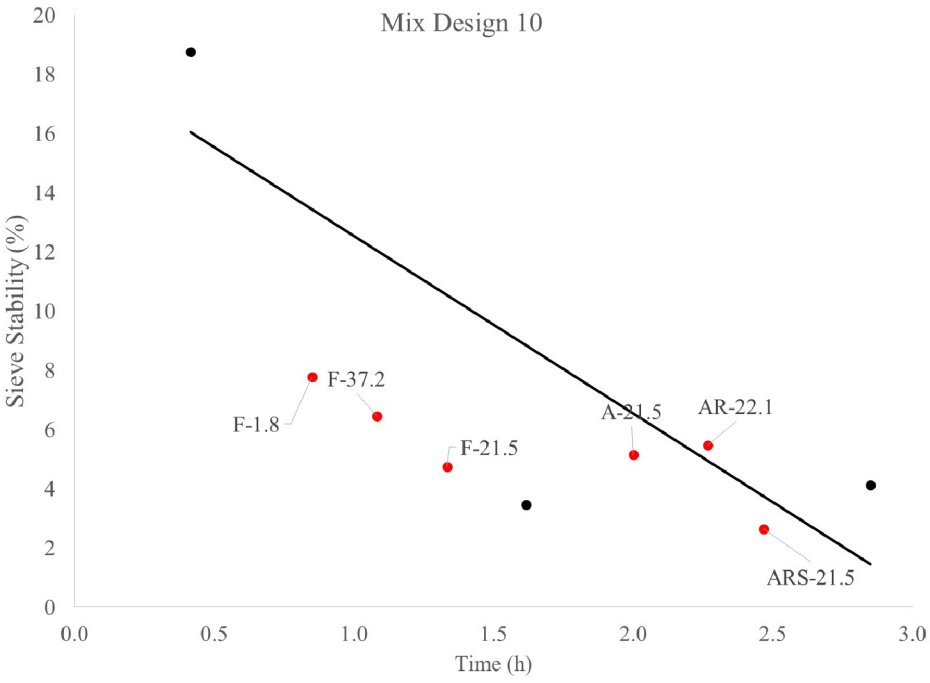

Figure A4.4. Sieve stability versus time for non-pumped (black) and pumped (red) samples for mix design 10.

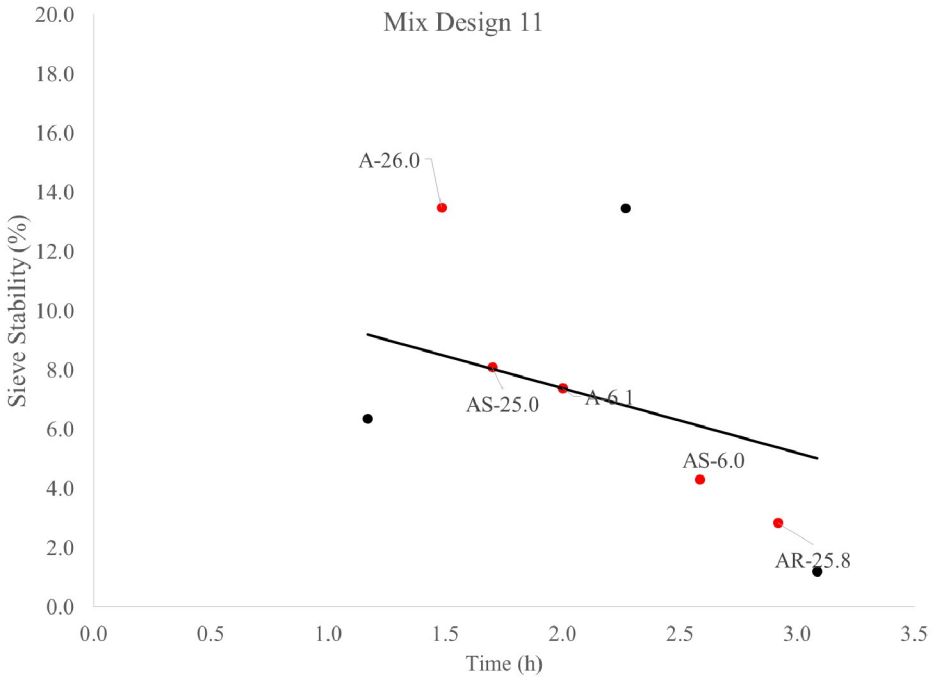

Figure A4.5. Sieve stability versus time for non-pumped (black) and pumped (red) samples for mix design 11.

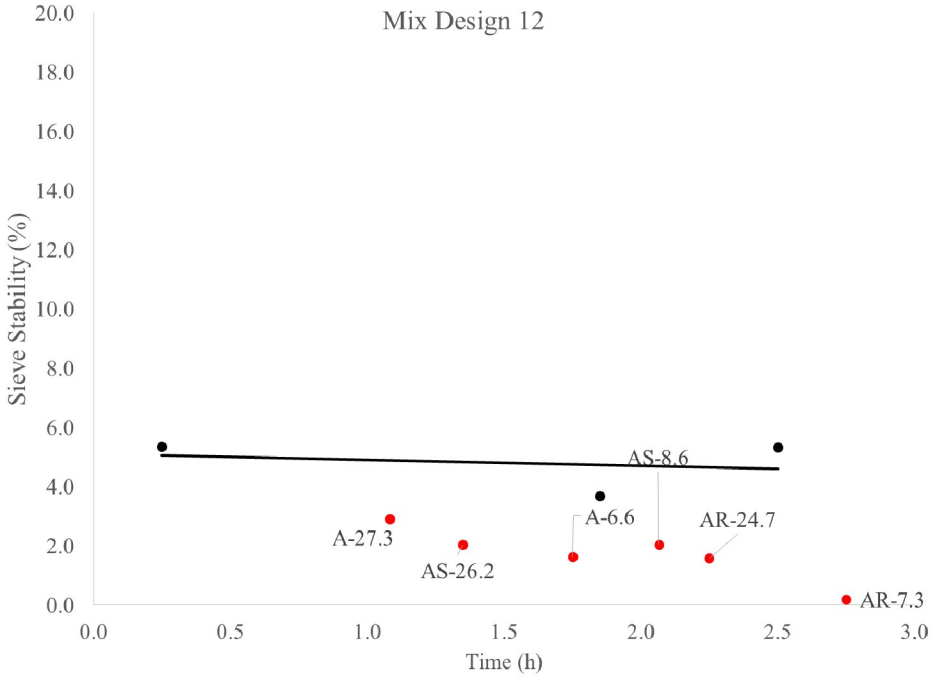

Figure A4.6. Sieve stability versus time for non-pumped (black) and pumped (red) samples for mix design 12.

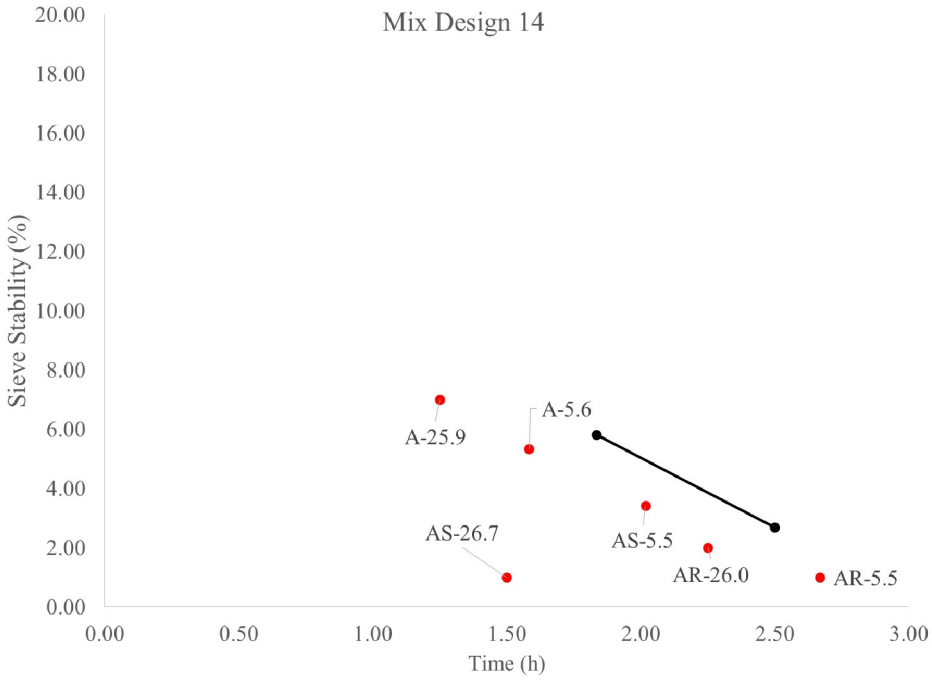

Figure A4.7. Sieve stability versus time for non-pumped (black) and pumped (red) samples for mix design 14.

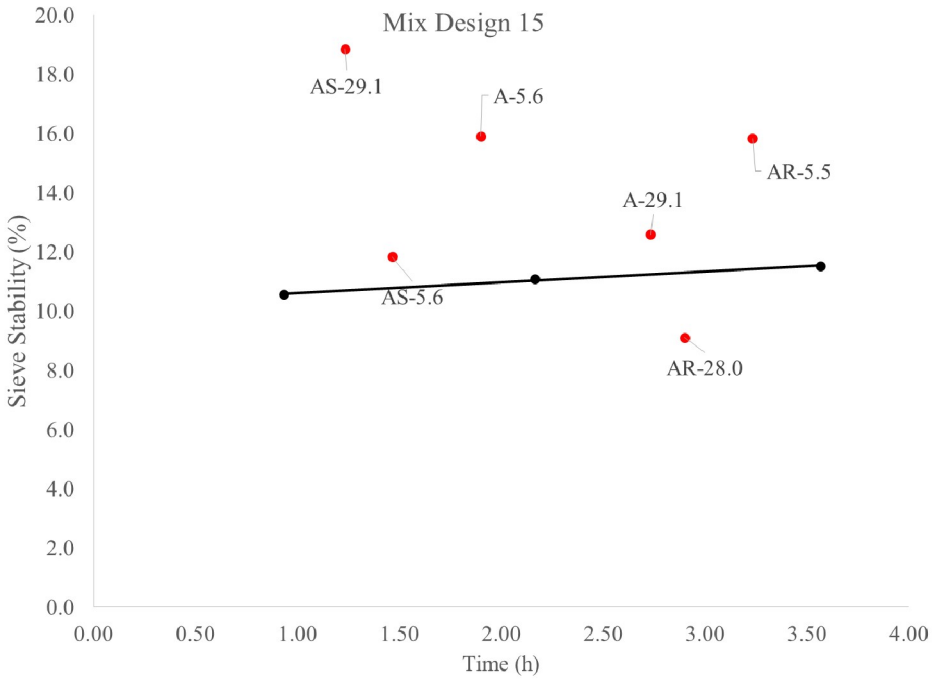

Figure A4.8. Sieve stability versus time for non-pumped (black) and pumped (red) samples for mix design 15.

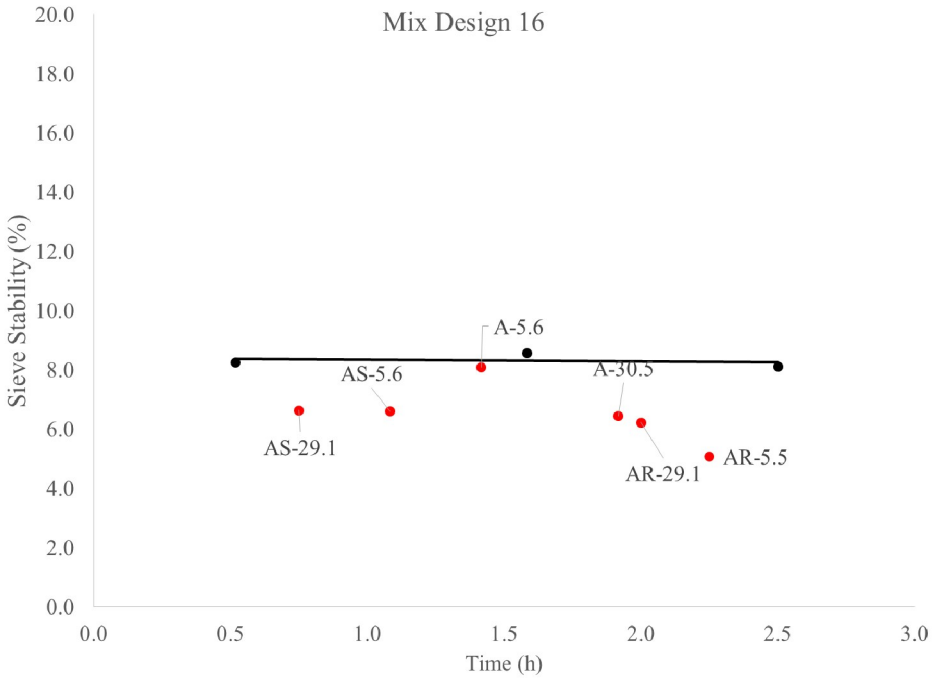

Figure A4.9. Sieve stability versus time for non-pumped (black) and pumped (red) samples for mix design 16.

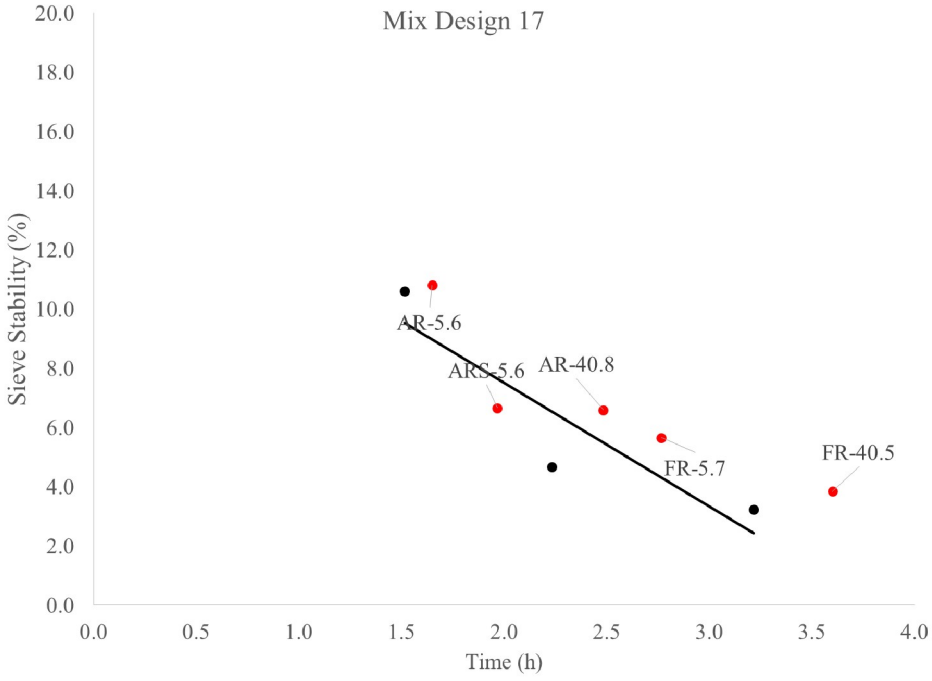

Figure A4.10. Sieve stability versus time for non-pumped (black) and pumped (red) samples for mix design 17.

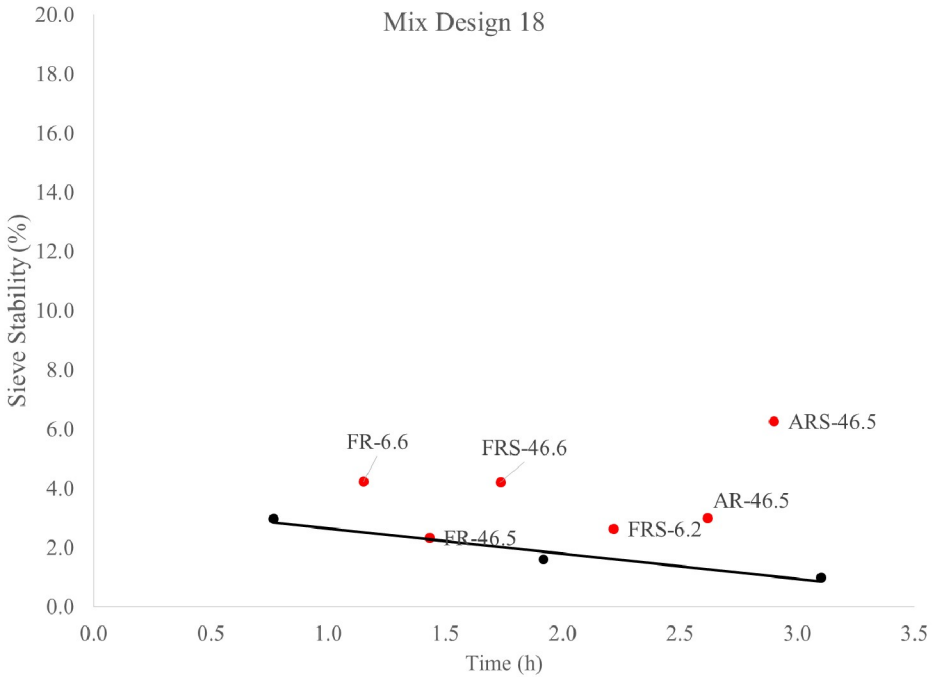

Figure A4.11. Sieve stability versus time for non-pumped (black) and pumped (red) samples for mix design 18.

A.5 Fresh concrete density

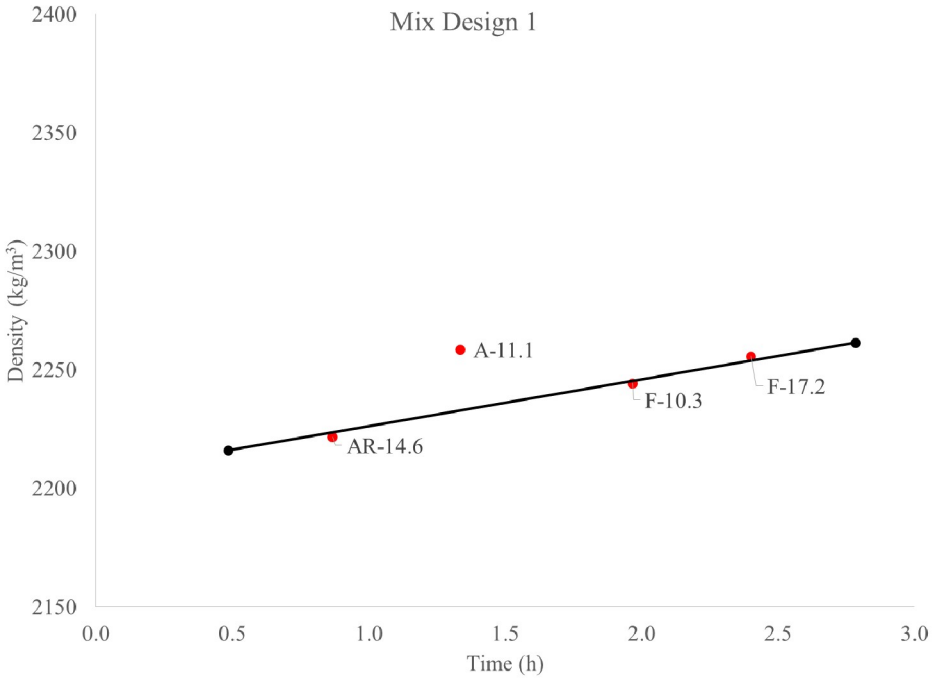

Figure A5.1. Density versus time for non-pumped (black) and pumped (red) samples for mixture 1.

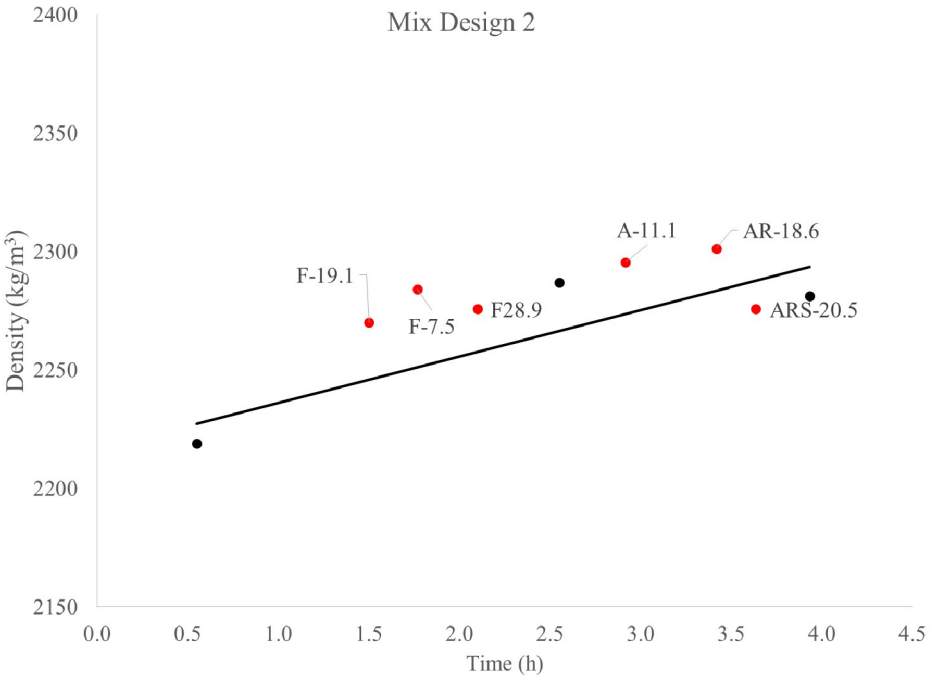

Figure A5.2. Density versus time for non-pumped (black) and pumped (red) samples for mixture 2.

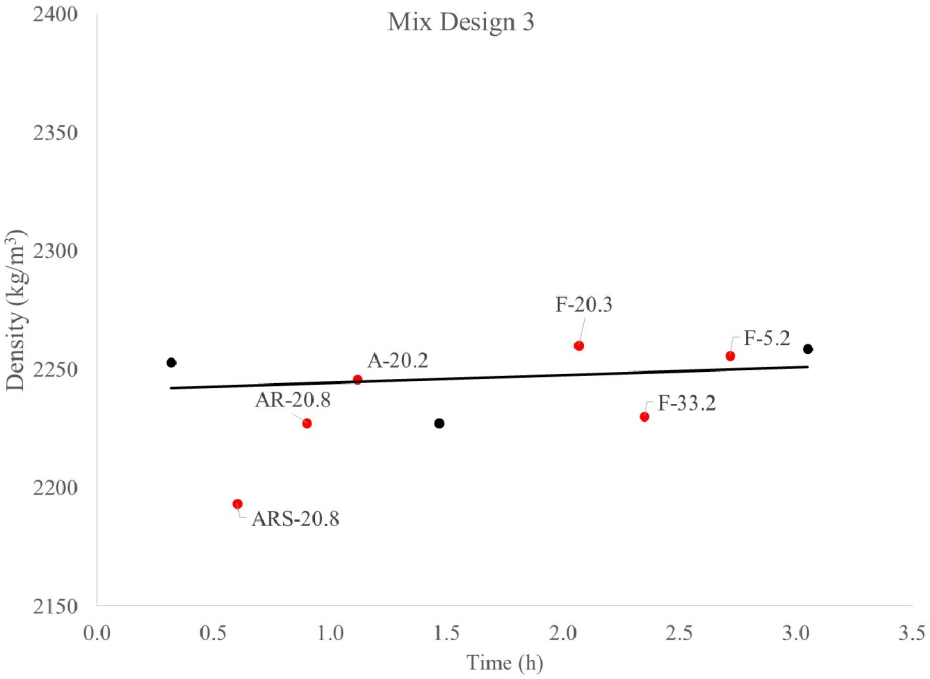

Figure A5.3. Density versus time for non-pumped (black) and pumped (red) samples for mixture 3.

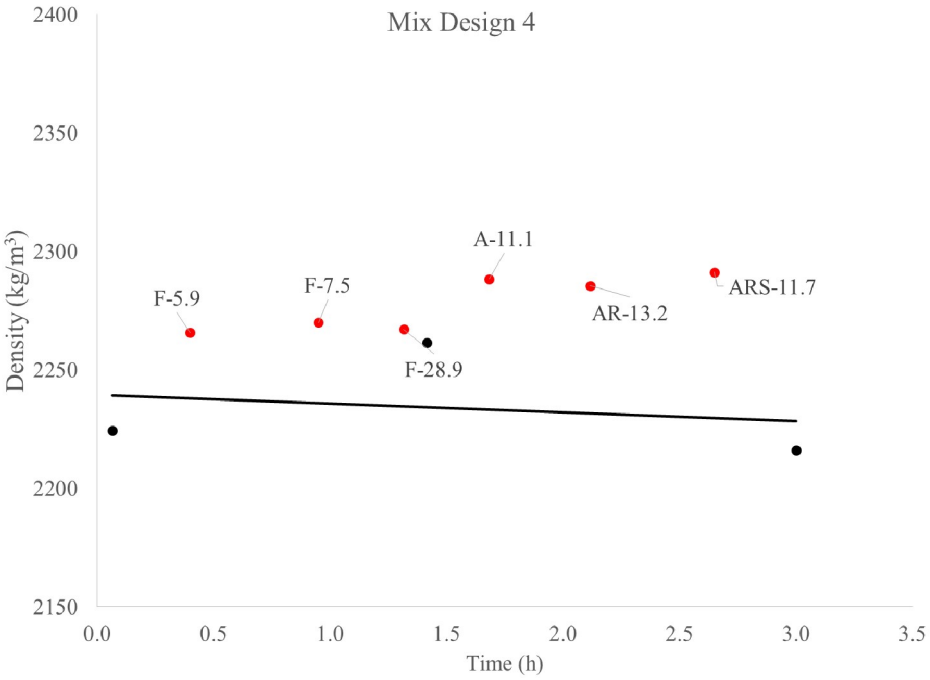

Figure A5.4. Density versus time for non-pumped (black) and pumped (red) samples for mixture 4.

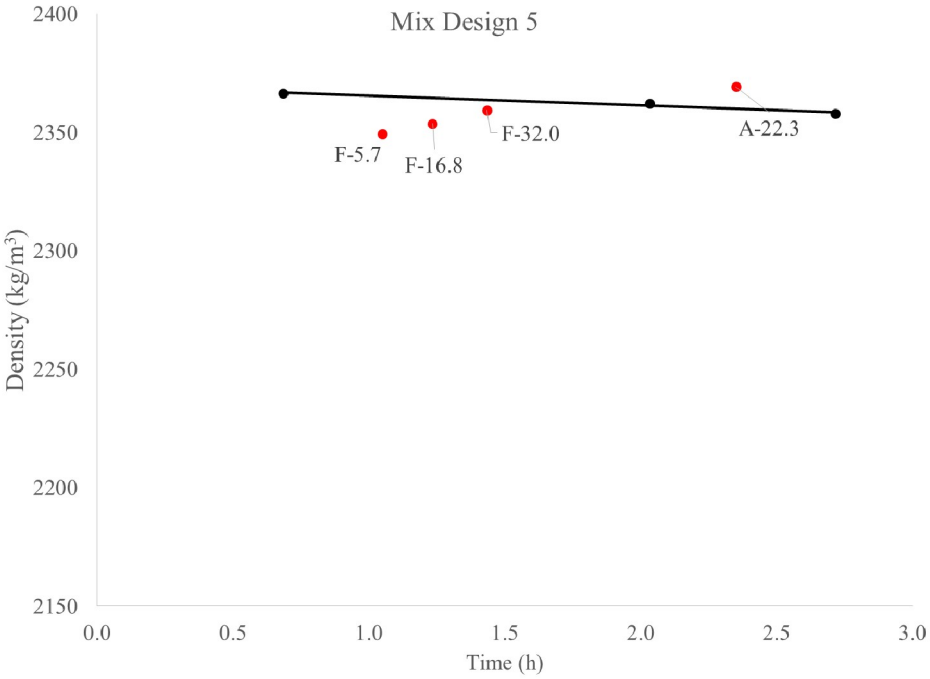

Figure A5.5. Density versus time for non-pumped (black) and pumped (red) samples for mixture 5.

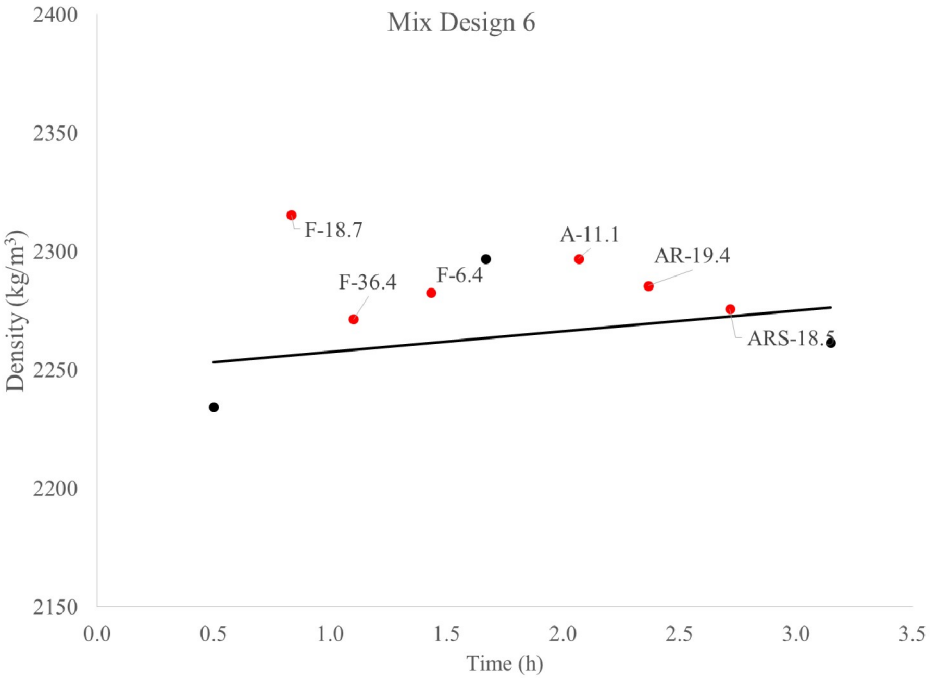

Figure A5.6. Density versus time for non-pumped (black) and pumped (red) samples for mixture 6.

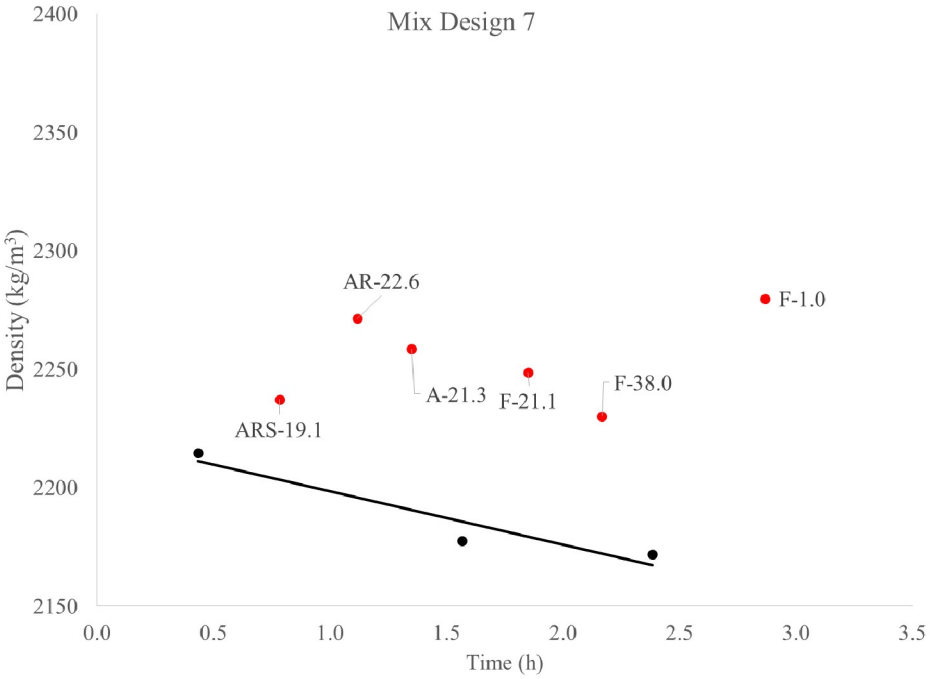

Figure A5.7. Density versus time for non-pumped (black) and pumped (red) samples for mixture 7.

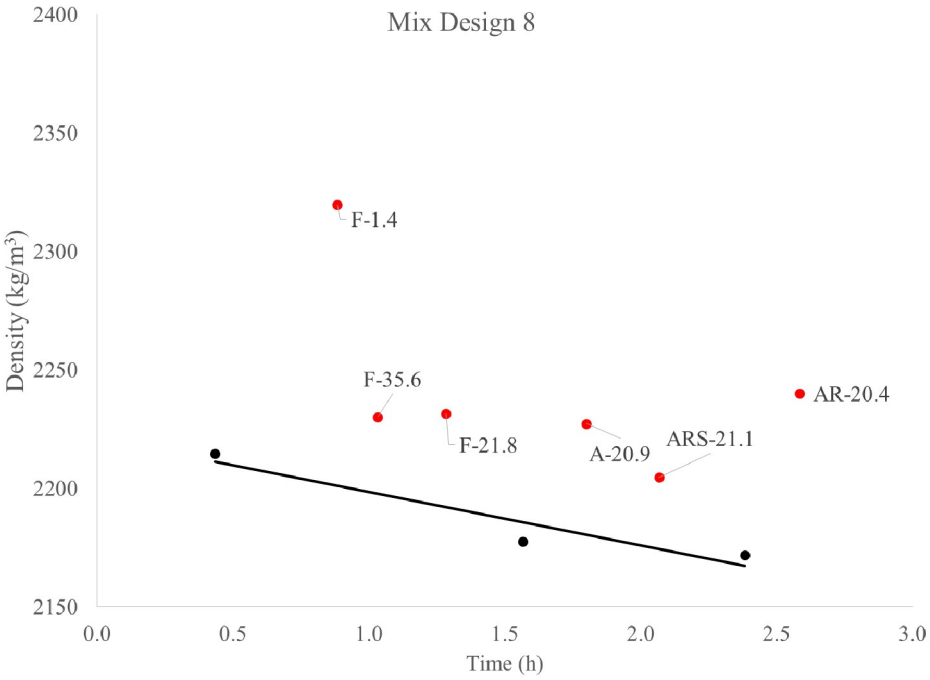

Figure A5.8. Density versus time for non-pumped (black) and pumped (red) samples for mixture 8.

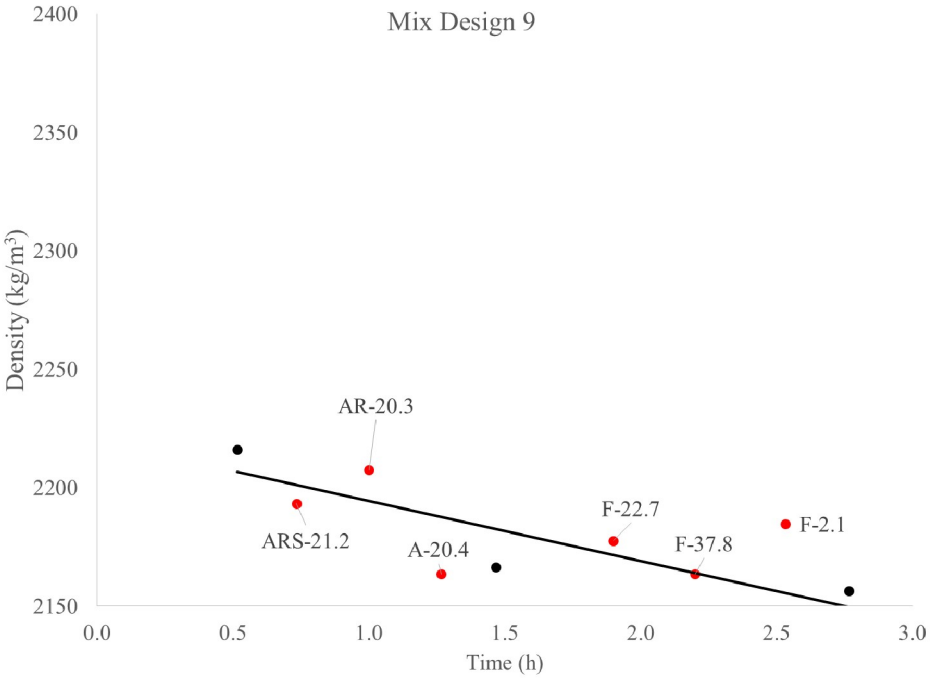

Figure A5.9. Density versus time for non-pumped (black) and pumped (red) samples for mixture 9.

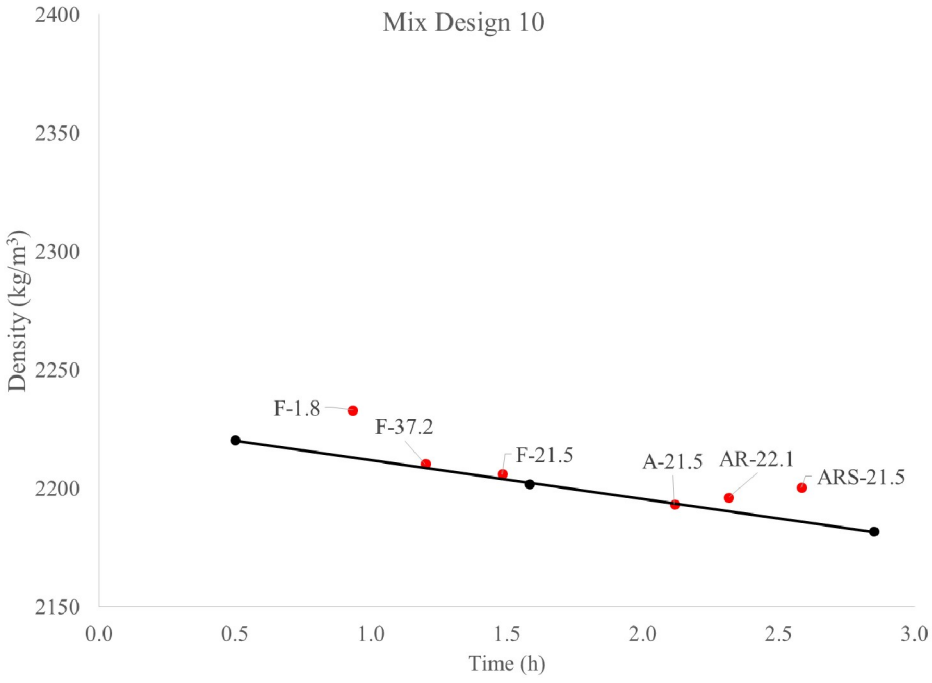

Figure A5.10. Density versus time for non-pumped (black) and pumped (red) samples for mixture 10.

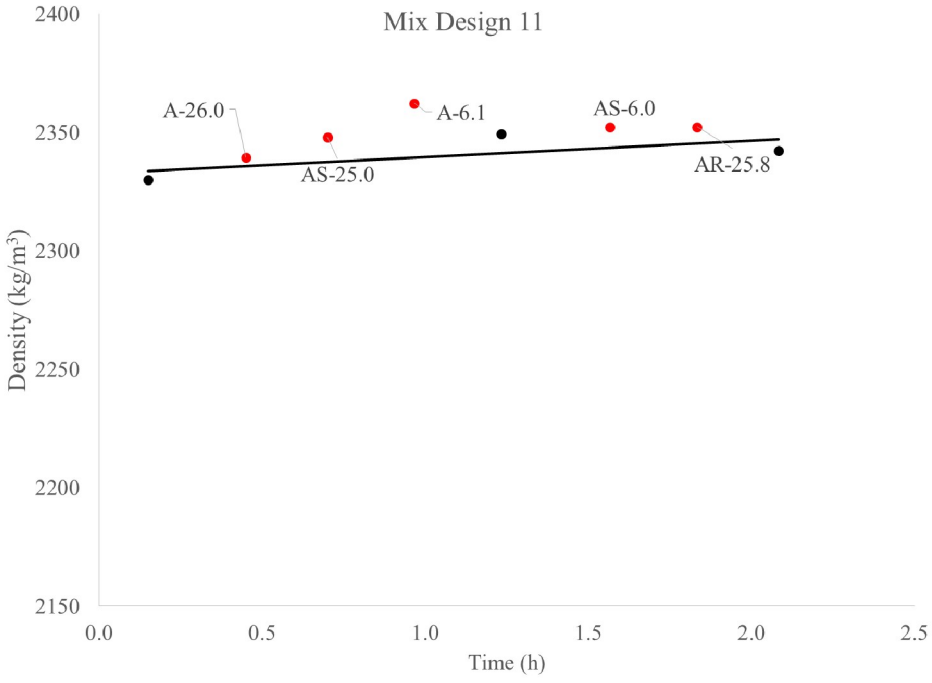

Figure A5.11. Density versus time for non-pumped (black) and pumped (red) samples for mixture 11.

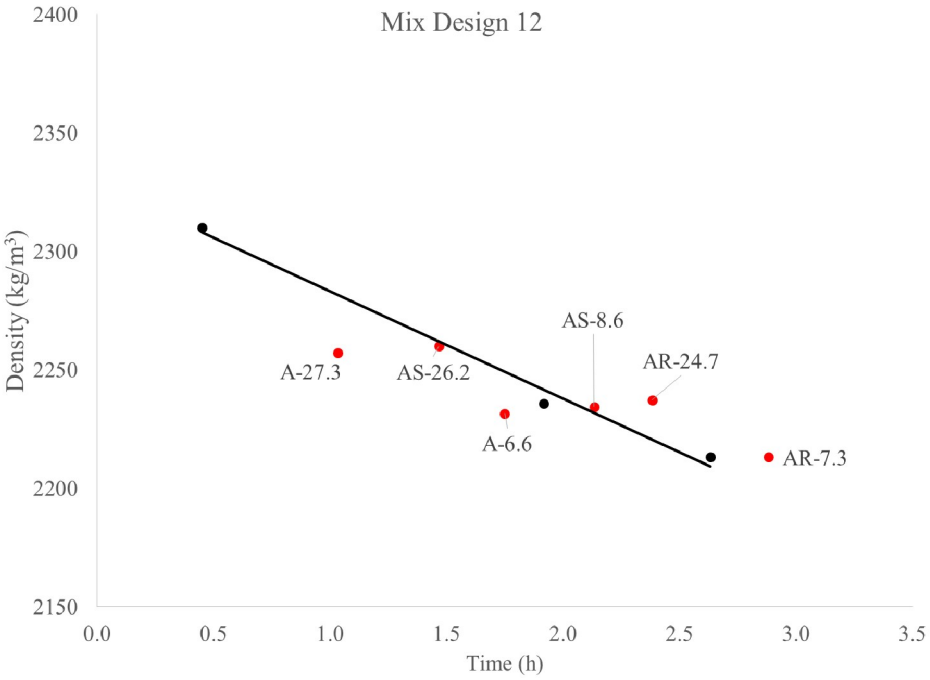

Figure A5.12. Density versus time for non-pumped (black) and pumped (red) samples for mixture 12.

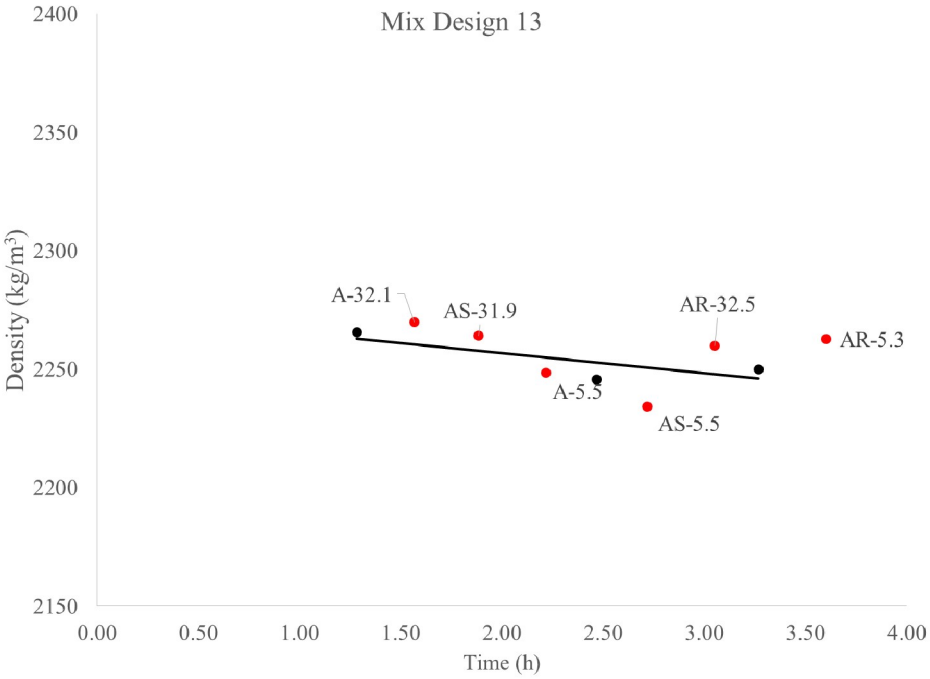

Figure A5.13. Density versus time for non-pumped (black) and pumped (red) samples for mixture 13.

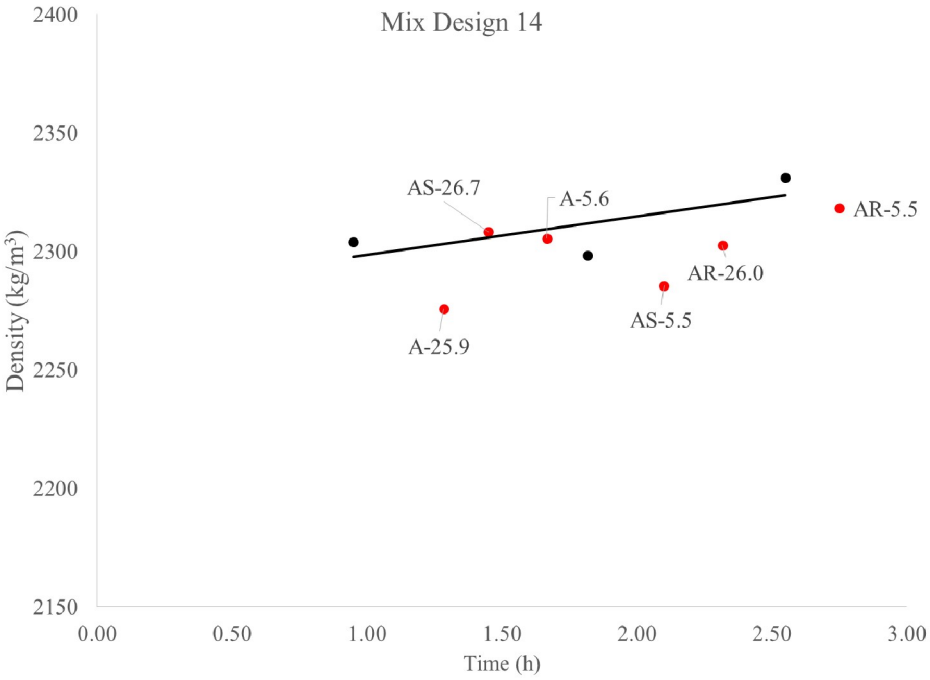

Figure A5.14. Density versus time for non-pumped (black) and pumped (red) samples for mixture 14.

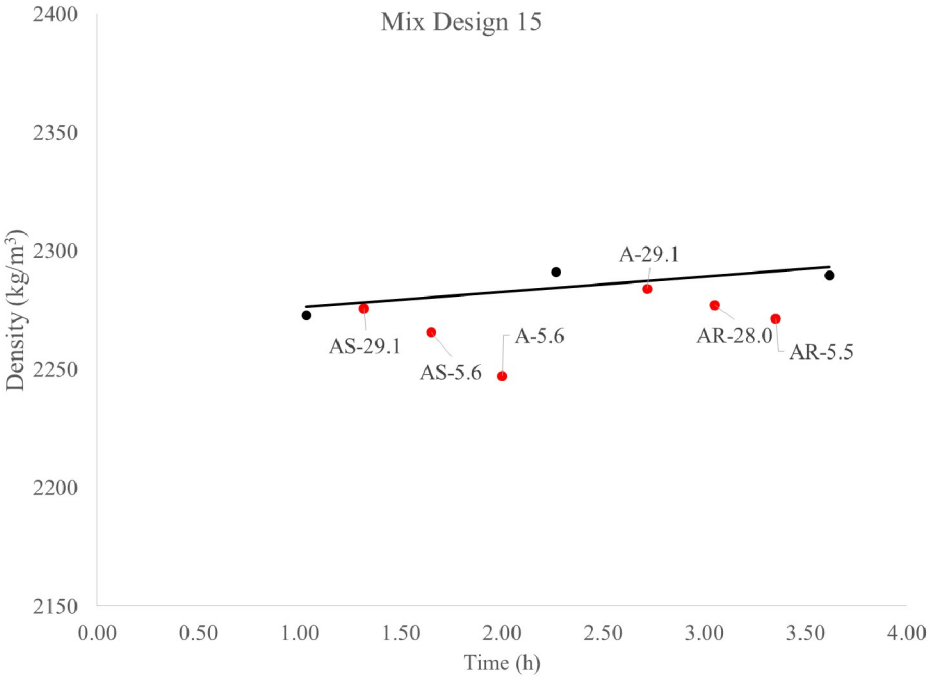

Figure A5.15. Density versus time for non-pumped (black) and pumped (red) samples for mixture 15.

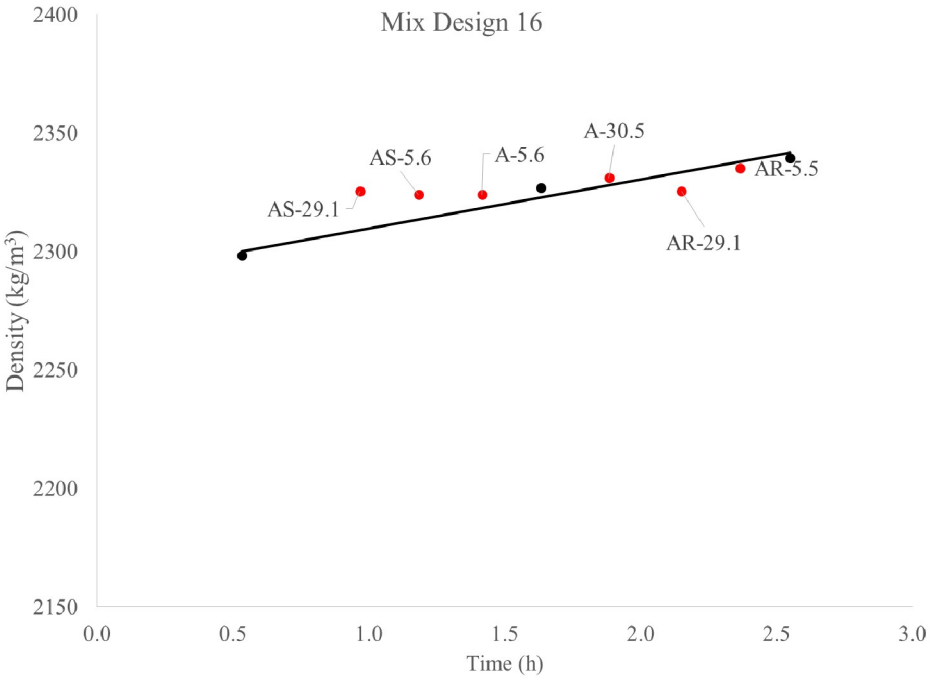

Figure A5.16. Density versus time for non-pumped (black) and pumped (red) samples for mixture 16.

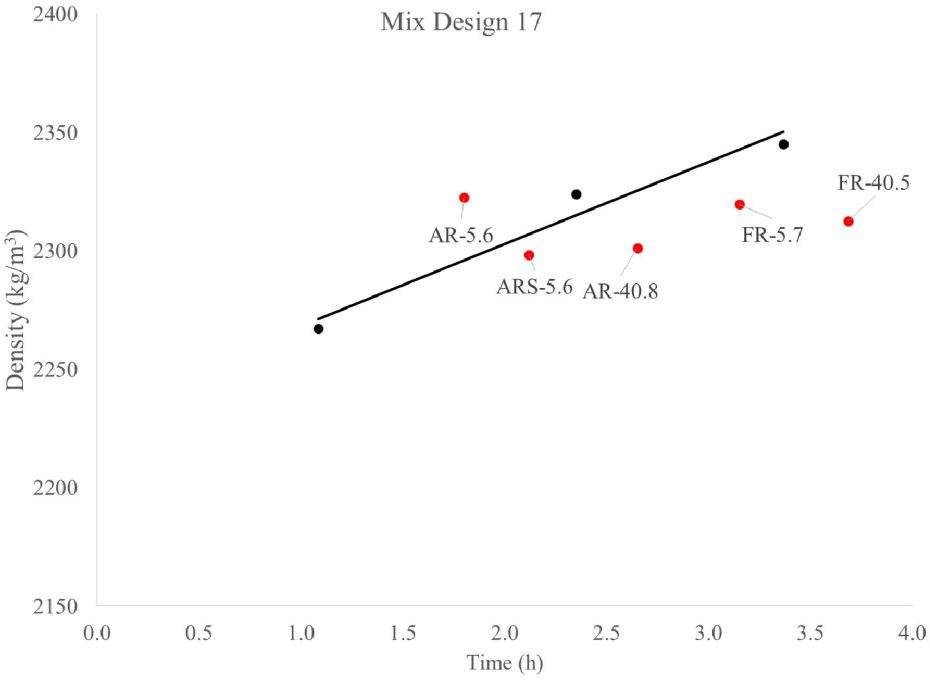

Figure A5.17. Density versus time for non-pumped (black) and pumped (red) samples for mixture 17.

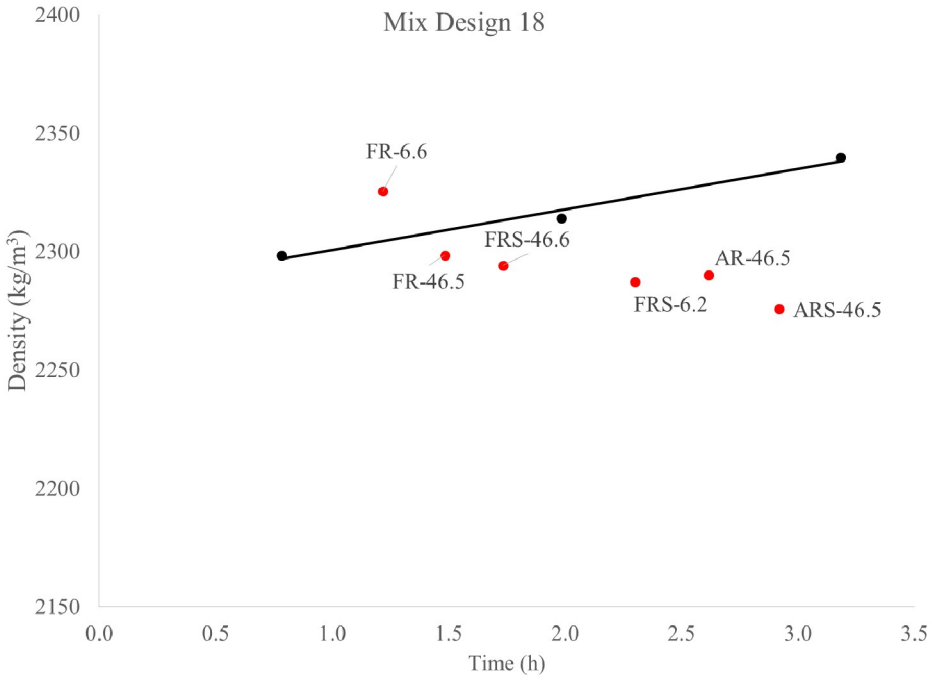

Figure A5.18. Density versus time for non-pumped (black) and pumped (red) samples for mixture 18.

A.6 Fresh concrete air content

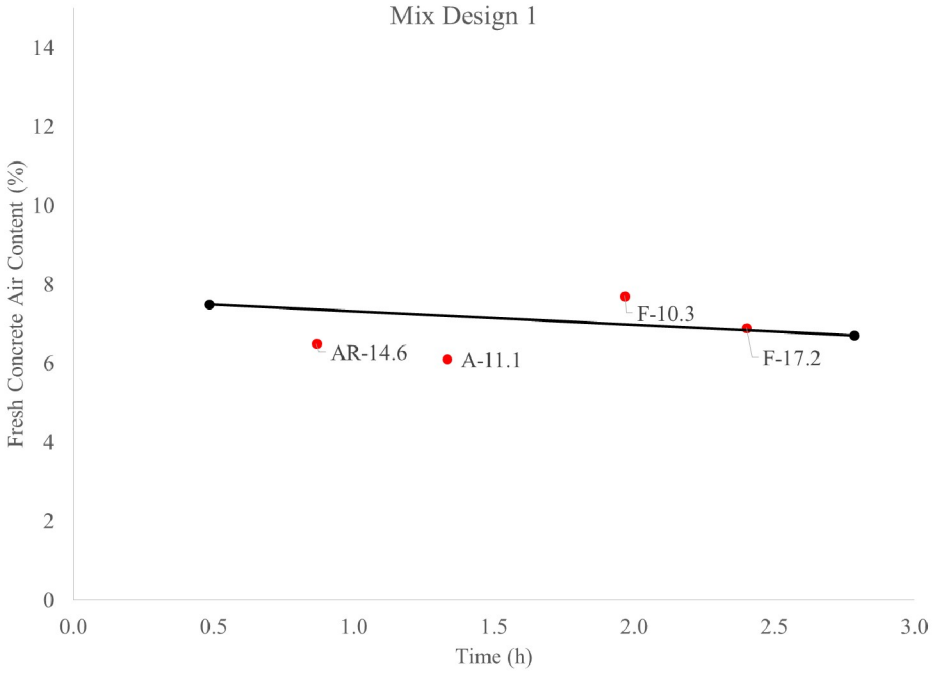

Figure A6.1. Fresh concrete air content versus time for non-pumped (black) and pumped (red) samples for mixture 1.

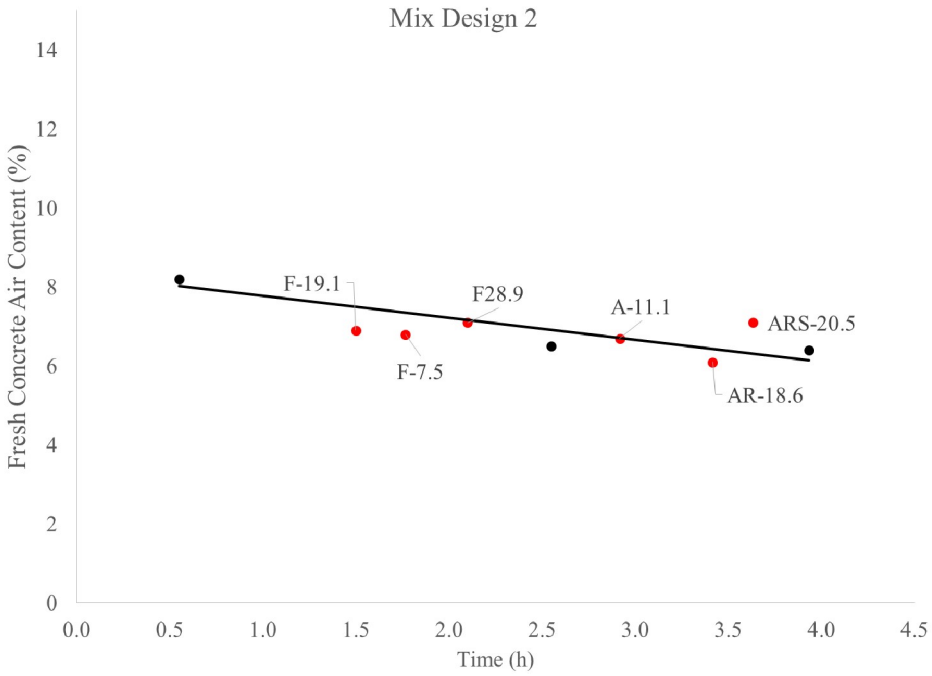

Figure A6.2. Fresh concrete air content versus time for non-pumped (black) and pumped (red) samples for mixture 2.

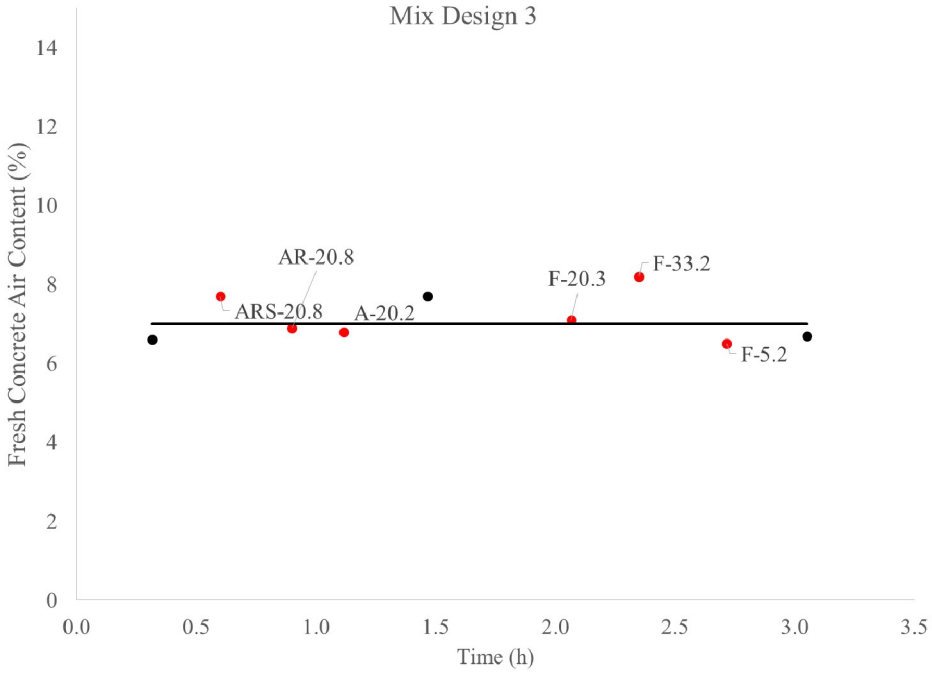

Figure A6.3. Fresh concrete air content versus time for non-pumped (black) and pumped (red) samples for mixture 3.

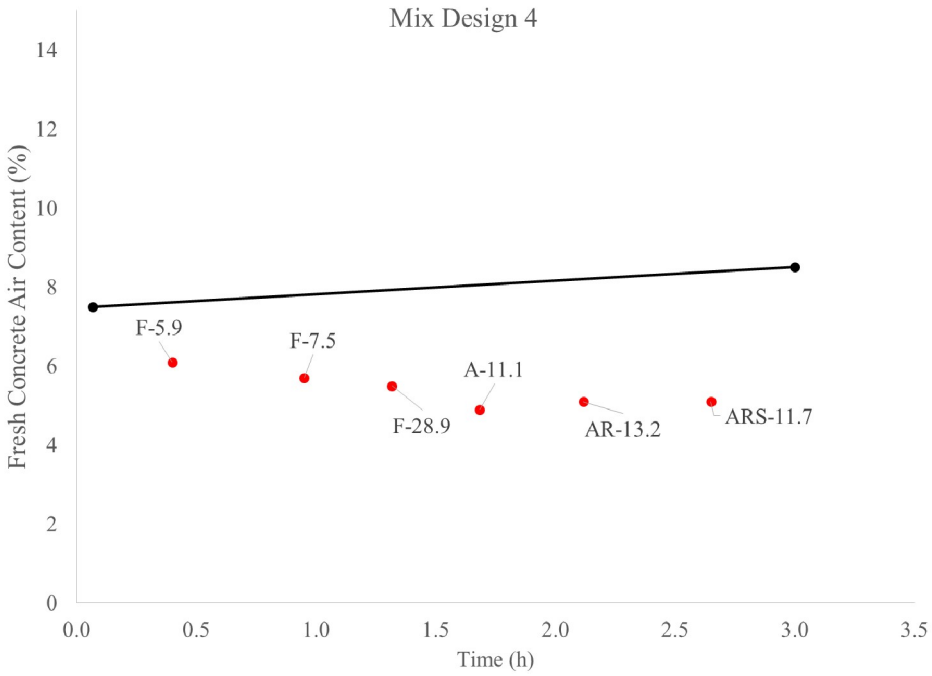

Figure A6.4. Fresh concrete air content versus time for non-pumped (black) and pumped (red) samples for mixture 4.

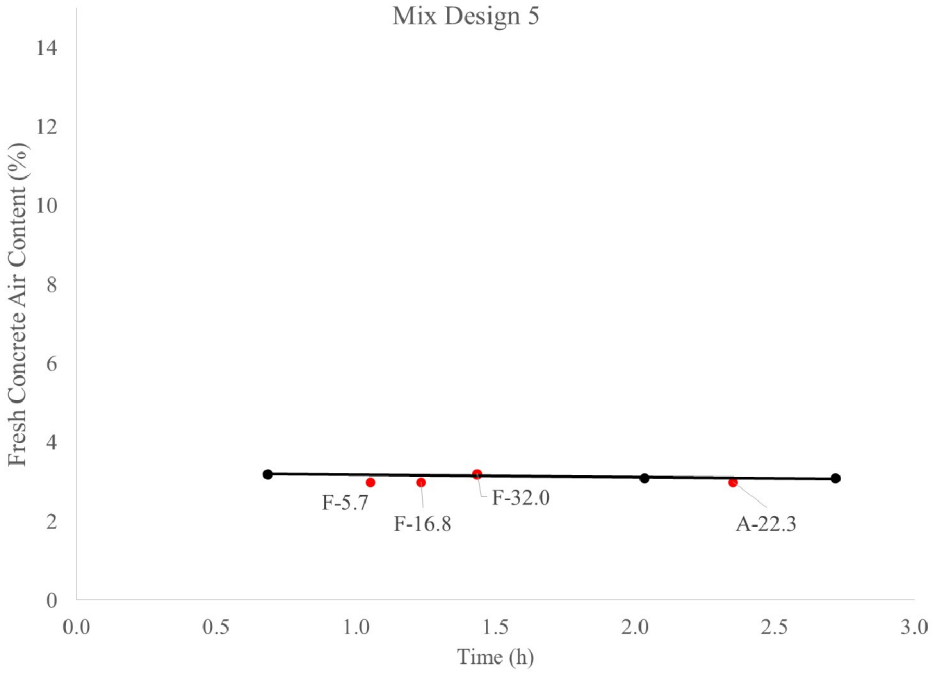

Figure A6.5. Fresh concrete air content versus time for non-pumped (black) and pumped (red) samples for mixture 5.

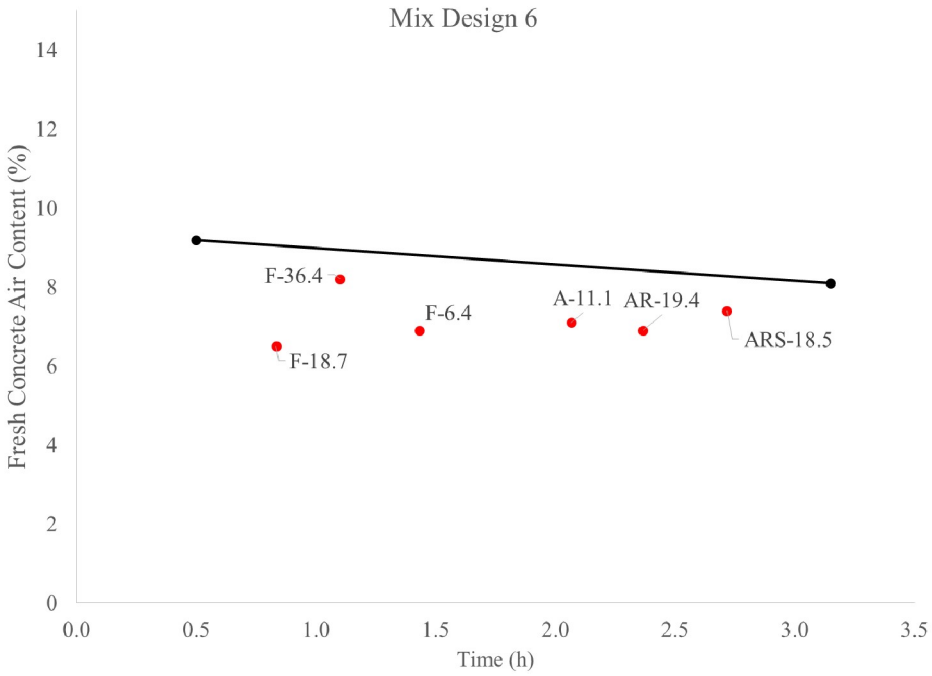

Figure A6.6. Fresh concrete air content versus time for non-pumped (black) and pumped (red) samples for mixture 6.

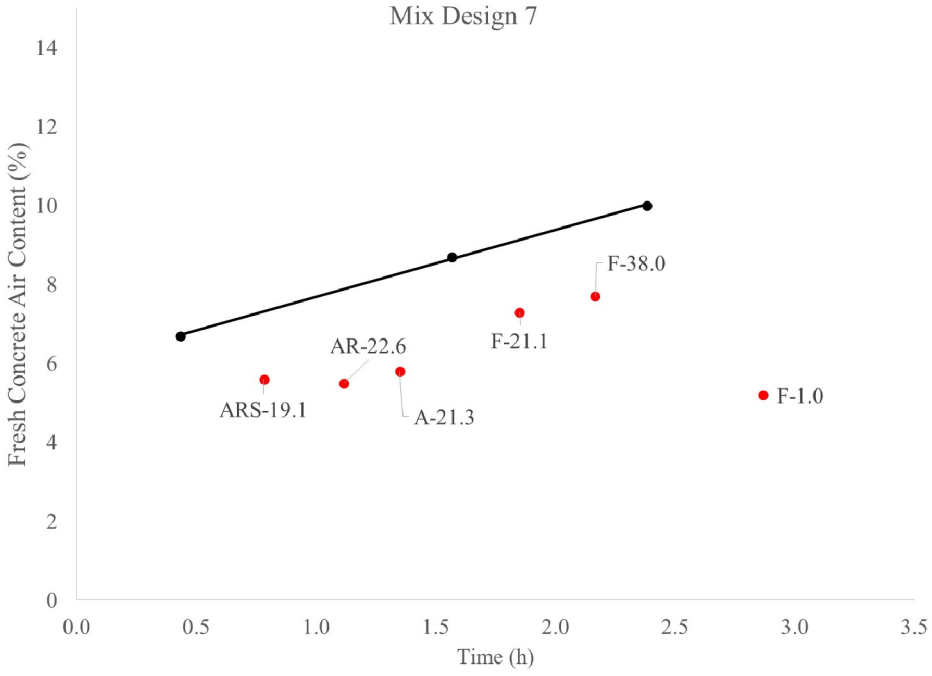

Figure A6.7. Fresh concrete air content versus time for non-pumped (black) and pumped (red) samples for mixture 7.

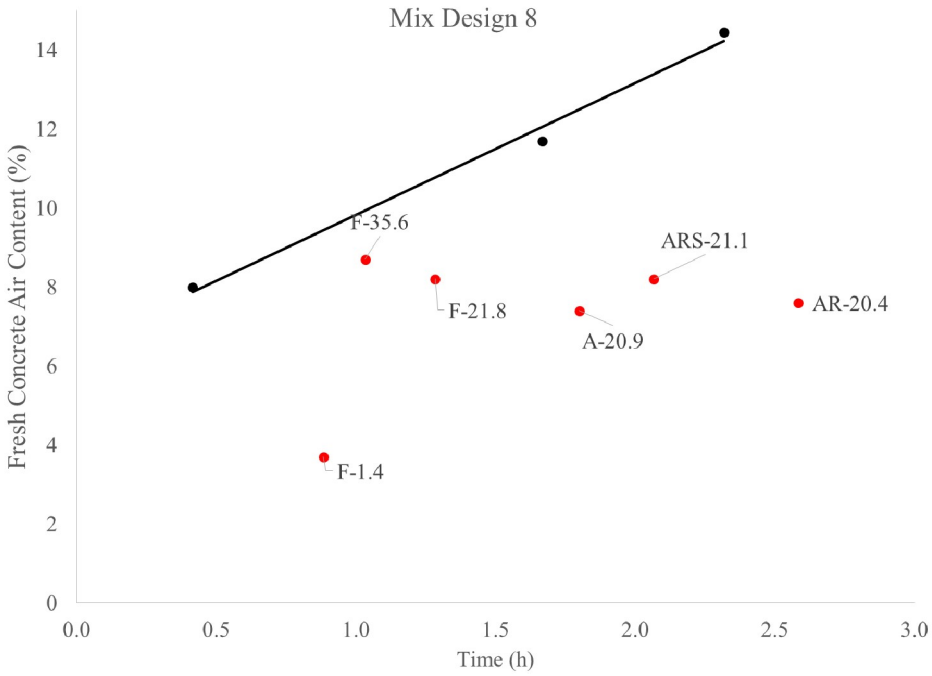

Figure A6.8. Fresh concrete air content versus time for non-pumped (black) and pumped (red) samples for mixture 8.

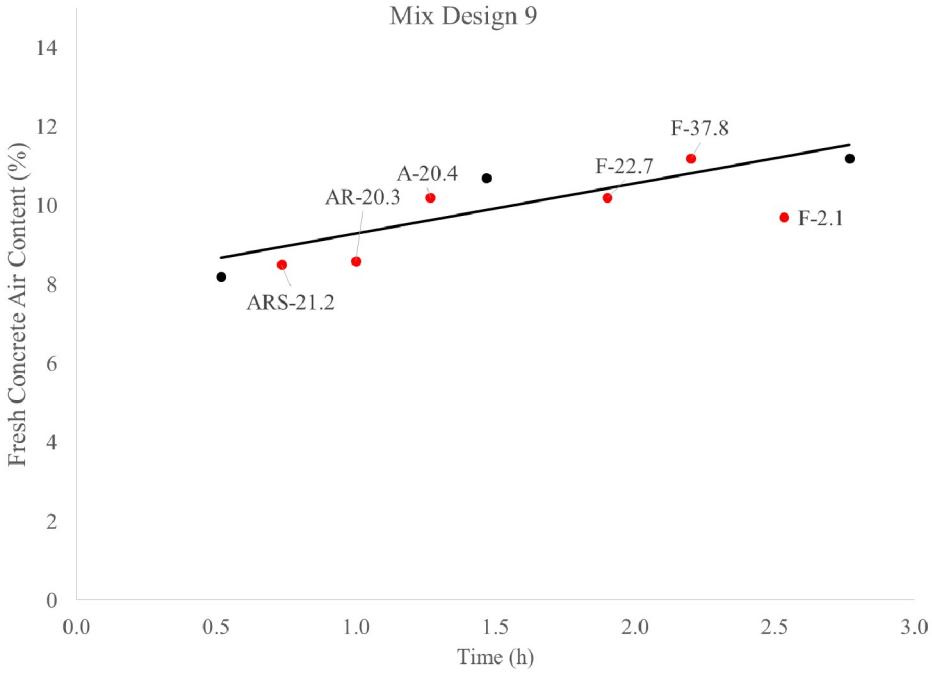

Figure A6.9. Fresh concrete air content versus time for non-pumped (black) and pumped (red) samples for mixture 9.

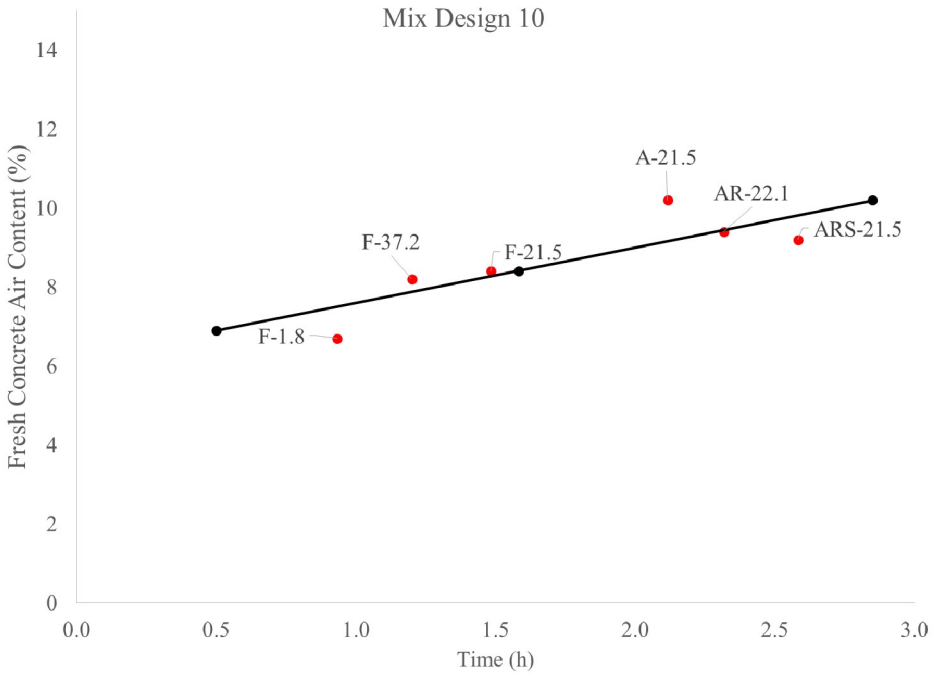

Figure A6.10. Fresh concrete air content versus time for non-pumped (black) and pumped (red) samples for mixture 10.

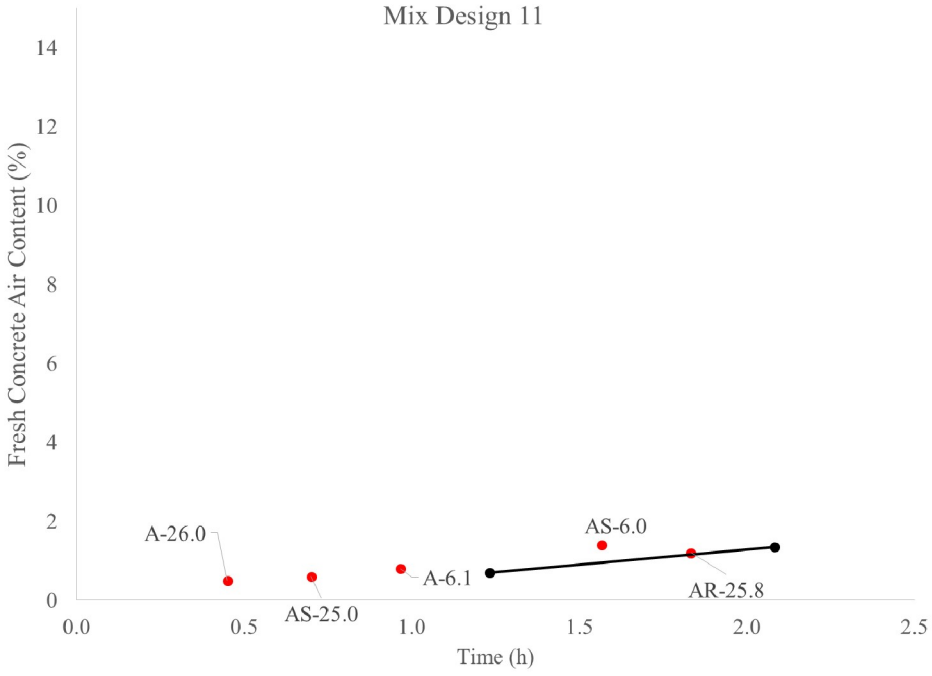

Figure A6.11. Fresh concrete air content versus time for non-pumped (black) and pumped (red) samples for mixture 11.

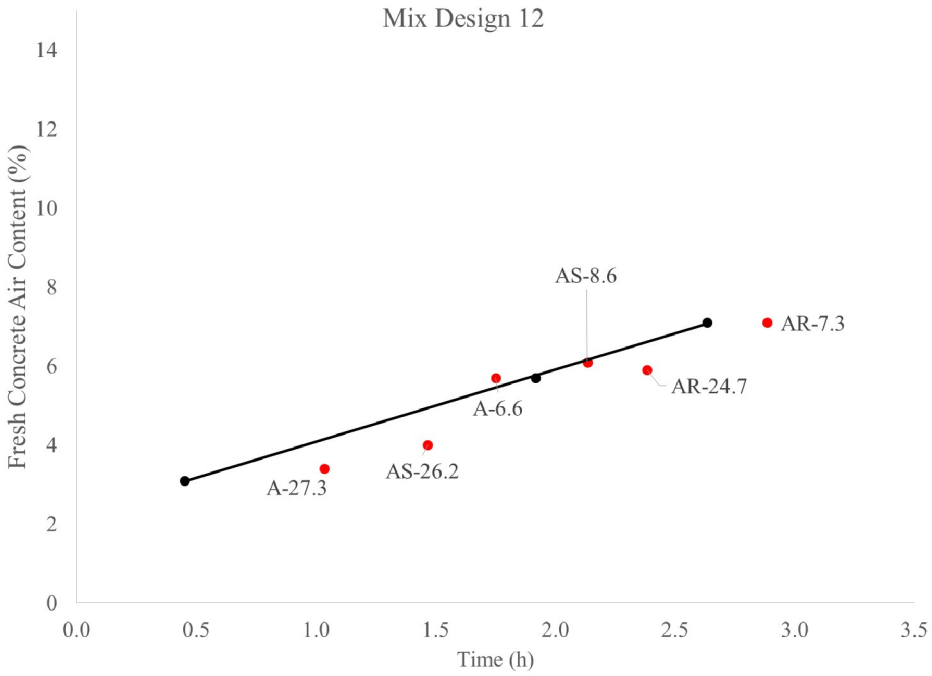

Figure A6.12. Fresh concrete air content versus time for non-pumped (black) and pumped (red) samples for mixture 12.

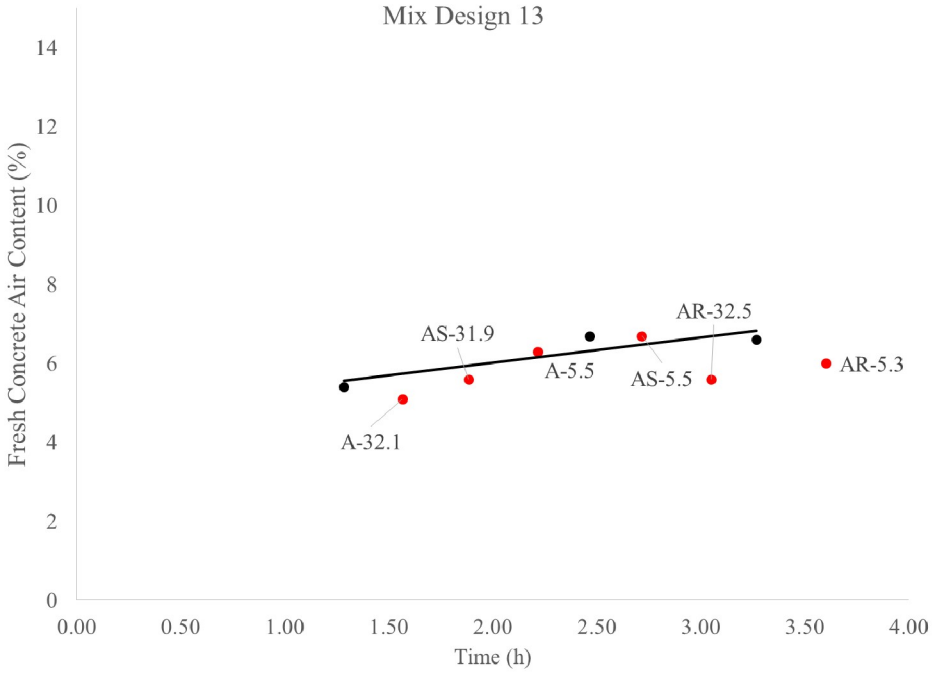

Figure A6.13. Fresh concrete air content versus time for non-pumped (black) and pumped (red) samples for mixture 13.

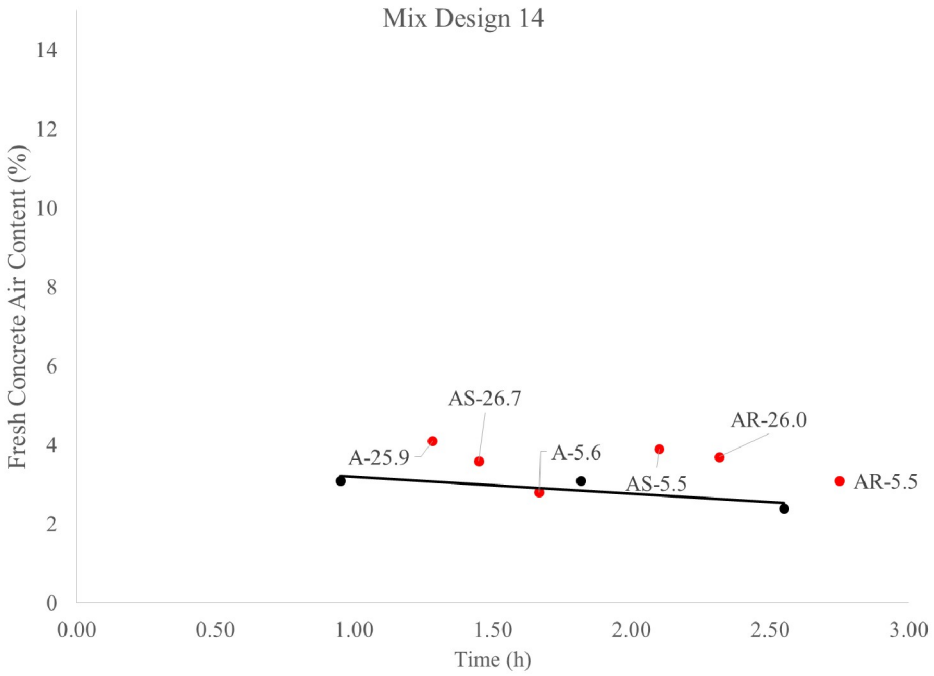

Figure A6.14. Fresh concrete air content versus time for non-pumped (black) and pumped (red) samples for mixture 14.

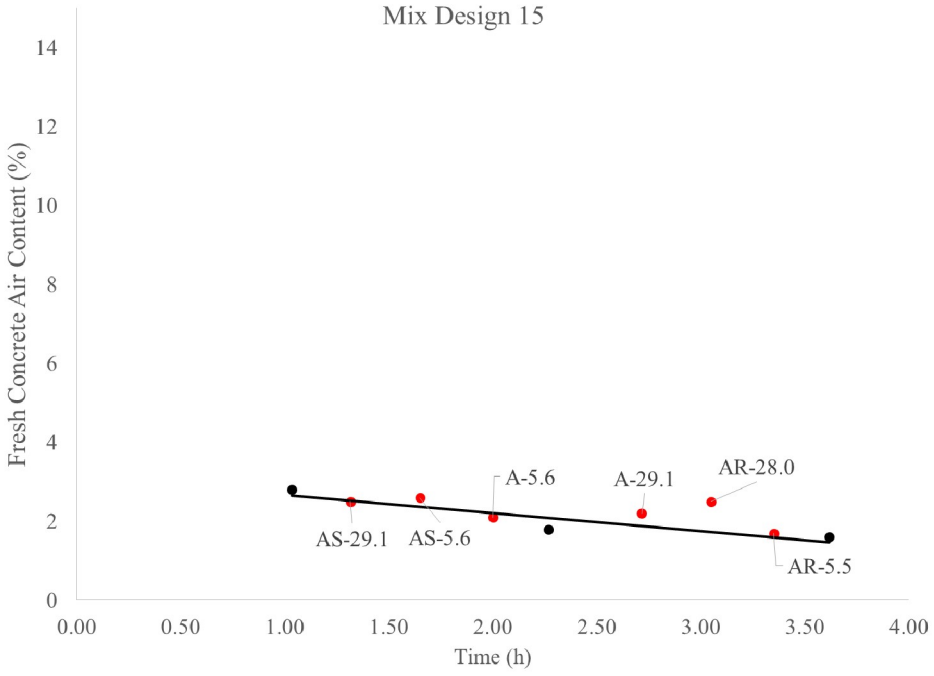

Figure A6.15. Fresh concrete air content versus time for non-pumped (black) and pumped (red) samples for mixture 15.

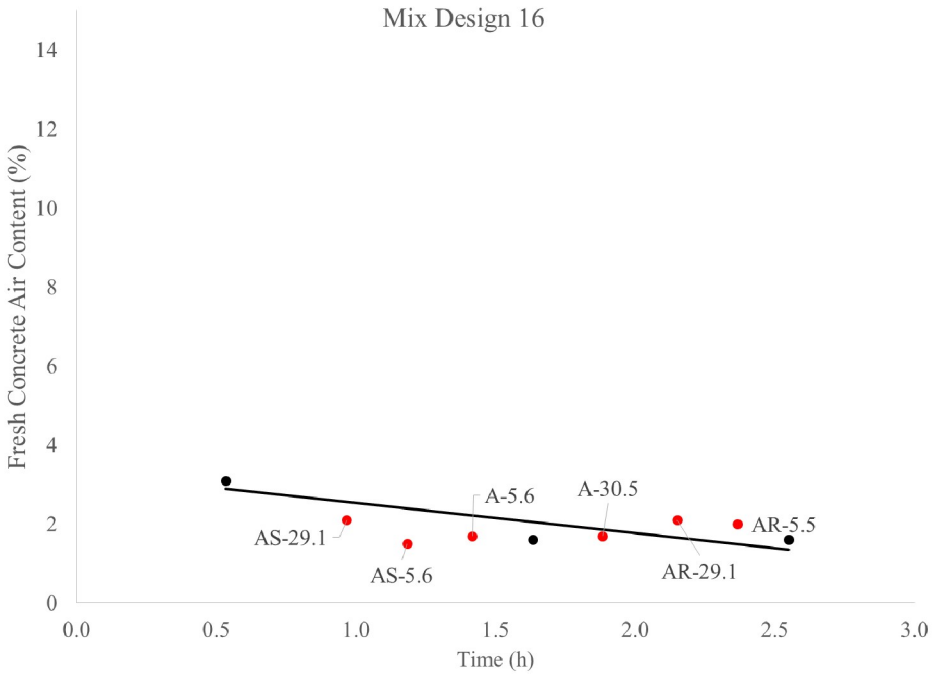

Figure A6.16. Fresh concrete air content versus time for non-pumped (black) and pumped (red) samples for mixture 16.

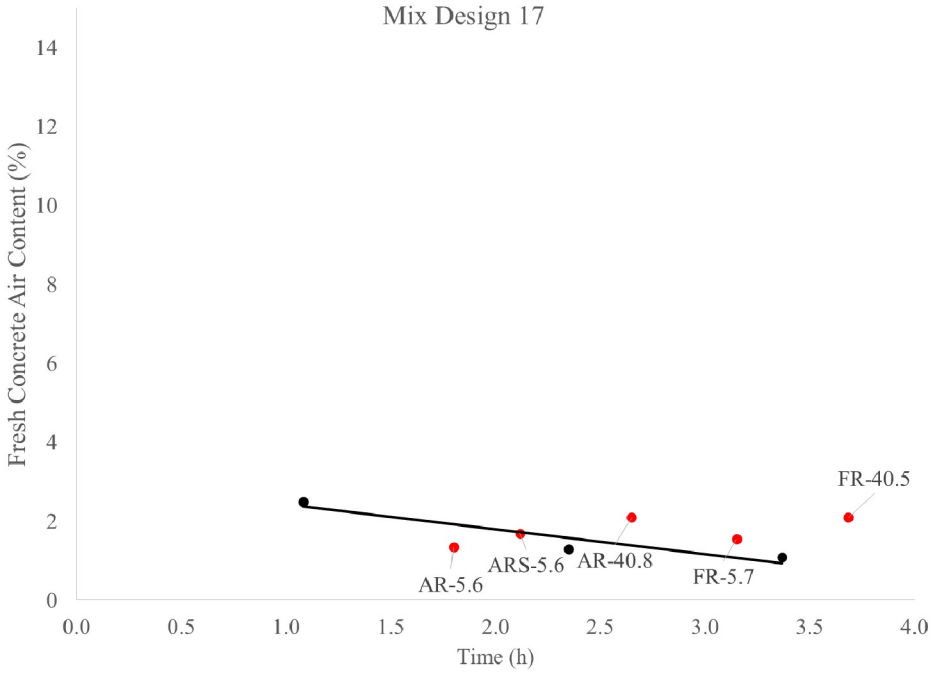

Figure A6.17. Fresh concrete air content versus time for non-pumped (black) and pumped (red) samples for mixture 17.

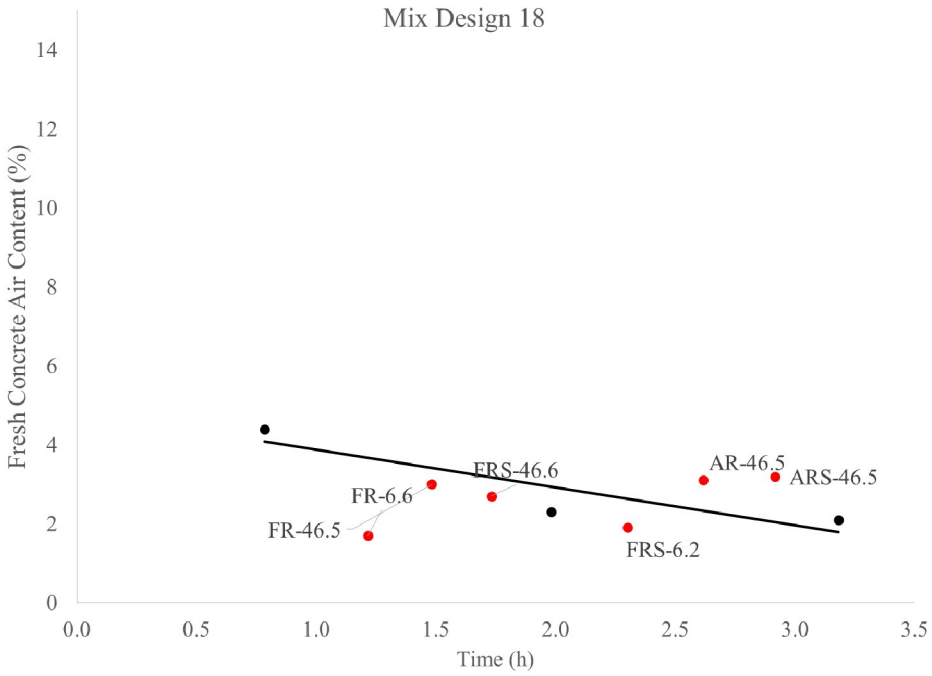

Figure A6.18. Fresh concrete air content versus time for non-pumped (black) and pumped (red) samples for mixture 18.

Appendix B: Changes in hardened concrete properties due to pumping

This appendix contains all time-plots of hardened properties for non-pumped (black) and pumped (red) samples;

- Section B.1: Gravimetric air content from cylinders
- Section B.2: Air content from Rapid Air analyzer
- Section B.3: Compressive strength
- Section B.4: Spacing factor
- Section B.5: Freeze-thaw resistance
- Section B.6: Scaling of top surfaces

B.1 Gravimetric air content from cylinders

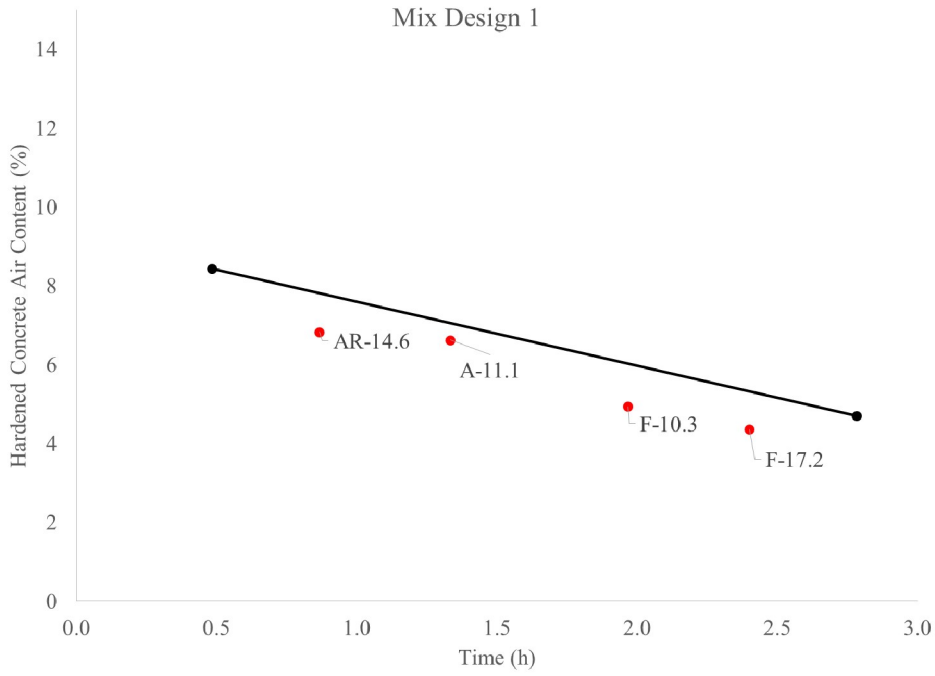

Figure B1.1. Hardened air content as a function of time for non-pumped (black) and pumped (red) samples for mixture 1.

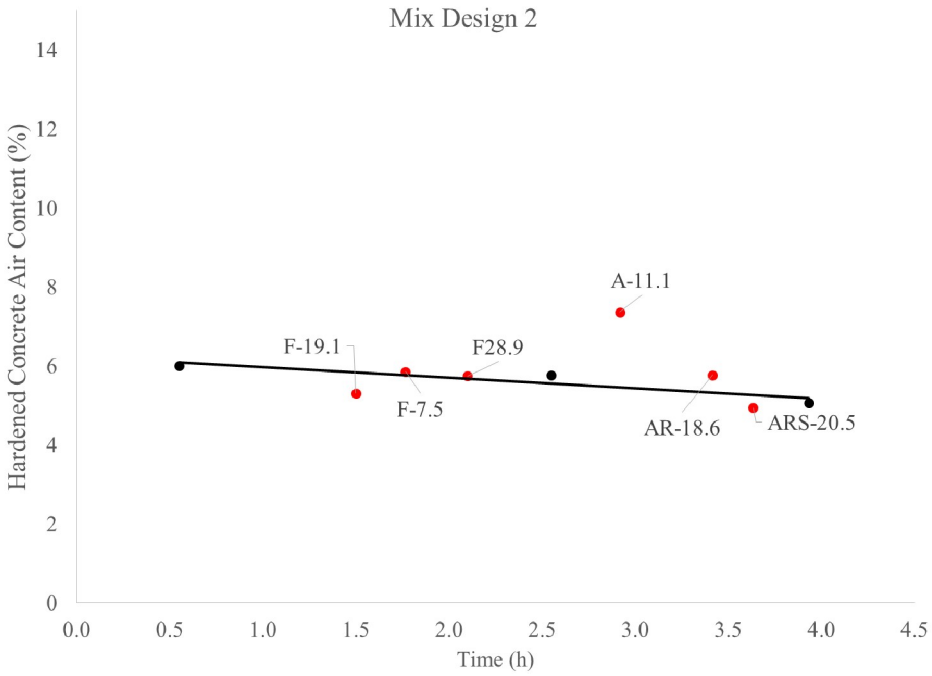

Figure B1.2. Hardened air content as a function of time for non-pumped (black) and pumped (red) samples for mixture 2.

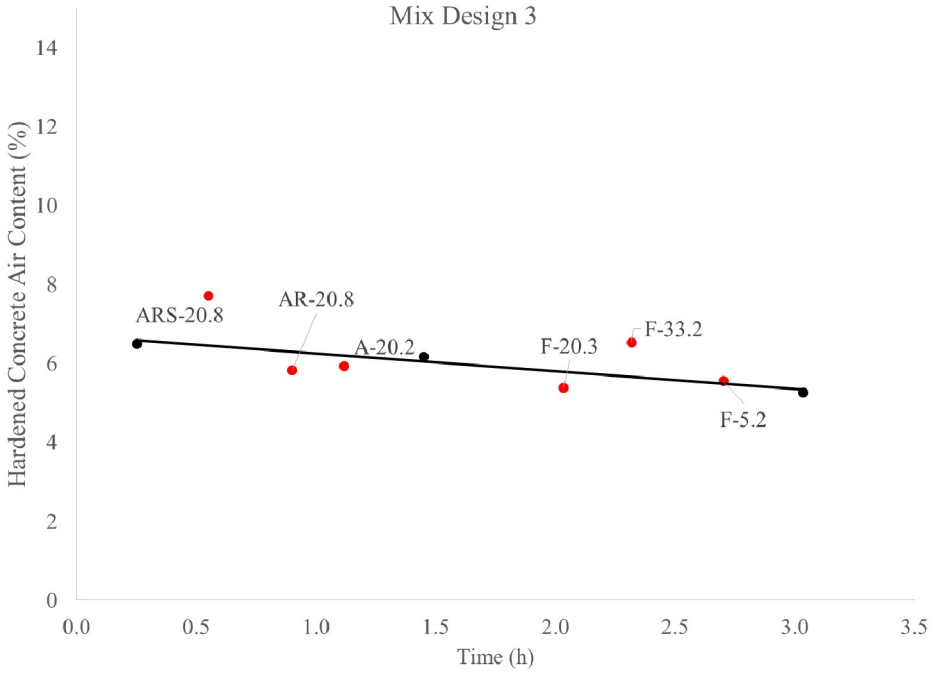

Figure B1.3. Hardened air content as a function of time for non-pumped (black) and pumped (red) samples for mixture 3.

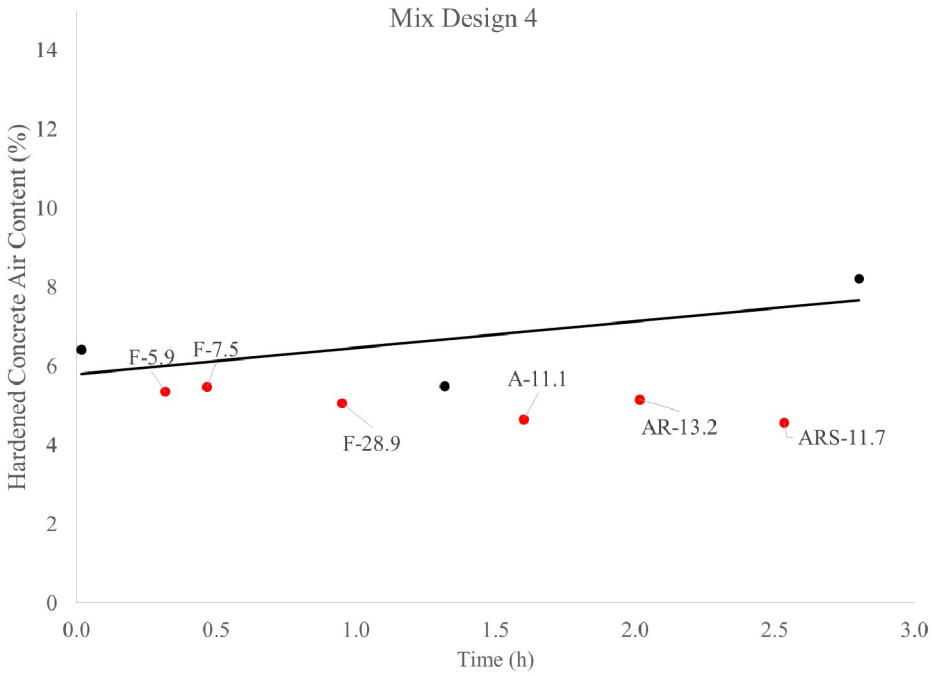

Figure B1.4. Hardened air content as a function of time for non-pumped (black) and pumped (red) samples for mixture 4.

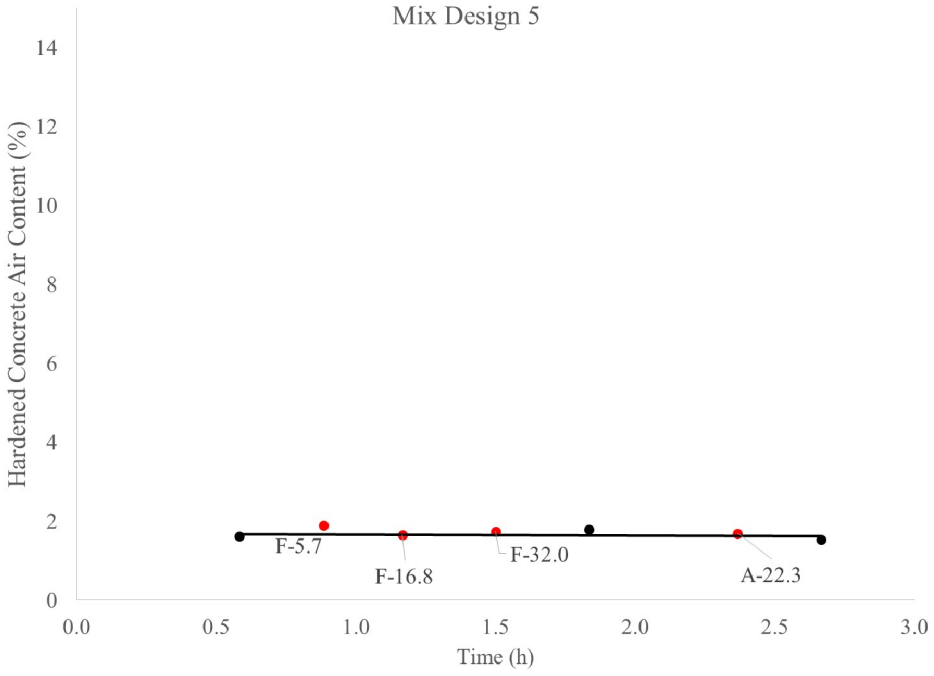

Figure B1.5. Hardened air content as a function of time for non-pumped (black) and pumped (red) samples for mixture 5.

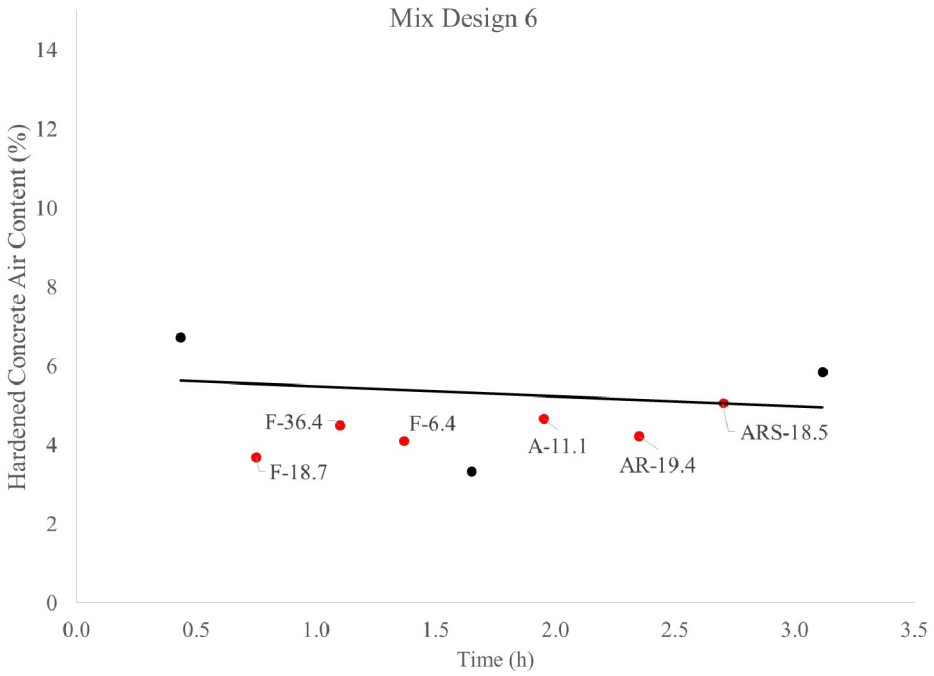

Figure B1.6. Hardened air content as a function of time for non-pumped (black) and pumped (red) samples for mixture 6.

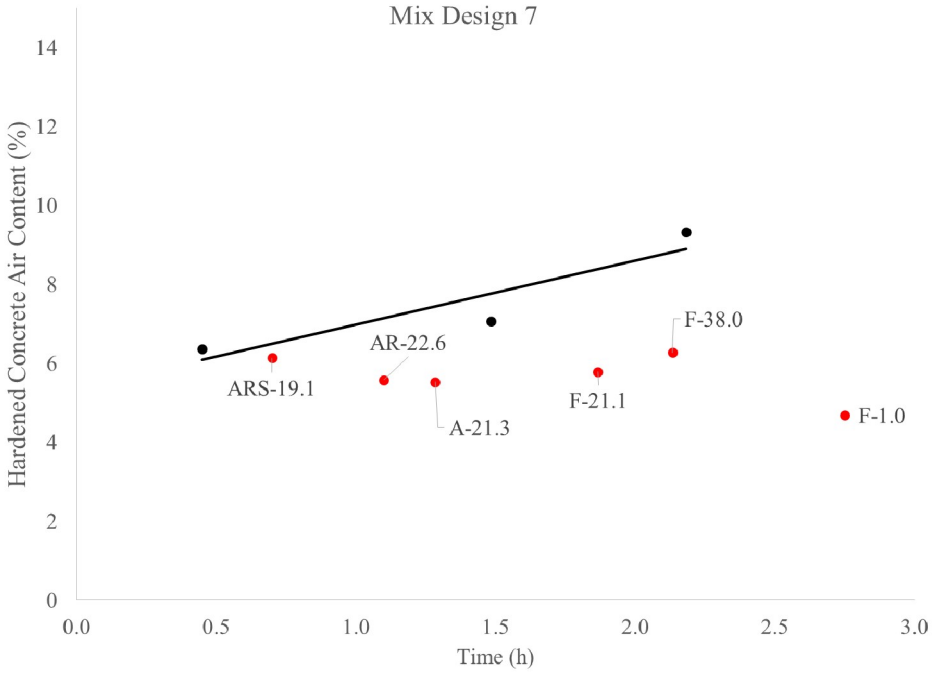

Figure B1.7. Hardened air content as a function of time for non-pumped (black) and pumped (red) samples for mixture 7.

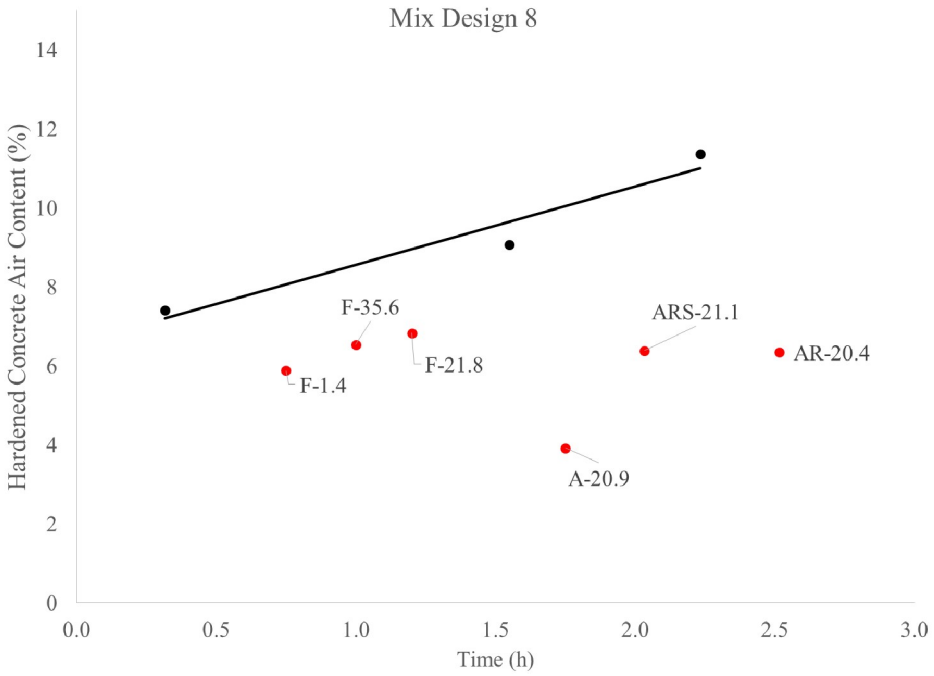

Figure B1.8. Hardened air content as a function of time for non-pumped (black) and pumped (red) samples for mixture 8.

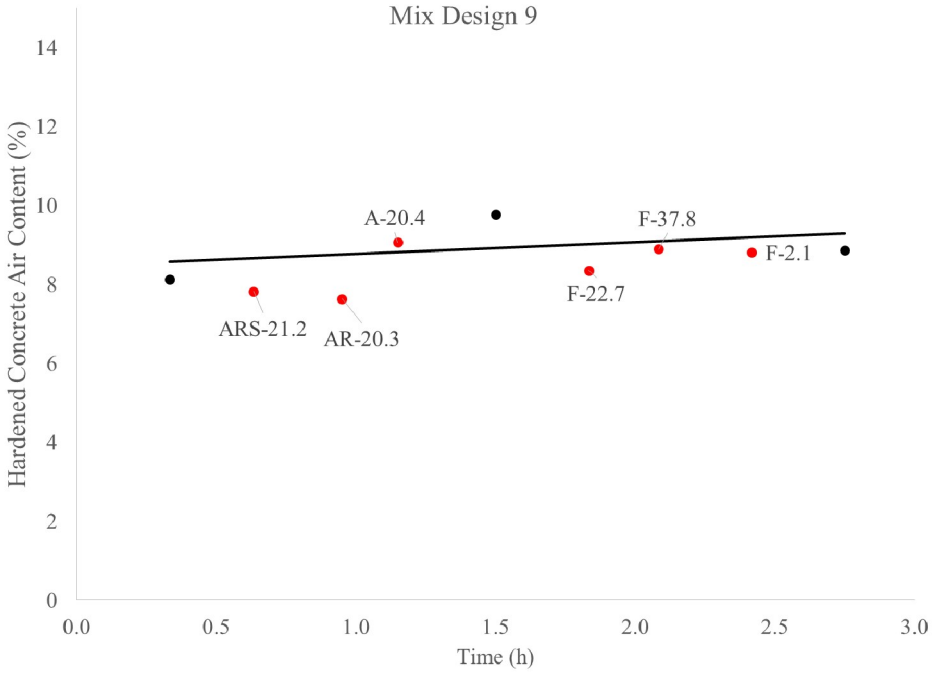

Figure B1.9. Hardened air content as a function of time for non-pumped (black) and pumped (red) samples for mixture 9.

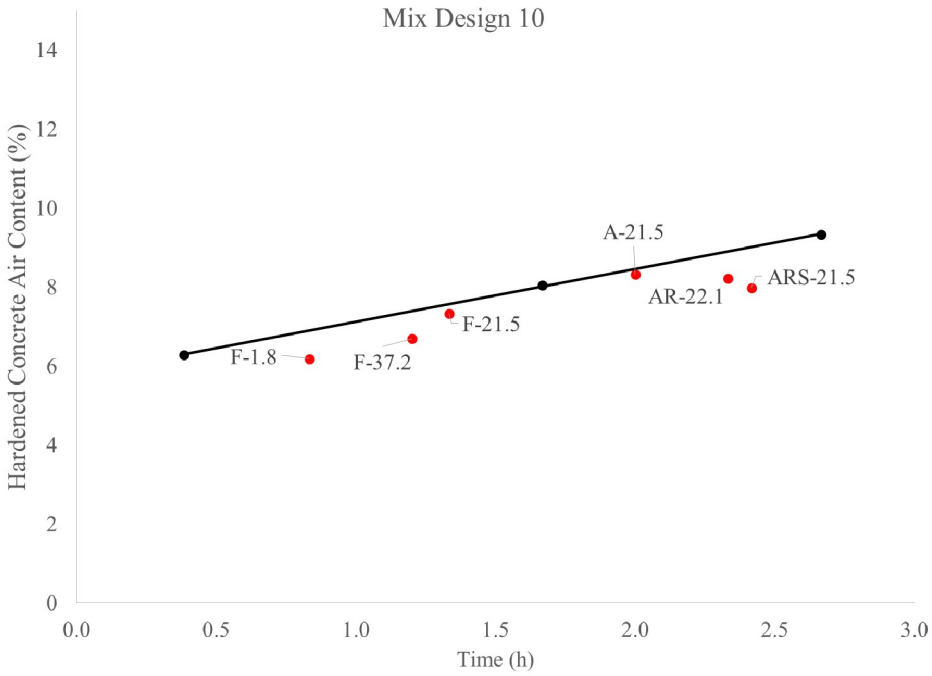

Figure B1.10. Hardened air content as a function of time for non-pumped (black) and pumped (red) samples for mixture 10.

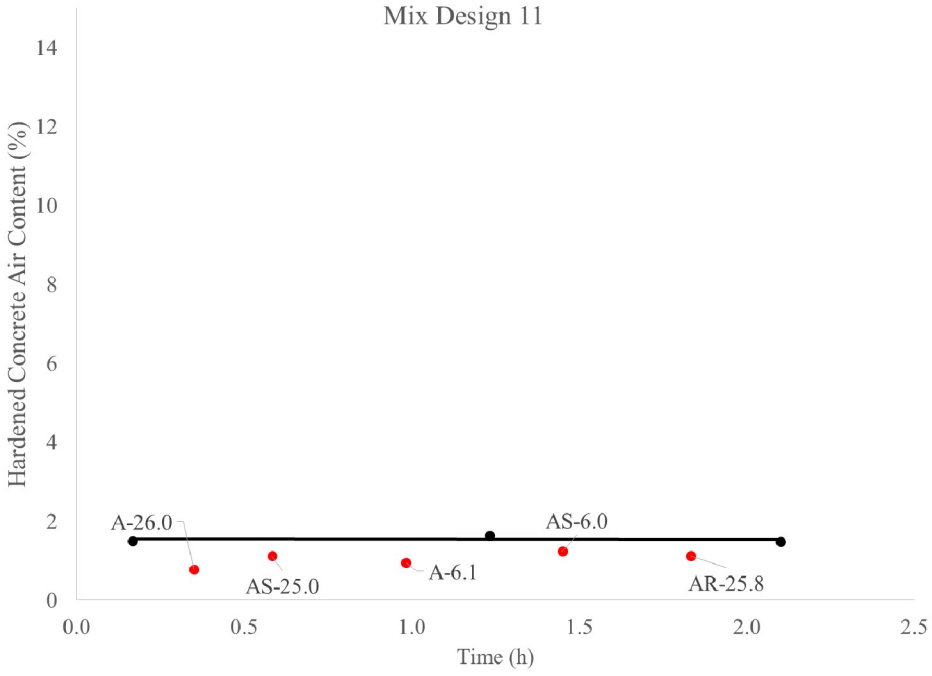

Figure B1.11. Hardened air content as a function of time for non-pumped (black) and pumped (red) samples for mixture 11.

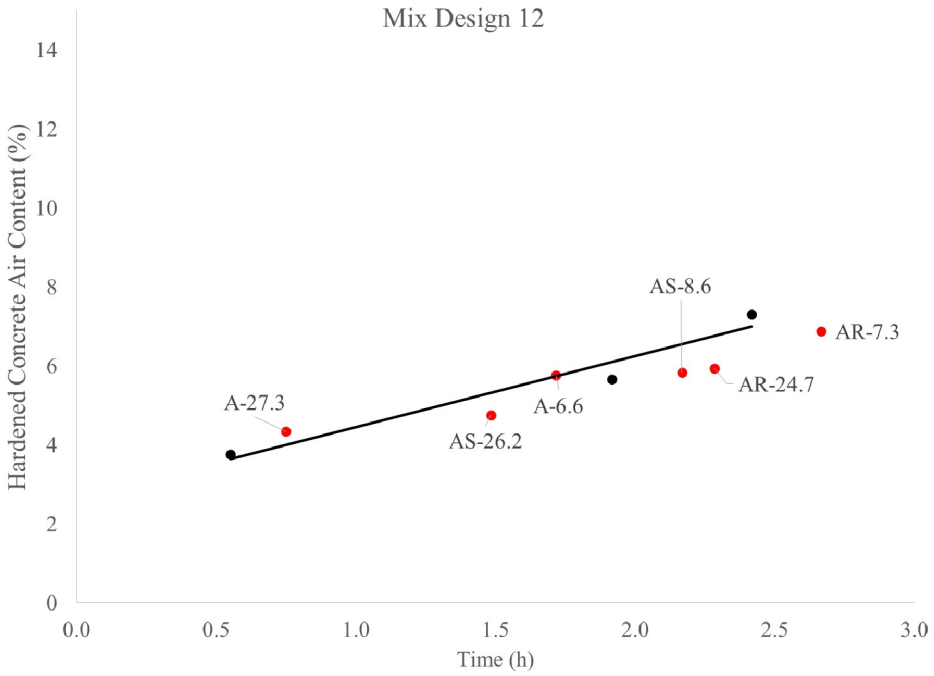

Figure B1.12. Hardened air content as a function of time for non-pumped (black) and pumped (red) samples for mixture 12.

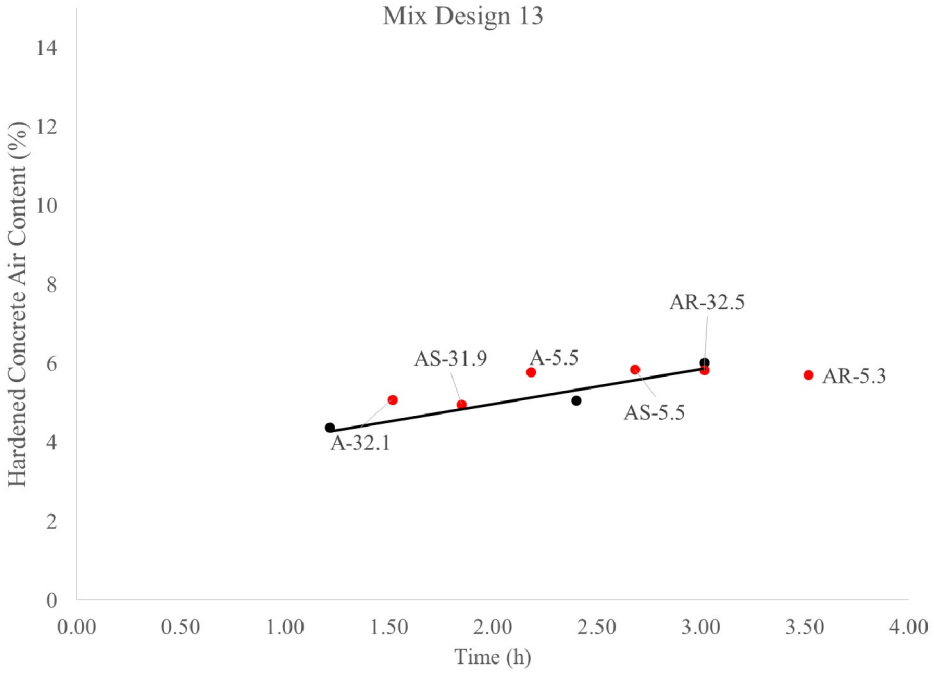

Figure B1.13. Hardened air content as a function of time for non-pumped (black) and pumped (red) samples for mixture 13.

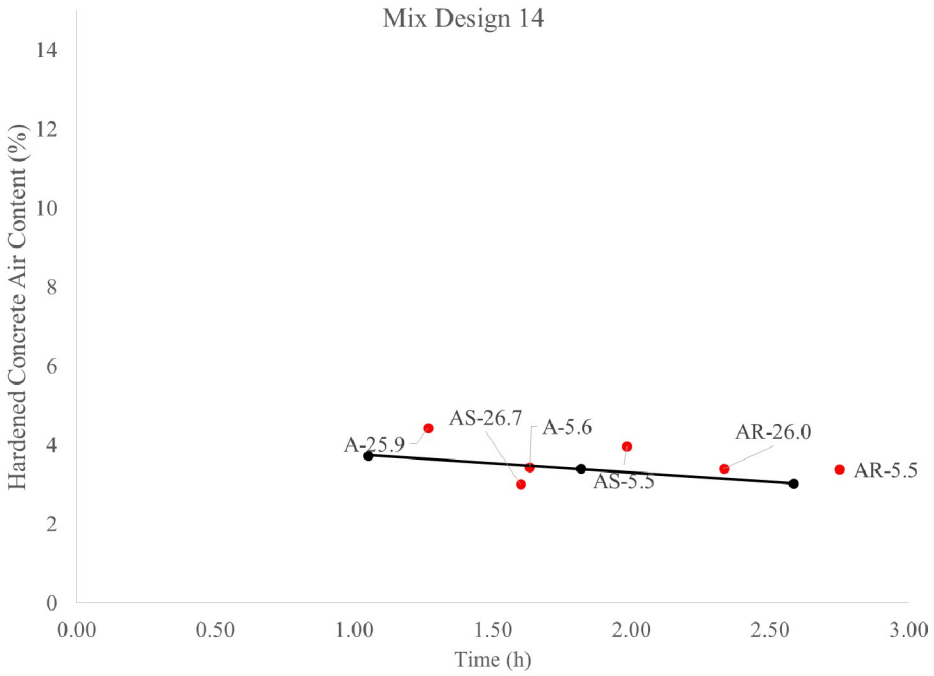

Figure B1.14. Hardened air content as a function of time for non-pumped (black) and pumped (red) samples for mixture 14.

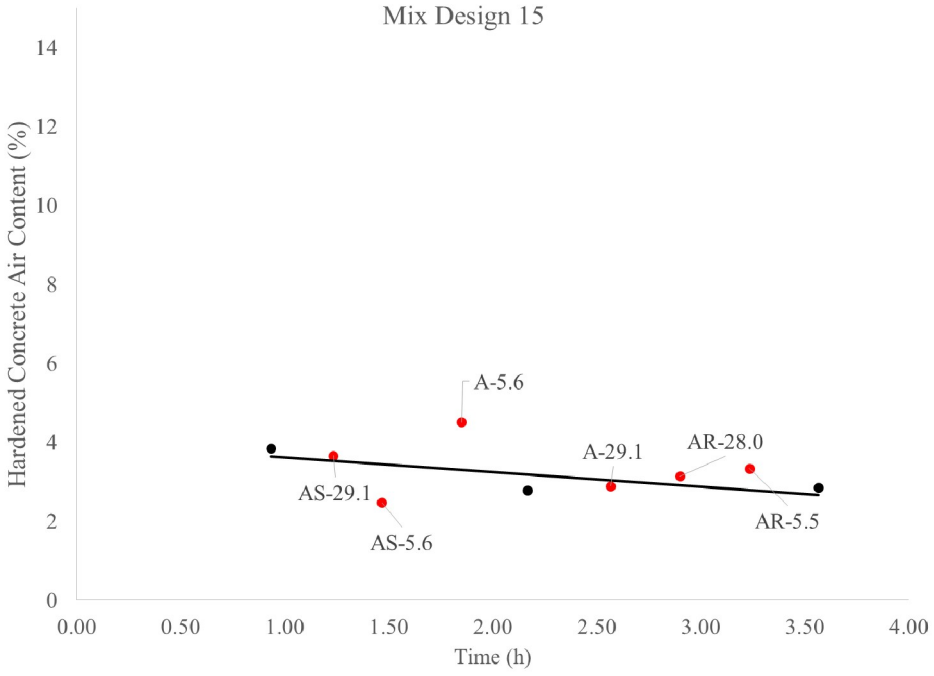

Figure B1.15. Hardened air content as a function of time for non-pumped (black) and pumped (red) samples for mixture 15.

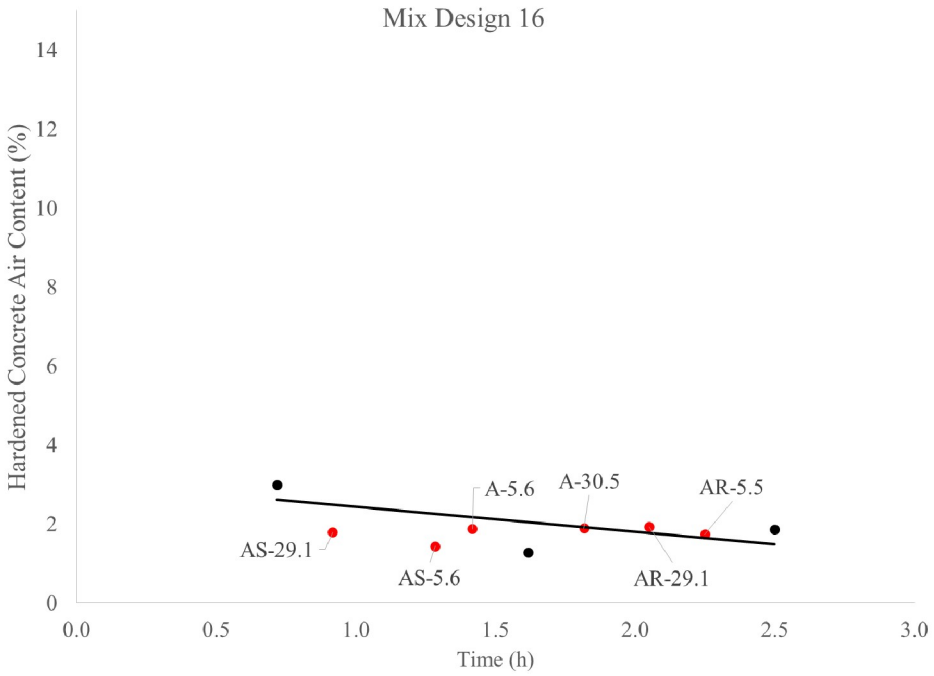

Figure B1.16. Hardened air content as a function of time for non-pumped (black) and pumped (red) samples for mixture 16.

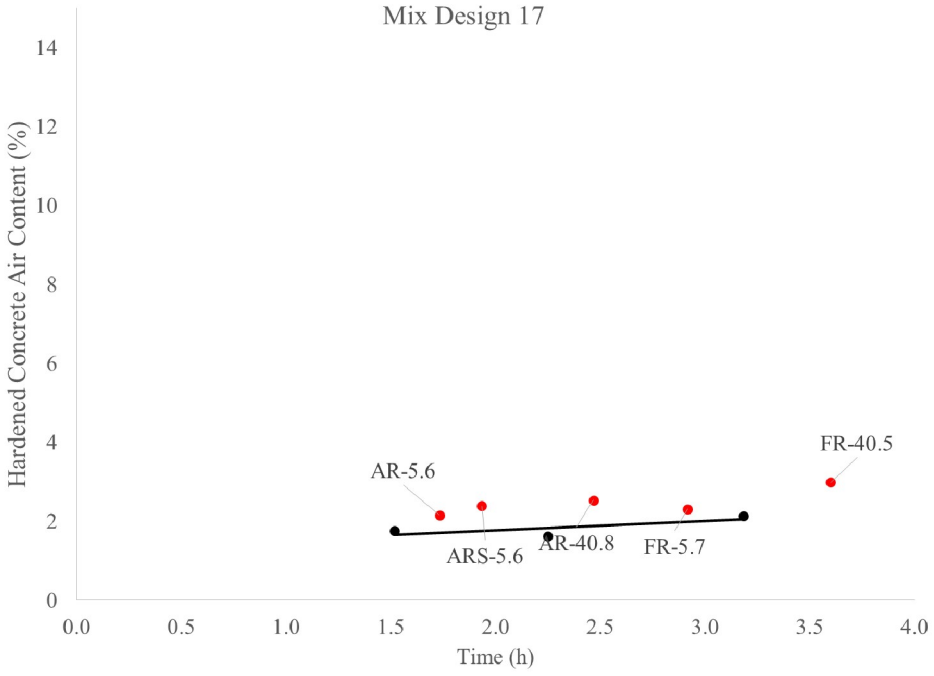

Figure B1.17. Hardened air content as a function of time for non-pumped (black) and pumped (red) samples for mixture 17.

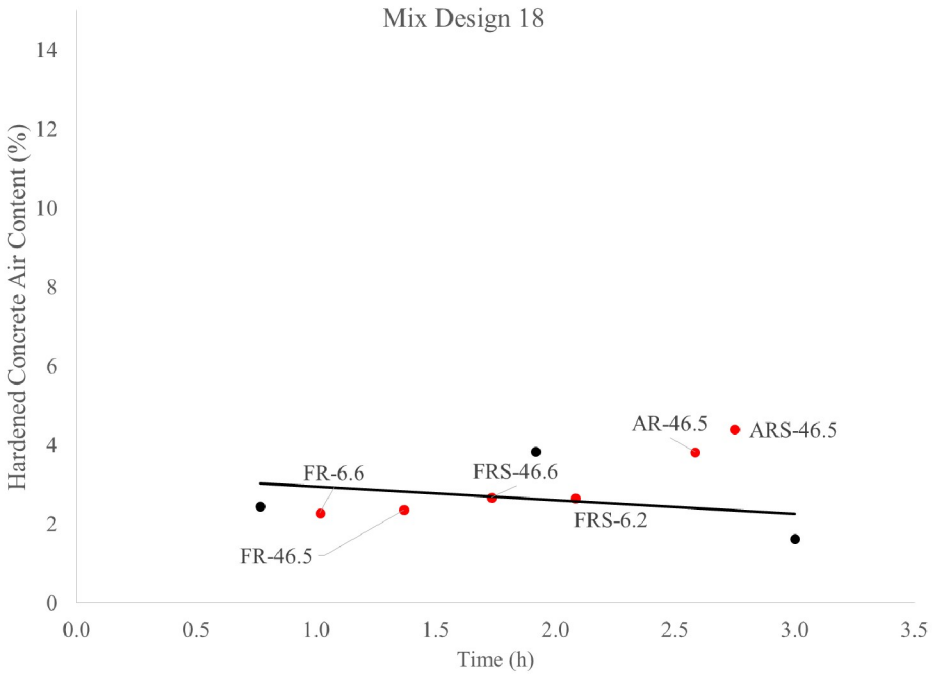

Figure B1.18. Hardened air content as a function of time for non-pumped (black) and pumped (red) samples for mixture 18.

B.2 Air content from Rapid Air Void Analyzer

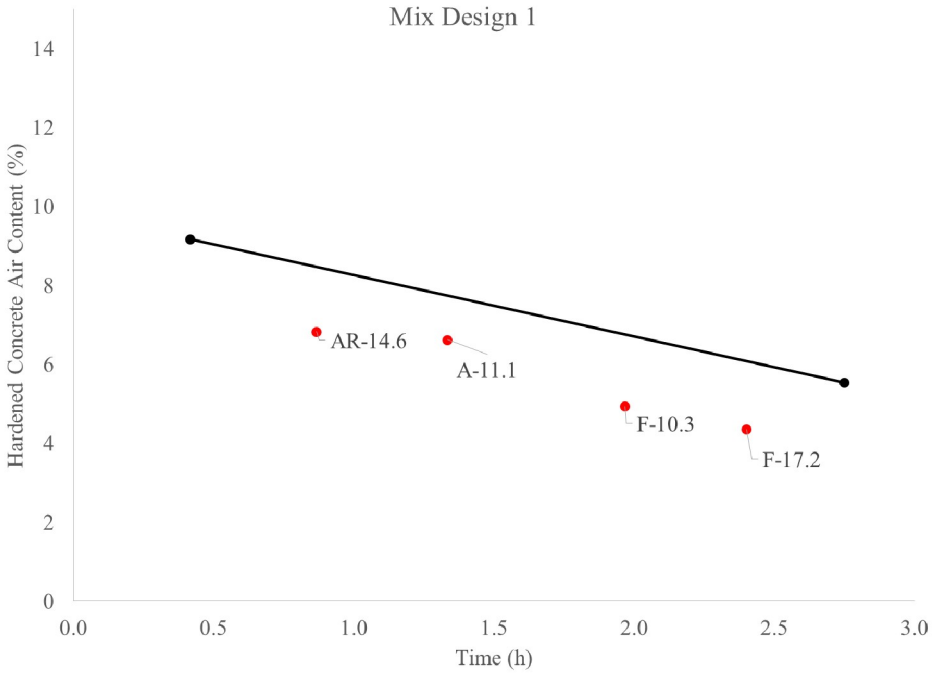

Figure B2.1. Hardened air content from Rapid Air as a function of time for non-pumped (black) and pumped (red) samples for mixture 1.

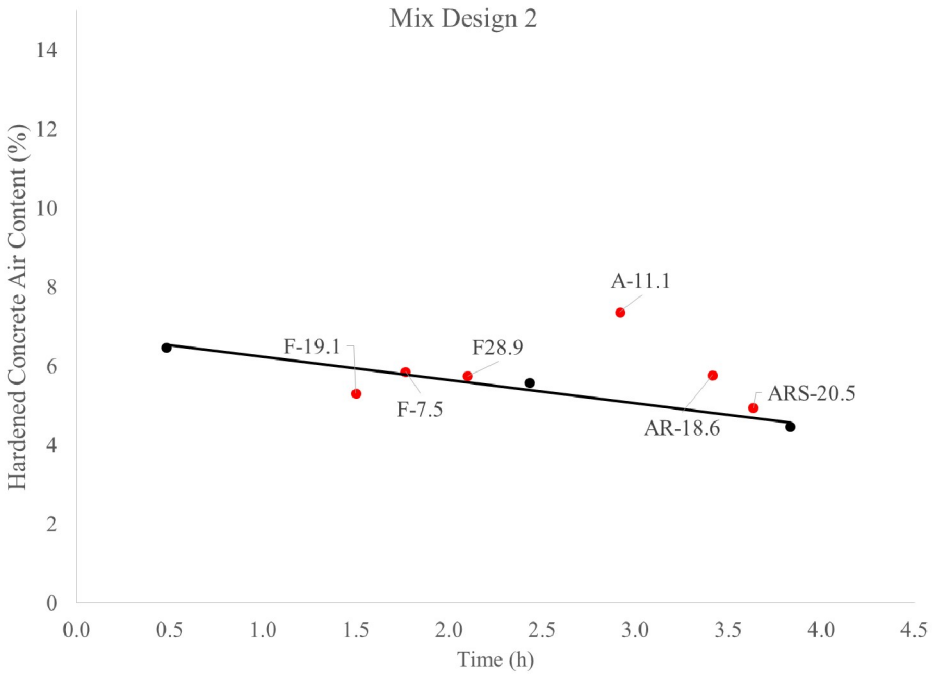

Figure B2.2. Hardened air content from Rapid Air as a function of time for non-pumped (black) and pumped (red) samples for mixture 2.

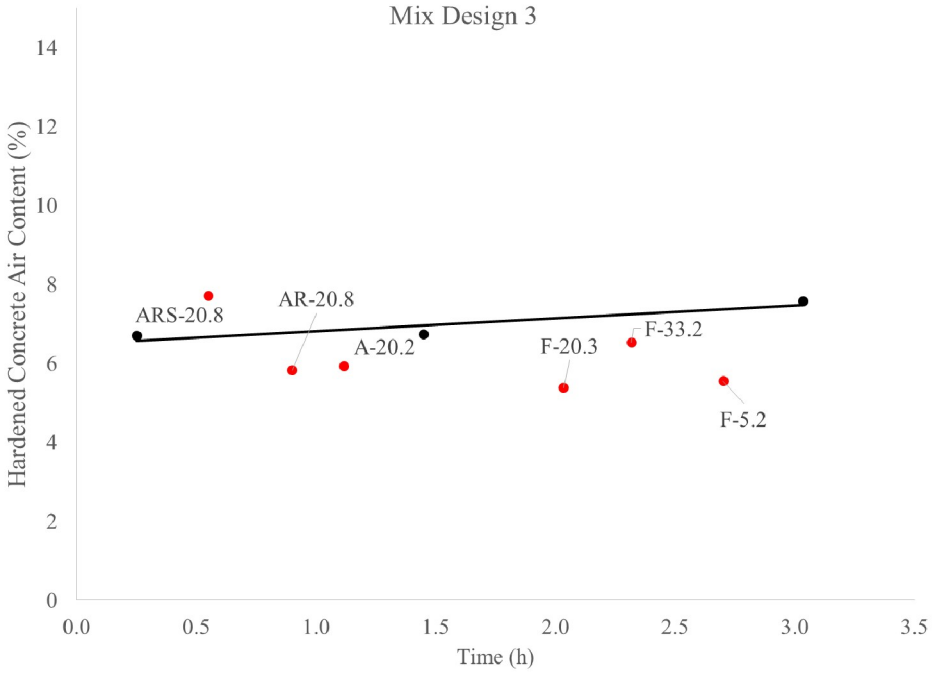

Figure B2.3. Hardened air content from Rapid Air as a function of time for non-pumped (black) and pumped (red) samples for mixture 3.

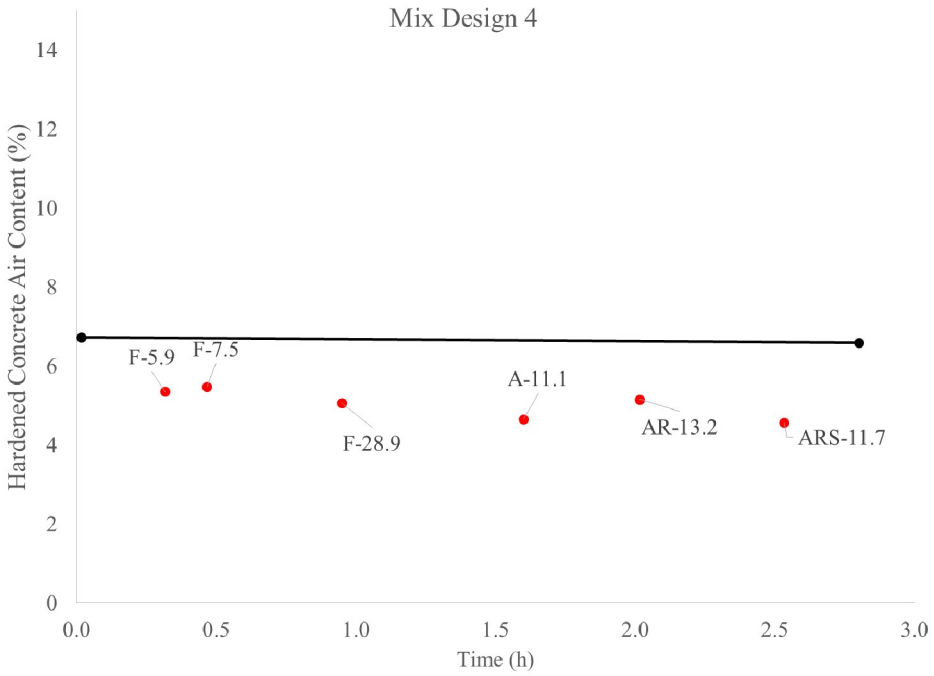

Figure B2.4. Hardened air content from Rapid Air as a function of time for non-pumped (black) and pumped (red) samples for mixture 4.

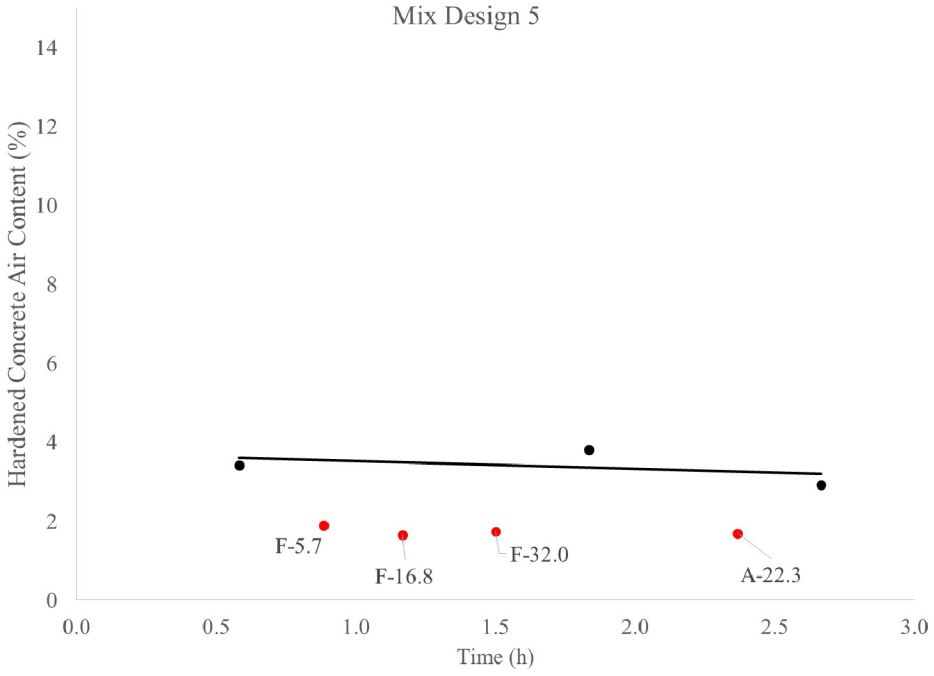

Figure B2.5. Hardened air content from Rapid Air as a function of time for non-pumped (black) and pumped (red) samples for mixture 5.

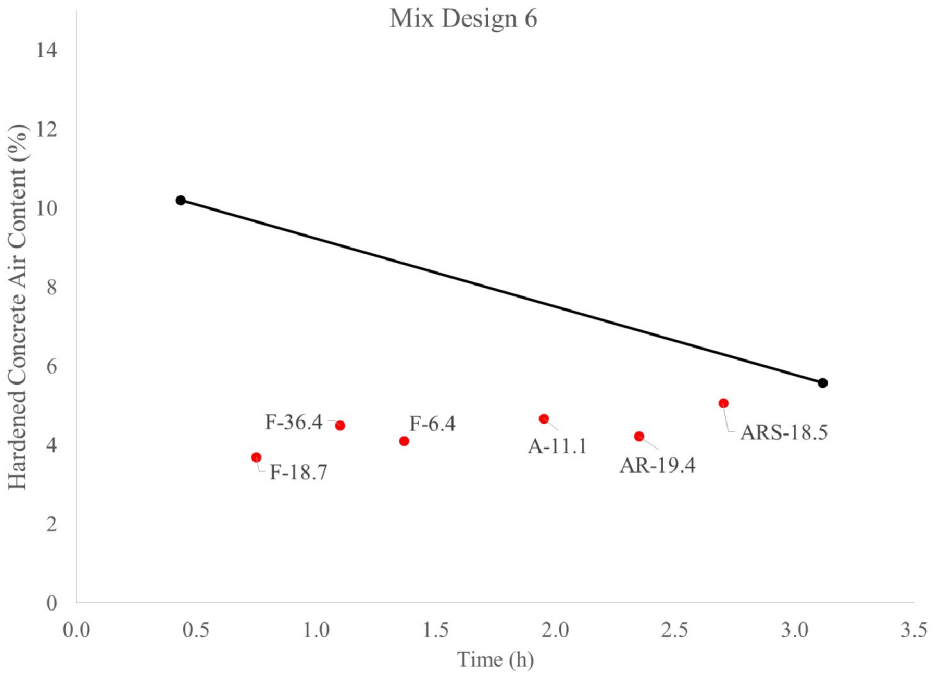

Figure B2.6. Hardened air content from Rapid Air as a function of time for non-pumped (black) and pumped (red) samples for mixture 6.

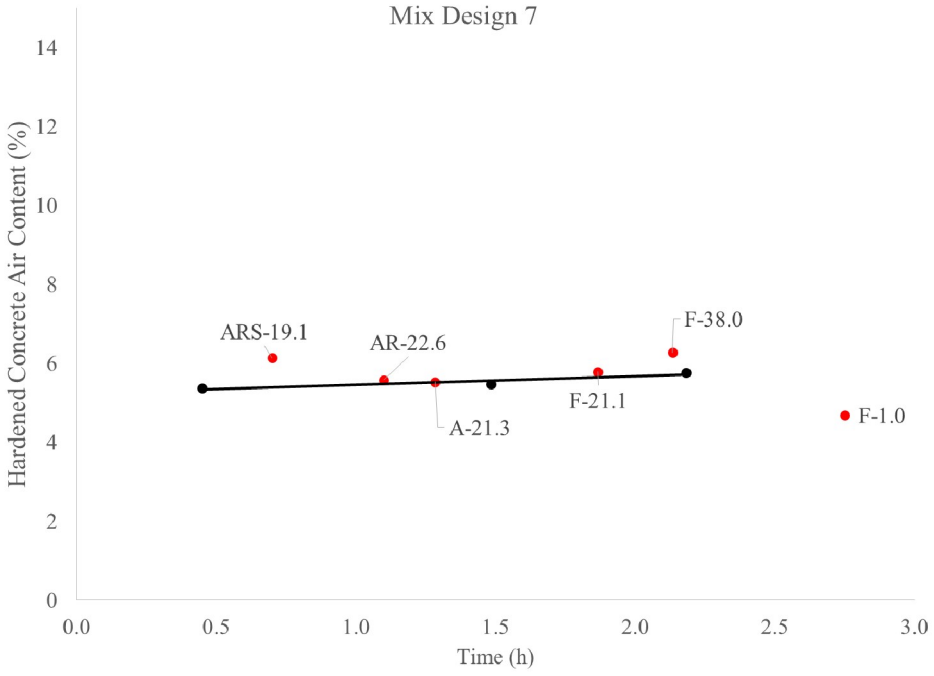

Figure B2.7. Hardened air content from Rapid Air as a function of time for non-pumped (black) and pumped (red) samples for mixture 7.

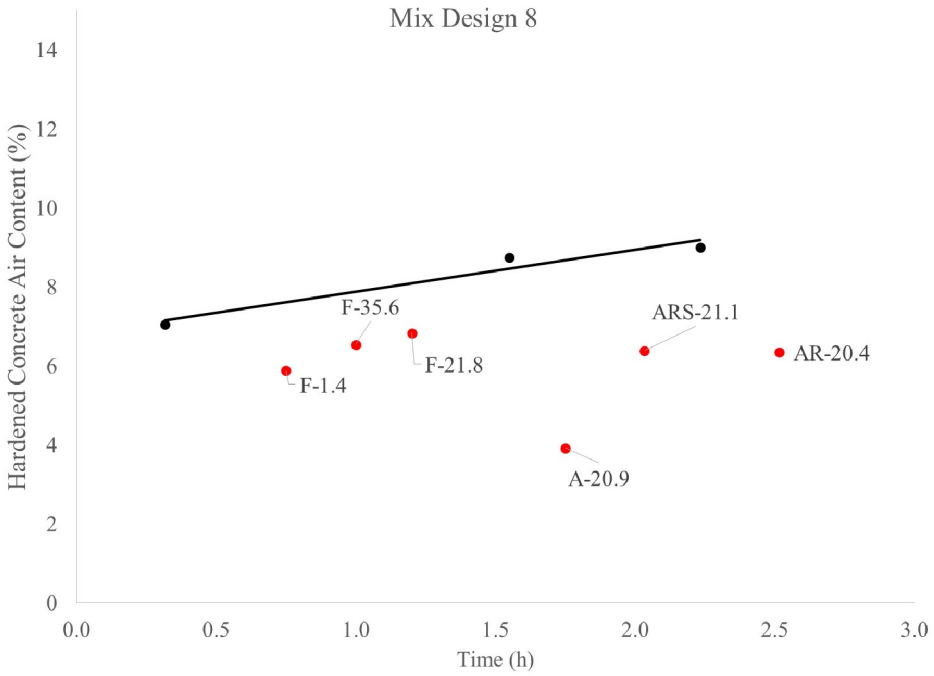

Figure B2.8. Hardened air content from Rapid Air as a function of time for non-pumped (black) and pumped (red) samples for mixture 8.

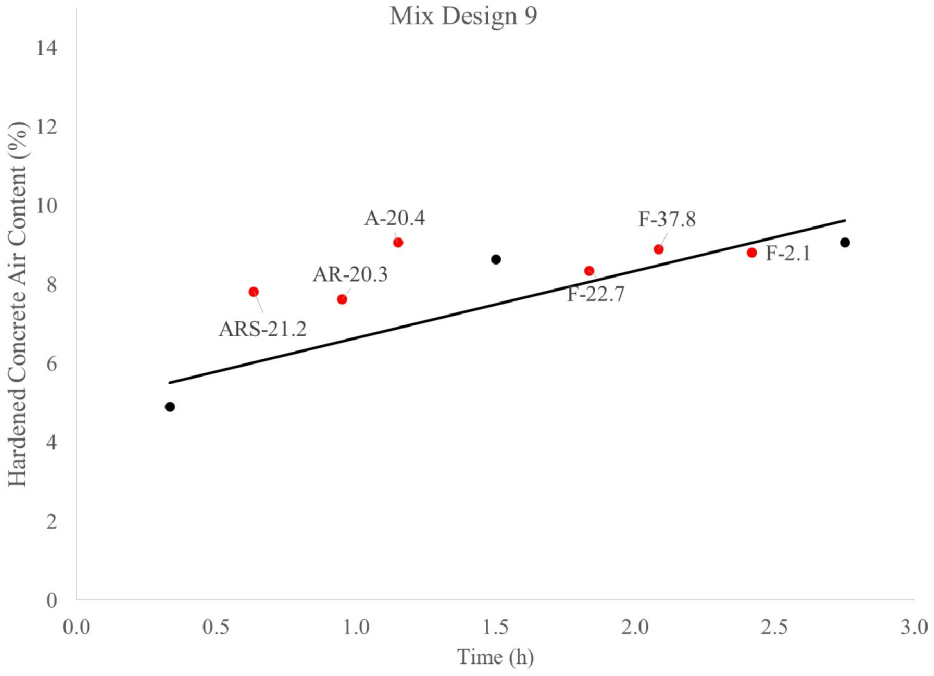

Figure B2.9. Hardened air content from Rapid Air as a function of time for non-pumped (black) and pumped (red) samples for mixture 9.

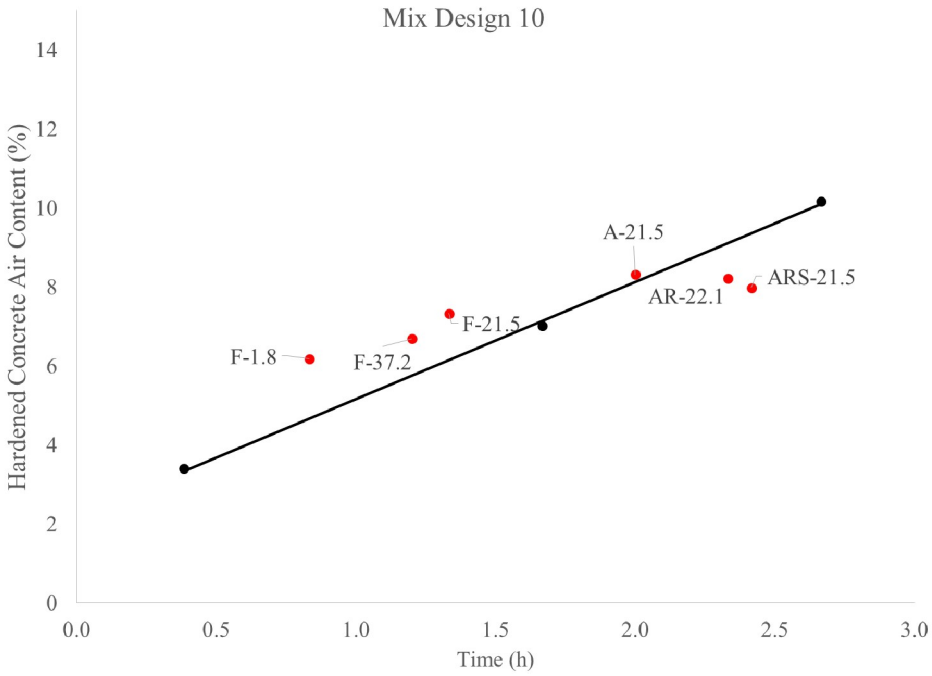

Figure B2.10. Hardened air content from Rapid Air as a function of time for non-pumped (black) and pumped (red) samples for mixture 10.

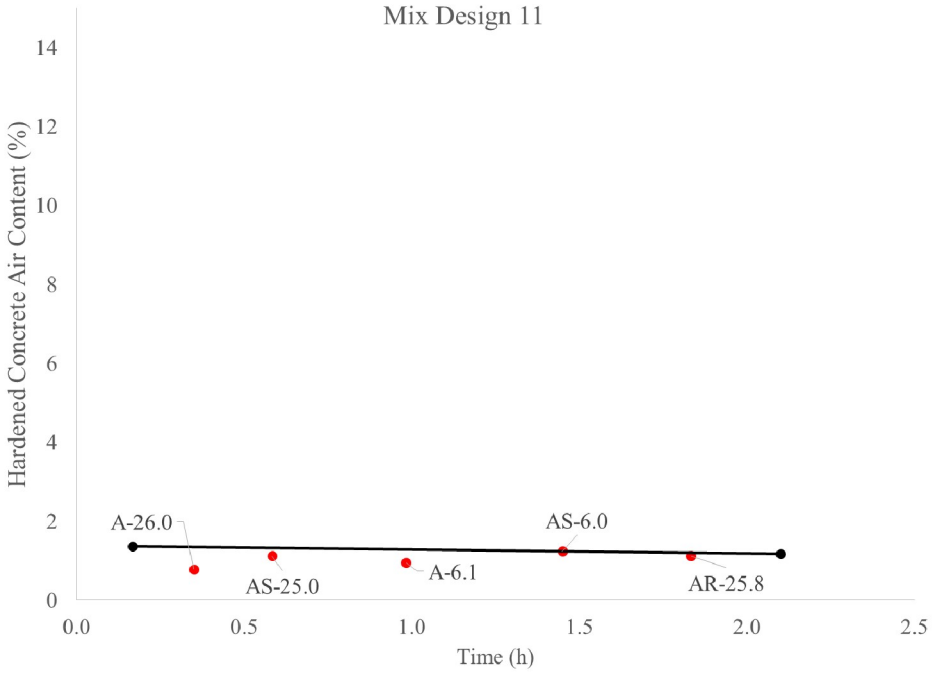

Figure B2.11. Hardened air content from Rapid Air as a function of time for non-pumped (black) and pumped (red) samples for mixture 11.

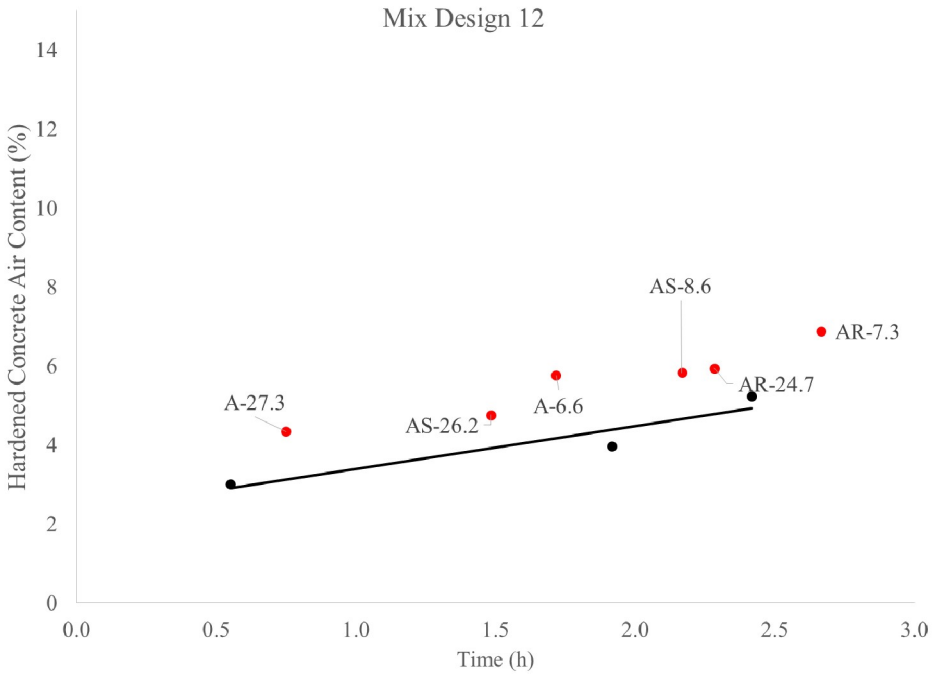

Figure B2.12. Hardened air content from Rapid Air as a function of time for non-pumped (black) and pumped (red) samples for mixture 12.

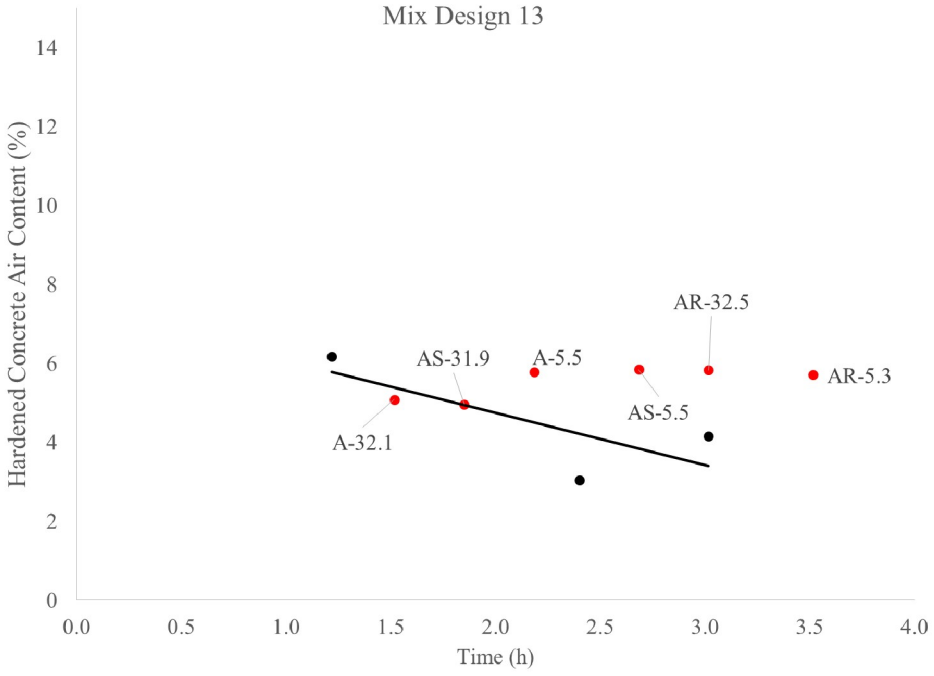

Figure B2.13. Hardened air content from Rapid Air as a function of time for non-pumped (black) and pumped (red) samples for mixture 13.

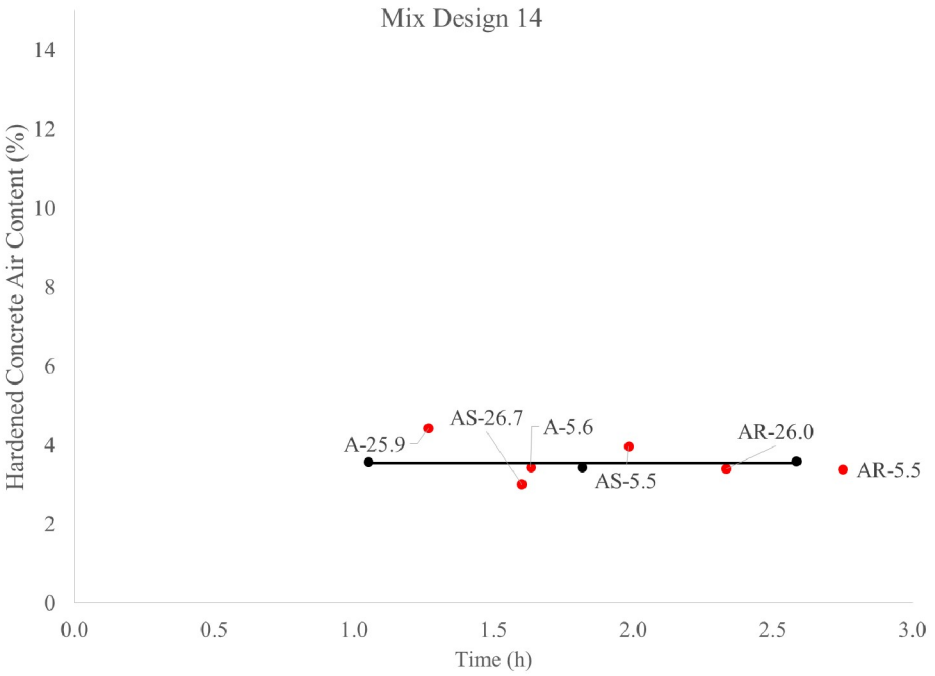

Figure B2.14. Hardened air content from Rapid Air as a function of time for non-pumped (black) and pumped (red) samples for mixture 14.

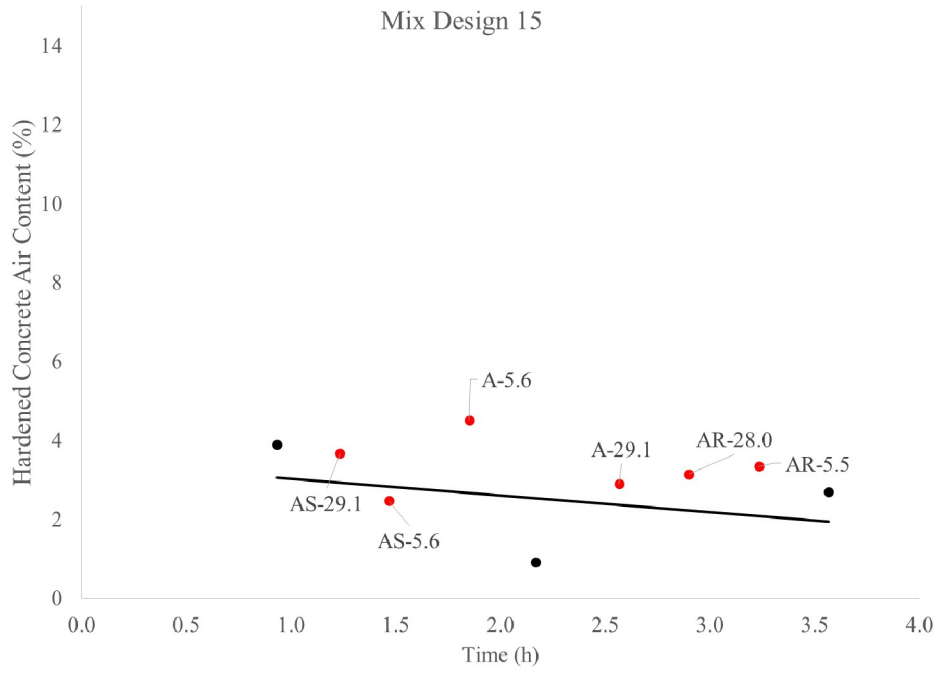

Figure B2.15. Hardened air content from Rapid Air as a function of time for non-pumped (black) and pumped (red) samples for mixture 15.

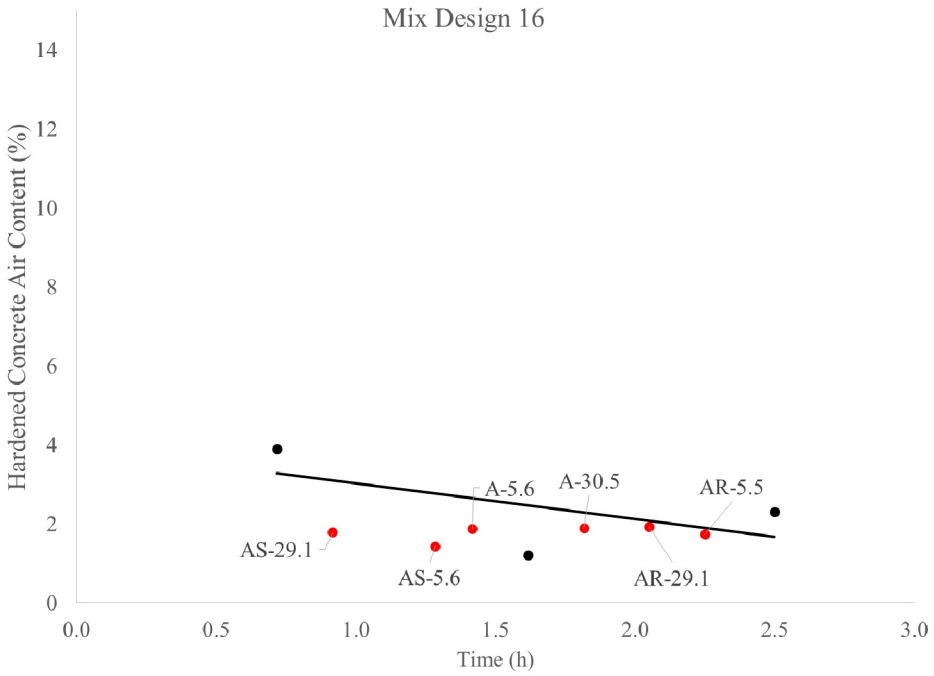

Figure B2.16. Hardened air content from Rapid Air as a function of time for non-pumped (black) and pumped (red) samples for mixture 16.

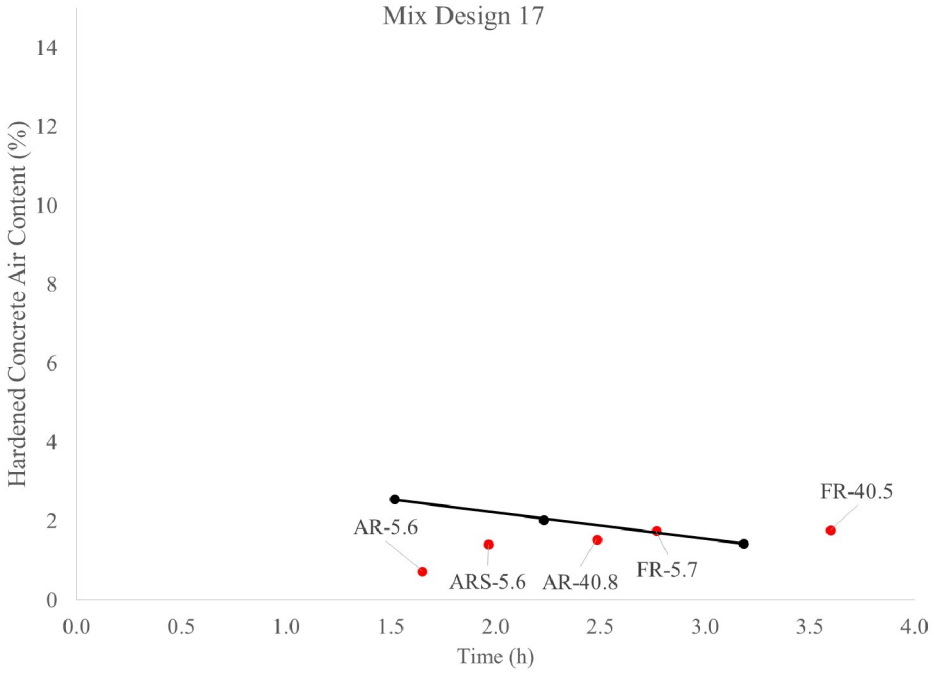

Figure B2.17. Hardened air content from Rapid Air as a function of time for non-pumped (black) and pumped (red) samples for mixture 17.

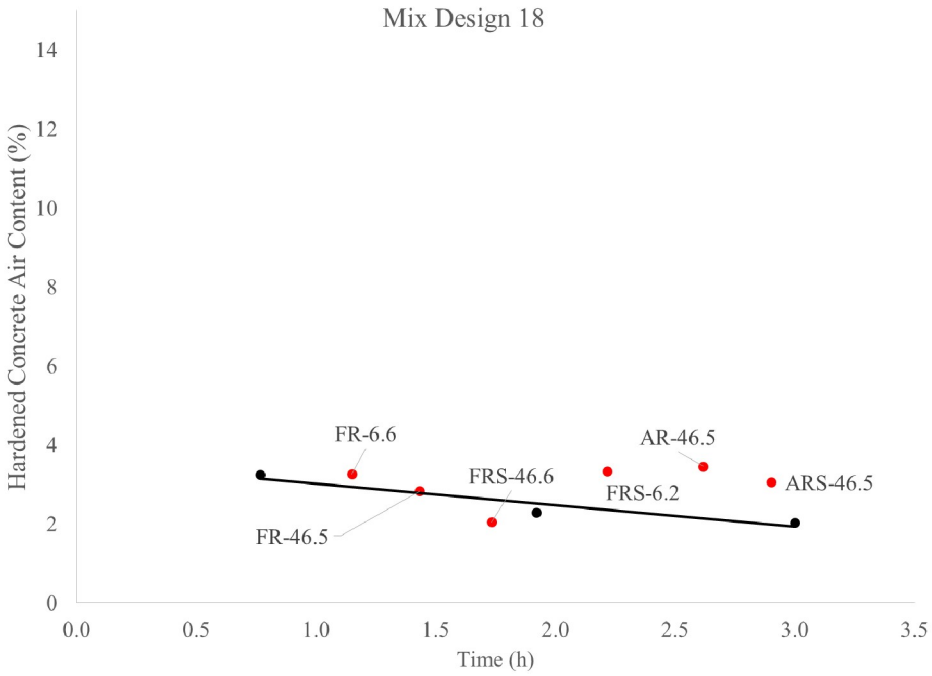

Figure B2.18. Hardened air content from Rapid Air as a function of time for non-pumped (black) and pumped (red) samples for mixture 18.

B.3 Compressive strength

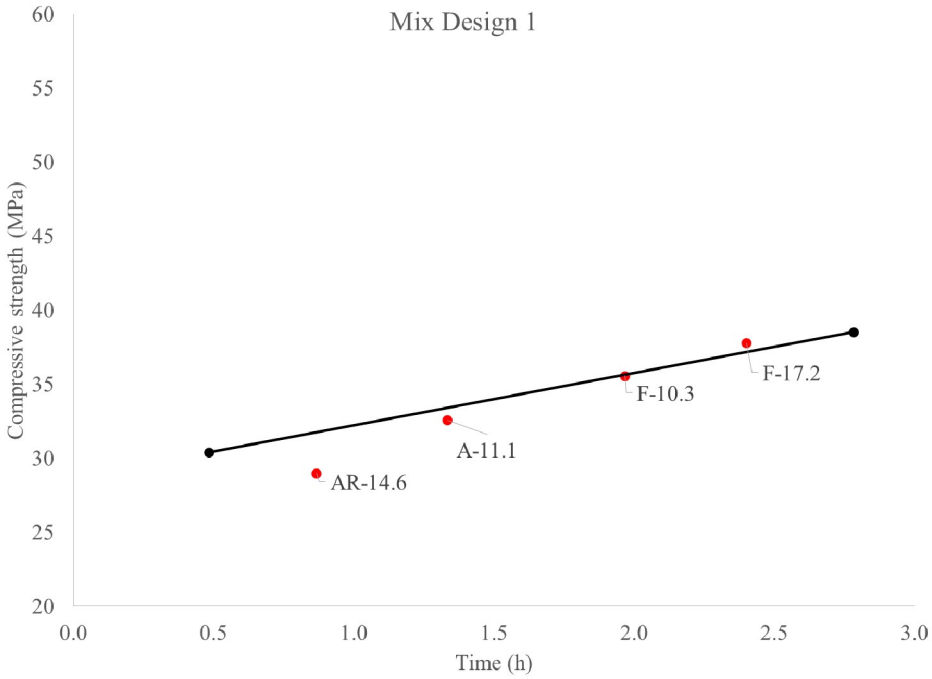

Figure B3.1. Compressive strength as a function of time for non-pumped (black) and pumped (red) samples for mixture 1.

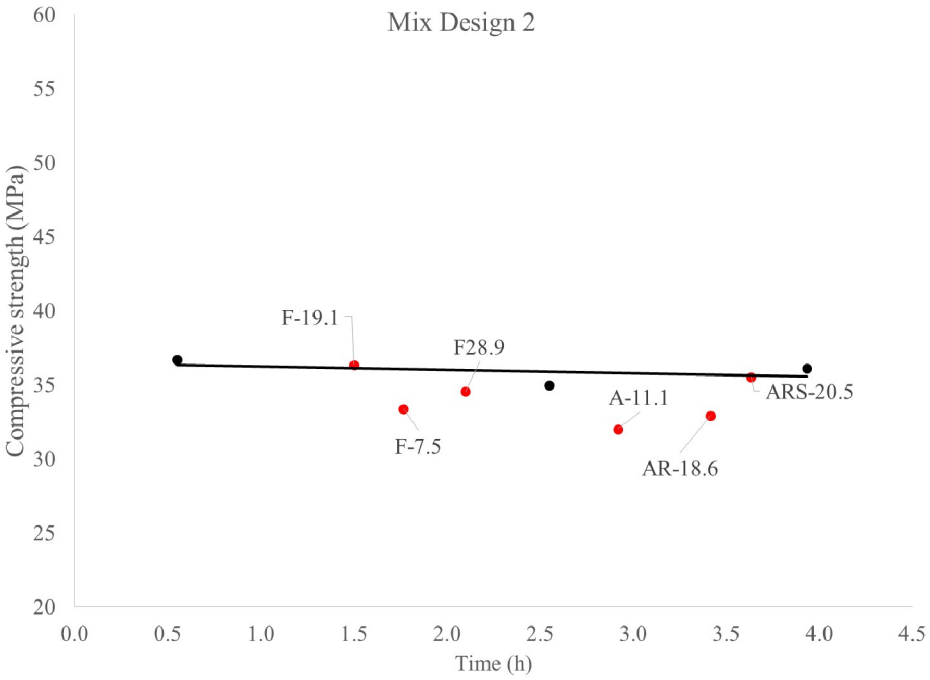

Figure B3.2. Compressive strength as a function of time for non-pumped (black) and pumped (red) samples for mixture 2.

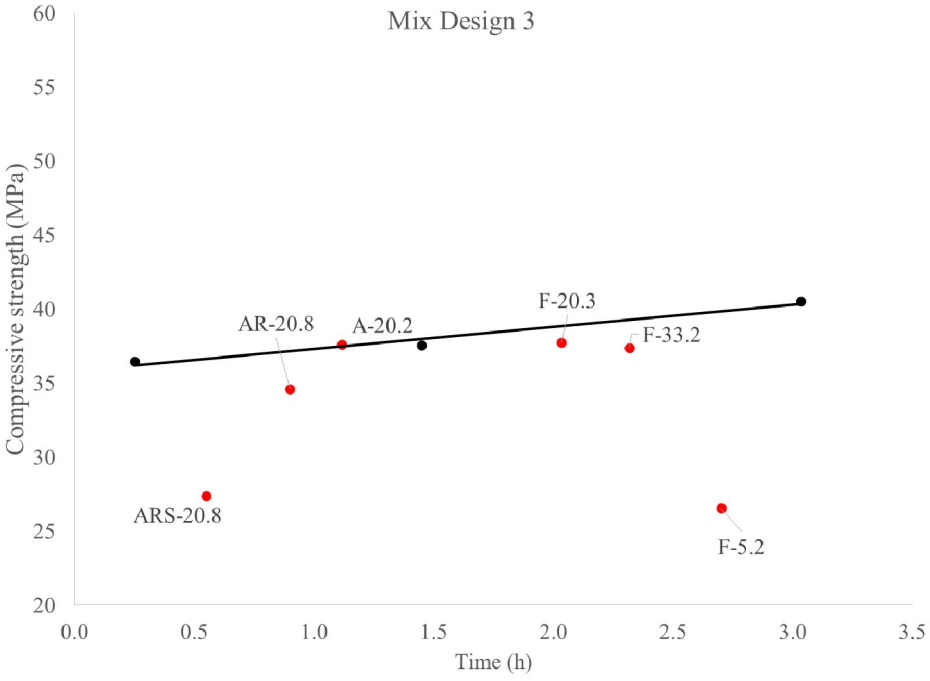

Figure B3.3. Compressive strength as a function of time for non-pumped (black) and pumped (red) samples for mixture 3.

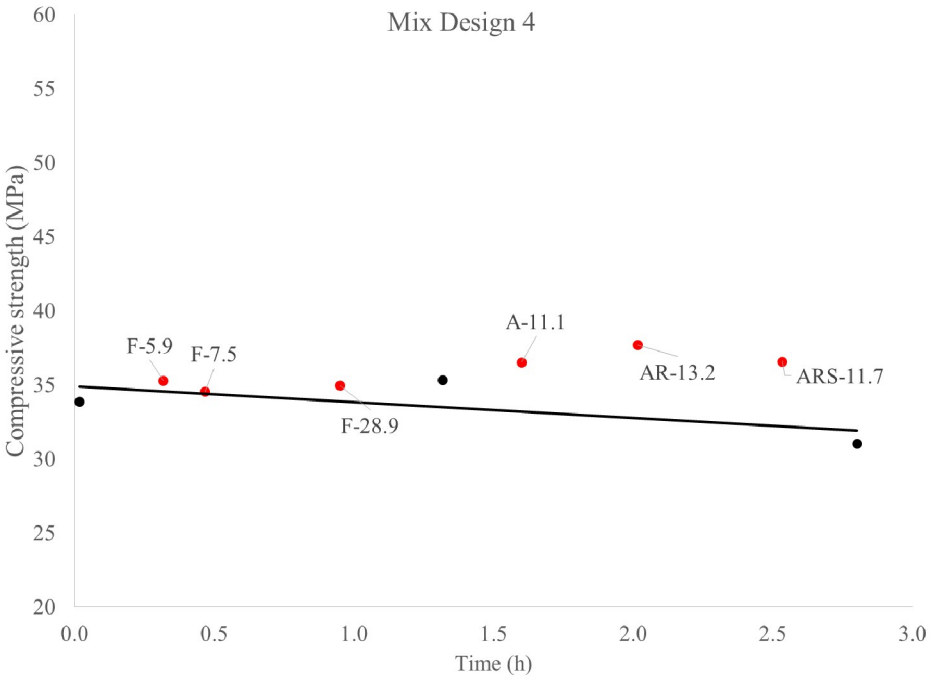

Figure B3.4. Compressive strength as a function of time for non-pumped (black) and pumped (red) samples for mixture 4.

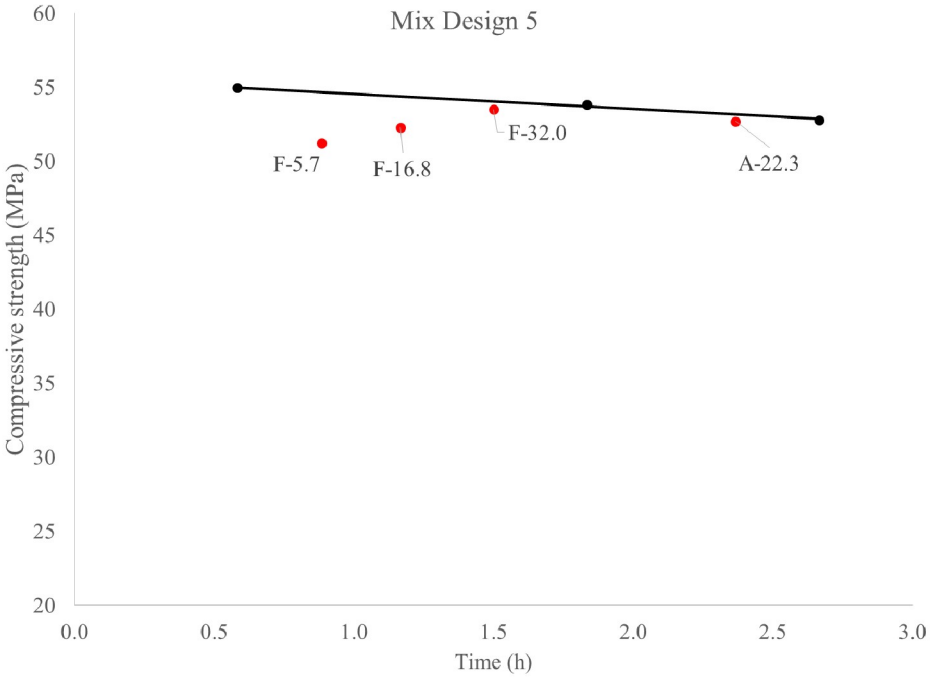

Figure B3.5. Compressive strength as a function of time for non-pumped (black) and pumped (red) samples for mixture 5.

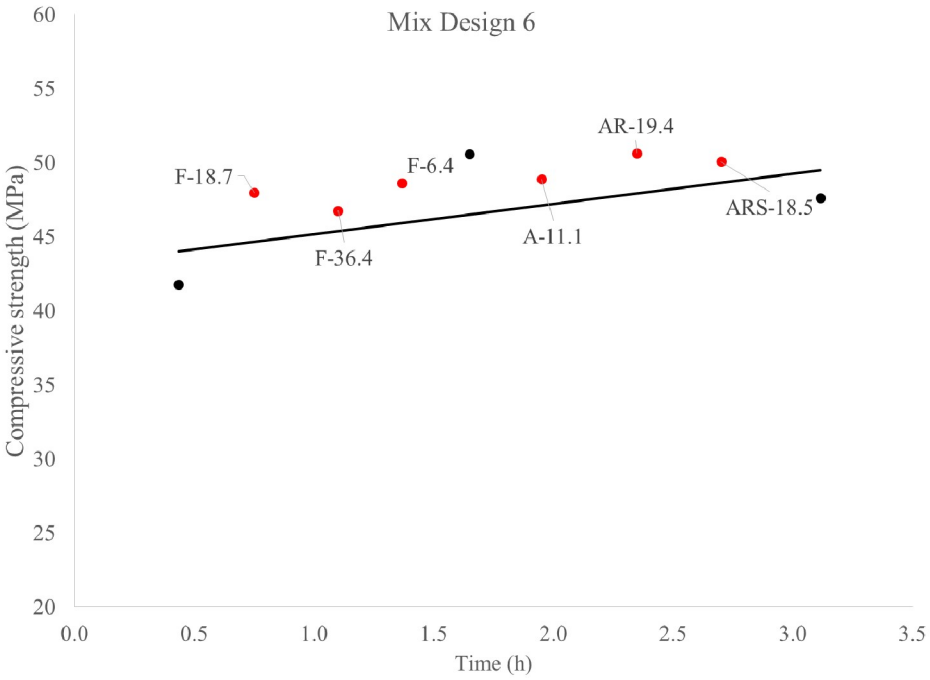

Figure B3.6. Compressive strength as a function of time for non-pumped (black) and pumped (red) samples for mixture 6.

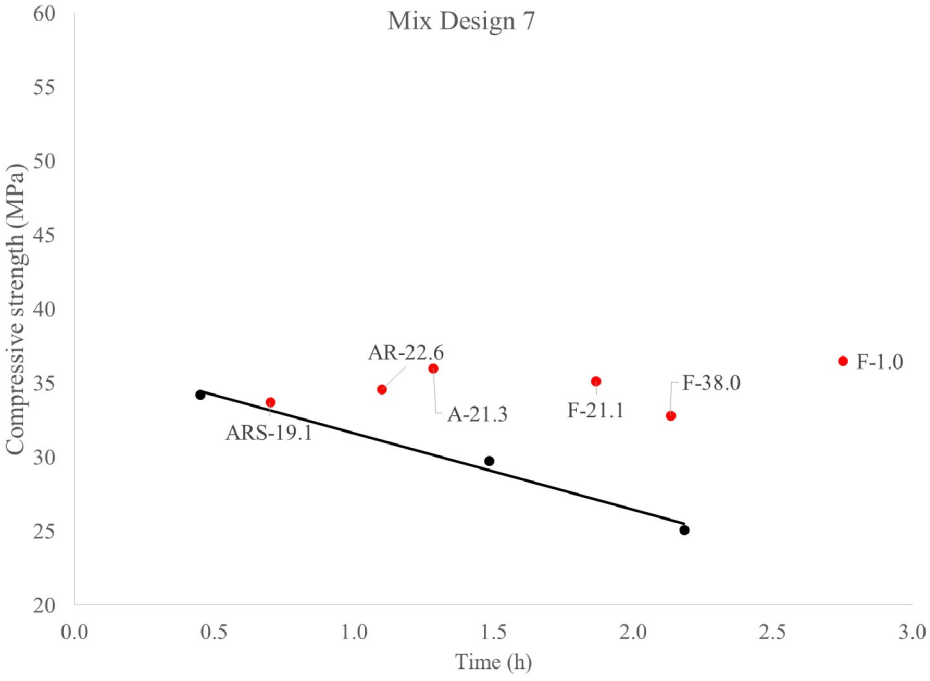

Figure B3.7. Compressive strength as a function of time for non-pumped (black) and pumped (red) samples for mixture 7.

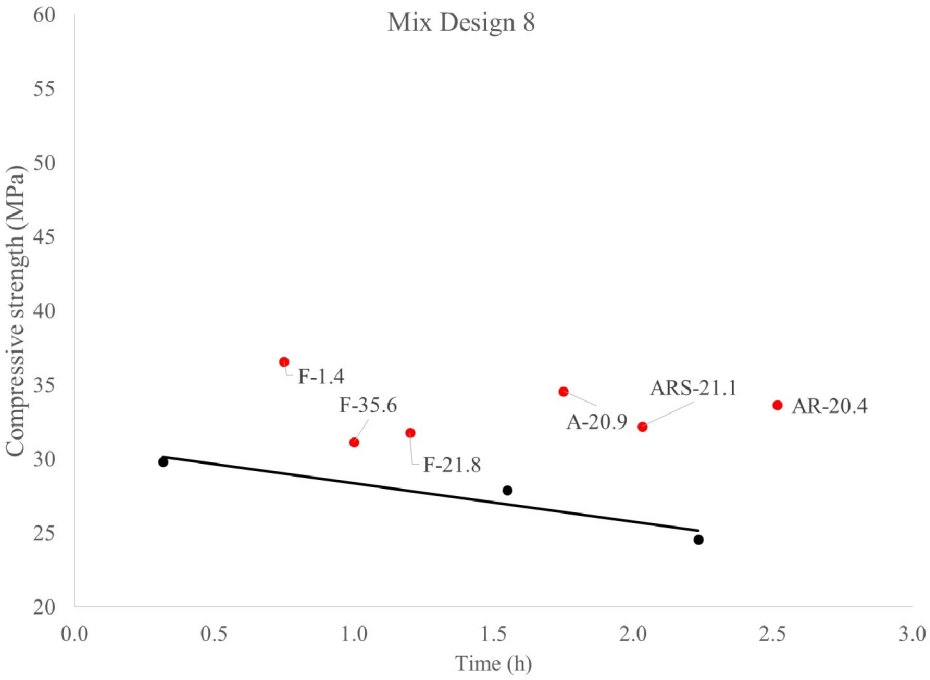

Figure B3.8. Compressive strength as a function of time for non-pumped (black) and pumped (red) samples for mixture 8.

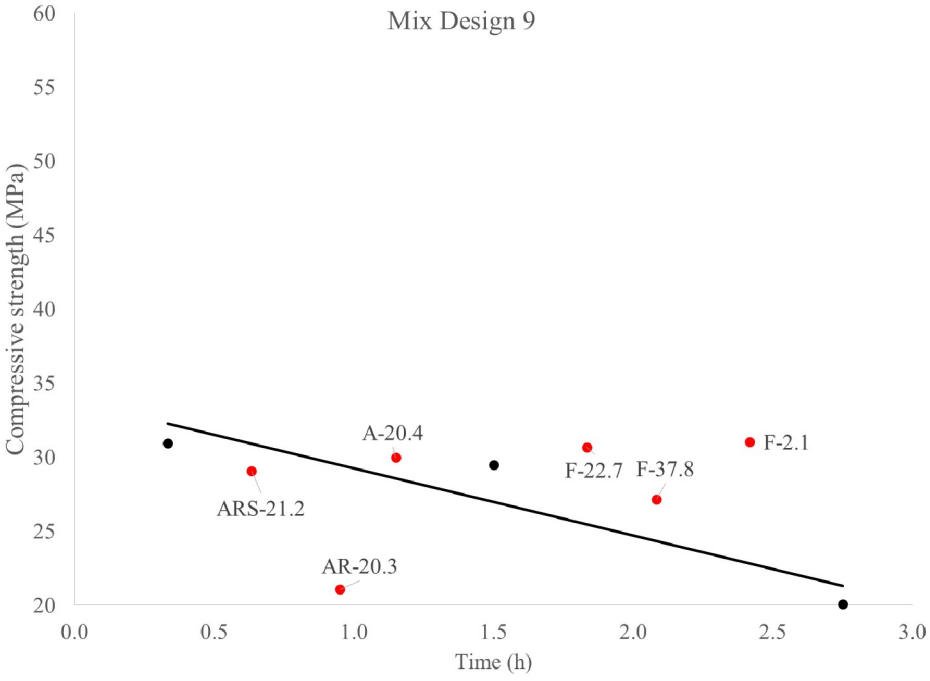

Figure B3.9. Compressive strength as a function of time for non-pumped (black) and pumped (red) samples for mixture 9.

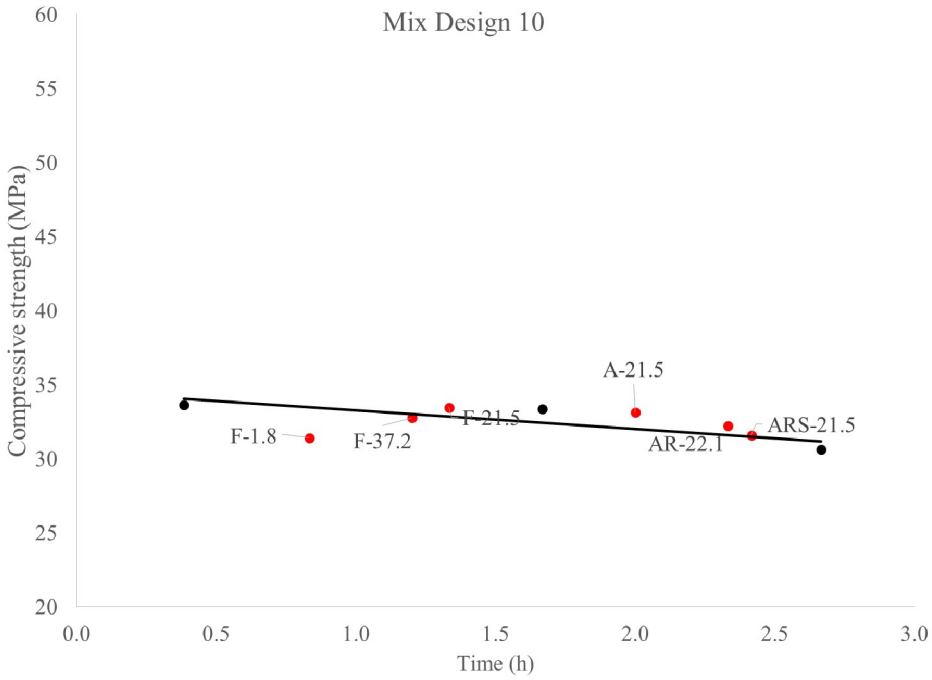

Figure B3.10. Compressive strength as a function of time for non-pumped (black) and pumped (red) samples for mixture 10.

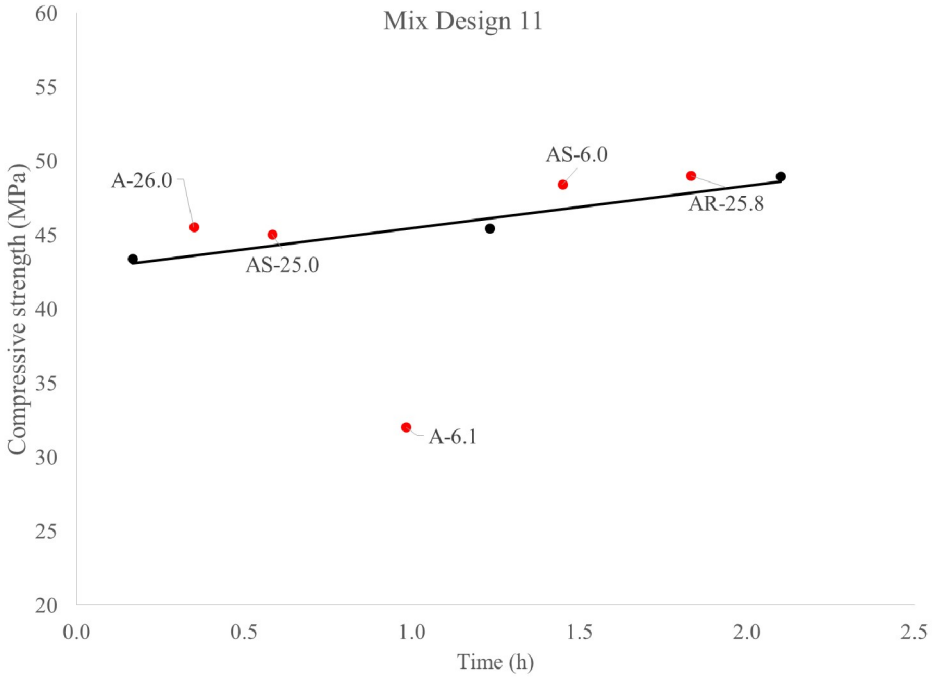

Figure B3.11. Compressive strength as a function of time for non-pumped (black) and pumped (red) samples for mixture 11.

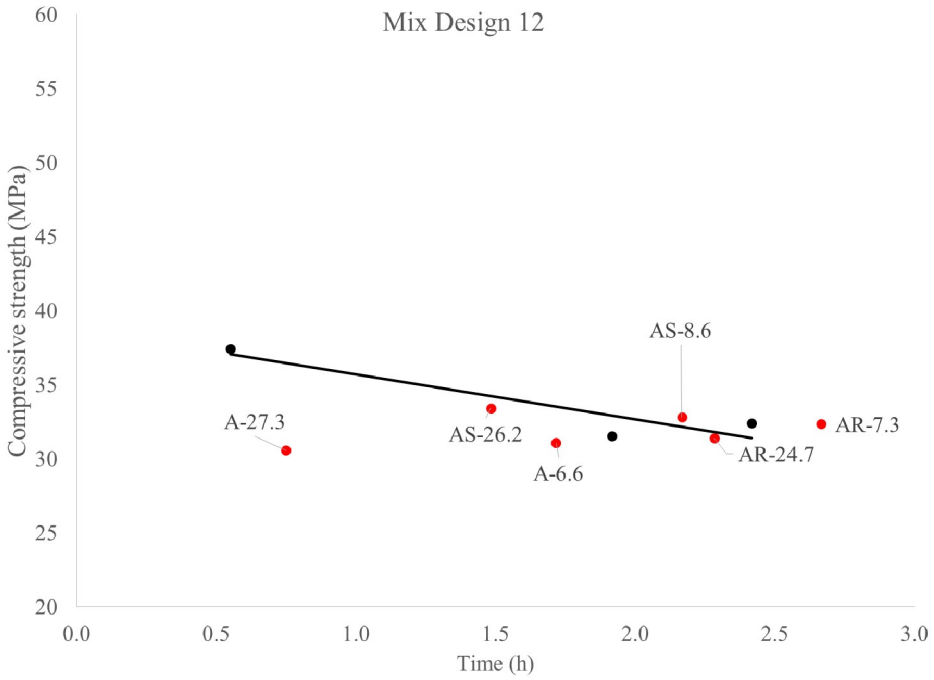

Figure B3.12. Compressive strength as a function of time for non-pumped (black) and pumped (red) samples for mixture 12.

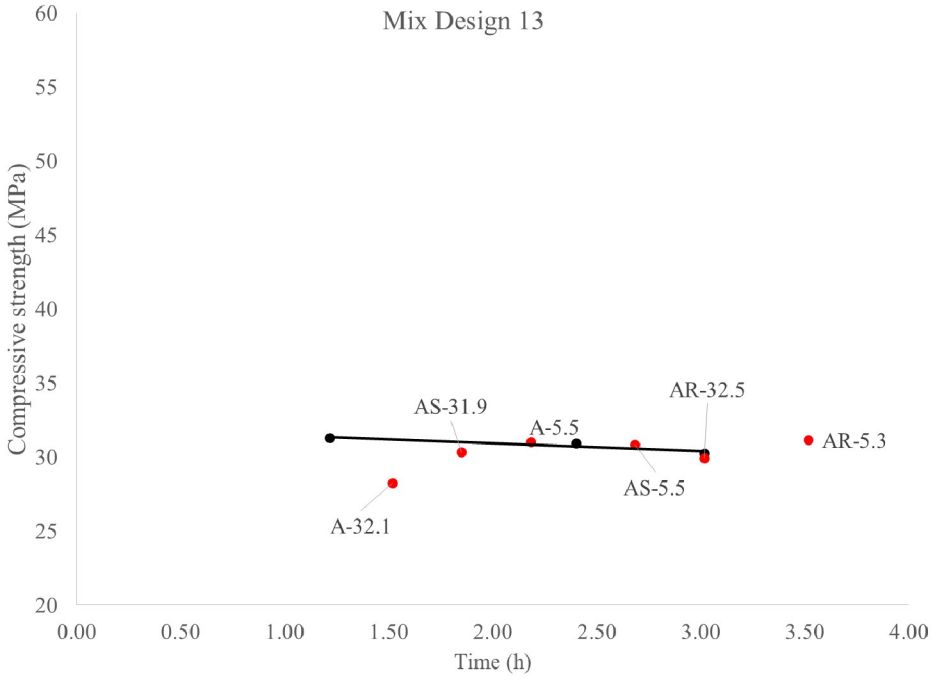

Figure B3.13. Compressive strength as a function of time for non-pumped (black) and pumped (red) samples for mixture 13.

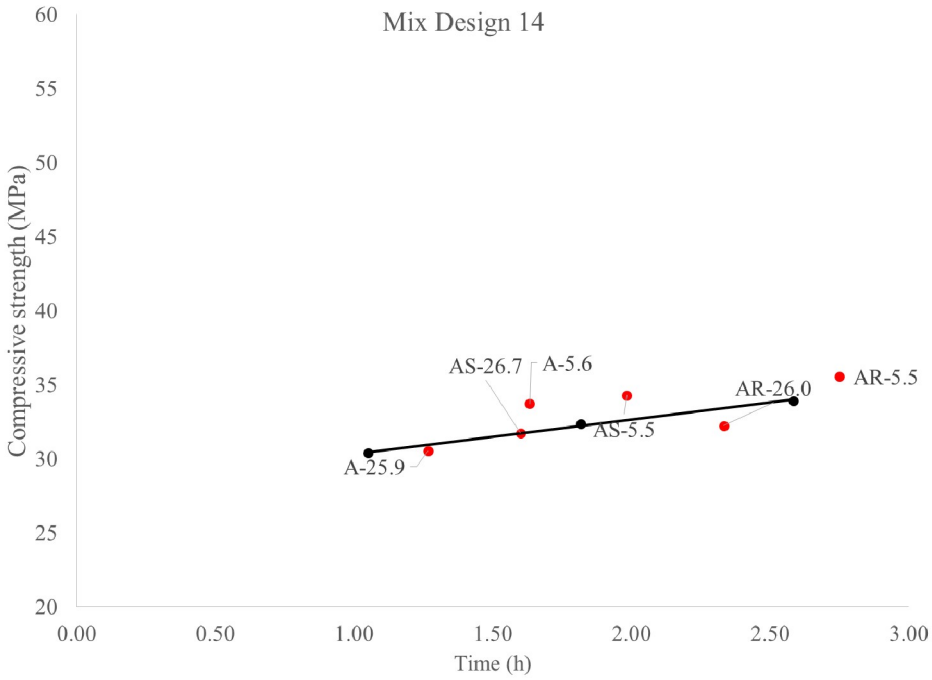

Figure B3.14. Compressive strength as a function of time for non-pumped (black) and pumped (red) samples for mixture 14.

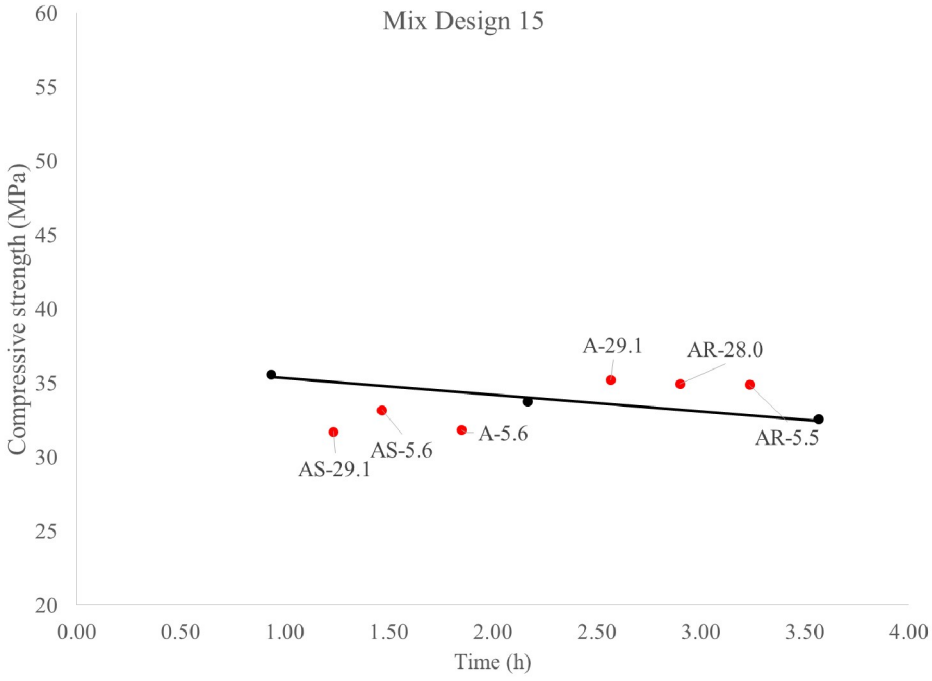

Figure B3.15. Compressive strength as a function of time for non-pumped (black) and pumped (red) samples for mixture 15.

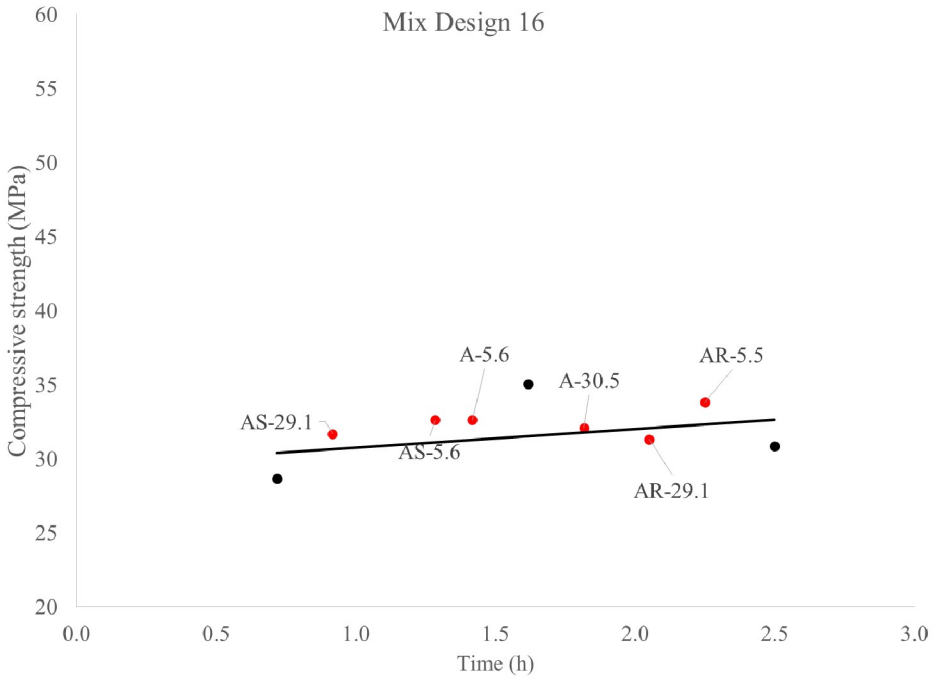

Figure B3.16. Compressive strength as a function of time for non-pumped (black) and pumped (red) samples for mixture 16.

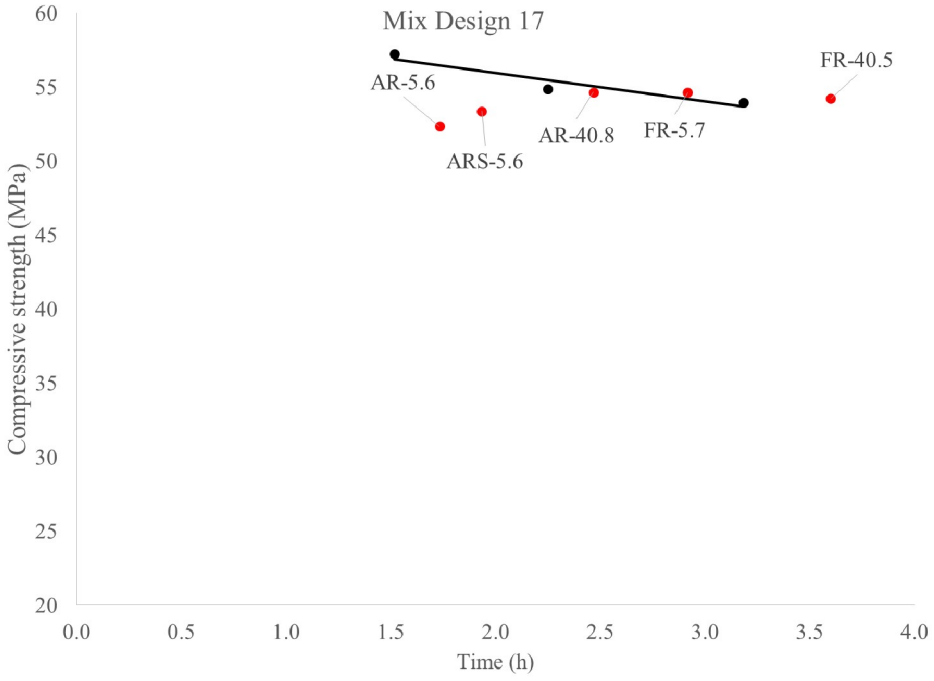

Figure B3.17. Compressive strength as a function of time for non-pumped (black) and pumped (red) samples for mixture 17.

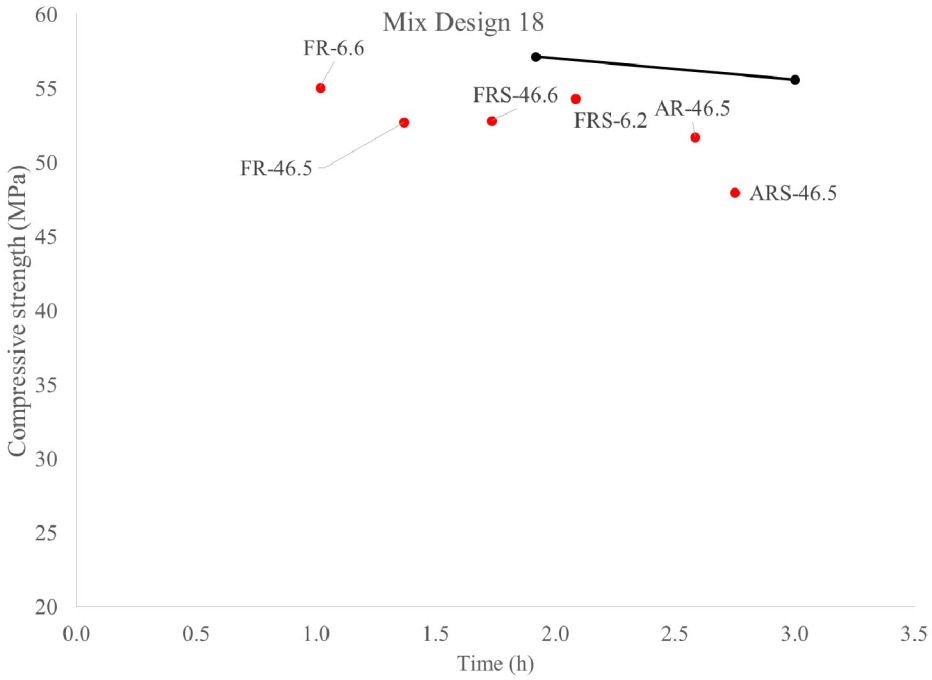

Figure B3.18. Compressive strength as a function of time for non-pumped (black) and pumped (red) samples for mixture 18.

B.4 Spacing factor

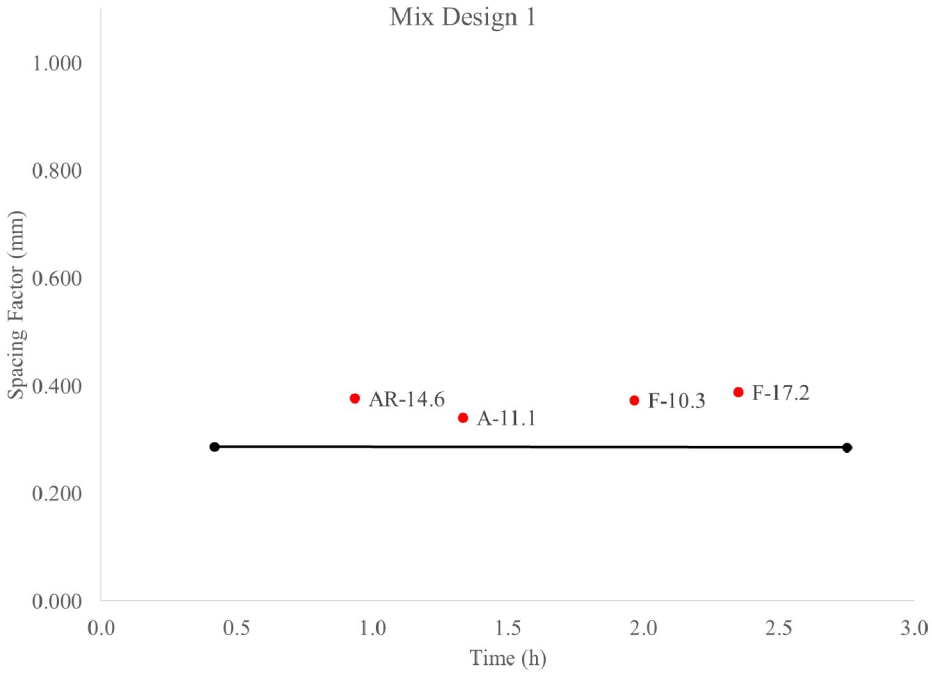

Figure B4.1. Spacing factor for non-pumped (black) and pumped (red) samples as a function of time for mix design 1.

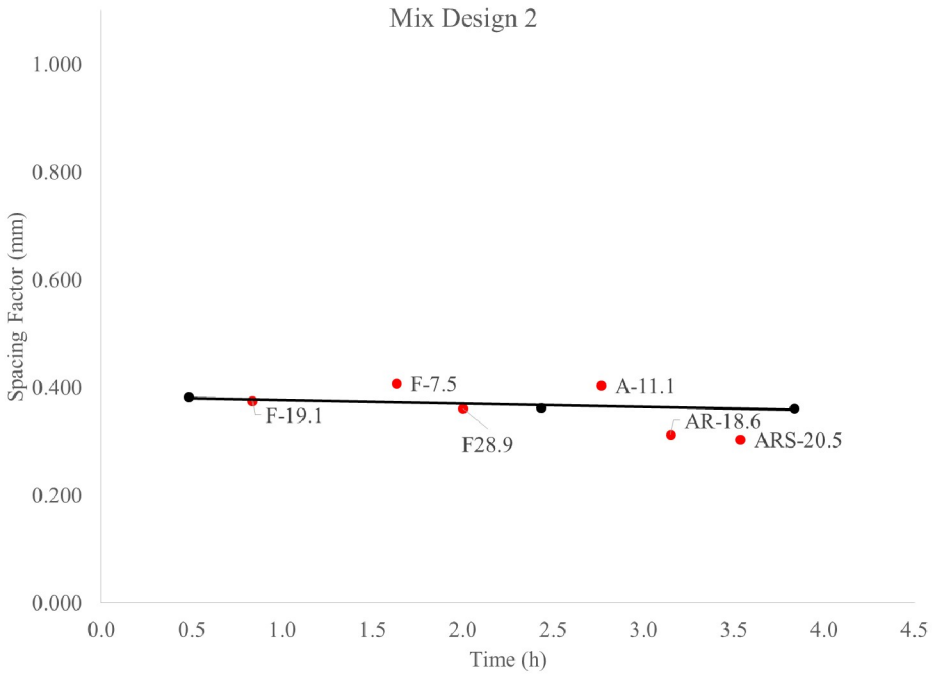

Figure B4.2. Spacing factor for non-pumped (black) and pumped (red) samples as a function of time for mix design 2.

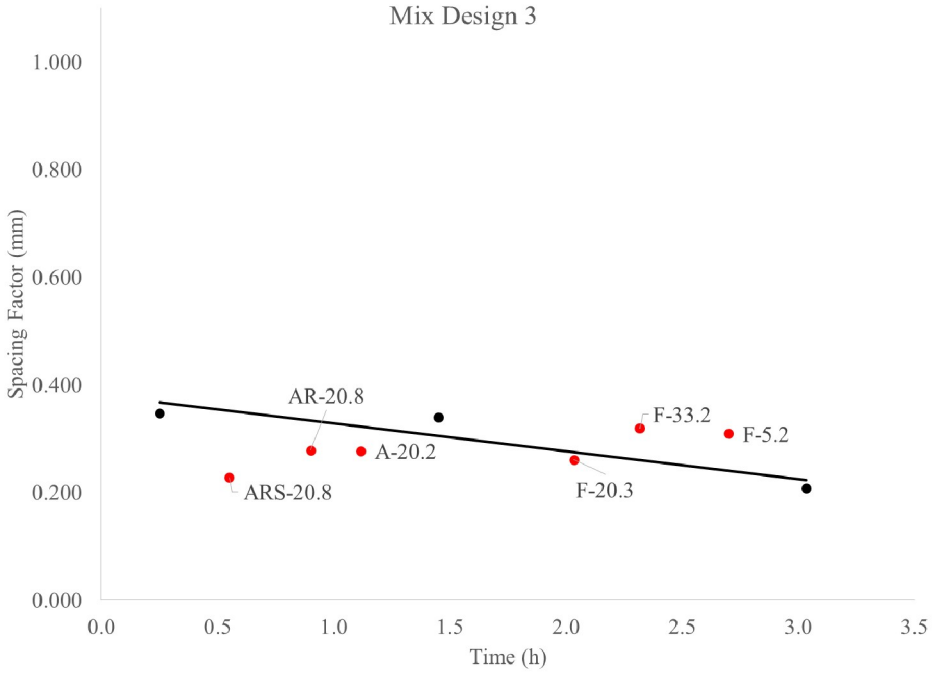

Figure B4.3. Spacing factor for non-pumped (black) and pumped (red) samples as a function of time for mix design 3.

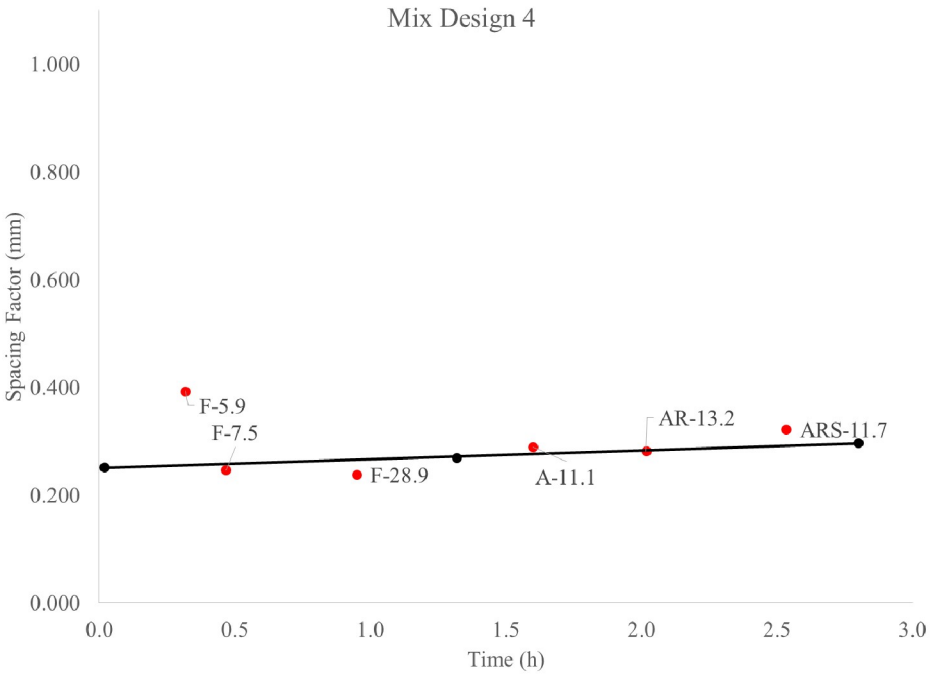

Figure B4.4. Spacing factor for non-pumped (black) and pumped (red) samples as a function of time for mix design 4.

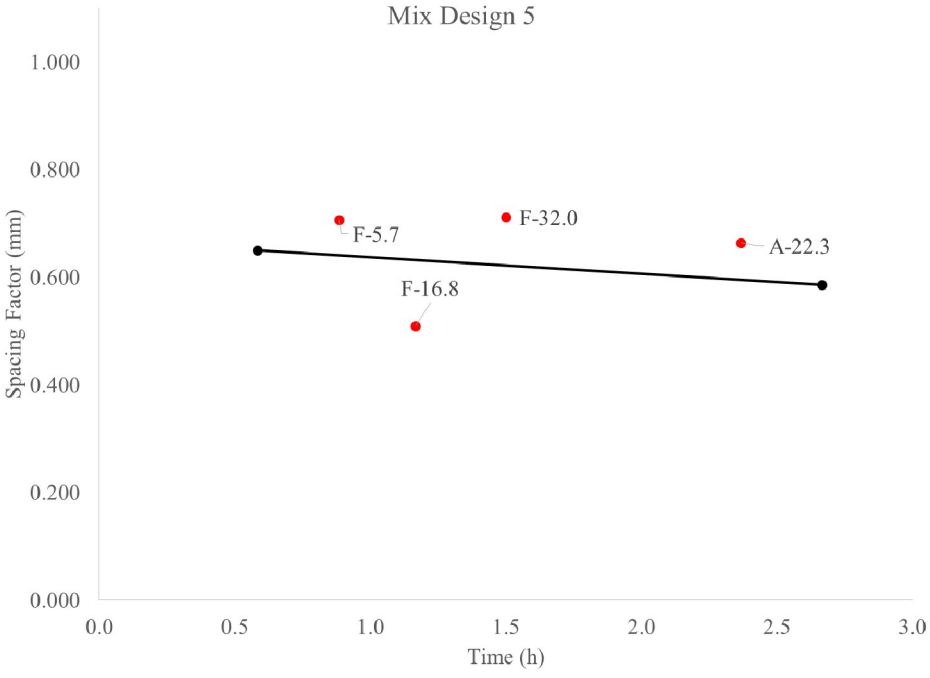

Figure B4.5. Spacing factor for non-pumped (black) and pumped (red) samples as a function of time for mix design 5.

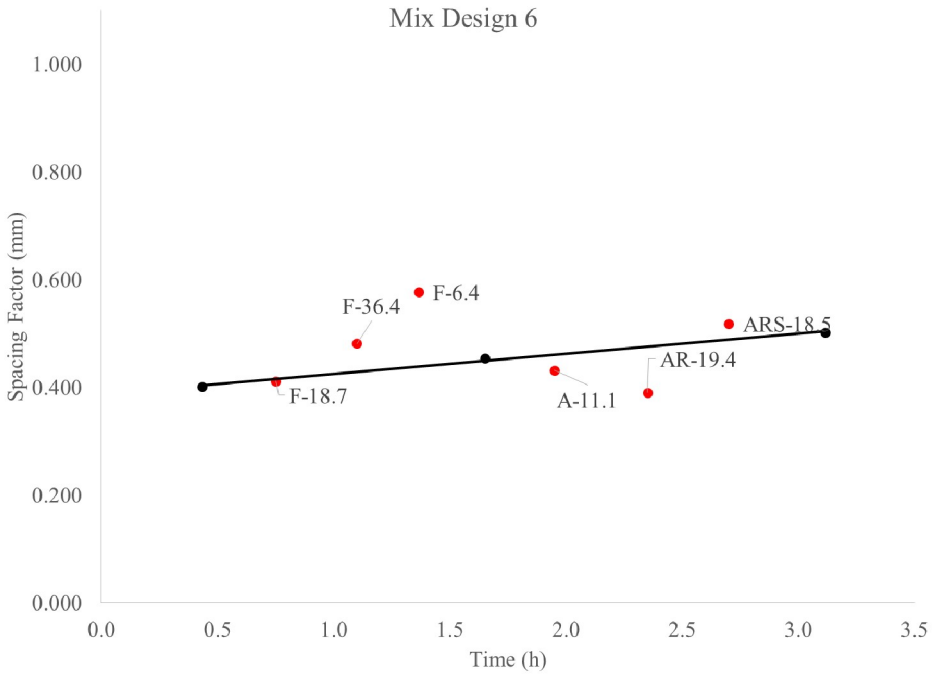

Figure B4.6. Spacing factor for non-pumped (black) and pumped (red) samples as a function of time for mix design 6.

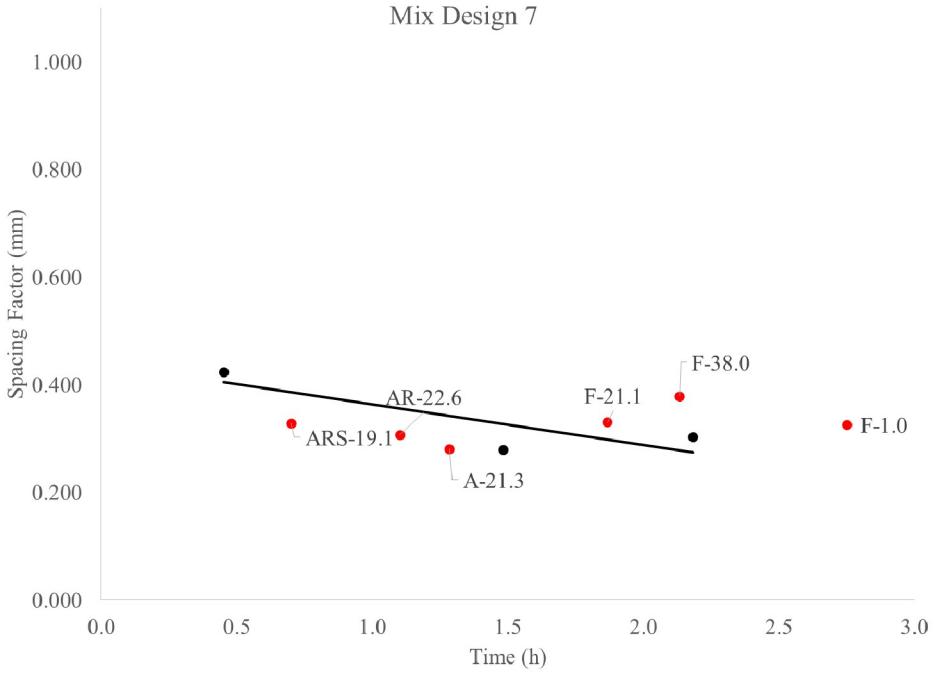

Figure B4.7. Spacing factor for non-pumped (black) and pumped (red) samples as a function of time for mix design 7.

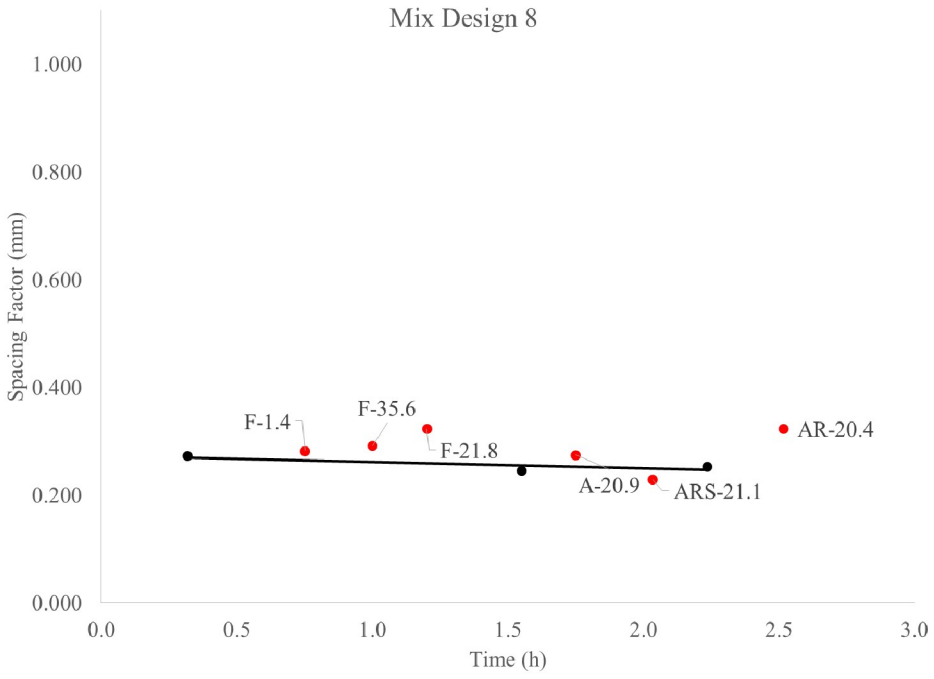

Figure B4.8. Spacing factor for non-pumped (black) and pumped (red) samples as a function of time for mix design 8.

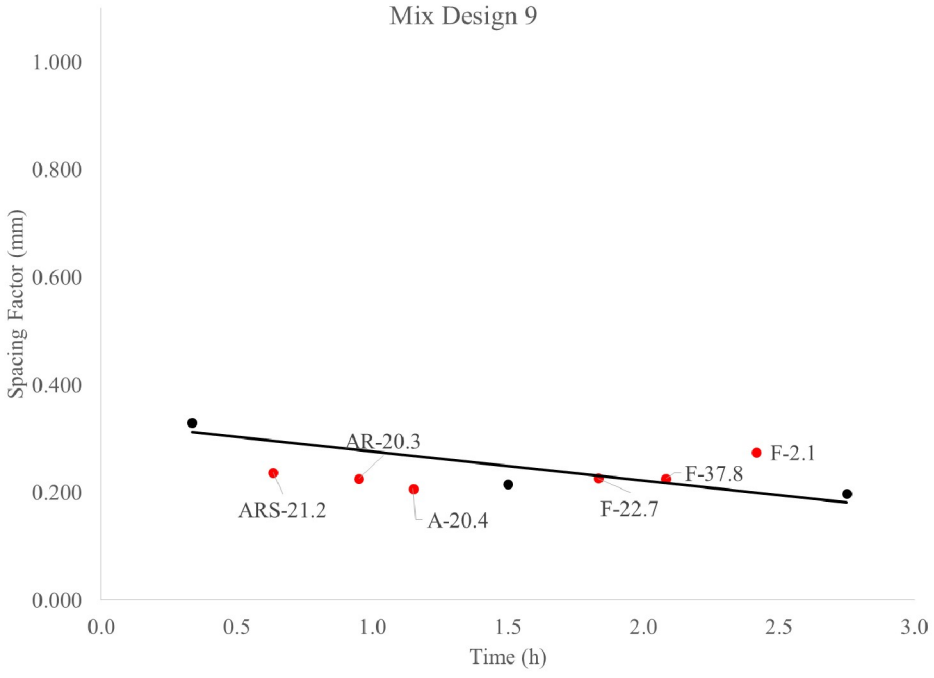

Figure B4.9. Spacing factor for non-pumped (black) and pumped (red) samples as a function of time for mix design 9.

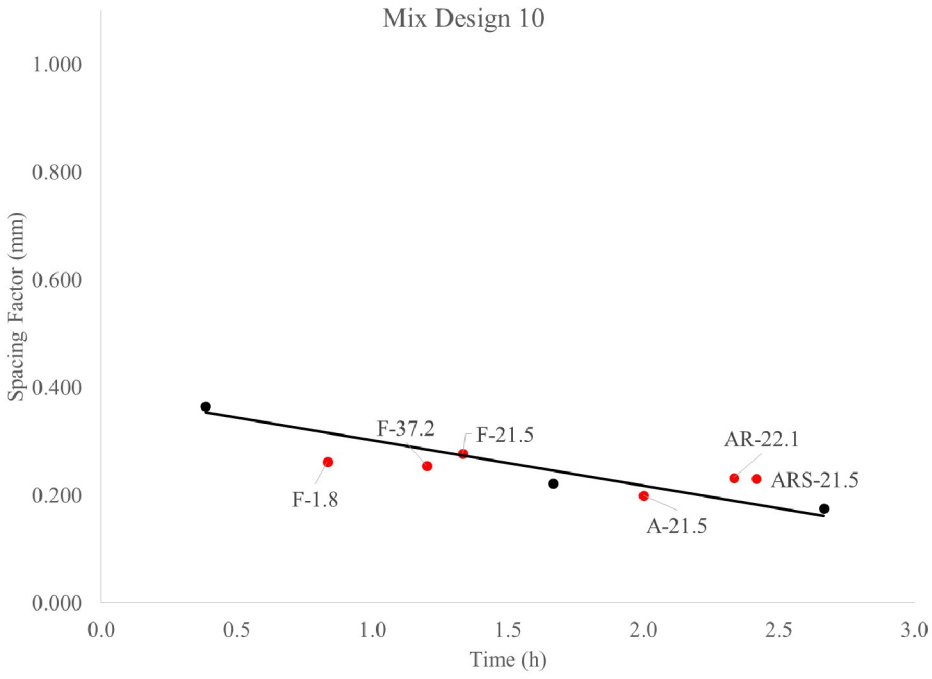

Figure B4.10. Spacing factor for non-pumped (black) and pumped (red) samples as a function of time for mix design 10.

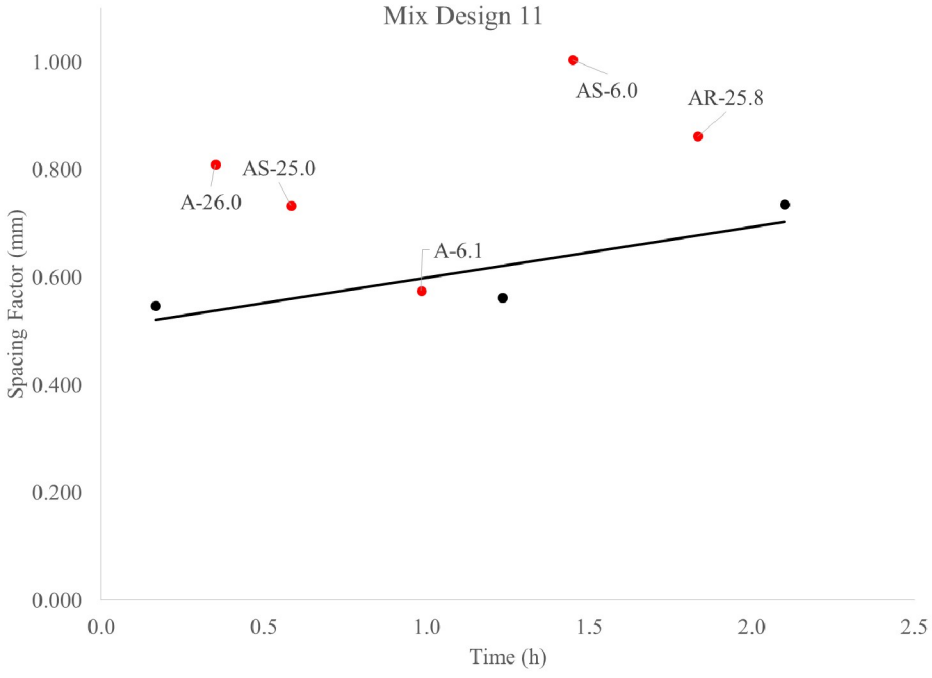

Figure B4.11. Spacing factor for non-pumped (black) and pumped (red) samples as a function of time for mix design 11.

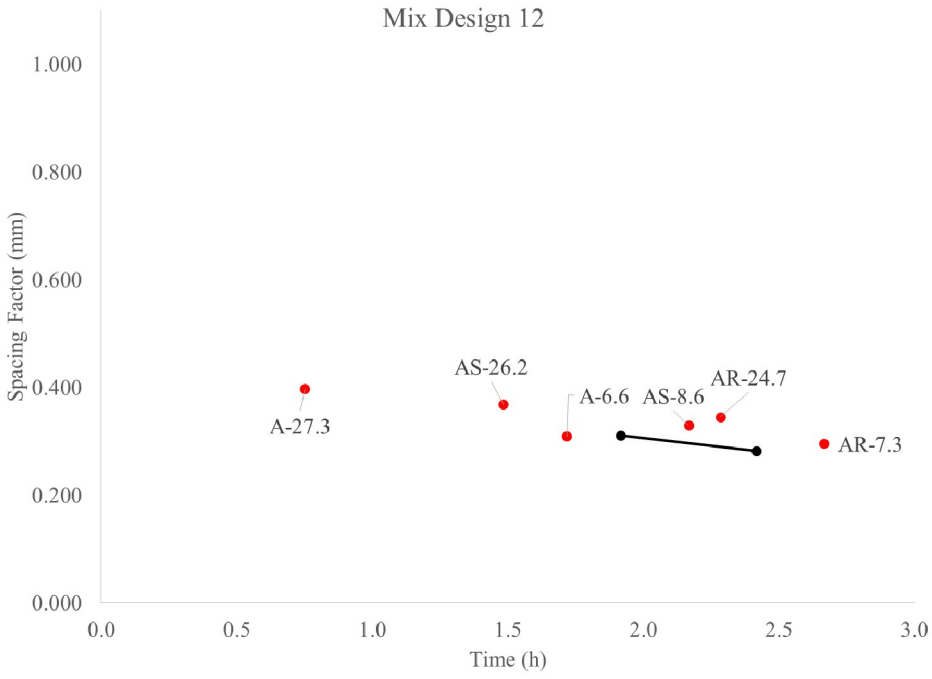

Figure B4.12. Spacing factor for non-pumped (black) and pumped (red) samples as a function of time for mix design 12.

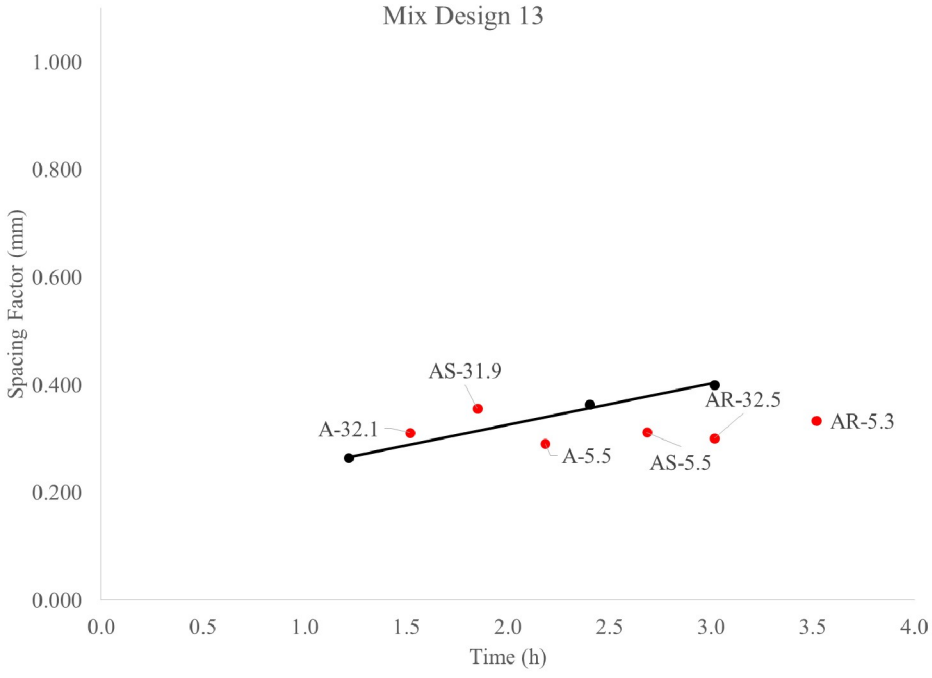

Figure B4.13. Spacing factor for non-pumped (black) and pumped (red) samples as a function of time for mix design 13.

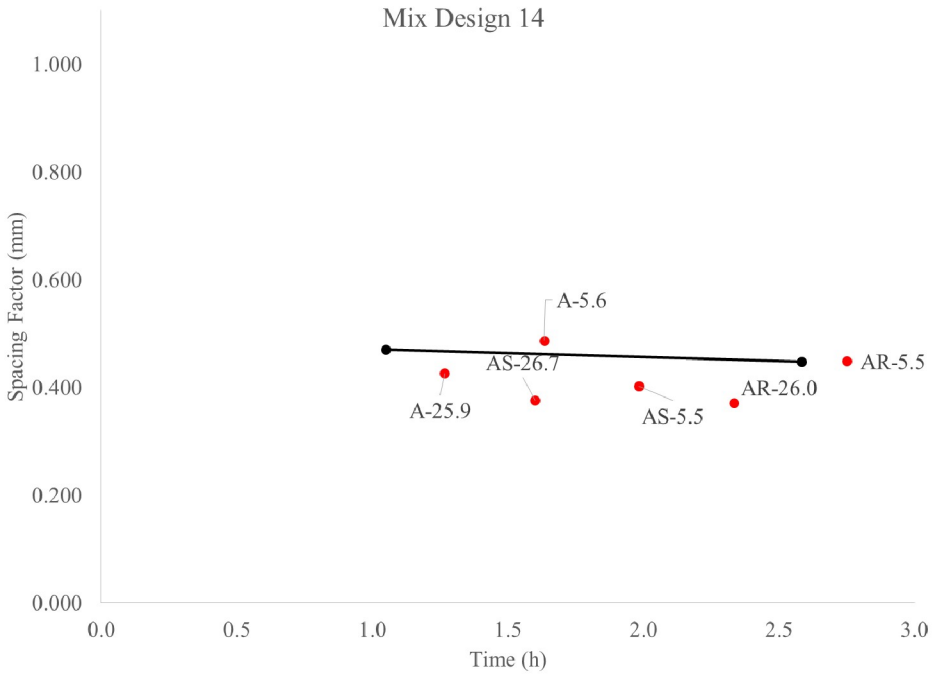

Figure B4.14. Spacing factor for non-pumped (black) and pumped (red) samples as a function of time for mix design 14.

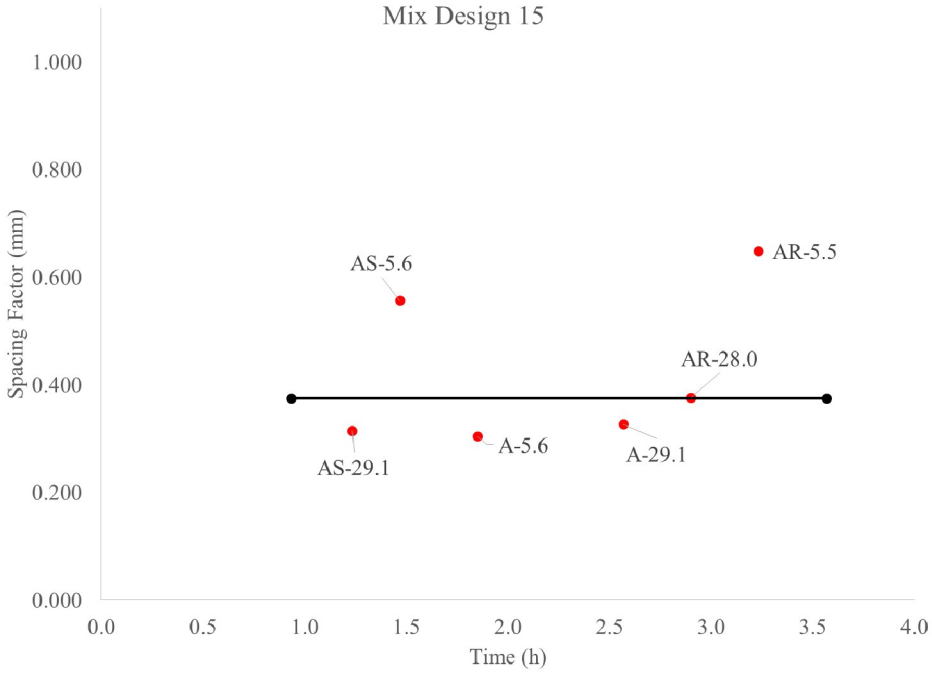

Figure B4.15. Spacing factor for non-pumped (black) and pumped (red) samples as a function of time for mix design 15.

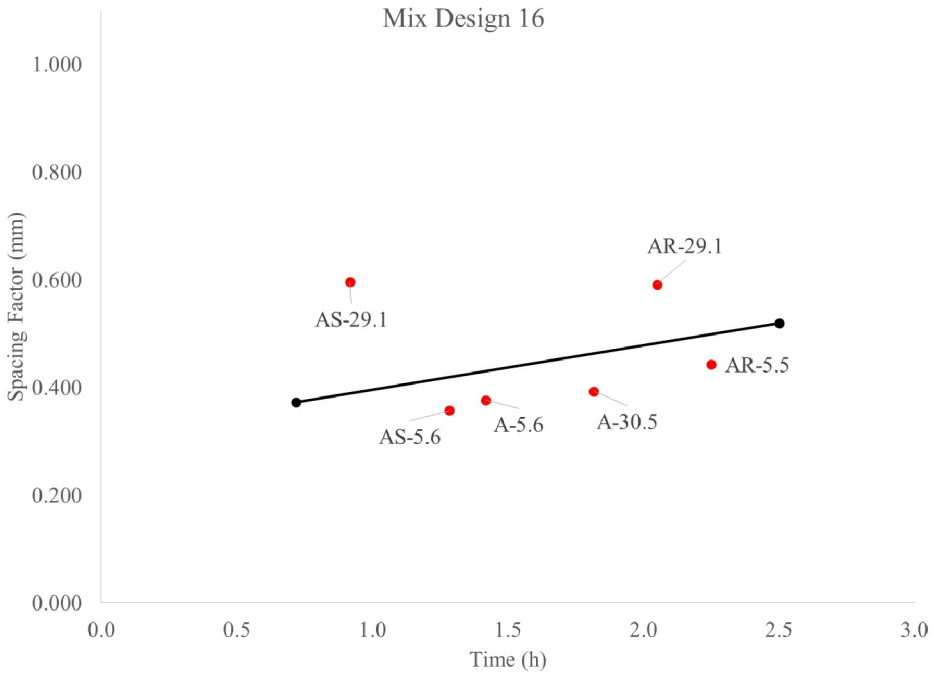

Figure B4.16. Spacing factor for non-pumped (black) and pumped (red) samples as a function of time for mix design 16.

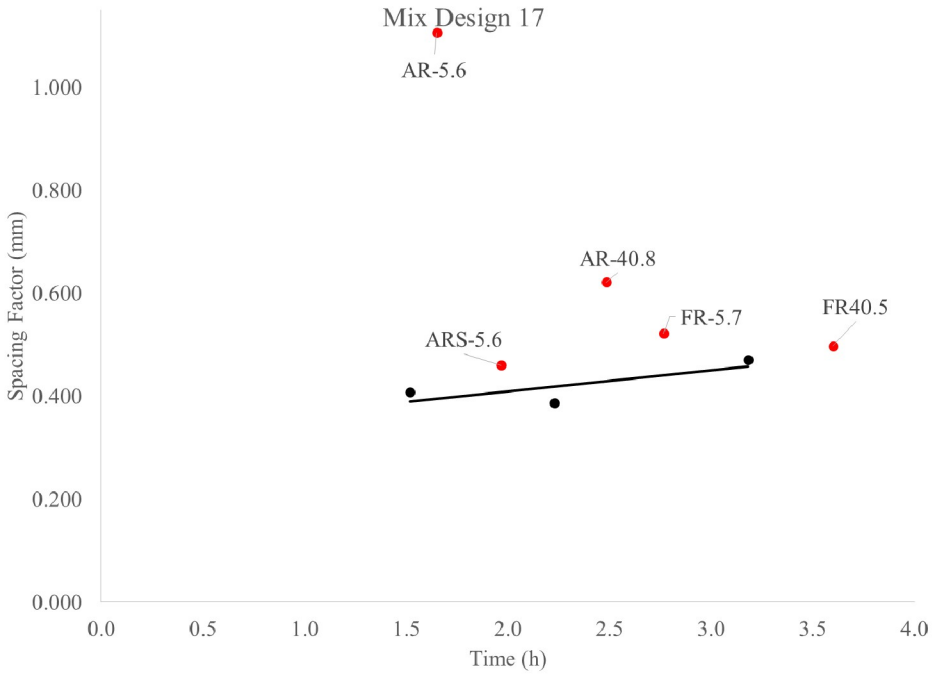

Figure B4.17. Spacing factor for non-pumped (black) and pumped (red) samples as a function of time for mix design 17.

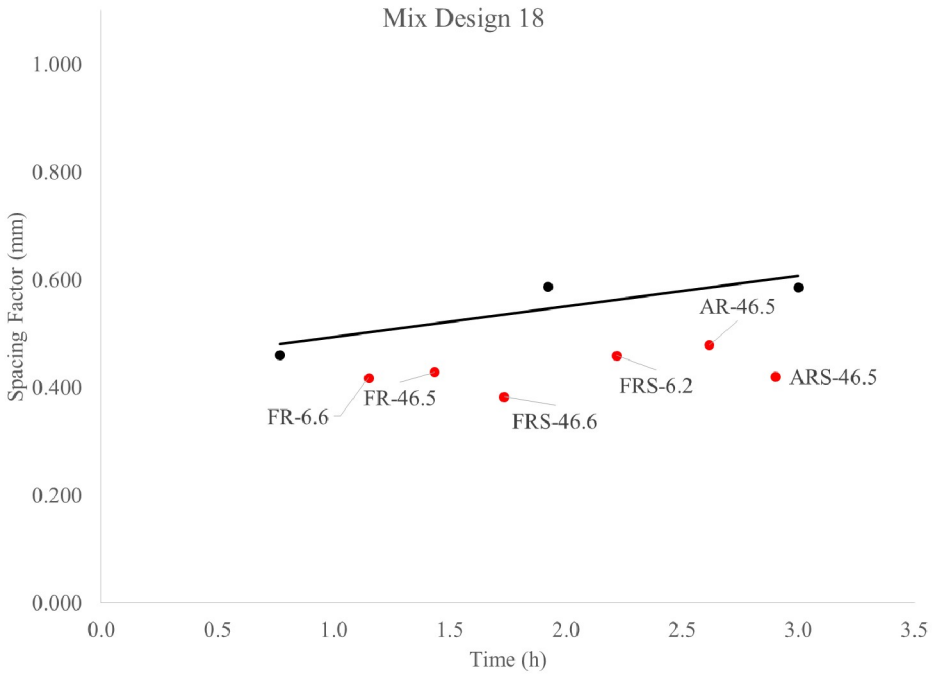

Figure B4.18. Spacing factor for non-pumped (black) and pumped (red) samples as a function of time for mix design 18.

B.5 Freeze-thaw resistance

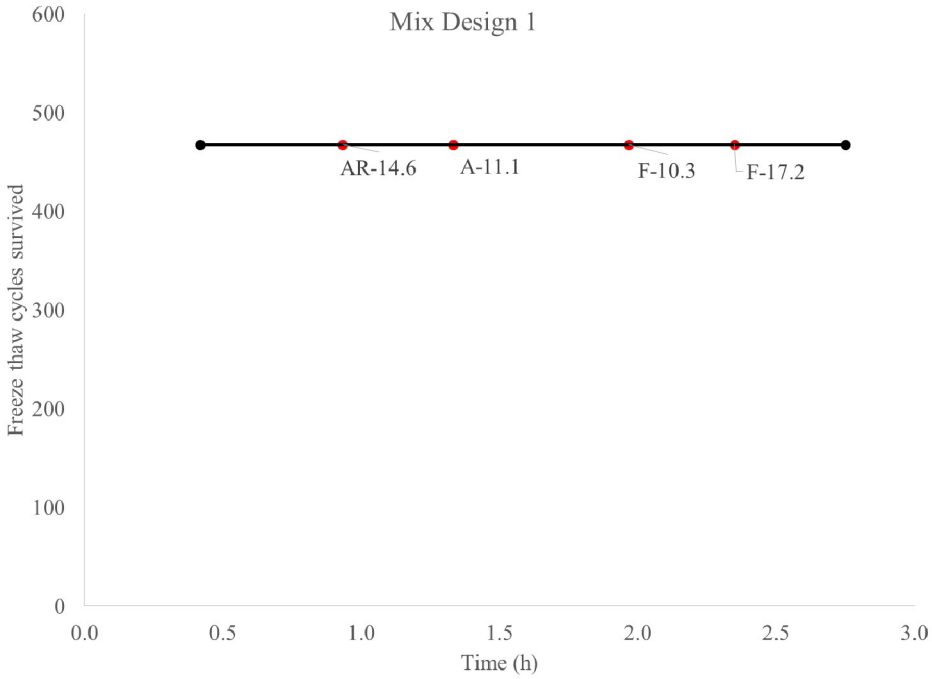

Figure B5.1: Number of cycles survived in freeze-thaw chamber for non-pumped (black) and pumped (red) samples for mix design 1.

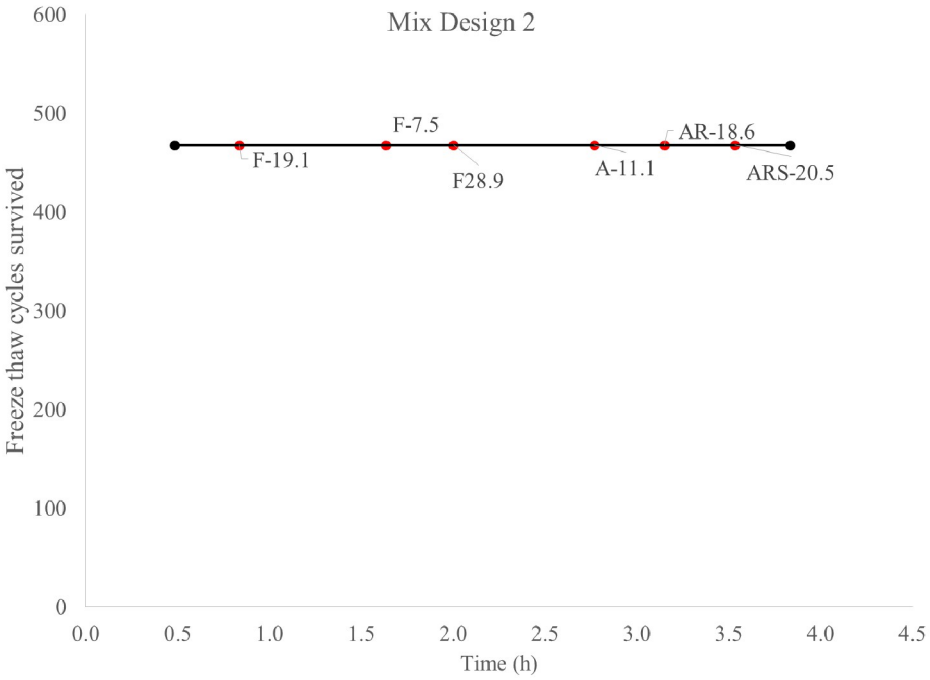

Figure B5.2: Number of cycles survived in freeze-thaw chamber for non-pumped (black) and pumped (red) samples for mix design 2.

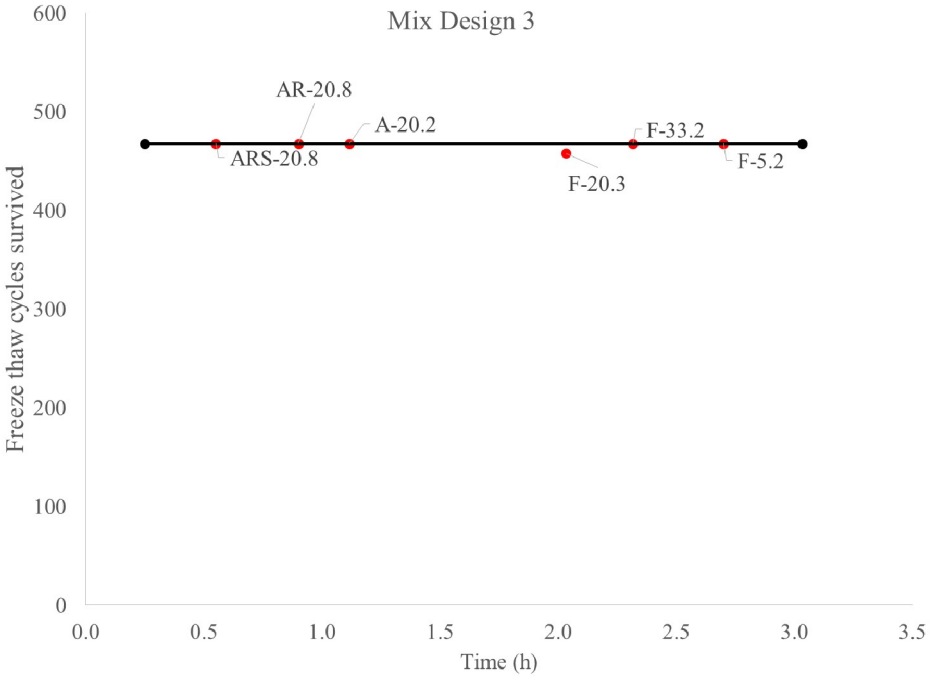

Figure B5.3: Number of cycles survived in freeze-thaw chamber for non-pumped (black) and pumped (red) samples for mix design 3.

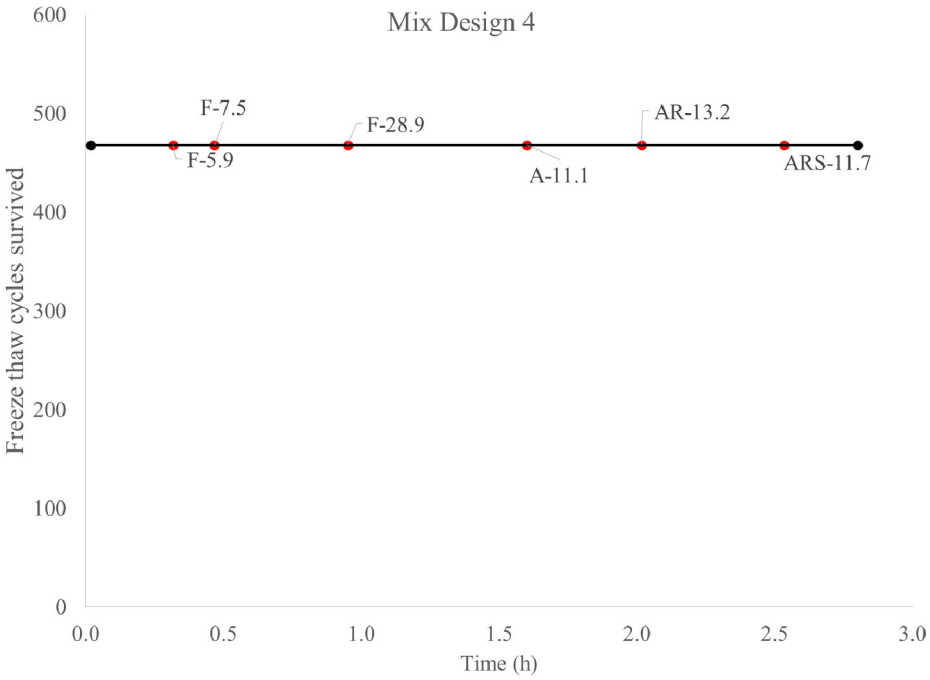

Figure B5.4: Number of cycles survived in freeze-thaw chamber for non-pumped (black) and pumped (red) samples for mix design 4.

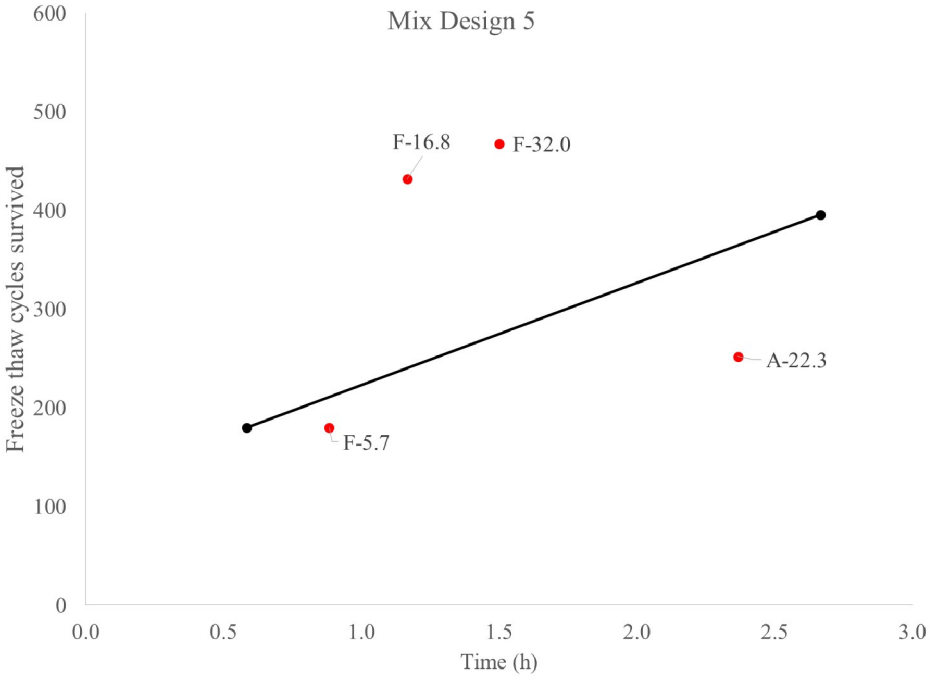

Figure B5.5: Number of cycles survived in freeze-thaw chamber for non-pumped (black) and pumped (red) samples for mix design 5.

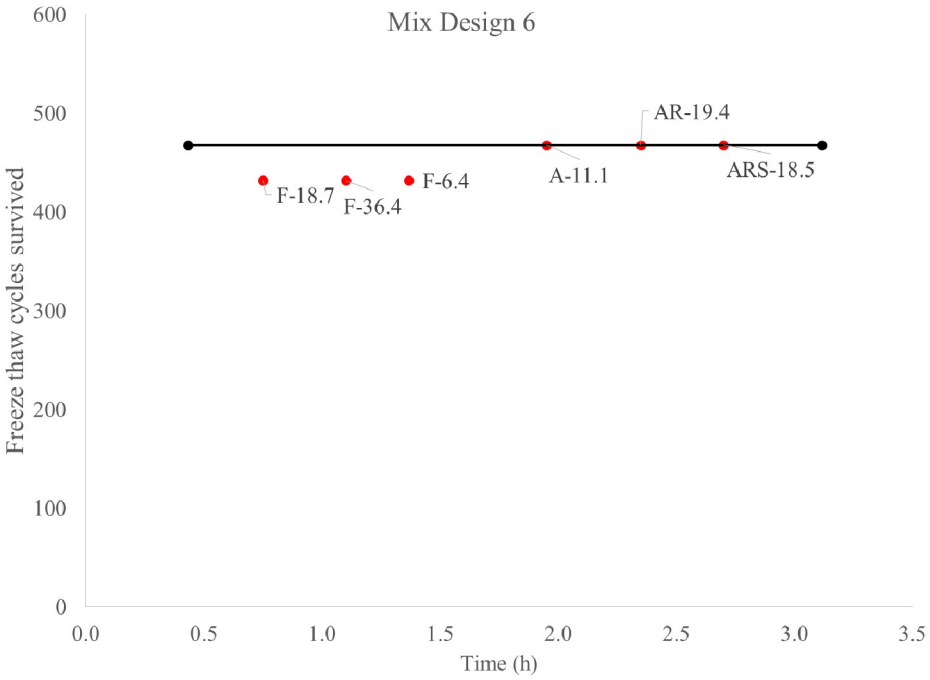

Figure B5.6: Number of cycles survived in freeze-thaw chamber for non-pumped (black) and pumped (red) samples for mix design 6.

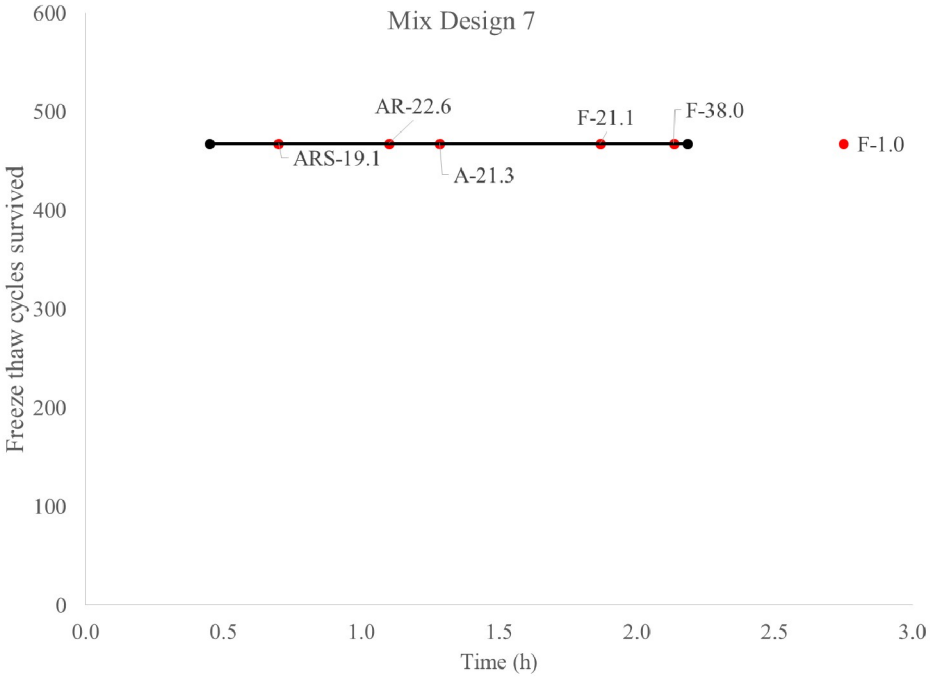

Figure B5.7: Number of cycles survived in freeze-thaw chamber for non-pumped (black) and pumped (red) samples for mix design 7.

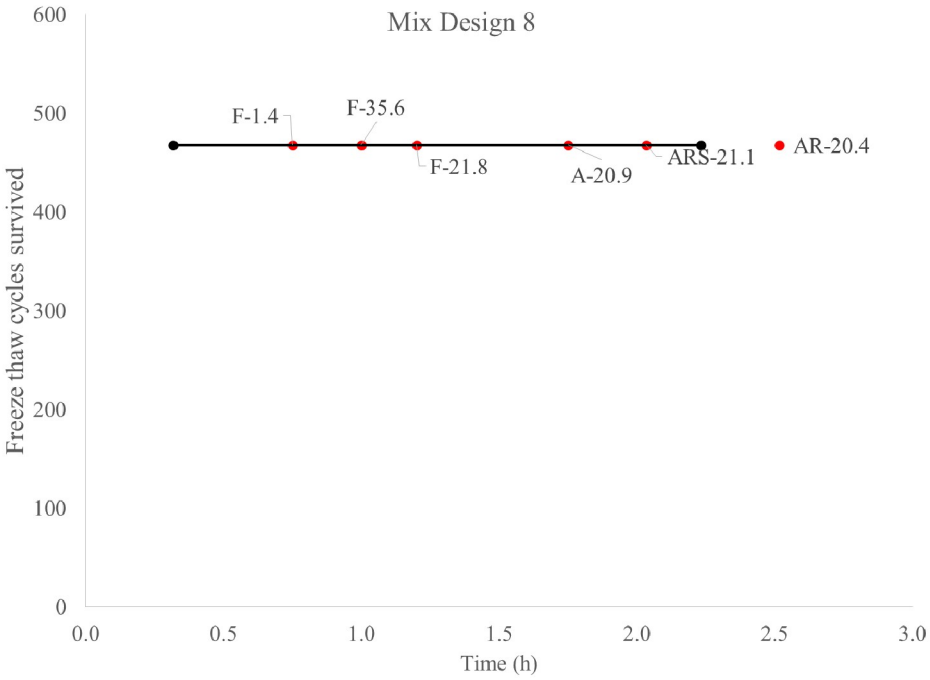

Figure B5.8: Number of cycles survived in freeze-thaw chamber for non-pumped (black) and pumped (red) samples for mix design 8.

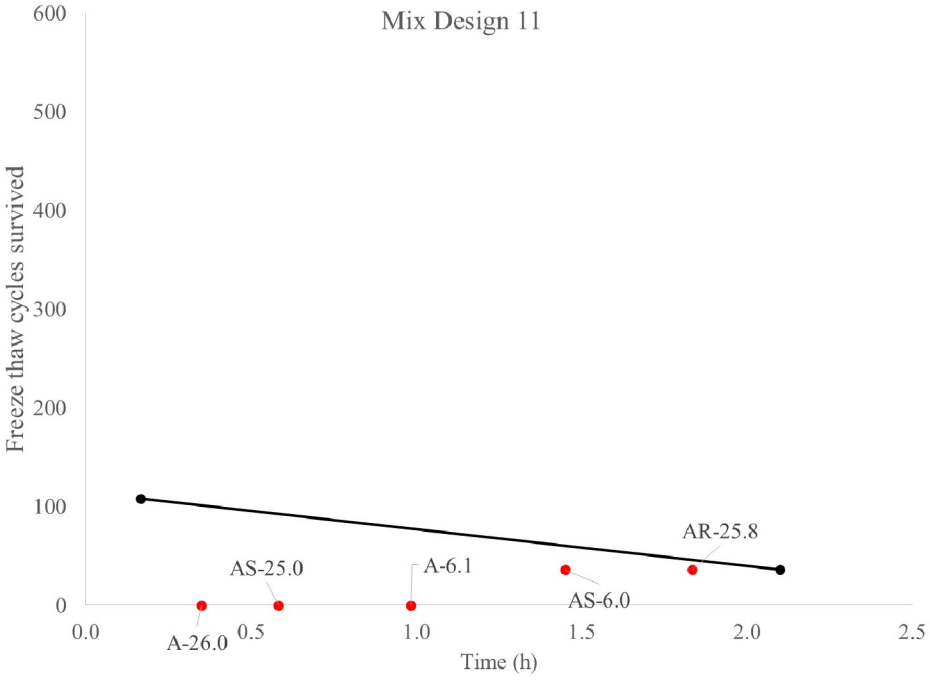

Figure B5.9: Number of cycles survived in freeze-thaw chamber for non-pumped (black) and pumped (red) samples for mix design 11.

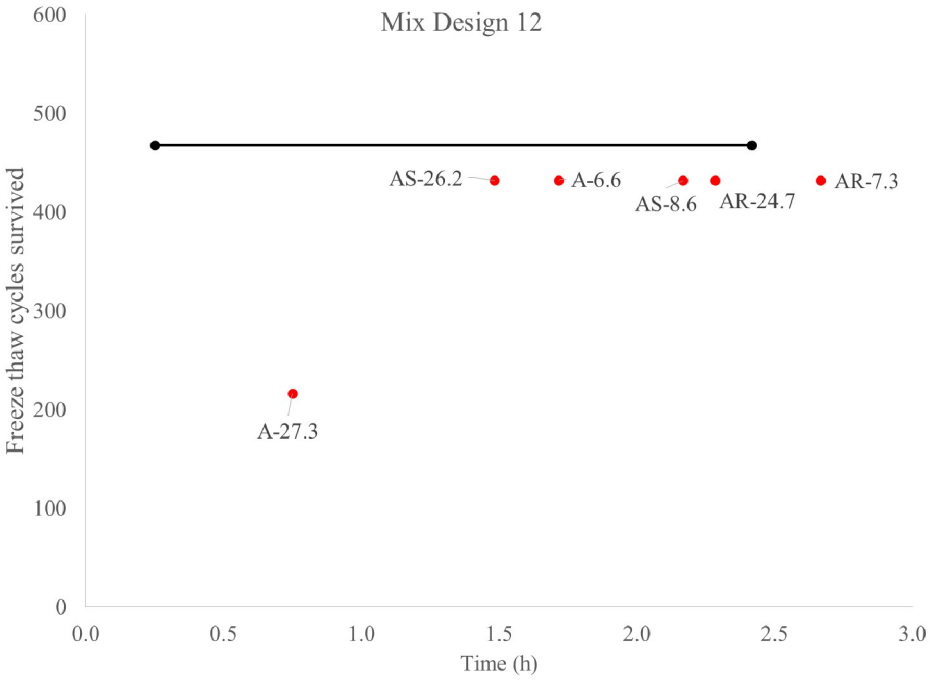

Figure B5.10: Number of cycles survived in freeze-thaw chamber for non-pumped (black) and pumped (red) samples for mix design 12.

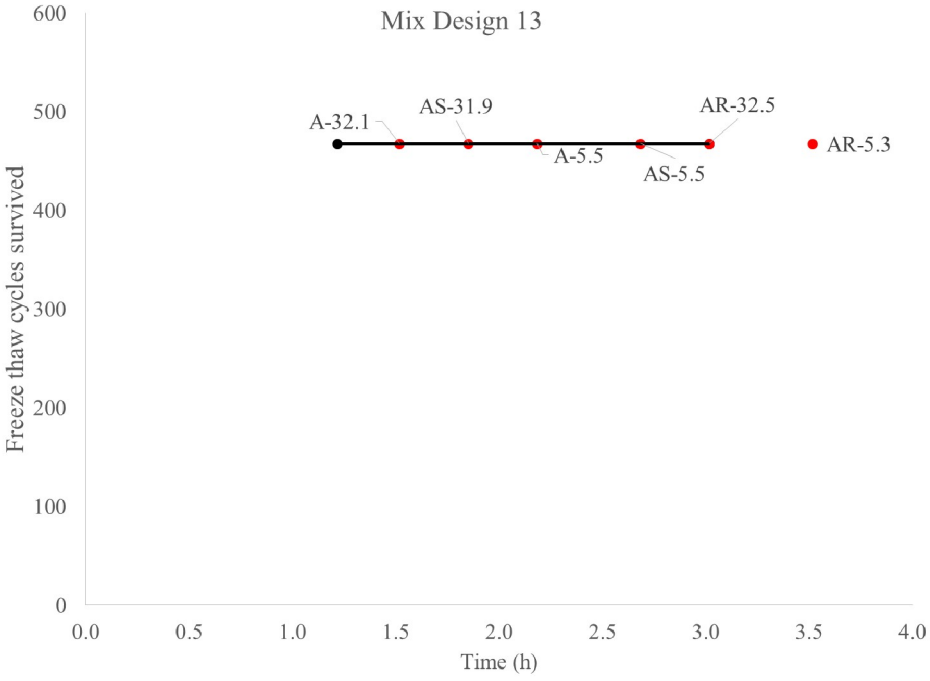

Figure B5.11: Number of cycles survived in freeze-thaw chamber for non-pumped (black) and pumped (red) samples for mix design 13.

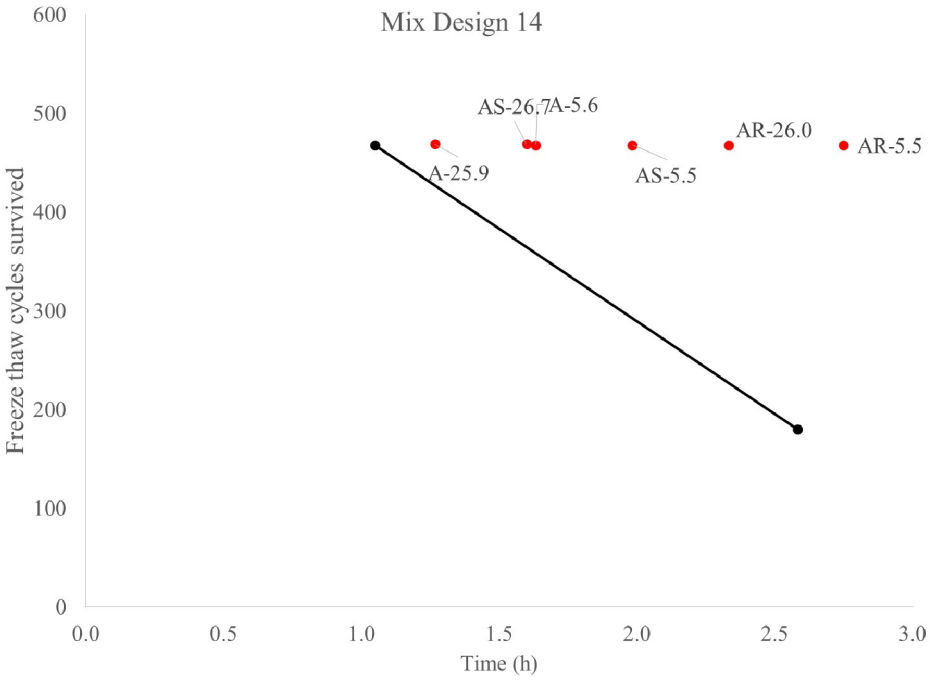

Figure B5.12: Number of cycles survived in freeze-thaw chamber for non-pumped (black) and pumped (red) samples for mix design 14.

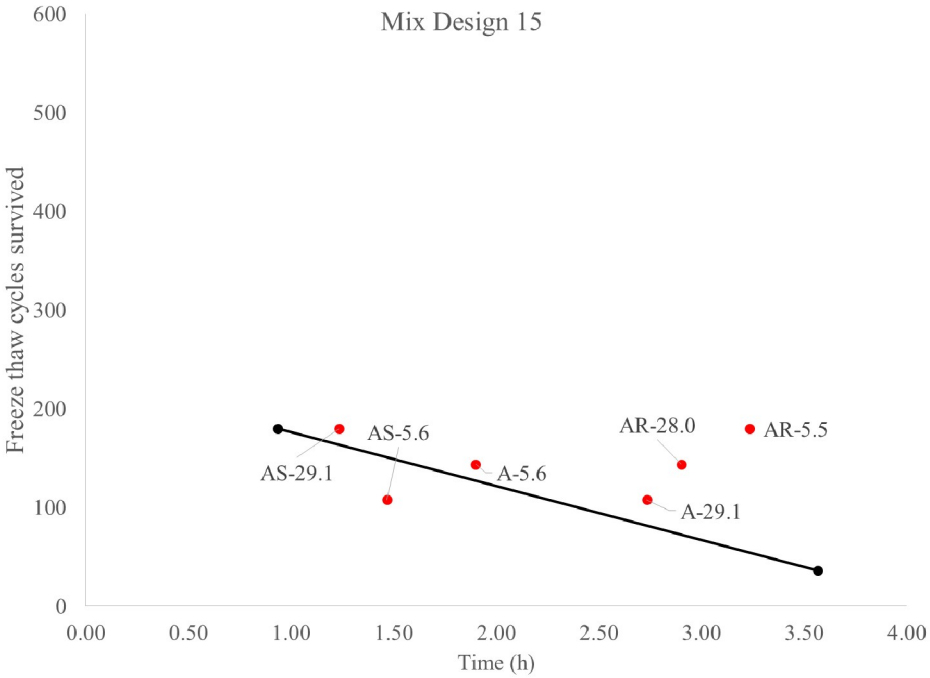

Figure B5.13: Number of cycles survived in freeze-thaw chamber for non-pumped (black) and pumped (red) samples for mix design 15.

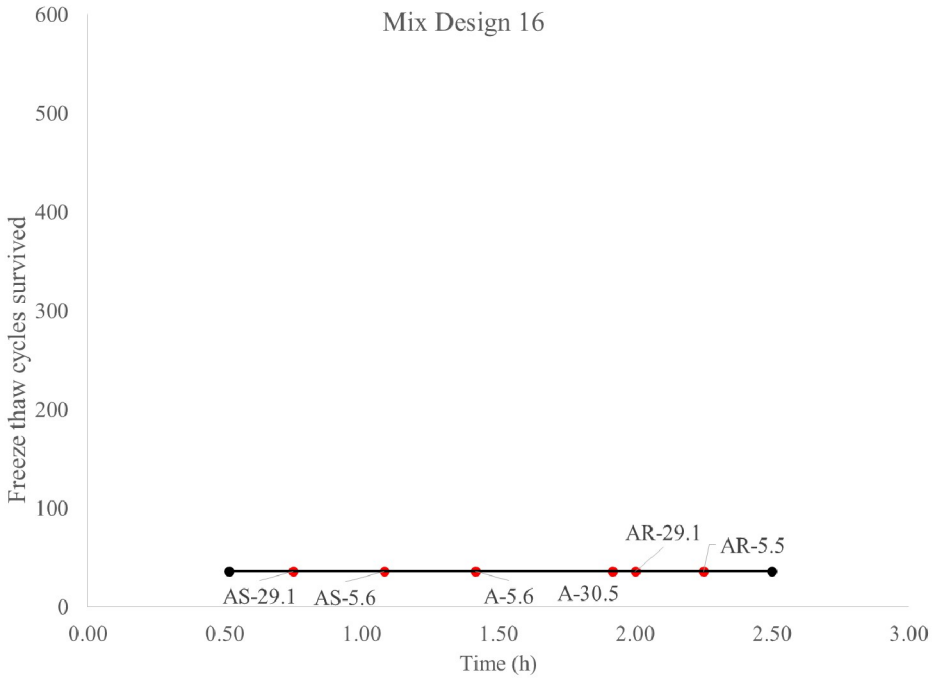

Figure B5.14: Number of cycles survived in freeze-thaw chamber for non-pumped (black) and pumped (red) samples for mix design 16.

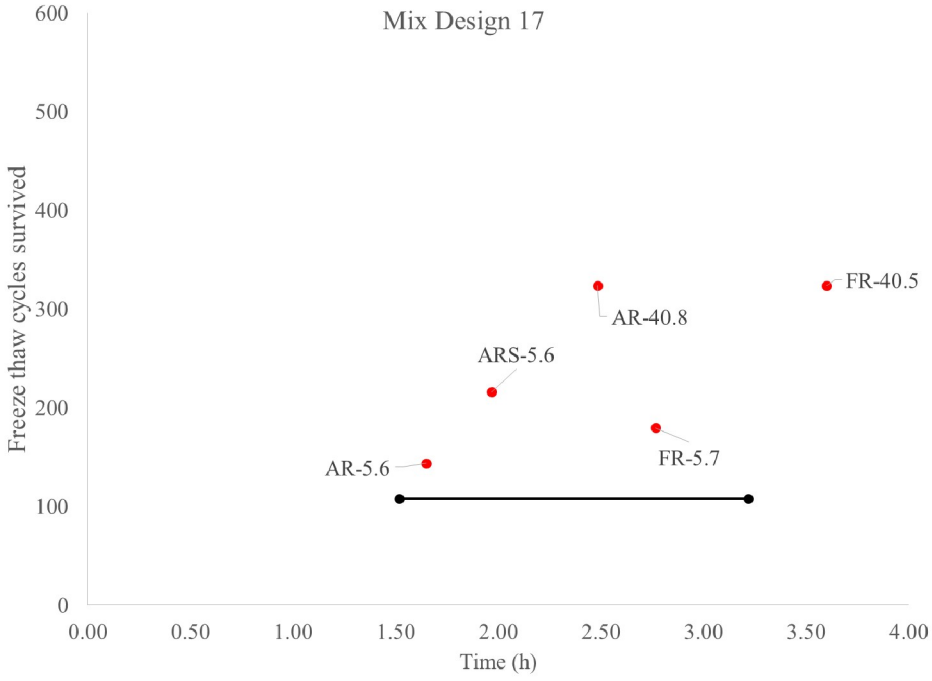

Figure B5.15: Number of cycles survived in freeze-thaw chamber for non-pumped (black) and pumped (red) samples for mix design 17.

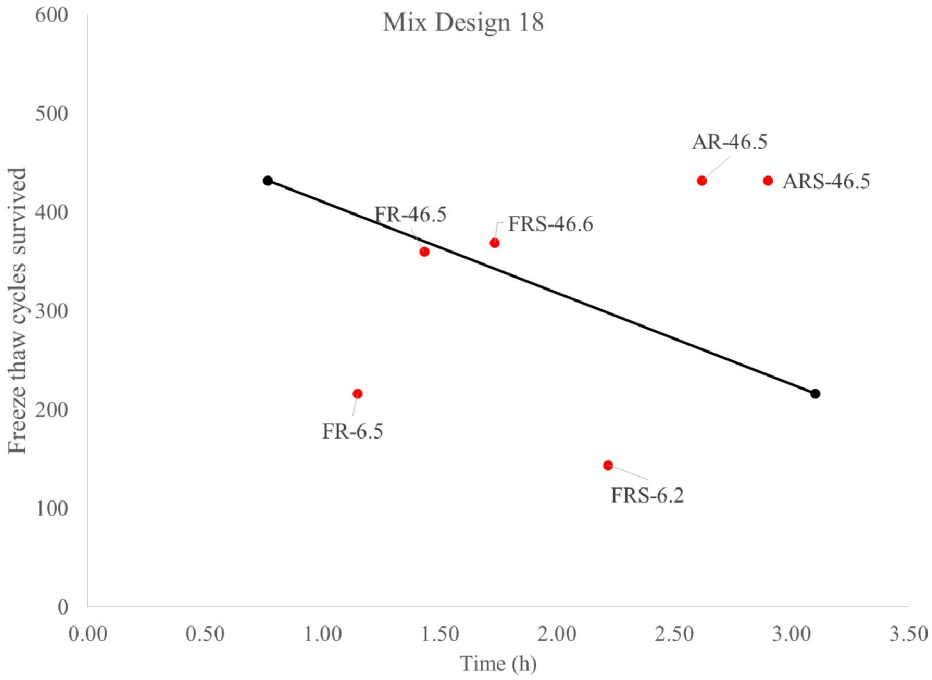

Figure B5.16: Number of cycles survived in freeze-thaw chamber for non-pumped (black) and pumped (red) samples for mix design 18.

B.6 Scaling of top surfaces of blocks

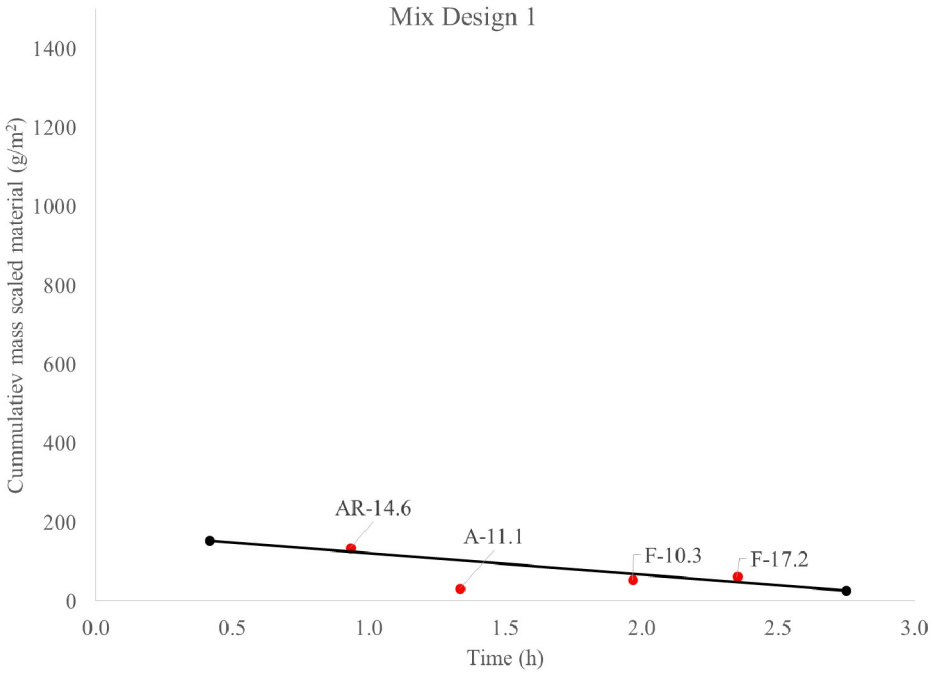

Figure B6.1: Cumulative scaling of the top of the blocks, non-pumped (black) and pumped samples (red), for mixture 1.

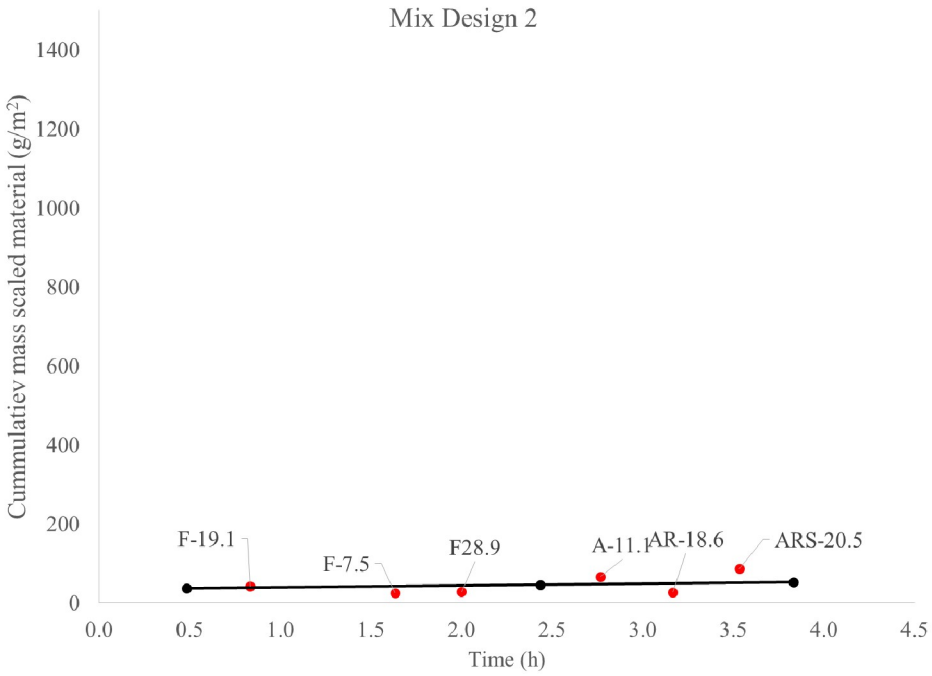

Figure B6.2: Cumulative scaling of the top of the blocks, non-pumped (black) and pumped samples (red), for mixture 2.

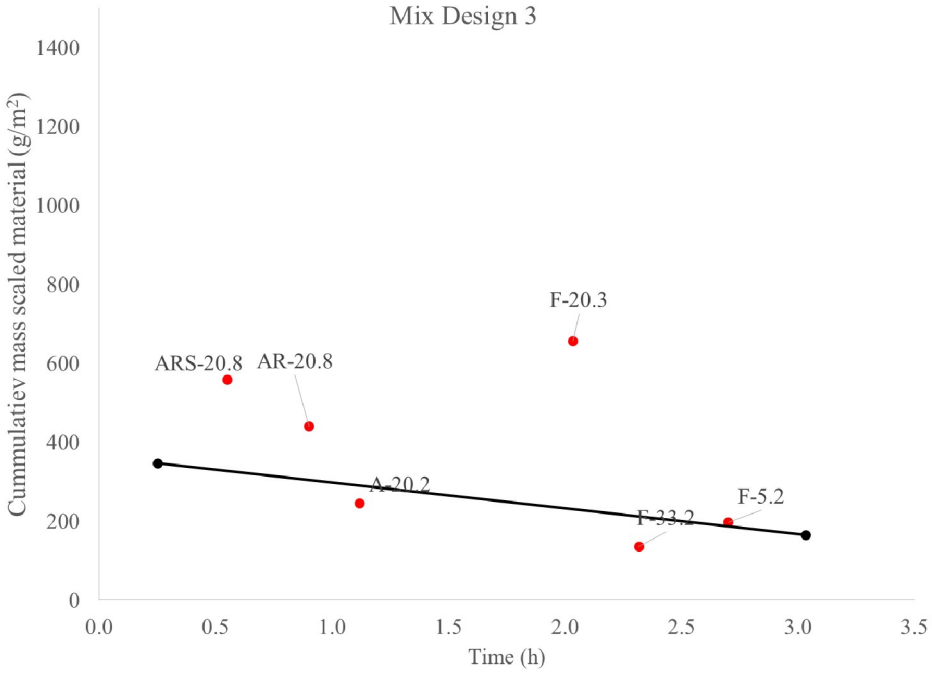

Figure B6.3: Cumulative scaling of the top of the blocks, non-pumped (black) and pumped samples (red), for mixture 3.

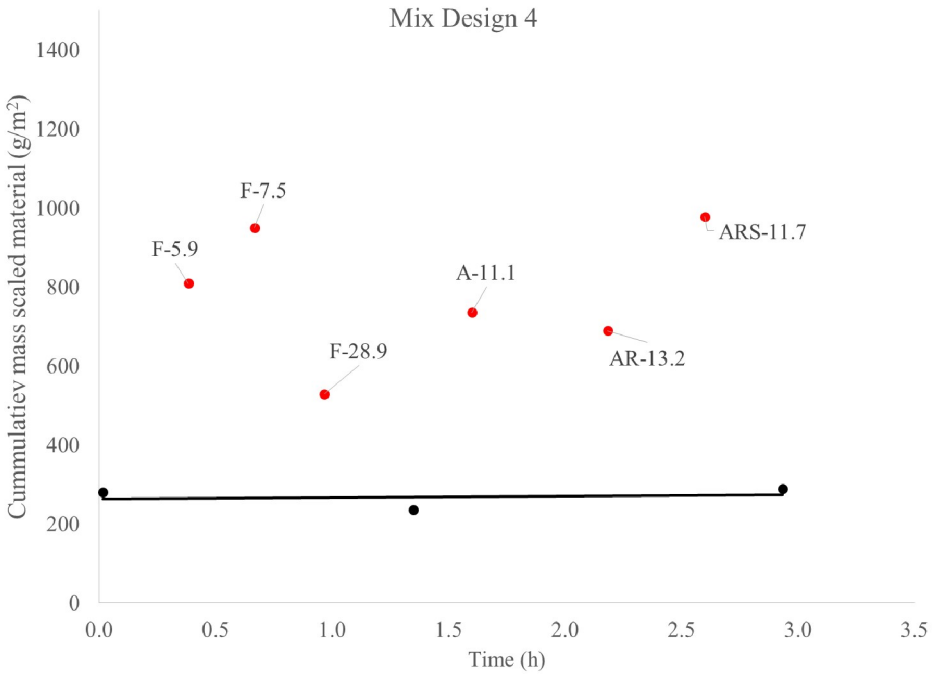

Figure B6.4: Cumulative scaling of the top of the blocks, non-pumped (black) and pumped samples (red), for mixture 4.

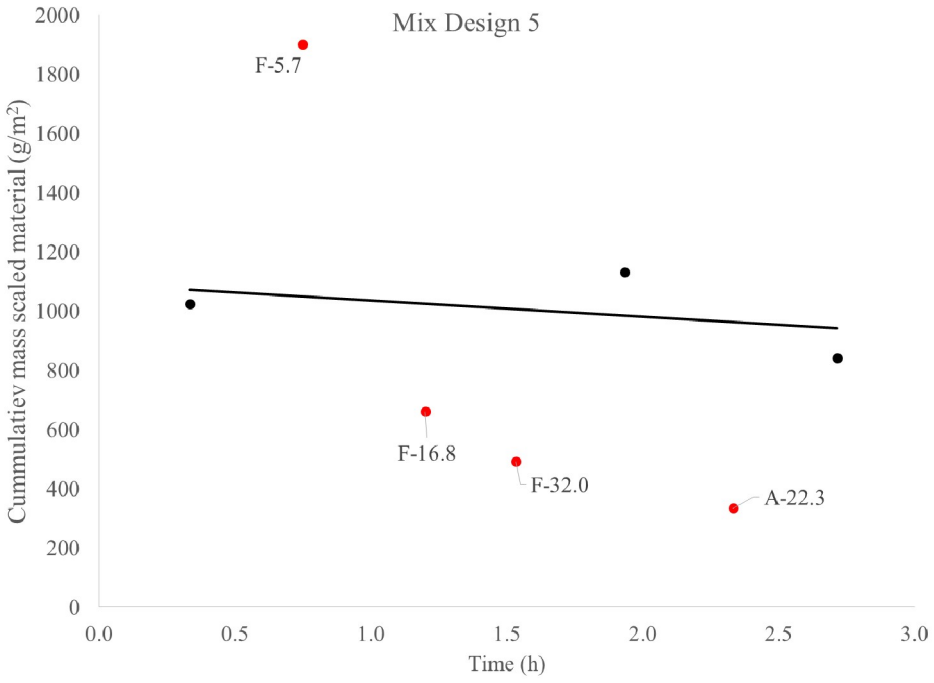

Figure B6.5: Cumulative scaling of the top of the blocks, non-pumped (black) and pumped samples (red), for mixture 5.

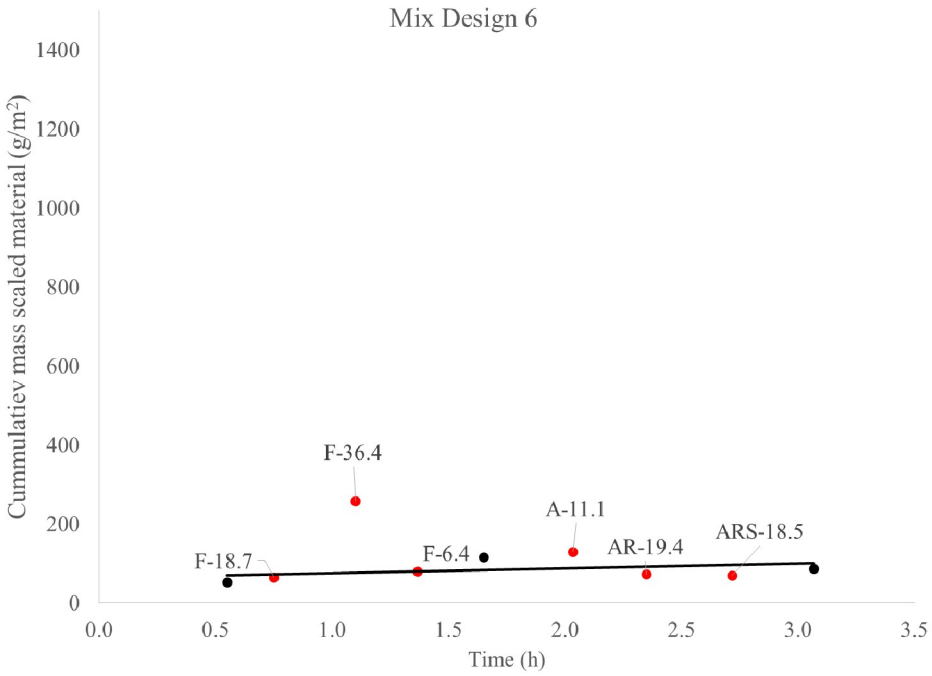

Figure B6.6: Cumulative scaling of the top of the blocks, non-pumped (black) and pumped samples (red), for mixture 6.

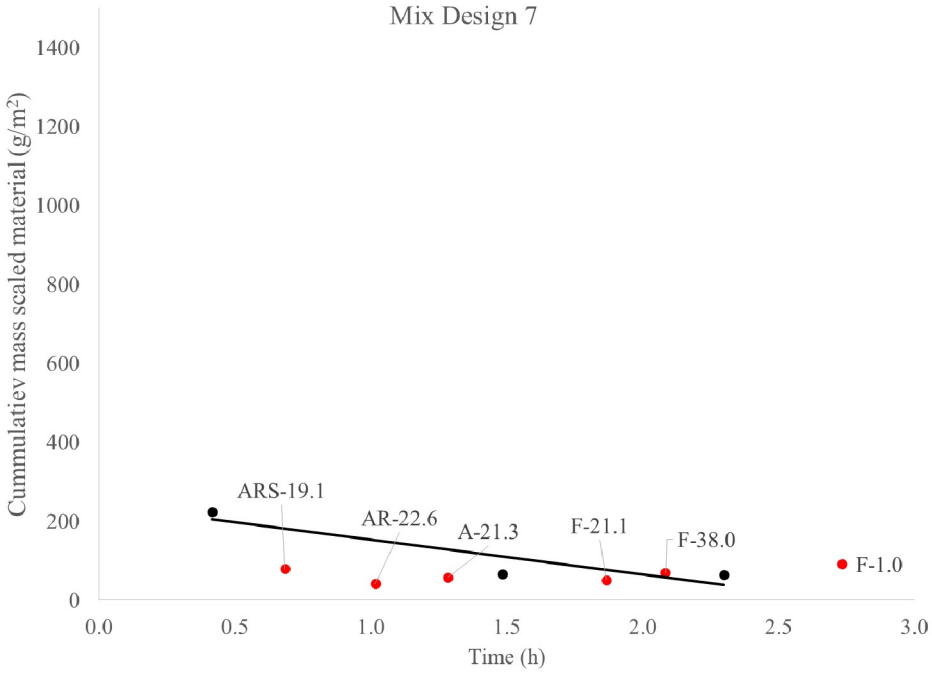

Figure B6.7: Cumulative scaling of the top of the blocks, non-pumped (black) and pumped samples (red), for mixture 7.

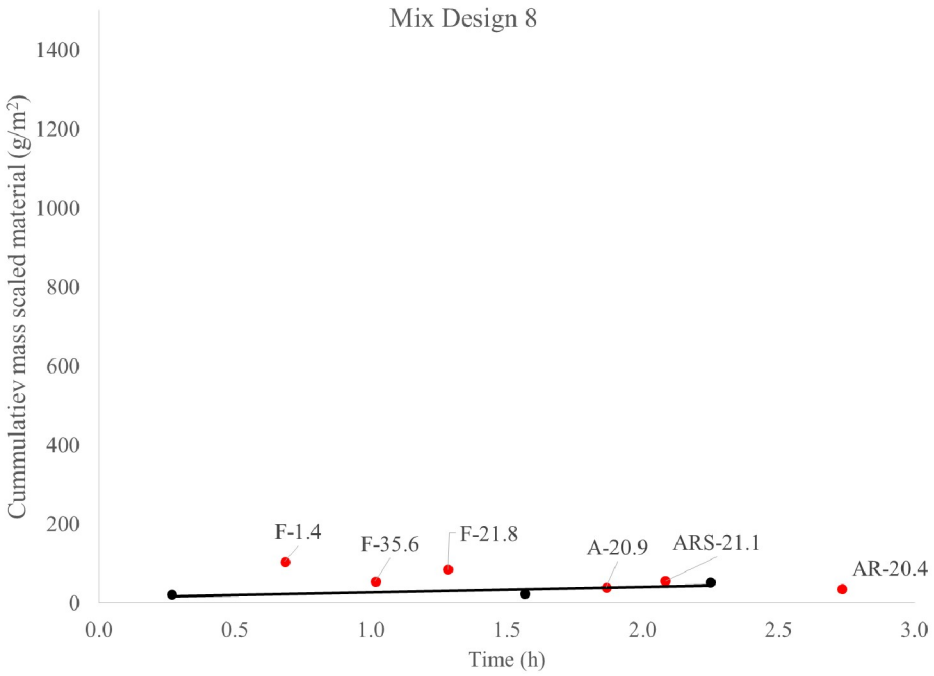

Figure B6.8: Cumulative scaling of the top of the blocks, non-pumped (black) and pumped samples (red), for mixture 8.

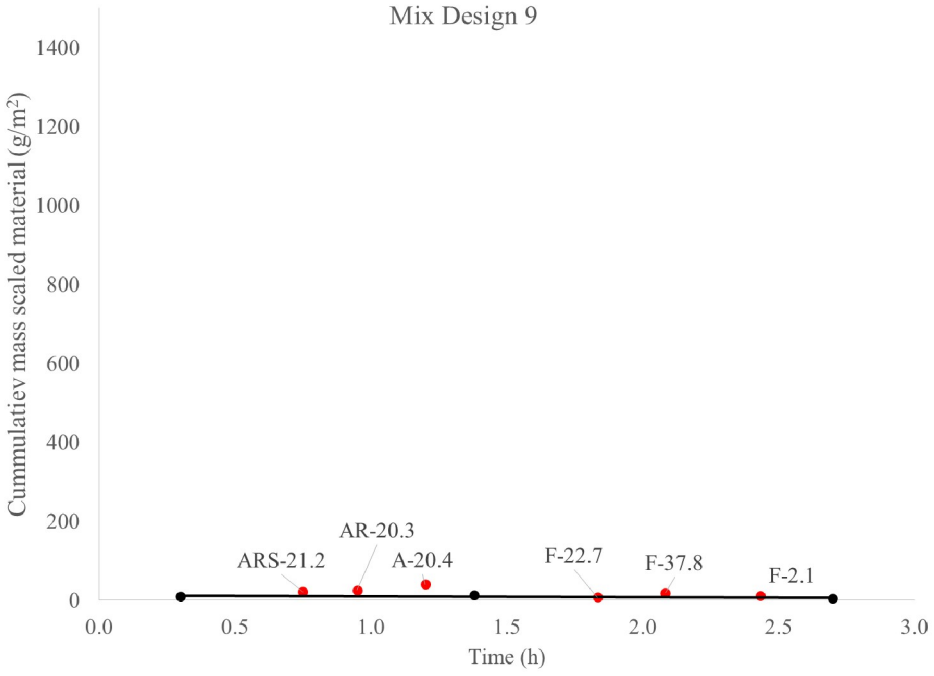

Figure B6.9: Cumulative scaling of the top of the blocks, non-pumped (black) and pumped samples (red), for mixture 9.

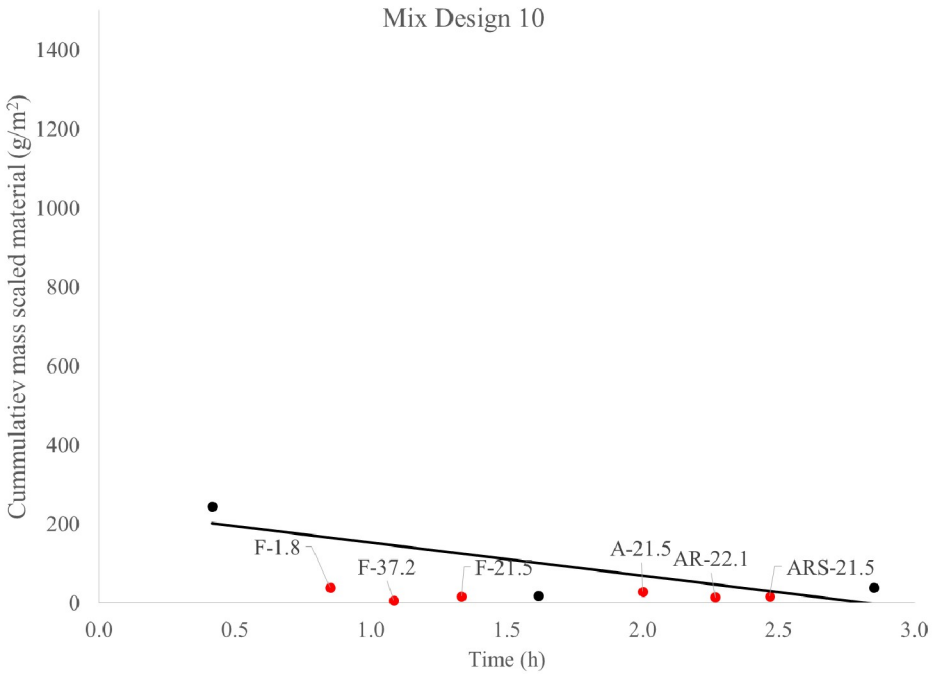

Figure B6.10: Cumulative scaling of the top of the blocks, non-pumped (black) and pumped samples (red), for mixture 10.

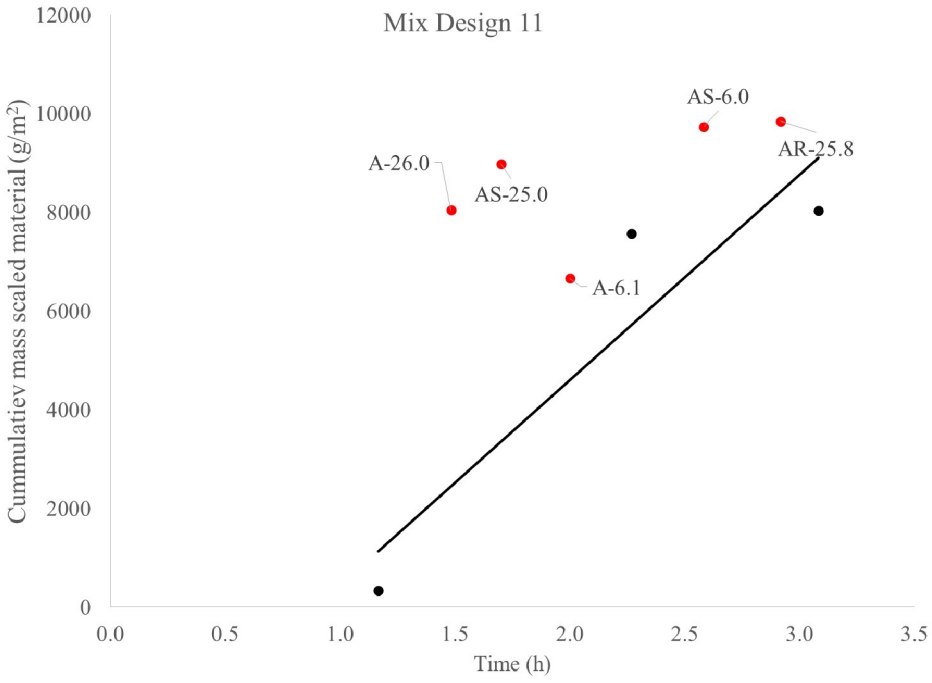

Figure B6.11: Cumulative scaling of the top of the blocks, non-pumped (black) and pumped samples (red), for mixture 11.

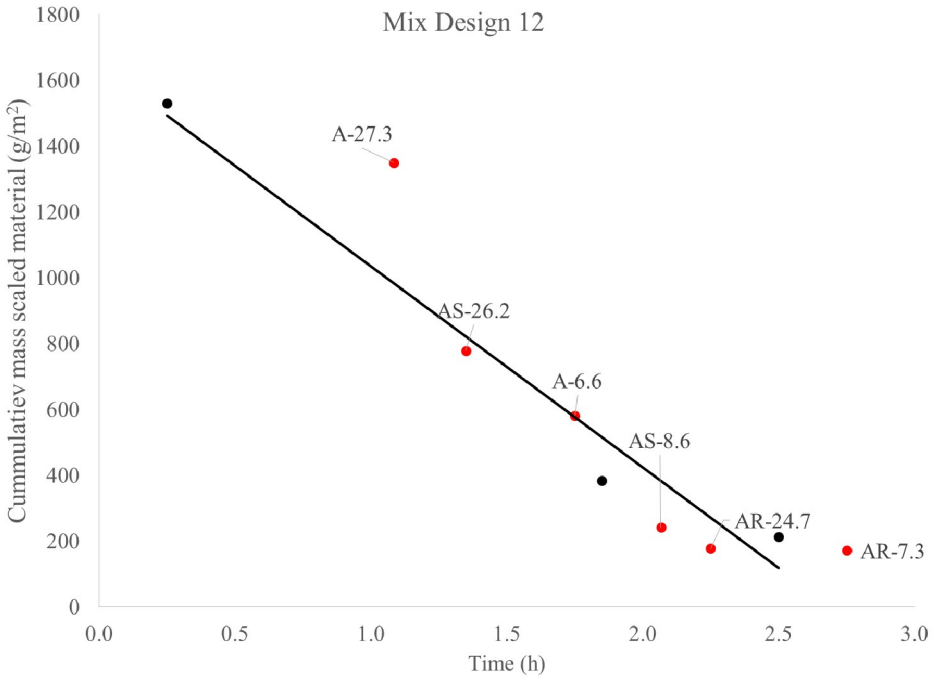

Figure B6.12: Cumulative scaling of the top of the blocks, non-pumped (black) and pumped samples (red), for mixture 12.

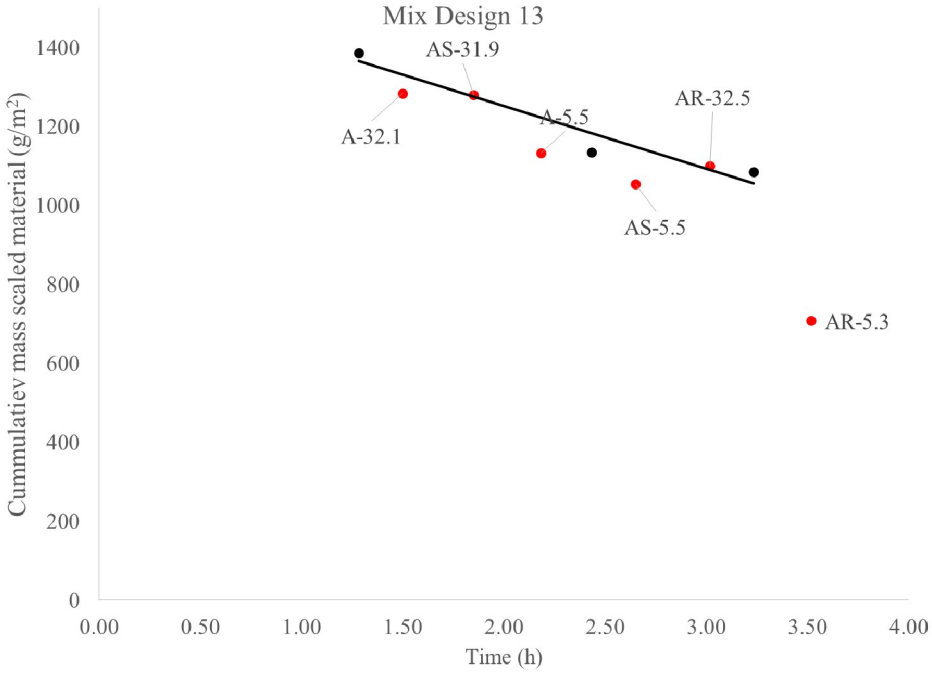

Figure B6.13: Cumulative scaling of the top of the blocks, non-pumped (black) and pumped samples (red), for mixture 13.

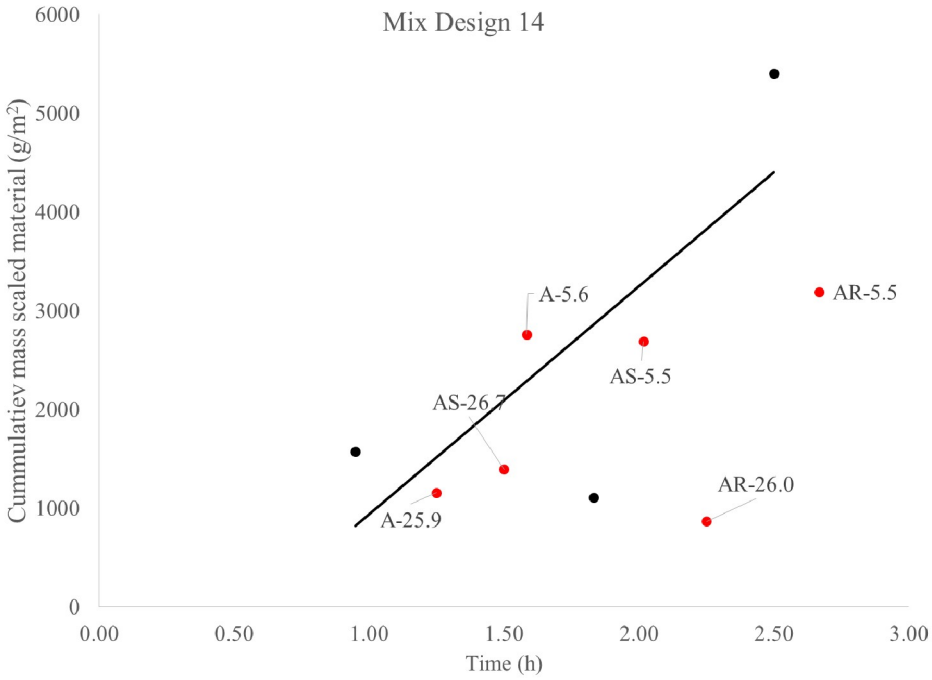

Figure B6.14: Cumulative scaling of the top of the blocks, non-pumped (black) and pumped samples (red), for mixture 14.

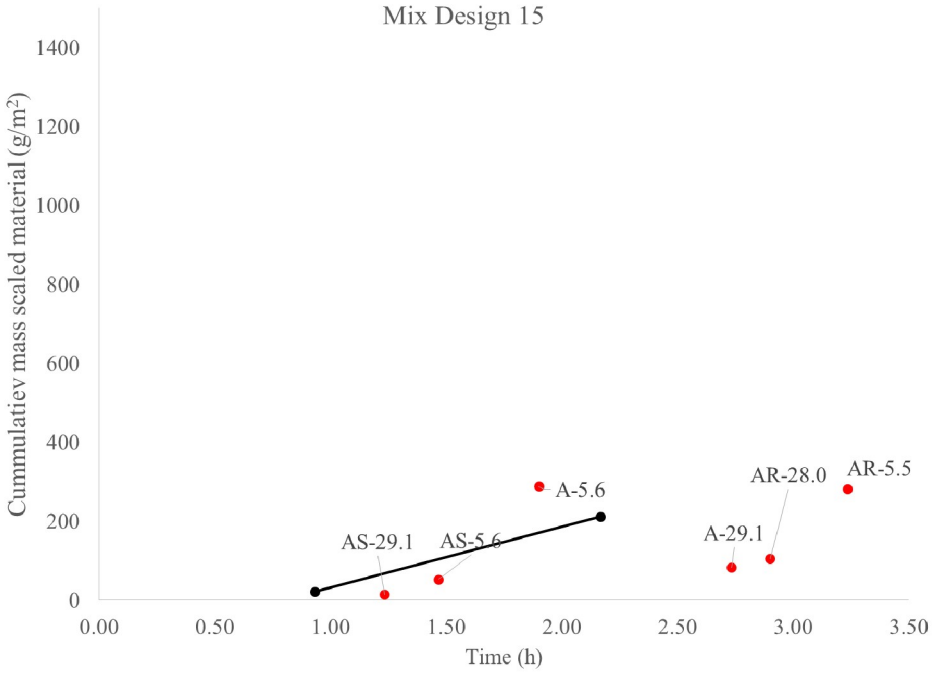

Figure B6.15: Cumulative scaling of the top of the blocks, non-pumped (black) and pumped samples (red), for mixture 15.

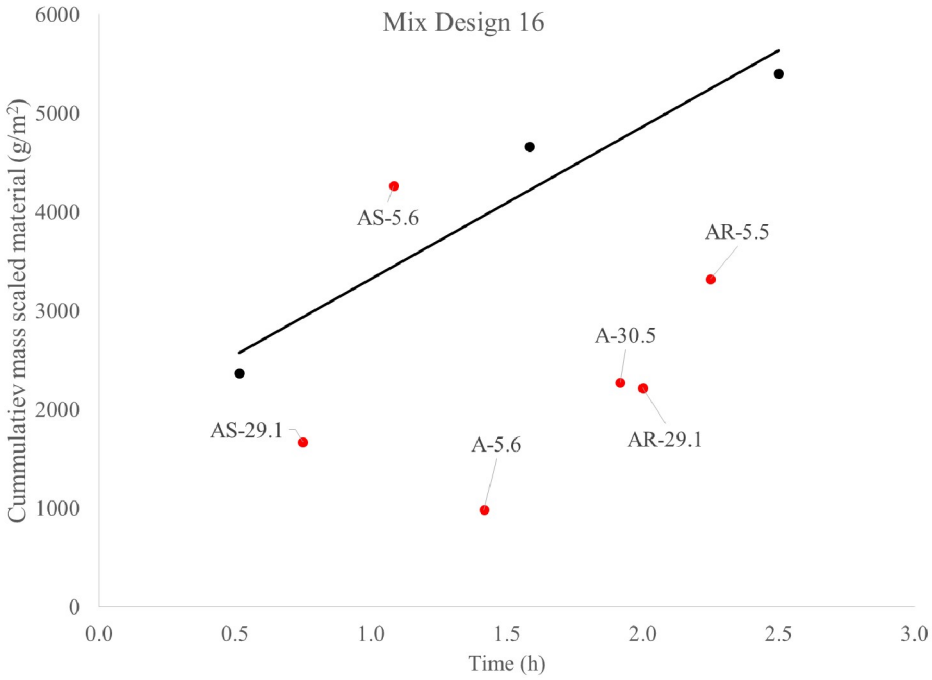

Figure B6.16: Cumulative scaling of the top of the blocks, non-pumped (black) and pumped samples (red), for mixture 16.

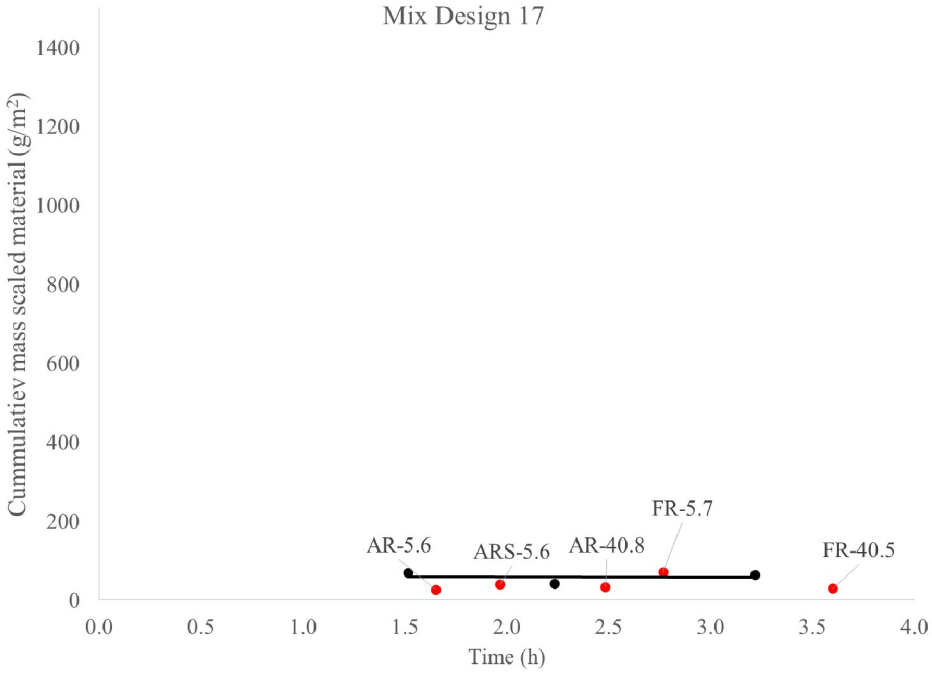

Figure B6.17: Cumulative scaling of the top of the blocks, non-pumped (black) and pumped samples (red), for mixture 17.

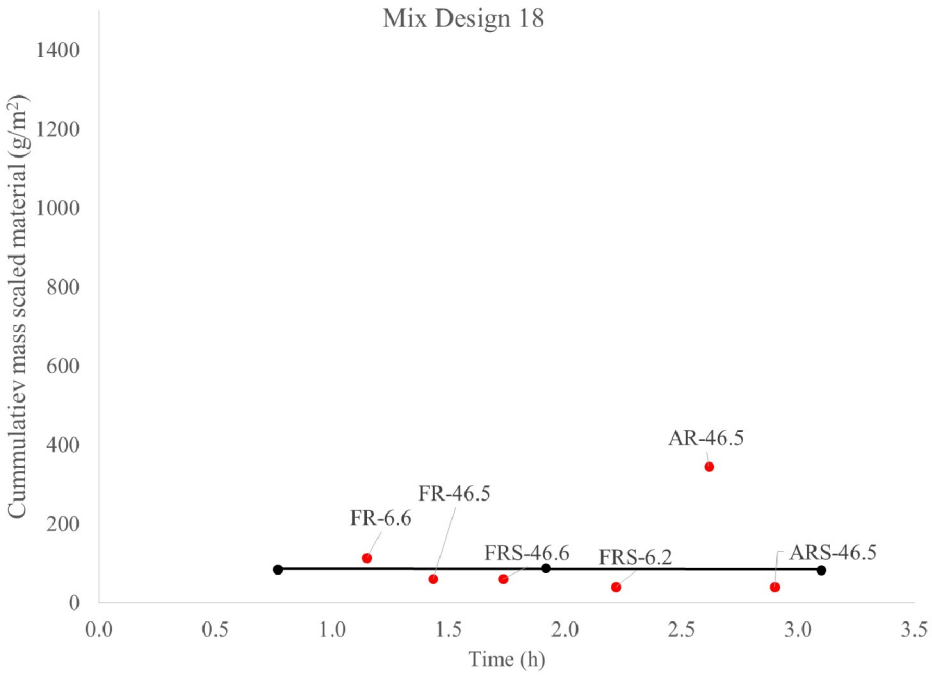

Figure B6.18: Cumulative scaling of the top of the blocks, non-pumped (black) and pumped samples (red), for mixture 18.

Appendix C: Freeze-Thaw Data

This appendix shows the raw data from the freeze-thaw tests.

Table C.1: Relative dynamic modulus for mix design 1.

		Mix Design 1					
		BT	AT	A-R	A	F	F
Flow rate	l/s			14.6	11.1	10.3	17.2
Time	h	0.4	2.8	0.9	1.3	2.0	2.4
Cycles	0	100	100	100	100	100	100
	36	103	101	98	98	104	98
	72	105	102	99	100	103	99
	108	103	102	99	102	103	102
	144	103	101	100	100	103	98
	180	103	100	98	100	101	98
	216	103	100	98	98	103	97
	252	102	101	99	101	105	98
	288	100	102	95	100	101	99
	324	101	98	95	96	100	93
	360	105	103	101	97	103	97
	396	101	100	97	96	100	95
	432	101	100	97	97	103	96
	468	101	100	98	98	102	96

Table C.2: Relative dynamic modulus for mix design 2.

		Mix Design 2							
		BT	AT	F	F	F	A	A-R	A-R(S)
Flow rate	l/s			19.1	7.5	28.9	11.1	18.6	20.5
Time	h	0.5	3.8	0.8	1.6	2.0	2.8	3.2	3.5
Cycles	0	100	100	100	100	100	100	100	100
	36	96	100	101	98	99	102	95	98
	72	99	96	96	97	98	98	95	101
	108	97	97	96	97	98	99	94	100
	144	97	96	96	98	100	99	96	98
	180	96	96	96	96	98	98	95	99
	216	96	96	95	97	95	97	94	97
	252	96	95	96	96	96	98	95	98
	288	97	93	96	98	97	101	96	99
	324	97	91	96	93	94	100	92	99
	360	92	94	91	91	95	96	92	97
	396	94	95	99	95	95	100	94	97
	432	97	94	94	93	95	96	94	97
	468	94	96	94	95	97	96	94	96

Table C.3: Relative dynamic modulus for mix design 3.

		Mix Design 3							
		BT	AT	A-R(S)	A-R	A	F	F	F
Flow rate	l/s			20.8	20	20.2	20.3	33.2	5.2
Time	h	0.3	3.0	0.6	0.9	1.1	2.0	2.3	2.7
Cycles	0	100	100	100	100	100	100	100	100
	36	99	98	97	99	98	99	97	99
	72	100	98	100	99	97	101	99	99
	108	102	100	101	100	100	101	99	102
	144	101	100	101	102	102	102	100	102
	180	100	99	96	97	96	98	97	99
	216	103	101	102	102	102	104	101	103
	252	100	100	99	95	99	97	95	97
	288	100	99	100	99	98	100	100	99
	324	100	98	99	101	97	98	98	100
	360	100	98	99	97	97	98	97	100
	396	100	98	98	97	98	99	97	99
	432	100	94	99	97	98	98	99	99
	468	100	100	100	100	99	99	100	102

Table C.4: Relative dynamic modulus for mix design 4.

		Mix Design 4							
		BT	AT	F	F	F	A	A-R	A-R(S)
Flow rate	l/s			5.9	7.5	28.9	11.1	13.2	11.7
Time	h	0.0	2.9	0.4	0.7	1.0	1.6	2.2	2.6
Cycles	0	100	100	100	100	100	100	100	100
	36	99	113	100	101	101	103	100	97
	72	107	104	103	104	107	106	105	101
	108	103	101	102	105	107	107	106	102
	144	102	103	95	100	103	103	101	98
	180	105	104	99	107	100	109	99	98
	216	107	104	104	109	108	110	107	105
	252	106	104	103	107	107	110	104	104
	288	105	104	104	107	108	108	106	103
	324	107	104	101	108	107	110	104	103
	360	106	103	103	106	105	110	107	104
	396	108	101	104	107	108	108	103	99
	432	106	105	104	105	107	110	108	104
	468	115	108	106	111	112	114	111	106

Table C.5: Relative dynamic modulus for mix design 5.

		Mix Design 5					
		BT	AT	F	F	F	A
Flow rate	l/s			5.7	16.8	32	22.3
Time	h	0.3	2.7	0.8	1.2	1.5	2.3
Cycles	0	100	100	100	100	100	100
	36	101	98	102	101	101	100
	72	97	92	101	102	100	100
	108	91	87	100	96	95	101
	144	83	91	100	102	97	100
	180	81	85	95	98	97	97
	216	76	82	X	103	101	97
	252	72	79		99	100	93
	288	67	76		97	98	X
	324	63	73		95	95	
	360	X	70		83	92	
	396		67		77	83	
	432		64		78		
	468		61		X	79	

Table C.6: Relative dynamic modulus for mix design 6.

		Mix Design 6							
		BT	AT	F	F	F	A	A-R	A-R(S)
Flow rate	l/s			18.68	36.38	6.37	11.143	19.4	18.5
Time	h	0.6	1.7	0.8	1.1	1.4	2.0	2.4	2.7
Cycles	0	100	100	100	100	100	100	100	100
	36	102	103	102	102	101	101	103	99
	72	105	107	107	106	103	104	105	98
	108	104	106	105	105	102	102	106	99
	144	107	110	111	107	106	106	108	104
	180	105	109	107	106	105	105	109	104
	216	109	110	107	107	105	105	108	104
	252	108	107	101	106	105	105	110	104
	288	108	107	107	106	100	105	110	101
	324	105	105	103	103	103	101	108	100
	360	108	110	99	102	100	105	107	101
	396	107	106	88	95	93	96	105	97
	432	106	108	80	88	90	102	105	100
	468	105	102	X	X	X	97	99	99

Table C.7: Relative dynamic modulus for mix design 7.

		Mix Design 7							
		BT	AT	A-R(S)	A-R	A	F	F	F
Flow rate	l/s			19.11	22.58	21.28	21.09	38.0	1.1
Time	h	0.4	2.3	0.7	1.0	1.3	1.9	2.1	2.7
Cycles	0	100	100	100	100	100	100	100	100
	36	101	100	100	100	100	101	99	103
	72	103	102	103	101	101	103	100	101
	108	99	100	102	102	101	102	102	97
	144	104	102	99	103	101	103	101	102
	180	98	97	99	96	98	100	91	97
	216	102	103	102	102	101	103	103	102
	252	105	102	105	100	100	104	103	102
	288	105	104	103	102	103	104	105	103
	324	105	104	103	103	103	103	96	103
	360	98	99	100	98	97	99	97	102
	396	108	106	107	106	106	107	106	102
	432	105	103	105	104	104	105	102	102
	468	105	101	98	102	100	102	98	96

Table C.8: Relative dynamic modulus for mix design 8.

		Mix Design 8							
		BT	AT	F	F	F	A	A-R(S)	A-R
Flow rate	l/s			1.4	35.56	21.84	20.92	21.1	20.4
Time	h	0.3	2.3	0.7	1.0	1.3	1.9	2.1	2.7
Cycles	0	100	100	100	100	100	100	100	100
	36	104	98	94	97	98	94	92	97
	72	100	100	100	97	99	100	99	99
	108	99	101	100	98	98	100	98	99
	144	98	102	95	97	95	96	96	100
	180	99	97	93	98	94	99	99	100
	216	100	103	100	102	101	102	102	101
	252	102	103	102	97	102	101	101	102
	288	101	103	102	102	101	100	102	100
	324	101	103	98	101	100	97	100	99
	360	100	101	102	100	101	100	100	101
	396	101	103	101	101	102	96	100	101
	432	99	102	100	102	99	96	101	100
	468	102	103	103	102	103	101	103	102

Table C.9: Relative dynamic modulus for mix design 11.

		Mix Design 11						
		BT	AT	A	A-(S)	A	A-(S)	A-R
Flow rate	l/s			26	25	6.1	6	25.8
Time	h	1.2	3.1	1.5	1.7	2.0	2.6	2.9
Cycles	0	100	100	100	100	100	100	100
	36	99	83	X	X	X	72	70
	72	97	X				X	X
	108	96						
	144	X						
	180							
	216							
	252							
	288							
	324							
	360							
	396							
	432							
	468							

Table C.10: Relative dynamic modulus for mix design 12.

		Mix Design 12							
		BT	AT	A	A-(S)	A	A-(S)	A-R	A-R
Flow rate	l/s			27.3	26.2	6.6	8.6	24.7	7.3
Time	h	0.3	1.9	1.1	1.4	1.8	2.1	2.3	2.8
Cycles	0	100	100	100	100	100	100	100	100
	36	95	100	96	95	97	96	98	98
	72	96	98	95	96	100	98	98	99
	108	96	100	94	96	93	94	99	99
	144	93	96	91	96	97	97	98	103
	180	89	94	82	92	94	93	95	95
	216	92	100	70	93	96	95	96	100
	252	68	97	X	96	96	94	76	95
	288	89	97		94	98	95	96	99
	324	86	96		94	95	99		103
	360	92	103		100	107	102	104	106
	396	82	102		96	102	97	103	103
	432	81	100		98	104	99	104	100
	468	79	100		X	X	X	X	X

Table C.11: Relative dynamic modulus for mix design 13.

		Mix Design 13							
		BT	AT	A	A-(S)	A	A-(S)	A-R	A-R
Flow rate	l/s			32.1	31.9	5.5	5.5	32.5	5.3
Time	h	1.3	3.2	1.5	1.9	2.2	2.7	3.0	3.5
Cycles	0	100	100	100	100	100	100	100	100
	36	99	101	102	101	102	101	100	99
	72	103	102	104	103	104	104	102	103
	108								
	144								
	180								
	216	101	101	103	99	103	104	104	102
	252	101	101	103	100	105	102	100	101
	288	100	102	101	101	104	102	101	101
	324	102	103	103	102	105	104	103	102
	360	101	102	103	99	104	101	104	102
	396	103	102	101	101	103	104	103	101
	432	97	99	101	98	101	101	100	97
	468	99	99	101	100	100	100	102	101

Table C.12: Relative dynamic modulus for mix design 14.

		Mix Design 14						
		BT	AT	A	A-(S)	A-(S)	A-R	A-R
Flow rate	l/s			25.9	26.7	5.5	26.0	5.5
Time	h	0.9	2.5	1.3	1.5	2.0	2.3	2.7
Cycles	0	100	100	100	100	100	100	100
	36	99	99	99	96	98	98	97
	72	98	90	99	98	98	98	97
	108	99	73	96	97	98	97	93
	144	99	70	98	97	97	96	93
	180	96	64	98	97	91	95	86
	216	97	X	98	97	96	93	X
	252	101		101	98	97	96	
	288	99		99	97	96	95	
	324	98						
	360	98						
	396	98						
	432	98						
	468	100		100	98	94		

Table C.13: Relative dynamic modulus for mix design 15.

		Mix Design 15							
		BT	AT	A-(S)	A-(S)	A	A	A-R	A-R
Flow rate	l/s			29.1	5.6	5.6	29.1	28.0	5.5
Time	h	0.9	3.6	1.2	1.5	1.9	2.7	2.9	3.2
Cycles	0	100	100	100	100	100	100	100	100
	36	100	96	102	101	105	105	103	104
	72	102	x	100	98	104	102	100	102
	108	96		101	99	98	97	98	93
	144	92		103	X	67	X	64	83
	180	101		100		X		X	106
	216	X		X					X
	252								
	288								
	324								
	360								
	396								
	432								
	468								

Table C.14: Relative dynamic modulus for mix design 16.

		Mix Design 16							
		BT	AT	A-(S)	A-(S)	A	A	A-R	A-R
Flow rate	l/s			29.1	5.6	5.6	30.5	29.1	5.5
Time	h	0.5	2.5	0.8	1.1	1.4	1.9	2.0	2.3
Cycles	0	100	100	100	100	100	100	100	100
	36	99	71	100	97	95	101	100	87
	72								
	108								
	144								
	180								
	216								
	252								
	288								
	324								
	360								
	396								
	432								
	468								

Table C.15: Relative dynamic modulus for mix design 17.

		Mix Design 17						
		BT	AT	A-R	A-R(S)	A-R	F-R	F-R
Flow rate	l/s			5.6	5.6	40.8	5.7	40.5
Time	h	1.5	3.2	1.7	2.0	2.5	2.8	3.6
Cycles	0	100	100	100	100	100	100	100
	36	88	93	92	99	96	92	102
	72	78	83	85	94	96	91	95
	108	76	79	80	87	95	81	97
	144	X	X	61	72	89	76	95
	180			X	71	89	75	95
	216				61	90	X	93
	252				X	85		84
	288					83		78
	324					77		75
	360					X		X
	396							
	432							
	468							

Table C.16: Relative dynamic modulus for mix design 18.

		Mix Design 18							
		BT	AT	F-R	F-R	F-R(S)	F-R(S)	A-R	A-R(S)
Flow rate	l/s			6.6	46.5	46.6	6.2	46.5	46.5
Time	h	0.8	3.1	1.2	1.4	1.7	2.2	2.6	2.9
Cycles	0	100	100	100	100	100	100	100	100
	36	93	94	97	102	100	96	97	97
	72	96	94	96	99	100	92	96	96
	108	96	91	94	101	100	89	97	99
	144	97	70	87	95	96	70	97	96
	180	97	71	87	100	96	X	97	96
	216	98	67	80	98	98		101	96
	252	93	X	X	93	94		99	95
	288	93			92	92		94	95
	324	91			87	87		93	91
	360	85			75	68		87	84
	396	78			X	X		83	80
	432	68						77	77
	468	X						X	X

Appendix D: Scaling data

Table D.1. Mass loss of samples (g) during scaling for mix design 1.

		Mix Design 1					
		BT	AT	A-R	A	F	F
Flow rate	l/s			14.6	11.1	10.3	17.2
Time	h	0.4	2.8	0.9	1.3	2.0	2.4
Cycles	5	1.5	0.0	1.6	0.0	0.0	0.0
	10	2.0	0.2	0.9	0.1	0.5	0.2
	15	0.9	0.2	0.7	0.2	0.4	0.9
	20	0.2	0.2	0.4	0.1	0.1	0.2
	25	0.2	0.1	0.4	0.1	0.2	0.3
	30	0.1	0.1	0.2	0.1	0.1	0.1
	35	0.1	0.1	0.2	0.3	0.3	0.3
	40	0.1	0.0	0.1	0.1	0.2	0.1
	45	0.0	0.0	0.0	0.0	0.0	0.0
	50	0.0	0.0	0.1	0.0	0.0	0.0
	Total	5.2	0.9	4.6	1.1	1.8	2.1

Table D.2. Mass loss of samples (g) during scaling for mix design 2.

		Mix Design 2								
		BT	MT	AT	F	F	F	A	A-R	A-R(S)
Flow rate	l/s				19.1	7.5	28.9	11.1	18.6	20.5
Time	h	0.5	2.4	3.8	0.8	1.6	2.0	2.8	3.2	3.5
Cycles	5	0.0	0.0	0.0	0.0	0.0	0.0	0.0	0.0	0.0
	10	0.2	0.2	0.2	0.3	0.2	0.2	0.3	0.1	0.3
	15	0.6	0.5	0.2	0.3	0.2	0.2	1.0	0.1	1.7
	20	0.1	0.2	0.1	0.2	0.1	0.1	0.3	0.1	0.4
	25	0.2	0.5	0.2	0.2	0.1	0.1	0.2	0.2	0.1
	30	0.0	0.1	0.1	0.1	0.0	0.1	0.0	0.1	0.1
	35	0.0	0.1	0.7	0.3	0.0	0.1	0.2	0.1	0.1
	40	0.1	0.0	0.2	0.0	0.1	0.1	0.0	0.1	0.1
	45	0.0	0.0	0.0	0.0	0.0	0.0	0.0	0.0	0.0
	50	0.0	0.0	0.0	0.0	0.1	0.0	0.0	0.0	0.0
	Total	1.3	1.6	1.8	1.4	0.9	1.0	2.3	0.9	2.9

Table D.3. Mass loss of samples (g) during scaling for mix design 3.

		Mix Design 3							
		BT	AT	A-R(S)	A-R	A	F	F	F
Flow rate	l/s			20.8	20	20.2	20.3	33.2	5.2
Time	h	0.3	3.0	0.6	0.9	1.1	2.0	2.3	2.7
Cycles	5	1.0	0.1	1.6	0.3	0.4	0.2	0.8	0.2
	10	2.3	1.4	1.3	3.2	2.6	3.7	0.8	0.3
	15	1.6	1.5	0.2	1.5	1.0	3.5	0.5	1.2
	20	2.0	1.0	1.9	3.1	2.2	5.1	0.8	1.6
	25	1.4	0.5	7.7	2.6	0.3	2.6	0.2	0.9
	30	0.4	0.3	0.3	1.4	0.3	1.4	0.2	0.6
	35	0.4	0.2	0.3	0.6	0.3	0.1	0.5	0.4
	40	0.6	0.2	1.2	0.3	0.2	0.5	0.6	0.6
	45	0.5	0.3	1.6	1.1	0.4	2.3	0.1	0.4
	50	1.4	0.1	3.0	0.9	0.7	2.8	0.0	0.6
	Total	11.7	5.7	19.0	14.9	8.3	22.3	4.6	6.7

Table D.4. Mass loss of samples (g) during scaling for mix design 4.

		Mix Design 4								
		BT	MT	AT	F	F	F	A	A-R	A-R(S)
Flow rate	l/s				5.9	7.5	28.9	11.1	13.2	11.7
Time	h	0.0	1.4	2.9	0.4	0.7	1.0	1.6	2.2	2.6
Cycles	5	0.4	1.2	1.2	5.5	19.8	9.2	12.2	0.5	7.4
	10	2.8	1.8	1.8	8.7	2.4	5.7	7.2	9.9	1.5
	15	0.8	0.6	0.6	3.6	1.9	0.5	1.8	0.8	0.5
	20	3.0	1.9	1.9	2.5	3.7	0.7	1.1	1.6	2.2
	25	1.1	0.5	0.5	1.0	1.5	0.3	0.6	0.3	0.3
	30	0.2	0.0	0.0	0.5	0.7	0.2	0.2	0.3	0.3
	35	0.1	0.0	0.0	0.1	0.3	0.1	0.0	1.0	0.1
	40	0.0	0.0	0.0	0.1	0.4	0.1	0.3	0.1	0.2
	45	0.2	0.5	0.5	2.0	0.7	0.0	0.4	3.5	12.9
	50	0.8	1.3	1.3	3.6	0.8	1.1	1.1	5.5	7.7
	Total	9.5	8.0	8.0	27.4	32.2	17.9	24.9	23.4	33.1

Table D.5. Mass loss of samples (g) during scaling for mix design 5.

		Mix Design 5						
		BT	MT	AT	F	F	F	A
Flow rate	l/s				5.7	16.8	32	22.3
Time	h	0.3	1.9	2.7	0.8	1.2	1.5	2.3
Cycles	5	5.0	3.3	3.3	5.7			0.6
	10	0.3	0.7	0.7	0.6		0.3	0.2
	15	1.4	2.3	2.3	21.1	5.2	0.6	1.3
	20	4.9	3.9	3.9	10.6	4.5	2.7	2.7
	25	1.6	4.9	4.9	6.6	5.8	3.0	2.7
	30	7.5	0.5	0.5	3.4	2.8	2.5	0.8
	35	4.9	7.1	7.1	3.8	1.5	2.8	1.0
	40	3.4	5.8	5.8	4.6	0.8	1.9	0.8
	45	2.6	4.9	4.9	3.7	0.4	1.4	0.5
	50	3.2	5.1	5.1	4.2	1.5	1.5	0.7
	Total	34.8	38.4	38.4	64.4	22.4	16.7	11.4

Table D.6. Mass loss of samples (g) during scaling for mix design 6.

		Mix Design 6								
		BT	MT	AT	F	F	F	A	A-R	A-R(S)
Flow rate	l/s				18.68	36.38	6.37	11.143	19.4	18.5
Time	h	0.6	1.7	1.7	0.8	1.1	1.4	2.0	2.4	2.7
Cycles	5	1.1	1.5	0.8	1.0	3.9	1.3	3.0	0.9	0.6
	10	0.2		0.1	0.3	0.5	0.3	0.5	0.1	0.2
	15	0.2	0.8	0.8	0.1	2.5	0.4	0.2	0.4	0.6
	20	0.1	0.5	0.7	0.1	1.1	0.5	0.1	0.4	0.5
	25	0.0	0.5	0.2	0.1	0.3	0.0	0.1	0.2	0.2
	30	0.1	0.3	0.1	0.1	0.3	0.0	0.1	0.1	0.0
	35	0.0	0.1	0.1	0.1	0.1	0.0	0.0	0.1	0.0
	40	0.0	0.0	0.1	0.0	0.1	0.0	0.0	0.0	0.0
	45	0.0	0.0	0.1	0.1	0.0	0.1	0.1	0.1	0.0
	50	0.1	0.1	0.1	0.3	0.0	0.1	0.2	0.2	0.1
	Total	1.8	3.9	2.9	2.2	8.7	2.7	4.4	2.5	2.3

Table D.7. Mass loss of samples (g) during scaling for mix design 7.

		Mix Design 7								
		BT	MT	AT	A-R(S)	A-R	A	F	F	F
Flow rate	l/s				19.11	22.58	21.28	21.09	38.0	1.1
Time	h	0.4	1.5	2.3	0.7	1.0	1.3	1.9	2.1	2.7
Cycles	5	0.5	1.2	0.6	1.9	0.5	1.0	0.3	0.4	0.4
	10	0.1	0.2	0.2	0.2	0.1	0.2	0.1	0.2	0.1
	15	0.0	0.3	0.0	0.1	0.1	0.1	0.2	0.2	0.3
	20	0.1	0.3	0.0	0.2	0.2	0.1	0.3	0.1	0.2
	25	0.0	0.0	0.2	0.0	0.1	0.2	0.1	0.1	0.3
	30	0.2	0.0	0.7	0.0	0.0	0.1	0.2	0.1	0.4
	35	1.8	0.1	0.1	0.1	0.1	0.1	0.1	0.2	0.4
	40	1.9	0.0	0.1	0.0	0.1	0.2	0.1	0.1	0.2
	45	1.2	0.0	0.1	0.1	0.1	0.0	0.3	0.3	0.6
	50	1.9	0.0	0.1	0.0	0.1	0.2	0.1	0.7	0.2
	Total	7.6	2.2	2.2	2.7	1.4	2.0	1.7	2.4	3.1

Table D.8. Mass loss of samples (g) during scaling for mix design 8.

		Mix Design 8								
		BT	MT	AT	F	F	F	A	A-R(S)	A-R
Flow rate	l/s				1.4	35.56	21.84	20.92	21.1	20.4
Time	h	0.3	1.6	2.3	0.7	1.0	1.3	1.9	2.1	2.7
Cycles	5	0.1	0.2	0.0	0.6	0.3	0.3	0.2	0.4	0.2
	10	0.2	0.4	0.1	0.2	0.2	0.2	0.1	0.2	0.1
	15	0.1	0.2	0.0	0.1	0.4	0.2	0.0	0.3	0.1
	20	0.0	0.8	0.0	0.1	0.1	0.1	0.1	0.2	0.0
	25	0.1	0.1	0.0	0.1	0.3	0.3	0.2	0.2	0.0
	30	0.0	0.0	0.0	0.2	0.1	0.5	0.0	0.2	0.1
	35	0.1	0.0	0.0	0.6	0.2	0.3	0.2	0.2	0.2
	40	0.1	0.0	0.0	0.4	0.1	0.4	0.1	0.1	0.1
	45	0.0	0.0	0.0	0.9	0.2	0.2	0.2	0.2	0.2
	50	0.1	0.0	0.1	0.4	0.1	0.4	0.1	0.1	0.1
	Total	0.7	1.8	0.3	3.5	1.9	2.9	1.3	1.9	1.2

Table D.9. Mass loss of samples (g) during scaling for mix design 9.

		Mix Design 9								
		BT	MT	AT	A-R(S)	A-R	A	F	F	F
Flow rate	l/s				21.2	20.3	20.4	22.7	37.8	2.1
Time	h	0.3	1.4	2.7	0.8	0.9	1.2	1.8	2.1	2.4
Cycles	5	0.0	0.1	0.0	0.2	0.1	0.0	0.1	0.1	0.0
	10	0.1	0.1	0.0	0.1	0.1	0.0	0.0	0.2	0.0
	15	0.0	0.0	0.0	0.2	0.0	0.8	0.0	0.0	0.0
	20	0.0	0.0	0.0	0.1	0.0	0.0	0.0	0.2	0.1
	25	0.0	0.0	0.0	0.0	0.0	0.0	0.0	0.0	0.1
	30	0.0	0.0	0.0	0.0	0.1	0.0	0.0	0.0	0.0
	35	0.0	0.1	0.0	0.0	0.0	0.0	0.0	0.0	0.0
	40	0.0	0.0	0.0	0.0	0.1	0.0	0.0	0.0	0.0
	45	0.0	0.1	0.0	0.0	0.0	0.0	0.0	0.0	0.0
	50	0.1	0.1	0.0	0.1	0.4	0.2	0.0	0.0	0.0
	Total	0.3	0.4	0.2	0.7	0.9	1.4	0.3	0.6	0.4

Table D.10. Mass loss of samples (g) during scaling for mix design 10.

		Mix Design 10								
		BT	MT	AT	F	F	F	A	A-R	A-R(S)
Flow rate	l/s				1.8	37.2	21.5	21.5	22.1	21.5
Time	h	0.4	1.6	2.9	0.9	1.1	1.3	2.0	2.3	2.5
Cycles	5	0.2	0.1	0.2	0.1	0.1	0.1	0.1	0.1	0.1
	10	0.1	0.3	0.1	0.8	0.0	0.2	0.8	0.0	0.2
	15	0.1	0.1	0.1	0.2	0.0	0.0	0.2	0.0	0.0
	20	0.2	0.1	0.1	0.0	0.0	0.1	0.0	0.0	0.1
	25	0.7	0.0	0.1	0.1	0.0	0.0	0.1	0.0	0.0
	30	1.2	0.0	0.1	0.0	0.0	0.0	0.0	0.0	0.0
	35	0.7	0.0	0.0	0.0	0.0	0.1	0.0	0.0	0.1
	40	1.4	0.0	0.1	0.0	0.0	0.0	0.0	0.0	0.0
	45	0.7	0.0	0.0	0.0	0.0	0.1	0.0	0.0	0.1
	50	3.0	0.1	0.6	0.0	0.0	0.0	0.0	0.0	0.0
	Total	8.3	0.6	1.3	1.3	0.2	0.6	1.3	0.2	0.6

Table D.11. Mass loss of samples (g) during scaling for mix design 11.

		Mix Design 11							
		BT	MT	AT	A	A-(S)	A	A-(S)	A-R
Flow rate	l/s				26	25	6.1	6	25.8
Time	h	1.2	2.3	3.1	1.5	1.7	2.0	2.6	2.9
Cycles	5	0.9	3.2	2.2	3.0	1.1	2.5	5.6	11.5
	10	0.4	9.6	11.8	8.1	4.4	10.0	12.2	23.0
	15	0.3	18.5	22.2	19.5	12.1	17.9	22.8	33.0
	20	0.2	16.9	18.9	23.4	14.7	20.8	22.1	23.0
	25	0.5	2.9	36.6	57.3	34.5	34.4	48.3	43.9
	30	0.7	51.0	35.9	57.5	46.2	38.9	51.0	49.6
	35	0.8	34.2	35.2	53.7	47.0	35.0	46.1	41.6
	40	1.0	0.3	3.8	2.7	3.9	0.9	0.4	1.1
	45	1.8	90.6	70.6	45.6	96.3	60.7	80.4	88.7
	50	4.9	29.5	35.2	2.2	44.4	4.7	41.4	18.5
	Total	11.4	256.8	272.4	272.9	304.6	225.9	330.2	334.0

Table D.12. Mass loss of samples (g) during scaling for mix design 12.

		Mix Design 12								
		BT	MT	AT	A	A-(S)	A	A-(S)	A-R	A-R
Flow rate	l/s				27.3	26.2	6.6	8.6	24.7	7.3
Time	h	0.3	1.9	1.9	1.1	1.4	1.8	2.1	2.3	2.8
Cycles	5	1.5	0.2	0.3	5.3	1.1	0.4	0.3	0.5	0.6
	10	1.7	0.3	0.3	4.7	0.6	0.4	0.2	0.3	0.5
	15	5.8	0.5	0.4	6.2	1.0	1.9	1.4	1.0	0.2
	20	2.0	0.2	0.2	1.8	0.3	0.7	0.3	0.2	0.2
	25	3.3	1.0	0.7	2.4	1.1	1.5	0.2	0.3	0.6
	30	4.9	1.9	0.9	4.3	1.9	2.8	1.6	1.1	1.7
	35	5.5	1.9	0.5	4.2	2.2	2.6	1.4	0.7	0.7
	40	5.4	1.8	0.7	3.1	2.2	2.5	1.6	0.6	0.8
	45	8.2	1.6	1.0	4.1	4.7	1.4	0.6	0.3	0.2
	50	13.5	3.6	2.3	9.6	11.3	5.6	0.6	1.0	0.2
	Total	51.9	13.0	7.2	45.8	26.4	19.7	8.2	6.0	5.8

Table D.13. Mass loss of samples (g) during scaling for mix design 13.

		Mix Design 13								
		BT	MT	AT	A	A-(S)	A	A-(S)	A-R	A-R
Flow rate	l/s				32.1	31.9	5.5	5.5	32.5	5.3
Time	h	1.3	2.4	3.2	1.5	1.9	2.2	2.7	3.0	3.5
Cycles	5	26.5	29.2	24.2	31.5	35.2	29.0	27.6	31.0	14.3
	10	12.8	3.2	3.8	3.3	3.2	3.8	4.5	2.4	2.2
	15	1.6	2.0	2.9	1.6	1.2	1.4	1.6	0.8	1.2
	20	1.1	0.8	1.3	0.6	0.6	0.6	0.8	0.4	1.1
	25	0.8	1.0	1.0	0.8	0.5	0.9	0.4	0.7	1.3
	30	1.1	0.5	0.9	0.7	0.5	0.4	0.5	0.2	0.4
	35	2.3	0.7	1.2	2.2	0.6	1.3	0.1	0.3	0.9
	40	0.0	0.5	0.8	1.3	0.6	0.6	0.1	0.3	1.2
	45	0.4	0.4	0.2	0.8	0.4	0.2	0.1	0.5	0.6
	50	0.4	0.2	0.5	0.9	0.7	0.3	0.1	0.6	0.8
	Total	47.0	38.5	36.8	43.5	43.4	38.4	35.7	37.3	24.0

Table D.14. Mass loss of samples (g) during scaling for mix design 14.

		Mix Design 14								
		BT	MT	AT	A	A-(S)	A	A-(S)	A-R	A-R
Flow rate	l/s				25.9	26.7	5.6	5.5	26.0	5.5
Time	h	0.9	1.8	2.5	1.3	1.5	1.6	2.0	2.3	2.7
Cycles	5	16.5	14.9	28.0	11.8	19.3	10.6	25.7	6.6	23.8
	10	3.0	5.1	16.5	2.5	15.3	14.8	8.4	4.4	24.1
	15	6.5	5.5	14.0	2.2	5.7	10.5	6.7	3.2	14.6
	20	6.6	4.8	12.6	1.4	2.7	6.6	5.3	1.9	17.1
	25	3.7	1.7	15.1		2.3	5.8	6.1	2.6	2.6
	30	2.4	2.3	22.6	4.3	1.0	9.0	8.0	2.4	14.5
	35	5.7	0.9	33.6	7.1	0.0	12.8	11.6	3.4	1.0
	40	3.9	0.9	23.5	4.9	0.4	10.5	8.8	2.7	5.4
	45	2.5	0.6	8.3	2.9	0.3	6.2	4.3	1.3	3.2
	50	2.7	0.8	8.9	2.2	0.3	6.8	6.4	0.8	2.0
	Total	53.3	37.7	183.1	39.3	47.3	93.6	91.1	29.4	108.3

Table D.15. Mass loss of samples (g) during scaling for mix design 15.

		Mix Design 15							
		BT	MT	A-(S)	A-(S)	A	A	A-R	A-R
Flow rate	l/s			29.1	5.6	5.6	29.1	28.0	5.5
Time	h	0.9	2.2	1.2	1.5	1.9	2.7	2.9	3.2
Cycles	5	0.4	4.1	0.2	0.1	3.9	0.7	0.9	3.6
	10	0.0	0.3	0.1	0.1	0.7	0.4	0.3	1.2
	15	0.0	0.9	0.1	0.1	0.5	0.4	0.4	1.2
	20	0.0	0.3	0.0	0.3	0.6	0.2	0.2	0.5
	25	0.1	0.4	0.1	0.7	2.0	0.4	0.6	1.2
	30	0.0	0.2	0.0	0.2	1.1	0.2	0.3	0.6
	35	0.0	0.1	0.0	0.1	0.1	0.0	0.0	0.1
	40	0.0	0.4	0.0	0.0	0.4	0.2	0.1	0.4
	45	0.1	0.2	0.0	0.1	0.2	0.2	0.5	0.4
	50	0.0	0.4	0.1	0.1	0.2	0.1	0.3	0.3
	Total	0.8	7.2	0.5	1.8	9.8	2.8	3.6	9.6

Table D.16. Mass loss of samples (g) during scaling for mix design 16.

		Mix Design 16								
		BT	MT	AT	A-(S)	A-(S)	A	A	A-R	A-R
Flow rate	l/s				29.1	5.6	5.6	30.5	29.1	5.5
Time	h	0.5	1.6	2.5	0.8	1.1	1.4	1.9	2.0	2.3
Cycles	5	7.9	7.9	37.7	8.7	17.7	3.3	11.2	12.2	26.8
	10	0.9	0.9	21.3	1.2	15.8	5.3	17.8	17.9	14.4
	15	12.8	12.8	14.5	11.6	15.5	8.7	11.6	14.2	16.8
	20	6.8	6.8	20.2	6.4	18.3	3.9	7.2	7.9	12.0
	25	12.6	12.6	16.0	11.1	30.5	3.9	9.9	14.1	18.1
	30	8.2	8.2	23.4	6.4	22.5	2.4	6.4	2.0	7.4
	35	0.1	0.1	6.9	0.4	0.7	1.9	0.3	0.2	0.1
	40	6.8	6.8	9.2	2.0	4.7	2.1	8.4	4.9	5.7
	45	12.2	12.2	26.8	8.2	15.0	0.8	3.7		8.7
	50	12.1	12.1	7.1	0.7	3.9	1.2	0.5	1.7	2.6
	Total	80.4	80.4	183.1	56.6	144.6	33.4	77.1	75.3	112.7

Table D.17. Mass loss of samples (g) during scaling for mix design 17.

		Mix Design 17							
		BT	MT	AT	A-R	A-R(S)	A-R	F-R	F-R
Flow rate	l/s				5.6	5.6	40.8	5.7	40.5
Time	h	1.5	2.2	3.2	1.7	2.0	2.5	2.8	3.6
Cycles	5	0.2	0.1	0.2	0.1	0.1	0.2	0.3	0.1
	10	0.2	0.1	0.2	0.1	0.2	0.2	0.3	0.1
	15	0.2	0.2	0.2	0.1	0.1	0.2	0.3	0.1
	20	0.2	0.1	0.2	0.1	0.2	0.2	0.3	0.1
	25	0.3	0.1	0.2	0.1	0.1	0.1	0.1	0.0
	30	0.2	0.2	0.3	0.0	0.1	0.1	0.1	0.1
	35	0.3	0.2	0.2	0.1	0.1	0.1	0.1	0.1
	40	0.4	0.2	0.3	0.2	0.1	0.2	0.3	0.1
	45	0.2	0.1	0.2	0.1	0.2	0.1	0.1	0.1
	50	0.1	0.1	0.1	0.1	0.1	0.1	0.3	0.1
	Total	2.4	1.4	2.2	0.9	1.4	1.2	2.4	1.0

Table D.18. Mass loss of samples (g) during scaling for mix design 18.

		Mix Design 18								
		BT	MT	AT	F-R	F-R	F-R(S)	F-R(S)	A-R	A-R(S)
Flow rate	l/s				6.6	46.5	46.6	6.2	46.5	46.5
Time	h	0.8	1.9	3.1	1.2	1.4	1.7	2.2	2.6	2.9
Cycles	5	0.5	0.5	0.5	0.7	0.4	0.4	0.1	1.4	0.1
	10	0.5	0.5	0.5	0.7	0.4	0.3	0.1	1.4	0.1
	15	0.5	0.5	0.5	0.7	0.4	0.4	0.1	1.3	0.1
	20	0.5	0.5	0.5	0.7	0.4	0.4	0.1	1.4	0.1
	25	0.1	0.2	0.2	0.2	0.1	0.1	0.2	0.6	0.2
	30	0.1	0.3	0.1	0.1	0.1	0.1	0.1	1.4	0.1
	35	0.2	0.2	0.2	0.3	0.1	0.1	0.2	1.2	0.2
	40	0.1	0.1	0.2	0.2	0.1	0.1	0.2	1.7	0.2
	45	0.2	0.1	0.1	0.1		0.2	0.2	1.0	0.2
	50	0.1	0.1	0.1	0.1		0.1	0.1	0.4	0.1
	Total	2.9	3.0	2.8	3.9	2.1	2.0	1.3	11.7	1.4